Ultrabroadband coherent Raman spectroscopy for reacting flows

Mazza, F.

DOI
10.4233/uuid:f51b273d-eac8-495b-b692-919eb54b9974

Publication date
2023

Document Version
Final published version

Citation (APA)
Mazza, F. (2023). *Ultrabroadband coherent Raman spectroscopy for reacting flows*. [Dissertation (TU Delft), Delft University of Technology]. https://doi.org/10.4233/uuid:f51b273d-eac8-495b-b692-919eb54b9974

ULTRABROADBAND COHERENT RAMAN SPECTROSCOPY FOR REACTING FLOWS

ULTRABROADBAND COHERENT RAMAN SPECTROSCOPY FOR REACTING FLOWS

Dissertation

for the purpose of obtaining the degree of doctor
at Delft University of Technology,
by the authority of the Rector Magnificus, prof. dr. ir. T.H.J.J. van der Hagen,
chair of the Board for Doctorates,
to be defended publicly on
Wednesday 4 October 2023 at 10:00 o'clock

by

Francesco MAZZA

Dottore magistrale in ingegneria aerospaziale,
Politecnico di Torino, Italy,
born in Macerata, Italy.

This dissertation has been approved by the promotors.

Composition of the doctoral committee:

Rector Magnificus,	chairperson
Prof. dr. ir. P. Colonna,	Delft University of Technology, promotor
Dr. ir. G. A. Bohlin,	Delft University of Technology, copromotor
Independent members:	
Prof. dr. D. J. E. M. Roekaerts,	Delft University of Technology
Prof. dr. W. M. G. Ubachs,	Vrije Universiteit Amsterdam
Prof. dr. ir. H. L. Offerhaus,	University of Twente
Dr. M. Marrocco,	ENEA, Italy
Dr. C. J. Kliewer,	Sandia National Laboratories, USA
Prof. dr. ir. W. de Jong,	Delft University of Technology, reserve member

This research is supported by the Applied and Engineering Science Domain (TTW) of the Dutch Research Council (NWO), grant number 15690.

Keywords: coherent Raman spectroscopy, gas-phase thermometry, time-resolved spectroscopy, femtosecond laser-induced filamentation, laser diagnostics, ro-vibrational spectroscopy, chemically reacting flows
Printed by: Ridderprint, https://www.ridderprint.nl/

Cover: F. Mazza

ISBN: 978-94-6366-725-8

---

*Author email: f.mazza@tudelft.nl

I told Leonard that reality is at best a collective hunch.
But that was just a line I stole from a female comedian.

Cormac McCarthy, *Stella Maris*

Abstract

The present dissertation covers the development of ultrabroadband femtosecond/picosecond coherent Raman spectroscopy (CRS) to measure temperature and species concentrations in gas-phase chemically reacting flows.

Since its first demonstration in 1965, CRS has been vastly employed as a non-linear optical spectroscopic technique to quantify scalars in gas-phase chemically reacting flows, and it is presently regarded as a benchmark to measure temperature and concentrations of major species in combustion environments. The commercial availability of ultrafast regenerative laser amplifiers has brought forth an astounding amount of advancements over the past ten years, with the development of time-resolved CRS techniques able to perform measurements on a timescale shorter than that of molecular collisions in gas-phase media. Hybrid femtosecond/picosecond (fs/ps) CRS in particular represents the current state-of-the-art for gas-phase thermometry with unprecedented accuracy and precision, achieved with remarkable spatial and temporal resolution. The high peak power provided by amplified fs laser systems enables spectroscopy to be realised in one- and two-dimensional imaging configurations acquiring single-shot images of the relevant scalar fields. Furthermore, the broad spectral bandwidth of fs laser pulses allows for a great simplification of the fs/ps CRS instrument. In two-beam fs/ps pure-rotational CRS a single broadband fs laser pulse coherently excites the whole rotational energy manifold of the target molecules, resulting in the coherent scattering of a spectrally narrow ps probe probe pulse. Moreover, the introduction of spectral broadening techniques prompted the development of ultrabroadband fs/ps CRS, where a single temporally-compressed supercontinuum pulse can excite, in principle, all the Raman-active modes of the target molecules. Ultrabroadband fs/ps CRS thus allows for the simultaneous investigation of the rotational and the vibrational motion of all the major species present in the probed volume, and could become the laser diagnostic tool for scalar determination in gas-phase chemically reacting flows, both in thermal equilibrium and in non-equilibrium conditions. For this to become a reality, however, a robust experimental protocol is needed for the implementation of ultrabroadband fs/ps CRS, which could be reliably employed behind the thick optical windows present in many practical experiments, such as those involving pressurised combustors and enclosed chemical reactors.

In this respect, the present thesis revolves around two main experimental developments. The first one concerns the implementation of fs laser-induced filamentation as the supercontinuum generation mechanism to perform ultrabroadband fs/ps CRS. The research demonstrated that fs laser-induced filamentation can be employed *in situ* to compress the excitation pulse directly behind thick optical windows and inside the chemically reacting flow under study. This ultrabroadband coherent light source is employed throughout the present research to perform single-shot fs/ps CRS measurements, over a spectral region ranging ~500-2000 cm^{-1}, the so-called "vibrational fingerprint region". Single-shot detection of four major combustion species –hydrogen, oxygen, carbon dioxide, and methane– is demonstrated in this region of the Raman spectrum, and fs/ps CRS thermometry based on each one of them is validated in a number of laboratory flames. The influence of the combustion environment on the non-linear optical phenomena underpinning fs laser-induced filamentation and on the resulting pulse self-compression is furthermore investigated, evaluating the impact of the local composition and temperature of the gas-phase optical medium.

The second experimental advancement addresses the need for an accurate quantification of the resulting spectral excitation bandwidth, with the development of a novel CRS experimental protocol. The conventional protocol entails the measurement of the non-resonant (NR) CRS signal *ex situ* in a non-resonant gas (typically argon), sequential to the CRS experiment, to map the spectral excitation profile. The novel protocol, on the contrary, is based on the generation of the NR CRS signal *in situ* in the combustion environment, simultaneous to that of the resonant CRS signal, thus removing a source of systematic bias in the spectral referencing. In order to practically implement this protocol, a polarisation-sensitive coherent imaging spectrometer is developed, which can simultaneously record the cross-polarised resonant and NR CRS signals in two distinct detection channels. The required polarisation angle to generate the resonant and NR CRS signals with orthogonal polarisation is theoretically determined, and the same angle is proven to realise the *in situ* referencing of any completely depolarised Raman transition. This referencing protocol is firstly applied to pure-rotational CRS thermometry on N_2 and O_2 in the pure-rotational region of the Raman spectrum, up to ~500 cm^{-1}. Thereupon the protocol is employed to realise ultrabroadband CRS on H_2, whose pure-rotational spectrum spans more than 1500 cm^{-1} at flame temperatures. The adoption of the *in situ* referencing protocol proves essential to perform accurate H_2 CRS thermometry behind the thick optical window. The novel protocol is also demonstrated on the ro-vibrational Raman spectrum of second vibrational mode (ν_2) of CH_4, which is completely depolarised, as are the Raman spectra associated to the least symmetric vibrations of more complex polyatomic molecules (e.g. heavier hydrocarbons). In this respect, ultrabroadband fs/ps CRS with *in situ* referencing of the spectral excitation efficiency could be employed not only to perform accurate thermometry in chemically reacting flows, but also to measure the concentrations of all the major molecular species in the probed volume.

In parallel to these experimental developments, the present research also involves the development of time-domain models for the pure-rotational and ro-vibrational CRS signals detected in the spectral window up to 2000 cm^{-1}. In particular the CH_4 ν_2 model is, to the best of the author's knowledge, the first of its kind to include more than 10 million spectral lines, proving the suitability of this modelling approach to complex polyatomic molecules, which could pave the way to the future application of quantitative ultrabroadband fs/ps CRS to investigate a broader set of chemically reacting flows.

All in all, the results collected in the present dissertation provide a basis for the direct use of ultrabroadband fs/ps CRS for scalar measurements in numerous and diverse practical applications in the applied science and engineering domain. The possibility of simultaneously measuring temperature and the concentrations of major species in chemically-reactive flows is paramount to understanding the physical and chemical processes at the base of many propulsion and power generation technologies. To name one, the *in situ* generation of the compressed excitation pulse provides a straightforward path to the use of ultrabroadband fs/ps CRS to perform spatially-resolved measurements of all the relevant scalar fields in high pressure combustion chambers. On the other hand, the ability of performing quantitative spectroscopy on complex polyatomic molecules is of great interest to many chemical engineering platforms, such as chemical reactors for the reforming of CH_4 in commodity hydrocarbons and carbon-neutral H_2.

Samenvatting

Deze dissertatie beschrijft de ontwikkeling van een ‘ultrabroadband’ femtoseconde/picoseconde coherente Raman spectroscopie (CRS) om temperaturen en species-concentraties in chemisch-reagerende ‘stromen’ in gasfase.

Sinds de eerste demonstratie in 1965, is CRS veelvuldig toegepast als non-lineaire spectroscopische techniek om scalairs in gasfase chemisch interacterende stromen te kwantificeren. Op dit moment wordt het gezien als benchmark/maatstaf voor het meten van temperaturen en concentraties van ‘major species’ in verbrandings-omgevingen. De commerciële beschikbaarheid van ultrasnelle regeneratieve laser versterkers heeft een enorme hoeveelheid voortgang en nieuwe inzichten met zich meegebracht in de afgelopen tien jaar, waaronder tijd-opgeloste CRS-technieken die metingen kunnen doen over tijdsspannes die korter zijn dan moleculaire botsingen in gasfase. Hybride femtoseconde/picoseconde (fs/ps) CRS vertegenwoordigt in het bijzonder de gouden standaard voor gasfase thermometrie met ongekende accuraatheid en precisie en met indrukwekkende spatiale en temporele resolutie. De hoge piekenergie van versterkte fs-laser systemen maken het binnen spectroscopie mogelijk om een- en twee-dimensionale beeldvormingsconfiguraties op te stellen, waardoor het mogelijk wordt om de relevante scalaire velden in één opname vast te leggen. Verder maakt de grote spectrale bandbreedte van fs-laser impulsen een grote versimpeling van het fs/ps CRS-instrument mogelijk. Bij 2-stralen fs/ps puur-rotationele CRS wordt een individuele broadband fs laser impuls gebruikt om op coherente wijze de gehele rotationele manifold van doel-moleculen te exciteren, resulterende in een coherente scattering van een nauwe spectrale probe probe impuls. Ook heeft de introductie van spectrale verbredings-technieken gezorgd voor de ontwikkeling van ultra broadband fs/ps CRS, waar een individuele temporally-compressed supercontinuum puls –in principe– alle Raman-actieve modi van de doel-moleculen can exciteren. Op deze wijze stelt ultrabroadband fs/ps CRS ons in staat om tegelijkertijd de rotationele en vibrationele motie van alle species in één getest volume te onderzoeken. Op deze wijze kan dit het laser-diagnostische instrument worden voor scalaire determinatie in chemisch interacterende stromen in gasfase, zowel bij condities van thermisch equilibrium en thermisch non-equilibrium. Om dit in de praktijk mogelijk te maken is een robuust protocol voor experimenten nodig voor de implementatie van ultrabroadband fs/ps CRS, die op betrouwbare wijze toegepast kan worden achter de grote optische ramen die we in veel praktische experimenten zien, zoals die bij druk-verbranders en gesloten chemische reactoren.

Daarom beschrijft deze dissertatie twee grote ontwikkelingen in experimentele toepassing. De eerste betreft de implementatie van fs-laser geïnduceerde filamentatie als supercontinuum genererend mechanisme om ultrabroadband fs/ps CRS uit te voeren. Uit het onderzoek blijkt dat fs laser geïnduceerde filamentatie *in situ* gebruikt kan worden om de excitatiepuls direct achter optische ramen samen te drukken en te concentreren in de chemisch interacterende stroom die bestudeerd wordt. Deze ultrabroadband coherente lichtbron is gedurende het onderzoek gebruikt om één-opname fs/ps CRS metingen te doen over een spectrale marge van ~500-2000 cm^{-1}, de zogenoemde vibrational fingerprint region. Single-shot detectie van vier grote verbrandingsspecies –waterstof, zuurstof, kooldioxide en methaan– is gedemonstreerd in deze regio van het Raman-spectrum en fsps CRS thermometrie gebaseerd op elk van deze vier is gevalideerd in een aantal laboratoriumvlammen. Verder is onderzoek gedaan naar de invloed van van de verbrandings-omgeving op de non-lineaire optische fenomenen die fs-Laser geïnduceerde filamentatie onderpinnen en naar de resulterende puls-zelf-compressie, waarbij de impact van lokale compositie en temperatuur van het gas-fase optische medium is geëvalueerd.

De tweede experimentele ontwikkeling adresseert de behoefte aan accurate kwantificering van de resulterende spectrale excitatie-bandbreedte, door de ontwikkeling van een nieuw protocol voor CRS-experimenten. Het conventionele protocol behelst de meting van het non-resonante (NR) CRS signaal *ex situ* in een non-resonant gas (meestal Argon), volgend op het CRS-experiment om het spectrale excitatie profiel in kaart te brengen. Het nieuwe protocol, daarentegen, is gebaseerd op de generatie van een NR CRS signaal *in situ* in de verbrandingsomgeving, gelijktijdig met die van het resonante CRS-signaal, waardoor een bron van systematische beïnvloeding in spectrale referentie verwijderd wordt. Om dit protocol praktisch te implementeren is een polarisatie-gevoelige coherente spectrometer ontwikkeld, die tegelijkertijd in twee kanalen cross-polarised resonante- en NR CRS signalen kan meten/opnemen. De noodzakelijke polarisatiehoek om de resonante en NR CRS signalen te genereren middels orthogonale polarisatie is theoretisch bepaald, waarna deze hoek effectief bewezen is in de *in situ* referencing van elke compleet gedepolariseerde Raman-transitie. Dit referencing-protocol is eerst toegepast op puur-rotationele CRS thermometrie van N_2 en O_2 in de puur-rotationele regio van het Raman-spectrum, tot en met ~500 cm^{-1}. Daarop is het protocol toegepast om ultrabroadband CRS te realiseren op H_2, waarvan het puur-rotationele spectrum meer dan 1500 cm^{-1} bestrijkt bij vlam-temperaturen. De adoptie van dit *in situ* referencing-protocol is essentieel bewezen om accurate H_2 CRS thermometrie achter een dik optisch raam uit te voeren. Het nieuwe protocol is ook bewezen voor het ro-vibrationele raman spectrum van de tweede vibrational modus (ν_2) van CH_4, welke compleet gedepolariseerd is, alsook de Raman spectra die geassocieerd zijn met de minst symmetrische vibraties van meer complexe polyatomische moleculen (bijv. Zwaardere koolwaterstoffen). Op deze wijze zou ultrabroadband fs/ps CRS met *in situ* referencing van de spectrale excitatie efficiëntie niet alleen toegepast kunnen worden voor accurate thermometrie in chemisch interacterende stromen, maar ook om concentraties van major moleculaire species in het onderzochte volume te meten.

Naast deze experimentele ontwikkelingen zijn –als onderdeel van deze dissertatie– ook time-domain modellen voor de puur-rotationele én ro-vibrationele CRS signalen ontwikkeld die gedecteerd worden in de spectrale marge tot en met 2000 cm^{-1}. In het bijzonder is het model voor CH_4 ν_2, naar beste kennis van de auteur, de eerste van dit type met meer dan 10 miljoen spectrale lijnen, waarmee de toepasbaarheid van dit type modellering voor complexe polyatomische bewezen wordt, waarmee toekomstige toepassingen van kwantitatieve ultrabroadband fs/ps CRS op een bredere set van chemisch interacterende stromen onderzocht kan worden.

Al in al, bieden de in dit proefschrift verzamelde resultaten een basis voor het directe gebruik van ultrabroadband fs/ps CRS voor scalaire metingen in talrijke en uiteenlopende praktische toepassingen in de toegepaste wetenschap en techniek. De mogelijkheid om gelijktijdig de temperatuur en de concentraties van de belangrijkste species in chemisch-reactieve stromen te meten is van het grootste belang voor het begrijpen van de fysische en chemische processen die aan de basis liggen van veel aandrijf- en energieopwekkingstechnologieën. Om er één te noemen: het *in situ* genereren van de gecomprimeerde excitatiepuls biedt een eenvoudige weg naar het gebruik van ultrabroadband fs/ps CRS om ruimtelijk-opgeloste metingen uit te voeren van alle relevante scalaire velden in verbrandingskamers onder hoge druk. Aan de andere kant is de mogelijkheid om kwantitatieve spectroscopie uit te voeren op complexe polyatomische moleculen van groot belang voor veel chemische engineeringplatforms, zoals chemische reactoren voor de reforming van CH_4 in basiskoolwaterstoffen en koolstofneutraal H_2.

Contents

Glossary

CARS *Coherent anti-Stokes Raman scattering*. Coherent Raman scattering where the scattered radiation has higher frequency than the incoming one.

CPA *Chirped pulse amplification*. Technique to amplify ultrashort laser pulses, based on the temporal stretch (chirp) of the optical pulse before its amplification, so as to reduced its peak power, and avoid damage of the optical components.

CPP *Chirped probe pulse* coherent Raman scattering. Time-resolved coherent Raman spectroscopy using a chirped femtosecond pulse as the probe to realise single-shot measurements.

CRS *Coherent Raman scattering*. Third-order non-linear optical process whereby an ensemble of coherently rotating-vibrating molecules inelastically scatter the incoming electromagnetic radiation resulting in its coherent re-emission.

CSRS *Coherent Stokes Raman scattering*. Coherent Raman scattering where the scattered radiation has lower frequency than the incoming one.

FOV *Field-of-view*. Spatial extent of the measurement field for a coherent Raman imaging spectrometer: in the present dissertation 1D CRS are reported, and the FOV represents the length of the measurement line.

FWHM *Full width at half maximum*. Conventional definition of the width of a curve as the distance between the two point where it falls to half of its maximum value.

FWM *Four-wave mixing*. Third-order non-linear optical process where the interaction of three input electromagnetic fields results in the generation of a fourth one.

GDD *Group delay dispersion*. Characteristic of an optical material quantifying its chromatic dispersion, defined as the second derivative of the spectral phase of an optical field with respect to the angular frequency.

GVD *Group velocity dispersion*. Characteristic of an optical material quantifying the amount of temporal chirp imposed on an optical pulse upon traversing a unit length of the material. The group velocity dispersion represents the group delay dispersion per unit length.

LE *Leading edge* of the filament. Defined as the foremost point of the filament in its propagation direction.

LSF *Line-spread function*. Measure of the resolution of an imaging device, quantified by its response to an edge function.

MEG *Modified exponential-gap* scaling law. Semi-empirical mode for the calculation of the rotational energy transfer rates in inelastic collisions.

NR *Non-resonant* non-linear optical process. In the present dissertation we consider the non-resonant coherent Raman scattering process as resulting from the four-wave mixing of the pump, Stokes and probe fields, without inducing any rotational-vibrational coherence in the optical medium.

OPA *Optical parametric amplification.* Technique to amplify an optical field at a specific frequency, via the difference frequency generation of an optical pump and an idler field.

RET *Rotational energy transfer.* Transfer of population between rotational energy states, within the same electronic and vibrational states, as a consequence of inelastic molecular collisions.

RPA *Random phase approximation.* Simplifying assumption made to compute the inelastic collisional dephasing rate of anisotropic CRS lines from the dephasing rate of isotropic lines associated to the initial final states in the corresponding transition.

RSTD *Relative standard deviation.* Relative measure of the dispersion of a statistical sample about average value, computed as the ratio between the standard deviation of the sample and the (absolute) mean value.

RWA *Rotating wave approximation.* Mathematical approximation introduced in the description of light-matter interaction to neglect coupling terms that oscillates at optical frequencies.

SHBC *Second-harmonic bandwidth compression.* Generation of a relatively narrowband picosecond optical pulse, via the sum-frequency generation of two chirp-conjugated broadband femtosecond pulses.

SNR *Signal-to-noise ratio.* Measure of the signal quality, quantified by the ratio between the desired signal and its noise.

SRS *Stimulated Raman scattering.* Third-order non-linear optical process whereby the coherent rotational-vibrational motion of the molecules, induced by the input pump and Stokes fields, results in a loss on the former and a gain on the latter.

TBP *Time-bandwidth product.* Product of the temporal duration and spectral bandwidth of an optical pulse, whose minimum value is limited according to the Fourier uncertainty principle.

TE *Trailing edge* of the filament. Defined as the aftmost point of the filament with respect to its propagation direction.

TL Fourier *transform-limitation.* A laser pulse is said to be transform-limited when it has the minimum temporal duration allowed by its bandwidth, according to the Fourier uncertainty principle.

Chapter 1

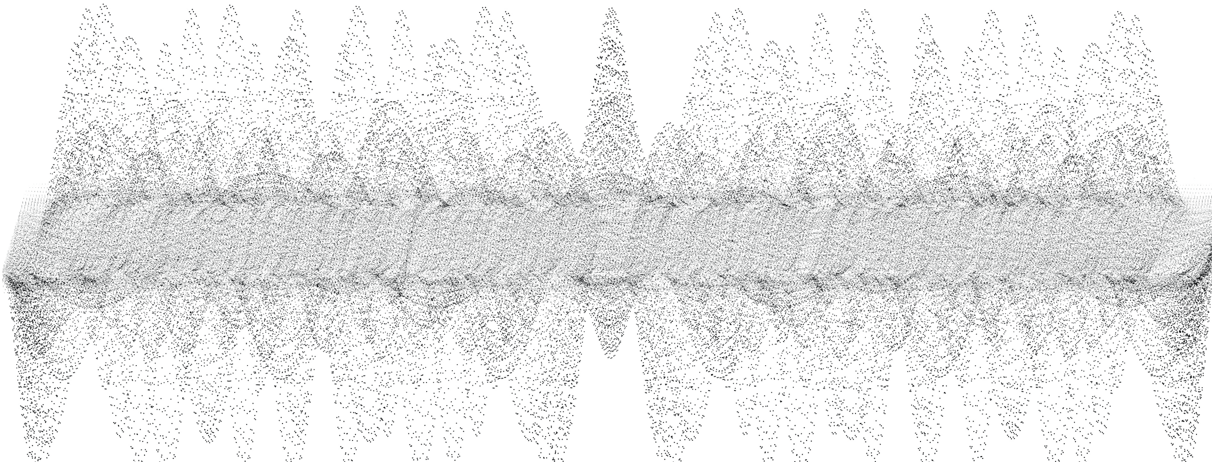

INTRODUCTION

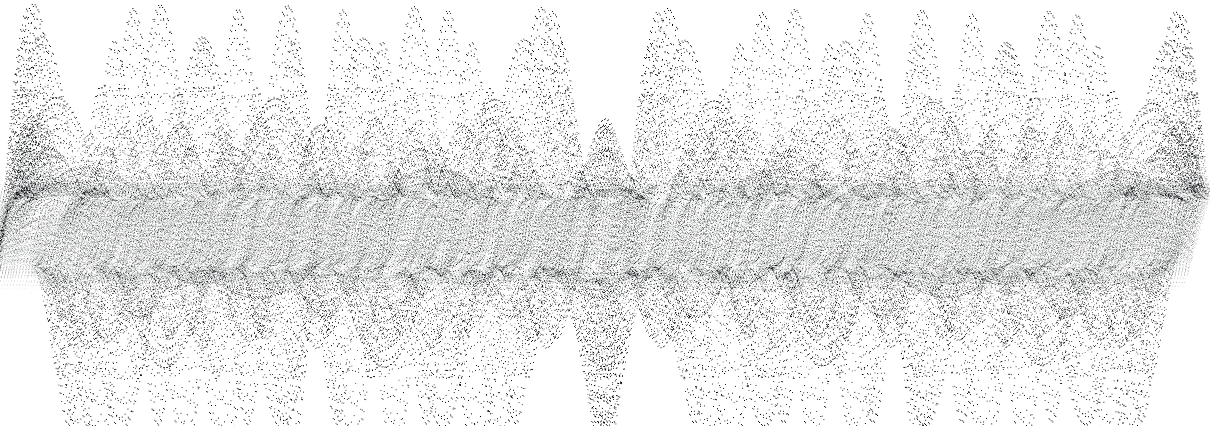

The present thesis concerns the development of coherent Raman spectroscopy (CRS), and its application to gas-phase diagnostics in chemically reacting environments [1]. In its conventional implementation, CRS employs three laser fields to probe the rotational and vibrational energy states of the target molecules in the gas-phase medium. The pump and Stokes fields coherently excite the rotational and/or vibrational motion of the molecules, so that they scatter the incoming probe field in a cooperative fashion, resulting in the generation of a fourth coherent field. This CRS signal carries information on the nature of the scattering molecules and on their rotational-vibrational Boltzmann distribution, thus allowing for an unambiguous identification of the chemical composition of the gas-phase medium and accurate measurements of the local temperature.

Since its advent in 1965 [2], CRS has found vast application in combustion diagnostics [3], providing non-intrusive, *in situ* measurements of temperature [4–8] and relative concentrations of major combustion species [9–12], its applications ranging from laboratory flames [6, 13] to full-scale engines [14–16]. The use of light-matter interaction to extract information on the local thermodynamic and chemical properties of the gas-phase flow allows for measurements to be performed under extremely challenging experimental conditions, such as in high temperature flames, that physical probes could not withstand. In addition, while the introduction of physical probes in a gaseous medium necessarily entails a modification of the flow field and can substantially alter the local properties one sets out to measure, this is not the case when light is used as a probe. The high spatial and temporal coherence of the light emitted by laser sources furthermore allows for spectroscopic measurements to be performed with a resolution unavailable to alternative measurement techniques. All these features make CRS the ideal experimental tool to quantify important scalars in chemically reacting flows, which are ubiquitous in applied science, and in aerospace engineering in particular.

With regard to the latter, the most obvious example is the combustion flow in aircraft or rocket engines, where the redox reaction between fuel and oxidiser increases the internal energy of the flow, for its later conversion into mechanical energy in the turbine and/or nozzle. Temperature represents one of the most important parameters controlling the evolution of the combustion process, as the rates of the underlying chemical reactions depend strongly, and in a non-linear way, on the local temperature in the gas-phase environment [17]. Hence, the temperature field not only determines the local heat released by the combustion reaction, but also controls the chemical pathways leading to the formation of pollutant species, such as carbon monoxide (CO), nitrogen oxides (NO_x) and particulate matter (soot). Small changes in the temperature field can propagate through the complex branching reactions, leading to utterly different emission profiles for the investigated combustion process. In this respect the availability of accurate experimental data is critical to validate predicting engineering models, and the requirements in terms of precision and accuracy of the employed diagnostics can be rather demanding. Consider, for example, methane combustion at the typical pressure and temperature found in an aircraft turbo-engine (inlet conditions: 30 atm, 900 K): an uncertainty of ~20 K (~1%) in the flame temperature results in a change of ~20% in the amount of thermal NO_x predicted by an Arrhenius-like rate equation [18]. In this respect, CRS represents the benchmark for high-temperature gas-phase thermometry, providing a measurement uncertainty in the order of ~1% in both its systematic bias (accuracy) and the measurement reproducibility (precision).

Next to thermometry CRS can be used to detect and measure the concentrations of major combustion species –whose spectra appear at distinct frequencies of the scattered radiation, depending on the specific rotational-vibrational energy of the target molecules, thus providing unique "fingerprints". In the context of combustion science, the use of multiplex spectroscopy to realise spatially-resolved measurements of the concentrations of major species allows for monitoring the molecular transport processes responsible of the flow mixing, as well as the chemical reaction, providing a direct estimation of the progress variable or mixture fraction. Moreover, the possibility of detecting virtually all the molecular species in the gas-phase environment under investigation makes CRS diagnostics suitable to less conventional measurement scenarios. For example, in burning metalised propellants, where CRS thermometry can be performed on by-products of the solid propellant pyrolysis, such as molecular hydrogen (H_2) [19].

In the past two decades, significant advancements in gas-phase CRS have been achieved with the introduction of ultrafast lasers, providing coherent light pulses with duration in the order of the picosecond (10^{-12} s) or the femtosecond (10^{-15} s). On such short timescales, molecular collision in the gas-phase medium can be "frozen" and time-resolved measurements can be realised, where the uncertainty due to the influence of the collisional environment on the CRS spectra can be eschewed, thus significantly improving the accuracy of CRS thermometry. The enhanced spectral stability of these laser sources reduced the mode noise and shot-to-shot amplitude fluctuations in the output pulses, significantly improving the reproducibility of the CRS measurements and the precision of CRS thermometry. These improvements in the fidelity of CRS thermometry pushed its measurement uncertainty towards the aforementioned ideal limit of 1%, such that time-resolved CRS is currently regarded as the gold standard for gas-phase thermometry [20]. Further advantages in the use of ultrafast laser sources to perform CRS are: (i) the high repetition rate, allowing single-shot measurements to be realised on the 1-10 kHz range, and (ii) the high peak power in fs laser pulses, allowing imaging measurements over one-dimensional (1D) [21] and two-dimensional (2D)[22] fields-of-view (FOVs). Furthermore, a laser pulse with duration lesser than ~50 fs has sufficient bandwidth to provide both the pump and Stokes frequencies required to excite the rotational motion of most combustion-relevant molecules. The typical CRS instrument can thus be simplified by employing a single fs laser pulse to excite the target molecules, and a relatively narrowband ps probe pulse to realise time-resolved measurements with sufficient spectral resolution: this two-beam fs/ps CRS technique [23] is at the core of the present research. Its main limitation, as compared e.g. to spontaneous Raman spectroscopy, is the need to excite the rotational-vibrational motion of the molecules beforehand. The spectral window that can be simultaneously interrogated on the basis of a single laser-shot is thus inherently limited by the bandwidth of the excitation pulse. This limitation can be overcome by employing pulse compression techniques to increase the bandwidth of the fs laser excitation pulse to hundreds of nanometres, such that the whole Raman spectrum can be simultaneously interrogated. This technique takes the name of "ultrabroadband fs/ps CRS" [24], and represents the current state-of-the-art for scalar determination in chemically reacting flows, allowing for simultaneous thermometry and wideband detection of all the major species in the probed volume [25], with potential for absolute concentration measurements.

Nevertheless, significant challenges still thwart a widespread adoption of ultrabroadband fs/ps CRS for scalar determination in practical measurements scenarios. This is particularly true for the use of ultrabroadband fs/ps CRS in high-pressure chambers, where the compression of the ultrabroadband fs laser excitation pulses needs to be achieved upon their transmission through thick optical windows and steep temperature and density gradients in the chemically reacting flow. As short fs pulses are especially sensitive to the frequency dispersion in different optical media, this can introduce a large uncertainty in ultrabroadband fs/ps CRS, or forestall it altogether: to date, gas-phase ultrabroadband fs/ps CRS measurements in closed environments have not been reported. The research illustrated in the present thesis is therefore aimed at developing a robust methodology for quantitative ultrabroadband fs/ps CRS in practical measurement scenarios.

The content of the thesis is organised as follows.

- Chapter 2 illustrates the background physics, describing: (i) the molecular rotational-vibrational energy manifold of simple diatomic molecules, (ii) the basic principles of light-matter interaction, with a particular focus on coherent Raman scattering, (iii) the use of ultrafast lasers to realise time-resolved CRS, hybrid fs/ps CRS in particular.
- Chapter 3 introduces the main research objective: the development of ultrabroadband fs/ps CRS for gas-phase diagnostics. Three main limitations to ultrabroadband fs/ps CRS are identified. First of all, the need to transport the compressed fs laser excitation pulse behind thick optical windows. Secondly, the uncertainty introduced by the unknown spectral excitation profile provided by the ultrabroadband fs laser pulse. Finally, the need for accurate models to simulate the ro-vibrational CRS spectra of complex polyatomic molecules.
- Chapter 4 addresses the first limitation by introducing fs laser-induced filamentation as an *in situ*-generated ultrabroadband coherent light source. The propagation and compression of fs laser pulses in the filamentation regime is briefly outlined at the beginning of the chapter. Thereupon the experimental setup for ultrabroadband fs/ps CRS with *in situ* filamentation, as demonstrated in Paper I [26], is described and the impact of the combustion environment on the filamentation process is discussed. The second part of the chapter demonstrate the use of *in situ* filamentation to perform single-shot ultrabroadband fs/ps CRS measurements in laboratory flames, behind a thick optical window. The impact of the window on the pulse propagation and its subsequent compression in the filamentation process, as reported in Paper III [27], is quantified.
- A novel experimental protocol, introduced in Paper II [28], is discussed in Chapter 5. This foresees the *in situ* measurement of the spectral excitation efficiency, concurrent to the fs/ps CRS experiment, and it is implemented by a polarisation approach and by the use of a polarisation-sensitive coherent imaging spectrometer. The impact of the experimental protocol on the measurement uncertainty in pure-rotational fs/ps CRS thermometry is first assessed by performing 1D imaging measurements across a laminar CH_4/air flame front. Thereupon, the novel experimental protocol is employed to realise accurate ultrabroadband fs/ps CRS thermometry on H_2 thermometry behind the thick optical window.
- Chapter 6 discusses the development and validation of time-domain models for the fs/ps CRS spectra of the four major combustion species investigated in the vibrational

fingerprint region: H_2, O_2, CO_2 and CH_4. The increasing complexity of the Raman spectra, with the number of molecular nuclei and vibrational degrees of freedom, is highlighted in the description of the time-domain fs/ps CRS models. In particular, the ro-vibrational spectrum associated to the second vibrational mode of CH_4 requires a rather large number of transitions to be taken into account to describe the intra-molecular coupling processes and its temperature dependence.

- Chapter 7 briefly outlines the potential of ultrabroadband fs/ps CRS for the *in situ* investigation of molecular transport processes and chemical reactions in gas-phase environments. Two examples are discussed: (i) the direct observation of H_2 differential diffusion in a laminar H_2/air diffusion flame, and (ii) the simultaneous detection of all the aforementioned major combustion species across a laminar CH_4/air diffusion flame front, highlighting the buoyant transport of CH_4 and its pyrolysis in the chemical reaction zone of the flame.
- Finally, Chapter 8 summarises the results and the present development of quantitative ultrabroadband fs/ps CRS for chemically reacting flows, and reviews the outlook for future developments of this technique.
- Appendix A provides a detailed description of the quantised rotational and vibrational motion of a diatomic molecule, and the derivation of the main equations reported in Chapter 2.
- Appendix B discusses the extension of this description to more complex polyatomic molecules. Some symmetry considerations are introduced, and their importance in determining the rotational-vibrational wave function of these molecules is discussed, with particular focus on the case of CH_4.
- Appendix C provides the general theoretical framework for the development of time-domain fs/ps CRS models and discusses the main simplifying assumption made to develop the specific models in Chapter 6.
- Appendix D outlines the polarisation theory of the CRS process, with particular regard to the polarisation strategy employed in Chapter 5 to implement the novel experimental protocol.

Chapter 2

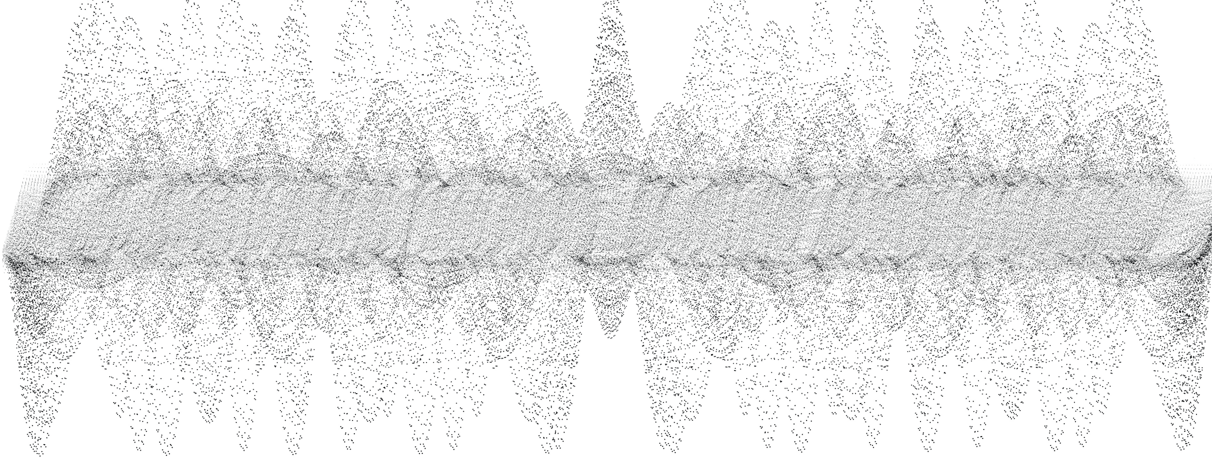

ROTATIONAL-VIBRATIONAL COHERENT RAMAN SPECTROSCOPY

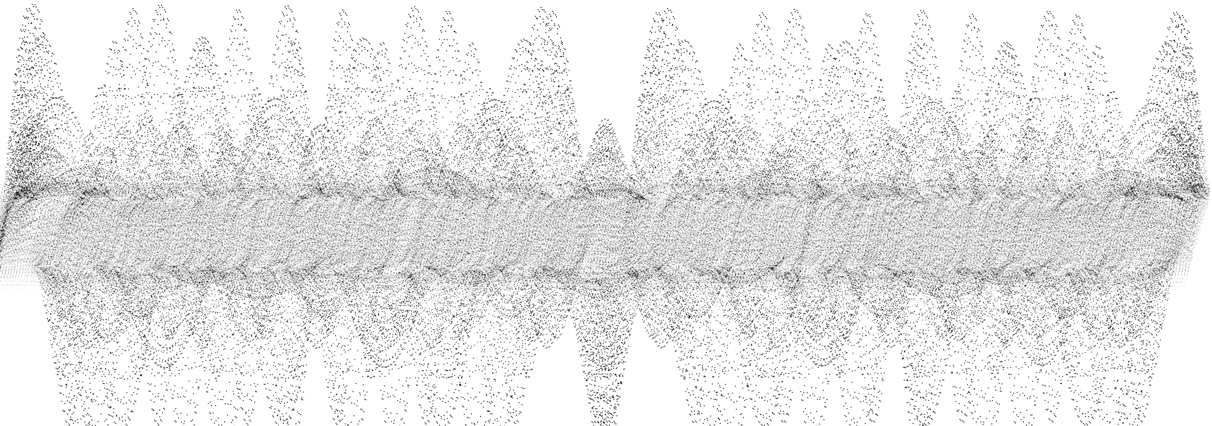

The use of laser-based optical spectroscopy for scalar measurements in chemically reacting flows relies on the interaction between the coherent electromagnetic (EM) radiation and the gas-phase medium [1]. Upon this light-matter interaction, the spectrum of the detected EM field carries information on the internal energy of the molecular components of the medium and, in particular, it reflects the Boltzmann statistics over their quantised rotational and vibrational energy states. Section 2.1 introduces simple classical models for the description of the rotational and vibrational motions of simple diatomic molecules, and summarises the main results of their canonical quantisation to provide a simple description of the discrete rotational-vibrational energy manifold.

Section 2.2 discusses the underlying physics and basic principles of spontaneous and coherent Raman scattering. Raman scattering is the inelastic scattering of the incident EM radiation by the optical medium: in this process both the internal energy of the molecules and the frequency of the input field change, so that the total energy of the system is conserved. The ro-vibrational energy distribution of the molecular constituents of the investigated gas can thus be measured by the spectrum of the scattered radiation. Spontaneous Raman scattering is an incoherent optical process, leading to the isotropic, incoherent emission of the scattered signal; furthermore, the typical Raman cross-section in the gas-phase is in the order of 10^{-29} cm^2/molecule·steradian [29]. The intensity of the scattered signal can be increased by many orders of magnitude if the emission of the scattered radiation can be stimulated, or if the molecules can be made to re-emit coherently, i.e. in a cooperative fashion [30]. Stimulated Raman spectroscopy (SRS) and coherent Raman spectroscopy implement precisely these two ideas. Both techniques involve a non-linear light-matter interaction [31], employing additional input laser fields to "drive" the rotational-vibrational motion of the target molecules, inducing a so called "Raman coherence" in the gas-phase medium. As a result, the scattered radiation is spatially and temporally coherent, showing the same properties of the emission from a laser [32]: this proves beneficial for remote optical diagnostics in harsh, luminous environments such as flames.

The commercial availability of ultrafast laser sources has prompted a stream of innovations in the past two decades [33, 34], with the development of time-resolved CRS and of imaging capabilities for gas-phase measurements. Contrary to the conventional frequency-domain implementation of CRS, based on the use of nanosecond (10^{-9} s) laser sources, time-domain CRS techniques employ ultrafast lasers to introduce a coherent excitation of the target molecules and probe its temporal evolution [35]. Laser pulses with duration ranging from ~10 ps down to ~10 fs thus provides sufficient temporal resolution to study molecular dynamics in the time domain [36]. Time-resolved CRS and its use for gas-phase diagnostics in chemically reacting flows is discussed in Section 2.3, with particular focus on the two-beam hybrid fs/ps CRS technique employed throughout the course of the present research.

2.1 Rotational-vibrational energy of molecules

Molecular spectroscopy allows the experimentalist to probe the internal energy of a molecule or the statistical distribution of an *ensemble* of molecules over the internal degrees of freedom. The internal energy of a molecule can be broken down as:

$$U = ZPE + E_{\text{electronic}} + E_{\text{vibrational}} + E_{\text{rotational}} + E_{\text{nuclear spin}} \tag{2.1}$$

ZPE is the zero-point energy, due to quantum fluctuations in the vacuum state of the EM field [32]. $E_{\text{electronic}}$ is the energy associated to the electronic configuration of the molecule as well as to the electron angular momentum, which include contributions due to the electron motion (orbital angular momentum) and to its inherent angular momentum (spin angular momentum). $E_{\text{vibrational}}$ is the energy associated to the relative motion of the nuclei in the binding EM potential. $E_{\text{rotational}}$ is the energy associated to the angular momentum due to the motion of the nuclei. $E_{\text{nuclear spin}}$ is the energy associated to the angular momentum due to the spin of the subatomic components in the nuclei. As an example, the potential energy curves of diatomic nitrogen in the three lowest electronic states are shown in Figure 2.1.

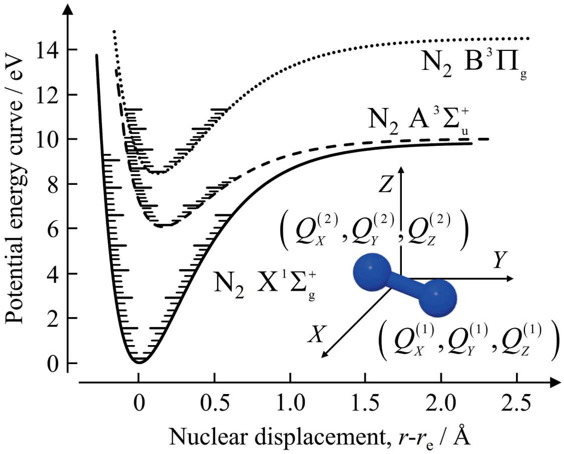

Figure 2.1: Internal energy of diatomic nitrogen (N_2). Potential energy curves of N_2 in the ground ($X^1\Sigma_g^+$) and first two excited ($A^3\Sigma_u^+$ and $B^3\Pi_g$) electronic states, different vibrational energy levels are marked within each electronic state. Molecule rendered using Jmol: an open-source Java viewer for chemical structures in 3D (http://www.jmol.org/).

Optical spectroscopic techniques, such as CRS, leverage the interaction of EM fields oscillating at optical frequencies with the target molecules to investigate their internal energy distribution. In this light-matter interaction, both the electronic state of the molecule and the rotational-vibrational motion of its nuclei can change. When the molecule transitions between two different electronic configurations one talks about electronic spectroscopy, and in particular *vibronic* and *ro-vibronic*, when the transition is accompanied by changes in the vibrational and in both vibrational and rotational energy, respectively. When the interaction involves only changes in the vibrational and/or rotational energy of the molecule, one talks about *ro-vibrational* and *pure-rotational* spectroscopy. The research discussed in the present thesis, with the only exception of Paper VI [37], is focused on pure-rotational and ro-vibrational spectroscopy, and its use to investigate the rotational and vibrational Boltzmann distributions in combustion environments.

The starting point in the description of rotational-vibrational CRS is the characterisation of the rotational and vibrational degrees of freedom of the molecular scatterers. As molecules are fundamentally quantum objects, this characterisation must take into account the quantised nature of their vibrational and rotational motion. This cumbersome task is not addressed directly in the present section, but deferred to Appendix A. In the following only the basic classical models for the vibrational and rotational motion of the simplest diatomic molecule are illustrated, and the main results concerning their quantisation are summarised.

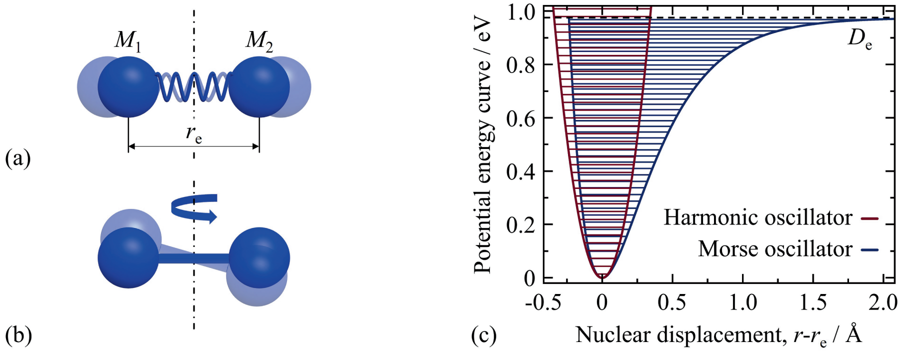

Figure 2.2: (a) Sketch of the classical harmonic oscillator model for the vibrational motion of a diatomic molecule. (b) Sketch of the rigid rotor model for the rotational motion of a diatomic molecule. (c) Harmonic (red) and Morse (blue) potential energy curves of N_2 in the ground electronic state, and their quantised vibrational energy states.

2.1.1 VIBRATIONAL ENERGY MANIFOLD

The simplest description of the vibrational motion of a diatomic molecule sees the molecule as a linear classical harmonic oscillator [38], i.e. an equivalent mass-spring system, as sketched in Figure 2.2(a).

The two nuclei are assimilated to point masses (M_1 and M_2) bound by an elastic force, with elastic constant k:

$$F_{\text{elastic}} = -\frac{dV_{\text{elastic}}(x)}{dx} = -kx \tag{2.2}$$

The potential energy associated to the elastic force in Equation (2.2) is given by:

$$V_{\text{elastic}}(x) = \frac{1}{2}kx^2 = m\omega^2 x^2 \tag{2.3}$$

Where $m = (M_1 M_2)/(M_1 + M_2)$ is the reduced mass of the system, and $\omega = \sqrt{k/m}$ is its angular frequency. The Hamiltonian function for the classical harmonic oscillator is well-known:

$$H = \frac{p^2}{2m} + \frac{1}{2}m\omega^2 x^2 \tag{2.4}$$

Where p is the linear momentum component along x.

Introducing the results of canonical quantisation for the motion of the harmonic oscillator (see Appendix A.1), the vibrational energy manifold is the discrete ladder sketched as the red curve in Figure 2.2(c), with energy levels:

$$E_{\mathrm{v}} = \left(v + \frac{1}{2}\right)\hbar\omega, \qquad v = 0, 1, 2, \cdots \tag{2.5}$$

Where v is the *vibrational quantum number.*

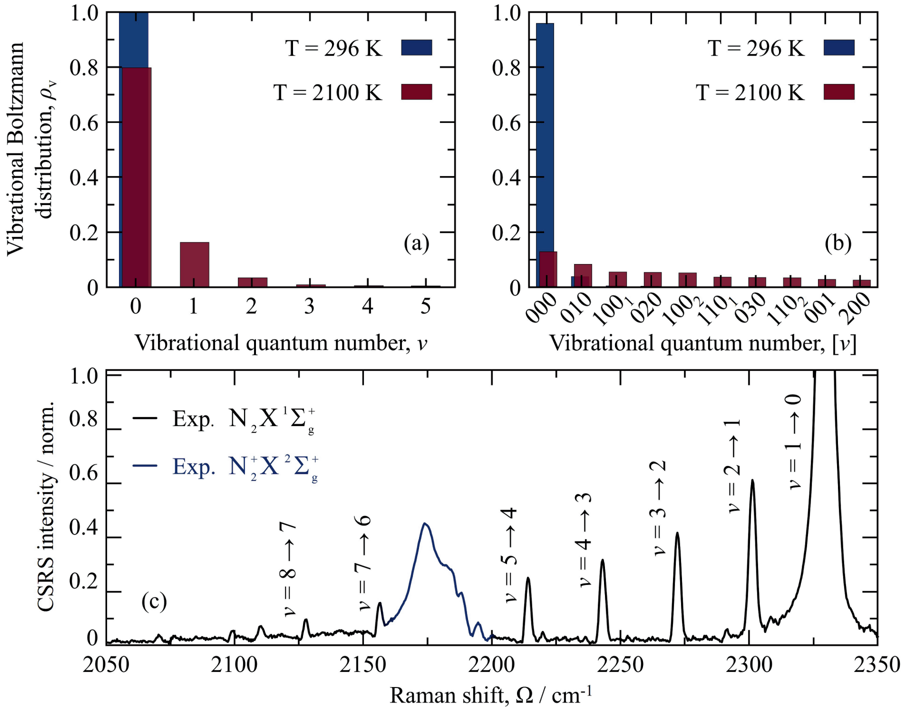

Figure 2.3: Vibrational Boltzmann distribution. (a) Boltzmann distribution of N_2 over the six lowest vibrational energy states, computed at room temperature and at a typical hydrocarbon flame temperature. At room temperature more than 99.9% of the molecules in the statistical ensemble occupy the vibrational ground state. At high temperature, the first four vibrational states are significantly populated. (b) Boltzmann distribution of CO_2 over the first ten vibrational energy states, computed at room temperature and at flame temperature. CO_2 is a polyatomic molecule with more than one vibrational mode. Some of these modes are significantly less energetic than the vibrational mode of N_2. Hence, more vibrational states are populated in the Boltzmann distribution computed at the same temperature. The notation for the different vibrational states of CO_2 is discussed in Section 6.3.1. (c) Ro-vibrational coherent Stokes Raman spectrum (CSRS) of N_2 acquired within the non-equilibrium (T_{rot}=296 K, T_{vib}>8000 K) plasma generated by fs laser-induced filamentation. The ro-vibrational CSRS spectrum clearly reflects the statistical distribution of the N_2 molecules over the quantised vibrational energy levels.

The classical harmonic oscillator model above assumes the electrostatic force exerted on the molecular nuclei to be linear in the internuclear distance, such that Hooke's law holds in Equation (2.2). This assumption is reasonable at the bottom of the potential curve in Figure 2.2(c), but for large nuclear displacements the electrostatic interaction between the nuclei and the bond electrons is no longer sufficient to hold the nuclei together and the molecule dissociates. A more realistic description of the vibrational motion of a diatomic molecule is then given by the Morse potential in Equation (2.6), which accounts for the vibrational dissociation of the molecule, as represented by the blue curve in Figure 2.2(c):

$$V(x) = D_\mathrm{e}\left[1 - e^{ax}\right]^2 \tag{2.6}$$

With D_e being the dissociation energy, and a a species-specific constant. Contrary to the quantum harmonic oscillator, there is no closed-formed solution to Schrödinger's equation when the Morse potential is employed, and the vibrational energy manifold is typically modified by introducing anharmonic corrections to Equation (2.5) in the form:

$$E(v) = \omega_\mathrm{e}\left[\left(v + \frac{1}{2}\right) - x_\mathrm{e}\left(v + \frac{1}{2}\right)^2 + y_\mathrm{e}\left(v + \frac{1}{2}\right)^3 + \cdots\right] \tag{2.7}$$

The spacing between the vibrational energy levels in the Morse potential thus reduces with v as shown in Figure 2.2 with important implications for vibrational spectroscopy.

The above description of the vibrational motion a single diatomic molecule can be extended to a statistical ensemble of identical molecules in the gas-phase medium. Assuming the ensemble to be in thermal equilibrium at temperature T, the statistical population of the discrete vibrational energy states v is described by the Boltzmann distribution:

$$\rho(v) = \frac{\exp(-\hbar E(v)/k_\mathrm{B}T)}{\sum_v \exp(-\hbar E(v)/k_\mathrm{B}T)} \tag{2.8}$$

Where k_B is the Boltzmann constant and the vibrational energy in each vibrational state $E(v)$ can be computed according to Equation (2.7). An example of the vibrational Boltzmann distribution of the N_2 and CO_2 molecules at three different temperatures is shown in Figure 2.3.

2.1.2 ROTATIONAL ENERGY MANIFOLD

Similar to the classical harmonic oscillator model employed in the previous paragraph, description of the quantised rotational motion of a diatomic molecule also moves from a simplified classical model. The simplest description of a rotating diatomic molecule is that of a rigid rotor, which assumes the internuclear distance to be constant during the rotational motion. The Hamiltonian function describing the motion of a rigid rotor is thus:

$$H = \frac{\boldsymbol{J}^2}{2I} \tag{2.9}$$

Where $\boldsymbol{J}$ is the angular momentum vector associated to the rotational motion of the molecule and I is the moment of inertia of the system. Note that this model assumes the angular momentum as deriving entirely from the rotational motion of the nuclei, thus neglecting other contributions due, e.g. to the rotational motion of the electrons. A more detailed survey of the different contributions to the total angular momentum of a molecule, and their relevance to molecular spectroscopy, is given in Appendix A.2.

The canonical quantisation of the Hamiltonian in Equation (2.9) leads to a discrete rotational energy manifold with energy levels:

$$E(J) = B_e J(J+1) \tag{2.10}$$

Where $B_e = \hbar/(4\pi c I)$ is the equilibrium rotational constant of the system (in cm^{-1} units), and J is the *total angular momentum quantum number.*

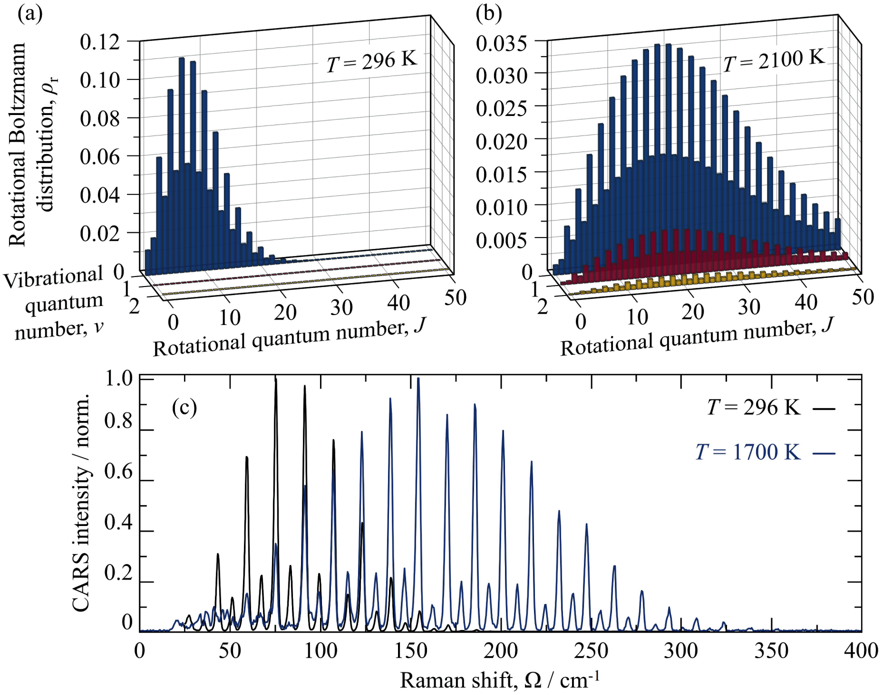

Figure 2.4: Rotational Boltzmann distribution. (a) Boltzmann distribution of N_2 over the first fifty rotational energy states, within the first three vibrational states, computed at room temperature. Even and odd rotational states show a 2:1 ratio due to the nuclear spin degeneracy of the N_2 molecule (see Appendix B.1). (b) Rotational Boltzmann distribution of the N_2 molecules at flame temperature (2100 K) within the first three vibrational states, which are significantly populated at this temperature. (c) Pure-rotational coherent anti-Stokes Raman spectra (CARS) of N_2 acquired in a room-temperature N_2 flow (black line) and across the reaction layer of a laminar premixed CH_4/air flame (blue line). The temperature difference is reflected on the envelope of the pure-rotational CARS spectrum, providing a direct measurement of the rotational Boltzmann distribution of the N_2 molecules.

The assumption of the molecule rotating rigidly is of course quite crude, and in open contradiction with the existence of a vibrational motion, whereby the internuclear distance is never constant. In analogy to the harmonic oscillator model, the rigid rotor one can also be corrected by introducing higher order terms, accounting for the distortion of the molecule in its rotational-vibrational motion. The first correction relates to the change in the internuclear distance due to the centrifugal force introduced by the rotational motion itself:

$$E(J) = B_e J(J+1) - D_e[J(J+1)]^2 \tag{2.11}$$

With D_e being the equilibrium centrifugal constant, not to be confused with the dissociation energy in Equation (2.6).

The vibrational motion of the molecule also affects its moment of inertia, and the resulting rotational-vibrational coupling can be accounted for by introducing a dependence of the rotational and centrifugal constant on the vibrational quantum number, as:

$$\begin{aligned} B_\mathrm{v} &= B_\mathrm{e} - \alpha\left(v + \tfrac{1}{2}\right) + \left[\gamma\left(v + \tfrac{1}{2}\right)^2 + \cdots\right] \\ D_\mathrm{v} &= D_\mathrm{e} - \beta\left(v + \tfrac{1}{2}\right) + \left[\varepsilon\left(v + \tfrac{1}{2}\right)^2 - \cdots\right] \end{aligned} \tag{2.12}$$

With α, β, γ, and ε being the rotational-vibrational interaction constants.

The rotational Boltzmann distribution for a canonical ensemble of diatomic molecules in thermal equilibrium at temperature T can then be computed as:

$$\rho(J) = (2J+1) g_\mathrm{s} \frac{\exp(-\hbar E(J)/k_\mathrm{B}T)}{\sum_J (2J+1)\exp(-\hbar E(J)/k_\mathrm{B}T)} \tag{2.13}$$

Where the $(2J+1)$ factor quantifies the multiplicity of rotational states with identical energy (*degenerate* states), but different projection along an arbitrarily defined axis (see Appendix A.2 for details). Figure 2.4 shows an example of the rotational Boltzmann distribution for an ensemble of N_2 molecules, in thermal equilibrium at three different temperatures. The 2:1 ratio in $\rho(J)$ for even and odd values of J is due to the factor g_s, which quantifies the degeneracy in the nuclear spin quantum number defined in Table A.1. This degeneracy has a significant impact on Raman spectroscopy and it is discussed in detail in Appendix B.

2.2 Light-matter interaction

As mentioned above, optical spectroscopy relies on light-matter interaction to extract information about the internal energy of a molecule, or to measure the statistical distribution of an ensemble of molecules. For the purpose of the present thesis a classical picture of this light-matter interaction will suffice: both the molecular electric dipole and the input EM fields are thus treated as classical objects. The quantisation of the molecular rotational-vibrational motion is then be introduced by assuming that the molecules have a discrete energy spectrum as described by Equation (2.7) and Equation (2.11).

The above quantisation of the rotational-vibrational motion of a diatomic molecule assumed the Born-Oppenheimer approximation for the decoupling of the internal energy degrees of freedom of the molecule. Under such assumption only the electrons, whose motion happens on a timescale of hundreds of attoseconds (10^{-18} s) [41], are fast enough to follow the oscillations of the optical field applied to the molecule. The light-matter interaction is thus described in terms of the interaction of the applied field with the molecule's electric multipole moments [39]:

$$\boldsymbol{Q} = \sum_n \sum_i \mathrm{e}_i \boldsymbol{r}_i^\mathrm{n} \tag{2.14}$$

This section is partly based on 🗎 *D. Long. The Raman effect* [39]. The description of coherent Raman scattering closely follows 🗎 *E. Potma and S. Mukamel. Theory of coherent Raman scattering* [40].

Where e_i is the charge of the i^{th} particle in the molecule, $\boldsymbol{r}_i$ are its Cartesian coordinates, and n represents the order of each term in the multipole expansion $-n = 1$ being the *dipole*, $n = 2$ the *quadrupole*, $n = 3$ the *octopole*, etc.

A common assumption in optical spectroscopy is the so called dipole approximation. The wavelength of an EM field oscillating at optical frequency is typically ~380-750 nm (1 nm = 10^{-9} m) for visible light, and from ~750 nm to ~1 mm for infrared (IR) light, while molecules have much smaller dimensions (e.g. $r_e \approx 1.5\,\text{Å}$ for N_2, $1\,\text{Å} = 10^{-10}$ m). Hence, the electric field can be assumed as spatially uniform over the extent of the molecule [32]. Only the first-order term in the multipole expansion in Equation (2.14), i.e. the electric dipole $\boldsymbol{p}(t) = e\boldsymbol{r}(t)$, is thus responsible for the light-matter interaction. A molecule is said to have a *permanent* dipole $\boldsymbol{p}_0$ when it presents an electric dipole in absence of an externally applied field: this permanent dipole is responsible for the absorption and emission behaviour of the molecule, which is said to be *IR-active*. Even in absence of a permanent dipole, a molecule can nonetheless have a so called *induced* dipole in response to an externally-applied field: the tendency of a molecule to form an instantaneous dipole when subjected to an external field is called its *polarisability*. Hence, applying the electric field $\boldsymbol{E}(t)$ to a molecule, the resulting electric dipole is:

$$\boldsymbol{p}(t) = \boldsymbol{p}_0(t) + \boldsymbol{\alpha}(t) \cdot \boldsymbol{E}(t) \tag{2.15}$$

Where $\boldsymbol{\alpha}$ is the polarisability tensor of the molecule.

2.2.1 RAMAN SCATTERING

The previous paragraph mentioned the absorption and emission of EM radiation by a molecule, the present thesis focuses on another form of light-matter interaction: scattering. According to Equation (2.15), the scattered radiation is the one emitted by the oscillating electric dipole induced by the input EM field. Considering an ensemble of N molecules with no permanent dipole and an input laser field, under the dipole approximation, the resulting polarisation in the optical medium is:

$$\boldsymbol{P}(t) = N\boldsymbol{p}(t) = \epsilon_0 \boldsymbol{\chi}^{(1)}(t)\boldsymbol{E}(t) \tag{2.16}$$

Where ϵ_0 is the vacuum susceptibility, and $\boldsymbol{\chi}^{(1)}$ is the macroscopic optical susceptibility of the optical medium. The superscript "(1)" highlights the fact that the resulting polarisation is linear in the amplitude of the input electric field $\boldsymbol{E}$. The scattering in Equation (2.16) is thus a *linear optical process.*

The molecular polarisability depends on the electric charge distribution in the molecules under consideration, and thus on the nuclear coordinates Q as:

$$\boldsymbol{\alpha}(t) = \boldsymbol{\alpha}_0(t) + \sum_k \frac{\partial \boldsymbol{\alpha}}{\partial Q_k}\bigg| Q_k + \frac{1}{2}\sum_{k,l} \frac{\partial^2 \boldsymbol{\alpha}}{\partial Q_k \partial Q_l}\bigg|_0 Q_k Q_l + \cdots \tag{2.17}$$

Where $Q_{k,l}$ are the normal coordinates associated to the rotational or vibrational nuclear motion with frequency $\omega_{k,l}$, and the subscript "0" means that the polarisability and its derivatives are evaluated in the equilibrium configuration.

Under the assumption of *electrical harmonicity*, the molecular polarisability in Equation (2.17) is linear in the normal coordinates Q_k. *Mechanical harmonicity* is furthermore assumed, so that the nuclear motion along the normal coordinates is that of the classical harmonic oscillator in Equation (2.4), with frequency Ω_k and phase δ_k:

$$Q_k(t) = Q_{k_0} e^{-i(\Omega_k t + \delta_k)} + \text{c.c.} = Q_{k_0} \cos(\Omega_k t + \delta_k) \tag{2.18}$$

Substituting Equation (2.18) into Equation (2.17), the polarisability has a harmonic component oscillating at the same frequency:

$$\boldsymbol{\alpha}_k(t) = \boldsymbol{\alpha}_0(t) + \left.\frac{\partial \boldsymbol{\alpha}}{\partial Q_k}\right|_0 Q_{k_0} \cos(\Omega_k t + \delta_k) \tag{2.19}$$

The applied laser field, oscillating at optical frequency ω_0 with phase ϕ_0, can be written as:

$$\boldsymbol{E}(t) = \boldsymbol{E}_0(t) e^{-i(\omega_0 t + \phi_0)} + \text{c.c.} = \boldsymbol{E}_0(\mathrm{t}) \cos(\omega_0 \mathrm{t} + \phi_0) \tag{2.20}$$

Substituting Equations (2.19) and (2.20) into Equation (2.16) one can finally write the induced macroscopic polarisation of the optical medium as:

$$\begin{aligned} \boldsymbol{P}(t) &= N\boldsymbol{\alpha}_0(t) \cdot \boldsymbol{E}_0 e^{-i\omega_0 t} + N \sum_k \left.\frac{\partial \boldsymbol{\alpha}}{\partial Q_k}\right|_0 Q_{k_0} \cdot \boldsymbol{E}_0 e^{-i[(\omega_0 - \Omega_k)t + \phi_0 - \delta_k]} + \text{c.c.} \\ &= N\boldsymbol{\alpha}_0(t) \cdot \boldsymbol{E}_0 \cos\omega_0 t + N \sum_k \left.\frac{\partial \boldsymbol{\alpha}}{\partial Q_k}\right|_0 Q_{k_0} \cdot \boldsymbol{E}_0 \big\{ \cos[(\omega_0 - \Omega_k)t - \phi_0 + \delta_k] + \\ &\quad \cos[(\omega_0 + \Omega_k)t + \phi_0 - \delta_k] \big\} \end{aligned} \tag{2.21}$$

The first term in Equation (2.21) represents the elastic scattering of the driving field $\boldsymbol{E}(t)$, called *Rayleigh scattering*. The second term represents *Raman scattering*, i.e. the inelastic scattering of the incident radiation, which is re-emitted at a different frequency, with a red-shifted component (*Stokes* radiation) at frequency $\omega_{\text{St}} = \omega_0 - \Omega_k$ and a blue-shifted component (*anti-Stokes* radiation) at frequency $\omega_{\text{aSt}} = \omega_0 + \Omega_k$.

The phase ϕ of the Raman-scattered radiation in Equation (2.21), depends on the harmonic motion of the molecule's nuclei. Assuming the rotational and vibrational degrees of freedom to be in thermal equilibrium, two distinct molecules have oscillating (nuclear) motion with no well-defined phase relationship ($\delta_i \neq \delta_j$ for $i \neq j$). The molecules thus form uncorrelated dipoles upon interaction with the incident laser radiation according to Equation (2.19), and the phase of the scattered radiation from two oscillating dipoles is uncorrelated as well. Spontaneous Raman scattering is thus an *incoherent optical process*[†].

In Equation (2.18) the nuclei have a harmonic motion with frequency Ω_k, and the inelastic scattering results in a change of the rotational-vibrational energy of the molecule. The amplitude of the scattered field is furthermore proportional to the polarisability change with the nuclear coordinates. The polarisability of a molecule thus play a critical role in determining its Raman activity, establishing so called *selection rules* for Raman scattering. Under the assumption of mechanical and electrical harmonicity [39] the selection rules for the change in vibrational state are:

[†] On the other hand, Rayleigh scattering is due to the molecular polarisability in the equilibrium configuration according to Equation (2.21) and, as such, does not depend on the nuclear motions. Rayleigh scattering is thus a *coherent optical process* [42].

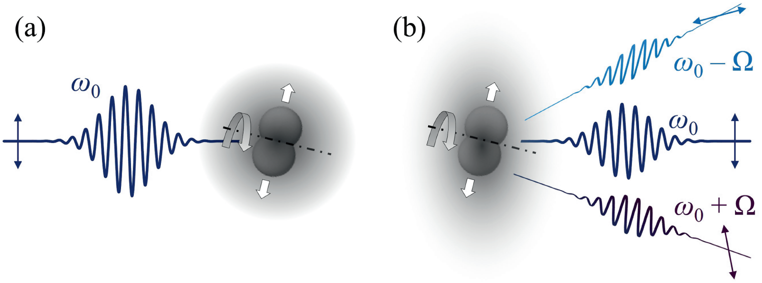

Figure 2.5: Linear optical scattering. (a) The first step in the scattering of the incoming radiation (with angular frequency ω_0) by a rotating-vibrating diatomic molecule is the interaction between the EM field and the electronic cloud surrounding the molecule, resulting in the generation of an instantaneous dipole. (b) The dipole re-emits a field with frequency components: ω_0 (elastic Rayleigh scattering), $\omega_0 - \Omega$ (inelastic Stokes Raman scattering) and $\omega_0 + \Omega$ (inelastic anti-Stokes Raman scattering). In the case of inelastic Raman scattering, the process is accompanied by a change in the internal energy of the molecule, corresponding to the change in the angular frequency of the emitted radiation by the amount Ω.

- $\Delta v = 0$, *pure-rotational* Raman scattering. The vibrational state of the molecule is unchanged in the scattering process and only the rotational state changes.
- $\Delta v = \pm 1$ *ro-vibrational* Raman scattering. The energy of the vibrational mode considered is changed by one quantum, i.e. the corresponding quantum number changes by one unit: this transitions define the so called *fundamental* band of the Raman spectrum, and its *hot bands*, when the change involves vibrational energy states higher than the ground state $v = 0$.

A detailed overview of the selection rules for rotational Raman scattering is beyond the scope of the present text, but can be found e.g. in *D. Long, The Raman effect: A unified treatment of the theory of Raman scattering by molecules* [39] and *P. Bernath, Spectra of Atoms and Molecules* [43]). Table 2.1 summarises the rotational Raman selection rules for the linear and spherical top rotors (see Appendix B) of interest, such as H_2 and CH_4. The selection rules for pure-rotational Raman spectroscopy are the same as for totally symmetric ro-vibrational Raman transitions in Table 2.1.

Table 2.1: Selection rules for the rotational Raman scattering in linear and spherical top molecules.

Rotor	**Vibrational degeneracy**	**Polarisation**	**Selection rules**
Linear	totally symmetric	polarised	$\Delta J = 0, \pm 2$
	degenerate	depolarised	$\Delta J = 0, \pm 1, \pm 2$
Spherical top	totally symmetric	polarised	$\Delta J = 0, \pm 2$
	doubly degenerate	depolarised	$\Delta J = 0, \pm 1, \pm 2$
	triply degenerate	depolarised	$\Delta J = 0, \pm 1, \pm 2$

The polarisation state reported in the table refer to the polarisation of the scattered radiation as compared to the polarisation of the incident field (assumed linear). The *depolarisation ratio* of the Raman-scattered radiation is defined as:

$$\rho \doteq \frac{I_\perp}{I_\perp + I_\parallel} \tag{2.22}$$

Where $I_\parallel$ and $I_\perp$ are, respectively, the polarisation components of the scattered field parallel and orthogonal to the incident field. The scattered light is said to be *completely polarised* if its polarisation is parallel to that of the incident radiation (i.e. $\rho = 0$), *depolarised* otherwise. The depolarisation ratio has a maximum theoretical value $\rho = 3/4$, when the Raman scattering is entirely due to the anisotropic polarisability of the molecule as defined in Equation (C.12), the scattered light is then said to be *completely depolarised.*

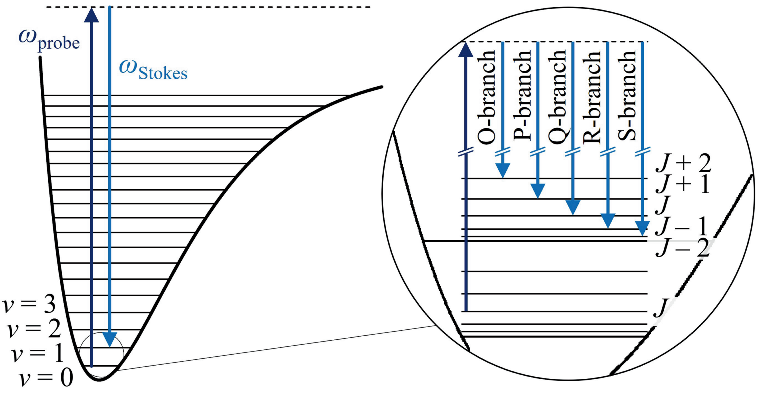

Figure 2.6: Selection rules for rotational-vibrational Raman scattering. The inelastic scattering of the incident radiation is accompanied by a change of the vibrational (v) and rotational (J) quantum numbers according to the selection rules: Δv=0, ±1 and ΔJ=0, ±1, ±2. The ro-vibrational transitions are labelled by the letters "O", "P", "Q", "R", and "S" to represent a change in the rotational quantum number by the amount -2, -1, 0, 1 and 2, respectively.

2.2.2 COHERENT RAMAN SCATTERING

The linear relationship between the polarisation of an optical medium and the incident EM field in Equation (2.16) can be thought of as a linearisation of the following Taylor expansion in $\boldsymbol{E}(t)$:

$$\boldsymbol{P} = \boldsymbol{P}^{(1)} + \boldsymbol{P}^{(2)} + \boldsymbol{P}^{(3)} + \cdots = \epsilon_0 \left(\boldsymbol{\chi}^{(1)} \cdot \boldsymbol{E} + \boldsymbol{\chi}^{(2)} : \boldsymbol{E}\boldsymbol{E} + \boldsymbol{\chi}^{(3)} \vdots \boldsymbol{E}\boldsymbol{E}\boldsymbol{E} + \cdots \right) \tag{2.23}$$

Where $\boldsymbol{P}^{(n)}$ is the n^{th}-order non-linear polarisation induced by the oscillating field $\boldsymbol{E}(\boldsymbol{r}, t)$, and $\boldsymbol{\chi}^{(n)}$ is the n^{th}-order non-linear susceptibility of the optical medium.

Coherent Raman scattering, the subject of this thesis, is a third-order non-linear optical process where the medium interacts with three fields oscillating at distinct frequencies, called the *pump*, the *Stokes* and the *probe* fields (indicated by the subscripts "1", "2", and "3", respectively):

$$P^{(3)}(\boldsymbol{r}, t) = \epsilon_0 \boldsymbol{\chi}^{(3)} \vdots \left[E_3(\boldsymbol{r}, t) E_2^*(\boldsymbol{r}, t) E_3(\boldsymbol{r}, t) \right] \tag{2.24}$$

Assuming that all the fields are co-propagating and have the same linear polarisation, and the molecular polarisability to be the scalar α, the description of the non-linear polarisation in the medium reduces to a scalar equation.

Consider a Raman-active molecule −described as a damped harmonic oscillator with resonance frequency Ω_k and damping coefficient Γ_k− under the action of the pump and Stokes fields, which oscillate at optical frequencies and are assumed as far detuned from any molecular resonance. Under the Born-Oppenheimer approximation the electrons are driven by the fields at the fundamental frequencies ω_i, as well as at the combinations frequencies $\pm(\omega_1 \pm \omega_2)$. In the following the focus is put on the frequency difference $\Omega = |\omega_1 - \omega_2|$, which is responsible for the coherent Raman scattering of the probe field. The electron motion, driven at frequency Ω, then couples to the nuclear motion through the change in molecular polarisability. The combined pump and Stokes fields thus exert an external force on the molecule, which determines a damped harmonic rotational-vibrational motion of its nuclei:

$$Q_k(t) = \frac{1}{m} \frac{\partial \alpha}{\partial Q_k}\bigg|_0 \frac{E_1 E_2^*}{\Omega_k^2 - 2i\Omega\Gamma_k - \Omega^2} e^{-i\Omega t} + \text{c.c.} \tag{2.25}$$

The amplitude of the nuclear oscillations is maximised when the frequencies of the pump and Stokes fields are tuned such that their difference is resonant to the rotational-vibrational mode, i.e. $\Omega = \Omega_k$.

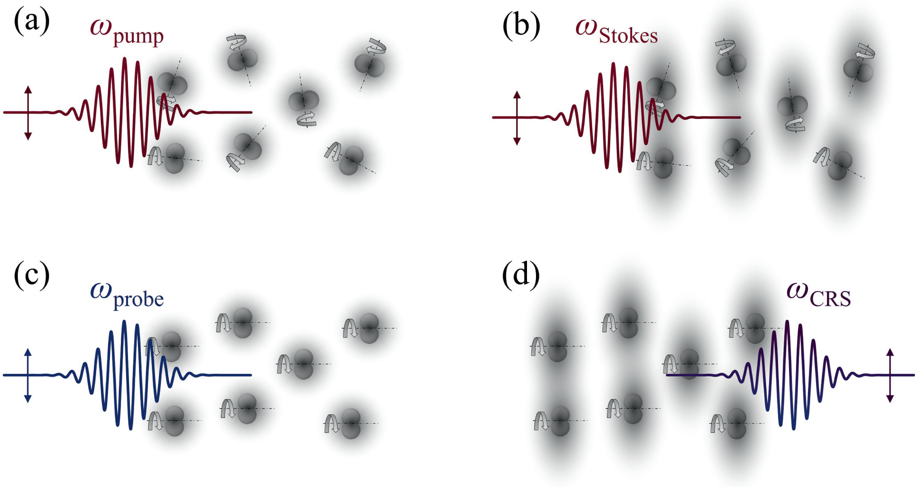

Figure 2.7: The non-linear coherent Raman scattering process. As a kind of four-wave mixing process, CRS involves the interaction between the molecules and four EM fields: (a) the pump field (ω_{pump}) interacts with the electrons producing instantaneous molecular dipoles, (b) the Stokes field (ω_{Stokes}) interacts with these dipoles, exerting a force that oscillates at the angular frequency Ω=$|\omega_{\text{pump}} - \omega_{\text{Stokes}}|$. When this force is resonant to a rotational-vibrational mode, it excites this mode producing a coherent molecular motion. This is represented as the alignment of the molecules in (c), followed by the interaction with the probe field (ω_{probe}), which generates new instantaneous dipoles. (d) Contrary to the spontaneous Raman scattering process, the dipoles oscillate in phase due to the interaction between the electrons and the nuclei, so that they re-emit coherent radiation at the frequencies ω_{CRS}=$\omega_{\text{probe}} \pm \Omega$.

The driven nuclear motion described by Equation (2.25) changes the optical properties of the material [40], so that all the incident light fields experience a different electronic polarisability while propagating through the optical medium. The resulting third-order polarisation is:

$$P^{(3)}(t) = P^{(3)}(\omega_1)e^{-i\omega_1 t} + P^{(3)}(\omega_2)e^{-i\omega_2 t} + P^{(3)}(\omega_{\mathrm{cS}})e^{-i\omega_{\mathrm{cS}} t} + P^{(3)}(\omega_{\mathrm{aS}})e^{-i\omega_{\mathrm{aS}} t} \tag{2.26}$$

The first two terms in Equation (2.26) represent *stimulated Raman scattering* (SRS). The third and fourth terms represent the coherent Raman scattering of the probe field, at the Stokes and anti-Stokes frequencies:

$$\begin{aligned}\omega_{\mathrm{cS}} &= -(\omega_1 - \omega_2) + \omega_3 = -\Omega + \omega_3 \\ \omega_{\mathrm{aS}} &= (\omega_1 - \omega_2) + \omega_3 = \Omega + \omega_3\end{aligned} \tag{2.27}$$

In this context the frequency difference Ω is commonly referred to as the *Raman shift*. The nomenclature *CSRS* and *CARS* is vastly adopted in the literature to distinguish between the coherent scattering at frequency ω_{cS} (Stokes) and ω_{aS} (anti-Stokes), respectively. In the present text the acronym CRS is consistently employed, with no particular regard to the specific process; when describing the experimental results, the notation CSRS (CARS) is introduced to specify that the spectra are acquired on the Stokes (anti-Stokes) side.

The amplitude of the coherently scattered radiation at e.g. the anti-Stokes frequency is given by:

$$P^{(3)}(\Omega) = \frac{N}{m}\left(\left.\frac{\partial\alpha}{\partial Q}\right|_0\right)^2 \frac{E_3E_2^*E_1}{\Omega_k^2 - 2i\Omega\Gamma_k - \Omega^2} = 6\epsilon_0\chi^{(3)}(\Omega)E_3E_2^*E_1 \tag{2.28}$$

Where the macroscopic third-order susceptibility $\chi^{(3)}$ of the medium is computed as:

$$\chi^{(3)}(\Omega) = \frac{N}{6m\epsilon_0}\left(\left.\frac{\partial\alpha}{\partial Q}\right|_0\right)^2 \frac{1}{\Omega_k^2 - 2i\Omega\Gamma_k - \Omega^2} \tag{2.29}$$

In classical terms, $\chi^{(3)}$ can be understood to represent the coordinated nuclear motion of the Raman-active molecules in the optical medium, under the external forcing by the combined (resonant) action of the pump and Stokes fields. Consider, for example, the pure-rotational CRS process represented in Figure 2.7. Assuming the pump and Stokes fields to be linearly polarised with same polarisation, their interaction with an ensemble of diatomic molecules results in the (periodic) alignment of the rotational axes of the molecules. The instantaneous electric dipoles generated in the following interaction with the probe field thus inherently oscillate in phase. This coherence of the microscopic dipoles results in the macroscopic (third-order) susceptibility of the optical medium $\chi^{(3)}$ and the emission of coherent radiation at the Stokes and anti-Stokes frequencies. The Raman scattering of the probe field can also be interpreted as the effect of the periodic modulation of the refractive index of the optical medium due to the coherent motion of its molecular components, as discussed in the seminal work of Maker and Terhune [2].

Figure 2.8 describes the same scattering process, highlighting the conservation of energy and momentum in the light-matter interaction. The notation employed in Figure 2.8 to represent the electronic, rotational and vibrational state of the molecule is detailed in Appendix B. As the individual fields are assumed to be off-resonant with respect to any ro-vibronic transition of the molecule, the quantum states of the molecule following the interaction with the pump and probe fields are not states of well-defined energy. These are referred to as *virtual states*. The lifetime of a virtual state is fundamentally limited by the uncertainty relation for energy [44]:

$$\Delta E\,\Delta t \sim \hbar \tag{2.30}$$

Where ΔE is the energy perturbation of the system, and Δt is the lifetime of the virtual state. For molecular species and laser fields relevant to combustion diagnostics, the detuning of the fields from any electronic transition is in the order of 10^5 cm^{-1}, resulting in a lifetime of tens to hundreds of attoseconds for the virtual states in Figure 2.8(a). As this timescale is much shorter than those of the rotational and vibrational motions, the electronic dephasing is typically assumed to be instantaneous.

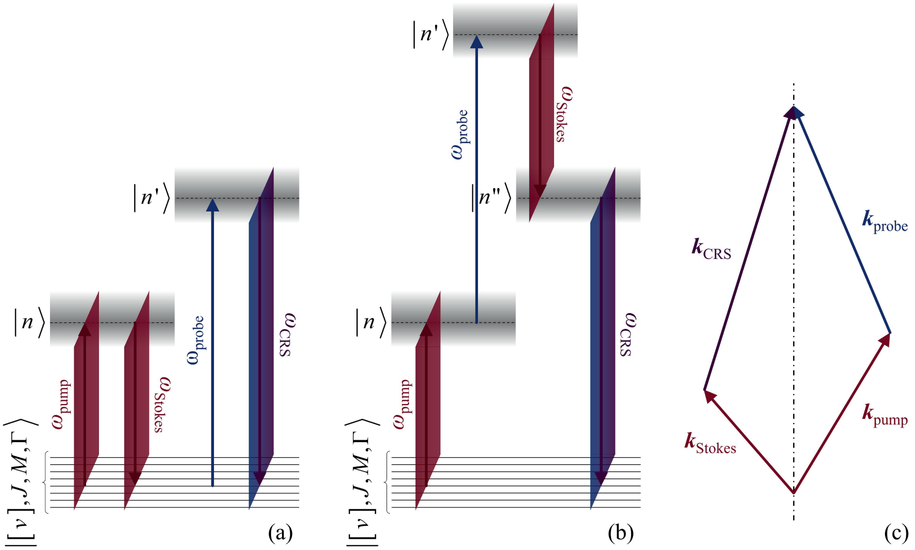

Figure 2.8: Conservation laws for the CRS process. Energy conservation in the parametric resonant (a) and non-resonant (b) CRS process: as the initial and final molecular states coincide in the energy diagrams, the energy is conserved in the light-matter interaction. In the case of a non-resonant process, the combination of the pump, Stokes and probe fields does not produce any coherent rotational-vibrational motion in the medium. These energy diagrams apply to a two-beam CRS process (as discussed in Section 2.3.1), where a single broadband laser pulse provides both the pump and the Stokes frequencies. (c) Phase-matching of the CRS process, representing the conservation of linear momentum: $\Delta\boldsymbol{k} = \boldsymbol{k}_1 - \boldsymbol{k}_2 + \boldsymbol{k}_3 - \boldsymbol{k}_{\text{CRS}}$. The planar BOXCARS phase-matching scheme sketched here allows for a perfectly phase-matched CRS process (i.e. $\Delta\boldsymbol{k} = 0$) with crossed-beam geometry, thus significantly improving the longitudinal resolution of the CRS measurements [45].

Figure 2.8(b) illustrate the existence of CRS even under fully non-resonant (NR) conditions. This is the case when the frequency difference between the pump and the Stokes fields is far-detuned from any rotational-vibrational transition, or when the scatterers do not possess any rotational-vibrational degree of freedom, as for monatomic species. The NR CRS process, also called NR *four-wave mixing* (FWM), cannot be understood in classical terms, but requires a semi-classical treatment of the molecules and the definition of virtual states, which provide a pathway for the NR CRS process as shown in Figure 2.8(b). Given the instantaneous dephasing of these virtual states, NR FWM can only happen when the pump, Stokes and probe field interact simultaneously with the molecular scatterers, i.e. when they overlap in time.

Like other non-linear optical processes, CRS has to satisfy conservation of linear momentum, expressed by the so called *phase-matching condition* [31]:

$$\Delta \boldsymbol{k} = \boldsymbol{k}_1 - \boldsymbol{k}_2 + \boldsymbol{k}_3 - \boldsymbol{k}_{\mathrm{CRS}} \tag{2.31}$$

Where the following sign convention is adopted: wave vectors for incident fields are summed, while wave vectors for emitted radiation are subtracted. Solving Maxwell's equation for the propagation of the CRS field in the non-linear optical medium, with wave vectors $\boldsymbol{k}_1$, $\boldsymbol{k}_2$ and $\boldsymbol{k}_3$ for the pump, Stokes and probe fields, yields [31]:

$$I^{(3)}(\omega_{\mathrm{CRS}}) = \frac{16\pi^4 \omega_{\mathrm{CRS}}^2}{n^4 c^4} \left|\chi(\Omega)\right|^2 I_1 I_2 I_3 l^2 \operatorname{sinc}^2\left(\frac{l\Delta k}{2}\right) \tag{2.32}$$

where n is the refractive index of the gas-phase medium, l is the interaction length of the incident fields, and the *sinc* function is defined as $\operatorname{sinc}(x) = \sin(x)/x$. The intensity of the CRS signal is thus maximised when the process is perfectly phase-matched, i.e. $\Delta k = 0$, and rapidly goes to zero for an increasing phase mismatch. While the CRS can be trivially phase-matched by adopting a collinear scheme, this results in an interaction length as long as the Rayleigh range of the laser sources employed, and poor spatial resolution in the longitudinal direction. The spatial sectioning of the probe volume can be dramatically improved in crossed-beam configurations: adopting a so called *BOXCARS* phase matching scheme [45], as shown in Figure 2.8(c), a longitudinal resolution in the order of ~1-2 mm can be achieved. Alternative phase matching schemes have been proposed, e.g. adopting a counter-propagating geometry for the pump and Stokes beams, which can result in an improvement of the spatial resolution by approximately one order of magnitude [46].

2.3 TIME-RESOLVED CRS

Through the third-order non-linear optical susceptibility in Equation (2.29), the CRS spectrum in Equation (2.32) carries information about the statistical distribution of the Raman-active molecules over their rotational and vibrational energy manifolds. For an ensemble of diatomic molecules in thermal equilibrium this correspond to the Boltzmann distribution in Equations (2.8) and (2.13): CRS can thus be employed to realise high-fidelity thermometry. The classical theory outlined in the previous paragraph provides a simple description of gas-phase CRS in the frequency domain, as realised by the use of narrowband laser sources, typically Nd:YAG lasers [33], which provide pulses with a duration of ~10 ns. This is significantly longer than the timescale of the rotational-vibrational motion of the target molecules, as well as of the typical dephasing of the Raman coherence −represented by the damping coefficient Γ in Equation (2.29). A detailed survey of the dephasing mechanism in gas-phase media is given in Section 2.3.2. While providing high spectral resolution, ns CRS instruments thus lack the temporal resolution required to measure molecular phenomena on these faster timescales.

The recent commercial availability of regenerative fs laser amplifiers, providing mJ-level energies [47] with pulse duration <100 fs, has brought forward the development time-resolved CRS techniques. These allow for the generating of the Raman coherence on a timescale small compared to molecular relaxation [48], and measuring its evolution in a time-resolved fashion, with furthermore significant advantages in terms of signal generation efficiency and measurement repetition rates [49]. The intensity of the CRS signal can be enhanced by increasing the amplitude of the coherent molecular oscillations in Equation (2.25), i.e. by maximising the molecular coherence [48]. If the duration of the pump and Stokes laser pulses is significantly shorter than the timescale for the corresponding rotational-vibrational motion, the excitation of the rotational-vibrational Raman coherence can be regarded as *impulsive* [50]. By employing a time-dependent density matrix (TDDM) formulation of the CRS process, Lucht and co-authors showed that the impulsive excitation by fs laser pulses can maximise the ro-vibrational coherence of gas-phase N_2 [51]. The use of ultrafast lasers also allows for the effective suppression of the NR CRS background due to the instantaneous electronic response of the optical medium. By delaying the probe pulse, its temporal overlap with the pump and Stokes can be minimised, effectively time-gating the NR CRS process [52]. Furthermore, ultrafast lasers can work at significantly higher repetition rates than ns ones, allowing for kHz-rate CRS in the case of regenerative fs laser amplifier systems [33], while 100 kHz rates have recently been achieved using a ps burst-mode laser [53]. Fs pulses were thus employed to perform CRS thermometry on combustion-relevant species, such as H_2 [54], N_2 and CO_2 [55]. In this context, the main limitation of fs CRS relates to the uncertainty principle in Equation (2.30): the high temporal resolution achieved by the coherent scattering of fs probe pulses comes at the price of a limited spectral resolution. As noted in Prince *et al.*, "[...] *Raman probe techniques with sufficient resolution (~15 cm^{-1}) to reasonably distinguish vibrational modes of interest have an inherent temporal resolution limit of ~1 ps*", with an even more stringent requirement to resolve the rotational structure of most molecules of interest (~5 cm^{-1}).

The need for single-shot measurements capabilities, especially in turbulent combustion environments, thus led to further developments in time-resolved CRS. Alongside the use coherent control techniques [56–61], and the development of chirped-probe pulse (CPP) CRS [62–68], *hybrid fs/ps CRS* was proposed to realise simultaneously time- and frequency resolved spectroscopy.

2.3.1 Hybrid femtosecond/picosecond (fs/ps) CRS

The combination of broadband fs pump and Stokes pulses and relatively narrowband ps probe pulses to realise simultaneously time- and frequency-resolved CRS measurements in liquid-phase toluene, rhodamine 6G and chloroform, was first demonstrated by Prince *et al.* in 2006 [69]. An analogous fs/ps CRS scheme, explicitly named "hybrid", was discussed in 2007 by Pestov *et al.* [70], who illustrated its use for rapid and specific detection of molecular markers for bacterial endospores [71].

Hybrid fs/ps CRS combines the concept of time-resolved fs CRS with a frequency-resolved probing of the Raman coherence by a narrowband ps probe. Hence, instead of measuring its temporal evolution via a sequence of fs probe pulses, as done in fs CRS, a single ps probe "reads" multiple quantum revivals (as illustrated in Figure 2.9, see also Appendix C) and "encodes" the underlying Raman frequencies on a frequency-resolved CRS spectrum. By appropriately tailoring the temporal envelope of the ps pulse and its duration, the dephasing effect of molecular collisions can be minimised, and time-resolved measurements of these collisional processes can be performed (see e.g. Paper VIII [72]). For gas-phase CRS this means that the impact of molecular collisions on the linewidth of the CRS spectra can be minimised by employing probe pulses shorter than the collisional timescale [73]: this mitigates a significant source of uncertainty, linked to the generally unknown collisional environment [74]. The time-resolved measurement of the collisional broadening of the N_2 and O_2 CRS spectra at pressures up to 20 bar was demonstrated in Ref. [75]. In addition, the suppression of the NR background already achieved by ps CRS is further optimised as the overlap between the fs excitation pulses and the ps probe pulse can by minimised and ideally avoided altogether, e.g. by employing a time-asymmetric probe pulse [76].

Over the last decade, hybrid fs/ps CRS has been developed into a state-of-the-art technique for gas-phase diagnostics in combustion environments [20, 68] as well as non-equilibrium plasmas [77–79]. In 2010 Miller and co-workers demonstrated the use of hybrid fs/ps CRS for kHz rate thermometry in high-temperature flames [80]. In a set of follow-up publications, the same research group applied hybrid fs/ps CRS for the investigation of the pure-rotational Raman spectra of N_2 and O_2 in combustion environments [73, 75, 76, 81]. Pure-rotational fs/ps CRS was then employed to perform simultaneous thermometry and relative O_2/N_2 concentration measurements in heated air by Kearney *et al.* [82], as well as in the product of flat hydrocarbon flames in Ref. [83].

Major advancements in gas-phase fs/ps CRS have been achieved thenceforth in the context of CRS imaging. The development of fs/ps CRS imaging built upon previous attempts based on ns CRS systems ([84–87]), and on the demonstration of one-dimensional (1D) CPP CRS by Kulatilaka *et al.*, where the high-peak power and efficient coherence generation provided by fs laser pulses allowed for single-shot 1D CRS thermometry at temperatures higher than 2000 K [21]. Nevertheless, the relatively large interaction length (~1.2 mm) limited the longitudinal resolution of this CPP CRS instrument, hampering the realisation of spatially-resolved measurements across the steep thermal gradient of a premixed CH_4/air flame. Pioneering work on pure-rotational fs/ps CRS imaging has been performed since 2012 by researchers at Sandia National Laboratories in Livermore, where Kliewer demonstrated a 1D pure-rotational CRS scheme, based on a counter-propagating phase-matching configuration, capable of achieving a longitudinal resolution of ~155 μm [46], one order of magnitude better than for the conventional BOXCARS configuration shown in Figure 2.8.

In this context, the most significant development for the interest of the present thesis was introduced one year later by Bohlin and Kliewer, with the development of *two-beam fs/ps CRS* [23]. This technique employs a single broadband fs laser pulse to excite the rotational Raman coherence of the target molecules, and a ps laser pulse as the narrowband probe to coherently scatter off them, as shown in Figure 2.9(a). The single fs laser pulse acts as a combined pump/Stokes pulse: constructive pump/Stokes frequency-pairs, at the resonant frequency difference Ω, are found within the broadband spectrum of the pulse and excite the corresponding Raman coherence. Employing imaging optics to realise pure-rotational two-beam fs/ps CRS, Bohlin and Kliewer could retrieve spatially resolved information over a ~10 mm 1D field-of-view (FOV), with a line-spread function (LSF) of ~84 μm, allowing them to resolve the steep gradient of a premixed CH_4/air flame. In subsequent works the LSF of the imaging system was reduced to ~60 μm [88] and ~40 μm

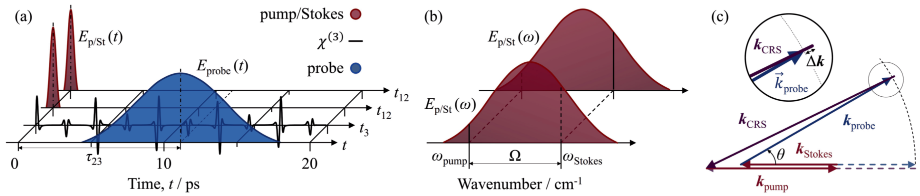

Figure 2.9: Two-beam fs/ps CRS. (a) Schematic of two-beam fs/ps CRS in the time domain. $E_{p/St}(t)$, and $E_{probe}(t)$ represent the temporal envelops of the combined pump/Stokes and probe pulses, respectively. $\chi^{(3)}$ is the non-linear optical susceptibility of the gas-phase medium due to the coherent motion of its molecular components. t_{12} and t_3 are the coherence timescales during the interaction with the input laser pulses, while τ_{23} is the intra-pulse delay. (b) Spectral excitation in two-beam fs/ps CRS. Constructive pump/Stokes frequency-pairs at Raman shifts $\Omega = |\omega_{pump} - \omega_{Stokes}|$ are found across the bandwidth of a single broadband fs excitation pulses. Since the pulse has finite bandwidth, the excitation efficiency decreases monotonically with increasing Raman shift. (c) Phase-matching of two-beam fs/ps CRS. The two-beam fs/ps CRS process sketched here can only be perfectly phase-matched (i.e. $\Delta\boldsymbol{k}=\boldsymbol{0}$) if all the laser beams are collinear. Adopting a crossed-beam geometry (i.e. $\theta \neq 0$), with crossing angle θ, necessarily results in a phase-mismatch that increases with larger Raman shifts and crossing angle [23].

[25], thus improving on the lateral resolution of 1D fs/ps CRS. In Paper V the LSF of the pure-rotational fs/ps CRS instrument is further improved by a factor two (i.e. 20 μm), by employing a ~400 nm probe.

Furthermore the interaction length in Ref. [23] could be easily tuned by changing the focusing properties and crossing angle (θ) between the pump/Stokes and probe beams, and a longitudinal resolution down to 50 μm was achieved in case of orthogonal crossing (i.e. $\theta = 90°$). It is important to notice, nevertheless, that the two-beam CRS fs/ps process is only perfectly phase-matched for a collinear geometry (i.e. $\theta = 0°$), as shown in Figure 2.9. Adopting a crossed-beam geometry results in a phase mismatch of the CRS process amounting to:

$$\Delta k = \Omega + k_3 - \sqrt{\left(\Omega + k_3 \cos\theta\right)^2 + \left(k_3 \sin\theta\right)^2} \tag{2.33}$$

If the angle θ is small, such that the envelope of the input laser fields can be assumed as constant along their interaction length (slowly varying amplitude approximation, SVAA), the phase-mismatch in Equation (2.33) reduces the intensity of the CRS signal according to the sinc^2 dependence in Equation (2.32). For larger crossing angles, on the contrary, the SVAA breaks down and the functional dependence of the pump/Stokes field amplitude on the propagation coordinate z must be taken into account and, assuming this be the Gaussian function $E_{12}(z) \propto \exp(-\alpha z^2)$, Equation (2.32) is modified as:

$$\begin{aligned} I^{(3)}(\omega_{CRS}) &= \frac{16\pi^4\omega_{CRS}^2}{n^4c^4}\left|\chi(\Omega)\right|^2 I_{12}^2 I_3\, l^2\, e^{(i\,\sqrt{2}\xi_2/\xi_1)^2}\left[\mathrm{erfi}^2\xi_2 - 4\Re(\xi_3) + |\xi_3|^2\right] \\ \xi_1 &= \sqrt{\alpha}\sin\theta \\ \xi_2 &= \frac{\Delta k}{2\xi_1} \\ \xi_3 &= \mathrm{erfi}(i\,z\,\xi_1 + \xi_2) \end{aligned} \tag{2.34}$$

Where erfi is the imaginary error function. Therefore an increment in crossing angle, and hence improved resolution, comes at the cost of a reduced excitation efficiency at larger Raman shifts [23, 89].

Bohlin *et al.* employed 1D pure-rotational two-beam fs/ps CRS to investigate the flame-wall interaction in a head-on quenching (HOQ) burner achieving time-resolved measurement of the temperature gradient, as the premixed CH_4/air flame approached the metal wall of the HOQ burner, and throughout the quenching process [90]. More recently, Escofet-Martin and co-authors have employed a similar CRS instrument to investigate transient heat transfer processes in the thermal boundary layer at the gas-wall interface [91]. Soon after their development of two-beam CRS, Bohlin and Kliewer extended its capability to snapshot two-dimensional (2D) hyperspectral imaging [22], and demonstrated its use to simultaneously map the temperature and relative O_2/N_2 concentration fields over sections of a premixed laminar CH_4/air flame [92]. Miller *et al.* later extended the repetition rate of this 2D pure-rotational two-beam fs/ps CRS technique to 1 kHz [93].

2.3.2 TIME-DOMAIN MODELLING OF HYBRID FS/PS CRS

Alongside the advantages discussed in the previous paragraph, hybrid fs/ps CRS allows for a significant simplification of the numerical modelling of the CRS spectrum in the time domain. The details of the time-domain modelling approach are deferred to Appendix C and only the main results, pertaining specifically to two-beam fs/ps CRS, are discussed below.

The input laser pulses are modelled in the time domain as plane waves with angular frequency ω and wave vector $\boldsymbol{k}$:

$$\boldsymbol{E}(\boldsymbol{r},t) = \boldsymbol{E}(t)\,e^{i[(\boldsymbol{k}\cdot\boldsymbol{r})-\omega t]} \tag{2.35}$$

Assuming for simplicity that the lasers pulses have same linear polarisation, and the CRS process to be perfectly phase-matched, the evolution of the third-order polarisation field in the gas-phase medium is described as:

$$\begin{aligned} P^{(3)}_{\mathrm{CRS}}(t,\tau_{23},\tau_{12}) = \left(\frac{i}{\hbar}\right)^3 E_3(t-t_3)\int_{-\infty}^{t} dt_{12}\,\chi^{(3)}(t_{12}) \\ E^*_{12}(t+\tau_{23}-t_{12})\,E_{12}(t+\tau_{23}-t_{12})\,e^{i(\omega_1-\omega_2)t_{12}} \end{aligned} \tag{2.36}$$

Where $E_{12}(t)$ represents the complex electric field of the combined pump/Stokes excitation pulse, t_{12} is the coherence timescale for the rotational-vibrational motion of the Raman-active molecules in the optical medium, and τ_{23} is the delay between the pump/Stokes and probe pulses.

Under the assumption of impulsive excitation of the rotational-vibrational coherence, Equation (2.36) is simplified as:

$$P^{(3)}_{\mathrm{CRS}}(t,\tau_{23}) = \left(\frac{i}{\hbar}\right)^3 E_3(t+\tau_{23})\chi^{(3)}(t) \tag{2.37}$$

The intensity spectrum of the CRS signal is finally computed as the (squared) Fourier transform of the time-dependent polarisation $P^{(3)}_{\mathrm{CRS}}(t)$:

$$I_{\mathrm{CRS}}(\omega) = \left|\mathscr{F}\left\{P^{(3)}_{\mathrm{CRS}}(t)\right\}\right|^2 \tag{2.38}$$

It is important to notice here that the assumption of impulsive excitation is formally equivalent to representing the temporal envelope of the pump/Stokes pulse as a Dirac delta. The pump/Stokes pulse is thus assumed to have an infinite bandwidth with homogeneous spectral density as implied by Equation (2.30). This is obviously non-physical, as even broadband fs laser pulse have a finite bandwidth, which ultimately limits the excitation bandwidth of the molecular Raman modes. The time-domain model in Equation (2.37) is not capable of rendering this behaviour and the experimental spectra need to be corrected for the finite bandwidth of the excitation pulse, so as to have a meaningful comparison to the model. The excitation efficiency at different Raman shifts is effectively mapped by the spectrum of the NR CRS emission, corresponding to the spectral autocorrelation of the combined pump/Stokes pulse [94]:

$$I_{\mathrm{NR}}(\omega) = \left|\mathscr{F}\left\{P^{(3)}_{NR}(t)\right\}\right|^2 \propto \left|\chi^{(3)}_{\mathrm{NR}} E_3(\omega) * \left[E_{12}(\omega) \star E_{12}(\omega)\right]\right|^2 \tag{2.39}$$

Where "$*$" and "$\star$" represent the convolution and correlation operator, respectively.

Hence, by measuring the NR CRS spectrum generated e.g. in a non-resonant gas (typically Ar), and by subdividing the resonant CRS spectrum by the NR one, the effect of the finite bandwidth of the excitation pulse can be factored out. This operation is part of the experimental CRS protocol and is called *spectral referencing*, and is the main topic of Chapter 5.

In the present thesis, the following simplified phenomenological description of the third-order susceptibility is adopted:

$$\begin{aligned}\chi^{(3)}(t) = \sum_{k} \sum_{[v]} \sum_{J,M,\Gamma} & X_k I^{(k)}_{\{[v]_f,J_f,M_f,\Gamma_f\}\leftarrow\{[v]_i,J_i,M_i,\Gamma_i\}} \\ & \exp\left[\left(i\omega^{(k)}_{\{[v]_f,J_f,M_f,\Gamma_f\}\leftarrow\{[v]_i,J_i,M_i,\Gamma_i\}} - \Gamma^{(k)}_{\{[v]_f,J_f,M_f,\Gamma_f\}\leftarrow\{[v]_i,J_i,M_i,\Gamma_i\}}\right)t\right]\end{aligned} \tag{2.40}$$

Where the labels "$|[v]_i,J_i,M_i,\Gamma_i\rangle$" and "$|[v]_f,J_f,M_f,\Gamma_f\rangle$" indicate the initial and final molecular states, according to the notation defined in Appendix B. The index k here represents the different Raman-active species present in the probe volume, each with mole fraction X_k.

Each damped harmonic contribution in Equation (2.40) represents, upon Fourier transforming $P^{(3)}_{\mathrm{CRS}}(t)$, an individual line in the CRS spectrum. The corresponding line strength $I^{(k)}_{\{\cdots\}_f\leftarrow\{\cdots\}_i}$ depends on the difference between the populations in the initial and final rotational-vibrational states of the Raman transition, as well as on its Raman cross-section.

The damping coefficient $\Gamma_{\{\cdots\}_f\leftarrow\{\cdots\}_i}$, already introduced in Equation (2.29), represents the dephasing rate of the coherent rotational-vibrational motion at Raman frequency $\omega_{\{\cdots\}_f\leftarrow\{\cdots\}_i}$. There are many physical phenomena contributing to the loss of Raman coherence, resulting in the broadening of the Raman linewidths, and an overview of the most prominent dephasing mechanisms is given in Appendix C. In the application of fs/ps CRS to gas-phase diagnostics –in particular at atmospheric pressure, as done in the present thesis– the main factor determining the dephasing of the rotational-vibrational Raman coherence on a ~100 ps timescale is the effect of inelastic collisions between the coherently rotating-vibrating molecules (the "*radiators*") and other collisional partners (the "*perturbers*"). The energy exchange in an inelastic collision determines a population transfer from the initial and final states, between which coherence was established by the (resonant) combined interaction with the pump and Stokes field. As discussed in the previous paragraph, one of the main advantages of the hybrid fs/ps CRS technique is the possibility of minimising the effect of molecular collisions, by probing the Raman coherence on a timescale of typically ∼10 ps.

Chapter 3

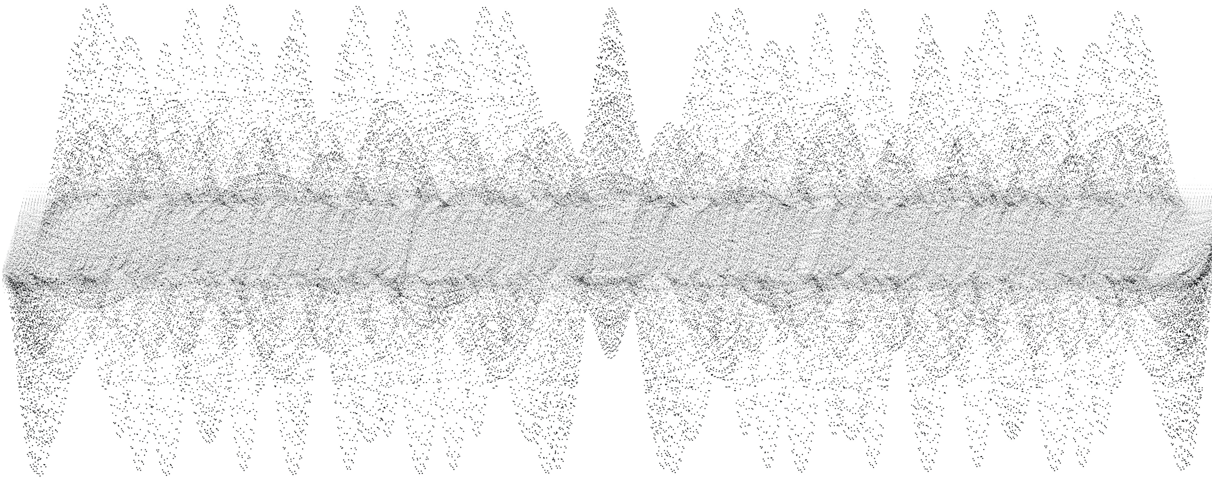

ULTRABROADBAND FS/PS CRS

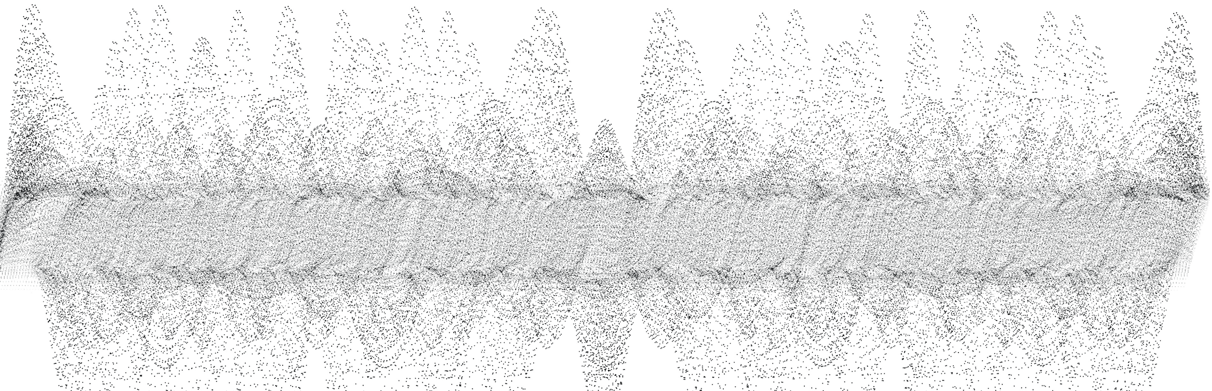

In the last decade, the use of pulse compression techniques to generate high-power laser pulses with duration down to a few fs allowed for extending the bandwidth of the fs pump/Stokes pulses to develop *ultrabroadband* fs/ps CRS [24].

The concepts of duration and bandwidth of a laser pulse, as well as the relationship between the two, have been somewhat presupposed in the previous chapter: a more proper introduction is given in the following. Consider the single-mode EM field in Equation (2.35) [32]: neglecting its spatial properties, the temporal evolution of $\boldsymbol{E}$ is described by a sinusoidal function with frequency ω and phase ϕ. Allowing for N frequencies (or modes) in the EM field, each with angular frequency ω_n and phase ϕ_n, the resulting electric field is [95]:

$$\boldsymbol{E}(t) = \sum_{n=0}^{N-1} \boldsymbol{E}_n \, e^{-i(\omega_n t + \phi_n)} + \text{c.c.} \tag{3.1}$$

If the modes have a fixed phase relationship, i.e. they are *coherent*, they give rise to a periodic interference pattern. A laser pulse can thus be defined as the localised constructive interference (also called a "*wave packet*") of the coherent modes in the emitted EM field centred at t_0. For an increasing number of modes, their destructive interference at $t \neq t_0$ leads to a faster dephasing of the wave packet, corresponding to a shorter duration of the laser pulse. The duration Δt of a laser pulse is thus inherently connected to the bandwidth $\Delta\omega$ of its spectrum, obtained by Fourier-transforming the time-domain electric field in Equation (3.1).

According to the Fourier uncertainty principle, a function and its Fourier transform cannot be simultaneously localised in the time-frequency domain [96]. Hence a laser pulse cannot have arbitrarily short duration and narrow bandwidth, their product (called the *time-bandwidth product*, TBP) having the lower bound:

$$\text{TBP} = \Delta t \, \Delta\omega \geq \text{c} \tag{3.2}$$

Where c is a constant determined by the functional form of the temporal and spectral envelopes of the laser pulse (e.g. $\text{c} = 2\ln 2/\pi$ for Gaussian pulses [95]). A laser pulse for which the inequality of Equation (3.2) is saturated is said to be *Fourier transform-limited* (TL): TL pulses thus have the shortest duration allowed by their bandwidth. Throughout the present thesis, laser pulses are assumed to be as Gaussian wave packets with spectrum:

$$\tilde{E}(\omega) = \frac{E_0 \, \Delta t}{2} \sqrt{\frac{\pi}{2\ln 2}} \, e^{-i\left[\frac{\Delta t^2}{8\ln 2}(\omega-\omega_0)^2 + \varphi(\omega)\right]} + \text{c.c.} \tag{3.3}$$

Where ω_0 is the *carrier frequency* of the optical pulse and φ is its *spectral phase.*

If φ is a linear function in ω –or, equivalently, ϕ is linear in time– Equation (3.4) describes a Gaussian TL pulse. In general, an optical pulse propagating through any optical material is subject to *group velocity dispersion* (GVD) or *chirp*, whereby non-linear components arise in the phase relationship between different frequency components. The spectral phase $\varphi(\omega)$ can then be expressed as a Taylor series about the carrier frequency as:

$$\varphi(\omega) = \sum_n k_{(n)} \frac{(\omega - \omega_0)^n}{n!} \tag{3.4}$$

where $k_{(n)}$ is the n^{th} derivative of the wave vector k with respect to the frequency ω.

In the two-beam fs/ps CRS technique employed in the present thesis, the excitation efficiency of the Raman modes is mapped by the spectral autocorrelation of the single combined pump/Stokes pulse, according to Equation (2.39). Assuming a TL pump/Stokes pulse with duration Δt, the resulting excitation bandwidth can be estimated as:

$$\Delta\omega_{\star} = \frac{\sqrt{2}\ln 2}{\pi c \Delta t} \tag{3.5}$$

With speed of light $c = 2.998 \cdot 10^{10}$ cm/s. Hence, in contrast to spontaneous Raman scattering, two-beam fs/ps CRS is inherently limited in the spectral window it can investigate by the bandwidth of the fs pump/Stokes pulse employed. The typical pulse duration provided by presently commercially-available regenerative fs laser amplifiers is in the order of a few tens of fs, such that the excitation bandwidth is limited to the *pure-rotational region* of the Raman spectrum up to ~500 cm^{-1}, as shown in Figure 3.1.

In the context of gas phase diagnostics, there is a number of motivations to extend the applicability of two-beam fs/ps CRS beyond the pure-rotational region:

- Pure-rotational CRS has been successfully applied in high-pressure combustion applications (e.g. in Ref. [97, 98]), but the collisional linewidths represent a source of uncertainty that can significantly impact CRS thermometry [99]. Time-resolved CRS alleviates this issue by probing the Raman coherence below the collisional timescale: effective collisional-independence of pure-rotational fs/ps CRS thermometry was demonstrated up to 15 bar by employing a 6.5 ps probe [73]. Nevertheless, the use of short ps probe pulses determines a poor spectral resolution, leading to the congestion of the pure-rotational region and to an unresolved rotational structure of the CRS spectra, especially for heavy molecules with small rotational constants such as CO_2 [83]. A possible strategy to overcome the congestion of the collisional-independent fs/ps CRS spectra at high pressure is to investigate the so-called *vibrational fingerprint region*[†] of the Raman spectrum, where the ro-vibrational Raman spectra of different species appear as isolated "fingerprints".
- Some molecules that play a significant role in combustion are not well-suited to be investigated by pure-rotational CRS. Important combustion products such as CO and H_2O have extremely low rotational Raman cross-sections, giving rise to weak CRS signals in flames [100, 101]. In the case of water vapour, CRS has been employed to investigate the ν_1 vibrational mode of H_2O (at ~3600 cm^{-1}) at temperatures as high as 2000 K [102–105]. A similar investigation by Nordström *et al.*, employing pure-rotational CRS, lead to the conclusion that "*due to the weak resonant signal, water vapor is an unsuitable candidate for CARS thermometry and relative concentration measurements in combustion*" [101]. This issue is even more relevant for spherical top polyatomic molecules such as CH_4, whose nuclear wave functions present a spherical symmetry such that they are not rotationally Raman active (in the ground vibrational state and neglecting vibrational-rotational coupling [106]).
- Another molecule of major interest in combustion, H_2, has an extremely large rotational constant, resulting in a pure-rotational spectrum which spans more than 1500

[†] The definition of the vibrational fingerprint region is borrowed from the literature on CRS microscopy, where the biologically-relevant Raman window is defined as Ω=500-3500 cm^{-1}, and the fingerprint region as Ω<1800 cm^{-1} [94].

cm^{-1} at flame temperatures, and the most significant rotational Raman transitions lie outside the pure-rotational Raman region [100], as shown in Figure 3.1.

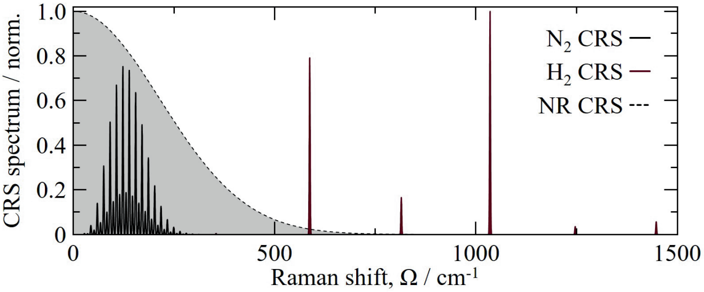

Figure 3.1: Pure-rotational two-beam fs/ps CRS. The implementation of two-beam hybrid fs/ps CRS employing commercially-available regenerative fs laser amplifiers, with typical pulse duration of a few tens of fs (35 fs represented here), limits the excitation efficiency to ~500 cm^{-1}. This fact hinders the application of gas-phase fs/ps CRS in those measurement scenarios where the investigation of a larger spectral window is necessary: one such case is the application of pure-rotational CRS to H_2, whose spectrum extends up to ~1500 cm^{-1} at T=700 K.

- In case of rotational-vibrational non-equilibrium, as often the case in plasma environments, it is necessary to independently measure the rotational and vibrational Boltzmann distributions. In line of principle the vibrational distribution is measured by the vibrational hot bands in the pure-rotational CRS spectrum, but their separation from the fundamental spectrum is typically <1 cm^{-1} [107], so that a probe duration much larger than ~15 ps is required to resolve the hot band structure. An alternative diagnostic approach is to simultaneously perform pure-rotational and ro-vibrational CRS: Dedic and co-authors demonstrated this in a dielectric barrier discharge by employing a dual-pump fs/ps CRS instrument [77], and later applied it to investigate the thermalisation dynamics in a plasma-assisted combustion environment [78].

Hence, there are clear benefits in increasing the instantaneous bandwidth of the fs pump/Stokes pulse to simultaneously interrogate the whole Raman spectrum. Tedder and co-authors, for example, employed a broadband ns dye laser with a bandwidth of ~18 nm FWHM to realise dual-pump CRS, simultaneously probing N_2, O_2, H_2, C_2H_4, CO and CO_2 over the region ~1000-2500 cm^{-1} [108].

Ultrabroadband fs/ps CRS makes use of a compressed *supercontinuum*[‡] as the pump/Stokes pulse to realise simultaneous spectroscopy in the pure-rotational and vibrational fingerprint regions of the Raman spectrum [24]. By extending the spectral excitation bandwidth up to ~4200 cm^{-1} (corresponding to vibrational frequency of H_2 [25]) all the fundamental Raman modes can be simultaneously excited by a single fs pump/Stokes pulse. Ultrabroadband fs/ps CRS can thus be applied to perform simultaneous thermometry and absolute concentration measurements of all the major molecular species present in the probed volume.

[‡] In the literature there is no clear-cut value for the pulse bandwidth defining a supercontinuum. In the present thesis a supercontinuum is defined as an optical pulse with bandwidth larger than ~40 nm, such that when compressed to the Fourier-transform limit its duration is lesser than 25 fs, comparable to the vibrational period of O_2 (see Paper I).

3.1 Pulse compression and ultrabroadband fs/ps CRS

The first application of ultrabroadband fs/ps CRS to gas-phase diagnostics employed a hollow-core optical fibre (or waveguide) filled with Ar at 0.15 MPa to generate the supercontinuum pulse [59]. Supercontinuum generation in hollow-core fibres relies on the third-order non-linear optical *Kerr effect*, whereby the refractive index of the optical medium the laser pulse propagates through depends quadratically on the amplitude of the electric field as:

$$n(t) = n_0 + \bar{n}_2 \langle E(t) \rangle^2 \tag{3.6}$$

Where n_0 is the linear refractive index of the optical medium. $\bar{n}_2$ is the non-linear refractive index, which can be computed from the third-order optical susceptibility of the medium as [31]:

$$\bar{n}_2 = \frac{3\chi^{(3)}}{4n_0} \tag{3.7}$$

The non-linearity of the refractive index introduces an intensity-dependent change in the phase of the optical pulse, called *self-phase modulation.* As the intensity of the electric field varies along the temporal envelope of the optical pulse, the non-linear time-dependent change in the phase $\phi(t)$ results in a variation of the instantaneous frequency: self-phase modulation thus generates new optical frequencies, broadening the fs laser pulse spectrum [31]. Additional dispersive optical elements, e.g. chirped mirrors, are usually employed to compress the pulse to its transform limit: few-cycle near-IR pulses down to ~5 fs can be generated thus [95].

Bohlin and Kliewer employed a hollow-core fiber and a set of chirped mirrors to generate a 7 fs compressed supercontinuum, which they employed as the pump/Stokes pulse in their two-beam quasi-phase-matching configuration [24]. Thereupon they demonstrated single-shot detection of the N_2, O_2, H_2, CO_2 and CH_4 CRS signals up to the C–H stretch region of the Raman spectrum at ~3200 cm^{-1}. They achieved a longitudinal resolution of ~500 μm, by adopting a crossing angle of 4° between the pump/Stokes and probe beams, and demonstrated 1D fs/ps CRS imaging over a ~3.5 mm measurement line. The same authors further developed gas-phase ultrabroadband fs/ps CRS imaging by achieving 2D hyperspectral imaging over the spectral range 0-4200 cm^{-1}, and employed this technique to investigate a H_2 jet flame, simultaneously recording the pure-rotational (S-branch) and ro-vibrational (Q-branch) spectra of H_2, as well as the ro-vibrational spectrum of O_2 [109]. Ultrabroadband fs/ps CRS imaging combines multiplex detection of combustion-relevant chemical species and spatio-temporally correlated measurement capability: this was demonstrated by 1D wideband chemical detection across a laminar flat premixed C_2H_4/air flame in Ref. [25]. The authors reported on 1D CRS measurements over the range 0-4200 cm^{-1} with a lateral resolution of 40 μm (as measured by the LSF of the imaging spectrometer), such that they could resolve the evolution of the chemical processes across the flame front, detecting reactants (e.g. C_2H_4, O_2) and products (e.g. CO), as well as intermediate species (e.g. H_2). As mentioned in the previous paragraph, besides providing wideband multiplex detection capability, ultrabroadband fs/ps CRS is the only viable approach to direct pure-rotational spectroscopy on H_2, whose spectrum spans more than 1500 cm^{-1} at flame temperatures. Building on the proof-of-principle of Ref. [109], Courtney *et al.* developed pure-rotational H_2 CRS thermometry, and quantified its performance against conventional pure-rotational N_2 CRS thermometry in a heated flow and in a diffusion flame on a Wolfhard-Parker slot burner [110].

Two-beam ultrabroadband fs/ps CRS has also been applied by researchers in Jena, to investigate the ro-vibrational spectrum of CO_2 at relatively high temperature (~900 K) and pressure (~8.5 bar) [111]: the experimental setup employed a hollow-core fibre and chirped mirrors to compress the pump/Stokes pulse to ~7 fs. The same research group has more recently demonstrated an alternative approach to ultrabroadband fs/ps CRS, based on the use of an optical parametric chirped pulse amplifier (OPCPA) [112]. In an OPCPA, a linearly chirped pump pulse is amplified in a non-collinear optical parametric amplifier (OPA) and subsequently compressed, providing a compressed supercontinuum output (<10 fs) with moderate pulse energy (~10 μJ) at high repetition rate (~100 kHz) [95]. In Ref. [112] the authors employed a single OPCPA to generated both the ultrabroadband 7 fs, 7.5 μJ pump/Stokes pulse and the 1.5 ps, 0.8 μJ probe pulse, at 200 kHz: they demonstrated CO_2 and H_2 CRS thermometry up to ~1100 K and CO concentration measurements in a gas oven. In a follow-up publication, the same experimental setup has recently been employed for the *in situ* investigation of carbon gasification in a CO_2 atmosphere [113]: the authors presented CO_2 thermometry and simultaneous CO concentration measurements during the gasification of carbonaceous feedstock.

An alternative approach for the efficient generation of ultrabroadband pump/Stokes pulses was introduced by Calegari and co-authors at Politecnico di Milano [114]: they demonstrated that fs laser-induced *filamentation* in Ar can result in the compression of near-IR fs pulses down to ~10 fs, and excite the ro-vibrational Raman modes of CO_2 at ~1400 cm^{-1} and of H_2 at ~4200 cm^{-1}. Fs laser-induced filamentation is the non-linear propagation of ultrashort laser pulses in transparent optical media [115] due to a combination of non-linear optical phenomena, in particular Kerr self-focusing and laser-induced ionisation due to multi-photon absorption or electron quantum tunneling [116]. In this regime, as the laser pulse propagates in the resulting plasma filament it experiences *self-compression* to a few- or even single-cycle pulse [117–119] (where a near-IR single-cycle pulse with a carrier wavelength of 800 nm has duration ~2.5 fs [120]). Researchers at Temple University combined fs laser-induced filamentation in air with hybrid fs/ps CRS, in a novel approach they called "*filament-assisted impulsive Raman spectroscopy*" (FAIRS) [121]. A remarkable novelty in their approach to ultrabroadband fs/ps CRS was the *in situ* use of the filament to compress the pump/Stokes pulse and excite the ro-vibrational wave packets of the target molecules [122].

3.2 LIMITATIONS OF ULTRABROADBAND FS/PS CRS

The present thesis concerns the development of ultrabroadband fs/ps CRS for the investigation of chemically reactive flows, employing *in situ* fs laser-induced filamentation. The experimental methodology developed in Ref. [121] is here identified as a viable approach to solve one of the standing limitations to the applicability of ultrabroadband fs/ps CRS in measurement scenario of practical interest: namely, the necessity of controlling the effective excitation bandwidth at the measurement location in optically-accessible measurement applications, such as high-pressure combustion chambers.

As a matter of fact, because of the significant GVD of its spectral components, the transmission of a compressed supercontinuum pulse through a thick optical window is a challenging engineering problem. The spectrochronographic properties of the pulse and the dispersion characteristics of the optical material must be known beforehand to effectively compensate the dispersion of the pulse as it propagates to the measurement location (e.g. by employing chirp mirrors). Additional factors can nonetheless change the GVD of the pulse in real measurement applications, such as the vibrations and the thermal and pressure loads on the optical windows of e.g. model rocket combustors, which introduce local strain in the optical material and change its refractive index. One such example is found in the recent application of two-beam fs/ps CRS thermometry in the post-detonation fireball produced by a commercial detonator and contained in a polycarbonate housing [123]. The authors reported a significant amount of non-linear chirp being introduced by the 13 mm-thick fused silica optical window providing optical access to the explosion containment chamber, such that the coherent excitation of the pure-rotational Raman spectrum of N_2, provided by their 35 fs pump/Stokes pulse, was limited to ~200 cm^{-1}. The situation described here could only be worse in the case of ultrabroadband two-beam fs/ps CRS, as supercontinuum pulses are inherently more "fragile", to the extent that a larger bandwidth results in a stronger dispersion of its spectral components, as understood by Equation (3.4). Hence, increasing the bandwidth of the fs pump/Stokes pulse could paradoxically reduce the effective Raman excitation bandwidth behind the optical window. Fs laser-induced filamentation offers a straightforward solution to this issue as relatively longer fs pulses, less sensitive to GVD, can be transmitted through thick optical windows and filamentation can be used *in situ* to compress them to a supercontinuum. In the present text, this strategy is named "*in situ* generation/*in situ* use" of the ultrabroadband coherent Raman excitation.

Achieving an ultrabroadband coherent excitation of the rotational-vibrational Raman modes in the probe volume represents only half the problem, when it comes to the robust application of ultrabroadband fs/ps CRS for quantitative measurements in chemically reactive flows. In order to have a meaningful comparison between the experimental CRS spectra and the theoretical models, and perform quantitative measurements, it is necessary to know the exact spectral excitation profile and adopt the spectral referencing protocol introduced in Section 2.3.1. This is typically done experimentally by measuring the NR CRS, which maps the excitation efficiency as a function of the Raman shift, as shown in Figure 3.1. The conventional experimental protocol thus requires performing the CRS experiment and sequentially measuring the NR CRS spectrum, generated in an optical material with no Raman-active modes in the spectral region investigated. This approach nevertheless cannot account for possible shot-to-shot fluctuations in the bandwidth of the fs pump/Stokes excitation pulse, since the resonant and NR CRS signals acquired sequentially are completely uncorrelated. The adoption of regenerative fs laser amplifiers, with a significantly more stable spectral output than older ns laser systems, improved the single-shot precision of CRS thermometry, reaching [25] (and recently surpassing [124, 125]) the "dream limit" of 1% at the high temperatures typically found in the flame products. On the other hand, typical pulse compression techniques employed to realise ultrabroadband fs/ps CRS can suffer from a reduced shot-to-shot spectral stability of the compressed supercontinuum. This was observed, for example, in the comparison between pure-rotational two-beam N_2 CRS thermometry realised employing a 45 fs pump/Stokes pulse and the 7 fs output of a hollow-core fibre, where the single-shot thermometric precision was reduced to ~5% [25]. In addition, the conventional *ex situ* referencing protocol cannot account for local changes in the GVD along the pump/Stokes beam path that may arise in chemically reactive flows, e.g. due to dynamic temperature gradients in the combustion environment. The research presented hereinafter addresses these limitations by introducing an alternative experimental protocol to measure the spectral excitation efficiency *in situ*, concurrently to the generation of the ultrabroadband fs/ps CRS signal. The uncertainty arising due to shot-to-shot fluctuations in the pulse self-compression and to the local boundary conditions to the pulse propagation in the filamentation regime within the reactive flow can thus be compensated by the referencing protocol.

Alongside the development of a robust experimental protocol, the practical use of ultrabroadband fs/ps CRS for quantitative gas-phase diagnostics requires the availability of spectroscopic models, ideally for all the Raman-active species significantly present in the probe volume. While such models have long been developed, validated and employed for simple diatomic molecules –N_2 being a prime example– the extension to heavier, more complex, polyatomic molecules is far from being a reality. Paper I detailed the development of one such model for the ro-vibrational spectrum of CO_2 and its validation at temperatures as high as 2100 K. The time-domain CRS code, similar to those developed by Kerstan *et al.* [111] and Gu *et al.* [67], includes the contribution from 180 rotational states and more than 180 vibrational states. The total number of resulting Raman transitions is still rather modest, compared to the millions of ro-vibrational transitions that need to be considered when modelling the CRS spectrum of even the simplest hydrocarbon, CH_4 [126]. In Paper IV, a time-domain model for the ro-vibrational Raman spectrum associated to the second normal vibrational mode (ν_2) of CH_4 –including more than 10 million Raman lines– is discussed and validated at temperatures up to ~800 K.

3.3 Research objectives

The goal of the doctoral research here reported is to overcome the three main limitations of ultrabroadband fs/ps CRS as gas-phase diagnostic tool, as they are elaborated upon in the previous paragraph. In this sense, the work reported on in Papers I to IV addressed three main research questions:

1. *How can fs laser-induced filamentation be employed in situ as a coherent light source to robustly perform ultrabroadband fs/ps CRS in chemically reacting flows behind thick optical windows?*
2. *To what extent can the performance of fs/ps CRS thermometry be improved by measuring the spectral excitation efficiency in situ?*
3. *To what extent can phenomenological time-domain CRS models be employed to perform high-fidelity fs/ps CRS thermometry on major combustion species in the vibrational fingerprint region of the Raman spectrum:* H_2*,* O_2*,* CO_2*, and* CH_4*?*

The first question can be further articulated into the following sub-questions:

1.1 What is the impact, on the pulse self-compression, of the local boundary conditions to fs laser-induced filamentation in a chemically reacting flow?

1.2 How does the transmission through a thick optical material affect the spectrochronographic properties of the fs excitation laser pulse? How do these, in turn, impact the pulse self-compression via fs laser-induced filamentation?

1.3 To what extent it is possible to control the GVD of the fs excitation laser pulse to optimise the *in situ* generation of the compressed supercontinuum?

These questions are addressed in Papers I and III, a detailed discussion is provided in Chapter 4.

The second research question is addressed in Papers II and III by answering the following:

2.1 How large is the measurement uncertainty borne into fs/ps CRS thermometry by the *ex situ* measurement of the spectral excitation efficiency?

2.2 Can a novel experimental protocol be devised for the *in situ* referencing of the spectral excitation efficiency? How can such a protocol be implemented in practice?

2.3 How much can this *in situ* referencing protocol improve the performance of ultrabroadband fs/ps CRS with *in situ* filamentation?

Chapter 5 discusses this novel experimental protocol.

The development and validation of time-domain models for pure-rotational H_2 and ro-vibrational O_2, CO_2, and CH_4 fs/ps CRS thermometry is discussed in Chapter 6.

Chapter 4

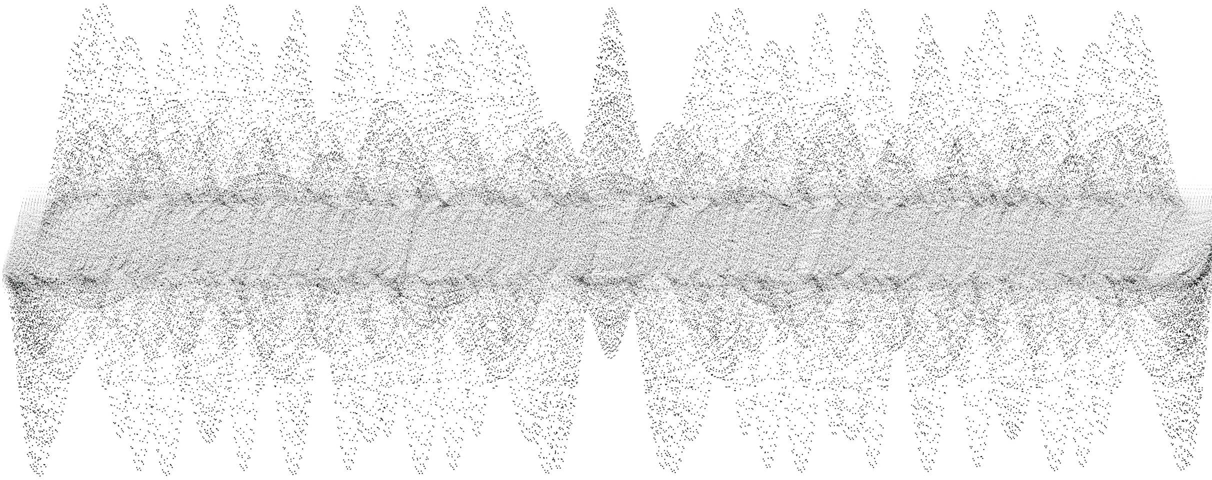

ULTRABROADBAND FS/PS CRS WITH IN SITU FILAMENTATION

The present chapter addresses the first research question, concerning the possible in situ use of fs laser-induced filamentation as a coherent light source to realise ultrabroadband fs/ps CRS behind thick optical windows. The development of ultrabroadband fs/ps CRS with in situ filamentation is discussed and the single-shot detection of the ro-vibrational Raman spectra of O_2 *and* CO_2 *is demonstrated in a canonical hydrocarbon flame. Upon the insertion of a thick optical window on the path of the fs excitation laser beam, the in situ generation of the compressed supercontinuum is proved and proof-of-principle ultrabroadband fs/ps CRS is demonstrated in two laboratory flames.*

Part of the results discussed in this chapter have been published in Papers I and III.

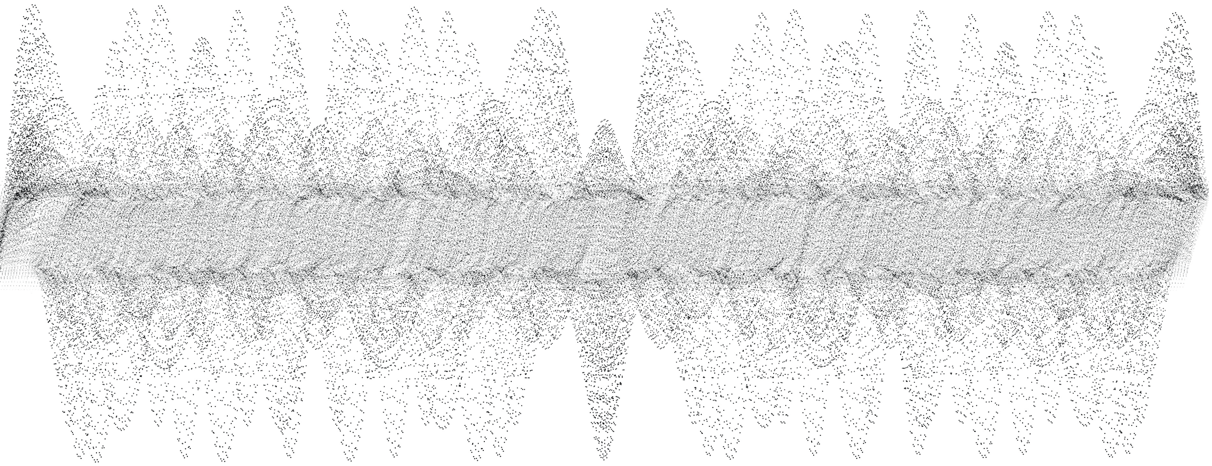

The first step towards the development of ultrabroadband fs/ps CRS for gas-phase chemically reactive flows is the implementation of *in situ* fs laser-induced filamentation as the ultrabroadband coherent light source. A detailed description of the complex physics of fs laser-induced filamentation is beyond the scope of the present text and the reader is referred to the specialised literature, such as Ref. [115, 116]. Only a brief overview of the filamentation of near-IR fs laser pulses in air is provided in the following.

The key phenomenon underpinning fs laser-induced filamentation is the aforementioned optical Kerr effected. In this third-order non-linear optical process the intensity of the electric field is large enough to determine a change of the refractive index of the medium the laser pulse is travelling through. When the non-linear component of the refractive index $\bar{n}_2$ dominates over the linear one, the propagation of the laser pulse is determined by its own temporal and spatial intensity profiles. The intensity of a typical laser beam is not homogeneous over it cross-section, but its spatial profile is usually described by a Gaussian function as depicted in Figure 4.1(a). When focused through a convex lens with focal length "f" the beam converges to a minimum waist radius defined by the so-called *Abbe diffraction limit*:

$$w_0 = \frac{\lambda}{4n\sin\left[\arctan\left({}^{d}/_{2\mathrm{f}}\right)\right]} \tag{4.1}$$

Where λ is the laser wavelength and d is the beam diameter before the lens. In the following this is referred to as the "linear" propagation regime for the fs laser pulse.

In optical Kerr effect the refractive index in Equation (4.1) depends on the local intensity of the electric field: the non-linear contribution to the refractive index thus depends on the radial coordinate across the beam profile, i.e. $n_2 = n_2(r,t)$. The resulting inhomogeneity of the refractive index makes the medium behave as a lens, determining the *self-focusing* of the beam via a positive feedback mechanism. As the beam intensity increases with z, moving towards the focal point, so does the Kerr effect enhancing the beam focusing itself.

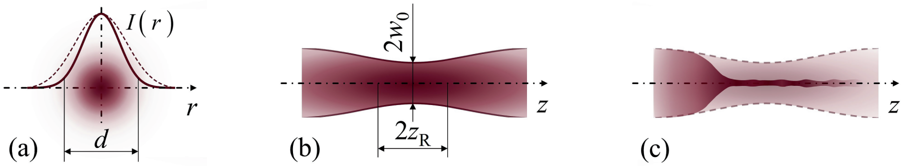

Figure 4.1: Linear and non-linear focusing of a fs laser beam. (a) Gaussian distribution of the field intensity over the beam cross-section, $I(r)$. The beam diameter is here defined as the distance between the points where $I(r)$ drops to $1/e^2$ of its maximum value. (b) Linear focusing of a Gaussian beam: the light converges to the minimum spot size w_0 allowed by the diffraction limit at the focal plane of the focusing optics. z_R is the corresponding *Rayleigh range*, over which the beam can be considered as collimated. (c) Non-linear focusing of the beam due to the optical Kerr effect: the local refractive index of the medium is modified according to $n(r){=}n_0{+}\bar{n}_2I(r)$ leading to a lensing effect that accelerates the beam focusing. This acceleration further steepens the intensity profile increasing the change in the local refractive index and thus the beam focusing and leading to the beam collapse.

The high local intensity of the electric field leads to additional non-linear optical effects, namely multi-photon ionisation and electron quantum tunneling ionisation. The generation of a plasma further changes the local properties of the optical medium, introducing an additional contribution to its refractive index:

$$n(r,t) = n_0 + \bar{n}_2 \langle E(r,t) \rangle^2 - \frac{\rho(r,t)}{2\rho_c} \tag{4.2}$$

With ρ being the local free electron density in the plasma; $\rho_c \doteq \epsilon_0 m_e \omega_0^2 / e^2$ is the critical plasma density [115], at which the plasma becomes opaque at the frequency ω_0 (with m_e and e being the electron charge and mass, respectively). As the plasma generation is dominated by non-linear optical field ionisation, its contribution to the refractive index is also non-linear in the electric field amplitude, and it counteracts the non-linear optical Kerr effect, determining a defocusing of the light and preventing its complete spatial collapse. There is a lag between the generation of the plasma and its defocusing effect on the laser beam: the leading (fore) portion of the pulse photoionises the gas medium, while the trailing (aft) portion experiences the variation of the refractive index due to the free electrons.

The propagation of a fs laser pulse in the filamentation regime is thus the result of the ensuing dynamic equilibrium of the non-linear refractive index terms in Equation (4.2). Kerr-self focusing increases the irradiance of the pulse leading to the generation of the plasma, when the plasma density is large enough for its effect to prevail the beam is defocused, this in turns reduces its irradiance and the plasma density to the point where the Kerr self-focusing term dominates again. This cycle of focusing and defocusing, as illustrated in Figure 4.2(a), is what determines the generation of the plasma filament, which acts a waveguide for the laser light, and goes on until the energy losses due to multi-photon absorption and inverse Bremsstrahlung determine the filament collapse and the final divergence of the beam in Figure 4.2(b).

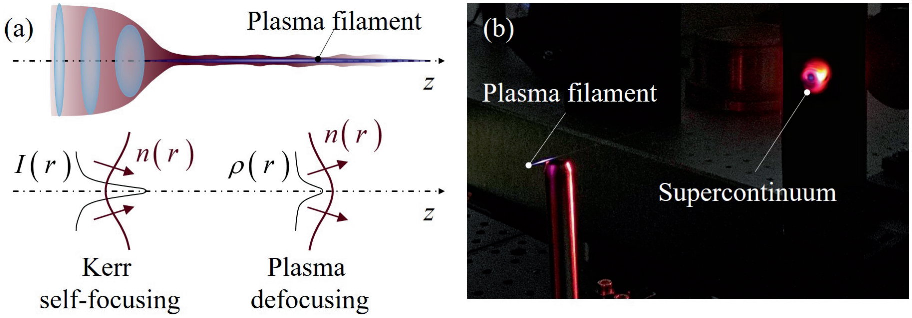

Figure 4.2: Fs pulse propagation in the filamentation regime. (a) Schematic of the focusing-defocusing cycle experienced by the beam in the filament propagation. The steep radial profile of the field intensity results in Kerr-self focusing, with the local optical gradient leading to the spatial collapse of the beam. This collapse is arrested by the defocusing effect of the plasma medium. (b) Picture of the filament generated in ambient air and of the supercontinuum output imaged on a plate: the coloured pattern emerging of the filament is the result of the self-phase modulation of the fs pulse, broadening the spectrum of the near-IR pulse such that it covers the whole visible region of the EM spectrum.

In the description above the propagation of the light in the filament is explained by the spatial distribution of the non-linear refractive index components over the cross-section of the laser beam. As shown by Equation (4.2) these terms also vary in time, leading to a time-dependent change in the phase of the different frequency components across the bandwidth of the fs laser pulse. Optical Kerr effect thus entails the self-phase modulation of the pulse, whereby its instantaneous frequencies evolve in time according to the equation [115]:

$$\omega(t) = -\frac{\partial\phi}{\partial t} \approx \omega_0 - \frac{n_2\omega_0}{c} z \frac{\partial I(r,t)}{\partial t} \tag{4.3}$$

With z being the propagation distance in the Kerr medium. Self-phase modulation results in the generation of new frequencies, proportionally to the slope of the pulse $\partial I/\partial t$: the leading portion of the pulse (for which $\partial I/\partial t < 0$) generates lower (red-shifted) frequencies, while the trailing portion generates higher (blue-shifted) frequencies. Similarly, the evolution of the free electron density with the propagation of the pulse in the filament determines a modulation of the pulse frequencies as [116]:

$$\omega(t) \approx \omega_0 + \frac{2\pi z e^2}{c m_e \omega_0} \frac{\partial\rho(r,t)}{\partial t} \tag{4.4}$$

The leading portion of the pulse obviously always travels in a neutral gas medium and only experiences a red broadening. The trailing portion of the pulse, on the other hand, experiences both self-phase modulation and the non-linear modulation in the plasma medium: both these effect contribute to a large broadening of the pulse to higher frequencies. Finally, this broadening of the pulse spectrum leads to its self-compression, as the newly-generated frequency components travel at different speed across the filament: in particular, the blue-shifted components generated in the trailing portion of the pulse travel faster in a plasma medium with a lesser refractive index according to Equation (4.2).

4.1 *IN SITU* GENERATION AND USE OF THE ULTRABROADBAND RAMAN EXCITATION

In the present doctoral research fs laser-induced filamentation is employed as the compressed supercontinuum generation mechanism to achieve an ultrabroadband excitation of the Raman-active modes in gas-phase combustion flows. A novel *in situ* generation/*in situ* use approach is adopted, whereby the filament is produced in close vicinity of the measurement location, introducing the CRS probe volume after the end of the filament. The compressed supercontinuum output by the filament inherently acted as a combined pump/Stokes pulse, exciting the coherent ro-vibrational motion of the molecules over a spectral region determined by the duration of the supercontinuum pulse itself.

Section 4.1.1 describes the experimental implementation of ultrabroadband fs/ps CRS, with *in situ* filamentation as the supercontinuum generation mechanism. A detail description of the optical setup is provided: the same setup served, with minor adjustments, in all the experiments reported in the present text. The use of ultrabroadband CRS with *in situ* filamentation as a combustion diagnostic tool is first demonstrated by performing ro-vibrational CRS simultaneously on CO_2 and O_2 in a laboratory flame.

The peculiar focusing properties of a fs laser pulse in the non-linear filamentation regime pose a challenge when it comes to the estimation of the CRS probe volume. A novel methodology for the characterisation of the supercontinuum divergence out of the filament and the resulting probe volume dimensions for ultrabroadband fs/ps CRS is introduced in Paper I. This is discussed in detail in Section 4.1.2.

Section 4.1.3 finally discussed the impact of the local composition and temperature of the gas-phase medium on the filamentation process, and on the resulting self-compression of the fs laser pulse. Experimental evidence is presented pointing to a strong dependence of *in situ* filamentation on the local boundary conditions in combustion flows.

4.1.1 Experimental setup for ultrabroadband CRS

The fs/ps CRS instrument employed in the present research was originally designed to perform pure-rotational fs/ps CRS 1D imaging in high-temperature environments, as detailed in Paper V. As shown in Figure 4.3, the optical setup can be roughly organised in two main sub-systems: the pulse generation on the left-hand-side and the signal detection on the right-hand-side.

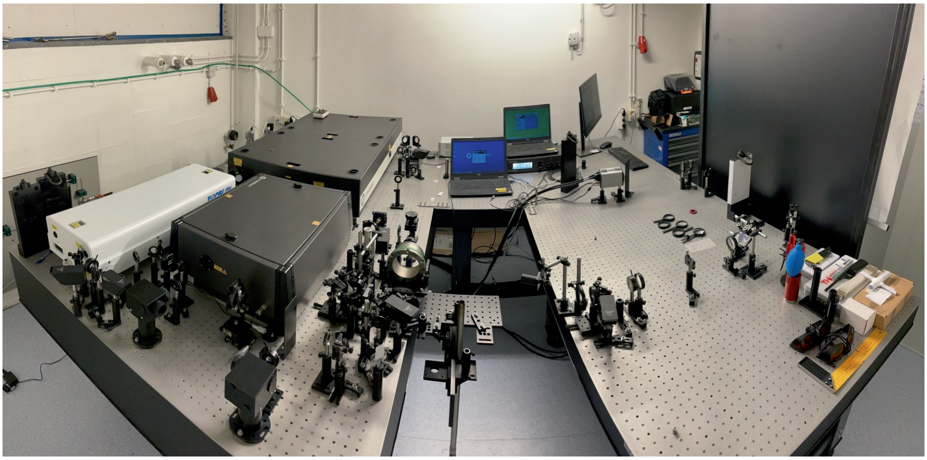

Figure 4.3: Picture of the experimental setup employed to realise ultrabroadband fs/ps CRS. The optical table on the left-hand side of the picture accommodates the laser system and the optics used to generate the fs pump/Stokes and the ps probe pulses, and to deliver them at the measurement location. On the right-hand side is the coherent imaging spectrometer employed to collect and record the CRS spectra.

A single regenerative Ti:Sapphire CPA system (Astrella, Coherent) is employed as the main coherent light source: this provides fs laser pulses with a bandwidth of 22.6 nm at 807 nm, a total pulse energy of ~7.5 mJ, and a repetition rate of 1 kHz. The output of the amplifier is split in two portions: a 65% split is compressed to a ~35 fs TL pulse and fed to a second-harmonic bandwidth compressor (SHBC, Light Conversion), which converts the fs pulse in a frequency-doubled (i.e. 403 nm) ~5 ps pulse, serving as the narrowband probe pulse. A 4f-pulse shaper is used to clean the spectrum of the probe pulse from the spectral sidebands originating from third-order chirp terms in the second-harmonic bandwidth compression of the fs pulse [125, 127, 128]. The pulse shaper consists of two high-resolution transmission grating (3039 lines/mm, Ibsen Photonics), two cylindrical lenses (focal length, f:=300 mm) and a mechanical slit in a 4f arrangement, as shown in Figure 4.4. By changing the slit width in the focal plane the bandwidth of the ps pulse can be tuned in the range ~2.7-5 cm^{-1}, changing the pulse duration in the range ~5-13 ps, with a corresponding pulse energy of ~1.2-0.3 mJ respectively [125]. A 400 nm half-wave plate is inserted at the output of the SHBC to optimise the diffraction efficiency of the transmission gratings in the pulse shaper (>90% for S-polarised light), while a thin film polariser ensures the linearity of the probe polarisation and a second half-wave plate controls its polarisation angle before the last focusing lens. The remainder of the CPA output energy is temporally compressed in an external grating compressor, whose position can be adjusted to control the amount of linear chirp in the fs pulse: negative chirp can thus be introduced in the pulse to compensate for the GVD arising along the beam path before the measurement location. The external compressor played a critical role in the optimisation of the supercontinuum generation via *in situ* filamentation behind thick optical windows, as is thoroughly discussed in Section 4.2. A combination of 800 nm half-wave plate and thin-film polariser is employed to tune the pulse energy and a second half-wave plate, placed after the polariser, controls the polarisation angle of the pump/Stokes pulse. The relative timing between the ps probe the fs pump/Stokes pulses is controlled by an automated delay line, composed of a retro-reflector mounted on a high-finesse translation stage, ensuring a <10 fs resolution in the timing of the pump/Stokes pulse relative to the probe.

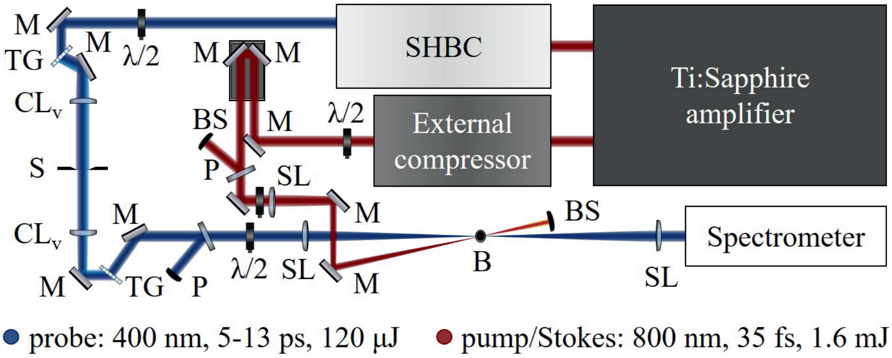

Figure 4.4: Schematic of the experimental setup employed to perform ultrabroadband two-beam fs/ps CRS. A single Ti:sapphire regenerative amplifier is employed to generate the 35 fs pump/Stokes and the ~5-13 ps probe pulses. *In situ* fs-laser induced filamentation is employed as the supercontinuum generation mechanism: the ultrabroadband pump/Stokes beam is crossed by the probe beam at a distance of ~4 mm after exiting the filament. TG, transmission grating; S, slit; CL, cylindrical lens with vertical (v) symmetry axes; $\lambda/2$, half-wave plate; B, burner; P, polariser; SL, spherical lens; M, mirror.

In Papers I, III and IV a 500 mm spherical lens is used to focus the fs beam and generate the filament: the beam has a diameter of ~10.6 mm and the beam waist at the focus is measured[*] to be ~60 μm, with a beam quality factor M^2 = 1.2. The peak irradiance of the pulse is thus computed to be >400 TW/cm^2: this results in the generation of a ~12.6 mm filament extending before the focal plane of the focusing lens.

Figure 4.5(a) shows a single-shot image of the filament in air, acquired with a commercial CMOS camera (Nikon D7500): the visible emission is mostly due to isotropic fluorescence

---

[*] This measurement is performed by attenuating the pulse energy to ~50 μJ, so as to avoid the onset of filamentation.

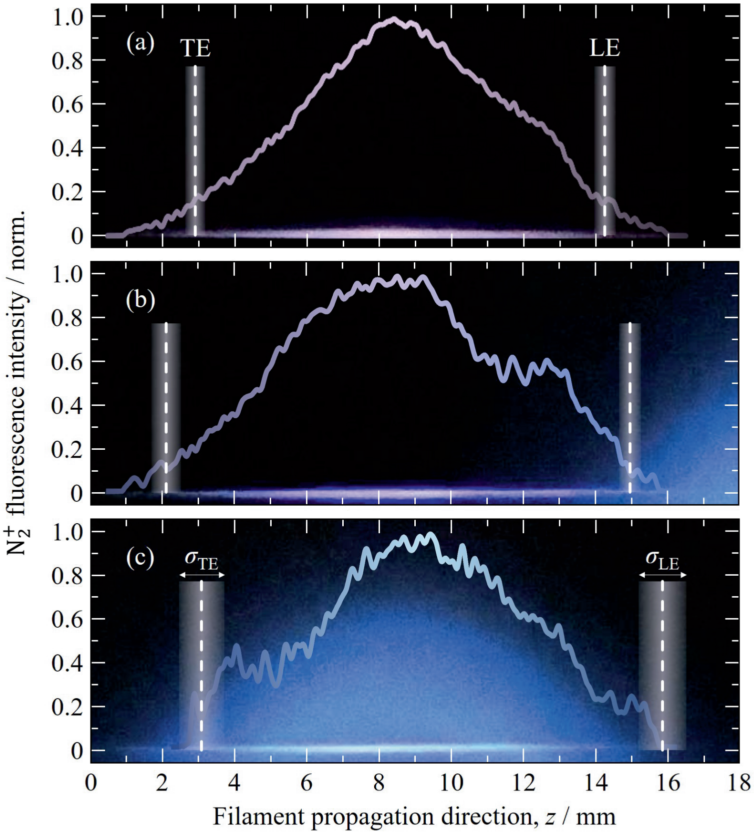

Figure 4.5: Plasma filament generated in air and in a hydrocarbon flame. (a) Filament generated in air by focusing a 35 fs ~1.5 mJ laser pulse through a 500 mm spherical lens. The visible emission from the filament is fluorescence of the N_2^+ ions at 391 and 428 nm. (b) Filament generated by the same pulse and focusing lens, partly extending in the hot products of a laminar premixed CH_4/air M-shaped flame. (c) Filament generated completely inside the products of the laminar flame. TE, trailing edge; LE, leading edge. The shaded areas represent the spatial jitter of the filament, estimated as the standard deviation (σ) of the TE and LE location measured shot-to-shot.

from the nitrogen cations (N_2^+), and the filament length is measured between the location where the integrated fluorescence trace drops to $1/e^2$ of the maximum value. A set of 250 single-shot images of the filament is acquired to assess the spatial jitter of the filament shot-to-shot: this is measured to be ~300 μm for the leading edge (LE) of the filament and ~330 μm for its trailing edge (TE).

The feasibility of ultrabroadband fs/ps CRS with *in situ* filamentation as a combustion diagnostics tool is firstly assessed by investigating the interaction of the filament and a typical hydrocarbon flame. Figure 4.5(b) shows a single-shot image of the filament generated (with the same pulse energy and under the same focusing conditions) partly inside the hot products of a laminar premixed CH_4/air flame, stabilised as a M-shaped flame on a Bunsen burner (the burner characteristics are detailed below). The focusing lens is then moved forward so as to push the filament completely inside the flame, as shown in Figure 4.5(c). The first remarkable observation is that the filament propagation is largely unaffected by the step temperature gradient and change in gas composition when generated partly or entirely inside the flame. As a matter of fact the filament length is measured to be ~13.1 mm in Figure 4.5(b) and ~13.0 mm in Figure 4.5(c). It should be noted that these latter measurements are also affected by an additional uncertainty in the definition of the filament edges due to the background emission from the flame chemiluminescence, which is subtracted in the image post-processing. This probably explains the larger spatial jitter, measured to be respectively ~440 μm and ~390 μm for the TE and LE of the filament in Figure 4.5(b), and ~700 μm and ~670 μm in Figure 4.5(c).

The fact that the filament propagation is not interrupted by the large drop in the effective refractive index in the hot product gases of the flame can be understood by this change affecting the optical Kerr effect and the plasma density to a similar extent. Both the beam self-focusing and the photo-ionisation processes discussed in the previous paragraph depend non-linearly on the gas density. The dynamic equilibrium of the Kerr self-focusing and plasma defocusing is thus maintained as the filament propagates through the flame. This is not to say, anyhow, that all the phenomena connected to fs laser-induced filamentation are unaffected by the presence of the flame. The reduction in the effective refractive index of the medium is indeed expected to affect the self-phase modulation of the pulse and thus the supercontinuum generation and its compression. This is also confirmed by the larger energy in the supercontinuum pulse output generated in the flame than in room-temperature air, as shown in Figure 4.6. Part of the input pulse energy is lost in the generation of the plasma medium so that the energy of the supercontinuum pulse is always lesser than the in the input one. A clear linear dependence is found between the input and output values. In ambient air the conversion efficiency in the supercontinuum generation via *in situ* filamentation is measured to be ~82%, while in the hot flame products this value increases to ~86%, attesting to the reduced photo-ionisation of the medium. The effect of the temperature and composition of the gas-phase medium on the pulse compression via

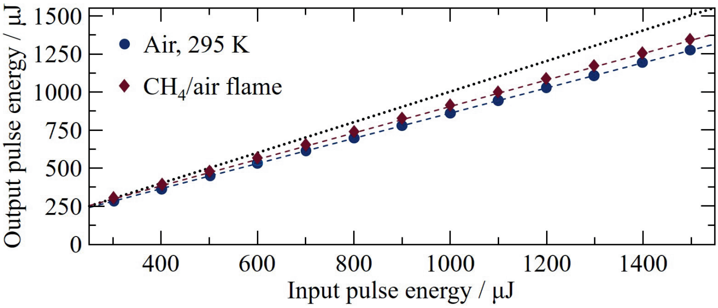

Figure 4.6: Power scaling of the compressed supercontinuum output by *in situ* filamentation in room-temperature air and in the products of a laminar premixed CH_4/air flame. The pulse energy is measured after the filament collapse and shows a linear dependence on the input fs laser pulse energy in the range 0.3–1.5 mJ. The dotted line represents the ideal case if no energy were lost in the filamentation process. Figure reproduced from Mazza *et al.* [26].

in situ filamentation is further discussed at the end of the present chapter.

The compressed supercontinuum output by the filament is employed as the combined pump/Stokes pulse in a cross-beam quasi-phase-matched configuration, where the probe beam, focused by a 300 mm spherical lens, is crossed at a shallow angle (~3-5°) by the pump/Stokes. The focusing lens for the fs laser beam is mounted on a linear translation stage, so as to control the longitudinal position of the filament with respect to the probe volume: the probe beam path intersected the output of the filament ~3-5 mm after its LE. The distance between the filament and the probe volume is determined as a trade-off between the maximisation of the CRS signal intensity and spatial resolution of the CRS measurements on the one hand, and the necessity to avoid a significant amount of ionisation inside the probe volume on the other. It should be noted that the optical Kerr effect determines a shift of the laser focus towards the focusing lens, such that the filament extends "backwards" with respect of the nominal focal plain of focusing lens. This behaviour is extremely beneficial when it comes to the *in situ* use of the filamentation to perform ultrabroadband CRS: the distance between the filament and the probe volume can be determined beforehand and is maintained (within the spatial jitter of the filament) even if the pulse energy is increased, as the filament grows backwards.

On the detection side of the optical setup, the ultrabroadband CRS signal is collimated by a 400 mm spherical lens and collected in a home-built spectrometer. This consists of:

- angle-tunable band-pass filter (bandwidth: ~1110 cm^{-1} FWHM, edge steepness: ~45 cm^{-1} 10-90%, Semrock) to reject the probe beam which almost co-propagates with the CRS signal in the shallow-angle two-beam fs/ps CRS configuration;
- spatial filter, composed of two 200 mm spherical lenses in a 2f arrangement and a mechanical slit placed at the focal plane, which suppresses the spatially-coherent amplified spontaneous emission (ASM) from the fluorescent N_2^+ ions in the filament (see Paper VI);
- Glan-laser polariser (Thorlabs), employed as the polarisation gate of the spectrometer to suppress the residual probe or to measure the polarisation of the CRS signal as a function of the input polarisation of the probe and pump/Stokes pulses;
- high-groove density transmission grating (3039 lines/mm, Ibsen Photonics) and imaging lens, the focal length of the lens is changed in different experiments to adjust the spectral window and resolution;
- sCMOS detector (Zyla 4.2, Andor).

The spectrometer configuration is adapted to different needs in the various experiments reported in Papers I to IV: the relevant modifications are detailed in the following chapters. Chapter 5 in particular describes the design of the polarisation-sensitive coherent imaging spectrometer developed for 1D CRS measurements, as discussed in Paper II.

The supercontinuum generated via *in situ* filamentation coherently excites all the rotational-vibrational Raman modes of the gas-phase medium up to ~2000 cm^{-1}, resulting in the coherent scattering of the narrowband probe pulse on both the Stokes and anti-Stokes sides. Figure 4.7 shows the corresponding NR CARS and CSRS signals over the spectral window 1100-1600 cm^{-1}. The CARS signal is measured to be ~20 times smaller than the CSRS one at 1553 cm^{-1}, i.e. at the location of the fundamental vibrational mode of O_2 (see Section 6.2.1). The theoretical $I_{\mathrm{CARS}}/I_{\mathrm{CSRS}}$ ratio, on the other hand, is predicted to be 1.29, owing to higher carrier frequency of the CARS signal in accordance with Equation (2.32) (see

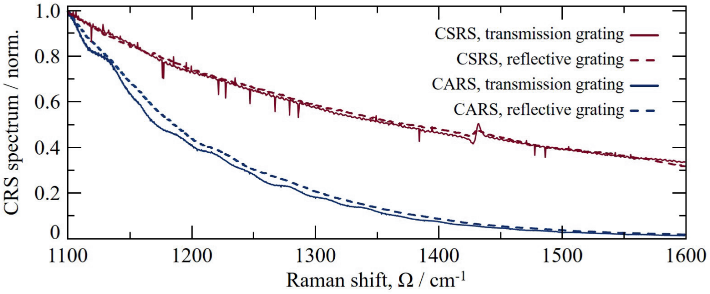

Figure 4.7: Ultrabroadband CARS and CSRS. The ultrabroadband NR CRS signals generated with *in situ* filamentation in Ar, and acquired in the spectral range 1100-1600 cm^{-1} on the anti-Stokes and anti-Stokes sides of the probe line. Two different diffraction gratings are tested: a high-groove density transmission grating (solid lines) and a ruled reflective grating (dashed lines). The CSRS signal is more than one order of magnitude stronger than the CARS signal at 1553 cm^{-1}. The small spectral feature visible at ~1430 cm^{-1} in the NR CSRS spectra is due to the coherent emission at ~428 nm from the electronically-excited N_2^+ ions in the filament [37]. Figure reproduced from Mazza *et al.* [26].

also Ref. [129]). Two different diffraction gratings are tested to disperse the CARS and CSRS signals in the spectrometer: (i) the above-mentioned high-groove density transmission grating, and (ii) a lower-groove density ruled reflective grating (1200 lines/mm, Thorlabs). The corresponding spectra in Figure 4.7 show a perfect agreement. The much lesser intensity of the detected ultrabroadband CARS signal could be partly explained by the transmission efficiency of the different optics employed in the spectrometer. Employing a ~400 nm probe, the CSRS signal is generated at lower frequencies in the visible portion of the EM spectrum, while the CARS signal has a blue shift towards the ultraviolet, where the transmission efficiency of the optical elements is typically quite poor. In order to maximise the signal intensity, especially at high temperature in combustion flows, ultrabroadband fs/ps CSRS is preferred in all the ultrabroadband experiments reported in Papers I, III and IV.

Ultrabroadband fs/ps CRS with *in situ* generation/*in situ* use of the compressed supercontinuum is demonstrated in Paper I by the single-shot detection of the ro-vibrational Raman spectra of O_2 and CO_2 in the laminar premixed CH_4/air flame shown in Figure 4.8(a). The flame is provided on a Bunsen burner, consisting of a seamless stainless steel pipe of ~12 mm inner diameter, with a length-to-diameter ratio (~100:1) chosen to dampen coherent flow structures at the outlet plane. Figure 4.8(b) shows an example of a single-shot ultrabroadband O_2-CO_2 fs/ps CSRS spectrum acquired in the products of the flame. The signal-to-noise ratio (SNR) of the single-shot spectra acquired at this flame condition is measured to be ~48. The ro-vibrational O_2 Raman spectrum has a fundamental Q-branch band (labelled here as "0 ← 1") centred at ~1553 cm^{-1}, and hot bands appearing at lower Raman shift in agreement with the compression of the vibrational levels in the Morse potential. The ro-vibrational CO_2 Raman spectrum is characterised by the ν_1+2ν_2 Fermi dyad, described in Section 6.3.1. The so-called "blue" Q-branch band appears at 1388 cm^{-1} and about seven hot bands are visible in the region up to ~1450 cm^{-1}. Since the vibrational energy manifold of CO_2 is more complex than that of diatomic O_2, at any given tempera-

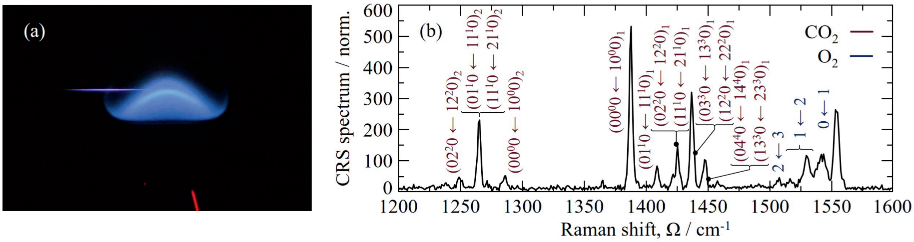

Figure 4.8: Ultrabroadband O_2-CO_2 fs/ps CSRS for combustion diagnostics. (a) Single-shot image of the filament generated in the product gases of a laminar premixed CH_4/air flame ($\phi = 0.77$) stabilised as a V-shaped flame. (b) Single-shot O_2-CO_2 CSRS spectrum acquired in the flame (Reproduced from Mazza *et al.* [26]). The red labels denote the Q-branch lines of the CO_2 Raman spectrum; blue labels are employed to indicate the fundamental and hot bands of the O_2 Q-branch spectrum.

ture the vibrational Boltzmann distribution spans over many more vibrational levels, as already observed in Figure 2.3. The "red" Q-branch is typically weaker and appears at lower Raman shifts, with a fundamental band at 1285 cm^{-1}, and three hot bands detectable at this flame temperature. Ro-vibrational O_2-CO_2 fs/ps CRS thermometry is validated in a set of experiments performed on the laminar premixed CH_4/air flame for varying equivalence ratio in the range 0.6-1.05. The results are discussed in Section 6.3.2.

4.1.2 Probe volume characterisation

The *in situ* use of the filament as a coherent light source complicates the determination of the CRS probe volume dimensions, as the fs laser pulse has different focusing properties in the filamentation regime than in the linear propagation one. Furthermore, its high irradiance hampers any direct measurement of the beam waist.

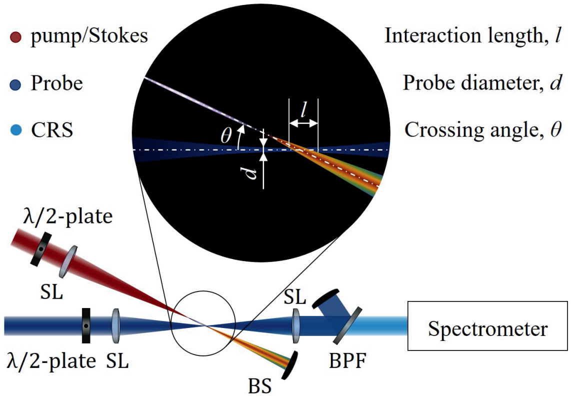

Figure 4.9: Schematic of the CRS probe volume. The probe beam crosses the supercontinuum some millimeters after the LE of the filament at an angle θ. The resulting probe volume is an ellipsoid, with lateral dimensions given by the diameter of the probe beam at the focus (d), and an interaction length (l) that depends on the supercontinuum beam waist and on the crossing angle.

Conventionally the probe volume dimensions can be estimated by geometrical calculations on the focusing properties of the beams and their crossing angle [125]. Alternatively, they are experimentally assessed by measuring the beam waists at their foci to know the lateral dimensions of the volume d, as shown in Figure 4.9. The interaction length l can be measured by [130]:

- Scanning a thin glass cover slip in the longitudinal direction through the probe volume. By measuring the variation in the intensity of the strong NR CRS signal generated in the solid-state material at the different locations it is possible to estimate the length of the probe volume.
- Scanning a knife-edge along the focus and measuring the intensity of the transmitted beams.
- Moving a thin gas jet along the probe volume and measuring the change in the CRS signal intensity.

The first two methods typically require attenuating the laser beam to avoid damaging the cover slip or knife-edge, while the third is hard to implement in practice, considering that the diameter of the gas jet needs to be much smaller than the probe volume, whose dimensions are usually <1 mm.

Tedder and co-authors introduced an alternative method for the direct imaging of the 3D probe volume, while maintaining the full laser power [130]. They placed a beam sampler after the focusing lens, splitting a ~7% portion of the beams and directing them towards a common intersection point, upon further attenuation via neutral density filters, the intersection volume was imaged onto a CCD camera mounted on a micrometer slide. The authors could thus perform a full reconstruction of the probe volume, by acquiring cross-sectional images at different longitudinal locations. Unfortunately, even this approach is not suitable to measure the probe volume under *in situ* filamentation conditions, because it still relies on the splitting of a small energy fraction off the laser beams to perform a direct imaging of their intersection at the foci. The problem at hand, on the contrary, requires one to maintain exactly the same filament properties to perform a representative measurement of the probe volume located at the end of the filament: hence the fs beam cannot be attenuated, nor a portion of its energy can be split off. To date there is no established procedure to measure the CRS probe volume with *in situ* filamentation.

In Paper I a novel methodology is introduced to estimate the probe volume under filamentation conditions, based on the measurement of the supercontinuum divergence out of the filament by the coherent imaging spectrometer sketched in Figure 4.10. The supercontinuum beam, diverging out of the filament, is collimated by a 200 mm spherical lens and a small portion is split off by a wedge plate to avoid interference from the two reflecting surfaces, and further attenuated by a thin-film polariser transmitting only a residual component of the S-polarised supercontinuum. This low-energy beam is then diffracted by the same reflective diffraction grating employed in Figure 4.7 and imaged by a 500 mm spherical lens onto a sCMOS detector (Zyla 4.2, Andor) with 1:2.5 magnification.

The inset in Figure 4.10 shows a picture of the supercontinuum dispersed onto a plate. The cross-section of the supercontinuum beam emitted by the filament has an annular structure, analogous to that observed for the self-seeded 428 nm lasing emission from filaments generated by 800 nm fs pulses in air by Liu *et al.* [131] and Chu *et al.* [132]. In order to measure the divergence of the supercontinuum after the collapse of the filament,

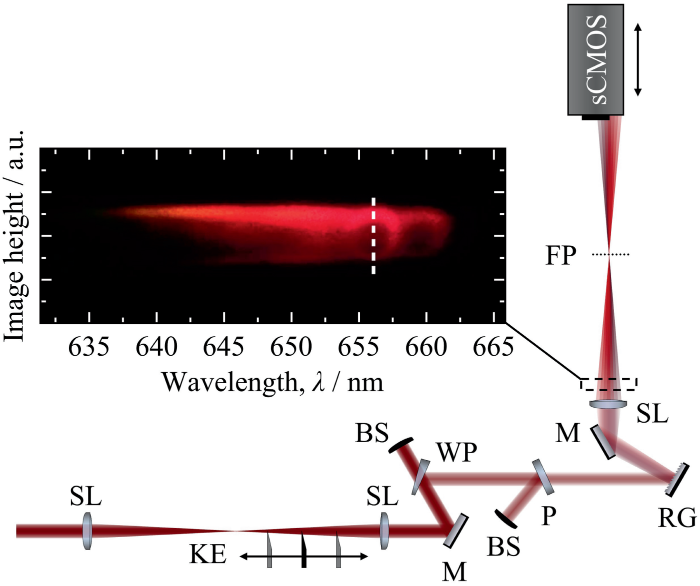

Figure 4.10: Schematic of the coherent imaging spectrometer employed to measure the divergence of the supercontinuum out of the filament generated in air. A knife-edge (KE) is inserted in the supercontinuum beam at 10 locations along the propagation direction (z). SL, spherical lens; M, mirror; BS, beam stop; WP, wedge plate; P, thin-film polariser; RG, reflective diffraction grating; FP, focal plane. Inset: spectral components of the conical white-light emission from the filament dispersed in the spectrometer. The divergence of the supercontinuum can, in principle, be investigated as a function of the wavelength.

a knife-edge is inserted at 10 locations, 5 mm apart from each other, along the propagation direction of the supercontinuum beam, as sketched in Figure 4.10. These locations are numbered consecutively from the closest to the filament at 36 mm from the CRS probe volume: this is the closest location where the knife-edge can be inserted without being destroyed by the high irradiance of the fs laser pulse. At each location the following operations are performed as part of the measurement routine:

1. The knife-edge is inserted and the sCMOS detector is moved longitudinally to find the corresponding image plane by minimising the line-spread function (LSF) of the illuminated edge.
2. An image of the beam cross-section with the knife-edge inserted is acquired before moving the knife-edge by 1 mm and acquiring a second image. This operation provides the spatial calibration of the image at each measurement location.
3. The knife-edge is removed from the laser beam and a sample of 100 single-shot images of the beam cross-section are acquired.

The intensity profile measured along the section line passing through the centre of the ring at location $z = 76.3$ mm is shown in Figure 4.11(a): the energy is not tangentially uniform over the ring. The edges of both the whole ring structure and the largest asymmetric feature are identified at the $1/e^2$ drop of the signal, and provide two alternative metrics to define the supercontinuum beam waist at each measurement location. Figure 4.11(b) shows the corresponding values measured along the propagation of the supercontinuum laser beam: independently of the criterion used to define the beam waist at each location, the beam is measured to diverge along a conical path (at least over the measured range), as showed by the linear trend in Figure 4.11(b). The diverging cone angle is measured to be ~3.2° and, projecting this trend backwards, the diameter of the supercontinuum pump/Stokes beam is estimated to be ~130 μm at the intersection with the probe beam, located ~4 mm after the end of the filament.

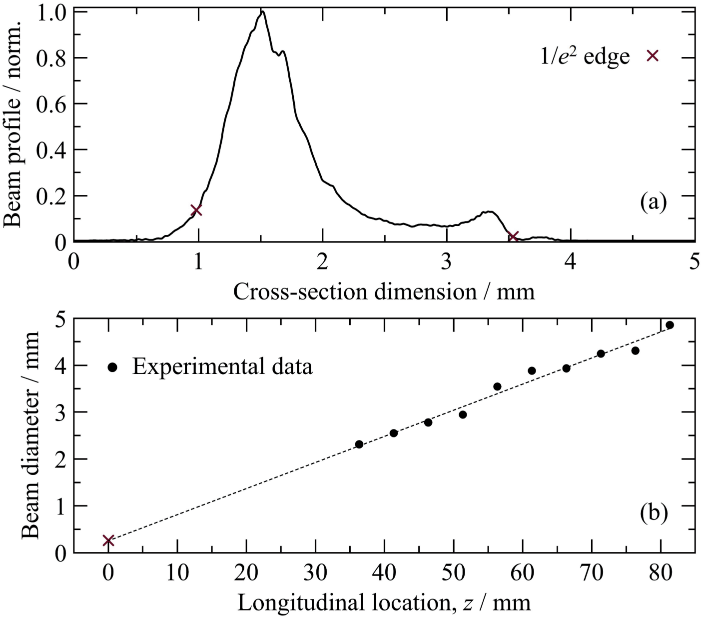

Figure 4.11: Measurement of the supercontinuum divergence out of the plasma filament. (a) Cross-sectional image of the supercontinuum at ~76 mm from the location of the probe volume. (b) Diameter of the supercontinuum measured at 10 locations (black circles): the linear growth of the beam diameter confirms the conical emission from the filament and allows for estimating the beam waist at the CRS probe volume (red marker).

The probe beam waist, on the other hand, can be assessed in a similar fashion as in Tedder *et al.* [130] —as its focusing properties are independent of the pulse energy in the linear focusing regime–, and it is measured to be ~30 μm ($1/e^2$). The interaction length is determined from the knowledge of the waists of the probe and pump/Stokes beams at the probe volume, and of their crossing angle. The latter is estimated by the measurement of the interaction length at low pulse energy (i.e. without generating a filament), by scanning a 100 μm cover slip along the longitudinal dimension of the probe volume. The interaction length, measured to be ~1.4 mm, combined with the pump/Stokes beam waist at low power (~60 μm), allows for estimating the crossing angle as:

$$\theta = \sin^{-1}\left(\frac{2w_{\text{pump/Stokes}}}{l}\right) \tag{4.5}$$

The crossing angle is thus measured to be ~4.7°. This value is finally used to estimate the interaction length under filamentation conditions, by inverting Equation (4.5) and employing the value of the supercontinuum beam waist estimated from the measurement of its divergence. The final result is $l \approx 3.3$ mm ($1/e^2$). The dimensions of the CRS probe volume with *in situ* filamentation are thus estimated to be: ~60 μm (height, $1/e^2$) x ~3.3 mm (length, $1/e^2$) x ~60 μm (width, $1/e^2$).

In conclusion to this paragraph it should be noted that, in Paper I, the divergence of the supercontinuum beam is only measured at ~655 nm and the same cone angle is assumed for all the frequencies in the spectrum of the supercontinuum. In line of principle, the coherent imaging spectrometer could be employed to measure the divergence of any frequency component in the compressed supercontinuum, and the methodology described above could provide a full reconstruction of the geometry of the beam diverging out of the filament. Future work should undertake this task to validate the assumption in Paper I and assess its impact on the evaluation of the probe volume dimensions: this point is further discussed in Chapter 8.

4.1.3 EFFECT OF GAS TEMPERATURE AND COMPOSITION ON *IN SITU* FILAMENTATION

As seen in Figure 4.5, the filament propagation is not affected by the presence of the flame on the beam path, but this is not as well the case for the pulse compression and supercontinuum generation. In fact, the phase modulation due to optical Kerr effect in Equation (4.3) and to the free electrons in the plasma medium in Equation (4.4) is significantly affected by the local properties of the gas-phase medium. In chemically reacting environments such as flames two main macroscopic variables show steep local gradients (as well as temporal, in the case of turbulent flames), which can significantly affect the supercontinuum generation: composition and temperature.

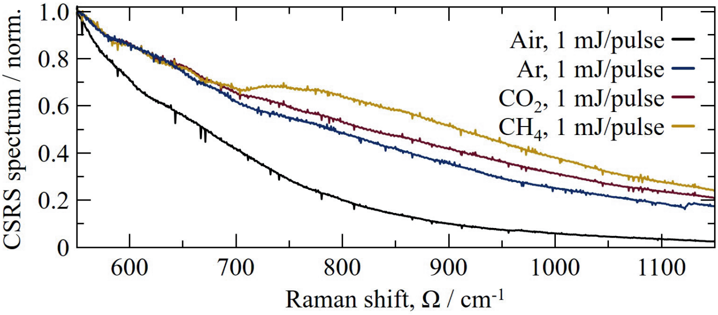

Figure 4.12: Effect of the local gas composition on the pulse compression via *in situ* filamentation. The filament is generated by a 1 mJ, 35 fs TL pulse at atmospheric pressure, in room-temperature flows of: air (black line), Ar (blue), CO_2 (red), and CH_4 (yellow). The different gases result in a widely different pulse self-compression: this effect can be explained by the magnitude of the electronic third-order susceptibility $\chi^{(3)}_{\mathrm{NR}}$ of the tested gases.

Different molecular species of course have different third-order optical susceptibility $\chi^{(3)}$: this not only affects their coherent Raman cross-section, but also determines a different magnitude of the optical Kerr effect experienced by the fs laser pulse when travelling through the corresponding gas, as seen in Equations (3.6) and (3.7). The effect of different combustion-relevant gases −air, Ar, CO_2, and CH_4− on the filamentation process is investigated by measuring the bandwidth of the ultrabroadband NR fs/ps CRS signal in the region ~500-1100 cm^{-1}, as shown in Figure 4.12. This spectral window is chosen because none of the gases tested have active rotational-vibrational modes in this region of the Raman spectrum. The gas flows are provided by compressed vessels and delivered through the burner pipe described in the previous paragraph. To avoid contamination of ambient air in the probe volume, a T-junction is mounted at the exit of the burner such that the laser beams can pass inside the junction while this is flown with the gas under investigation.

The results in Figure 4.12 show that the compressed supercontinuum output by the filament has the largest bandwidth when generated in CH_4, and the lowest in air, while a similar bandwidth is measured in Ar and CO_2. Table 4.1 reports the (electronic) non-resonant third-order susceptibilies of many combustion-relevant species: the magnitude of $\chi^{(3)}_{\text{NR}}$ provides a good explanation of the different pulse compression achieved via *in situ* filamentation in the different gases tested. It should be noted that the polyatomic species with Raman modes that can be excited within the bandwidth of the fs pulse have an additional (resonant) Raman-induced contribution to the optical Kerr effect:

Table 4.1: Electronic third-order susceptibilities $\chi^{(3)}_{\text{NR}}$ of various combustion-relevant gases. All the values are given in cm^3/erg·amagat.

Species	Reference	$\chi^{(3)}_{\text{NR}}$
N_2	[133]	$7.90\cdot10^{-18}$
O_2	[133]	$7.98\cdot10^{-18}$
H_2	[133]	$5.90\cdot10^{-18}$
Ar	[133]	$9.46\cdot10^{-18}$
CO_2	[133]	$11.80\cdot10^{-18}$
CH_4	[133]	$22.70\cdot10^{-18}$
H_2O	[134]	$17.40\cdot10^{-18}$
Propane (C_3H_8)	[134]	$90.90\cdot10^{-18}$
n-Butane (*n*-C_4H_{10})	[134]	$113.70\cdot10^{-18}$

$$\bar{n}_2 = \frac{3}{4n_0}\left(\chi^{(3)}_{\text{NR}} + \chi^{(3)}_{\text{Raman}}\right) \tag{4.6}$$

If the assumption of impulsive excitation of said Raman modes applies, the contribution of the rotational-vibrational coherence to the optical Kerr effect is negligible and the non-linear refractive index is only due to the non-resonant electronic contribution in Equation (4.6). The large variation in the bandwidth of the compressed supercontinuum generated by *in situ* filamentation in the tested gases can significantly impact the use of fs laser induced filamentation to realise ultrabroadband fs/ps CRS in chemically reacting flows. Consider for example a non-premixed hydrocarbon/air flame, depending on the geometry of the problem, the composition of the flow the filament propagates through can vary significantly: in the oxidiser stream the average $\chi^{(3)}_{\mathrm{NR}}$ would be ~7.92·10^{-18} cm^3/erg·amagat, while in the fuel stream it could be significantly larger, from 22.7·10^{-18} cm^3/erg·amagat for CH_4 to >100·10^{-18} cm^3/erg·amagat for heavier hydrocarbons.

The large temperature gradient developed across the chemical reaction zone of a flame can also significantly impact the amount of self-compression produced by the filament as it propagates through it. Deconvolving the relative contributions due to composition and temperature in a flame is not straightforward. The effect of the temperature gradient on *in situ* filamentation can nonetheless be appreciated by comparing the ultrabroadband NR CRS spectra acquired in Ar and in the products of a laminar H_2/air diffusion flame, as shown in Figure 4.13. The only major product of H_2 combustion is water vapour, so that the product gases of the flame are a mixture of N_2 and H_2O, whose non-resonant third-order susceptibility is expected to be larger than that of air, according to the values in Table 4.1. Hence, neglecting the effect of temperature on *in situ* filamentation one would expect the pulse compression to be larger in the flame products. On the contrary, a significant reduction in the Raman excitation bandwidth is observed in Figure 4.13, meaning that the large reduction in the effective refractive index across the temperature gradient determines a lesser compression of the pulse. As described in the introductory section to the present chapter, the propagation of a fs pulse in the filamentation regime can be seen as the result of the balancing act between the non-linear Kerr self-focusing and plasma defocusing. The introduction of a temperature gradient along the filament axis reduces the local density of the gas-phase medium, decreasing both the non-linear refractive index $\bar{n}_2$ and the plasma density ρ in Equation (4.2), so that the filament propagation is virtually unaffected as observed in Figure 4.5. On the other hand, the magnitude of the non-linear optical processes underpinning the filamentation process (i.e. Kerr effect and photo-ionisation) can be significantly reduced.

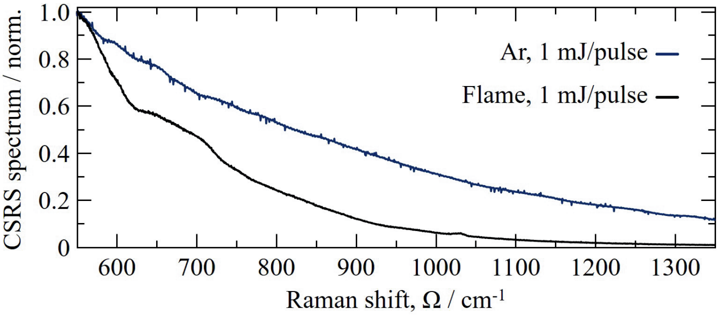

Figure 4.13: Effect of the local gas temperature on the pulse compression via *in situ* filamentation. The filament was generated by a 1 mJ, 35 fs TL pulse in room-temperature Ar (blue line) and in the hot products of a laminar H_2/air diffusion flame (black). The pulse self-compression via *in situ* filamentation in the flame is significantly lesser than in Ar.

The effects of the local composition and temperature of the gas-phase medium on the pulse self-compression pose an additional challenge to the implementation of ultrabroadband fs/ps CRS with *in situ* filamentation as a combustion diagnostic tool. As a matter of fact, the dependence of the effective excitation bandwidth on the local boundary conditions to the filamentation process represents a large source of uncertainty and can negatively impact the diagnostics, as shown in Chapter 5.

4.2 ULTRABROADBAND FS/PS CRS BEHIND THICK OPTICAL WINDOWS

A discussed in Chapter 3, the need to transport the ultrabroadband excitation laser pulse behind thick optical windows can significantly limit the applicability of ultrabroadband fs/ps CRS in measurement scenarios of practical interest. One of the main research questions formulated in Section 3.3 concerns the *in situ* use of fs laser-induced filamentation to generate the compressed supercontinuum directly behind thick optical windows. In Paper III the first proof-of-principle demonstration of this approach is provided: ultrabroadband fs/ps CRS with *in situ* filamentation is performed in a laboratory flame behind a 22 mm-thick BK7 glass optical window.

The optical window is placed approximately 200 mm after the 500 mm pump/Stokes focusing lens, as shown in Figure 4.14(a), the maximum distance of the window from the lens being limited by the onset of filamentation inside the bulk glass material. Solid materials typically have non-linear optical susceptibilities that are orders of magnitude larger than gases. Therefore laser pulses with peak power in the megawatt range can propagate through filaments in the optical material, whereas a peak power in the gigawatt range is needed in gases [135]. Hence, if the window is placed too close to the focal plane of the lens, the local irradiance of the focusing fs beam can be sufficient to lead to filamentation inside the glass. The supercontinuum thus generated diverges after the filament collapse at the solid-gas interface, so that it cannot be used as an ultrabroadband pump/Stokes pulse at the probe volume. Quite recently, Zhao and co-authors have demonstrated the filamentation of the ~1 ps high-energy (60 mJ) pulse generated by a thin-disk laser, and used the supercontinuum to perform simultaneous ro-vibrational O_2-N_2 fs/ps CARS in room-temperature air [136]. The authors argued that the use of ps pulses, rather than fs ones, could mitigate the impact of the GVD imparted by the thick optical medium and avoid the need for its compensation e.g. by using a grating compressor as discussed in Paper III. They demonstrated this by placing glass windows of different thickness (1 mm, 6 mm, and 12 mm) after the focusing lens: these had to be placed 17 cm after the 3 m focusing lens (at ~1/15 of the focal length) to avoid the filamentation of the high-energy ps pulse. Furthermore, the length of the filament in Ref. [136] was ~80 cm, limiting the use of ps laser-induced filamentation to large-scale applications, such as furnaces. Despite being more sensitive to the GVD of the optical material, fs pulses can be more efficiently compressed via laser-induced filamentation, with a much stronger spectral broadening than achieved by filamentation of ps laser pulses [137]. Hence, employing a relatively low-energy (~1.5 mJ) fs laser pulse, the filament length almost two orders of magnitude smaller and the optical window can be placed much farther from the focusing lens (at ~2/5 of the focal length), thus achieving a larger flexibility. Figure 4.14(b) shows a single-shot ro-vibrational O_2-CO_2 CSRS spectrum acquired in the same flame of Figure 4.8: in this case the optical window is placed on the pump/Stokes beam path. The 1.495 mJ pulse energy in the fs beam is transmitted through the optical window with a measured loss of 116 μJ, due to partial reflection by the window. The remaining 1.379 mJ are sufficient to compress the

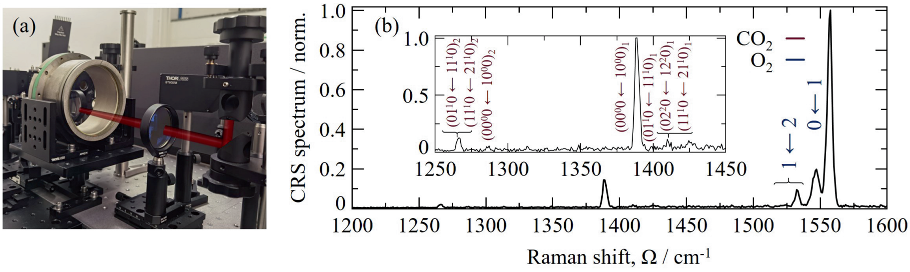

Figure 4.14: Ultrabroadband fs/ps CRS behind a thick optical window. (a) The fs pump/Stokes pulse is compressed by *in situ* filamentation behind the 22 mm BK7 optical window, placed ~20 cm after the focusing lens (f:=500 mm). (b) Single-shot ro-vibrational CO_2-O_2 CSRS spectrum acquired in a laminar premixed CH_4/air flame (ϕ=0.6) behind the optical window.

pulse to ~17 fs, as measured by the NR CRS acquired in Ar. The estimation of the fs pulse duration via the NR CRS spectrum is discussed in Sections 4.2.1 and 4.2.2.

In Paper III, *in situ* filamentation is employed to realise ultrabroadband fs/ps CRS on the pure-rotational Raman spectrum of H_2 in a laminar H_2/air diffusion flame. As already pointed out in Section 3.1, H_2 has a rotational constant significantly larger than other heavier diatomic molecules, such as N_2 and O_2, so that its pure-rotational spectrum spans over 1500 cm^{-1} at flame temperature. Pure-rotational H_2 CRS thermometry could only recently be realised in an open flame by employing ultrabroadband fs/ps CRS [110]. Figure 4.15 presents an example of a single-shot H_2 CRS spectrum, spanning the region 300-1500 cm^{-1}, acquired in the flame experiment reported in Paper III. This is the first-ever example of pure-rotational fs/ps H_2 CRS realised behind a thick optical window.

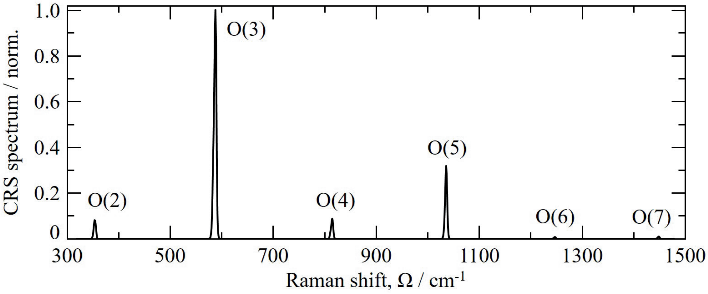

Figure 4.15: Single-shot pure-rotational H_2 CSRS spectrum acquired in a laminar H_2/air diffusion flame, behind the 22 mm-thick BK7 optical window. Six rotational lines –from O(2) (corresponding to the pure-rotational transition $J = 0 \leftarrow 2$) at 354 cm^{-1} to O(7) (transition $J = 5 \leftarrow 7$) at 1447 cm^{-1}– are detected simultaneously in the spectral region 300-1500 cm^{-1} and within the dynamic range of the sCMOS detector.

Instrumental to the pulse compression via *in situ* filamentation behind the optical window is the use of the external grating compressor mentioned in Section 4.1.1, which allows for compensating the temporal chirp introduced by the optical window, and to control the fs pulse duration prior its filamentation. This is demonstrated in Paper III by measuring the excitation bandwidth provided by the fs pump/Stokes pulse –as mapped by the NR CRS spectrum, which measures the spectral autocorrelation of the pulse according to Equation (2.39)– as a function of its temporal chirp. Figure 4.16(a) shows 1000 shot-averaged

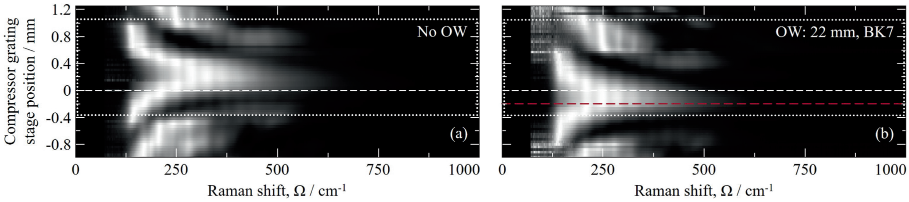

Figure 4.16: Effect of pump/Stokes GVD on the NR CRS signal. (a) 1000-shot-averaged NR CARS spectra recorded, by varying the position of the compressor grating, in a flow of CH_4 without the optical window. The white dashed line identifies the condition of a near-TL pulse. (b) Corresponding NR CARS spectra after the introduction of the BK7 optical window on the pump/Stokes beam path. The red dashed line identifies the condition of a TL pulse obtained after transmission through the window. The dotted boxes represent the region of interest analysed in Paper III. Figure reproduced from Mazza *et al.* [27].

NR CARS spectra, acquired in a room-temperature CH_4 flow for different settings of the external compressor. The pump/Stokes pulse energy is attenuated to 50 μJ to avoid the onset of photo-ionisation and fs laser-induced filamentation and the dashed line represents the spectral excitation provided by a 35 fs TL pulse. The spectral region $\lessapprox$150 cm^{-1} is affected by the band-pass filter used to suppress the probe pulse. The temporal chirp introduced to the fs pump/Stokes pulse by the external compressor has a dramatic impact on the spectral excitation profile mapped by the NR CRS spectrum. Not only the excitation bandwidth is reduced as the chirp increases, but multiple spectral side-bands appear next to the central excitation peak the further the pulse is temporally stretched. The existence of symmetrical side-bands on the Stokes side of the Raman spectrum is also confirmed.

The effect of the 22 mm-thick BK7 glass window can be appreciated by comparing this behaviour with the one in Figure 4.16(b): the whole NR CRS surface is shifted by ~0.4 mm, in terms of position of the diffraction grating in the external compressor. That is to say that the grating compressor employed in the present fs/ps CRS instrument is more than capable of compensating the chirp introduced by 22 mm of BK7 glass, and a TL pulse can be delivered to the measurement location behind the optical window.

4.2.1 MEASUREMENT OF THE FS PULSE CHIRP

The TL condition for the pump/Stokes pulse in Figure 4.16 is identified by comparing these experimental spectra to a time-domain model for the NR CRS signal, as discussed in the following.

For a two-beam hybrid fs/ps CRS process the NR CRS spectrum can be computed according to Equation (2.39). The pump/Stokes laser field is modelled in the time-domain as a Gaussian pulse of duration Δt = 35 fs, its Fourier transform yielding a Gaussian spectrum in the form of Equation (3.3), where the spectral phase can be expressed as the Taylor series in Equation (3.4). In order to derive a closed-form solution the series is stopped to the second order, including only the quadratic phase term arising due to the GVD of the pulse, i.e. its linear chirp:

$$\tilde{E}_{\mathrm{p/St}}(\omega) = \frac{E_0\,\Delta t}{2}\sqrt{\frac{\pi}{2\ln 2}}\,e^{-i\left[\frac{\Delta t^2}{8\ln 2}(\omega-\omega_0)^2+k_0+k_1(\omega-\omega_0)+\frac{k_2}{2}(\omega-\omega_0)^2\right]} + \text{c.c.} \tag{4.7}$$

Where k_0 is a negligible phase factor [rad], k_1 is the *group delay* (GD) experienced by the pulse as it propagates in the optical material [fs], and k_2 is the *group delay dispersion* (GDD) [fs^2].

Non-linear chirp terms, e.g. due to the *third-order dispersion* (TOD) of the pulse propagating in condensed-phase optical media, could significantly alter the spectrochronographic properties of the fs pulse, as illustrated in Figure 4.17. In Paper III, these higher-order contributions are nevertheless assumed to be negligible. This assumption is justified by the experimental observation that the presence of the optical window only introduces a minor shift in the NR CRS spectra in Figure 4.16, with no substantial change in the envelope of the spectra themselves. The possible TOD of the pump/Stokes pulse arising in the glass material is thus neglected and the window is assumed to only contribute a quadratic phase term to Equation (4.7).

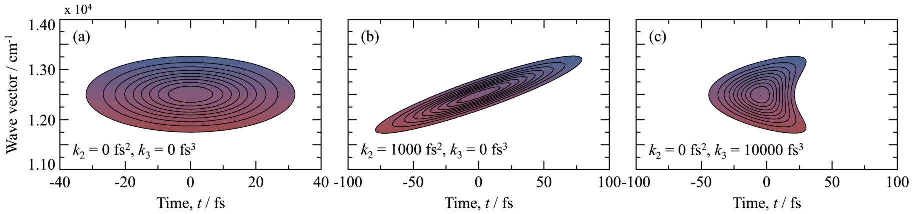

Figure 4.17: Wigner function of the pump/Stokes pulse. The Wigner function [95] provides a visual representation of the spectrochronographic properties of an optical pulse, depicting simultaneously its spectral and temporal envelope. (a) 35 fs TL pump/Stokes pulse at 806 nm. (b) Linear chirp due to a GDD of 1000 fs^2. (c) Quadratic chirp due to a TOD of 10000 fs^3.

The spectral autocorrelation of the pump/Stokes pulse can then be calculated as:

$$\begin{aligned}\left(\tilde{E}_{\mathrm{p/St}}\star\tilde{E}_{\mathrm{p/St}}\right)(\Omega) &= \int_{-\infty}^{+\infty} d\omega\,\tilde{E}^{*}_{\mathrm{p/St}}(\omega)\tilde{E}_{\mathrm{p/St}}(\omega+\Omega) \propto \exp\left[-\left(\frac{\ln 2}{\Delta\omega^2_{\mathrm{p/St}}}+i\frac{k_2}{2}\right)\Omega^2\right]\\ &\cdot\int_{-\infty}^{+\infty} d\omega\,\exp\left\{\frac{4\ln 2}{\Delta\omega^2_{\mathrm{p/St}}}\left[\Omega+\frac{(\omega-\omega_{\mathrm{p/St}})}{2}\right]^2 - i\varphi_2\Omega\frac{\omega-\omega_{\mathrm{p/St}}}{2}\right\}\end{aligned} \tag{4.8}$$

Where $\Delta\omega_{\mathrm{p/St}}$ represents the bandwidth of the pump/Stokes pulse, which is computed according to Equation (3.3) with $c = 2\ln 2/\pi$ for a 35 fs TL Gaussian pulse. Equation (4.8) has an analytical solution in the form:

$$\left(\tilde{E}_{\mathrm{p/St}}\star\tilde{E}_{\mathrm{p/St}}\right)(\Omega) \propto \sqrt{\pi(4\ln 2 + i\varphi_2\Delta\omega^2_{\mathrm{p/St}})}\exp\left[\left(-\frac{4\ln 2}{\Delta\omega^2_{\mathrm{p/St}}}+i\varphi_2\right)\Omega^2\right] \tag{4.9}$$

It is interesting to analyse the behaviour of the complex exponential function in Equation (4.9), as represented in Figure 4.18(a) and compared to the experimental NR CRS

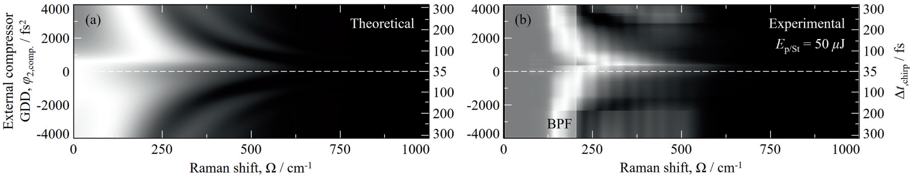

Figure 4.18: Time-domain modelling of the NR CRS signal. (a) Synthetic NR CARS spectra simulated by Equation (4.9) for different values of the quadratic phase φ_2. (b) 1000-shot-averaged NR CARS spectra acquired for different position of the grating compressor: the quadratic phase and pulse duration are measured by fitting these experimental spectra to the theoretical model. The white dashed line identifies the condition of a near-TL pulse. Figure reproduced from Mazza *et al.* [27].

spectra in Figure 4.18(b). The real part of the complex exponential is a Gaussian function whose bandwidth coincide, for a TL pulse with zero GDD, to the autocorrelation bandwidth computed in Equation (3.5). The imaginary part of the exponential, on the other hand, introduces a non-linear oscillation due to the quadratic component of the spectral phase: the spectrum of the NR CRS signal thus shows quadratic oscillations with a proportionality constant given by the GDD of the optical pulse. This model well describes the behaviour of the experimental NR CARS spectra as a function of the pulse dispersion introduced by the external compressor in Figure 4.18(b). A large GDD effect on the second-harmonic generation (SHG) in a non-linear crystal was experimentally measured by Broers *et al.* [138]. The authors observed a non-monotonic SHG spectrum, with an increasing number of local maxima for larger values of the linear chirp. This behaviour is, at least qualitatively, analogous to the one observed for the stimulated Raman excitation in Figure 4.18, and was explained by Broers and co-authors as the result of interference between the coherent excitation pathways available at each instant in time across the bandwidth of the fs pulse [138].

The time-domain NR CRS model is employed to generate a library of synthetic spectra, for varying input values of the pulse GDD in the range 0-5000 fs^2, to fit the experimental data in Figure 4.18(b). This allows for estimating the GDD of the optical window to be 424 fs^2, with the pump/Stokes pulse being stretched to ~47 fs. This quantification of the chirp introduced by the optical window furthermore confirms the ability of the external compressor to easily compensate it and control the quadratic phase of the pump/Stokes pulse delivered at the measurement location. As a matter of fact, the external compressor can introduce a GDD in excess of ±4000 fs^2, as shown in Figure 4.18, so that much thicker optical windows could be employed without limiting the capabilities of the fs/ps CRS instrument.

4.2.2 Pulse compression behind the optical window

Paper III furthermore demonstrates that the quadratic phase of the fs pulse has a significant impact on its filamentation and self-compression. At each grating position in Figure 4.16(b), the energy of the fs pulse is increased to ~1.5 mJ (measured before the optical window) to compress it via *in situ* filamentation, both in room-temperature air and CH_4. The comparison between the ultrabroadband NR CARS spectra generated by a TL input pulse in CH_4 and in air, in Figure 4.19, shows that fs laser-induced filamentation is characterised by a stronger self-phase modulation in CH_4, resulting in a larger broadening of the pump/Stokes pulse. This result confirms the observation discussed in Section 4.1.3.

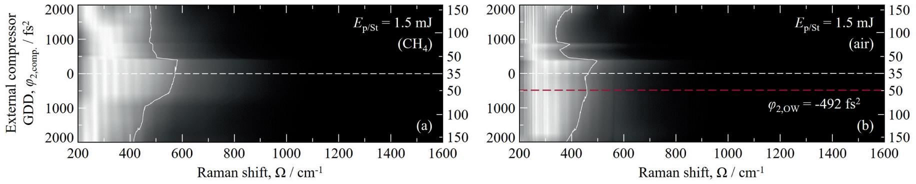

Figure 4.19: Effect of the ro-vibrational wave packet on the pulse compression. (a) 1000 shot-averaged ultrabroadband NR CARS spectra generated via *in situ* filamentation in a CH_4 flow behind the optical window, for a varying amount of GDD introduced by the external compressor. The dashed white line identifies the TL condition for the input fs pulse before filamentation, while the solid white line is the contour of the HWHM excitation bandwidth. (b) Corresponding ultrabroadband NR CARS spectra generated by *in situ* filamentation in air. The red dashed line identifies the compressor settings employed to optimise the pulse compression in the flame. In both experiments the filament is generated under the focusing conditions discussed in Section 4.1.1, for an input pulse energy of 1.5 mJ (measured before the optical window). Figure reproduced from Mazza *et al.* [27].

As for the impact of the temporal chirp of the input laser pulse on the filamentation process, the two gases also show remarkable differences as highlighted by the contour plots (solid white line), which identify the resulting half-width-at-half-maximum (HWHM) excitation bandwidth over the spectral range 200-1600 cm^{-1}. For moderate amounts of GDD in the input laser pulse (i.e. $|k_2| < 500$ fs^2), the bandwidth of the compressed supercontinuum generated by *in situ* filamentation in CH_4 is almost unaffected. Larger amounts of pulse dispersion result in a dramatic and monotonic decrease in the excitation bandwidth. This behaviour is easily interpreted in terms of the reduced instantaneous peak power of the fs laser pulse when stretched in time, resulting in a lower intensity of the electric field in Equation (4.3). In terms of its third-order optical susceptibility, responsible for the optical Kerr effect at the onset of fs laser-induced filamentation, CH_4 can be treated as a non-resonant molecule. As detailed in the next chapter, the vibrational modes of CH_4 lie at higher frequencies (>1300 cm^{-1}) than accessible, via stimulated Raman scattering, by the bandwidth of a 35 fs laser pulse. In addition, as discussed in Appendix B, CH_4 is a spherical top molecule with no rotational degree of freedom in its electronic and vibrational ground state. Hence, the 35 fs laser pulse employed in the experimental setup cannot excite any coherent rotational-vibrational wave packet in the CH_4 flow. The pulse self-compression in the filamentation process thus relies entirely on the electronic part of the third-order optical susceptibility of the CH_4 medium.

The molecular components of air (i.e. N_2 and O_2), on the other hand, have the whole rotational energy manifold available within the bandwidth of the 35 fs pump/Stokes pulse. In parallel to the non-resonant electronic contribution to $\chi^{(3)}$, there is a Raman-induced contribution to the optical Kerr effect due to the rotational wave packets of N_2 and O_2. An example of how the macroscopic coherence in ensembles of diatomic molecules introduces periodic oscillations of the non-linear refractive index of the optical medium can be found in Avram *et al.*. The authors derived the expression of the coherent states for a 3D Morse oscillator and calculated the contribution of the vibrational Raman-induced wave packet to the optical Kerr effect. The relative magnitude of the electronic and nuclear components of $\chi^{(3)}$ depends, among other things, on the duration of the laser pulse employed. If this duration is much smaller than the rotational period of the molecules the non-linear optical response is entirely due to the electronic susceptibility [139]. This is the very same argument invoked to claim an impulsive excitation of the ro-vibrational Raman modes in the time-domain CRS theory (see Section 2.3.2). Therefore, introducing a small amount of chirp to the fs pulse can enhance the optical Kerr effect and the self-pulse compression during the filamentation process in air, as shown in Figure 4.19(b). Two local maxima of the HWHM excitation bandwidth are found for an input GDD of the pulse of about ±500 fs^2. This result is in very good agreement with the experimental observation of a dramatic decrease of the critical power required to trigger the filamentation of fs near-IR pulses in air, reported e.g. by Liu and Chin [140]. In the flame experiment outlined in the next section, the pulse compression and thus the Raman excitation bandwidth are found to be optimised for a negative input GDD of -492 fs^2, coinciding with the lower local maximum in the contour line in Figure 4.19(b).

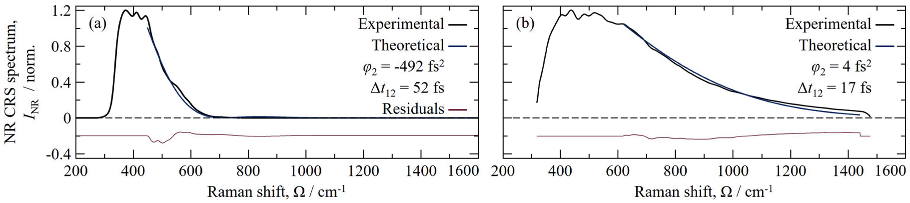

Figure 4.20: Pulse compression via fs laser-induced filamentation. (a) 1000 shot-averaged NR CRS spectrum of the chirped input fs laser pulse optimised for pulse compression via *in situ* filamentation in the flame environment. (b) 1000 shot-averaged ultrabroadband NR CRS spectrum generated by *in situ* filamentation in an Ar flow. Figure reproduced from Mazza *et al.* [27].

The time-domain NR CRS model discussed in the previous paragraph is extended in Paper III to measure the pulse compression achieved by fs laser-induced filamentation. This extension relies on the assumption that the supercontinuum pulse output by the filament maintains an essentially Gaussian spectrum, so that the closed-form solution for the pulse autocorrelation in Equation (4.9) can be applied to the description of the ultrabroadband NR CRS spectrum. The validity of this working assumption could be questioned to the extent that an asymmetrical broadening of the pulse spectrum, with a strong blue shift, has been experimentally observed in filamentation of tightly-focused near-IR laser pulses in air [141, 142]. This was attributed to a large contribution of the non-linear refractive index of the dense plasma medium. The assumption in Paper III is somewhat justified by the fact that the focusing geometry employed there (with numerical aperture NA $\approx$ 0.01) is much less tight than in the experiments by Liu *et al.* (NA $\approx$ 0.12 [141]) and Vaičaitis *et al.* (NA = 0.15 [142]), as well as by the lesser density of the plasma medium in the hot combustion environment.

The time-domain NR CRS model is thus employed to fit the ultrabroadband NR CSRS spectrum generated by *in situ* filamentation to a two-dimensional library of synthetic spectra, computed for a pulse duration varying in the range 5-35 fs, as well as for a GDD in the range ±2000 fs^2. In the flame experiment, the pulse compression is optimised directly on the NR CSRS spectrum measured *in situ*, in the laminar H$_2$/air flame, behind the optical window. The pulse energy is first attenuated to record the NR CSRS spectrum generated (in Ar) by the fs laser pulse without filamentation, as shown in Figure 4.20(a), which is then fitted to measure a GDD of -492 fs^2, as mentioned above. This pulse is then compressed in the filamentation process as shown in Figure 4.20(b), where the spectrum is fitted to measure a pulse duration of 17 fs with virtually no residual chirp.

Chapter 5

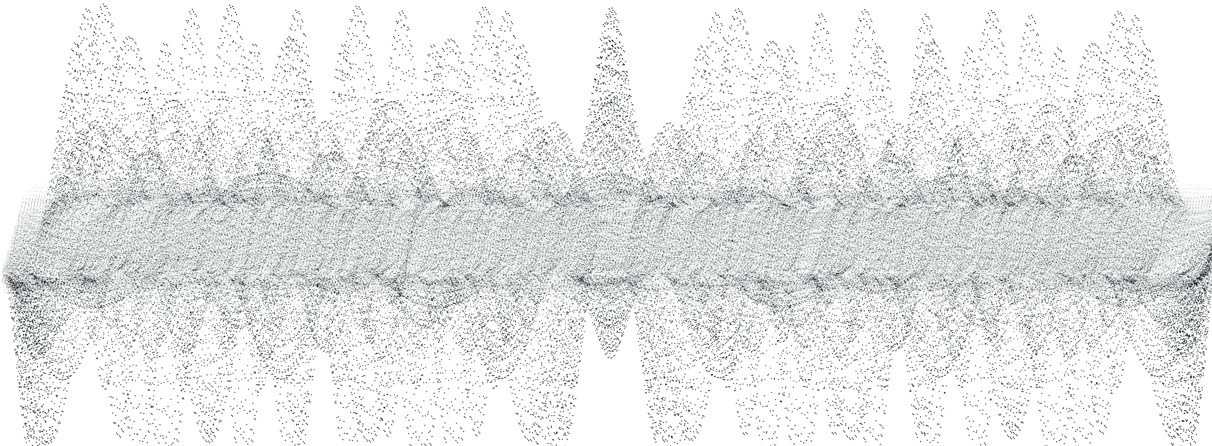

IN SITU REFERENCING OF THE SPECTRAL EXCITATION EFFICIENCY

The present chapter illustrates the development of a novel experimental protocol for the in situ referencing of the spectral excitation efficiency. This addresses the second research question, concerning the uncertainty introduced in gas-phase fs/ps CRS thermometry by the unknown effective excitation bandwidth, provided by the fs pump/Stokes pulse upon its propagation in the chemically reacting flow. The novel in situ referencing protocol is firstly compared to the conventional ex situ one by pure-rotational N_2-O_2 CRS imaging thermometry across a laminar premixed CH_4/air flame front. Thereupon, its extension to ultrabroadband fs/ps CRS is demonstrated for pure-rotational H_2 CRS thermometry across a diffusion H_2/air flame front.

Part of the results discussed in this chapter have been published in Papers II and III.

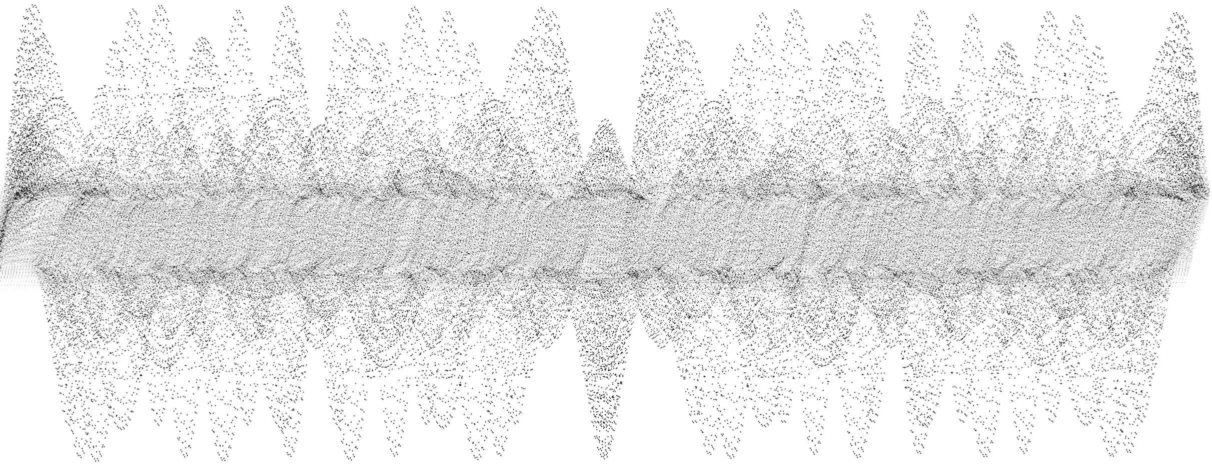

The effective spectral excitation of the Raman modes provided by the broadband fs pump/Stokes pulse represents an inherent source of uncertainty to fs/ps CRS. As discussed in Section 3.1 the excitation bandwidth is limited by the finite bandwidth of the fs excitation laser pulse. The effect of the finite bandwidth of the pump/Stokes pulse on the CRS spectrum can be accounted for in the time-domain CRS code by modelling the temporal envelope of the pump/Stokes pulse in Equation (2.36). This approach was indeed discussed in the first publication on hybrid fs/ps CRS [69]. To accurately simulate the CRS signal in real experimental scenarios one would also need to modify Equation (2.36) to account for the exact phase of the fs laser pulse at the measurement location, including the effects of the possible GDD and TOD arising along the beam path. The resulting modulation of the excitation pulse, especially in terms of its phase, can dramatically change the effective spectral excitation profile as experimentally proven in Figure 4.16. Including these effects in the time-domain model of the CRS process often requires resorting to the TDDM formalism and integrating the evolution of the system under the interaction Hamiltonian [143].

When it comes to the application of time-resolved CRS as a diagnostic tool for chemically reactive flows, maintaining a detailed knowledge of the properties of the fs laser pulse at the measurement location is rather unfeasible. Even more so considering the use of ultrabroadband fs/ps CRS in measurement scenarios of practical interest (e.g. high-pressure combustion chambers), where the phase of the pulse can be severely distorted by its transmission through thick optical windows and by the local temperature and composition of the gas flow along the laser beam path. In this case, the question of the effective spectral excitation of the Raman spectrum can be approached more effectively by measuring the NR CRS signal, mapping the spectral excitation efficiency of the fs pump/Stokes pulse. The conventional experimental protocol for a CRS experiment thus includes the sequential measurement of the NR CRS signal in a non-resonant gas. The effect of the finite excitation bandwidth is then accounted for by *spectral referencing*, i.e. subdividing the resonant CRS spectra by the NR spectrum. This experimental approach has the advantage of taking into account additional effects such as the imperfect phase-matching for two-beam fs/ps CRS with a crossed-beam geometry [23, 89], and the transmission and detection efficiency curves of the spectrometer.

The conventional spectral referencing protocol described above is here labelled as "*ex situ*", because the NR CRS signal is measured sequential to the CRS experiment and under rather different experimental conditions: typically, in room-temperature Ar. The spectral reference provided by the NR CRS signal measured *ex situ* cannot perfectly map the effective spectral excitation profile available in the CRS experiment, as it does not account for the local flow conditions along the beam path to the measurement location. Furthermore, the spectral excitation profile can show significant shot-to-shot variations, due to the inherent spectral noise of the coherent light source employed. The dynamic nature of the optical medium in turbulent flows is an additional source of noise: variations in the local temperature and composition fields along the propagation of the fs excitation laser pulse can introduce shot-to-shot variations in the effective excitation bandwidth at the measurement location. An example of the limited representativeness of the NR CRS spectrum acquired *ex situ* is found in Retter *et al.* [19], where the authors performed ro-vibrational H_2 fs/ps CARS thermometry in the the multi-phase reaction zone of a solid

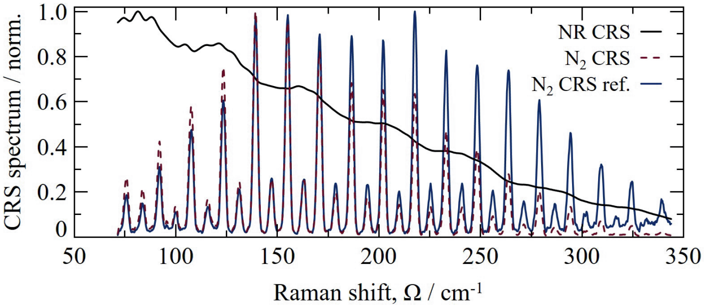

Figure 5.1: Conventional referencing of the pure-rotational fs/ps CRS signal. The experimental pure-rotational N_2 CARS spectrum (dashed red line), acquired in the high-temperature products of a laminar premixed CH_4/air flame, is subdivided by the NR CRS spectrum generated *ex situ* in room-temperature Ar (solid black line). The solid blue line is the resulting referenced spectrum, which can be meaningfully compared to the time-domain CRS model to extract the local temperature.

propellant flame. Over the course of the 2 hour-long experiment they observed significant variations in the spectrum of the NR CARS signal acquired in room-temperature air in the spectral range 3900-4200 cm^{-1}. They attributed these changes to the behaviour of the OPA employed to generate the Stokes pulse in their three-beam fs/ps CRS instrument, and quantified the resulting thermometric imprecision to be ~3% in validation measurements performed on a Hencken burner.

The imprecision arising from shot-to-shot variations in the excitation bandwidth has long been recognised as a limitation to gas-phase CRS thermometry, and the concurrent detection of the resonant and NR CRS signals has been proposed to mitigate this uncertainty. Grisch and co-workers demonstrated simultaneous ro-vibrational CRS on H_2 and H_2O, at representative operational conditions in a high-pressure rocket combustor, by employing a broadband ns CRS instrument. They performed ro-vibrational CRS thermometry and deduced the H_2O concentrations by measuring the modulation of the resonant H_2O signal over the continuum NR background [14]. Before transporting the laser beams inside the combustion chamber via optical fibers, the authors focused them in an atmospheric-pressure Ar flow and recorded the NR CRS signal to monitor the shot-to-shot fluctuations in the pulse energies and the spectral shape of the broadband Stokes laser. A similar approach, with sequential focusing of the beams to record the shot-to-shot spectral reference, had been demonstrated already in 1985 by Pealat and co-authors, who claimed that "*referencing on a shot-to-shot basis improved the mean slightly and produced marginal gains in the standard deviation of individual measurements*" [144]. Van Veen and Roekaerts, on the other hand, identified in the spectral excitation profile the "*main bottleneck to obtaining high-quality N_2 CARS spectra and to arriving at species as well as accurate temperature values*" [145]. They employed an echelle spectrometer to simultaneously measure the spectra of the ro-vibrational N_2 CRS signal, as well as of their modeless dye laser, which was then used to compute the spectral excitation profile. The CRS thermometry validation measurements performed in a McKenna burner resulted in a remarkable precision of 1.5%, comparable to present state-of-art fs/ps CRS instruments [146]. The authors speculated that fluctuations in the measurements platform could be the limiting factor, and that the precision of their CRS instrument might in fact be better than 1%. Recently Barros and co-authors have indeed observed such instabilities in a laminar flame stabilised on a McKenna burner and, by subtracting their dynamics, they have achieved a precision of 0.5% at 2081 K by ro-vibrational N_2 fs/ps CARS thermometry [124]. In Papers II and V analogous fluctuations are observed in a laminar premixed CH_4/air stabilised on a Bunsen burner, where the flame front dynamics is tracked over the acquisition time by pure-rotational N_2-O_2 fs/ps CRS imaging, with a temporal resolution of 1 ms. More recently, Lauriola and co-authors developed a ps burst-mode vibrational CRS instrument and demonstrated its use to perform N_2 thermometry at 100 kHz [53]: they observed that the bandwidth of the NR CRS spectrum changed over the burst, increasing the measurement imprecision. This was compensated for by splitting 8% of the Stokes and pump/probe beams and focusing them in 3 mm-thick glass window to realise the concurrent generation of the NR CRS signal.

These works proved that the concurrent generation of the NR CRS signal for spectral referencing is an effective solution to the shot-to-shot fluctuations in the spectral excitation profile, and can significantly improve the precision of gas-phase CRS thermometry and concentration measurements. Nevertheless, all the approaches illustrated above resorted to an *ex situ*, even if concurrent, generation of the NR CRS signal: they could only account for the noise in the laser source employed, while they neglected that arising along the beam path due to fluctuations in the gas-phase optical medium. Paper II introduces an alternative referencing protocol, based on the concurrent *in situ* generation of the NR CRS signal, which is thereupon extended to ultrabroadband fs/ps CRS with *in situ* filamentation in Paper III.

This work builds on an old idea firstly advanced by Farrow and co-workers in 1982 [5], who demonstrated for the first time the simultaneous detection of resonant and non-resonant CRS signals in two distinct detection channels. The authors employed the polarisation control scheme pioneered by Oudar *et al.* [147] to minimise the NR background in the ro-vibrational Q- and O-branch spectra of N_2, and compared CRS thermometry to calibrated thermocouple measurements in a diffusion flame. The O-branch spectrum, consisting of 5 spectral lines in the 2157-2172 cm^{-1} spectral region investigated in this work is completely depolarised (see Section 2.2.1). Hence, the polarisation approach of Ref. [147] not only allowed for a significant reduction of the NR background in the resonant spectrum, but the NR signal itself could be detected with minimal interference of the resonant component, yielding "*a more ideal normalization spectrum (spectrally smoother)*" [5]. The authors compared the temperature measured by (i) conventional N_2 Q-branch CRS with *ex situ* referencing (ii) ro-vibrational O-branch CRS with *in situ* referencing, and (iii) thermocouples. They found the three measurements to agree within the experimental uncertainty in the homogeneous region of the flame, with results: (i) 1816 ± 50 K, (ii) 1826 ± 50 K, and (iii) 1833 ± 60 K. Nevertheless, it should be noted that the spectral window investigated in this work was relatively small, so that the *in situ* NR CRS spectrum was almost flat over the measured ~15 cm^{-1}, and the impact of the referencing protocol on ro-vibrational N_2 CRS thermometry was not investigated. In a later publication the same research group applied the *in situ* referencing protocol to measure the relative concentrations of CO in an atmospheric CH_4/air flat flame [11]. They exploited the overlap of the ro-vibrational CO CRS Q-branch spectrum in the region ~2100-2180 cm^{-1} with the ro-vibrational N_2 O-branch spectrum, and with line S(9) in the pure-rotational spectrum of H_2 at 2130 cm^{-1}. The authors reported an improvement of the reproducibility of the normalised measurements, which was observed to approach the shot-noise limit (estimated to be 1.2%) for a single laser pulse, in a dedicated room-temperature experiment in a 10 atm CO/Ar mixture. The significant impact of the referencing protocol was attributed to the large shot-to-shot variations of the laser fields provided by multi-mode lasers, resulting in a measured standard deviation of the non-normalised CRS spectra larger than 12%. Despite the promising results of Farrow and co-authors, the *in situ* referencing approach to CRS thermometry and concentration measurements was not applied in later works.

Paper II combines a polarisation-based *in situ* referencing approach with the imaging capabilities of pure-rotational fs/ps CRS (see Paper V for details about the pure-rotational fs/ps CRS imaging instrument). An innovative polarisation-sensitive coherent imaging spectrometer is designed to simultaneously measure the two cross-polarised one-dimensional CRS signals extending over ~1.3 mm, in distinct detection channels. This design represents a significant improvement with respect to the two-channel detection system of Farrow *et al.*. As a single polariser is needed to separate the resonant and NR CRS signal components, and a single sCMOS detector acquires both spectral images at high repetition rate. Furthermore, spectral images of the resonant and NR CRS signals can be simultaneously recorded with excellent spatial resolution (~40 μm) over the one-dimensional FOV. Pure-rotational N_2-O_2 fs/ps CRS imaging thermometry with *in situ* referencing is thus demonstrated across a laminar premixed CH_4/air flame front. The novel referencing protocol is compared to the conventional one, the latter being performed by measuring the NR CRS signal in room-temperature Ar sequential to the flame experiment. In contrast to the limited spectral window required to perform ro-vibrational N_2 CRS thermometry in Ref. [5], the pure-rotational N_2 spectrum spans more than 300 cm^{-1} at high temperature. An accurate measurement of the spectral excitation profile is thus critical to perform accurate thermometry, as shown in Figure 5.1.

The theory of polarisation control for the generation of the two-beam fs/ps CRS signal is outlined in Appendix D. The polarisation angle of the resonant and NR CRS signals are derived as functions of the relative polarisation angle between the linearly polarised pump/Stokes and probe beams, as well as of the depolarisation ratio of the Raman spectrum. A detailed description of the coherent imaging spectrometer introduced in Paper II is provided in Section 5.1. Section 5.2 illustrates the application of the *in situ* referencing protocol to pure-rotational N_2-O_2 fs/ps CARS imaging thermometry. Finally, the application of the *in situ* referencing protocol to ultrabroadband fs/ps CRS with *in situ* filamentation is presented in Section 5.3.

5.1 Polarisation-sensitive coherent imaging spectrometer

The main differences in the optical setup presented in Section 4.1.1 and the one in Paper II concern: (i) the focusing optics used to realise pure-rotational N_2-O_2 fs/ps CARS imaging, and (ii) the introduction of a novel polarisation-sensitive coherent imaging spectrometer to implement the *in situ* referencing protocol.

As shown in Figure 5.2, 1D fs/ps CARS imaging is realised by focusing the pump/Stokes and probe beams via cylindrical lenses with focal lengths f:=300 and 500 mm, respectively. The symmetry axes of the lenses are vertically aligned (denoted as "$CL_{(v)}$" in the figure) to generate a vertical measurement line. The length of said line is adjusted by introducing astigmatic focusing via two horizontally aligned cylindrical lenses ("$CL_{(h)}$") with focal lengths f:=1000 and 300 mm on the pump/Stokes and probe beam path, respectively. The probe beam thus extends to ~1.3 mm at its vertical focus, while the pump/Stokes beam is focused at the same location on a ~4 mm long line, both lines being measured with a sCMOS beam profiler (WinCamD, Dataray). This arrangement ensures that the peak irradiance of the pump/Stokes pulse, estimated to be ~18 TW/cm^2, is sufficiently low not to result in the photo-ionisation of the gas-phase medium. The beams are crossed at a shallow angle (~3°), resulting in a probe volume of ~1.3 mm (height) x ~0.6 mm (length) x ~30 μm (width, FWHM).

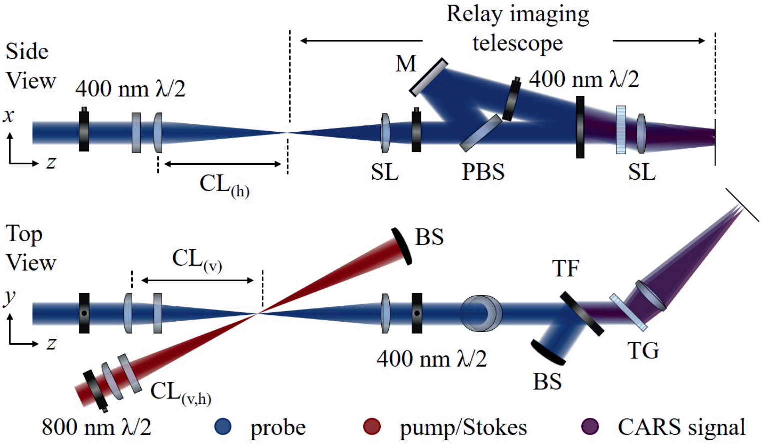

Figure 5.2: The polarisation-sensitive coherent imaging spectrometer used for spatially divided detection of the resonant and NR 1D CRS signals. The subscripts "v" (vertical) and "h" (horizontal) represent the alignment of the symmetry axes of the cylindrical lenses (CL). Two separate detection channels for P- and S-polarised light, with orientation determined with respect to the transmission grating (TG), are relay-imaged with ~1:1 magnification from the signal generation plane to the camera plane. M, mirror; $\lambda/2$ half-wave plate; PBS, polarisation beam splitter; BS, beam stop; TF, tunable band-pass filter; SL, spherical lens. Figure reproduced from Mazza *et al.* [28].

The CARS signal generated over the resulting ~1.3 mm FOV is then collected by the coherent imaging spectrometer, as shown in Figure 5.2. A 400 mm spherical lens, mounted on a linear translation stage, collimates the vertical dimension of the CRS beam with 3:4 magnification, while the horizontal one diverges because of the astigmatism in the focusing scheme. A single thin-film polariser is employed to discriminate the resonant and NR CARS signals in two distinct detection channels. As sketched in Figure D.2, under polarisation-separation conditions (i.e. $\phi = \tan^{-1}\sqrt{6} \approx 67.8°$) the resonant and NR CARS signals are linearly polarised with polarisation angles, $\beta \approx -50.7°$and $\delta \approx 39.2°$, measured with respect to the vertically-aligned pump/Stokes polarisation. A 400 nm half-wave plate is inserted after the collection lens to align the polarisation of the resonant and NR CRS signal components to the transmission and reflection axes of the polariser, respectively.

The S-polarised NR CRS signal is reflected by the polariser into the NR detection channel, where a second 400 nm half-wave plate turns its polarisation by $\pi/2$. Thus both signals are S-polarised with respect to the high-density transmission grating of the spectrometer, ensuring a transmission efficiency >90%. A tunable-angle band-pass filter is inserted before the grating to suppress the probe, which almost perfectly co-propagates with the CRS signal for the nearly phase-matched geometry and shallow crossing angle employed. The two signals are imaged 1:1 onto two regions of the sCMOS detector, each 100 pxl (height) x 2048 pxl (width), by a 400 mm imaging lens. The imaging properties of the spectrometer are quantified by inserting a knife-edge at the location of the probe volume, which is thus relay-imaged onto the imaging plane of the telescope. Placing the detector at this plane the LSF of the image is measured to be ~40 μm. Figure 5.3 illustrates the simultaneous single-shot detection of the resonant and NR CRS signals generated across a laminar premixed CH_4/air flame front. The NR CRS spectra recorded in Channel 2 provides the *in situ* spectral reference to normalise the resonant CARS spectra in Channel 1.

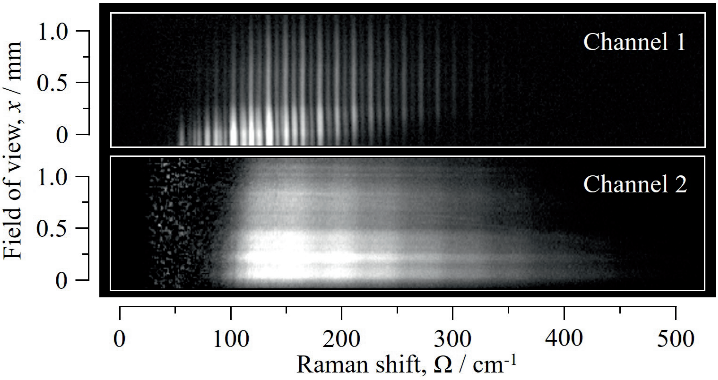

Figure 5.3: Single-shot fs/ps CARS imaging in the pure-rotational region of the Raman spectrum, with simultaneous detection of the resonant and NR CARS signals. The measurements are performed across a laminar premixed CH_4/air flame front (ϕ=0.95). The resonant CARS signal in "Channel 1" shows the effect of the temperature and composition gradient across the flame front. In the lower portion of the image the low-temperature spectra of N_2 and O_2 are visible. Progressing in the reaction zone, O_2 is consumed and the heat released in the reaction results in the spread of the rotational Boltzmann distribution to higher rotational energy states. “Channel 2” indicates the detection channel for the broadband NR CARS signal. Figure reproduced from Mazza *et al.* [28].

The ability of this spectrometer to discriminate the polarisation of the detected signals is extensively employed throughout the present research to: (i) implement the *in situ* referencing protocol in Papers II and III; (ii) identify the nature of additional non-linear optical processes in Papers VI and VII [148]; (iii) implement a novel time-resolved CRS-based detection technique for H_2O in Paper VIII. The first application is discussed in detail through the rest of the present chapter.

5.2 COHERENT RAMAN IMAGING THERMOMETRY WITH *IN SITU* REFERENCING

The use of the *in situ* referencing protocol is first demonstrated in Paper II by performing pure-rotational O_2-N_2 fs/ps CARS imaging thermometry across a laminar premixed CH_4/air flame front. An example of the single-shot detection of the resonant and NR CARS spectra, recorded simultaneously in the pure-rotational region up to 500 cm^{-1}, is shown in Figure 5.3. The change in the local temperature and composition of the medium is evident along the measurement line, which is placed orthogonal to the flame front. In the reactant mixture the spectra present the signatures of both O_2 and N_2, and only the lowest rotational energy states are populated according to Boltzmann statistics. Progressing across the chemical reaction layer, the temperature increases significantly while O_2 is consumed, such that for $x \gtrapprox 0.3$ mm only the pure-rotational spectrum of N_2 is clearly identified, and higher rotational states become populated. The effect of the temperature change is also evident in the reducing intensity of both the resonant and NR CARS signals along the measurement line, in agreement with the quadratic scaling of the CRS signal intensity with the number density of the molecular scatterers. In order to establish the location of the reaction zone along the measurement line, conventional pure-rotational fs/ps CARS is performed on the spectra acquired at a probe delay of ~27 ps. At this delay there is no significant overlap between the pump/Stokes and probe laser pulses, so that the NR CRS signal is time-gated, and the *ex situ* referencing protocol is adopted, normalising the resonant CARS spectra by the NR CARS spectrum acquired in Ar. The resulting temperature and relative O_2/N_2 concentration, measured across the laminar flame front, are shown in Figure 5.4.

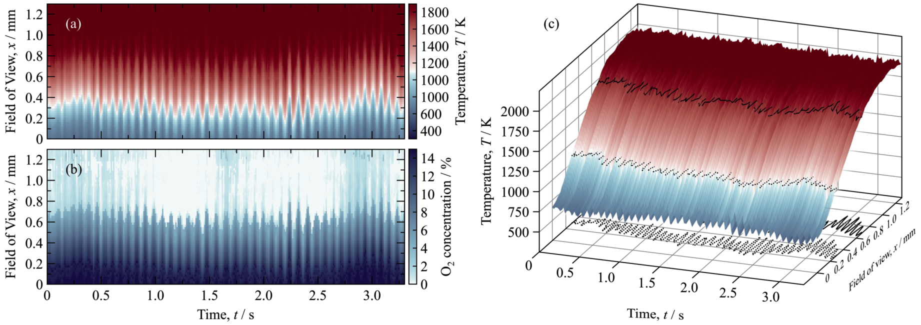

Figure 5.4: Flame front tracking via single-shot fs/ps CRS imaging. (a) Temperature profile measured by pure-rotational O_2-N_2 CARS over the ~1.3 mm FOV. The temperature profile is tracked over 300 single-shot frames acquired at ~91 Hz: clear oscillations in the flame front at ~13 Hz (as also reported in Ref. [125]) are visible. (b) Relative O_2/N_2 concentrations measured over the FOV. (c) Conditional mapping of the flame front, by measuring the temperature at a fixed distance from the flame front location, defined as the inflection point in the temperature profile (at ~1200 K).

As expected, the local temperature and O_2 concentration show a strong inverse correlation: the temperature increases across the reaction zone of the flame, due to the heat release of the combustion reaction, where O_2 is consumed. The opposite trend of the temperature and concentration gradients is confirmed through the whole temporal sequence in Figure 5.4(a) and (b), consisting of 300 single-shot frames acquired at ~91 Hz. This acquisition rate is sufficient to resolve the ~13 Hz oscillations in the flame platform, also observed in Ref. [125] and attributed to buoyancy-driven fluctuations in the combustion flow. In order to assess the thermometric precision of the fs/ps CARS instrument, and compare the performance of the two referencing protocols, the temperature is measured conditional to the position of the flame front at each single-shot frame. The latter is defined as the location of the inflection point of the temperature profile (at T = 1192 K) across the one-dimensional laminar premixed CH_4/air flame (ϕ = 0.95), as predicted by the CHEM1D code [149]. This location is tracked over the acquisition time as illustrated by the dashed line in Figure 5.4(c). Paper II reports the temperature statistics at a distance of ~390 μm from the flame front, represented by the solid line in Figure 5.4(c). The average temperature measured of this location is 1843 K, resulting in an accuracy of -1.5%, assuming a true temperature of 1870 K according to the numerical simulation. Adopting this conditional approach the thermometric precision is estimated to be 1.2%, almost three times better than the 3.1% standard deviation of the temperature statistics collected at the fixed location along the measurement line (at x = 0.82 mm). This fact points to the precision of the fs/ps CRS instrument being fundamentally limited by the physical oscillations in the flame employed for its calibration.

Adopting a probe delay of ~3 ps the resonant and NR CARS spectra are concurrently generated and recorded, so that both the conventional *ex situ* and the *in situ* referencing protocols can be adopted, to compare their impact on fs/ps CARS thermometry. The *ex situ* NR CARS spectra, acquired in room-temperature Ar sequentially to the flame experiment, are shown in Figure 5.5(a), while the NR spectra acquired *in situ* are presented in Figure 5.5(b). Note that in this case the NR CARS spectrum at each location along the FOV is normalised to its maximum value, so that the effect of the temperature gradient observed in Figure 5.3 is not visible in Figure 5.5(b). The NR CARS spectra acquired *ex-* and

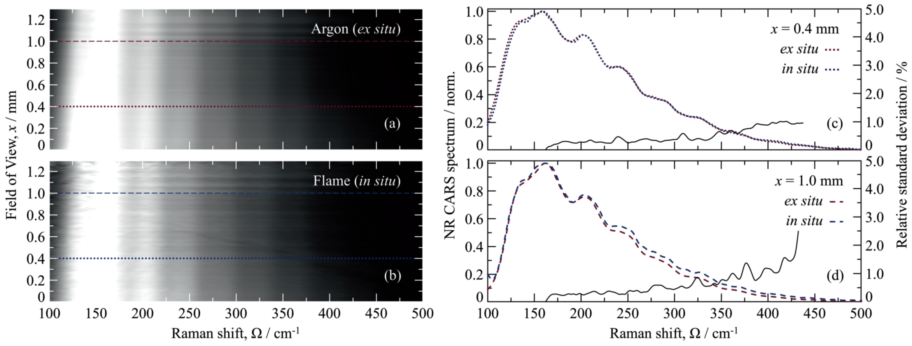

Figure 5.5: *Ex situ* and *in situ* measurement of the spectral excitation profile for pure-rotational fs/ps CARS imaging. (a) NR CARS spectrum measured in room-temperature Ar (*ex situ*) over the ~1.3 mm FOV of the 1D fs/ps CARS imaging instrument described in Ref. [125]. (b) NR CARS spectrum measured *in situ* concurrently to the pure-rotational O_2-N_2 CARS signal across a laminar premixed CH_4/air flame front. (c) Comparison of the excitation profiles measured *ex-* (red) and *in situ* (blue) at x=0.4 mm over the FOV, in the pre-heat zone of the flame front: the two profiles almost perfectly overlap at this location. The solid black line represents the RSTD of the NR CARS spectra acquired *in situ* over the spectral range employed for pure-rotational O_2-N_2 CARS. (d) Comparison of the excitation profiles measured *ex-* (red) and *in situ* (blue) in the products of the flame at location x=1 mm. The *ex situ* referencing protocol entails an overestimation of the temperature at this location.

in situ have a similar envelope, but an important difference is identified when comparing these spectra at two distinct locations along the measurement line. At location x=0.4 mm, corresponding to the average location of the flame front as defined above, the two average NR CARS spectra perfectly coincide. Hence, the *ex situ* referencing protocol does not introduce any systematic bias in the temperature measured by pure-rotational fs/ps CARS at this location.

In the hot product gases of the flame at location x=1 mm the average profile of the NR CARS spectrum measured in Ar is lower than the corresponding average profile measured *in situ*: the conventional referencing protocol thus introduces a systematic overestimation of the temperature at this location. This variation of the systematic bias introduced by the referencing protocol over the measurement line, in the flame experiment, is explained in Paper II by the gradient of the effective refractive index across the flame front. This entails a difference in the GDD imparted over different portions of the fs pump/Stokes beam as it propagates through the flame. The relatively cold gas-phase medium in the reactants and pre-heat zone of the flame introduces a larger temporal chirp than the more rarefied hot product gases do, so that the effective excitation bandwidth varies across the flame front. This behaviour of course cannot be rendered by the NR CARS signal acquired in the homogeneous environment of the room-temperature Ar flow, whose refractive index is almost identical to that of room-temperature air (at 800 nm, n=1.00027 for Ar [150] and n=1.00028 for dry air [151], both at standard pressure and temperature).

An undetected leakage of the NR CARS signal into the resonant detection channel of the coherent imaging spectrometer –possibly due to the imperfect separation of the two polarisation components by the thin-film polariser–, results in the contamination of the resonant spectra acquired at ~3 ps in the flame experiment of Paper II. This skews the spectral envelope and results in a significant underestimation of the local temperature 390 μm from the flame front, independently of the spectral referencing protocol employed. The *ex situ* referencing yields 1696±11 K, while the *in situ* protocol results in 1674±18 K. Nevertheless, the leakage only affects the resonant CARS signal, so that a meaningful comparison between the two protocols can still be drawn. The observed change in the effective excitation bandwidth over the measurement line, as mapped by the *in situ* NR CARS signal, results in a systematic bias of varying magnitude being introduced by the *ex situ* referencing protocol. As observed in Figure 5.5(c), at the flame front the excitation bandwidth is correctly mapped by either NR CARS spectrum so the the specific referencing protocol does not affect the resulting measurement. This is confirmed by fs/ps CARS thermometry resulting in 1210±18 K adopting the *ex situ* referencing protocol, and 1207±19 K with the *in situ* one. In the flame products, ~390 μm from the flame front location, the reduced GVD of the optical medium, and consequently larger effective excitation bandwidth, can only be accounted for by the *in situ* protocol. The conventional referencing protocol results in a temperature overestimation of 22 K, corresponding to a systematic uncertainty of ~1.3%.

These results show that the spectral referencing protocol can have an important impact on the accuracy of pure-rotational fs/ps CRS thermometry in combustion environments, in particular when short fs laser pulses (<50 fs) are employed to impulsively excite the rotational Raman coherence. The introductory chapter of the present text discussed the importance of developing high-fidelity metrology for scalar determination in chemically reacting flow. In particular, the need for accurate thermometry measurements in high-temperature combustion processes is argued in view of the significant impact that even a ~1% uncertainty in the measured temperature can have in the prediction of the chemical pathways and the formation of pollutant species. The results in Paper II therefore point to the need of adopting the *in situ* referencing protocol in the pursuit of exact CARS thermometry, consistently improving its accuracy below the limit of 1%.

5.3 ULTRABROADBAND FS/PS CRS WITH *IN SITU* REFERENCING OF THE SPECTRAL EXCITATION

In Paper III the *in situ* referencing protocol is applied to ultrabroadband fs/ps CRS with *in situ* filamentation to perform accurate pure-rotational H_2 CRS thermometry behind the thick optical window discussed in the previous chapter.

The impact of the spectral referencing protocol on the accuracy of ultrabroadband fs/ps CRS is expected to be more significant than the one assessed in Paper II for pure-rotational N_2-O_2 CRS. As a matter of fact, the shorter the temporal duration of a fs laser pulse, the larger its sensitivity to the GVD of the optical medium it propagates through, as pointed out in Section 3.2. The *ex situ* referencing protocol therefore introduces a larger bias to pure-rotational H_2 CRS thermometry employing the 17 fs output of the filament as the ultrabroadband pump/Stokes pulse. This is be even more relevant as the pulse compression is achieved *in situ* via fs laser-induced filamentation. Section 4.1.3 presents experimental evidence of the impact of the boundary conditions to the filamentation process on the pulse self-compression.

Both the local composition of the gas-phase medium and its temperature are found to significantly affect the bandwidth of the compressed supercontinuum generated via *in situ* filamentation in Figures 4.12 and 4.13. The introduction of the *in situ* referencing protocol can also significantly improve the single-shot reproducibility of ultrabroadband fs/ps CRS measurements, if the supercontinuum light source employed has poor spectral stability. For example, Bohlin and Kliewer attributed the large uncertainty in the single-shot determination of the relative concentrations of CH_4 and H_2 (estimated to be 13% and 4%, respectively) to the shot-to-shot spectral fluctuations of the supercontinuum generated in a hollow-core fiber [24].

The pure-rotational H_2 spectrum is chosen in Paper III as the perfect case to demonstrate the combination of the *in situ* referencing protocol with the *in situ* generation/*in situ* use of the compressed supercontinuum, to realise accurate ultrabroadband fs/ps CRS thermometry behind the optical window. Pure-rotational Raman spectra are completely depolarised, such that the same polarisation settings employed in Paper II can be used in the application of the *in situ* referencing protocol to H_2. Furthermore, the pure-rotational spectrum of H_2 spans >1500 cm^{-1} at high temperature, such that CRS thermometry on this species is particularly sensitive to the spectral referencing protocol employed. The details of this experiment are discussed in Section 5.3.1.

Following work provides experimental confirmation of the possibility of extending the polarisation-based *in situ* referencing protocol to any depolarised Raman transition, besides pure-rotational ones. Section 5.3.2 discusses the application of the *in situ* referencing protocol to the ro-vibrational Raman spectrum associated to the ν_2 mode of CH_4, which appears in the vibrational fingerprint region in close proximity to the ro-vibrational spectra of O_2 and CO_2.

5.3.1 *IN SITU* REFERENCING OF THE PURE-ROTATIONAL H_2 CRS SPECTRUM

In order to implement the *in situ* referencing protocol for ultrabroadband fs/ps CRS some modifications are introduced to the polarisation-sensitive coherent imaging spectrometer described above, as shown in Figure 5.6.

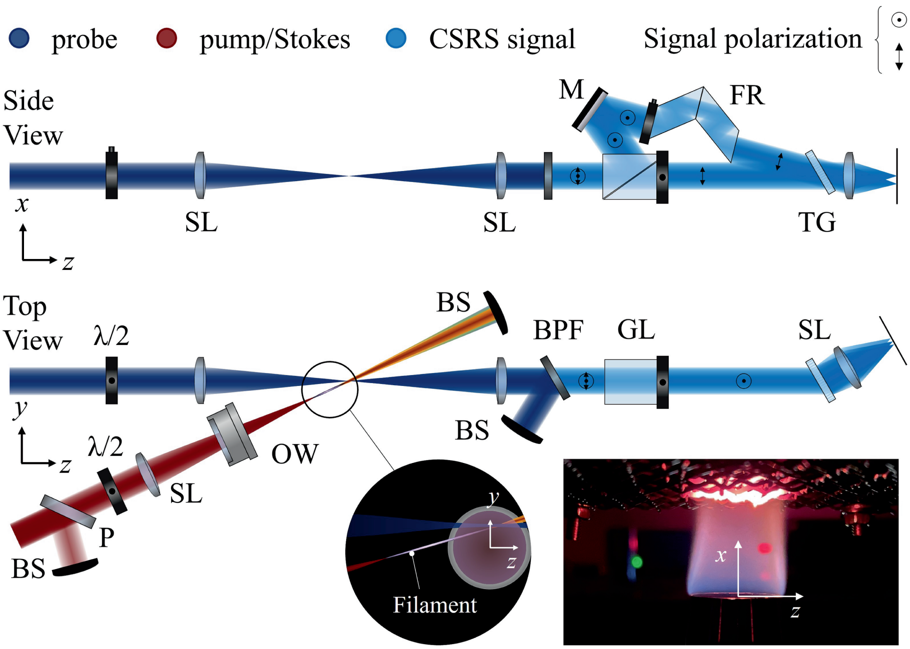

Figure 5.6: Schematic of the ultrabroadband polarisation-sensitive coherent imaging spectrometer. A Glan-laser polariser (GL) is employed to separate the cross-polarised resonant and NR CRS signals, while a Fresnel rhomb (FR) rotates the polarisation of the ultrabroadband NR CRS signal so as to maximise the diffraction efficiency of the transmission grating (TG). A thin-film polariser (P) ensures the linearity of the polarisation state for the fs pulse prior filamentation. A 22 mm BK7 optical window (OW) is mounted on the fs beam path, ~20 cm after the 500 mm focusing lens. SL, spherical lens; $\lambda/2$, half-wave plate; M, mirror; TF, tunable band-pass filter; BS, beam stop. Signal polarisation: ↕, in-plane polarisation; ⊙, out-of-plane polarisation. Figure reproduced from Mazza *et al.* [27]. Inset: orientation of the filament propagation with respect to the laminar H_2/air diffusion flame front.

Since the ultrabroadband CSRS signal acquired over the spectral region ~300-1500 cm^{-1} spans over ~24.5 nm, a single broadband Fresnel rhomb is used to turn the polarisation in the NR CSRS detection channel of the spectrometer to maximise the diffraction efficiency of the transmission grating. The polarisation angles of the linearly-polarised pump/Stokes and probe pulses are set so as to satisfy the polarisation-separation condition in Equation (D.14), and to generate the resonant signal in transmission through the Glan-laser polariser employed as the polarisation gate in the spectrometer. A thin film polariser mounted on the pump/Stokes beam path is used to both attenuate the pulse energy –to characterise the effect of its temporal chirp, as discussed in the previous sections– and to ensure the linearity of the pump/Stokes polarisation. This is critical to the successful combination of the polarisation-based *in situ* referencing protocol and the supercontinuum generation via *in situ* filamentation, as it is known that the combination of electronic Kerr non-linearity, electron plasma and molecular alignment in the filament result in an ultrafast rotation of the polarisation ellipse during the filamentation of elliptically-polarised fs pulses [152]. Linearly-polarised fs pulses, on the other hand, have been experimentally demonstrated to maintain their polarisation state during the filamentation process as well as in the post-filament propagation. By minimising the polarisation ellipticity of the pump/Stokes pulse before the focusing lens, the polarisation theory outlined in Appendix D is successfully applied to generate cross-polarised ultrabroadband resonant and NR CSRS signals. A fast-focusing lens (f:=100 mm) is used to image the signals onto the sCMOS detector with a dispersion of 0.93 cm^{-1}/pixel and an overall detection band of 1900 cm^{-1}, ultimately limited to 1200 cm^{-1} by the band-pass filter. The supercontinuum output by the filament and the probe beam are crossed at a ~3° angle approximately 2 mm after the end of the filament, so that, according to the procedure and results presented in Section 4.1.1 the probe volume dimensions are estimated to be: ~20 μm (height, FWHM) x ~2.5 mm (length, FWHM) x ~20 μm (width, FWHM).

Figure 5.7(a) shows the ultrabroadband NR CSRS spectra (black line, average of 1200 single-shot spectra) acquired at 17 measurement location across a laminar H_2/air diffusion flame front. The probe volume is placed ~0.5 mm above rim of a Bunsen burner (the details of this experiment are discussed in Section 6.1.2), and moved radially from the centre of the burner at location y=0 mm to up to y=8 mm, corresponding to the last location in the flame front where the H_2 CSRS signal is acquired with sufficient SNR to perform thermometry. These *in situ* spectral references are compared with the NR CSRS spectrum acquired in a room-temperature argon flow (red line), revealing a dramatic difference in the spectral excitation bandwidth as measured *ex situ* and the effective bandwidth available in the combustion environment. This confirmed the observations in Section 4.1.3: the pulse compression via *in situ* filamentation has a strong dependence on the local boundary conditions, i.e. chemical composition and temperature of the gas-phase medium, to the filamentation process itself. This fact is also highlighted by the progressive decrease of the excitation bandwidth in the progression from the centre of the burner towards the high-temperature reaction zone of the flame front. The change in the spectral excitation

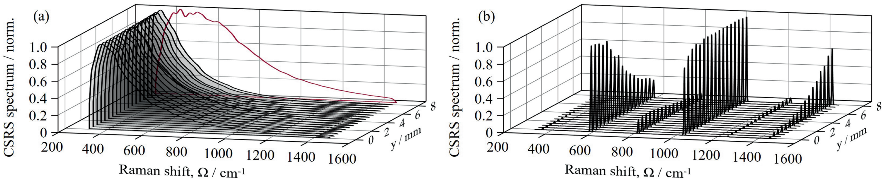

Figure 5.7: Ultrabroadband fs/ps CSRS across the H_2/air flame front. (a) 1200 shot-averaged ultrabroadband NR CSRS spectra acquired *in situ* (black lines) over 17 locations from the centre of the burner (y=0 mm) to the flame front (y=8 mm), and *ex situ* in room-temperature Ar (red line). (b) Single-shot ultrabroadband H_2 CSRS spectra acquired from the centre of the burner to the flame front. Up to six pure-rotational lines are detected simultaneously over the 300-1500 cm^{-1} spectral range. Figure reproduced from Mazza *et al.* [27].

bandwidth is quantified by the application of the time-domain NR CRS model discussed in the previous chapter, to measure the pulse compression at the different flame locations. At the centre of the burner the pulse self-compression leads to an average pulse duration of 26 fs with a residual positive chirp quantified to ~100 fs^2, while moving to the higher temperature region in the flame front the compression is reduced to 30 fs with a ~100 fs^2 GDD. The pulse compression is thus significantly lower in the flame than in the room-temperature Ar flow, and it reduces moving towards the flame front because of the three-dimensional curvature of the flame. At location y=0 mm the filament crosses the flame front almost perpendicularly. On the contrary, over the burner rim (y=9.5 mm) the filament is parallel to the flame front and propagates for a larger distance inside the high-temperature reaction zone, where the reduced effective refractive index negatively impacts the self-phase modulation and photo-ionisation processes.

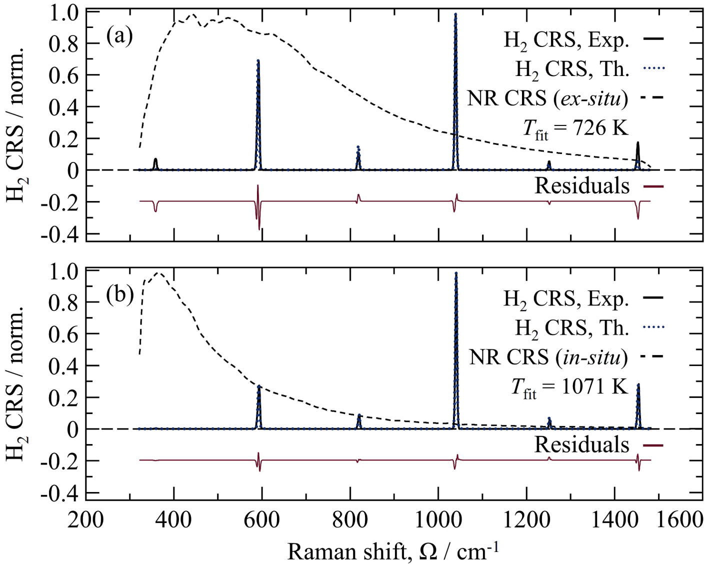

Figure 5.8: Impact of the referencing protocol on pure-rotational H$_2$ CRS thermometry. (a) Single-shot ultrabroadband H$_2$ CSRS spectrum acquired in the flame at location y=6 mm, normalised by the NR CRS signal acquired in argon (*ex situ*). The spectrum is fitted to the time-domain CSRS code to measure the local temperature to T=726 K. (b) The same spectrum is normalised by the NR CRS signal simultaneously acquired in the flame (*in situ*), and fitted to measure T=1071 K. Figure reproduced from Mazza *et al.* [27].

Figure 5.8 provides a direct comparison between the *ex situ* and *in situ* referencing protocols applied to a single-shot pure-rotational H$_2$ CSRS spectrum acquired at location y=6 mm. The significant difference between the pulse compression realised by fs laser-induced filamentation in Ar (*ex situ*) –resulting in a 17 fs compressed supercontinuum– and in the flame is reflected dramatically on the normalised resonant spectra in Figure 5.8. The use of the conventional *ex situ* referencing protocol thus results in a largely skewed spectrum as shown by the large misfit to the time-domain model (dotted blue line), in Figure 5.8(a). The experimental spectrum is severely distorted upon the *ex situ* referencing such that its envelope does not correctly represent the pure-rotational Boltzmann distribution of the H_2 molecules in the probed volume. On the other hand, when employing the correct excitation profile, as mapped by the *in situ* NR CSRS spectrum, a more meaningful comparison to the model is possible. This is particularly evident in the good agreement shown by the experimental and synthetic spectra in Figure 5.8(b), in correspondence of lines O(2) and O(7), which are in contrast completely skewed in Figure 5.8(a). As shown in the figure, the conventional *ex situ* referencing protocol introduces a massive systematic bias of ~350 K (32%), as compared to the temperature measured by pure-rotational N_2 CARS, rendering the pure-rotational H_2 CRS thermometry an all but useless tool for combustion diagnostics. On the contrary, by adopting the *in situ* referencing protocol the temperature estimates by pure-rotational H_2 CSRS and pure-rotational N_2 CARS agree within 0.35% over the 1200 single-shot spectra acquired at this location in the flame. A detailed characterisation of the precision and accuracy of pure-rotational H_2 CSRS is given in Section 6.1.2.

The results of Paper III demonstrate the possibility of performing accurate ultrabroadband fs/ps CRS measurements behind thick optical windows, by combining the *in situ* generation/*in situ* use of the compressed supercontinuum, via fs laser-induced filamentation, with the *in situ* referencing protocol. The application of this protocol is also proposed to significantly improve relative (and possible absolute) concentration measurements via ultrabroadband fs/ps CRS. The accurate measurement of the effective spectral excitation efficiency of the different Raman modes, paired with a reliable knowledge of the Raman cross-section of the different molecules, would allow for determining the concentrations of all the Raman-active species present in the probed volume.

5.3.2 *IN SITU* REFERENCING OF THE RO-VIBRATIONAL CH_4 ν_2 CRS SPECTRUM

The practical implementation of the *in situ* referencing protocol –setting the linear polarisation of the input laser fields so as to generate cross-polarised resonant and NR CRS signals– depends on the depolarisation ratio of the Raman spectrum of interest. According to Equation (D.14) for a completely-depolarised Raman transition (i.e. ρ=3/4) the polarisation-separation condition is satisfied by employing a probe polarisation angle of ~67.5°. The same condition thus apply to all pure-rotational Raman spectra, independently of the chemical species, but also to the completely-depolarised ro-vibrational bands of more complex polyatomic molecules. One such example is the ro-vibrational Raman spectrum of the ν_2 mode of CH_4 [153].

Figure 5.9 presents the first demonstration of the cross-polarised CH_4 ν_2 and NR CSRS signals generated in a room-temperature CH_4 flow, simultaneously recorded in the two detection channels of the polarisation-sensitive coherent imaging spectrometer described in the previous paragraph. A sample of 2000 single-shot NR CSRS spectra is recorded in room-temperature Ar to provide the *ex situ* spectral referencing profile. Since these have no correlation to the resonant CH_4 ν_2 CSRS spectra, the *ex situ* NR spectra are averaged to obtain the smooth referencing profile (dashed red line) in Figure 5.9(a). On the other hand, this profile carries no information on shot-to-shot fluctuations in the pulse compression via *in situ* filamentation (shaded blue area).

The different spectral excitation profiles mapped by the NR CSRS spectra acquired *ex situ* in Ar and *in situ* in CH_4 highlight the effect of the gas composition on the pulse

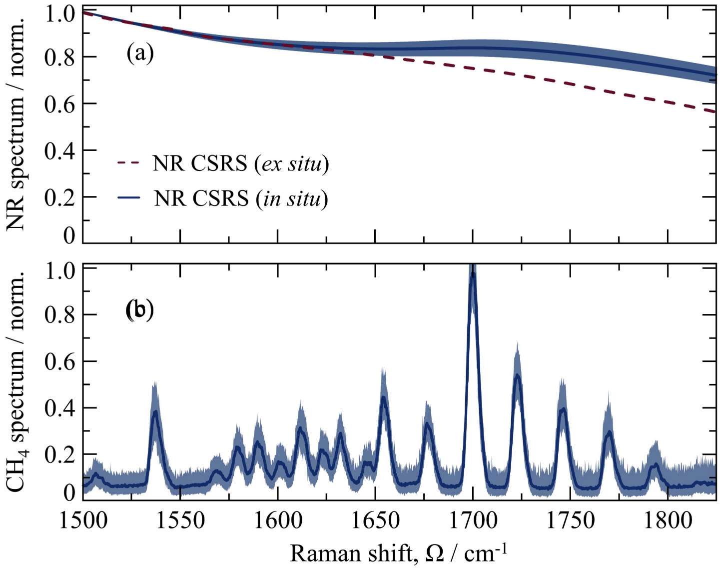

Figure 5.9: Application of the *in situ* referencing protocol to the CH_4 ν_2 CRS spectrum. (a) NR CSRS spectra acquired in the vibrational fingerprint region ~1500-1800 cm^{-1} in room-temperature Ar (*ex situ*) and simultaneously to the resonant CSRS signal in CH_4 (*in situ*). A sample of 2000 single-shot NR CSRS spectra is acquired in Ar and averaged to obtain a smooth excitation profile (dashed red line). The solid blue line represents the sample average of the NR CSRS spectra acquired *in situ*, while the shaded area quantifies the shot-to-shot fluctuation of the excitation provided by *in situ* filamentation in the CH_4 flow. (b) CH_4 ν_2 CSRS spectra normalised, according to the *in situ* protocol, by the NR CSRS signal acquired simultaneously in CH_4.

compression via *in situ* filamentation. As expected, considering the larger electronic third-order susceptibility of CH_4 compared to Ar, *in situ* filamentation in the former led to a larger pulse compressor. In addition, the NR CSRS spectra measured *in situ* show a non-monotonic behaviour: this difference is observed consistently when performing experiments on *in situ* filamentation in Ar and CH_4, over different spectral regions at different pulse energy. Figure 5.9(b) shows a high-resolution ro-vibrational CH_4 ν_2 CSRS spectrum acquired simultaneously to the NR CSRS spectrum in the region ~1500-1800 cm^{-1}. The solid line represents the average over the sample of 2000 single-shot spectra, while the shaded area represents shot-to-shot fluctuations in the spectral envelope. The stability of the pulse compression via *in situ* filamentation is confirmed by comparing the fluctuations in the resonant CRS spectra upon application of the *ex* and *in situ* referencing, with no significant change between the two.

These experimental results confirm that the *in situ* referencing protocol can be effectively applied to the depolarised ν_2 mode spectrum of CH_4, and could be employed to perform accurate concentration measurements, e.g. in CH_4 pyrolysis reactors for H_2 production. This technique could also be employed for the *in situ* investigation of more complex molecules, whose polarisability tensor associated to some of the least-symmetric vibrational modes typically results in completely-depolarised ro-vibrational Raman spectra, as depolarisation ratios in Raman scattering are determined by symmetry properties [39].

This is the case, for instance, of heavier hydrocarbons such as C_2H_4, C_2H_6 and dymethil ether [154], as well as of other chemical compounds of interest for combustion and atmospheric science, such as water vapour [155] and sulfur hexafluoride (SF_6) [156].

Chapter 6

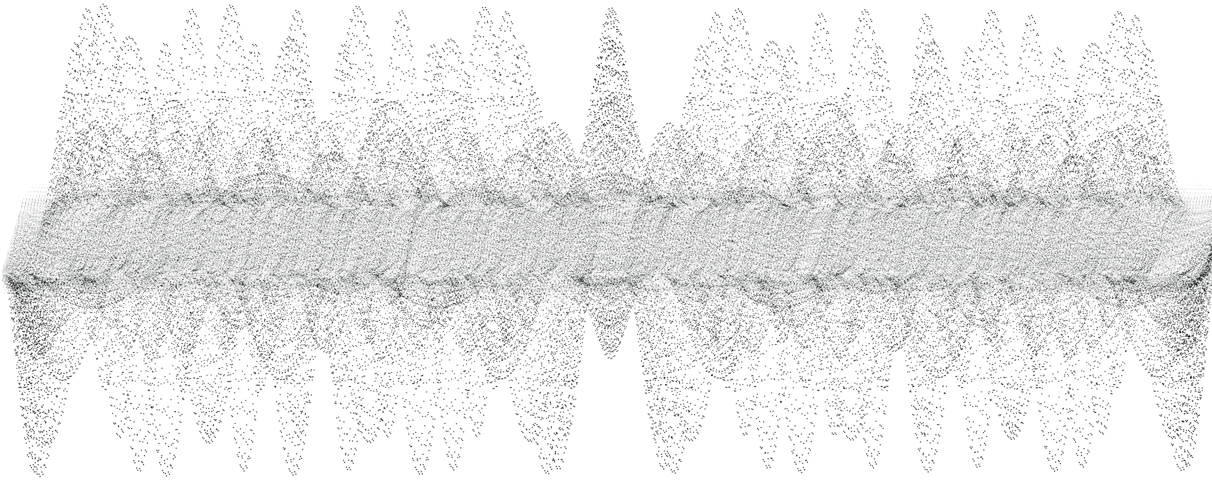

ULTRABROADBAND FS/PS CRS IN THE FINGERPRINT REGION

The present chapter discusses the development of time-domain fs/ps CRS models for simulating the Raman spectra of the major combustion species investigated in the vibrational fingerprint region: H_2, O_2, CO_2 and CH_4. The use of these models to perform high-fidelity fs/ps CRS thermometry on each of these species is demonstrated in a set of laboratory flames. The validation experiments are detailed and the results summarised.

Part of the results discussed in this chapter have been published in Papers I, III and IV.

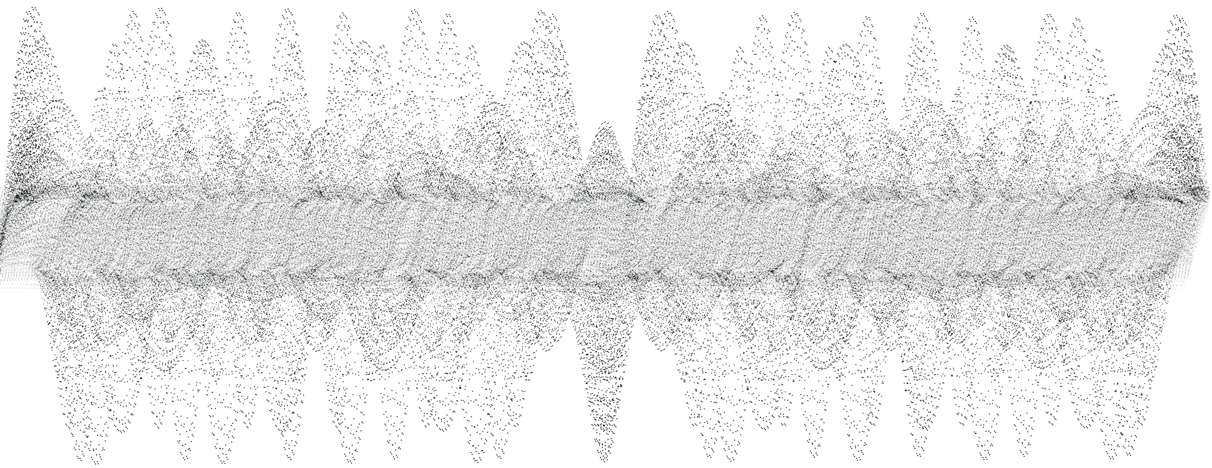

The results presented in Papers I and III demonstrate the possibility of employing *in situ* filamentation as the compressed supercontinuum generation mechanism to perform fs/ps CRS in enclosed combustion environments.

The last step in the development of ultrabroadband fs/ps CRS with *in situ* filamentation as a robust diagnostic technique for quantitative measurements in chemically reacting flow is to address the time-domain modelling of the fs/ps CRS spectra. Quantitative fs/ps CRS requires the availability of reliable spectroscopic models as a means of comparison for the experimental data. The work in Papers II and V makes use of well-established models for the pure-rotational fs/ps CRS spectra of N_2 and O_2 [82, 83]: these are validated in Paper V by performing pure-rotational N_2-O_2 CARS thermometry and relative concentration measurements across a laminar premixed CH_4/air flame.

In parallel to the experimental developments discussed in Chapters 4 and 5, the research published in Papers I, III and IV focuses on the extension of said models to the Raman spectra of some major combustion species in the vibrational fingerprint region. This spectral region is of particular interest for the application of ultrabroadband fs/ps CRS in chemically reactive flows, as it offers a window to investigate gas-phase processes, identifying a large number of relevant species with high chemical specificity. The present research focuses on four major combustion species: H_2, O_2, CO_2, and CH_4.

The combination of *in situ* filamentation with the *in situ* referencing protocol, to achieve accurate pure-rotational H_2 CRS thermometry behind the thick optical window, is discussed in the previous chapter. The impact of the spectral referencing protocol is assessed by fitting the experimental data, acquired in a laminar H_2/air diffusion flame, to a time-domain fs/ps CRS model. The model is described in Section 6.1.1, while the validation experiment and the results are detailed in Section 6.1.2.

The application of ultrabroadband fs/ps CRS to perform simultaneous ro-vibrational O_2 and CO_2 CSRS thermometry is demonstrated, in Paper I, in a laminar premixed CH_4/air flame. Section 6.2 details the time-domain ro-vibrational O_2 fs/ps CRS model, and discusses its validation for flame thermometry.

While the development of such a model for O_2 is a straightforward extension of the well-established model for ro-vibrational N_2 fs/ps CRS (see e.g. Ref. [157, 158]), the application of the modelling approach discussed in Section 2.3.2 to more complex polyatomic molecules is still largely an open research question. The number of vibrational modes of a molecule grow with the number of its atomic nuclei, so that the accurate modelling of the Raman spectra for even relatively simple polyatomic molecules (such as CO_2 and CH_4) requires the availability of detailed spectroscopic databases. The development of a time-domain model for the ro-vibrational fs/ps CRS spectrum of CO_2 is discussed in Section 6.3.2: the model included up to 180 vibrational bands, and is validated at temperatures as high as 2200 K in Paper I.

Finally, Section 6.4 deals with the time-domain fs/ps CRS model developed for the ν_2 mode of CH_4: this model includes more than ten million spectral line and, to the best of the author's knowledge, it the first of its kind to include such a large number of Raman transitions.

6.1 Pure-rotational fs/ps CRS on H_2

The simplest molecule investigated, within the context of the present doctoral research, by means of ultrabroadband fs/ps CRS, is the simplest diatomic molecule H_2. As highlighted in multiple occasions through the present text, the exceptionally large rotational constant of H_2 results in its pure-rotational spectrum extending way beyond the pure-rotational region of the Raman spectrum and into the vibrational fingerprint region. This also entails that only few rotational states are significantly populated even at relatively high temperatures and the pure-rotational H_2 spectrum thus shows a strong temperature sensitivity. In addition, the dynamic range of the detector can also limit the number of rotational lines simultaneously detected, as the intensities of adjacent even and odd lines differ by about one order of magnitude in the H_2 CRS spectrum, as seen in Figure 4.15.

Chapter 4 presents the first demonstration of pure-rotational H_2 fs/ps CSRS behind a thick optical window via *in situ* filamentation. The application of the *in situ* referencing protocol for the concurrent measurement of the ultrabroadband excitation bandwidth provided by the compressed supercontinuum output by the filament is discussed in Chapter 5. The present section addresses the validation of pure-rotational H_2 fs/ps CRS thermometry with *in situ* generation/*in situ* use and *in situ* referencing of the ultrabroadband excitation. Section 6.1.1 presents the time-domain model employed to simulate the pure-rotational H_2 fs/ps CSRS spectrum as a function of temperature. The validation of this model is performed in a laminar H_2/air flame and the performance of pure-rotational H_2 fs/ps CRS thermometry, in terms of its precision and accuracy, is assessed in the comparison with conventional pure-rotational N_2 fs/ps CARS thermometry. This validation experiment and its results are discussed in Section 6.1.2.

6.1.1 Time-domain model for pure-rotational H_2 CRS

The time-domain model employed to simulate the pure-rotational H_2 fs/ps CSRS spectrum in Paper III is a straightforward implementation of the theory summarised in Section 2.3.2. H_2 is the simplest diatomic molecule and, as such, its pure-rotational Raman spectrum is computed in the time domain along the very same lines of the pure-rotational N_2 CRS model in Paper V. The main differences between these two species concern their pure-rotational Raman frequencies and the molecule-specific parameters introduced in Appendix C to compute: (i) the anisotropic polarisability of the molecule γ^2, (ii) the Placzek-Teller coefficient for the pure-rotational O-branch transitions $b_{\text{O-branch}}$, (iii) the Herman-Wallis factor F_γ, and (iv) the nuclear spin degeneracy g_s.

Because of the small mass of its nuclei, not only does the H_2 molecule have a sparse rotational energy manifold, but the exact frequencies associated to the different rotational levels strongly depend on the higher-order correction terms introduced in Equations (2.11) and (2.12). In Paper III, these frequencies are taken from Komasa *et al.* who calculated the ro-vibrational levels of H_2 and D_2 with extremely high accuracy, including even relativistic and quantum electrodynamics corrections, to compare with experimental measurements by precision spectroscopy [159].

The polarisability anisotropy γ^2 defined in Equation (C.12) quantifies the coupling between the electrons and the nuclei in the rotational motion of the diatomic molecule considered, and is responsible for stimulated Raman interaction between the molecule and the input pump and Stokes fields according to Equation (2.28). Assuming the polarisability anisotropy of H_2 to be independent of the vibrational (v) and total angular momentum quantum (J) numbers, γ^2 becomes a simple scaling factor in Equation (C.11), which could be ignored in the simulation of the pure-rotational H_2 CSRS spectrum. On the other hand, the time-domain model in Paper III is also employed to measure the relative H_2/N_2 concentrations in a laminar H_2/air diffusion flame, as discussed in the next chapter. The simultaneous modelling of the pure-rotational H_2 and N_2 CSRS spectra requires the introduction of the specific value of γ^2 for the two species under consideration: these are taken from Ref. [160].

The Placzek-Teller coefficient in Equation (C.11) quantifies the coupling probability of the angular momenta between the initial and final ro-vibrational states of the Raman transition considered, i.e. the probability of a molecule to change its total angular momentum from initial state J_i to the final J_f through the resonant (combined) interaction with the pump and Stokes fields. In the case of a simple linear rotors (see Appendix B) and linearly polarised laser fields, the Placzek-Teller coefficient for an O-branch transition is computed according to the algebraic formula:

$$b_{\text{O-branch}}(J) = \frac{3J(J-1)}{2(2J+1)(2J-1)} \tag{6.1}$$

The strong coupling between the rotational and vibrational motions of the lightweight H_2 molecule affects the Raman cross section of the molecule, and hence the strength of the pure-rotational Raman lines, as much as their position. This has been demonstrated to have a significant impact on CRS thermometry performed on the Q-branch of the ro-vibrational H_2 Raman spectrum [161]. The rotational-vibrational coupling is introduced in the pure-rotational Raman cross-section of Equation (C.11) by the (anisotropic) Herman-Wallis factor F_γ, which is computed in Paper III according to the formula given by Tipping and Ogilvie [162]:

$$F_\gamma(J) = \left[1 + \frac{\eta^2}{\chi}\left(J^2+3J+3\right)\right]^2 \tag{6.2}$$

Where η=$2B_e/\omega_e$ is the ratio between the equilibrium values of the rotational (B_e=60.8 cm^{-1} [163]) and vibrational (ω_e=4401 cm^{-1} [163]) constants. χ is here the ratio between the first two terms in the Taylor expansion of the polarisability anisotropy as a function of the internuclear distance (χ=0.38 [160]).

The significant difference observed in the intensity of even and odd lines in the pure-rotational H_2 CSRS spectrum in Figure 4.15 is a consequence of the nuclear spin degeneracy of the molecule, as illustrated in Appendix B for the case of N_2. In the case of H_2, the ^{1}H nuclei are protons with nuclear spin i=1/2 so that they have a combined nuclear spin wave function corresponding to the singlet state (para-hydrogen, I=0 and M_I=0)

$$|I,M_I\rangle = |0,0\rangle = \frac{1}{2}\left(|\uparrow\downarrow\rangle - |\downarrow\uparrow\rangle\right) \tag{6.3}$$

or to the triplet state (ortho-hydrogen, I=1 and M_I=0, ±1)

$$|I,M_I\rangle = \begin{cases} |1,1\rangle = |\uparrow\uparrow\rangle \\ |1,0\rangle = \frac{1}{2}\left(|\uparrow\uparrow\rangle + |\downarrow\downarrow\rangle\right) \\ |1,-1\rangle = |\downarrow\downarrow\rangle \end{cases} \tag{6.4}$$

Multiplying the wave functions in Equations (6.3) and (6.4) by the rotational wave function and applying the exclusion principle, the nuclear spin degeneracy factor, g_s in Equation (B.1), for the H_2 molecule is:

$$\begin{aligned} g_s &= 1 \quad J \text{ even} \\ g_s &= 3 \quad J \text{ odd} \end{aligned} \tag{6.5}$$

which explains the 1:9 ratio between even and odd lines in the pure-rotational H_2 spectra in Figure 4.15. The nuclear spin degeneracy factor in Equation (6.5) is thus introduced in Equation (2.13) to compute the rotational Boltzmann population of H_2 for temperature ranging from 200 K to 2000 K, in steps of 10 K.

It should be mentioned that the pure-rotational H_2 CSRS code in Paper III does not include any model for the collisional linewidths. This is justified by the fact that the validation experiment are performed in an atmospheric flame, and the probe pulse delay is <10 ps to simultaneously generate the resonant and NR CSRS spectra: the fs/ps CRS measurements are thus effectively collisional-independent.

6.1.2 VALIDATION OF PURE-ROTATIONAL H_2 CRS THERMOMETRY WITH *IN SITU* REFERENCING

In Paper III, pure-rotational H_2 CSRS thermometry with *in situ* referencing of the ultra-broadband spectral excitation efficiency is validated in a laminar H_2/air diffusion flame, behind the 22 mm-thick optical window. The flame is provided on a Bunsen burner, consisting of a ~60 cm-long seamless stainless steel pipe of ~19 mm inner diameter, tapered to the outlet section to reduce the heat losses due to heat conduction to the bulk metal. Contrary to the flame experiments in Papers I and II (described in Section 4.1.1), the flame employed to validate pure-rotational H_2 CSRS in Paper III is a diffusion flame, produced by a laminar fuel flow of 2 SLPM mixing with ambient air (oxidiser flow) to produce a combustible mixture. The fuel flow consists of 50% H_2 and 50% N_2: the two flows are independently regulated by digital flow controllers (Bronkhorst) and mixed before entering the burner pipe. Seeding the flow with N_2 makes it possible to perform pure-rotational N_2 CARS thermometry across the whole flame front as shown in Figure 6.1(a), and validate the pure-rotational H_2 CSRS code.

Spatially-resolved fs/ps CRS measurements are performed at 25 radial locations across the flame front –from the centre of the fuel stream at location y=0 mm, to the oxidiser stream ~3 mm beyond the burner rim (y=12.5 mm)–, approximately 0.5 mm above the burner rim. A steel mesh is placed ~15 mm above the burner to stabilize the flame. At each radial location a sample of 1200 single-shot frames, consisting of both the pure-rotational H_2 and the NR CSRS signals are recorded, as shown in Figure 5.7. Up to six rotational lines of the pure-rotational Raman spectrum of H_2 –from O(2) at 354 cm^{-1} to O(7) at 1447 cm^{-1}– can be detected within the spectral detection window and dynamic range of the spectrometer. The progression in the H_2 CSRS spectra from the centre of the burner towards the reaction zone of the flame front highlights the shift in the rotational Boltzmann distribution with the increasing temperature.

The time-domain H_2 CSRS model is thus employed to fit the experimental spectra and extract the local temperature across the flame front, as shown in Figure 6.1. The NR CSRS spectrum acquired *ex situ* in Ar cannot faithfully map the effective excitation profile provided by the compressed supercontinuum generated via *in situ* filamentation. The *ex situ* referencing protocol results in a significant underestimation of the temperature by pure-rotational H_2 CRS thermometry (red markers) throughout the whole flame front as shown in Figure 6.1(a). The resulting temperature underestimation is more significant the more the pulse compression via *in situ* filamentation is affected by the temperature increase in the flame, as seen in Figure 5.7(a). The systematic bias of pure-rotational H_2 fs/ps CRS thermometry with *ex situ* referencing varies from −10-20% at relatively low temperature at the centre of the burner, up to -80% at location y=7.5 and 8 mm, as shown in Figure 5.7(b). On the other hand, when employing the *in situ* referencing protocol the accuracy of pure-rotational H_2 fs/ps CRS thermometry is better than 1% for most measurement locations across the flame front.

In terms of precision, the performance of pure-rotational H_2 fs/ps CRS with *in situ* referencing is comparable to that of to conventional pure-rotational N_2 fs/ps CRS, with a standard deviation over the 1200 single-shot spectra in each sample estimated in the range 1-3% for measurements up to location y=6.5 mm. At the last three measurement locations, the reduction in the SNR due to the higher temperature and the almost complete consumption of the H_2 fuel negatively impacts the measurement precision, increasing the standard deviation up to 9% at location y=8 mm.

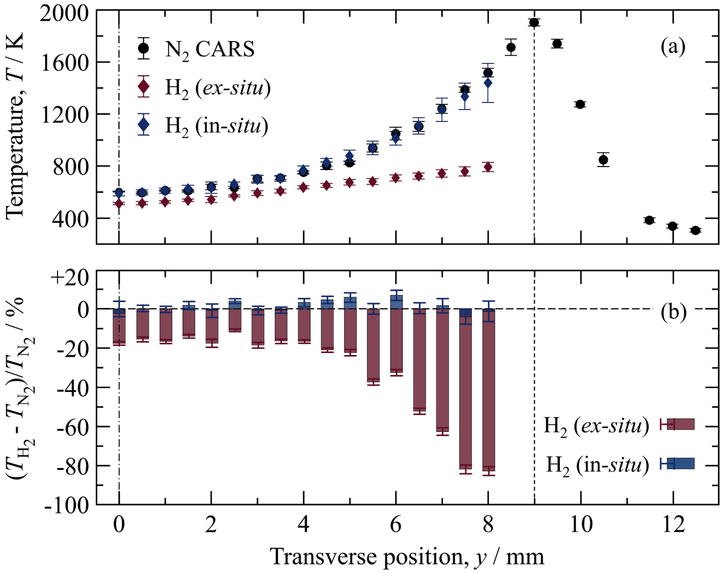

Figure 6.1: Pure-rotational H_2 CSRS thermometry. (a) Comparison between the temperature profile across the laminar H_2/air diffusion flame front by conventional pure-rotational N_2 CARS and ultrabroadband H_2 CSRS thermometry. The conventional *ex situ* referencing protocol leads to a significant underestimate of the temperature. (b) Accuracy and precision of ultrabroadband H_2 CSRS thermometry, assuming conventional N_2 CARS as a reference. Figure reproduced from Mazza *et al.* [27].

6.2 Ro-vibrational fs/ps CRS on O_2

The second molecular species investigated in the vibrational fingerprint region by ultrabroadband fs/ps CRS is O_2.

Its large abundance in ambient air and its vibrational constant ($\omega \approx 1556$ cm^{-1} [164]) being significantly smaller than that of N_2 ($\omega \approx 2320$ cm^{-1} [165]) make O_2 a natural candidate for the first application of ultrabroadband fs/ps CRS with *in situ* filamentation in Paper I. Obviously O_2 is also a major combustion species, being the main oxidiser in most gas-phase combustion environments, and ro-vibrational O_2 CRS thermometry at high-temperature has been investigated in laboratory flames ([166, 167]) and applied in furnaces [168] and spray flames [169]. The availability of an accurate O_2 CRS technique for *in situ* thermometry and simultaneous concentration measurements relative to other major combustion species (see e.g. Ref. [16, 168]) is furthermore critical in oxy-fuel flames [170]. The absence of N_2 in such combustion environments requires CRS thermometry to be simultaneously performed on two species to reconstruct the whole temperature profile across the whole chemical reaction zone of the flame [14].

As seen in Figures 4.8 and 4.14 the the fundamental vibrational band and (at least) the first hot band of the ro-vibrational O_2 CSRS spectrum can be detected on a single-shot basis in the hot products of a lean hydrocarbon flame. The *in situ* generation of the compressed supercontinuum via fs laser-induced filamentation makes it possible to perform these measurements behind the thick optical window. In Paper I ro-vibrational O_2 fs/ps CRS thermometry is demonstrated by comparing the experimental spectra to a time-domain CSRS ro-vibrational O_2 model, whose details are discussed in Section 6.2.1. The validation experiments, conducted in the products of a laminar CH_4/air flame for varying equivalence ratio ϕ=0.6-1.05, are presented in Section 6.2.2.

6.2.1 Time-domain model for ro-vibrational O_2 CRS

O_2 is a homonuclear diatomic molecule, whose vibrational and rotational energy manifolds are well described by the theory laid out in Appendix A. With respect to other homonuclear diatomics such as H_2 and N_2, the description of the O_2 molecules is slightly more complicated, as its ground electronic state $X^3\Sigma_g^-$ has two unpaired electrons [12, 171] such that the molecule has non-zero electron spin angular momentum (S=1) as introduced in Appendix A.2. The coupling of this angular momentum component with the nuclear angular momentum (represented by the quantum number N, see Table A.1) leads to the total rotational eigenstates being the triplet states J=N, $N \pm 1$. The rotational-vibrational Raman lines are thus split by a small frequency component (~480 MHz for pure-rotational transitions), which gives rise to a slow beating of the time-domain fs/ps CRS spectrum. Courtney and Kliewer measured this beating in the pure-rotational O_2 spectrum by two-beam fs/ps CARS, and demonstrated that it can have a significant impact on O_2 CARS thermometry for probe delays larger than 100 ps [172]. The time-domain modelling of the ro-vibrational O_2 fs/ps CSRS spectrum is simplified, in Paper I, by neglecting the electron spin-nuclear angular momentum coupling and treating the triplet states as degenerate. This assumption is justified by the probe delay being well below 100 ps in the validation experiments and the O_2 CSRS spectrum being dominated by the Q-branch, whose rotational line splitting is lesser than for the O- and S-branch transitions [164].

Under this assumption, the time-domain model is a straightforward implementation of the theory summarised in Chapter 2. The quantised levels in the rotational-vibrational energy manifold of O_2 are computed by employing the molecular constants experimentally determined by Rouillé and co-workers in Ref. [164]. The time-domain model includes the fundamental (v=0← v=1) and the first two vibrational hot bands (v=1← v=2 and v=2← v=3), and rotational states up to N=119 are taken into account. Equations (C.10) and (C.11) are then employed to compute the strength of each rotational line in the ro-vibrational O-, Q, and S-branch spectra of O_2. The Placzek-Teller coefficient for the O-branch transitions is given in Equation (6.1), the coefficients for the Q- and S-branch transitions are calculated as:

$$\begin{aligned} b_{\text{Q-branch}}(J) &= \frac{J(J+1)}{(2J-1)(2J+3)} \\ b_{\text{S-branch}}(J) &= \frac{3(J+1)(J+2)}{2(2J+1)(2J+3)} \end{aligned} \tag{6.6}$$

The isotropic and anisotropic Herman-Wallis factors (respectively, F_α and F_γ) as well as the polarisability invariants (α^2 and γ^2) in Equation (C.11) are computed according to the algebraic formulas given by Buldakov *et al.* [173].

Under the atmospheric conditions investigated in Paper I, the dephasing of the O_2 CRS signal is attributed to the RET in inelastic collisions between the coherently vibrating O_2 molecules responsible for the coherent scattering process and other molecular perturbers in the gas-phase medium. The collisional dephasing of each rotational line in the Q-branch spectrum includes the effect of O_2-O_2 (self-perturbing) and O_2-N_2 collisions and the corresponding dephasing rate is computed according to the *sum rule*:

$$\Gamma_{\{[v]_f,J\}\leftarrow\{[v]_i,J\}} = \sum_{k\neq j}\gamma_{kj} \tag{6.7}$$

Where γ_{kj} represents the collisional transition rate between the j^{th} and k^{th} rotational states. The upward and downward collisional rates are computed according to the MEG scaling law [174] as:

$$\begin{aligned} \gamma_{ji} &= \alpha p\left(\frac{T_0}{T}\right)^n\left(\frac{1+aE_i/k_BT\delta}{1+aE_i/k_BT}\right)\exp\left[\frac{-\beta(E_j-E_i)}{k_BT}\right] \\ \gamma_{ij} &= \frac{2J_i+1}{2J_j+1}\exp\left[\frac{-\beta(E_j-E_i)}{k_BT}\right]\gamma_{ji} \end{aligned} \tag{6.8}$$

Where p is the pressure, T_0=296 K is the reference temperature, E_i and E_j represent the ro-vibrational energy in the lower and upper states of the transition, and α, β, δ, a and n are the fitting parameters for the scaling law, depending on the collisional system considered. The fitting parameters for both the O_2-O_2 and the O_2-N_2 collisional system are taken from Ref. [175].

This model is employed to perform ro-vibrational O_2 fs/ps CRS thermometry in a canonical hydrocarbon flame by comparing the experimental spectra to a library of synthetic ro-vibrational O_2 CSRS spectra, computed for an input temperature ranging 250-2300 K, in steps of 50 K.

6.2.2 Validation of ro-vibrational O_2 CRS thermometry

Paper I reports validation measurements for the time-domain ro-vibrational O_2 CSRS model, performed on a laminar premixed CH_4/air flame provided on the Bunsen burner described in Section 4.1.1. The CH_4 and air flows are provided by separated pressurised vessels, independently regulated by rotametres (Omega), and mixed before entering the burner. The volumetric flow rate of the combustible mixture is maintained below 5 SLPM, with a resulting Reynolds number $<$1000, thus ensuring a laminar flow at the burner outlet. The equivalence ratio of the combustible mixture is varied in the fuel-lean regime from ϕ=0.6, up to slightly fuel-rich conditions (ϕ=1.05). The probe volume is placed ~7 mm above the tip of the conical flame. The two leanest flames measured (i.e. ϕ=0.6 and 0.66) are stabilized as V-shaped flames to avoid their lean blow-off, by employing a 4 mm diameter steel rod placed at a height of ~12 mm above the burner rim: in these flame conditions the probe volume is located ~5 mm above the rod, as seen in Figure 4.8(a).

In the product gases of the lean flame the significant amount of unburnt O_2 allows for the simultaneous detection the ro-vibrational O_2 and CO_2 CSRS spectra in the 1100-1600 cm^{-1} region as shown in Figure 4.8(b). Nevertheless, the quality of the SNR at the highest temperature tested in Paper I is deemed insufficient to provide a reliable experimental validation: 40 laser shots are thus averaged in the validation experiment. The experimental spectra are fitted to both the ro-vibrational O_2 CSRS model above and a ro-vibrational CO_2 CSRS model, which is discussed in the next section. The two species are fitted independently from each other –thus providing a cross-validation of the two time-domain models– by segmenting the experimental spectrum in regions corresponding to different spectral features: in particular, the region 1475-1575 cm^{-1} is employed to perform ro-vibrational O_2 fs/ps CRS thermometry. Figure 6.2 shows an example of the resulting spectral fit reconstructed over the whole 1200-1600 cm^{-1} region, for a 40-shot averaged spectrum acquired in the second leanest flame tested (ϕ = 0.66).

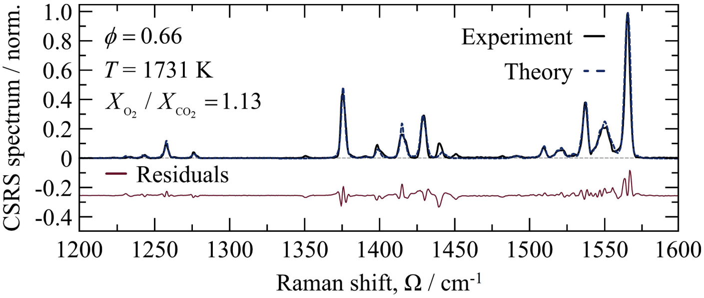

Figure 6.2: 40-shot averaged ro-vibrational CO_2 and O_2 CSRS spectra acquired in the hot product gases of a laminar premixed CH_4/air flame for ϕ=0.66 (solid black line). The experimental spectra are fitted to the time-domain CRS models discussed in Sections 6.2.1 and 6.3.1 (dashed blue line) to measure the gas temperature. The red line represents the residuals of the spectral fit, offset by -0.25 for clarity. Figure reproduced from Mazza *et al.* [26]

Table 6.1 summarises the different values of the equivalence ratio used for the experimental validation of ro-vibrational O_2-CO_2 CRS thermometry, and the resulting temperature estimates. For an increasing equivalence ratio in Table 6.1 the concentration of unburnt O_2 in the product gases of the flame is reduced, reaching 0 at stoichiometric conditions

(ϕ=1). For ϕ=0.93 the ro-vibrational O_2 CSRS signal can be detected, but the SNR is too low to perform quantitative spectroscopy on it, and only the CO_2 CSRS signal is employed to perform thermometry on the two richest flames tested. The accuracy of ro-vibrational CRS thermometry is calculated by using the adiabatic flame temperature, computed by the one-dimensional laminar flame code CHEM1D [149], as the target temperature. In addition, conventional pure-rotational N_2 CARS thermometry is performed at the same flame conditions, by attenuating the fs pump/Stokes pulse below the filamentation threshold (~80 μJ/pulse).

Table 6.1: Comparison of ultrabroadband fs/ps CRS thermometry in the products of the laminar premixed CH_4/air flame at different equivalence ratios. For ϕ>0.84 the O_2 CSRS signal is too weak to provide a reliable estimation of the gas temperature. The results of ro-vibrational thermometry, performed on the 40-shot averaged ro-vibrational CSRS spectra of O_2 and CO_2, are compared to the adiabatic flame temperature and to the results of single-shot pure-rotational O_2-N_2 CARS thermometry. Table reproduced from Ref. [26]

Equivalence ratio	**Adiabatic flame temperature**	**Pure-rotational N_2-O_2 CARS**			**Ro-vibrational CO_2 CSRS**			**Ro-vibrational O_2 CSRS**		
ϕ	$T_{ad.}$	$T_{avg.}$	$\frac{T_{avg.}-T_{ad.}}{T_{avg.}}$	$\frac{\sigma_T}{T_{avg.}}$	$T_{avg.}$	$\frac{T_{avg.}-T_{ad.}}{T_{avg.}}$	$\frac{\sigma_T}{T_{avg.}}$	$T_{avg.}$	$\frac{T_{avg.}-T_{ad.}}{T_{avg.}}$	$\frac{\sigma_T}{T_{avg.}}$
[–]	[K]	[K]	[%]	[%]	[K]	[%]	[%]	[K]	[%]	[%]
0.60	1669	1622	−2.9	0.4	1619	−3.1	1.5	1636	−2.0	2.0
0.66	1775	1783	+0.5	0.4	1711	−3.7	1.2	1711	−3.7	1.0
0.77	1951	1909	−2.2	0.3	1836	−6.3	1.1	1787	−9.1	1.5
0.84	2059	2019	−2.0	0.4	1939	−6.2	1.1	2045	−0.7	5.4
0.93	2167	2086	−3.9	0.4	2081	−4.1	0.8	–	–	–
1.05	2226	2132	−4.4	0.5	2113	−5.3	0.7	–	–	–

6.3 RO-VIBRATIONAL FS/PS CRS ON CO_2

Increasing in molecular complexity, the third species investigated in the vibrational fingerprint region of the Raman spectrum is CO_2. This is a triatomic molecule that shares a number of characteristics with the simpler diatomic molecules discussed in the previous sections, owing to its being a linear rotor. In addition, CO_2 belongs to the same point group of any homonuclear diatomic molecule ($D_{\infty h}$), as discussed in Appendix B, and therefore has a centre of symmetry. In view of this, it is subject to the *rule of mutual exclusion*, stating that no normal mode of a molecule with a centre of symmetry can be both IR- and Raman-active [43].

As shown in Figure 6.3, CO_2 has three normal vibrational modes. The first vibrational mode (ν_1) is the symmetric stretch of the C–O bonds: as the molecule maintain its $D_{\infty h}$ symmetry, it has no permanent dipole and its thus IR-inactive. On the other hand in this vibrational mode the molecule has a non-zero polarisability, which makes the mode Raman-active. The second (ν_2) and third (ν_3) vibrational modes of CO_2 –respectively, the bending and asymmetric stretch of the O–C–O bonds– on the contrary, have a permanent dipole that make the molecule IR-active and Raman-inactive. Hence, the symmetric stretch is the only mode responsible for the vibrational Raman scattering of the CO_2 molecule.

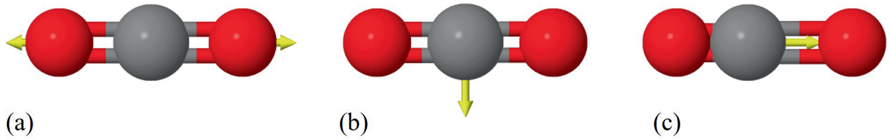

Figure 6.3: The vibrational modes of CO_2. (a) The first vibrational mode (ν_1, at 1428 cm^{-1}) is the symmetric stretch of the C–O bonds. (b) The second vibrational mode (ν_2, at 659 cm^{-1}) is the bend of the O–C–O bonds. (c) The third vibrational mode (ν_3 at 2463 cm^{-1}) is the asymmetric stretch of the C–O bonds. Molecules rendered using Jmol: an open-source Java viewer for chemical structures in 3D (http://www.jmol.org/).

CO_2 is of course a major product of the combustion of hydrocarbon fuels, as well the main greenhouse gas in terms of radiative forcing [176], and as such is of inherent interest for combustion diagnostics. Over the last forty years, multiple studies have demonstrated the use of CRS on the ro-vibrational Raman spectrum of CO_2 to perform quantitative measurements in laboratory flames as well as in practical combustion applications (see e.g. [15, 16, 67, 170, 177, 178]).

In stark contrast to pure-rotational H_2 fs/ps CRS, which requires the use of a compressed supercontinuum due to the sparse rotational energy manifold of H_2, the application of pure-rotational fs/ps CRS to CO_2 is complicated by the small rotational constant of this molecule ($B = 0.39$, roughly one fifth of the rotational constant of N_2). The pure-rotational Raman spectrum of CO_2 spans less than 200 cm^{-1} even at 2000 K, imposing strong requirements on the spectral resolution of the fs/ps CRS instrument: a probe pulse longer than 25 ps is needed to resolve individual lines in the pure-rotational CO_2 CRS spectrum at atmospheric pressure. The use of shorter ps probe pulses, as required to perform time-resolved measurements in high-pressure combustion applications, results in either one of two pitfalls, as illustrated by the synthetic spectra in Figure 6.4, simulated at two different probe delays employing a 5 ps probe pulse. As the duration of the pulse is comparable to the revival period of the pure-rotational coherence, as shown in Figure 6.4(a), only one revival peak in the time-domain optical response is sampled by the probe pulse. This results in (i) a poor spectral resolution in the frequency domain, if the probe overlaps with one (fractional) revival of the molecular response, as shown in Figure 6.4(a) for a probe delay of 10 ps, or (ii) a suppression of the signal generation, as the probe pulse falls between two consecutive revival peaks, e.g. for a probe delay of 5 ps.

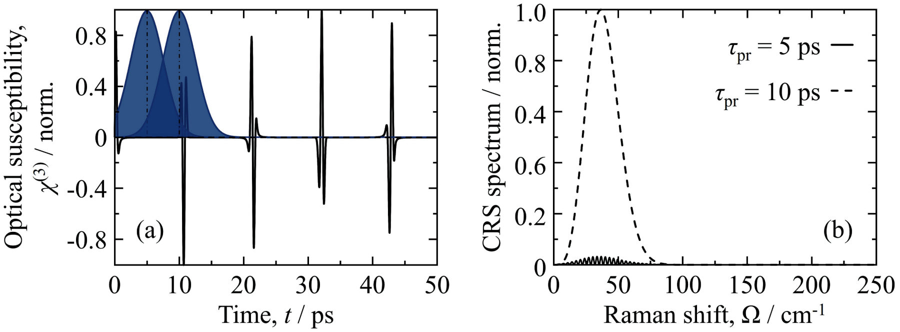

Figure 6.4: Pure-rotational CO_2 CRS. (a) Pure-rotational coherence of gas-phase CO_2 at room temperature (296 K): the interferogram representing the molecular coherence has a revival time of ~42.8 ps. By employing a short 5 ps probe pulse, only one revival structure can be read at a time. (b) Pure-rotational CO_2 CRS spectra simulated for τ_{probe}=5 and 10 ps: the short duration of the probe pulse results in a poor spectral resolution. In addition, when the probe pulse arrives between two fractional revivals of the Raman coherence (e.g. at 5 ps), the CRS process is almost entirely suppressed.

This fact clarifies the need for a robust time-domain fs/ps CRS model to perform quantitative measurements on the ro-vibrational Raman spectrum of CO_2 at temperatures higher than 2000 K. In Paper I such a model is reported, taking into account up to 180 vibrational bands as discussed in Section 6.3.1, and validated in a canonical premixed CH_4/air flame at temperatures as high as ~2100 K. The validation experiment has been already described in Section 6.2.2 and only a brief discussion of the main results for ro-vibrational CO_2 fs/ps CRS thermometry is given in Section 6.3.2.

6.3.1 Time-domain model for ro-vibrational CO_2 CRS

As mentioned in the previous paragraph, the symmetric stretch mode is the only one responsible for the vibrational Raman-activity of the CO_2 molecule. Nevertheless, its dense vibrational manifold entails that multiple vibrational states are populated according to Boltzmann statistics even at low temperature, as seen in Figure 2.3. The time-domain ro-vibrational CO_2 CSRS code in Paper I therefore includes up to 180 vibrational states and 120 rotational lines within each vibrational band. The vibrational states of CO_2 are labelled following the notation in Herzberg [179]: $[v] = [v_1 v_2^l v_3]$. The quantum number l here quantifies the additional angular momentum component arising from the bending motion of the molecule when $v_2 \neq 0$. In this case the molecule is not linear anymore and it can acquire an angular momentum component about the original internuclear axis z. This *vibrational angular momentum* is quantised with quantum number l=$-v_2$, v_2+2,..., v_2-2,

v_2, and the rotational energy term in Equation (2.11) is modified according to:

$$F([v],J) = B_{[v]}\left[J(J+1)-l^2\right] - D_{[v]}\left[J(J+1)-l^2\right]^2 \tag{6.9}$$

The Raman frequencies associated to the 180 vibrational bands considered in the time-domain model of Paper I are take from Ref. [180], and Equation (6.9) is employed for the calculation of the rotational frequencies within each vibrational band.

As the vibrational angular momentum quantum number in Equation (6.9) is squared, vibrational energy states with active bending mode are $(l+1)$-fold degenerate: more specifically, each sub-state with a non-zero vibrational angular momentum quantum number is twice degenerate. In analogy to the Λ-doubling due to spin-orbit coupling [181] the same notation employed for the electronic configuration of diatomic molecules (e.g. $\mathrm{X}^1\Sigma_g^+$ for the ground state of N_2) is used to label the vibrational wave function of CO_2, as shown in Figure 6.5. Capital Greek letters represent the value of l: "Σ" meaning l=0, "Π" l=1, and so on following the labelling of the electronic orbitals with the Latin alphabet. The subscript "g" and "u" identify symmetric ("*gerade*") and anti-symmetric ("*ungerade*") vibrational wave functions, respectively.

As already seen in the case of H_2, the symmetry of the wave function plays a critical role in the calculation of the Boltzmann distribution, since it constrains the values of the nuclear spin degeneracy factor g_s according to Pauli's exclusion principle. For the specific case of CO_2, g_s is respectively 1 and 0 for even and odd rotational states in those vibrational states characterised by an even symmetry of the wave function, while the opposite holds for anti-symmetric states.

In addition, the existence of vibrational angular momentum components needs to be accounted for in the total angular momentum of the molecule and, in particular, in the calculation of the Placzek-Teller coefficient for the coupling of the angular momenta in a Raman transition. Since the vibrational angular momentum is parallel to the internuclear axis, when it is in a degenerate bending state the CO_2 molecules behaves as a prolate symmetric top molecule [39] (see Appendix B), and the Placzek-Teller coefficients for a Q-branch band are calculated as:

$$b_{\text{Q-branch}}(J,l) = \frac{\left[J(J+1)-3l^2\right]^2}{J(J+1)(2J-1)(2J+3)} \tag{6.10}$$

The ro-vibrational Raman spectrum of CO_2 is further complicated by a phenomenon known as *Fermi resonance*, whereby the wave functions associated to different vibrational modes of the molecules can mix when they have the same symmetry and almost the same energy [182]. Looking at Figure 6.5 for example, it is evident that such a resonance is possible between state $10^00\Sigma_g^+$ (where only one quantum is assigned to the symmetric stretch) and state $02^00\Sigma_g^+$, where two quanta are assigned to the bending mode with zero vibrational angular momentum quantum number. As the ν_1 mode has almost twice the frequency of the ν_2 mode, all the vibrational states where only the symmetric stretch is active (i.e. $[v] = [n0^00]$) are Fermi-resonant with even overtones of the bending mode ($[v] = [0(2n)^l0]$). Fermi resonance results in the appearance in the Raman spectrum of the Raman-inactive $2\nu_2$ lines, and the anharmonic terms in the exact rotational-vibrational Hamiltonian determine a "repulsion" of the spectral lines [43]. Hence, the Raman spectrum

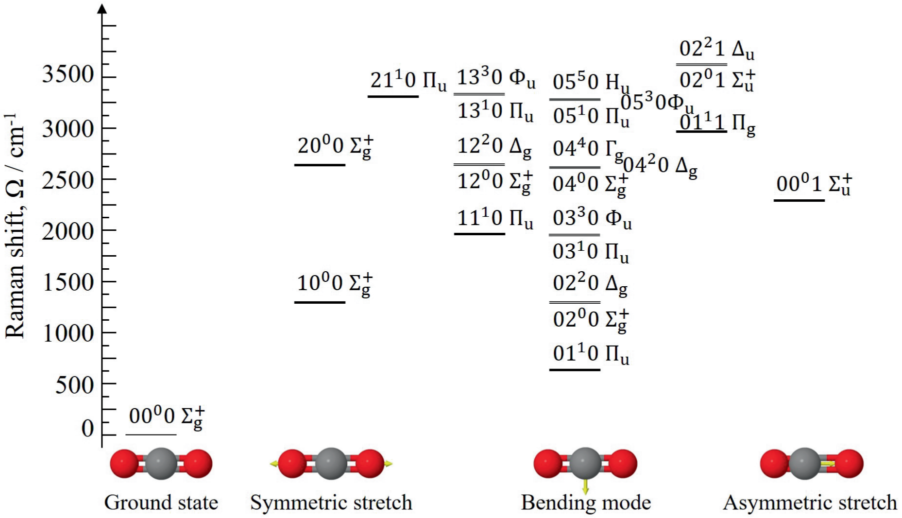

Figure 6.5: Vibrational energy manifold of CO_2 up to 3500 cm^{-1}. Vibrational states characterised by an active bending mode (i.e. $v_2 \neq 0$) are (v_2+1)-fold degenerate, as the vibrational angular momentum has quantised values $l = -v_2, -v_2+2, \dots, v_2-2, v_2$. Each degenerate bending with non-zero vibrational angular momentum (i.e. $l \neq 0$) is doubly degenerate, and capital Greek letters are used to label these states: Σ, Π, Δ, Γ, Φ, and H representing l=1, 2, 3, 4, 5, and 6, respectively. Two different vibrational states characterised by the same vibrational wave function symmetry and having similar energy show a Fermi resonance. Molecules rendered using Jmol: an open-source Java viewer for chemical structures in 3D (http://www.jmol.org/). Figure reproduced from Mazza *et al.* [26].

the shape of a ν_1+2ν_2 Fermi dyad with fundamental bands at 1285 cm^{-1} (the "red" dyad [183]) and 1388 cm^{-1} (the "blue" dyad [184]), as shown in Figures 4.8 and 4.14.

The values of the isotropic (α^2) and anisotropic (γ^2) transition polarisability invariants are taken from Lemus *et al.*, who used an algebraic approach to compute the vibrational dipole moments for 180 vibrational bands in the spectral range 1100-1600 cm^{-1} [180]. On the other hand, no reliable measurements of the dependence of these transition dipole moments on the rotational energy states could be found in the literature and the same value is assumed for all the rotational transitions within the same vibrational band.

Similarly, the polarisability anisotropy of the CO_2 molecule is not known with sufficient accuracy and only the isotropic contribution to the CO_2 Q-branch spectrum is considered [67]. This assumption is justified in the light of the extremely small value of the depolarisation ratio of the fundamental vibrational band in the CO_2 Raman spectrum at 1388 cm^{-1}, experimentally measured to be 0.027 [185].

The dephasing rate of each of the rotational lines in the ro-vibrational CO_2 Q-branch CSRS spectrum, due to self-perturbing $CO_2 - CO_2$ collisions is computed according to the MEG model in Equations (6.7) and (6.8) with fitting parameter taken from Ref. [186].

Analogously to the case of O_2 discussed in the previous section, the time-domain ro-vibrational CO_2 CSRS model is used to compute a library of synthetic spectra, for temperatures ranging, in steps of 50 K, from 250 K to 2300 K.

6.3.2 VALIDATION OF RO-VIBRATIONAL CO_2 CRS THERMOMETRY

The details of flame experiment performed to validate ro-vibrational O_2-CO_2 fs/ps CRS have already been discussed in Section 6.2.2.

As mentioned above, the experimental ultrabroadband spectra are segmented in three spectral regions corresponding to different spectral features: the "red" CO_2 Q-branch spectrum in the region 1200-1300 cm^{-1}, the "blue" CO_2 Q-branch spectrum in the region 1350-1450 cm^{-1}, and the O_2 Q-branch in the region 1475-1575 cm^{-1}. The temperature is thus measured independently by fitting the O_2 and the CO_2 "blue" Q-branch CSRS spectra. Single-shot CO_2 fs/ps CRS thermometry is demonstrated in Paper I by fitting the single-shot spectra acquired in the lean flame shown in Figure 4.8: the temperature is measured to be 1921 K over a sample of 1000 single-shot spectra, thus resulting in an accuracy of -1.5%, as compared to the adiabatic flame temperature of 1951 K.

40-shot averaged spectra are furthermore fitted to extend the validation of the time-domain ro-vibrational CO_2 CSRS model at temperatures higher than 2000 K: the results are summarised in Table 6.1. The inaccuracy of ro-vibrational CO_2 fs/ps CRS thermometry, despite not insignificant when compared to the adiabatic flame temperature computed by the 1D laminar flame code, is comparable to the one of pure-rotational N_2-O_2 CRS thermometry performed in the same flame conditions. In particular at the highest temperature tested ($\phi = 0.95$ and 1.05), the temperature measured independently by the two CRS techniques agrees to within 0.9%.

6

The single-shot precision of ro-vibrational CO_2 fs/ps CRS is assessed in Paper I on the measurements performed at relatively lower temperature, in the lean flame condition ϕ=0.77. With a standard deviation of 27 K, the single-shot precision is estimated thus to be 1.4%, in line with the values reported in the literature for ro-vibrational N_2 fs/ps CRS performed in a similar flame [146]. The 40-shot-averaged measurements reported in Table 6.1 show an interesting trend, as far as the precision of CO_2 fs/ps CRS is concerned. As the flame temperature increased, the relative standard deviation decreases from 1.5% for ϕ= 0.60 to 0.7% for ϕ= 1.05. This behaviour is partly attributed, in Paper I, to the increased CO_2 concentrations in the products of the flame for increasing values of ϕ. Furthermore, at higher temperatures many more vibrational states become thermally populated according to Boltzmann distribution, increasing the number of Raman transitions probed in the ro-vibrational CO_2 CRS spectrum. This results in a more robust spectral fit than what performed at lower temperatures, or on simpler diatomic molecules such as O_2, whose ro-vibrational CRS spectrum shows at most two vibrational hot bands, as seen in Figure 6.2.

6.4 RO-VIBRATIONAL FS/PS CRS ON THE ν_2 MODE OF CH_4

Paper IV presents the first application of ultrabroadband CRS with *in situ* filamentation to investigate the so-called "*dyad* region" of the ro-vibrational Raman spectrum of CH_4 between ~1200 cm^{-1} and 2000 cm^{-1}.

As discussed in Appendix B, the CH_4 molecule is a spherical-top rotor belonging to the tetrahedral point symmetry group T_d, with four normal modes of vibrations represented in Figure 6.6. The first vibrational mode (ν_1) is the *symmetric stretch* of the C–H bonds of the molecules, with vibrational (angular) frequency 2932 cm^{-1}: this mode is non-degenerate,

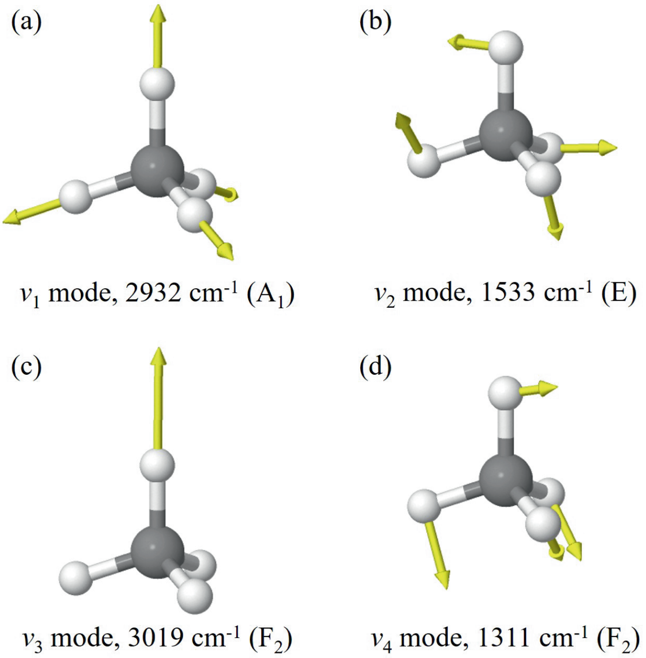

Figure 6.6: Vibrational modes of the CH_4 molecule. (a) The first vibrational mode, ν_1 at 2932 cm^{-1} in the Raman spectrum, is the symmetric stretch of the four C–H bonds, whereby the molecule maintains the spherical symmetry $\Gamma = A_1$. (b) The second vibrational mode, ν_2 at 1533 cm^{-1}, is the E-symmetric bending of the H–C–H bonds. (c) ν_3 at 3019 cm^{-1}, is the asymmetric stretch of the C–H bonds, with symmetry label $\Gamma = F_2$. (d) ν_3 at 3019 cm^{-1}, is the least symmetric bend of the H–C–H bonds, with symmetry label $\Gamma = F_2$. Molecules rendered using Jmol: an open-source Java viewer for chemical structures in 3D (http://www.jmol.org/). Figure reproduced from Mazza *et al.* [187].

and the associated symmetry label is A_1*. Since this vibrational mode preserves the original symmetry of the molecule in its ground vibrational state, the CH_4 molecule has no permanent dipole in state $|[v_1, 0, 0, 0]\rangle$: the ν_1 mode is thus Raman-active, but IR-inactive. The second vibrational mode (ν_2) is the doubly-degenerate ($\Gamma = E$) *twisting bend* of the H–C–H bonds, at 1533 cm^{-1}. The third vibrational mode (ν_3) is the triply-degenerate ($\Gamma = F_2$) *asymmetric stretch* of the C–H bonds, at 3019 cm^{-1}. The last normal vibrational mode (ν_4) is the triply-degenerate ($\Gamma = F_2$) *scissoring bend* of the H–C–H bonds, at 1311 cm^{-1}. The second, third and fourth normal vibrational modes reduce the symmetry of the molecule introducing a permanent dipole, so that these modes are both IR- and Raman-active.

Since the the vibrational stretching modes ν_1 and ν_3 have approximately twice the energy of the bending modes ν_2 and ν_4, the resulting ro-vibrational IR and Raman spectra are organised in isolated vibrational bands called "*polyads*" [188], allowing for the construction of effective Hamiltonian and transition moment operators (dipole moment for the IR

---

*The subscript "1" ("2") in the symmetry labels indicates the (anti-)symmetry of the vibrational wave function with respect to the symmetry operation σ defined in Appendix B [38].

spectrum, polarisability for the Raman one) adapted to the following polyad scheme [189]. A vibrational mode of the CH_4 molecule belongs to the polyad P_n

$$n = \sum_{j=1}^{j=4} i_j v_j \tag{6.11}$$

with n being the *polyad number*, v_j the vibrational quantum number for the j^{th} vibrational mode ν_j, and (i_1, i_2, i_3, i_4)=(2, 1, 2, 1) the polyad scheme for the CH_4 molecule. The polyad number then satisfies the relationship:

$$n = 2(v_1 + v_3) + v_2 + v_4 \tag{6.12}$$

The first polyad (P_0, also referred to as the "*monad*") obviously represents the ground vibrational state of the CH_4 molecule; the "*dyad*" P_1 consists of the fundamental ν_2 and ν_4 bending modes, occurring at ~1500 cm^{-1}; the "*pentad*" of the fundamental ν_1 and ν_3 stretching modes, as well as of the overtones ($2\nu_2$ and $2\nu_4$) and combination ($\nu_2 + \nu_4$) of the bending modes at ~3000 cm^{-1}, *etc.* [188]

CRS techniques have been applied to investigate the pentad region in the Raman spectrum of CH_4: high-resolution continuous-wave (CW) SRS [190, 191] and CRS [192–195] measurements allowed to assign individual rotational lines within the isotropic Q-branch spectrum of the symmetric C–H stretch mode, and to investigate the collisional RET in gas-phase mixtures of CH_4 with He, Ar, and N_2 [196–198]. CH_4 ν_1 CRS has also been employed as a combustion diagnostic tool to measure the local gas temperature in furnaces, laminar flames and supercritical LOX/CH_4 combustion [168, 199, 200]. More recently, time-resolved CRS techniques have been applied to measure relative CH_4 concentrations in binary mixtures with N_2 [201], and to realise imaging thermometry at temperatures up to 1000 K [126]. Bohlin and Kliewer also demonstrated single-shot detection of the CH_4 Raman spectrum in the pentad region via ultrabroadband fs/ps CARS in a gas cell [24] as well as in a SWQ burner [90]: rotational thermometry and relative concentration measurements of N_2, O_2, H_2, CO_2, and CH_4 could be simultaneously performed via the ultrabroadband approach.

Paper IV presents what, to the best of the author's knowledge, is the first-ever CRS investigation of the CH_4 Raman spectrum in the dyad region. The spectrum in this region consists of the ro-vibrational lines due to the ν_2 and ν_4 vibrational modes, but the latter is much weaker than the first [154, 202] and cannot be detected. In the following reference is only made to the CH_4 ν_2 mode spectrum.

In order to perform quantitative CH_4 ν_2 CRS measurements a time-domain CRS model is developed, which includes more than ten million Raman transitions, involving ro-vibrational states up to the *tetradecad* (i.e. the P_4 polyad at ~6200 cm^{-1}). The spectral constants employed in the model were provided by Prof. Thomas Butterworth from the University of Maastricht and Dr. Cyril Richard and Prof. Vincent Boudon from the University of Burgundy. The details of the time-domain modelling of the CH_4 ν_2 CRS spectrum are discussed in Section 6.4.1.

Section 6.4.2 discusses the experimental observation of a strong coherence beating of the experimental CH_4 ν_2 fs/ps CRS spectra acquired at room temperature. This effect is attributed to the Coriolis-splitting of the ro-vibrational lines, as demonstrated by the comparison with the time-domain ro-vibrational CH_4 ν_2 CSRS model.

Ultrabroadband fs/ps CRS with *in situ* filamentation is furthermore employed in Paper IV to perform spatially-resolved measurements across a laminar CH_4/air diffusion flame front. Ro-vibrational CH_4 ν_2 CSRS thermometry is validated against ro-vibrational CO_2 CSRS at temperatures as high as 800 K: the results are discussed in Section 6.4.3

6.4.1 Time-domain model for ro-vibrational CH_4 ν_2 CRS

The modelling framework for the time-domain CH_4 ν_2 CSRS signal reported in Paper IV is the same as outlined in Chapter 2 and employed in the previous sections. Nonetheless, the higher complexity of the CH_4 molecule, as compared to simple diatomics or even linear triatomic CO_2, leads to a much larger number of ro-vibrational transitions to be taken into account [126]. Furthermore symmetry considerations, more complex than those outlined in the previous section for CO_2, play a critical role in constraining the symmetry of the total molecular wave function, and thus its physical realisation. A more detailed discussion of this point is deferred to Appendix B.2.

In order to compute the time-domain non-linear optical response associated to the ν_2 vibrational mode of CH_4 the associated Raman frequencies and Raman cross-sections need be known. For this purpose Paper IV employs the values computed at the University of Burgundy [189, 203] and available in the MeCaSDa spectroscopic database (accessible at http://vamdc.icb.cnrs.fr/PHP/methane.php). This spectral database was employed by Butterworth and co-authors to develop a spontaneous Raman model for the ν_1 mode spectrum of CH_4 and perform rotational-vibrational thermometry in a non-equilibrium pulsed microwave plasma, which was validated up to 860 K [204]. More recently, Chen and co-authors used the same database to develop a time-domain CARS model for the ν_1 mode of CH_4 and validated ro-vibrational CH_4 ν_1 fs/ps CRS thermometry in a tube furnace at temperatures up to 1000 K. The spontaneous Raman line-strengths in the MeCaSDa database are computed adopting a tetrahedral formalism developed for the analysis of spherical top molecules [188], which removes inter-polyad contributions to the higher order using implicit contact transformations [205], while retaining inter-polyad contributions due to the strong coupling between vibrational states within individual polyads.

The Raman line strength for the transition between the ro-vibrational energy states $|[v]_i, J_i, \Gamma_i\rangle$ and $|[v]_f, J_f, \Gamma_f\rangle$ can be expressed as:

$$I_{\text{Raman}} \propto \rho_{\{[v]_i,J_i,\Gamma_i\}}(T_0)\left(S_0\mathscr{I}^2_{\{[v]_f,J_f,\Gamma_f\}\leftarrow\{[v]_i,J_i,\Gamma_i\}} + S_2\mathscr{A}^2_{\{[v]_f,J_f,\Gamma_f\}\leftarrow\{[v]_i,J_i,\Gamma_i\}}\right) \tag{6.13}$$

Where S_0 and S_2 are the Stones coefficients, which depend on the the observation geometry in a spontaneous Raman experiment [204]. $\mathscr{I}$ and $\mathscr{A}$ are the transition values of the isotropic and anisotropic components of the polarisability tensor defined in Equation (C.12):

$$\begin{aligned} \mathscr{I} &= \langle [v]_f, J_f, \Gamma_f | \hat{a} | [v]_i, J_i, \Gamma_i \rangle \\ \mathscr{A} &= \langle [v]_f, J_f, \Gamma_f | \hat{\gamma} | [v]_i, J_i, \Gamma_i \rangle \end{aligned} \tag{6.14}$$

The Raman cross-section for the ro-vibrational CH_4 ν_2 spectrum can thus be computed by the spontaneous Raman line-strengths in the spectral database by factoring out the

Boltzmann population computed at the reference temperature (T_0=1450 K). The coherent Raman line-strengths are thus computed as:

$$I_{\mathrm{CRS}} = \frac{\rho_{\{[v]_f,J_f,\Gamma_f\}} - \rho_{\{[v]_i,J_i,\Gamma_i\}}}{\rho_{\{[v]_i,J_i,\Gamma_i\}}\big|_{T_0}} \, I_{\mathrm{Raman}} \qquad (6.15)$$

The time-domain model in Paper IV includes self-perturbed collisional dephasing coefficients $\Gamma^{(\mathrm{CH_4-CH_4})}_{\{[v]_f,J_f,\Gamma_f\}\leftarrow\{[v]_i,J_i,\Gamma_i\}}$, computed according to the MEG scaling law given in Equations (6.7) and (6.8). The application of this scaling law to compute the collisional dephasing of the CH_4 ν_2 Q-branch spectrum is based on the extension of the sum rule in Equation (6.7) beyond its rigorous definition, which is only valid for isotropic non-degenerate vibrational transitions. To a first approximation, the effect of collisional re-orientation is neglected and the CH_4 ν_2 transitions are treated as if they were completely isotropic and non-degenerate. This is of course a rough approximation, but it has a precedent in the work of DePristo and co-authors, who successfully extended the sum rule to model the collisional line broadening of the P- and R-branch lines in the absorption spectra of CO_2 [206]. The application of the MEG scaling law to model the collisional dephasing of the anisotropic CH_4 ν_2 Q-branch spectrum is thus justified in view of the fact that experiments are only performed at atmospheric pressure, so that collisional re-orientation and intra-branch coupling can be reasonably neglected. A further simplification introduced in Paper IV is to assume the same dephasing rate for all the irreducible representations of the rotational wave function corresponding to the same total angular momentum in Table B.3 [198]. Similarly, the same RET rates computed for the fundamental Q-branch lines are applied to all the vibrational hot bands. Following the time-domain modelling of the CH_4 ν_1 CRS spectrum in Chen *et al.*, the species-specific parameter a in Equation (6.8) is set to 2, and the fitting parameters are reduced to α and β at standard pressure and temperature conditions (i.e. $\delta = 1$ and $n = 0$) [126].

Figure 6.7(a) illustrates the dephasing of the spectrally-integrated CH_4 ν_2 Q-branch spectrum, measured in a flow of CH_4, for probe delays varying in the range ~30-210 ps in steps of 5 ps. Under standard pressure and temperature conditions, the effect of inelastic collisions is virtually negligible for values of the probe delay lesser than ~80 ps, where the dynamic behaviour of the integrated CH_4 CSRS signal is dominated by a strong coherence beating, as addressed in the next section. The experimental behaviour is fitted in Paper IV to the MEG model to simultaneously determine the scaling parameters α and β, which are fitted to 4.45E-2 and 1.52 respectively. The theoretical evolution of the CSRS signal in absence of collisional dephasing is also shown as the dashed line in Figure 6.7(a): for probe delays greater than ~80 ps the collisions start to dominate the signal dynamics determining a change of about two orders of magnitude at 200 ps. The satisfactory agreement of the experimental data and MEG scaling law proves that, at least to a first approximation, the sum rule in Equation (6.7) can be extended to model the effectively collisional dephasing of the anisotropic CH_4 ν_2 Q-branch spectrum at atmospheric pressure. Figure 6.7. The state-to-state relaxation rates computed by Equation (6.8) including the fitted values of α and β are thus used to calculate the Q-branch linewidths in the time-domain CH_4 ν_2 CSRS model.

The dephasing rates for the O-, P-, R- and S-branch transitions, on the other hand, are computed from the Q-branch ones by introducing the *random phase approximation* (RPA),

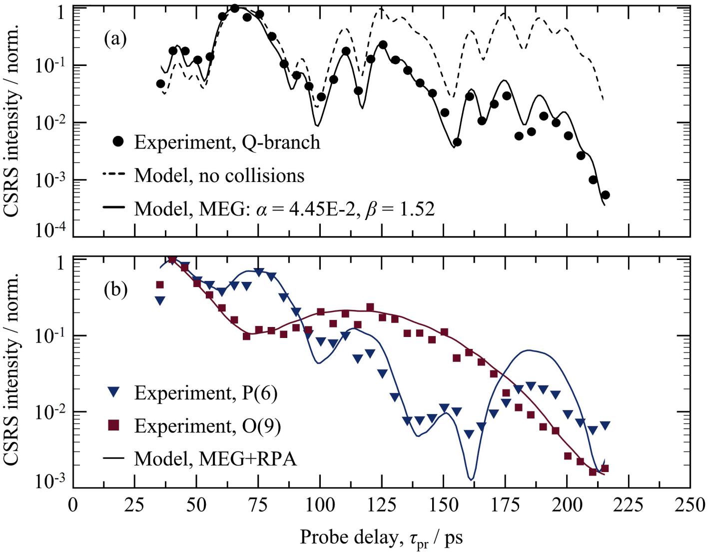

Figure 6.7: Experimental and modelled dephasing of the CH$_4$ ν_2 CSRS spectrum. (a) The collisional dephasing of the Q-branch spectrum under standard pressure and temperature conditions is measured in the range ~30-210 ps (circles) and fitted to the MEG scaling law (solid line) to determine the values of the α and β parameters. For comparison the theoretical behaviour of the spectrum in absence of collisions is also shown as the dashed line. (b) Two isolated lines in the P- and O-branch spectra illustrate the comparison between the experimental dephasing of the CSRS signal and the theoretical behaviour computed by employing the RPA. Figure reproduced from Mazza *et al.* [187].

whereby the collisional dephasing of a spectral line involving a change in the rotational quantum number depends only on the dephasing rate of the rotational states involved in the transition [206, 207], as:

$$\Gamma_{\{[v]_f,J_f\}\leftarrow\{[v]_i,J_i\}} = \frac{1}{2}\left(\Gamma_{\{[v]_f,J_i\}\leftarrow\{[v]_i,J_i\}} + \Gamma_{\{[v]_f,J_f\}\leftarrow\{[v]_i,J_f\}}\right) \tag{6.16}$$

Figure 6.7(b) shows the comparison between the theoretical dephasing of two isolated lines in the O- and P-branches of the CH$_4$ ν_2 CSRS spectrum calculated including these linewidths and the experimental data. A very good agreement is found for the dephasing of line O(9), while in the case of line P(5) the agreement between the experimental and theoretical dephasing is quite satisfactory up to ~150 ps, but an insufficient dumping of the coherence beating is found in the predicted dynamics at larger probe delays. All in all, these results prove that to a first approximation both the MEG scaling law and the RPA can be applied to predict the self-perturbed dephasing of the CH$_4$ ν_2 CSRS signal under standard pressure and temperature conditions.

6.4.2 TIME-RESOLVED CORIOLIS EFFECT ON THE ν_2 MODE SPECTRUM OF CH$_4$

The experimental CH$_4$ ν_2 CSRS spectrum shows a stark dynamic behaviour even for probe delays <80 ps, i.e. on a timescale where the effect of molecular collisions can be safely neglected at atmospheric pressure. This behaviour is interpreted in Paper IV as the effect of coherence beating between unresolved lines in the CSRS spectrum. In particular the beating of seemingly well-resolved rotational lines in the P- and R-branch spectra points to the existence of a fine splitting mechanism, which is attributed to an additional energy term introduced by Coriolis forces.

The effect of non-inertial Coriolis forces on the rotational-vibrational motion of the CH_4 molecule was first experimentally observed in 1935 by Nielsen and Nielsen in the ν_4 band of its IR absorption spectrum [208], and explained in a series of theoretical papers by Jahn as the gyroscopic coupling of the ν_2 and ν_4 vibrational modes [209–212]. Analogous to the description in classical mechanics, Coriolis effect is manifested in the motion of the molecular nuclei as a non-inertial force, arising from the gyroscopic coupling of the vibrational and rotational motion [213]. A simple depiction of Coriolis effect on the CH_4 molecule is given in Figure 6.8: in the inertial frame of reference XYZ, the nuclei of the molecule move linearly with respect to one another in to the ν_2 vibrational mode, and rigidly in the rotational motion about the Z axis. In the molecule-fixed reference xyz the combination of the rotational and vibrational motions gives rise to a non-inertial perturbation, interpreted as a fictitious Coriolis force. This force introduces an additional bending component to the vibrational motion, with same frequency as the inertial vibrational mode [38].

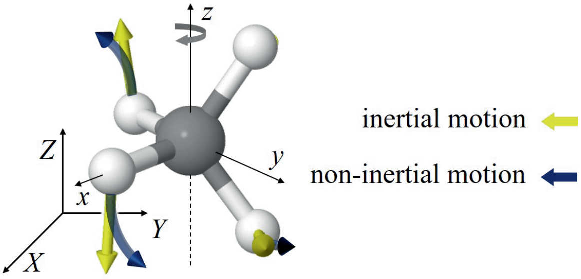

Figure 6.8: Coriolis effect in the coupling in the rotational-vibrational motion of the CH_4 molecule. The yellow vectors in the molecule sketch represent the motion of the ^1H nuclei in the inertial reference frame XYZ. In the Eckart (molecule-fixed) frame xyz, the coupling of the rotational motion about e.g. the z axis results in the appearance of a fictitious Coriolis force, which introduces a tangential velocity component in the non-inertial motion (blue vectors). Molecule rendered using Jmol: an open-source Java viewer for chemical structures in 3D (http://www.jmol.org/).

To within the harmonic oscillator and rigid rotor approximations, i.e. assuming a complete decoupling of the vibrational and rotational motions of the CH_4 molecules, the corresponding rotational-vibrational Hamiltonian is symmetrical with respect to rotations of the total angular momentum in the Eckart frame xyz, so that the K-states all have the same energy and each rotational state is $(2J+1)^2$-fold degenerate (see Appendix B). The introduction of rotational-vibrational coupling terms in the Eckart Hamiltonian, due to non-inertial fictitious (centrifugal and Coriolis) forces breaks this symmetry, resulting in a split of the $|J,K\rangle$ rotational sub-states. In Ref. [211] Childs and Jahn demonstrated that the Coriolis coupling terms in the Eckart Hamiltonian transform according to the F_1 irreducible representation of T_d. A first-order Coriolis interaction between two vibrational states can thus occur if the following condition is satisfied:

$$\Gamma(\psi_{v_i}) \times \Gamma(\psi_{v_j}) \supset F_1 \tag{6.17}$$

Hence, only the triply-degenerate ν_3 and ν_4 vibrational modes, with irreducible representation F_2, present a first-order Coriolis splitting of the ro-vibrational levels [214]. On the other hand, the symmetry condition in Equation (6.17) allows for a second-order gyroscopic coupling between the ν_2 and ν_4 modes [215], which results in a split of the $|J,K\rangle$ rotational sub-states in Table B.3.

The fine structure of the Coriolis-split rotational lines in the ν_2 Raman spectrum of CH_4 was experimentally observed by Thomas and Welsh [216], and later assigned by Champion at the Laboratoire de Spectronomie Moléculaire of the University of Burgundy [217, 218]. The spectral database employed in Paper IV was computed at the University of Burgundy, including the effect of the second-order Coriolis coupling between the ν_2 and ν_4 modes. The time-domain model is thus able to faithfully reproduce the strong coherence beating of the unresolved Coriolis-split rotational lines in the experimental CH_4 ν_2 CSRS spectrum, as shown in Figure 6.9.

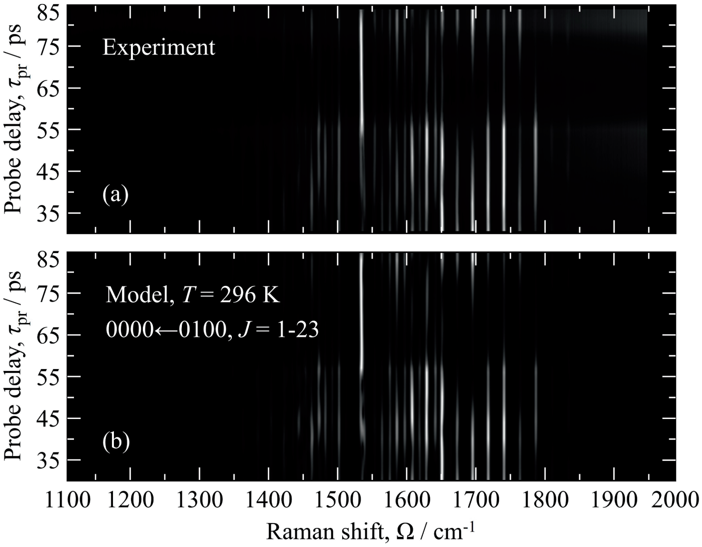

Figure 6.9: Coherence beating in the spectrochronogram of the CH_4 ν_2 CSRS signal. (a) Experimental ultrabroadband CSRS spectra acquired in a room-temperature CH_4 flow in the spectral region ~1100-2000 cm^{-1}, for probe delays varying in the range ~30-85 ps with a 2.2 ps step. (b) Synthetic CSRS spectra computed by the time-domain model by including only the fundamental ro-vibrational transitions 0000 ← 0100 and rotational states up to J=23. Figure reproduced from Mazza *et al.* [187].

The Coriolis effect is particularly evident in the coherence beating of the (otherwise well-resolved) odd rotational lines in the P- and R-branches of the CH_4 ν_2 CSRS spectrum. As a matter of fact, the rotational structure of the Q-branch is completely unresolved for the 4.1 cm^{-1} (top-hat) probe employed in this experiment, while the rotational O-and S-branch lines, spaced as $2B(2J+3)$, overlap with the even lines of the P- and R-branch spectra, spaced as $2B(J+1)$. Neglecting the rotational-vibrational coupling and assuming a negligible contribution from the vibrational hot bands at room temperature, odd lines in the P- and S-branch spectra should be perfectly resolved and would not give rise to any coherence beating. This contradicts the experimental observation, as

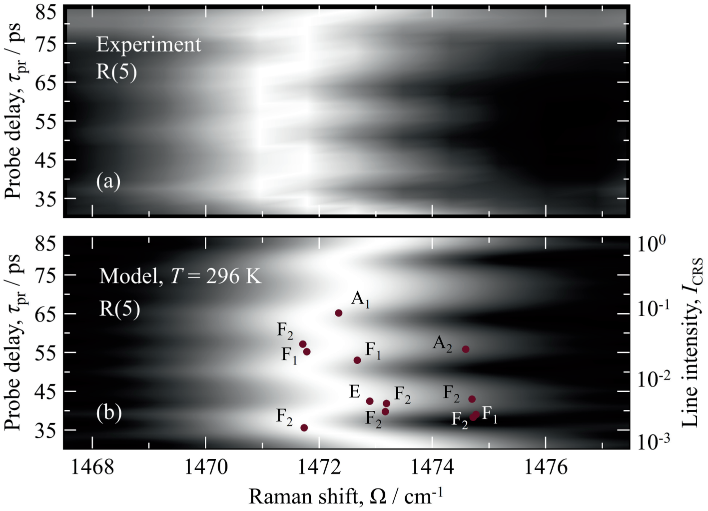

Figure 6.10: Coriolis splitting of the well-resolved R(5) line in the CH$_4$ ν_2 CSRS spectrum. (a) Coherence beating between the unresolved Raman transitions between the irreducible representations of the ro-vibrational wave functions $|[0,0,0,0], J=5\rangle$ and $|[0,1,0,0], J=4\rangle$, split by Coriolis effect. (b) The Coriolis split of the Raman line is included in the time-domain model, where the individual symmetry components are considered independently in terms of Raman frequency and line-strength. These are indicated by the red circles for each of the Coriolis-split Raman lines, corresponding to two A-labelled states, one E state, and nine F states.

illustrated in Figure 6.10(a) for the P(5) line in the CH$_4$ ν_2 CSRS spectrum recorded for a probe delay varying in steps of 2.2 ps in the range 30-85 ps. In order to rule out the possible coherence beating arising from unresolved vibrational hot bands, the time-domain CSRS spectra in Figure 6.10(b) are simulated including only the fundamental ν_2 Raman transitions. The spectrochronogram in Figure 6.10(a) thus illustrates the time-domain behaviour of the Raman transition $|[0000], 5, (2\mathrm{E} \oplus 9\mathrm{F})\rangle \leftarrow |[0100], 6, \mathrm{E} \times (2\mathrm{A} \oplus 2\mathrm{E} \oplus 9\mathrm{F})\rangle$: the coherence beating of the P(5) line arises from the Coriolis-splitting of the rotational sub-states, resulting in 12 unresolved lines whose position, rotational symmetry labels and CSRS intensities are represented by the red circles. Hybrid fs/ps CRS on CH$_4$ thus provides a means to investigate the intra-molecular coupling in the time domain, as the Coriolis coupling of the ν_2 and ν_4 vibrational modes is manifested in the time-resolved coherence beating of Figures 6.9 and 6.10.

These results demonstrate the ability of the time-domain CH$_2$ ν_2 CSRS model to render the complex ro-vibrational motion of the CH$_4$ molecule at room temperature, accurately reproducing its coherence beating. This validation is a first important step towards the application of the time-domain model to perform direct ro-vibrational fs/ps CRS thermometry on the ν_2 mode spectrum of CH_4 at higher temperatures, where the complexity of the Raman spectrum increases enormously as vibrational hot bands must be accounted for.

6.4.3 VALIDATION OF RO-VIBRATIONAL CH_4 ν_2 CRS THERMOMETRY

In order to validate the time-domain CH_4 ν_2 CSRS code at elevated temperatures, spatially-resolved ultrabroadband fs/ps CRS measurements are performed at 25 locations across a laminar CH_4/air diffusion flame in Paper IV. The flame is provided on the same Bunsen burner of Paper III, described in Section 6.1.2; a pure CH_4 flow is provided from a pressurised vessel and regulated by a digital flow controller (Bronkhorst) so that the flow velocity at the outlet section of the burner is estimated to be ~2.7 cm/s. This low velocity results in a very small Reynolds number (~35) thus guaranteeing a laminar CH_4 flow, which, upon mixing with the surrounding ambient air, produces the laminar diffusion flame. A steel mesh is furthermore placed ~15 mm above the burner to stabilise the flame. The spatially-resolved fs/ps CRS measurements are performed ~1 mm above the burner rim, by moving the probe volume from the centre of the fuel stream (at y=0 mm) in steps of 0.5 mm up into the oxidiser stream at y=12.5 mm.

The CH_4 ν_2 signal can be detected in the 1200-2000 cm^{-1} region of the single-shot fs/ps CSRS spectra up to location y=6.5 mm, where the average temperature is measured to be ~800 K by ro-vibrational CO_2 fs/ps CRS thermometry. In order to validate the time-domain model up to this temperature, 10-shot-averaged spectra are recorded at each measurement location: CH_4 ν_2 fs/ps CRS thermometry can thus be performed up to y=6.5 mm. This is validated by comparison to ro-vibrational CO_2 fs/ps CRS thermometry, performed independently on the "blue" Q-branch spectrum of CO_2, which can detected at all the 25 measurement locations across the flame front (see Section 7.2 for details). Figure 6.11(a)

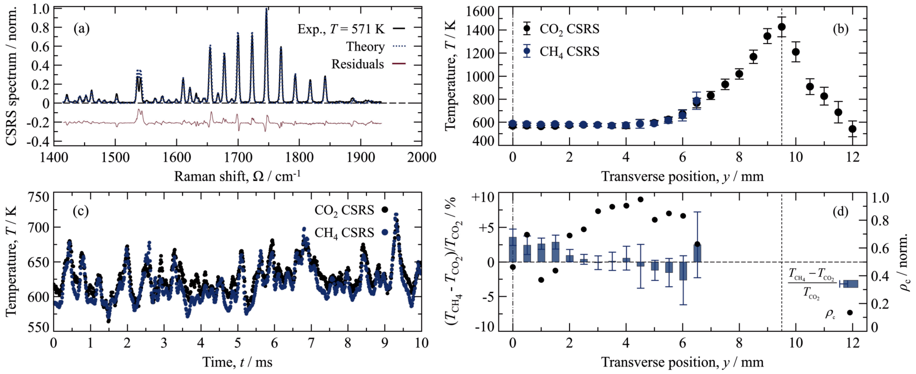

Figure 6.11: Ro-vibrational CH_4 ν_2 fs/ps CSRS thermometry. (a) 10 shot-averaged CH_4 ν_2 CSRS spectrum acquired in the flame (y=0 mm) and compared to the time-domain CRS model. (b) Average temperature profile across the flame front measured by ro-vibrational CO_2 (black markers) and CH_4 ν_2 CSRS thermometry (blue markers). (c) Temporal dynamics of the local temperature measured at y=5.5 mm by ro-vibrational CH_4 ν_2 and CO_2 CSRS thermometry. (d) Accuracy and precision of CH_4 ν_2 CSRS thermometry: accuracy (blue bars) is better than 3% at all measurement locations, precision is limited by the physical fluctuations of the flame. Concordance correlation (black dots) quantifies the agreement of the temperature dynamics measured by CO_2 and CH_4 ν_2 CSRS at each location. Figure reproduced from Mazza *et al.* [187].

presents an example of the fitting of the experimental CH_4 ν_2 CSRS spectrum acquired at the centre of the burner (y=0 mm). This contour fit includes all the five ro-vibrational branches of the CH_4 ν_2 spectrum in the region ~1400-1950 cm^{-1}. At locations y=4-6.5 mm the fit is limited to the P- and O-branch spectra, as the R- and S-branch lines overlap to the hot bands of the "blue" CO_2 dyad at higher temperature, while the Q-branch overlaps significantly with the ro-vibrational O_2 spectrum moving towards the oxidiser stream. The resulting temperature profiles in the fuel stream up to location y=6.5 mm and across the whole flame front, measured respectively by ro-vibrational CH_4 ν_2 and CO_2 CSRS thermometry, are shown in Figure 6.11(b). A good agreement is obtained for each spectrum within the 1000-frame sample acquired at each measurement location, as shown in Figure 6.11(c) for location y=0 mm.

This agreement is quantified in Paper IV by computing a concordance correlation coefficient as in Ref. [219]:

$$\rho_c = \frac{2\sigma_{\mathrm{CO_2,CH_4}}}{\sigma^2_{\mathrm{CO_2}} + \sigma^2_{\mathrm{CH_4}} + \left(\mu_{\mathrm{CO_2}} - \mu_{\mathrm{CH_4}}\right)^2} \tag{6.18}$$

Where $\mu_{\mathrm{CO_2}}$ and $\mu_{\mathrm{CH_4}}$ are the mean temperatures measured by CO_2 and CH_4 CSRS, respectively, with standard deviation $\sigma_{\mathrm{CO_2}}$ and $\sigma_{\mathrm{CH_4}}$, and covariance $\sigma_{\mathrm{CO_2,CH_4}}$. The ρ_c values given in Figure 6.11(d) thus quantify the correlation between the local temperature measured by CH_4 ν_2 and CO_2 CSRS, independently of the possible systematic bias in the former, and of the temperature fluctuations in the sample. The accuracy of CH_4 ν_2 CSRS thermometry is found to be better than 3% at all measurement locations, while the limiting factor in the thermometric precision is identified in the oscillations of the flame, as evident in the common fluctuations of the temperature profiles in Figure 6.11(c). By Fourier transforming these temporal sequences $T_{\mathrm{CH_4}}$ and $T_{\mathrm{CO_2}}$, common frequencies in the corresponding spectra can be identified and attributed to physical fluctuations in the flame. Following the methodology employed in Ref. [124], these common frequencies in the spectral range ~0.1-12.5 Hz are filtered off, thus suppressing the physical oscillations in $T_{\mathrm{CH_4}}$ and $T_{\mathrm{CO_2}}$ and leaving the inherent noise in the fs/ps CRS measurements. The resulting precision of CH_4 ν_2 CSRS thermometry is estimated to be better than 2% at all measurement locations.

Chapter 7

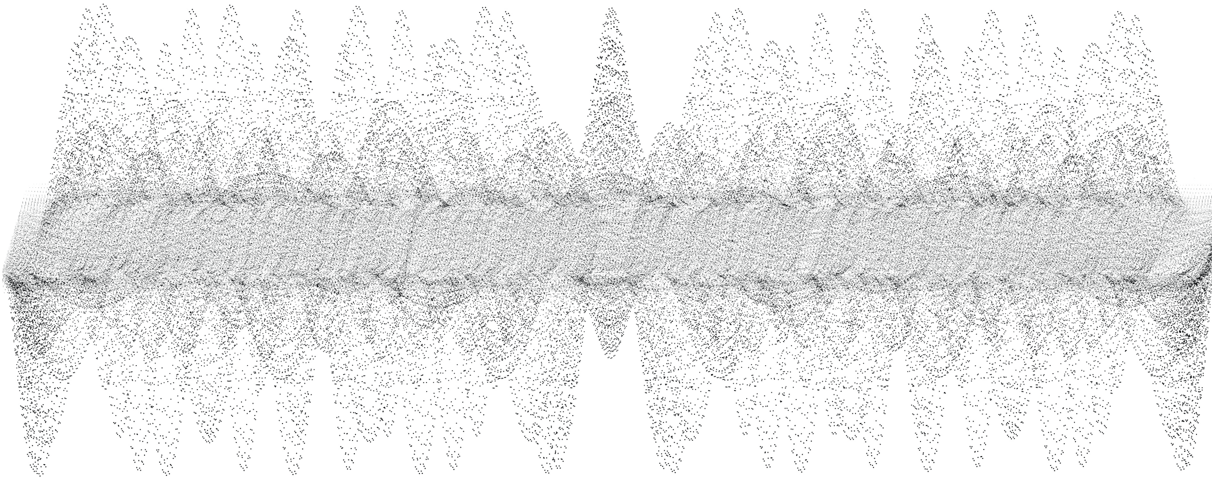

ULTRABROADBAND FS/PS CRS FOR COMBUSTION DIAGNOSTICS

The present chapter discusses some preliminary results demonstrating the use of ultrabroadband fs/ps CRS with in situ filamentation to investigate chemical and molecular transport processes in chemically reacting flows. The differential diffusion of the H_2 *molecule in a laminar* H_2*/air diffusion flame is experimentally observed by the spatially-resolved fs/ps CRS measurements of the local temperature and absolute concentrations of* N_2 *and* H_2 *in the fuel stream. The simultaneous detection of four major combustion species across a laminar* CH_4 *air diffusion flame sheds light on the buoyancy of* CH_4 *in the fuel stream and its pyrolysis, which produces* H_2 *in the reaction zone of a laminar* CH_4*/air diffusion flame.*

Part of the results discussed in this chapter have been published in Papers III and IV.

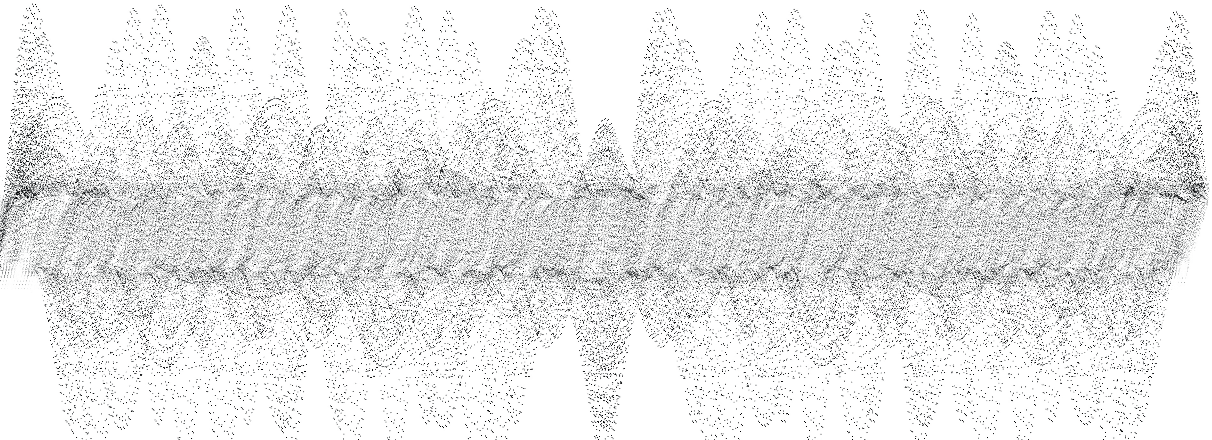

The results discussed in Chapters 4 to 6 answer the research questions formulated in Section 3.3, elucidating the development of quantitative ultrabroadband fs/ps CRS with *in situ* filamentation as a combustion diagnostic tool. The present chapter discusses the application of spatially-resolved ultrabroadband fs/ps CRS measurements to investigate chemical and molecular transport processes in different laboratory flames.

Section 7.1 details the direct observation of H_2 differential diffusion in a laminar H_2/air diffusion flame. This is demonstrated in Paper III by performing simultaneous pure-rotational N_2 fs/ps CRS thermometry and absolute N_2 and H_2 concentration measurements. The pure-rotational Raman coherence of both the N_2 and H_2 is excited by the compressed supercontinuum pump/Stokes pulse generated by *in situ* filamentation behind the thick optical window.

The second application of ultrabroadband fs/ps CRS with *in situ* filamentation as a combustion diagnostics tool is presented in Paper IV. This concerns the detection of the four major combustion species discussed in the previous chapter across a laminar CH_4/air diffusion flame.

7.1 CRS in a H_2/air diffusion flame

The first example, illustrating the suitability of ultrabroadband fs/ps CRS to investigate transport processes on a molecular scale in chemically reacting flow, is the direct observation of H_2 *differential diffusion* in the laminar H_2/air diffusion flame of Paper III.

The term "differential" refers to the fact that each species in a multi-component flow has a different diffusion velocity [220]. A different but related phenomenon observed in the combustion of H_2 is called "*preferential*" diffusion, referring to the mass diffusivity (D) being larger than the thermal diffusivity (α) [221], as quantified by a non-unitary Lewis number, defined as the ratio of the two diffusivity constants:

$$\mathrm{Le} \doteq \frac{\alpha}{D} \tag{7.1}$$

An assumption often made in the simplest description of e.g. laminar premixed flames is that of unit Lewis number, such that the heat diffusion is assumed to have the same magnitude as the mass diffusion in the combustion flow [17].

In the combustion of H_2, or where H_2 transport has a significant impact on the flame propagation [222], this assumption can lead to significant misrepresentations of the combustion dynamics and local flame structure [223]. As a matter of fact, the light weight of the H_2 molecule reflects on its high diffusivity, according to Graham's law [220], thus determining the existence of strong preferential and differential diffusion in H_2/air flames. Despite these effects being well-known in combustion science, to the best of the author's knowledge, they have never been directly observed, but only indirect experimental confirmations of their impact on the combustion process exists. Meier and co-authors, for example, employed spontaneous Raman scattering to characterise two turbulent H_2/N_2/air jet diffusion flames, and discussed the effect of the differential diffusion of H_2 as determining a super-adiabatic flame temperature, as plotted against the local O_2 mole fraction [223].

Paper III reports the direct observation of differential diffusion of H_2 towards the reaction zone of the laminar H_2/air diffusion flame described in Section 6.1. In order to investigate the local molecular transport processes in this flame, a second set of spatially-resolved

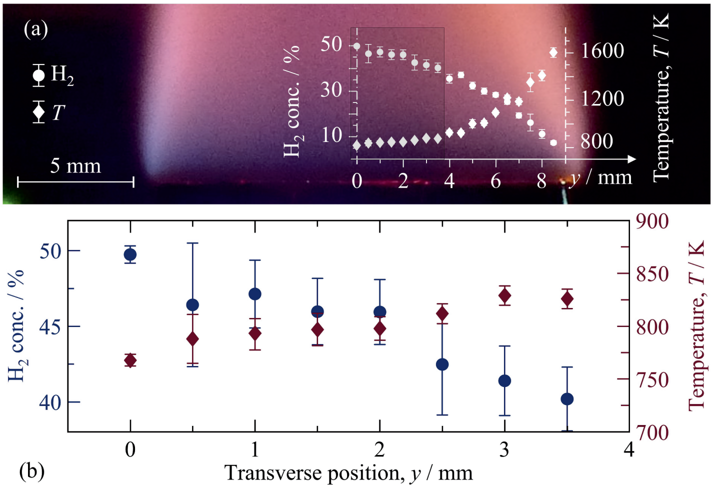

Figure 7.1: Differential diffusion of the H_2 molecules. (a) Temperature and relative H_2/N_2 concentration profiles measured by ultrabroadband fs/ps CSRS in a laminar H_2/air diffusion flame. (b) Detail of the measured scalars in the fuel stream up to 3.5 mm from the centre of the burner: the temperature increases by ~50 K over this range, due to the heat transfer from the chemical reaction zone, while the H_2 concentration reduces significantly from 50% in the centre of the fuel stream to 40% at location y=3.5 mm. The change in the relative H_2/N_2 concentration is attributed to the large mass diffusivity of H_2, which is thus more easily transported to the chemical reaction zone in the flame. Figure reproduced from Mazza *et al.* [27].

measurements is performed, at the same radial locations employed for the validation of the time-domain H_2 CSRS model, ~1 mm above the burner rim. The spectrometer is modified to perform high-resolution pure-rotational fs/ps CSRS in the spectral region ~50-600 cm^{-1}: a slower-focusing spherical lens (f:=400 mm) is employed as the imaging lens, resulting in a signal dispersion on the sCMOS sensor of ~0.27 cm^{-1}/pixel. The pure-rotational CSRS spectra of N_2 and O_2, as well as the first two lines of the pure-rotational spectrum of H_2 –O(2) at 354 cm^{-1} and O(3) at 587 cm^{-1}– are employed to simultaneously measure the local temperature and the relative O_2/N_2 and H_2/N_2 concentrations at each radial location across the flame front. The resulting temperature and relative H_2/N_2 concentration profiles are shown in Figure 7.1(a).

The fuel stream at the burner outlet consists of a mixture of 50% H_2-50% N_2, providing the N_2 CARS signal employed to validate pure-rotational H_2 fs/ps CRS thermometry. The simultaneous detection of the N_2 and H_2 CARS signal thus results in absolute concentration measurements of these two species, thus allowing for the *in situ* monitoring of the molecular transport processes within the fuel stream. The differential diffusion of H_2 is more pronounced at the centre of the fuel stream, as highlighted in Figure 7.1(b), where a detail of the temperature and absolute H_2 concentration profiles over the radial locations 0-3.5 mm is provided. Progressing from the centre of the burner to location y=3.5 mm, the H_2 concentration is reduced from 50% to 40% (i.e. a relative variation of 20%). The measured temperature, on the other hand, increases only so slightly from ~780 K, at the centre of the burner, to ~830 at location y=3.5 mm. This increment of ~50 K (i.e. ~6.4%) is attributed in Paper III to the heat transfer from the high-temperature reaction zone, rather than to the onset of the combustion reaction in the pre-heat region of the flame front.

The reducing H_2 concentration thus reflects the diffusion of H_2 ahead of N_2 towards the reaction zone of the flame, where it is consumed in the chemical reaction. In this sense, the measured concentration profile in Figure 7.1(b) provides a direct experimental observation of the differential diffusion of H_2 in this flame.

7.2 CRS IN A CH_4/AIR DIFFUSION FLAME

Beside the validation of the time-domain CRS model, Paper IV demonstrates the use of ultrabroadband fs/ps CRS to detect four major combustion species across the laminar CH_4/air diffusion flame in Figure 7.2.

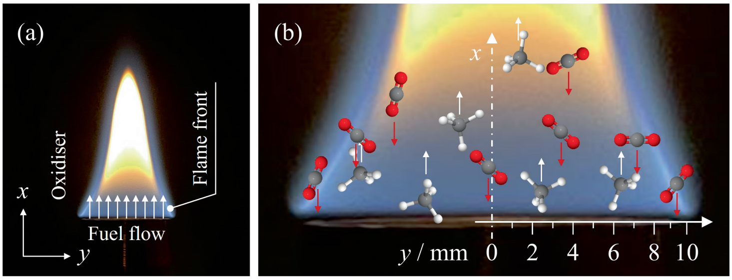

Figure 7.2: Molecular transport in laminar CH_4/air diffusion flame. (a) Picture of the laminar CH_4/air diffusion flame provided on the Bunsen burner. (b) Schematic of the buoyancy-driven transport of the CH_4 molecules and the back-diffusion of the heavier CO_2 molecules produced in the reaction zone of the flame. Molecules rendered using Jmol: an open-source Java viewer for chemical structures in 3D (http://www.jmol.org/).

The pure-rotational spectrum of H_2 is detected along with the ro-vibrational spectra of O_2, CO_2 and CH_4 in the vibrational fingerprint region ~1100-2000 cm^{-1}, as shown in Figure 7.3. The ro-vibrational CH_4 ν_2 spectrum spans from 1300 to 1950 cm^{-1}, as shown in the CSRS spectrum acquired in the fuel stream at location y=1 mm, in Figure 7.3(a). This spectrum partly overlaps with the fundamental and first hot band in the Q-branch of the Fermi-split ro-vibrational CO_2 spectrum, which dominates the vibrational fingerprint region of the Raman spectrum in the flame. The small spectral feature at 1553 cm^{-1}, on the other hand, is identified as to the ro-vibrational Q-branch spectrum of O_2.

Figure 7.3(b) shows the CSRS spectrum acquired in the reaction zone of the flame (y=8.5 mm). At this location, CH_4 is almost entirely consumed in the reaction with O_2, and the heat realised in the reaction raises the local temperature, as attested by the detection of the first hot band in the ro-vibrational O_2 spectrum and of several hot bands in the spectrum of CO_2. The more complex structure of the vibrational energy manifold of the triatomic CO_2 molecule, as compared to diatomic O_2, explains on the one hand its larger specific heat capacity and on the other the spreading of the vibrational Boltzmann distribution over a larger number of vibrational states. Figure 7.3(c) illustrates the CSRS spectrum in the oxidiser stream, dominated by the ro-vibrational spectrum of O_2, with well-resolved the S- and O-branch spectra on the lower- and higher-frequency side of the unresolved Q-branch. A small amount of CO_2 is also detected at this location (y=11.5 mm) in the ambient air constituting the oxidiser stream for the flame investigated in Paper IV.

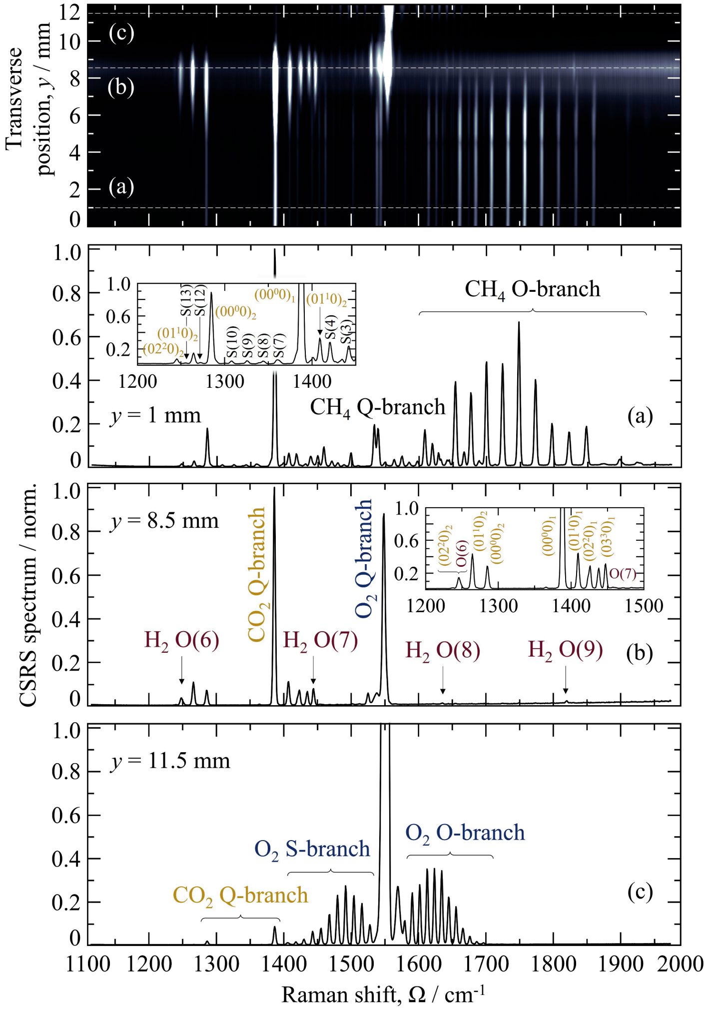

Figure 7.3: 10 shot-averaged ultrabroadband CSRS spectra in the vibrational fingerprint region measured across the laminar CH_4/air diffusion flame. Gamma compression was employed in the image post-processing to highlight some spectral features. (a) Fuel stream (y=1 mm): low-temperature ro-vibrational spectra of CO_2 and CH_4. (b) Reaction layer (y=8.5 mm): at temperatures greater than ~1300 K CH_4 undergoes pyrolysis producing H_2, which is then rapidly consumed. Four lines of the pure-rotational H_2 CSRS spectrum are detected in the spectral region ~1100–2000 cm^{-1}. (c) Oxidizer stream (y=11.5 mm): the oxidizer is ambient air so that the CSRS spectrum is dominated by the ro-vibrational O_2 Q-branch at ~1553 cm^{-1}; a small amount of CO_2 diffuses into the oxidizer stream. Figure reproduced from Mazza *et al.* [187].

The detection of these four major combustion species within the vibrational region of the Raman spectrum provides valuable insights into the molecular transport processes within the fuel stream and the pyrolysis of CH_4 in the chemical reaction zone of the flame.

The abundance of CO_2 at the centre of the fuel stream is explained in Paper IV as the result of the gravity-driven transport of this heavier molecule within the flow of much lighter CH_4. Due to its larger molecular mass (m_{CO_2}=44), the CO_2 produced in the reaction zone of the conical diffusion flame diffuses against the flow of buoyant CH_4 (m_{CH_4}=16). The resulting internal recirculation of CO_2 within the fuel stream has a two-fold effect on the temperature profile across the flame front, as independently measured by ro-vibrational CO_2 and CH_4 ν_2 fs/ps CRS thermometry. The local temperature at the centre of the fuel stream (y=0 mm) is increased to ~600 K by the mixing of the fresh CH_4 flow with the hot CO_2 flow. On the other hand, CO_2 has a larger specific heat capacity than the molecular components of air ($C_{CO_2,p}$=37.35 J/mol·K, $C_{O_2,p}$=29.39 J/mol·K and $C_{N_2,p}$=29.12 J/mol·K at 300 K). Hence, when introduced as a diluent in the combustible mixture, CO_2 acts as heat sink, resulting in a drastic reduction of the flame temperature [224]. This is observed in Paper IV, where the maximum temperature measured across the flame front (~1430 K at location y=9.5 mm, see Figure 6.11) is significantly lower than expected for a laminar axisymmetric CH_4/air diffusion flame [225], and comparable to the effect of a 20% CO_2 dilution in a laminar premixed CH_4/air flame (ϕ=0.8) [226].

Four lines belonging to the pure-rotational O-branch spectrum of H_2 are also visible in Figure 7.3(b): O(6) at 1246 cm^{-1}, O(7) at 1447 cm^{-1}, O(8) at 1637 cm^{-1} and O(9) at 1815 cm^{-1}. H_2 is produced by methane *pyrolysis*, i.e. by the thermal decomposition of the CH_4 molecules, which typically happens at temperatures higher than ~1300 K at atmospheric pressure and in absence of catalytic species [227].

This fact is of particular interest in view of the potential application of ultrabroadband fs/ps CRS with *in situ* filamentation to study the chemical reforming of CH_4 for carbon-neutral H_2 production within catalytic or plasma reactors [227, 228]. The pure-rotational H_2 and ro-vibrational CH_4 ν_2 spectra could be acquired simultaneously in the vibrational fingerprint region up to ~2000 cm^{-1}. An accurate measurement of the relative H_2/CH_4 concentrations would require the simultaneous measurement of the NR CRS signal to map the effective excitation bandwidth and implement the *in situ* referencing protocol. As remarked above, the ν_2 mode spectrum of CH_4 is completely depolarised, such that the same polarisation angle $\phi = \arctan\sqrt{6}$ could be employed to simultaneously apply the *in situ* referencing to the Raman spectra of H_2 and CH_4 in the vibrational fingerprint region. Accurate concentration measurements of these two critical species could thus be performed by ultrabroadband fs/ps CRS with *in situ* referencing of the spectral excitation, providing a means for the *in situ* monitoring of the CH_4 conversion process in chemical reactors.

Chapter 8

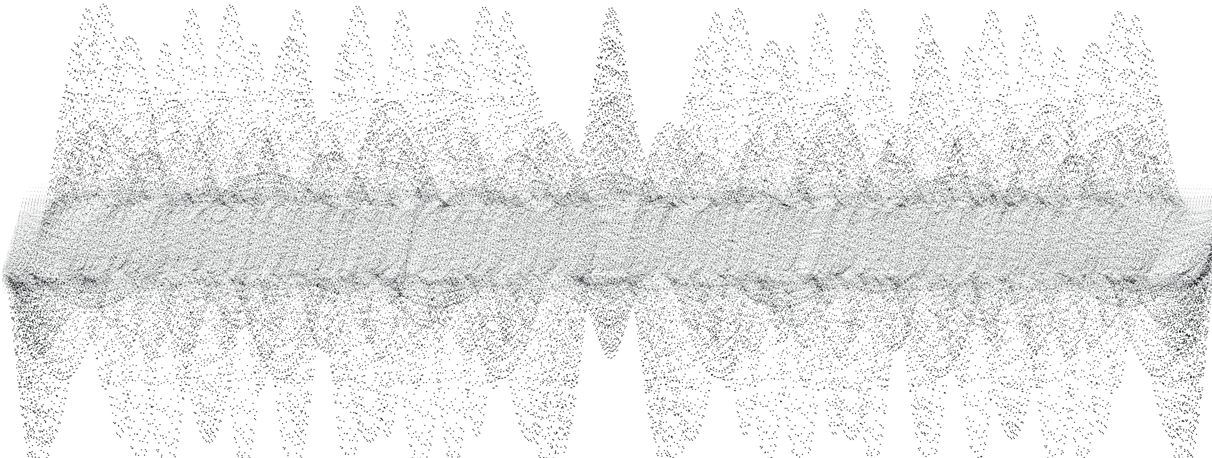

CONCLUSION AND OUTLOOK

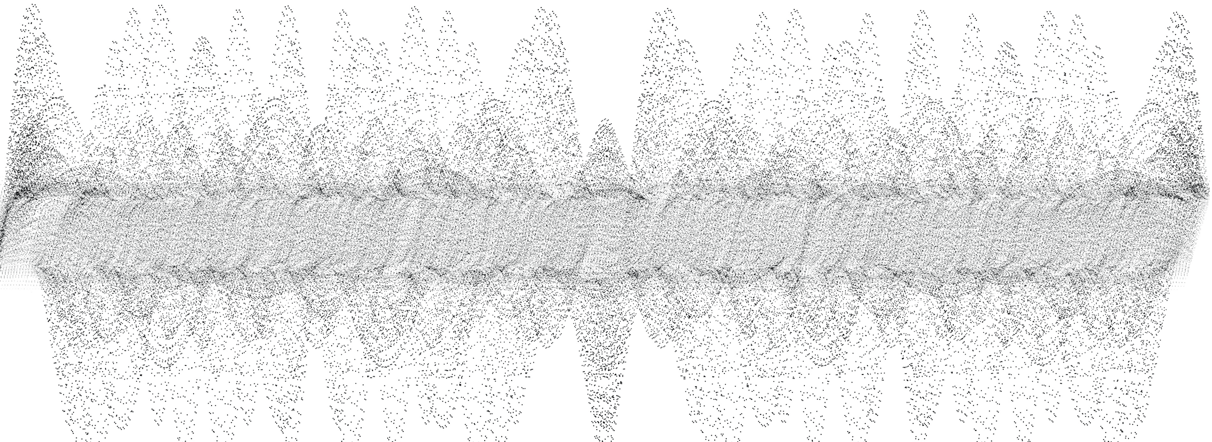

The present dissertation reports on the development of ultrabroadband fs/ps CRS for scalar measurements in chemically reacting flows, with a particular focus on its application as a combustion diagnostic tool. Moving from a number of significant advances in gas-phase CRS demonstrated in the last decade, this research aims at developing a quantitative ultrabroadband fs/ps CRS technique that could be robustly applied in measurements scenarios of practical interests.

In this perspective, two major hurdles are identified to the application of ultrabroadband fs/ps CRS outside the ideal, simplified settings of the experiments carried out in optical laboratories, where the boundary conditions can be well characterised and arbitrarily chosen: (i) the necessity of transmitting frail supercontinuum pulses through thick optical materials, and (ii) the *a priori* unknown dependence of the effective spectral excitation efficiency on the local boundary conditions in the pulse transmission to the measurement location. A third element to be considered, when aiming at the use of in the vibrational fingerprint region of the Raman spectrum for quantitative CRS measurements in the gas phase, is the need of accurate spectroscopic models. Time-domain CRS models for diatomic molecules, in particular N_2, have long been developed, validated in a range of operational pressure and temperature condition [229, 230], and employed in diverse practical measurement scenarios [19, 78, 90, 123, 231, 232]. Polyatomic molecules, on the other hand, are still largely unexplored and only recently some efforts have been spent on the development of time-domain ro-vibrational CRS models for some of the simplest combustion-relevant polyatomic molecules, such as CO_2 [67, 111] and CH_4 [126].

Therefore, the doctoral research here reported is articulated along the lines of the research questions formulated in Section 3.3, and addresses the three aforementioned challenges to the use of ultrabroadband fs/ps CRS for quantitative gas-phase diagnostics.

The first main research question is framed as:

1. *How can fs laser-induced filamentation be employed in situ as a coherent light source to robustly perform ultrabroadband fs/ps CRS in chemically reacting flows behind thick optical windows?*

In this respect, one of the most important outputs of the present doctoral research is the demonstration of *in situ* filamentation as a straightforward and effective strategy to perform ultrabroadband fs/ps CRS behind thick optical windows.

In particular, fs laser-induced filamentation proves to be an efficient and robust supercontinuum generation mechanism. Even a modest fs pulse energy (<1.5 mJ) is sufficient to achieve the *in situ* self-compression of the pump/Stokes pulse to <20 fs (as measured in Ar), enough to perform single-shot ultrabroadband fs/ps CRS in the fingerprint region up to 2000 cm^{-1}, as demonstrated in Papers I, III and IV. A robust filament propagation is shown through steep concentration and temperature gradients in the combustion flow, and the compressed supercontinuum output is measured to have an excellent spectral stability shot-to-shot, limiting the impact of the spectral noise on the reproducibility of the fs/ps CRS measurements. Nevertheless, the *in situ* use/*in situ* generation of the compressed supercontinuum has so far only been demonstrated in laminar laboratory flames. The filament generation and the fs laser pulse self-compression in turbulent chemically reacting flows should be the subject of future research activities, aimed at demonstrating the suitability of fs laser-induced filamentation as the supercontinuum generation mechanism for ultrabroadband fs/ps CRS in turbulent environments.

Since the use of fs laser-induced filamentation in the context of fs/ps CRS is a recent development, no established methodology exists for the determination of the CRS probe volume dimensions with *in situ* filamentation. Paper I introduces a novel experimental approach to address this question, by measuring the divergence of the supercontinuum beam output by the filament through a coherent imaging spectrometer. These measurements are carried out, in Paper I, on a single wavelength (at ~655 nm), and the same divergence angle is assumed for all the relevant wavelengths in the spectrum of the supercontinuum beam. Future work should investigate the validity of this assumption and assess its impact on the estimated probe volume dimensions. Nevertheless, the methodology proposed in Paper I is entirely general and the coherent imaging spectrometer described in Section 4.1.2 could be readily employed to characterise the wavelength-dependence of the supercontinuum divergence, resulting in a more sophisticated description of the CRS probe volume.

In situ filamentation is furthermore employed in Paper III to realise the first demonstration of ultrabroadband fs/ps CRS in the gas phase behind a thick optical window. The introduction of an external grating compressor in the fs/ps CRS instrument is instrumental to this achievement, as the compressor unit can easily compensate the GDD introduced by the window, granting a fine control over the quadratic spectral phase of the fs pulse, to optimise its *in situ* compression in the combustion environment. The combination of GDD control and *in situ* filamentation of relatively low-energy fs pulses grants the ultrabroadband fs/ps CRS instrument a large flexibility in terms of the minimum distance between the optical windows and the focal plane of the fs beam, which would be critical in practical measurement scenarios. A parametric investigation of the impact of the focusing geometry for the fs pump/Stokes beam on its self-compression during the filament propagation should be carried out as a follow-up study. Moreover, the dependence of the supercontinuum beam divergence out of the filament, and the resulting dimensions of the CRS probe volume, on the focusing geometry should be assessed.

It is also worth mentioning here that fs laser-induced filamentation could be the gateway to stand-off fs/ps CRS in the gas-phase, exploiting the backward coherent emission from excited atomic [233–235] and molecular species [236–238] in the filament. This *in situ*-generated "air lasing" emission could be used to probe the rotational-vibrational coherence induced by the compressed supercontinuum pulse, thus realising stand-off fs/ps CRS measurements for single-ended probing in enclosed environments or atmospheric monitoring [239, 240]. Furthermore, spectral imaging measurements reported on in Paper VI reveal a coherent emission from electronically-excited N_2^+ ions within sub-filamentary structures with diameter (~10 μm) smaller than the diffraction limit of the probe beam (~20 μm). Hence air lasing could be employed as a probe for ultrabroadband fs/ps CRS with the potential for spatially-resolved measurements beyond the diffraction limit.

The second research question concerns the uncertainty introduced in fs/ps CRS thermometry by the spectral referencing protocol. The question is formulated as:

2. *Is it possible to improve the performance of fs/ps CRS thermometry by measuring the spectral excitation efficiency in situ?*

As pointed out in Section 2.3.1, the excitation bandwidth of the two-beam fs/ps CRS instrument is limited by the bandwidth of the single combined fs pump/Stokes pulse, and a spectral referencing protocol is implemented to measure the resulting spectral excitation efficiency. In the practical application of fs/ps CRS, this efficiency depends on the spectrochronographic properties of the fs pump/Stokes pulse at the measurement location, i.e. upon its propagation through optical material and the gas-phase medium in the chemically reacting flow. The conventional experimental protocol –foreseeing the *ex situ* measurement of the spectral excitation profile as mapped by the NR CRS signal, typically generated in room-temperature Ar– therefore introduces an inherent uncertainty in fs/ps CRS thermometry.

Hence, the second cornerstone in the present research is the development of a novel experimental protocol for the *in situ* referencing of the spectral excitation efficiency. A simple polarisation theory of the gas-phase CRS process establishes the input linear polarisation of the pump/Stokes and probe laser fields that allows for the simultaneous generation of cross-polarised resonant and NR CRS signals. A novel coherent imaging spectrometer is introduced in Paper II for the simultaneous recording of these signals in two distinct detection channels. The application of the *in situ* referencing protocol is firstly demonstrated on conventional pure-rotational N_2 CRS thermometry, realised in two-beam 1D imaging configuration, and the results are compared the conventional experimental protocol. The spectral referencing protocol is shown to introduce a systematic bias in fs/ps CRS thermometry, depending on the measurement location across the laminar premixed CH_4/air flame front investigated. In the hot products of the flame, the difference in the density of the gas-phase medium along the fs beam path results in a lesser GDD of the pulse and, therefore, in a larger excitation bandwidth than measured by the NR CRS spectrum recorded *ex situ*. The conventional *ex situ* referencing protocol is thus demonstrated to result in a ~1.3% overestimation of the temperature measured in the product gases of the flame.

The need for an *in situ* referencing protocol to perform accurate fs/ps CRS measurements becomes even more relevant when fs laser-induced filamentation is employed as the *in situ* supercontinuum generation mechanism. The investigation of *in situ* filamentation in combustion environments, as reported in Section 4.1.3, demonstrates a strong dependence of the underlying non-linear optical phenomena on the local composition and temperature of the gas-phase flow, with temperature gradients in particular limiting the ultimate pulse compression achievable by fs laser-induced filamentation.

The novel *in situ* referencing protocol introduced in Paper II is therefore employed in Paper III to measure the ultrabroadband excitation of the pure-rotational spectrum of H_2 over more than 1000 cm^{-1}, in a laminar H_2/air diffusion flame. On the one hand, the *in situ* measurement of the NR CRS signal allows for estimating the duration and quadratic spectral phase of the compressed supercontinuum generated via fs laser-induced filamentation at different locations across the flame front, quantifying the impact of the local temperature and composition of the gas-phase medium on the pulse self-compression. On the other hand, the *in situ* referencing protocol proves crucial to achieve accurate pure-rotational H_2 fs/ps CRS thermometry: while the *ex situ* referencing introduces a systematic underestimation of the temperature as large as 80%, the accuracy of H_2 fs/ps CRS thermometry with *in situ* referencing is better than 1% at most measurement locations.

While these results demonstrate the critical need for *in situ* measurements of the effective spectral excitation efficiency to perform accurate H_2 fs/ps CRS thermometry, the impact of the referencing protocol on fs/ps CRS concentration measurements is yet to be explored. As demonstrated in the case of the ro-vibrational ν_2 mode spectrum of CH_4, the *in situ* referencing protocol can be applied, with the same relative polarisation angle between the pump/Stokes and probe fields, to any completely depolarised Raman spectrum. Hence, two-beam fs/ps CRS with *in situ* referencing of the ultrabroadband excitation efficiency could be used to simultaneously investigate the pure-rotational region of the Raman spectrum, as well as most of the bending vibrational modes of complex polyatomic molecules in the fingerprint region. One such application would the investigation of the chemical conversion of CH_4 into H_2 by pyrolysis in either catalytic or plasma reactors. Ultrabroadband fs/ps CRS could provide accurate H_2/CH_4 concentration measurements and allow for monitoring the chemical conversion process, with high spatio-temporal resolution and mode specificity in the investigation of the vibrational excitation of the CH_4 molecule [241].

Nevertheless, the issue of the spectral referencing for strongly polarised Raman spectra –such as the isotropic Q-branch spectra of most diatomic molecules, as well as the Q-branch spectrum of CO_2 [242]– is still open and new strategies needs to be developed to apply the *in situ* referencing protocol to these spectra.

Lastly, the need for accurate spectroscopic models to simulate the ro-vibrational fs/ps CRS spectra of complex polyatomic molecules in the vibrational fingerprint region is considered:

3. *To what extent can phenomenological time-domain CRS models be employed to perform high-fidelity fs/ps CRS thermometry on major combustion species in the vibrational fingerprint region of the Raman spectrum: H_2, O_2, CO_2, and CH_4?*

The complexity of the rotational-vibrational motion of a polyatomic molecule grows with the number of nuclei and chemical bonds. This is not only due to the growing number of normal vibrational modes, but also to (i) the possible resonance between individual vibrational modes –as in the case of the ν_1+$2\nu_2$ Fermi resonance in the Raman spectrum of CO_2–, and (ii) the higher-order coupling between the vibrational and rotational degrees of freedom of the molecule –as in the Coriolis effect observed in the Raman spectrum of the ν_2 mode of CH_4. Furthermore, at any given temperature, the larger number of normal vibrational modes for polyatomic molecules obviously reflects on a larger number of vibrational energy states being significantly populated according to Boltzmann statistics. The Raman spectra of polyatomic molecules thus have more pronounced vibrational hot bands than those of the simplest diatomic molecules, as observed in the case of CO_2 (see e.g. Figures 2.3 and 4.8). While this fact can increase the temperature sensitivity of fs/ps CRS thermometry performed on polyatomic molecules, as shown in the comparison between ro-vibrational O_2 and CO_2 fs/ps CRS (see Sections 6.2.2 and 6.3.2), it also makes the need for accurate spectroscopic models more demanding.

The present doctoral research covers the development of time-domain fs/ps CRS models for four major combustion species in the vibrational fingerprint region of the Raman spectrum, in order of complexity: H_2, O_2, CO_2, and CH_4. All the models are based on a simplified phenomenological description of the CRS process, as outlined in Appendix C, whereby the fs pump/Stokes laser pulse is assumed to impulsively excite the rotational-vibrational coherence of the target molecules, and the resulting macroscopic third-order susceptibility is computed as the interferogram in Equation (2.40). All the models are compared to the experimental CRS spectra acquired in the laboratory flames discussed in Chapter 6, providing a validation at temperatures up to: ~1450 K for the pure-rotational H_2 CRS model, ~2050 K and ~2100 K for the ro-vibrational O_2 and CO_2 CRS models, respectively, and ~800 K for the ro-vibrational CH_4 ν_2 CRS model.

These results demonstrate the wide applicability of the phenomenological description in Equation (2.40) to model the time-domain CRS spectra not only of simple diatomic molecules (H_2 and O_2), but also of more complex polyatomic molecules (CO_2 and CH_4). The time-domain CH_4 ν_2 CRS model in particular includes more than 10 million spectral lines, which is, to the best of the author's knowledge, the largest spectroscopic database ever employed in a time-domain CRS model for quantitative gas-phase fs/ps CRS. In this respect, the modelling efforts reported in Papers I and IV represent a first important step towards the development of a fully quantitative ultrabroadband fs/ps CRS technique for scalar determination in chemically reacting flows, and could pave the way to the application of fs/ps CRS to new domains of gas-phase diagnostics [243]. The time-domain model developed for ro-vibrational CH_4 ν_2 CRS, for example, could be readily extended to more complex spherical top molecules such as SF_6 [244], for which comprehensive spectroscopic databases already exist [245].

Nonetheless, while the pulse compression provided by *in situ* filamentation is clearly sufficient to excite the Raman coherence for molecular modes in the vibrational fingerprint region up to ~2000 cm^{-1}, the measured pulse duration of 17 fs should raise some concerns about the assumption of an impulsive excitation of the ro-vibrational Raman modes in this region. Such a pulse duration is indeed comparable to, if only slightly shorter than, e.g. the vibrational periods of CO_2 ($\tau_{\text{vib}} \approx 24.9$ fs) and O_2 ($\tau_{\text{vib}} \approx 21.5$ fs). Future research efforts should therefore be devoted to investigating the validity limits of this assumption, and to developing more accurate models that might take into account the experimental time-domain envelope of the pump/Stokes pulse.

Finally, it should be noted that the time-domain CRS models for the four major combustion species discussed in the present theses are validated at moderate-to-high temperatures for fs/ps CRS thermometry, but could be readily extended to perform simultaneous concentration measurements. This would require a careful experimental calibration of the numerical codes at different concentrations, to validate values reported in the literature for the Raman-cross section of the different molecular species. The availability of validated time-domain CRS models for all the major combustion species, paired with the *in situ* referencing protocol, could establish ultrabroadband fs/ps CRS as the state-of-the-art for accurate absolute concentration measurements in gas-phase environments.

In conclusion, the present research demonstrates that a straightforward path exists towards the use of ultrabroadband fs/ps CRS as a robust diagnostic tool for scalar determination in practical measurement scenarios, and lays the ground work for the development of quantitative ultrabroadband fs/ps CRS in chemically reacting flows.

Appendix A

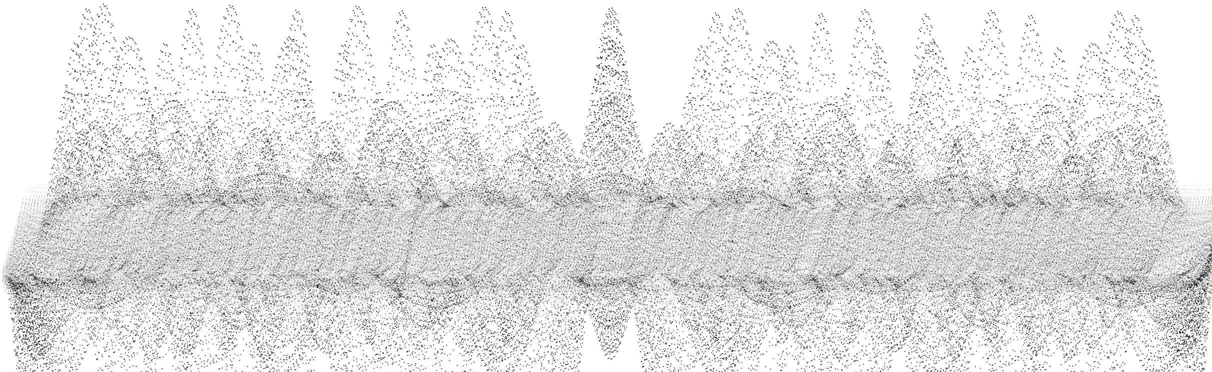

QUANTISATION OF THE ROTATIONAL-VIBRATIONAL ENERGY

The present appendix illustrates the fundamentals of the canonical quantisation of the rotational and vibrational motions of simple diatomic molecules, whose results are employed to describe spontaneous and coherent Raman scattering in Chapter 2.

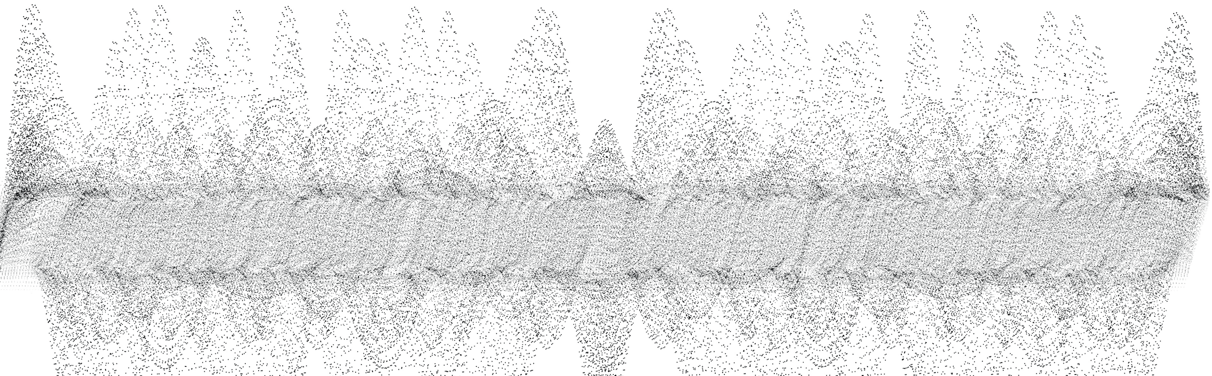

Consider a simple diatomic molecule as sketched in Figure 2.1: each of its sub-atomic components (i.e. nuclei and electrons) is described, according to quantum mechanics, by the wave function $|\psi(\mathbf{r},t)\rangle$, whose temporal evolution is prescribed by the *time-dependent Schrödinger's equation* [44]:

$$i\hbar\frac{\partial|\psi\rangle}{\partial t}=\hat{H}|\psi\rangle=-\left(\frac{\hbar^2}{2m}\right)\Delta|\psi\rangle+V(\boldsymbol{r})|\psi\rangle \tag{A.1}$$

Where $\hat{H}$ is the Hermitian operator representing the quantum equivalent of the classical Hamiltonian function H, defined as the difference between the kinetic ($-\hbar^2\Delta/2m$) and potential (V) energies of the system under consideration. In rigorous terms, the entire molecule as a physical system should have a wave function $|\psi\rangle$ assigned to it, depending on the whole set of coordinates associated to its components. However it is customary to invoke the *Born-Oppenheimer approximation*, whereby the contributions due to different coordinates are treated as independent of each other, and the molecular wave function can be factored as [246]:

$$|\psi\rangle=|\psi_{\mathrm{e}}\rangle|\psi_{\mathrm{s}}\rangle|\psi_{\mathrm{v}}\rangle|\psi_{\mathrm{r}}\rangle|\psi_{\mathrm{t}}\rangle \tag{A.2}$$

Where ψ_{e} is the part of the wave function that depends on the electronic coordinates (including the electron spin), ψ_{s} depends on the nuclear spin coordinates, ψ_{v} depends on the vibrational nuclear coordinates, ψ_{r} depends on the rotational nuclear coordinates, and ψ_{t} depends on the molecular coordinates.

The Born-Oppenheimer approximation thus entails neglecting the possible coupling between the different degrees of freedom. This has important implications in the light-matter interaction described in Section 2.2, as decoupling the electron and nuclear motion allows one to assume that only the former is fast enough to follow the oscillations of externally-applied EM fields at optical frequencies (~10^{11}-10^{16} Hz). On the other hand, the coupling between the vibrational and rotational motion of the nuclei plays an essential role in molecular spectroscopy, and it is taken into account via first- and second-order correction terms to ro-vibrational energy of diatomic molecules in Appendices A.1 and A.2, and of polyatomic molecules in Appendix B.

As mentioned in the introduction of Chapter 2, the internal energy contributions associated to the electronic and nuclear spin coordinates is of no concern for the present thesis: hence, the task a hand is to define the vibrational $|\psi_{\mathrm{v}}\rangle$ and rotational $|\psi_{\mathrm{r}}\rangle$ wave functions of a diatomic molecules and the corresponding energy levels. Intuitively these wave functions can be understood as describing the motion of the two nuclei in Figure 2.1 in the reference frame defined by the nuclear coordinates. Their motion along the internuclear axis results in the molecular vibrations, while the rigid motion about the centre of mass of the system determines the molecular rotation about an arbitrary axis in the plane orthogonal to the internuclear axis. In absence of external forces, the stationary states of these motions are found by solving the eigenvalue problem of the *time-independent Schrödinger's equation*:

$$\hat{H}|\psi\rangle=E|\psi\rangle \tag{A.3}$$

Where the eigenvalues E represent the only observable values of the rotational-vibrational energy, i.e. the only possible outcomes of an experimental measurement. The quantisation of the rotational-vibrational energy thus entails discrete molecular spectra, with spectral lines corresponding to specific transitions between these energy states.

A.1 QUANTISATION OF THE VIBRATIONAL MOTION

The description of the vibrational motion of a diatomic molecule moves from the assumption that this behaves as a linear classical harmonic oscillator [38]. The two nuclei, with masses M_1 and M_2, are bound by an electrostatic potential, modelled as the elastic force along the internuclear axis x:

$$F_{\text{elastic}} = -\frac{dV_{\text{elastic}}(x)}{dx} = -kx \tag{A.4}$$

Where k is the equivalent elastic constant of the system. Defining the reduced mass of the system as $m = (M_1 M_2)/(M_1 + M_2)$, the vibrating molecule is described by an equivalent mass-spring system with harmonic (angular) frequency $\omega = \sqrt{k/m}$. The potential energy associated to the elastic force in Equation (A.4) is given by:

$$V_{\text{elastic}}(x) = \frac{1}{2}kx^2 = m\omega^2 x^2 \tag{A.5}$$

The dynamics of such a system are described in terms of the well-known Hamiltonian function:

$$H = \frac{p^2}{2m} + \frac{1}{2}m\omega^2 x^2 \tag{A.6}$$

Where p is the linear momentum component along x. Solving the Hamilton-Jacobi equations with the Hamiltonian in Equation (A.6) gives the textbook solution for motion of a classical harmonic oscillator [213].

Following the canonical quantisation procedure introduce by Paul Dirac in 1926, the quantisation of this motion can be carried out by operating the substitutions [247]:

$$\begin{aligned} x &\longrightarrow \hat{x} \\ p &\longrightarrow \hat{p} = -i\hbar\frac{d}{dx} \end{aligned} \tag{A.7}$$

Where $\hat{x}$ and $\hat{p}$ are Hermitian operators acting on the Hilbert space of the wave functions $|\psi\rangle$. Introducing the transformations of Equation (A.7) in Equation (A.6) the system Hamiltonian is recast as the operator:

$$\hat{H}_{\text{v}} = -\frac{\hbar^2}{2m}\frac{d^2}{d^2x} + \frac{1}{2}m\omega^2\hat{x}^2 \tag{A.8}$$

It is now possible to rewrite the Schrödinger's equation for the molecular vibrational wave function, by substituting the Hamiltonian of Equation (A.8) into Equation (A.1):

$$\frac{d^2\,|\psi_{\text{v}}\rangle}{dx^2} + \left(\frac{2mE_{\text{v}}}{\hbar^2} - \frac{\omega^2 x^2}{\hbar^2}\right)|\psi_{\text{v}}\rangle \tag{A.9}$$

Finally, the time-independent Schrödinger's equation can be solved to find the observable vibrational energy levels of the diatomic molecule, i.e. the eigenvalues of $\hat{H}_{\text{v}}$ [44]:

$$E_{\text{v}} = \left(v + \frac{1}{2}\right)\hbar\omega, \quad v = 0, 1, 2, \cdots \tag{A.10}$$

The corresponding vibrational wave functions (i.e. the eigenstates $|v\rangle$) are given in terms of the Hermite polynomials H_v, represented over the potential energy curve in Figure A.1:

$$|v\rangle = \frac{1}{\sqrt{2^v v! \pi^{1/2}}} \exp\left(-\frac{\omega m}{2\hbar}(r-r_\mathrm{e})^2\right) H_\mathrm{v}\left(\sqrt{\frac{\omega m}{\hbar}}(r-r_\mathrm{e})\right) \tag{A.11}$$

The potential energy curve as well as the vibrational energy levels and wave functions have been obtained from the assumption the that the vibrational motion obeys Hooke's law in Equation (A.4). This assumption holds well as long as the internuclear distance r is close to its equilibrium value r_e, while for $r \to \infty$ the electrostatic potential binding the nuclei is negligible and the molecule dissociates into two neutral atoms. The energy required to overcome the electrostatic potential is thus called the *dissociation energy* D_0. For vibrational energies larger than D_0 then the internuclear distance can grow with no upper bound without a corresponding increment in the potential energy V [38]. This is a clear deviation from the behaviour predicted by the linear harmonic oscillator model adopted thus far. A more realistic description of the vibrational motion is found by adopting the Morse potential curve shown in Figure A.1(a):

$$V(x) = D_\mathrm{e}\left[1-e^{ax}\right]^2 \tag{A.12}$$

Where D_e is the dissociation energy measured relative to the equilibrium potential energy and a is an experimental constant depending on the electronic state of the molecule considered. There are no analytical solutions to the time-independent Schrödinger's equation when the anharmonic potential energy in Equation (A.12) is employed and the vibrational energy term values are modified by introducing higher-order terms of a power series in $\left(v+\frac{1}{2}\right)$:

$$G(v) = \omega_\mathrm{e}\left[\left(v+\frac{1}{2}\right) - x_\mathrm{e}\left(v+\frac{1}{2}\right)^2 + y_\mathrm{e}\left(v+\frac{1}{2}\right)^3 + \cdots\right] \tag{A.13}$$

Hence, in the anharmonic potential, the vibrational energy levels are not equally spaced as predicted by the quantum harmonic oscillator model, but the spacing decreases for larger values of the vibrational quantum number v.

It is worth noting here an important fact about Schrödinger's equation: since Equation (A.1) is linear in $|\phi\rangle$, any linear combination of the eigenfunctions $|v\rangle$ is also a valid solution to it. The general form of the vibrational wave function for a diatomic molecule is then:

$$|\psi_\mathrm{v}\rangle = \sum_v c_v |v\rangle \quad c_v \in \mathbb{C} \tag{A.14}$$

Equation (A.14) is said to represent a *coherent superposition* of vibrational eigenstates $|v\rangle$: in the present dissertation reference is often made to *vibrational coherence* to mean vibrational states of the form in Eq. A.14. As the present thesis deals with statistical ensembles of molecules in gas-phase media, it is useful to represent the state of a molecule by means of the so called *density operator* $\hat{\rho}$, which evolves according to the *Liouville-von Neumann equation*:

$$i\hbar\frac{\partial\hat{\rho}}{\partial t} = \left[\hat{H},\hat{\rho}\right] \tag{A.15}$$

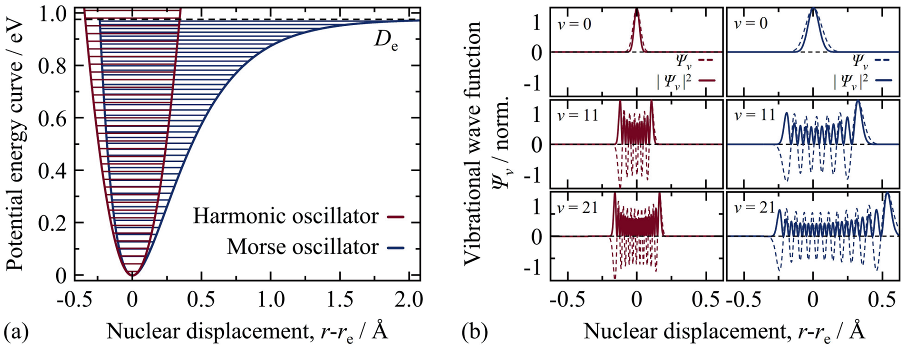

Figure A.1: The vibrational energy manifold of a diatomic molecule. (a) The harmonic (red) and Morse (blue) potential energy curves of N_2 in the ground electronic state are represented along with the corresponding vibrational energy states. The harmonic potential has a quadratic dependence on the nuclear displacement from the equilibrium position according to Hooke's law, resulting in equidistant energy levels. The mechanical anharmonicity of the Morse potential, on the other hand, determines a reducing energy gap between increasingly higher vibrational states up to the dissociation energy D_e. (b) Vibrational wave function associated to the vibrational quantum numbers v = 0, 11, and 21 in the harmonic (red) and Morse (blue) potential energy curves, computed according to Equation (A.11) and by solving Schrödinger's equation with the potential in Equation (A.12), respectively.

The vibrational state of a diatomic molecule in a statistical ensemble is then represented by the operator:

$$
\begin{aligned}
\hat{\rho}_{\mathrm{v}} &= |\psi_{\mathrm{v}}\rangle\langle\psi_{\mathrm{v}}| = \sum_{v}\sum_{v'} c_v c^*_{v'}\,|v\rangle\langle v'| && \text{coherent state} \\
\hat{\rho}_{\mathrm{v}} &= \sum_{v} p_v\,|v\rangle\langle v| \quad p_v \in \mathbb{R} && \text{mixed state}
\end{aligned}
\tag{A.16}
$$

The first definition in Equation (A.16) applies to a coherent superposition in the sense outlined above, while the second definition represents a statistical mixture of vibrational eigenstates, each one weighted by its own probability p_v. The latter is the case for an ensemble of molecule in thermal equilibrium, whose probability distribution over the vibrational energy states is given by Boltzmann statistics:

$$
\hat{\rho}_{\mathrm{Th}} = \frac{\exp(-\hat{H}/k_{\mathrm{B}}T)}{\mathrm{Tr}[\exp(-\hat{H}/k_{\mathrm{B}}T)]} \tag{A.17}
$$

Substituting the vibrational energy term for an anharmonic oscillator in Equation (A.13) into Equation (A.17) the vibrational Boltzmann distribution is computed for an ensemble of diatomic molecules in thermal equilibrium, at temperature T:

$$
\rho(v) = \frac{\exp(-\hbar G(v)/k_{\mathrm{B}}T)}{\sum_v \exp(-\hbar G(v)/k_{\mathrm{B}}T)} \tag{A.18}
$$

An example of the vibrational Boltzmann distribution of the N_2 and CO_2 molecules at three different temperatures is shown in Figure 2.3.

A.2 QUANTISATION OF THE ROTATIONAL MOTION

In order to describe the rotational motion of a diatomic molecule and operate its quantisation, it is necessary to introduce the angular momentum. The starting point is the definition of the classical angular momentum $\boldsymbol{l}$ for a single particle, with tensor of inertia $\boldsymbol{I}$ and angular velocity $\boldsymbol{\omega}$ defined in the Cartesian reference frame XYZ with unit vectors $\boldsymbol{i}$, $\boldsymbol{j}$, and $\boldsymbol{k}$:

$$\boldsymbol{l} = l_X\boldsymbol{i} + l_Y\boldsymbol{j} + l_Z\boldsymbol{k} = \boldsymbol{I}\cdot\boldsymbol{\omega} \tag{A.19}$$

In a body-fixed frame xyz (unit vectors $\boldsymbol{i}'$, $\boldsymbol{j}'$, and $\boldsymbol{k}'$), Galilean relativity and conservation of the angular momentum entail that the rotation of the reference axes is compensated by changes in the angular momentum components as:

$$\frac{dl_x}{dt}\boldsymbol{i}' + \frac{dl_x}{dt}\boldsymbol{j}' + \frac{dl_x}{dt}\boldsymbol{k}' + \boldsymbol{\omega}\times\boldsymbol{l} = \boldsymbol{0} \tag{A.20}$$

Equation (A.19) can then be recast as three scalar equations:

$$\begin{aligned}
\frac{dl_x}{dt} + \left(\frac{1}{I_y} - \frac{1}{I_z}\right) l_y l_z = 0\\
\frac{dl_y}{dt} + \left(\frac{1}{I_z} - \frac{1}{I_x}\right) l_z l_x = 0\\
\frac{dl_z}{dt} + \left(\frac{1}{I_x} - \frac{1}{I_y}\right) l_x l_y = 0
\end{aligned} \tag{A.21}$$

Similar to the canonical quantisation of the linear harmonic oscillator, the angular momentum of the single-particle system here considered can be quantised by introducing the angular momentum operator:

$$\hat{\boldsymbol{l}} = \boldsymbol{r}\times\hat{\boldsymbol{p}} = -i\hbar\boldsymbol{r}\times\nabla \tag{A.22}$$

The three scalar components of the angular momentum operator satisfy the commutation relations:

$$\left[\hat{l}_i, \hat{l}_i\right] = i\hbar\epsilon_{i,j,k}\hat{l}_k \tag{A.23}$$

Where $\epsilon_{i,j,k}$ is the Levi-Civita symbol, taking values ±1 for even and odd permutation of the indexes i, j and k. The commutation relations in Equation (A.23) imply that the projections of the angular momentum along two orthogonal axes cannot be measured simultaneously, according to the uncertainty principle. It is also useful to define the Casimir operator as the squared modulus of the *total angular momentum* $\hat{l}$:

$$\hat{\boldsymbol{l}}^2 = \hat{l}_i^2 + \hat{l}_l^2 + \hat{l}_k^2 \tag{A.24}$$

The operator $\hat{\boldsymbol{l}}^2$ commutes with all the components of the momentum operator, i.e. $\left[\hat{\boldsymbol{l}}^2, \hat{l}_{i,j,k}\right]=0$, meaning that it is possible to simultaneously measure the total angular momentum of the system and its projection over an arbitrarily chosen axis. It is customary (see e.g. Ref. [44]) to choose z as the quantisation axis, the conservation of the angular momentum along this axis leads to an eigenvalue problem with solution:

$$l_z = \hbar m, \quad m = 0, \pm 1, \pm 2, \cdots \tag{A.25}$$

From the conservation of the total angular momentum l^2 follows naturally that the modulus of the eigenvalues l_z must have an upper boundary l, such that l_z=m=$-l$, $-l+1$,..., $l-1$, l. The eigenvalues of the Casimir operator then are found to be:

$$\boldsymbol{l}^2 = \hbar^2 l(l+1), \quad l = 0, 1, 2, \cdots \tag{A.26}$$

From the commutation of the $\hat{\boldsymbol{l}}^2$ and $\hat{l}_z$ operators, follows that they have common eigenstates, denoted as $|l,m\rangle$. The quantisation of the angular momentum for a single particle in the Euclidian 3D space is summarised by the following equations:

$$\begin{aligned} \hat{\boldsymbol{l}}^2 |l,m\rangle &= \hbar^2 l(l+1) |l,m\rangle \\ \hat{l}_z |l,m\rangle &= \hbar m |l,m\rangle \end{aligned} \tag{A.27}$$

Finally, the Hamiltonian H of the system can be written in terms of the angular momentum l^2 [213], so that the corresponding operator is:

$$\hat{H} = \frac{\hat{\boldsymbol{l}}^2}{2I} \tag{A.28}$$

As it is obvious from its definition, the (rotational) Hamiltonian commutes with the Casimir operator, and the eigenstates of the momentum operators $\hat{\boldsymbol{l}}^2$ and $\hat{l}_z$ also represent states of well-defined rotational energy:

$$\hat{H} |l,m\rangle = \frac{\hbar^2}{2I} l(l+1) |l,m\rangle \tag{A.29}$$

Of the stationary states defined by Equation (A.29), those which differ only in the value of m have the same rotational energy: this follows from the fact that the direction of the quantisation axis z is chosen arbitrarily [44]. Hence, the energy levels $|l,m\rangle$ of a system whose angular momentum is conserved are (2l+1)-times degenerate. These (2l+1) degenerate rotational sublevels are sometimes referred to as "Zeeman states" [248]. The rotational eigenfunctions $|l,m\rangle$ are Laplace's spherical harmonics:

$$Y_l^m(\theta,\phi) = \frac{1}{\sqrt{(2\pi)}} e^{im\phi} (-1)^m i^l \sqrt{(2l+1)\frac{(l-m)!}{2(l+m)!}} P_l^m(\cos\theta) \tag{A.30}$$

Where P_l^m are the associated Legendre polynomials. The spherical harmonics associated to an angular momentum quantum number l=0,..., 3 are shown in Figure A.2. These can be interpreted as the wave functions associated to different degrees of alignment with respect to the chosen quantisation axis z.

The above model for the quantisation of angular momentum can be applied to the different angular momentum components in a diatomic molecule [38]. These are summarised in Table A.1, along with the associated quantum number and eigenvalues, and sketched in Figure A.3. In the following, the total angular momentum of the investigated molecules is assumed as only due to the nuclear motion, thus neglecting the electronic and nuclear spin components. While this assumption holds well for e.g. N_2 and H_2, which have

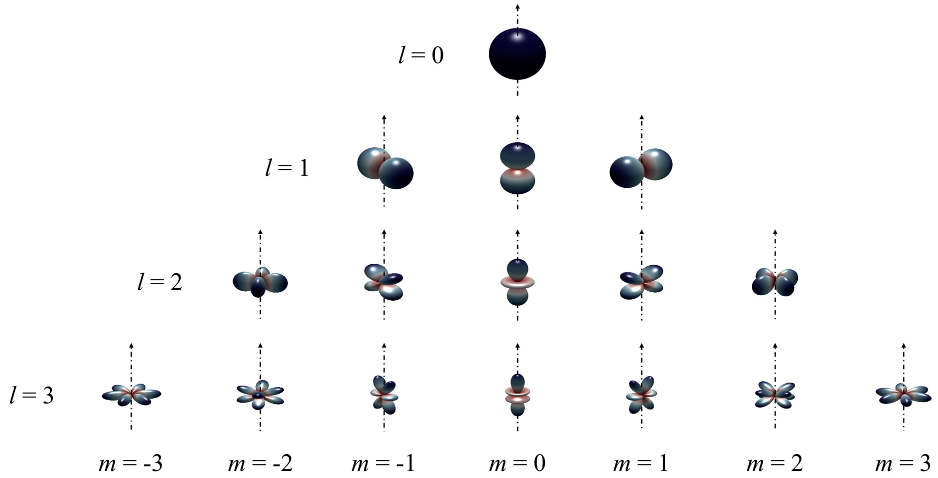

Figure A.2: Angular momentum wave functions. The wave function associated with the eigenstates of the rotational Hamiltonian in Eq. A.29 has the form of Laplace's spherical harmonics as in Eq. Equation (A.30), where the quantum number l represents the discrete values of the angular momentum, while m represents its projection along the quantisation axis z. The case m=|l| represent the alignment of the angular momentum to the to the quantisation axis, while the case m=0 represents its anti-alignment.

null electron spin angular momentum (S,L=0), it does not so for O_2, which has S=1 and whose coupling between the electron spin and nuclear angular momentum can influence its rotational spectrum (see e.g. Ref. [172]). Nevertheless, within the scope of the present thesis this assumption produces reasonable results and is retained in the description of all homonuclear diatomic species of interest (i.e. N_2, O_2 and H_2).

The quantisation of the angular momentum described above can now be applied to define the rotational states $|J,M\rangle$ of a diatomic molecule. The first step is the assumption of the nuclear motion being described by the *rigid rotor* model, whereby the internuclear distance is assumed to be constant and equal to r_e through the molecular motion. The rotational Hamiltonian for this system is then:

$$\hat{H}\,|J,M\rangle = \frac{\hbar^2}{2I}J(J+1)\,|J,M\rangle \tag{A.31}$$

In analogy to the vibrational energy term in Equation (A.13), the rotational energy of the rigid rotor can be expressed in units of angular frequency as [249]:

$$F(J) = B_e J(J+1) \tag{A.32}$$

Where B_e is the rotational constant of the system (in cm^{-1} units), defined as:

$$B_e = \frac{\hbar}{4\pi c I} \tag{A.33}$$

The assumption of the molecule behaving as a rigid rotor is in obvious contrast to the vibrational motion described in Appendix A.1: the internuclear distance is not constant, but

Table A.1: Quantisation of the angular momentum components of a rotating molecule.

Physical variable	**Quantum number**	**Quantised value**	**Value of quantum number**
Electron orbital angular momentum	L	$\hbar\sqrt{L(L+1)}$	$L = 0, 1, 2, \cdots$
Z-component of L	M_L	$\hbar M_L$	$M_L = 0, \pm 1, \cdots, \pm L$
Electron spin angular momentum	S	$\hbar\sqrt{S(S+1)}$	$S = 0, \frac{1}{2}, 1, \cdots$
Z-component of S	M_S	$\hbar M_S$	$M_S = 0, \pm\frac{1}{2}, \cdots, \pm S$
Nuclear spin angular momentum	I	$\hbar\sqrt{I(I+1)}$	$I = 0, \frac{1}{2}, 1, \cdots$
Z-component of I	M_I	$\hbar M_I$	$M_I = 0, \pm\frac{1}{2}, \cdots, \pm I$
Nuclear angular momentum	N	$\hbar\sqrt{N(N+1)}$	$N = 0, 1, 2, \cdots$
Z-component of N	M_N	$\hbar M_N$	$M_N = 0, \pm 1, \cdots, \pm N$
Total angular momentum	J	$\hbar\sqrt{J(J+1)}$	$J = 0, 1, 2, \cdots$
Z-component of J	M	$\hbar M$	$M = 0, \pm 1, \cdots, \pm J$
z-component of J	K	$\hbar K$	$K = 0, \pm 1, \cdots, \pm J$

changes about the equilibrium value r_e. Two first-order corrections are then introduced to the rotational energy term of Equation (A.32). The first correction introduces the centrifugal distortion of the molecular bond: the existence of non-inertial centrifugal forces in the molecule-fixed reference frame (*Eckart frame*[*]) increases the internuclear distance r and the inertia of the molecule I, thus reducing the effective rotational constant B. This effect is modelled by introducing a correction term proportional to the rotational energy of the molecule in the form:

$$F(J) = B_e J(J+1) - D_e[J(J+1)]^2 \tag{A.34}$$

Where D_e is here the equilibrium centrifugal constant, not to be confused with the dissociation energy in Equation (A.12). Higher-order correction terms might be introduced in Equation (A.22) to account for the mechanical anharmonicity [38], i.e. the fact that the vibrational motion is not properly described by the simple harmonic oscillator, but requires a more accurate potential curve (e.g. Morse's potential in Eq. A.12). This very same effect is at the base of the vibrational-rotational coupling, introduced as an additional first-order correction to Equation (A.32) by including the dependence of the rotational and centrifugal

---

[*] Non-inertial forces in the body-fixed frame of reference can also lead to second-order effects, such as the Coriolis coupling of different vibrational modes in polyatomic molecules (see Appendix B).

constants on the vibrational quantum number [163]:

$$\begin{aligned} B_\text{v} &= B_\text{e} - \alpha\left(v+\tfrac{1}{2}\right) + \left[\gamma\left(v+\tfrac{1}{2}\right)^2 + \cdots\right] \\ D_\text{v} &= D_\text{e} - \beta\left(v+\tfrac{1}{2}\right) + \left[\varepsilon\left(v+\tfrac{1}{2}\right)^2 - \cdots\right] \end{aligned} \tag{A.35}$$

With α, β, γ, and ε being the rotational-vibrational interaction constants.

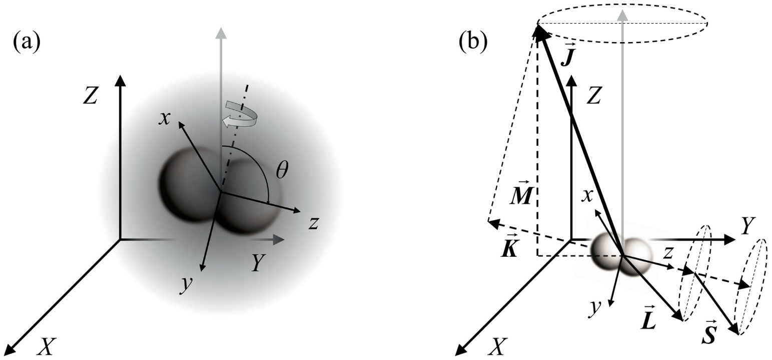

Figure A.3: Angular momentum of a diatomic molecule. (a) The rotating H_2 molecule represented in the inertial reference frame XYZ and molecule-fixed frame xyz. The angle θ represents the *molecular orientation* angle, defined as the angle between the inertial axis Z and the molecule-fixed internuclear axis z. (b) Angular momentum components for the H_2 molecule in the XYZ reference frame and their projections on the z axis.

In analogy to the density operator used to represent the vibrational state of the molecule, the rotational wave function $|J,M\rangle$ can be used to define coherent and mixed rotational states:

$$\begin{aligned} \hat{\rho}_\text{r} &= |\psi_\text{r}\rangle\langle\psi_\text{r}| = \sum_{J,M}\sum_{J',M'} c_{J,M}c^*_{J',M'}\,|J,M\rangle\langle J',M'| && \text{coherent state} \\ \hat{\rho}_\text{r} &= \sum_{J,M} p_{J,M}\,|J,M\rangle\langle J,M| && \text{mixed state} \end{aligned} \tag{A.36}$$

Assuming a canonical ensemble of diatomic molecules, the thermal distribution of Equation (A.17) is recast to compute the rotational Boltzmann distribution:

$$\rho(J) = (2J+1)\frac{\exp(-\hbar F(J)/k_\text{B}T)}{\sum_J (2J+1)\exp(-\hbar F(J)/k_\text{B}T)} \tag{A.37}$$

Where the ($2l$+1) factor represents the rotational multiplicity due to the degeneracy of the $|J,M\rangle$ states with the projection quantum number M, and is sometimes indicated as g_r. As the M quantum number is defined with respect to an inertial reference frame its degeneracy can only be lifted by providing and external reference, e.g. in the form of an EM field which couples to the nuclear motion. This is known as the Zeeman [250], Stark [251], or Autler-Townes effect [252], depending on whether an external magnetic, electrostatic or EM field is applied.

Appendix B

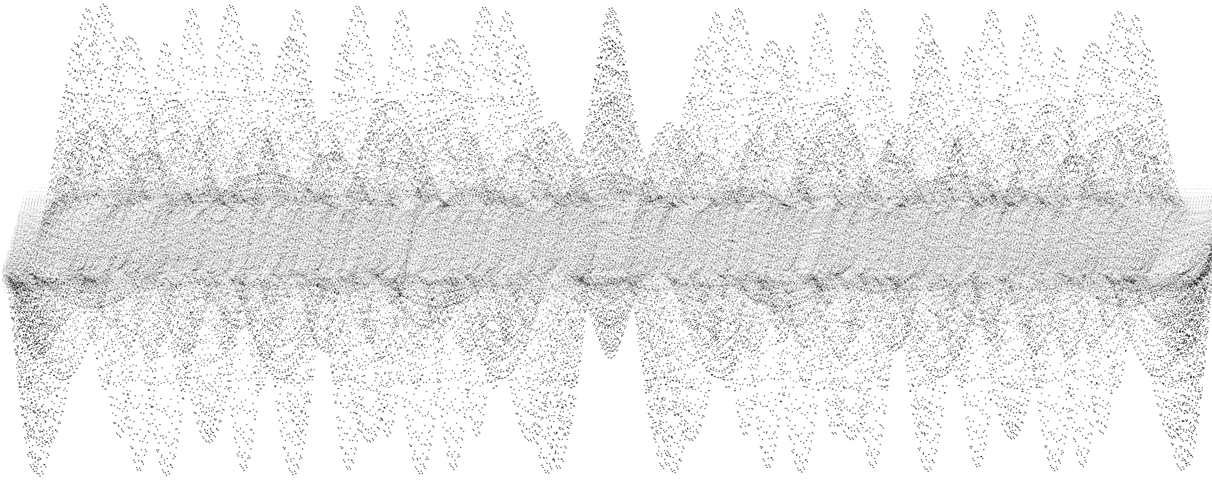

POLYATOMIC MOLECULES

The present appendix discusses the extension of the models in Appendix A, employed to describe the rotational-vibrational motion of simple diatomic molecules, to the more complex case of polyatomic molecules. Some symmetry considerations based on group theory are provided, and their application to the wave function of CH_4 is discussed.

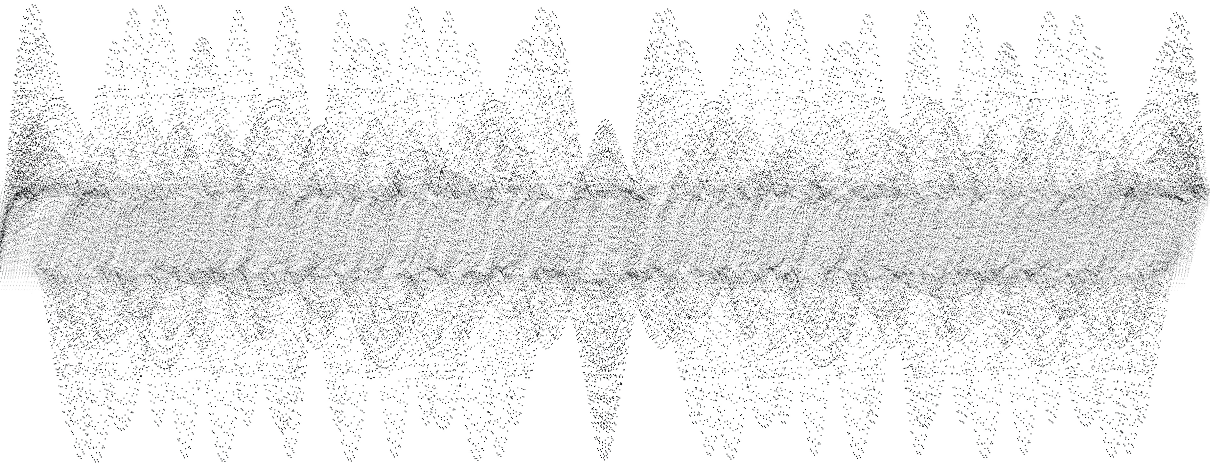

The rotational-vibrational motion in polyatomic molecules is significantly more complicated than in diatomic ones, owing to the increased number of nuclei and bonds. Consider a N-atomic molecule in the inertial frame of reference XYZ: 3 degrees of freedom are assigned to the i^{th} nucleus, corresponding to the coordinates $\left(Q_X^{(i)}, Q_Y^{(i)}, Q_Z^{(i)}\right)$. The whole molecule will thus have $3N$ degrees of freedom associated to the nuclear coordinates, i.e. to the translational, rotational and vibrational motions. Molecular translation entails the rigid motion of all the nuclei with equal velocity components (v_X, v_Y, v_Z) along the reference axes: 3 degrees of freedom are thus associated to the translational kinetic energy of the molecule. Similarly, a maximum of three degrees of freedom are associated to the rotational motion of the molecule with angular velocity components $(\omega_X, \omega_Y, \omega_Z)$. In the case of linear molecules, assuming the nuclei to be point masses, the moment of inertia about the internuclear axis will be null: hence, only 2 degrees of freedom are associated to their rotational motion. The vibrational degrees of freedom of a N-atomic molecule are thus $(3N-6)$ in the most general case or $(3N-5)$ for linear molecules, and to each a different vibrational wave function is associated. The number of these vibrational modes can grow significantly with the complexity of the molecule considered: relatively simple hydrocarbon molecules, such as acetylene (C_2H_2), ethylene (C_2H_4), or ethane (C_2H_6), have respectively 7, 13, and 18 vibrational modes.

B.1 SYMMETRY OF POLYATOMIC MOLECULES

The problem of describing the vibrational motion of polyatomic molecules can be greatly simplified by introducing the concept of molecular symmetry and the connected results of group theory. Every molecule possesses elements of symmetry, corresponding to the symmetry operations [38]:

- I, *identity element of symmetry*, for which no operation is performed on the molecule;
- C_n, *n-fold axis of symmetry*, for which the molecule is symmetric when rotated about this axis by $2\pi/n$ rad;
- σ, *plane of symmetry*, for which the molecule is symmetric under reflection of the nuclear coordinates with respect to this plane;
- i, *centre of symmetry*, for which the molecule is symmetric under reflection of the nuclear coordinates with respect to this point;
- S_n, *n-fold rotation-reflection axis of symmetry*, for which the molecule is symmetric under rotation of $2\pi/n$ rad about such axis, and subsequent reflection of the nuclear coordinates with respect to a plane orthogonal to the axis and through the centre of the molecule.

Molecules sharing the same symmetry elements are then said to belong to the same *point group*. Two point groups are relevant to the molecules treated in the present thesis. The first point group is $D_{\infty\text{h}}$, representing linear molecules with an inversion centre: homonuclear diatomic molecules such as N_2, O_2 and H_2, and triatomic CO_2 all belong to this group. CH_4, which will be thoroughly discussed in Appendix B.2, belongs to the tetrahedral point group T_d.

Group theory allows one to identify so called *irreducible representations* of the wave function describing the vibrational motion of the molecule under consideration [253]. Vibrational wave functions that present the same symmetry, i.e. have the same irreducible representation, share the same energy, and can then be considered degenerate representations of the same *normal* vibrational mode. In the example of CH_4, of the 9 possible vibrational modes, one is non-degenerate, one is doubly-degenerate, and two are triply-degenerate: CH_4 has only four normal vibrational modes (see Appendix B.2). As a first approximation, these normal vibrational modes can be treated as independent of each other, and each one can be modelled as a harmonic oscillator, thus extending the theory outlined in Appendix A.1. To each irreducible wave function is associated a quantum number v, and a symmetry label Γ_v to represent its vibrational degeneracy: the labels "A", "E" and "F" are employed to indicate non-degenerate, doubly-degenerate and triply-degenerate vibrations, respectively.

Considering a N-atomic molecule in the body-fixed reference frame xyz, the tensor of inertia $\boldsymbol{I}$ can be diagonalised by defining the principal momenta axes *abc*, and the diagonal elements (I_a, I_b, I_c) are called the *principal moments of inertia*. Conventionally, the principal moments of inertia are defined such that I_a is the minimum moment of inertia, while I_c is always the maximum. Depending on the value of the principal moments of inertia, the following classification of the molecular rotors is defined:

- *Symmetric top* molecules have two identical moments of inertia, while the third one can be lesser or greater;
    - *Prolate symmetric top* molecules have $I_c = I_b > I_a$. A linear molecule (e.g. diatomic) is a particular example of a prolate symmetric rotor, since $I_c = I_b$ and $I_a = 0$.
    - *Oblate symmetric top* molecules have $I_c > I_b = I_a$. An example of an oblate symmetric rotor is the planar benzene (C_6H_6) molecule.
- *Asymmetric top* molecules have $I_c > I_b > I_a$. The water molecule (H_2O) is an example of an asymmetric rotor.
- *Spherical top* molecules have $I_c = I_b = I_a$. Spherical rotors are highly symmetric, and include all molecules in the tetrahedral point group (e.g. CH_4).

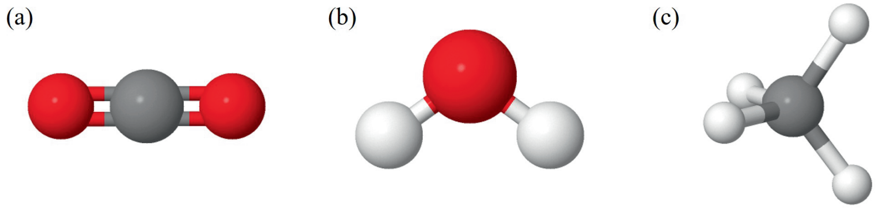

Figure B.1: Polyatomic molecules. (a) Sketch of the CO_2 molecule, an example of a linear molecule with I_c=I_b and I_a=0 (symmetric top rotor). (b) Sketch of the H_2O molecule, an asymmetric top rotor with I_c>I_b>I_a. (c) Sketch of the CH_4 molecule, a spherical top rotor with I_c=I_b=I_a. Molecules rendered using Jmol: an open-source Java viewer for chemical structures in 3D (http://www.jmol.org/).

The quantum numbers necessary to describe the rotation of a polyatomic molecule, according to the rigid rotor model in Appendix A.2, depend on which operators commute with the rotational Hamiltonian. In prolate symmetric top molecules, for example, neglecting the electron angular momentum and nuclear spin, $\hat{\boldsymbol{J}}^2$, $\hat{J}_Z$ and $\hat{J}_z$ all commute with $\hat{H}_\mathrm{r}$, and the rotational state is described by the quantum numbers $(J,M,K)^{\dagger}$. On the other hand, there are no closed-form solutions for the rotational energy term of asymmetric and spherical top molecules [38]. A detailed description of the rotational energy manifold of polyatomic molecules and its effect on their CRS spectra (see e.g. [254–258]) is beyond the scope of the present thesis. The focus here will be put on linear CO_2 and tetrahedral CH_4, and details about their rotational energy manifold will be discussed in Section 6.3.1 and Section 6.4.1, respectively.

In the following, the total wave function representing the rotational-vibrational motion of a polyatomic molecule are indicated as $|[v],J,M,\Gamma\rangle$, where $[v]$ represents the set of vibrational quantum numbers associated to the normal vibrational modes, and $\Gamma=\Gamma_\mathrm{v}\times\Gamma_\mathrm{r}$ is the product of the vibrational and rotational symmetry labels. Assuming an ensemble of polyatomic molecules in thermal equilibrium, the rotational-vibrational Boltzmann distribution is then computed as:

$$\rho([v],J,\Gamma) = g_v g_r g_s \frac{\exp\Big(-\hbar\big[G([v])+F(J)\big]/k_\mathrm{B}T\Big)}{Z} \tag{B.1}$$

Where Z is the partition function, and g_v, g_r and g_s represent the multiplicity of wave functions due to vibrational, rotational, and nuclear spin degeneracy. The latter is worth mentioning here, as it is responsible for the 2:1 alternation of even and odd J-states in the rotational Boltzmann population of N_2 shown in Figure 2.4. As pointed out in Table Table A.1, for a nuclear spin quantum number I there exist $(2I+1)$ degenerate spin sub-states corresponding to M_I=0, ±1,..., $\pm I$. The overall symmetry of the molecular wave function is then given, neglecting the electron wave function, by the product of the symmetry labels of the rotational, vibrational, and the nuclear spin wave functions. According to *Pauli's exclusion principle* this overall symmetry is constrained under the operation of exchange of identical nuclei, so that only certain combinations of Γ_v, Γ_r and Γ_s are physically realisable [259]. In the example of N_2, the nuclei are bosons with integer nuclear spin quantum number i=1 and, assuming the molecule to be in the ground electronic and vibrational states, the overall wave function must by symmetric with respect to their exchange. The nuclear spin wave function is asymmetric for odd values of I (*para-nitrogen*) −corresponding to the spin triplet I=1, and M_I=0, ±1− and symmetric for even values (*ortho-nitrogen*) −the sextet I=0, M_I=0 and I=2, M_I=0, ±1, ±2. Analogously, the rotational wave function is (a)symmetric for (odd) even values of J. The constraint on the overall molecular wave function being symmetric implies that only even values of J are admissible for ortho-nitrogen, and only odd for para-nitrogen. The nuclear spin multiplicity thus reads

$$\begin{aligned} g_\mathrm{s} &= 6 \quad J \text{ even} \\ g_\mathrm{s} &= 3 \quad J \text{ odd} \end{aligned} \tag{B.2}$$

The more complex case of the nuclear spin degeneracy in polyatomic CH_4 is discussed in the following section.

[†] The projection of the angular momentum on the molecule-fixed quantisation axis z introduces an additional energy term to Equation (A.32) as $(A_\mathrm{v}-B_\mathrm{v})K^2$, where A_v and B_v are the rotational constants about the a and b principal axes of inertia, defined as in Equations (A.33) and (A.35). In a diatomic molecule the z axis is defined as the internuclear axis (see Figure A.3), hence $J_z = 0$ and K=0, and the rotational energy term reduces to Equation (A.32).

B.2 THE RO-VIBRATIONAL ν_2 MODE OF CH_4

The exclusion principle for the CH_4 molecule can be formulated as follows: as the ^{1}H nuclei are protons and obey the Fermi-Dirac statistics, the total molecular wave function $|\psi\rangle$ must be symmetrical with respect to all proper rotations of the T_d point group, meaning that $|\psi\rangle$ must have a symmetry label "A". Since the translational and electronic wave functions are completely symmetrical, the exclusion principle then constrains the combination of the vibrational, rotational and nuclear spin wave functions in Equation (A.2) as:

$$\Gamma\left(|\psi_\mathrm{v}\rangle\right) \times \Gamma\left(|\psi_\mathrm{r}\rangle\right) \times \Gamma\left(|\psi_\mathrm{s}\rangle\right) \supseteq \mathrm{A} \tag{B.3}$$

where the product of the symmetry labels Γ is defined according to the rules in Table B.1.

Table B.1: Direct product of wave function representations. Table reproduced from Ref. [38].

	A	E_1	E_2	F
A	A	E_1	E_2	F
E_1	E_1	E_2	A	F
E_2	A	E_2	A	E_1
F	F	F	F	$A \oplus E_1 \oplus E_2 \oplus 2F$

The symmetry labels of the vibrational wave function $|\psi_\mathrm{v}\rangle$ for the four normal modes of CH_4 are summarised in Figure 6.6. The nuclear spin wave functions $|\psi_\mathrm{s}\rangle$ form a basis for the representation of the group of permutations of identical nuclei, which are equivalent to rotations. CH_4 has four identical ^{1}H nuclei, each consisting of only one proton with spin i=1/2 and two possible projections (m_i=±1/2) with corresponding eigenstates $|\uparrow\rangle$ and $|\downarrow\rangle$, so that 16 possible combinations of these eigenstates exist, which span the space of all possible nuclear spin wave functions for the CH_4 molecule. With the exception of the states $|\uparrow\uparrow\uparrow\uparrow\rangle$ and $|\downarrow\downarrow\downarrow\downarrow\rangle$, which have total nuclear spin I=2 and spin projections M_I=±2 respectively, the other wave functions do not have a well-defined total nuclear spin, so that it is impossible to establish their symmetry with respect to the exchange of identical nuclei. This problem is solved by defining the linear combinations (i.e. the superposition spin states) in Table B.2, for which the nuclear spin quantum number can be defined, along with its projection on the quantisation axis and its symmetry with respect to the exchange of two identical nuclei (Γ_s). Since wave functions which have the same symmetry are ($2I$+1)-degenerate (unless this symmetry is somehow broken), 5 irreducible representations are found for the nuclear spin wave function: A_1 is five-fold degenerate, E_1 and E_2 are non-degenerate, and $F_{1,x}$, $F_{1,y}$, and $F_{1,z}$ are three-fold degenerate.

The irreducible representation of the rotational wave function of CH_4 in terms of the total angular momentum quantum number J was derived by Bright Wilson Jr. by applying the methods of group theory in Ref. [259]: his results are summarised in Table B.3. Considering a specific ro-vibrational state for the CH_4 molecule $|[v],J,\Gamma\rangle$, one can thus compute the vibrational (g_v), rotational (g_r) and nuclear spin (g_s) multiplicity factors in the ro-vibrational Boltzmann distribution in Equation (B.1), considering only those representations of the molecular wave function that are not symmetry-forbidden. Combining the product rules in Table B.1 and the exclusion principle, as formulated in Equation (B.3), one

Table B.2: Molecular superposition of the nuclear spin eigenstates with well defined nuclear spin angular momentum (I) and projection (M_I). Table reproduced from https://www.nist.gov/pml/methane-symmetry-operations/methane-symmetry-operations-nuclear-spin-functions.

Nuclear spin wave function, $\lvert\psi_s\rangle$	I	M_I	Γ_s
$\lvert\uparrow\uparrow\uparrow\uparrow\rangle$	2	2	A_1
$\frac{1}{2}\big(\lvert\downarrow\uparrow\uparrow\uparrow\rangle+\lvert\uparrow\downarrow\uparrow\uparrow\rangle+\lvert\uparrow\uparrow\downarrow\uparrow\rangle+\lvert\uparrow\uparrow\uparrow\downarrow\rangle\big)$	2	1	A_1
$\frac{1}{\sqrt{6}}\big(\lvert\uparrow\downarrow\uparrow\downarrow\rangle+\lvert\downarrow\uparrow\downarrow\uparrow\rangle+\lvert\uparrow\downarrow\downarrow\uparrow\rangle+\lvert\downarrow\uparrow\uparrow\downarrow\rangle+\lvert\uparrow\uparrow\downarrow\downarrow\rangle+\lvert\downarrow\downarrow\uparrow\uparrow\rangle\big)$	2	0	A_1
$\frac{1}{2}\big(\lvert\uparrow\downarrow\downarrow\downarrow\rangle+\lvert\downarrow\uparrow\downarrow\downarrow\rangle+\lvert\downarrow\downarrow\uparrow\downarrow\rangle+\lvert\downarrow\downarrow\downarrow\uparrow\rangle\big)$	2	-1	A_1
$\lvert\downarrow\downarrow\downarrow\downarrow\rangle$	2	-2	A_1
$\frac{1}{\sqrt{12}}\big(2\lvert\uparrow\uparrow\downarrow\downarrow\rangle+2\lvert\downarrow\downarrow\uparrow\uparrow\rangle-\lvert\uparrow\downarrow\uparrow\downarrow\rangle-\lvert\downarrow\uparrow\downarrow\uparrow\rangle-\lvert\downarrow\uparrow\uparrow\downarrow\rangle-\lvert\uparrow\downarrow\downarrow\uparrow\rangle\big)$	0	0	E_1
$\frac{1}{2}\big(\lvert\uparrow\downarrow\uparrow\downarrow\rangle+\lvert\downarrow\uparrow\downarrow\uparrow\rangle-\lvert\downarrow\uparrow\uparrow\downarrow\rangle-\lvert\uparrow\downarrow\downarrow\uparrow\rangle\big)$	0	0	E_2
$\frac{1}{2}\big(-\lvert\downarrow\uparrow\uparrow\uparrow\rangle+\lvert\uparrow\downarrow\uparrow\uparrow\rangle-\lvert\uparrow\uparrow\downarrow\uparrow\rangle+\lvert\uparrow\downarrow\downarrow\downarrow\rangle\big)$	1	1	$F_{2,x}$
$\frac{1}{\sqrt{2}}\big(\lvert\uparrow\downarrow\uparrow\downarrow\rangle-\lvert\downarrow\uparrow\downarrow\uparrow\rangle\big)$	1	0	$F_{2,x}$
$\frac{1}{2}\big(\lvert\uparrow\downarrow\downarrow\downarrow\rangle-\lvert\downarrow\uparrow\downarrow\downarrow\rangle+\lvert\downarrow\downarrow\uparrow\downarrow\rangle-\lvert\downarrow\downarrow\downarrow\uparrow\rangle\big)$	1	-1	$F_{2,x}$
$\frac{1}{2}\big(\lvert\downarrow\uparrow\uparrow\uparrow\rangle-\lvert\uparrow\downarrow\uparrow\uparrow\rangle-\lvert\uparrow\uparrow\downarrow\uparrow\rangle+\lvert\uparrow\uparrow\uparrow\downarrow\rangle\big)$	1	1	$F_{2,y}$
$\frac{1}{\sqrt{2}}\big(\lvert\downarrow\uparrow\uparrow\downarrow\rangle+\lvert\uparrow\downarrow\downarrow\uparrow\rangle\big)$	1	0	$F_{2,y}$
$\frac{1}{2}\big(-\lvert\uparrow\downarrow\downarrow\downarrow\rangle+\lvert\downarrow\uparrow\downarrow\downarrow\rangle+\lvert\downarrow\downarrow\uparrow\downarrow\rangle-\lvert\downarrow\downarrow\downarrow\uparrow\rangle\big)$	1	-1	$F_{2,y}$
$\frac{1}{2}\big(-\lvert\downarrow\uparrow\uparrow\uparrow\rangle-\lvert\uparrow\downarrow\uparrow\uparrow\rangle+\lvert\uparrow\uparrow\downarrow\uparrow\rangle+\lvert\uparrow\uparrow\uparrow\downarrow\rangle\big)$	1	1	$F_{2,z}$
$\frac{1}{\sqrt{2}}\big(\lvert\uparrow\uparrow\downarrow\downarrow\rangle-\lvert\downarrow\downarrow\uparrow\uparrow\rangle\big)$	1	0	$F_{2,z}$
$\frac{1}{2}\big(\lvert\uparrow\downarrow\downarrow\downarrow\rangle+\lvert\downarrow\uparrow\downarrow\downarrow\rangle-\lvert\downarrow\downarrow\uparrow\downarrow\rangle-\lvert\downarrow\downarrow\downarrow\uparrow\rangle\big)$	1	-1	$F_{2,z}$

obtains the multiplication rules in Table B.4. The vibrational multiplicity factor takes of course value g_v=1, 2, or 3 for non-degenerate and doubly- and triply-degenerate vibrational modes, respectively.

Table B.3: Irreducible representations of the rotational wave function of CH_4, with $p = 0, 1, 2, 3, 4$, or, 5. Table reproduced from Ref. [259].

$J = 6p$	$(2J+1)\big[(p+1)\,A \oplus 2p\,E \oplus 9p\,F\big]$
$J = 6p+1$	$(2J+1)\big[p\,A \oplus 2p\,E \oplus 3(3p+1)\,F\big]$
$J = 6p+2$	$(2J+1)\big[p\,A \oplus 2(p+1)\,E \oplus 3(3p+1)\,F\big]$
$J = 6p+3$	$(2J+1)\big[(p+1)\,A \oplus 2p\,E \oplus 3(3p+2)\,F\big]$
$J = 6p+4$	$(2J+1)\big[(p+1)\,A \oplus 2(p+1)\,E \oplus 3(3p+2)\,F\big]$
$J = 6p+5$	$(2J+1)\big[p\,A \oplus 2(p+1)\,E \oplus 3(3p+3)\,F\big]$

The rotational multiplicity is due to two distinct components, as highlighted in table B.3: the (2J+1) factor is due to the degeneracy of the Z-projection quantum number M=-J, -J+1,..., J-1, J (see Appendix A.2), which cannot be lifted by internal molecular forces, but only by the application of an external EM field (e.g. in the Stark effect). For the purpose of the research reported in Paper IV, the ($2J$+1) Zeeman states are here always considered as degenerate. The other multiplicity component arises from the ($2J$+1)-fold degeneracy of the total angular momentum projection on the body-fixed reference frame (K=-J, -J+1,..., J-1, J), whose symmetry components are provided at each entry in Table B.3. Nevertheless, this degeneracy is lifted in the ν_2 vibrational mode of CH_4 by Coriolis effect, as discussed in Section 6.4.2. Finally, the value of nuclear spin multiplicity (g_s=5, 2, or 3) depends on the specific ro-vibrational state considered as the multiplication rules in Table B.4 constrain the physically-realisable combinations of ro-vibrational and nuclear spin wave functions.

Table B.4: Multiplication table for the irreducible representation labels. Table reproduced from Ref. [38].

	A	E	F
A	$A = A$	$E \not\supset A$	$F \not\supset A$
E	$E \not\supset A$	$(2A \oplus E) \supseteq A$	$F \not\supset A$
F	$F \not\supset A$	$F \not\supset A$	$(A \oplus E \oplus 2F) \supseteq A$

Appendix C

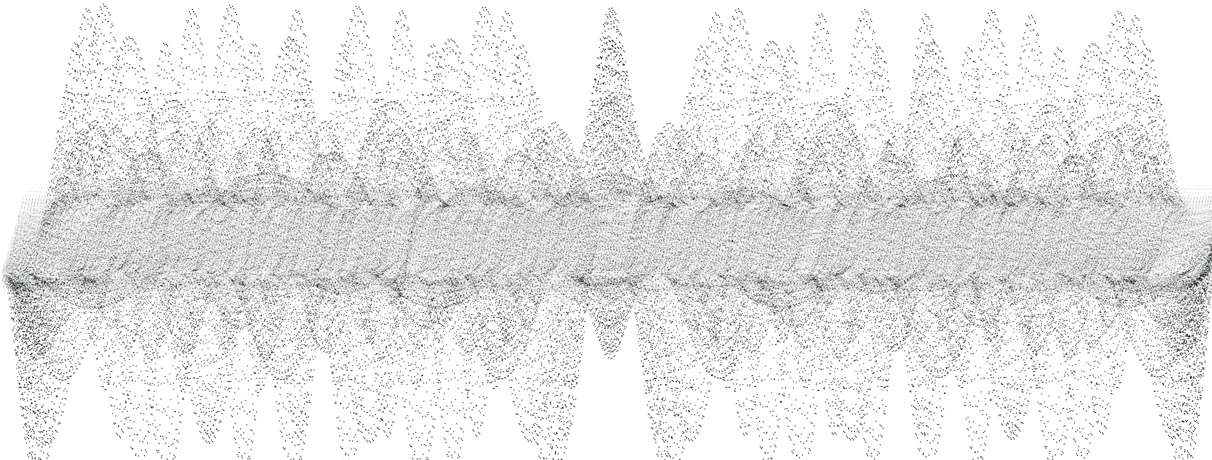

TIME-DOMAIN MODELLING OF HYBRID FS/PS CRS

The present appendix provides some details on the time-domain modelling of the fs/ps CRS process outlining the main assumptions needed to simplify the mathematical description. The main quantities used to compute the CRS line strengths and the Raman cross-sections are also defined.

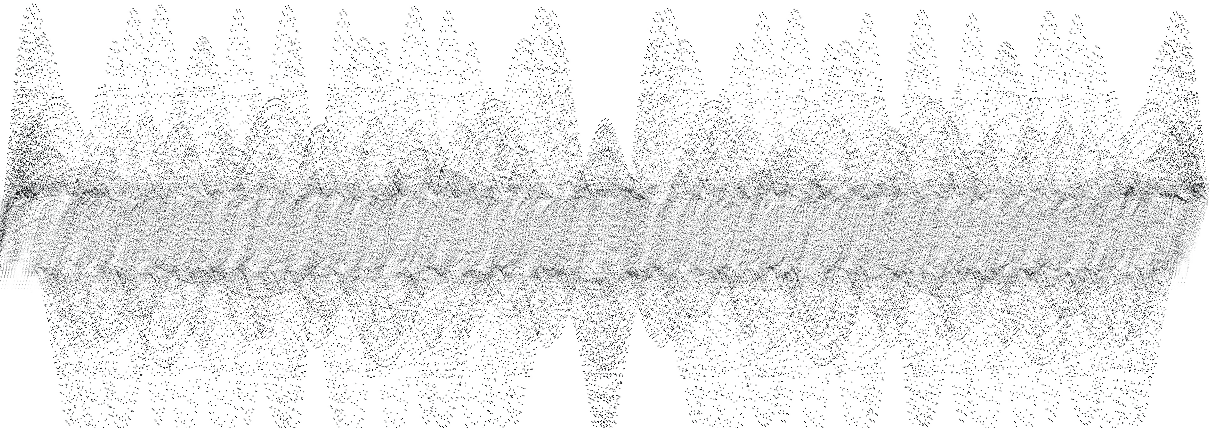

The description of the hybrid fs/ps CRS process in the time-domain summarised in Section 2.3.2 follows the theoretical treatment by Prince *et al.* [69].

The first step is to define the complex electric field as the sum of the pump, Stokes and probe laser pulses, with electric field amplitude $\boldsymbol{E}_i(t)$, carrier (angular) frequency ω_i, and wave vector $\boldsymbol{k}_i$:

$$\boldsymbol{E}(\boldsymbol{r},t) = \boldsymbol{E}_1(t+\tau_{23}+\tau_{12})\,e^{i[(\boldsymbol{k}_1\cdot\boldsymbol{r})-\omega_1 t]} + \boldsymbol{E}_2(t+\tau_{23})\,e^{i[(\boldsymbol{k}_2\cdot\boldsymbol{r})-\omega_2 t]} + \boldsymbol{E}_1(t)\,e^{i[(\boldsymbol{k}_3\cdot\boldsymbol{r})-\omega_3 t]} \tag{C.1}$$

Where τ_{12} and τ_{23} represent the delay between the Stokes and pump pulses, and the probe and Stokes pulses, respectively. The non-linear polarisation induced by the interaction of $\boldsymbol{E}(\boldsymbol{r},t)$ with the gas-phase optical medium is given by Equation (2.24).

As the duration of the fs pump and Stokes pulses is comparable to, or smaller than, the timescale of the nuclear motion of the Raman-active molecules, the interaction between the pulses and the optical medium must be treated as time-dependent [157]. Under the assumption of (i) parallel polarisation of all the laser pulses, (ii) rotating wave approximation (RWA) [260] for the light-matter interaction, and (iii) phase matched CRS process $\boldsymbol{k}_{\text{CRS}}=\boldsymbol{k}_1-\boldsymbol{k}_2+\boldsymbol{k}_3$, the third-order polarisation is computed as the convolution of the third-order susceptibility with the electric field in Equation (C.1):

$$\begin{aligned} P^{(3)}(t,\tau_{23},\tau_{12}) = \left(\frac{i}{\hbar}\right)^3 \int_{-\infty}^{t} dt_3 \int_{-\infty}^{t_3} dt_2 \int_{-\infty}^{t_2} dt_1\, \chi^{(3)}(t-t_3,t_3-t_2,t_2-t_1) \\ E_3(t_3)\,E_2^*(t_2+\tau_{23})\,E_1(t_1+\tau_{23}+\tau_{12})\,e^{-i\omega_3 t_3}\,e^{i\omega_2 t_2}\,e^{-i\omega_1 t_1}\,e^{i(\omega_3-\omega_2+\omega_1)t} \end{aligned} \tag{C.2}$$

Where t_i is the coherence timescale during the interaction of the medium with the i^{th} laser pulse, as illustrated in Figure C.1. The third-order optical susceptibility can be written as the sum of two distinct contributions: $\chi^{(3)}_{\text{CRS}}$, representing the resonant contribution due to the coherent rotational-vibrational motion of the molecular scatterers, and $\chi^{(3)}_{\text{NR}}$, the purely non-resonant contribution due to the electronic response of the medium.

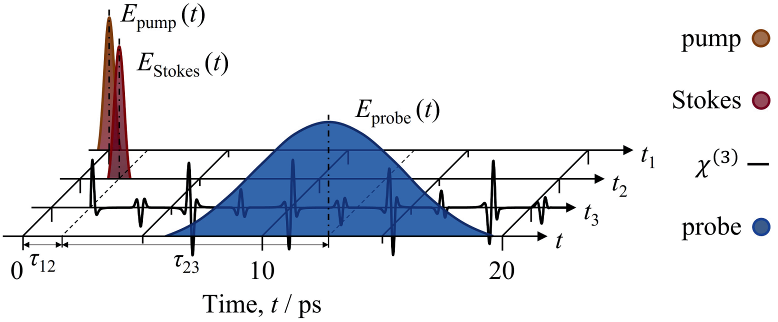

Figure C.1: Schematic of hybrid fs/ps CRS in the time domain: $E_{\text{pump}}(t)$, $E_{\text{Stokes}}(t)$, and $E_{\text{probe}}(t)$ represent the temporal envelops of the input laser pulses; $\chi^{(3)}$ is the non-linear optical susceptibility of the gas-phase medium due to the coherent motion of its molecular components; t_1, t_2, and t_3 are the coherence timescales during the interaction with the input laser pulses; τ_{12} and τ_{23} are the intra-pulse delays.

Under the assumption of far detuned optical pulses, upon its interactions with the pump and probe (and Stokes, in case of a NR pathway) pulses the molecule is in a virtual state, for which an instantaneous dephasing is assumed as discussed in Section 2.2.2. The non-linear susceptibility of the medium can then be written as:

$$\begin{aligned}\chi^{(3)}_{\mathrm{CRS}}(t-t_3,t_3-t_2,t_2-t_1) &= \delta(t-t_3)\,\chi^{(3)}(t_3-t_2)\,\delta(t_2-t_1)\\ \chi^{(3)}_{\mathrm{NR}}(t-t_3,t_3-t_2,t_2-t_1) &= \delta(t-t_3)\,\delta(t_3-t_2)\,\delta(t_2-t_1)\end{aligned} \tag{C.3}$$

Where $\delta(t)$ is the Dirac delta distribution. Using the well-known *sifting* property of δ, the NR third-order polarisation field in the medium can then be written as:

$$P^{(3)}_{\mathrm{NR}}(t,\tau_{23},\tau_{12}) = \left(\frac{i}{\hbar}\right)^3 E_3(t+\tau_{23}+\tau_{12})\,E_2^*(t+\tau_{12})\,E_1(t) \tag{C.4}$$

Similarly the resonant contribution to the third-order polarisation field in the medium can be simplified as:

$$\begin{aligned}P^{(3)}_{\mathrm{CRS}}(t,\tau_{23},\tau_{12}) = \left(\frac{i}{\hbar}\right)^3 E_3(t-t_3)\int_{-\infty}^{t} dt_2\,\chi^{(3)}(t_2)\\ E_2^*(t+\tau_{23}-t_2)\,E_1(t+\tau_{23}-t_2+\tau_{12}-t_1)\,e^{i(\omega_1-\omega_2)t_2}\end{aligned} \tag{C.5}$$

The research discussed in the present thesis is carried out employing the two-beam fs/ps CRS instrument detailed in Paper V [125]. As discussed in Section 2.3.1, the two-beam CRS phase-matching scheme makes use of a single broadband fs pulse to deliver the pump and Stokes frequencies. The time-domain modelling of the two-beam CRS process can then be simplified by introducing a single complex electric field to represent the combined pump/Stokes excitation pulse $\boldsymbol{E}_{12}(t)e^{i(\boldsymbol{k}_{12}\cdot\boldsymbol{r}-\omega_{12}t)}$, substituting this field into Equation (C.5) yields:

$$\begin{aligned}P^{(3)}_{\mathrm{CRS}}(t,\tau_{23},\tau_{12}) = \left(\frac{i}{\hbar}\right)^3 E_3(t-t_3)\int_{-\infty}^{t} dt_{12}\,\chi^{(3)}(t_{12})\\ E_{12}^*(t+\tau_{23}-t_{12})\,E_{12}(t+\tau_{23}-t_{12})\,e^{i(\omega_1-\omega_2)t_{12}}\end{aligned} \tag{C.6}$$

Where t_{12} represents the coherence timescale for the rotational-vibrational motion of the Raman-active molecules in the optical medium, after the interaction with the combined pump/Stokes pulse, as shown in Figure C.2.

As discussed in Section 2.3, if the temporal envelope of the pump/Stokes pulse has a duration much smaller than the rotational-vibration motion of the target molecules, the Raman coherence is generated impulsively. This is modelled mathematically by the so-called *sudden approximation* [261], whereby the convolution in Equation (C.6) reduces to the value of the third-order susceptibility computed at time t. The third-order polarisation field is then simplified thus:

$$P^{(3)}_{\mathrm{CRS}}(t,\tau_{23}) = \left(\frac{i}{\hbar}\right)^3 E_3(t+\tau_{23})\chi^{(3)}(t) \tag{C.7}$$

Finally, the intensity spectrum of the CRS signal is computed by Fourier transforming the time-dependent polarisation, and taking its squared modulus:

$$I_{\mathrm{CRS}}(\omega) = \left|\mathscr{F}\left\{P^{(3)}_{\mathrm{CRS}}(t)\right\}\right|^2 \tag{C.8}$$

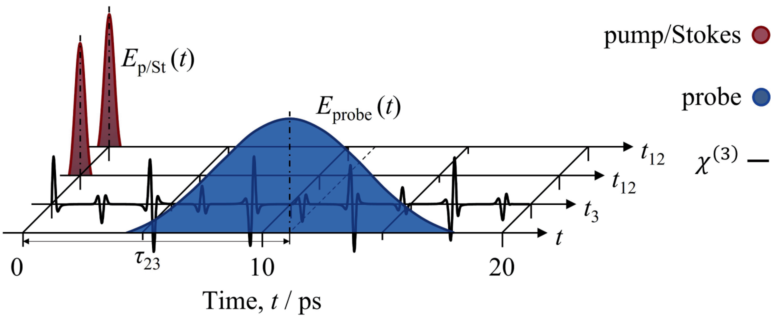

Figure C.2: Schematic of two-beam fs/ps CRS in the time domain: $E_{\mathrm{p/St}}(t)$ represents the temporal envelop of the single combined pump/Stokes pulse; τ_{23} is the probe pulse delays.

The theory outlined above allows for a straightforward description description of the CRS process in the time domain, provided that the third-order susceptibility of the optical medium is known. $\chi^{(3)}$ can be properly computed solving the TDDM equations, with the interaction-free rotational-vibrational Hamiltonian to describe the quantised internal energy structure of the Raman active molecules, and the interaction Hamiltonian derived under the dipole approximation. This was done e.g. by Patnaik *et al.* in Ref. [262], and Gu *et al.* in Ref. [143]. Alternatively, a simplified phenomenological description of $\chi^{(3)}$ can be adopted, whereby the time-dependent optical response of the medium is modelled as the interferogram of damped harmonic contributions, due to the individual rotational-vibrational Raman transitions (see Figure C.3):

$$\begin{aligned}\chi^{(3)}(t) = \sum_{k}\sum_{[v]}\sum_{J,M,\Gamma} X_k I^{(k)}_{\{[v]_f,J_f,M_f,\Gamma_f\}\leftarrow\{[v]_i,J_i,M_i,\Gamma_i\}} \\ \exp\left[\left(i\omega^{(k)}_{\{[v]_f,J_f,M_f,\Gamma_f\}\leftarrow\{[v]_i,J_i,M_i,\Gamma_i\}} - \Gamma^{(k)}_{\{[v]_f,J_f,M_f,\Gamma_f\}\leftarrow\{[v]_i,J_i,M_i,\Gamma_i\}}\right)t\right]\end{aligned} \tag{C.9}$$

Where the labels "$|[v]_i,J_i,M_i,\Gamma_i\rangle$" and "$|[v]_f,J_f,M_f,\Gamma_f\rangle$" indicate the initial and final molecular states. The index k here represents the different Raman-active species present in the probe volume, each with mole fraction X_k; $\omega^{(k)}_{\{\cdots\}_f\leftarrow\{\cdots\}_i}$ is of course the angular frequency of the Raman transition, and $\Gamma^{(k)}_{\{\cdots\}_f\leftarrow\{\cdots\}_i}$ is the damping coefficient representing the dephasing rate of the rotational-vibrational Raman coherence (not to be confused with the symmetry labels in the subscripts). Each complex exponential term in Equation (C.9) represents an individual line in the CRS spectrum $I_{\mathrm{CRS}}(\omega)$, and the corresponding line intensity depends quadratically on the mole fraction of the molecular scatterers, as well as on the line strength $I^{(k)}_{\{\cdots\}_f\leftarrow\{\cdots\}_i}$.

The strength of a CRS spectral line can be computed as the product of the *Raman cross-section* $\frac{\delta\sigma}{\delta\Omega}$ and the difference between the molecular populations in rotational-vibrational states involved in the Raman transition $\Delta\rho$:

$$I^{(k)}_{\{[v]_f,J_f,M_f,\Gamma_f\}\leftarrow\{[v]_i,J_i,M_i,\Gamma_i\}} \propto \Delta\rho(T)\left(\frac{\delta\sigma}{\delta\Omega}\right)_{\{[v]_f,J_f,M_f,\Gamma_f\}\leftarrow\{[v]_i,J_i,M_i,\Gamma_i\}} \tag{C.10}$$

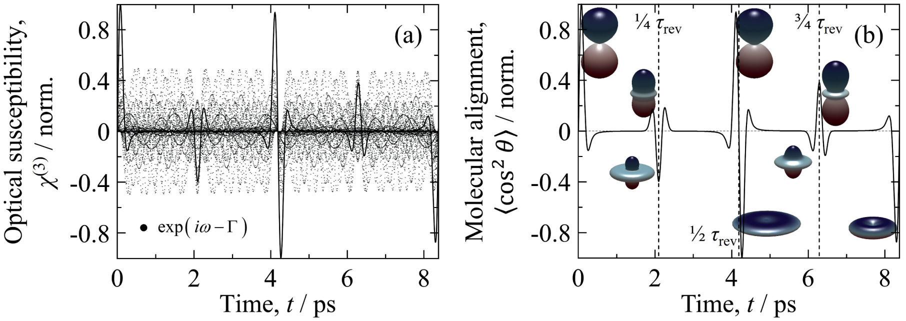

Figure C.3: Temporal evolution of the Raman coherence. (a) The third-order optical susceptibility of the gas-phase medium is modelled as the interferogram of the molecular Raman modes with frequencies $\omega^{(k)}_{\{[v]_f,J_f,M_f,\Gamma_f\}\leftarrow\{[v]_i,J_i,M_i,\Gamma_i\}}$. The interference of the different modes gives rise to a periodic modulation of the non-linear refractive index of the medium showing quantum revivals. Shown here is the pure-rotational coherence of a room-temperature ensemble of N_2 molecules. (b) The quantum revival exhibited by the pure-rotational Raman coherence can be interpreted as due to a periodic field-free alignment of the molecular rotors (see Appendix A.2), following the impulsive alignment induced by the pump/Stokes pulse to its own polarisation plane. In the case of N_2, the revival period is τ_{rev}=8.38 ps: at half this period, the molecules show a nearly-classical behaviour with perfect anti-alignment, as measured by the expectation value of the molecular alignment $\langle \cos^2(\theta) \rangle = -1$. The Raman coherence also shows fractional revivals (e.g at $1/4\tau_{\mathrm{rev}}$), where the molecules have a partial alignment (or anti-alignment) to the polarisation plane of the excitation field. Alignment probability densities reproduced from Weber *et al.* [263], using the tool in Ref. [264].

Assuming the optical medium to be a gas in thermal equilibrium at temperature T, the molecular populations in the initial and final rotational-vibrational energy states can be computed according to the Boltzmann distribution in Equation (B.1).

The cross-section of a Raman transition quantifies the transition probability, accounting for (i) the polarisability of the molecules, (ii) the coupling of angular momenta in the interaction between the molecules and the applied fields [265], and (iii) the coupling of the rotational and vibrational motions. Assuming the incident pulses to be linearly polarised, the Raman cross-section can be expressed in terms of the isotropic (a^2) and anisotropic (γ^2) transition polarisability invariants [39] as:

$$\left(\frac{\delta\sigma}{\delta\Omega}\right)_{\{[v]_f,J_f,M_f,\Gamma_f\}\leftarrow\{[v]_i,J_i,M_i,\Gamma_i\}} \propto a^2 F_a(J) + \frac{4}{45}\gamma^2 b_{\{[v]_f,J_f,M_f,\Gamma_f\}\leftarrow\{[v]_i,J_i,M_i,\Gamma_i\}} F_\gamma(J) \tag{C.11}$$

With polarisability invariants defined as:

$$\begin{aligned} a &= \frac{1}{3}\left[|\alpha_{xx}+\alpha_{yy}+\alpha_{zz}|^2\right] \\ \gamma &= \frac{1}{2}\left[|\alpha_{xx}-\alpha_{yy}|^2+|\alpha_{yy}-\alpha_{zz}|^2+|\alpha_{zz}-\alpha_{xx}|^2\right] \\ &\quad+\frac{3}{4}\left[|\alpha_{xy}+\alpha_{yx}|^2+|\alpha_{zx}+\alpha_{xz}|^2+|\alpha_{yz}+\alpha_{zy}|^2\right] \end{aligned} \tag{C.12}$$

For simple diatomic molecules the transition polarisability invariants can be easily computed according to closed-form expressions given e.g. in Buldakov *et al.* for N_2 and O_2

[173]. In the case of more complex polyatomic molecules, more sophisticated mathematical tools (e.g. algebraic description of the vibrational excitation) are employed to compute the transition moments of the molecular polarisability. For example, Lemus and coworkers used an algebraic approach to compute the transition polarisability of CO_2 [180, 266] (see Section 6.3.1), while Boudon and co-workers employed a tensorial formalism to derive the polarisability of spherical top molecules, such as CH_4 [267] (see Section 6.4.1).

The coupling of the angular momenta in the Raman transition between two rotational-vibrational states is quantified by the Placzek-Teller coefficients $b_{\{\dots\}_f \leftarrow \{\dots\}_i}$ [268], for which closed formulas can be obtained, following Altmann and Strey [269], employing a spherical representation of the polarisability tensor $\boldsymbol{\alpha}$ and Wigner 3-j symbols. The exact formulas depend on the nature of the molecular rotor considered (e.g. spherical top) and can be rather cumbersome, hence only the Placzek-Teller coefficients for linear rotors are explicitly given in Section 6.2.1.

The effect of the rotational-vibrational coupling on the line strength in the Raman spectrum of diatomic molecules is quantified in Equation (C.11) by the Herman-Wallis factors, F_a and F_γ [270]. These can play a significant role in pure-rotational CRS, especially at high temperatures [271] and for lightweight molecules such as H_2 [272] (see Section 6.1.1), and many formulas have been proposed to compute F_γ [162, 173, 273, 274].

The damping coefficient $\Gamma_{\{\dots\}_f \leftarrow \{\dots\}_i}$ in Equation (C.9) represent the dephasing rate of the coherent rotational-vibrational motion at Raman frequency $\omega_{\{\dots\}_f \leftarrow \{\dots\}_i}$. A number of physical mechanisms contribute to the dephasing of the Raman coherence in the gas-phase medium, and are briefly summarised here:

- *Spontaneous emission*, a molecule in the coherent rotational-vibrational state considered can couple to a lower energy state via spontaneous emission of one (or more) photons. For molecules with no permanent dipole moment (as is the case for homonuclear diatomics) in the ground electronic state, a single-photon transition between to rotational-vibrational energy states is forbidden: in this case the coherence dephasing via spontaneous emission happens on a timescale of seconds [262]. This mechanism is thus neglected in the present thesis.
- *Frequency spread*, if the rotational-vibrational energy levels are degenerate, and this degeneracy is lifted for any reason, the resulting spread of the frequencies involved in the transition leads to their interference and to the dephasing of the corresponding coherence. This dephasing mechanism is further discussed in the application of fs/ps CRS to the ro-vibrational spectrum of CH_4 in Section 6.4.2;
- *Doppler effect*, due to the velocity distribution of the Raman-active molecules in the gas, which introduces a Gaussian broadening of the Raman transition. The resulting frequency spread limits the lifetime of the Raman coherence. The magnitude of the Doppler effect is dictated by the thermal velocity of the molecules according to their Maxwell-Boltzmann distribution: at atmospheric pressure and above this is limited by molecular collisions and Doppler broadening is typically negligible.
- *Molecular collisions*, the interaction between the coherent molecules (the *radiators*) and the bath of colliders in the surrounding environment is the main dephasing mechanism of the Raman coherence in the gas-phase at atmospheric conditions. Molecular collisions can be broadly subdivided in two kinds:
  - *Inelastic collisions*, responsible for the loss of rotational-vibrational Raman co-

herence as population is transferred between the rotational and/or vibrational energy states. Considering the N_2 molecule at room temperature, the *rotational energy transfer* (RET) rate ($\Gamma_{\mathrm{RET}} \sim 2.7 \times 10^{10} s^{-1}$) is orders of magnitude larger than the *vibrational energy transfer* (VET) rate ($\Gamma_{\mathrm{VET}} \sim 10^{6} s^{-1}$) [262], so that it typically represents the major contribution to the collisional dephasing of the gas-phase CRS signal;

- *Elastic collisions* or pure dephasing (quantum decoherence), in classical terms this can be interpreted as a molecular re-orientation upon collision. Owschimikow and co-author have experimentally demonstrated that, under standard pressure and temperature conditions, the contribution of elastic collisions to the dephasing of the rotational Raman coherence of N_2 is negligible [275].

The collisional dephasing of the rotational-vibrational Raman coherence can significantly impact gas-phase CRS measurements, especially in high pressure environments, such as internal combustion engines [98] or aeronautical combustors [231]. Hence, the RET process between a number the Raman-active species and other combustion-relevant species had been the object of significant research efforts, both numerical and experimental [74, 175, 274, 276, 277]. Many approaches are found in the literature concerning the modelling of the RET in molecular collisions, but the most beaten track is to employ so-called *dynamical scaling laws* to fit experimental linewidth data sets provided by inverse or stimulated Raman scattering [249]. The most commonly employed scaling laws are the *energy-corrected sudden exponential law* (ECS) [206], and the *modified exponential-gap* (MEG) [174]. The MEG scaling law is employed in the present thesis to extract the collisional dephasing rate of self-perturbed CH_4 from the complex time-domain dependence of the CH_4 CRS signal: this work is discussed more in details in Section 6.4.1.

The introduction of time-resolved CRS techniques, on the other hand, allowed for the direct measurement of the collisional dephasing of the rotational-vibrational Raman coherence. Magnitskiĭ and Tunkin were the first to employ a ps laser to measure the dephasing time of the Q(1) line of H_2 in the Dicke narrowing regime [278]. Following studies have provided direct measurements of the collisional line broadening coefficients for a number of combustion-relevant species [171, 230, 279–283]. As discussed in Section 2.3.1, the influence of molecular collisions can be minimised in the hybrid fs/ps CRS scheme by operating below the typical collisional timescale, at least for moderate pressure applications (up to ~20 bar [33]), by employing a short ps probe pulse (<10 ps), while collisional broadening needs to be taken into account at larger pressures [284]. In the present thesis, the temporal resolution provided by hybrid fs/ps CRS has been exploited to measure the collisional dephasing of the Raman coherence of the CH_4 molecule in mixtures with other combustion-relevant species (see Paper IV).

Appendix D

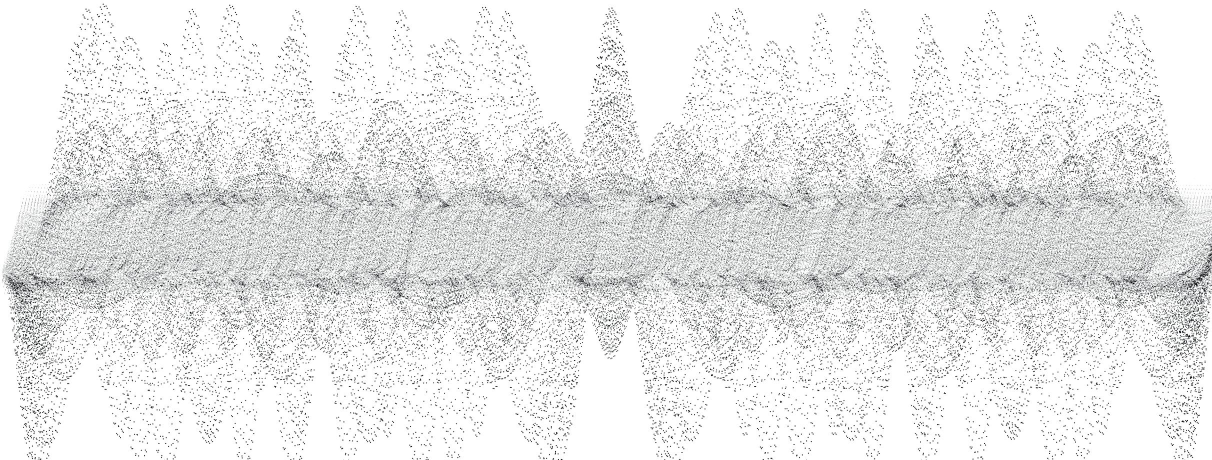

POLARISATION THEORY OF CRS

The present appendix introduces the theoretical description of the polarisation of the CRS field as a function of the, assumed linear, polarisation of the pump, Stokes and probe fields. Assuming the pump and Stokes fields to be combined in a single fs excitation pulse, the relative angle of the probe polarisation resulting in cross-polarised resonant and NR CRS signals is derived in terms of the depolarisation ratio of the Raman spectrum. This solution represents the cornerstone for the development of the polarisation-based in situ referencing protocol introduced in Chapter 5.

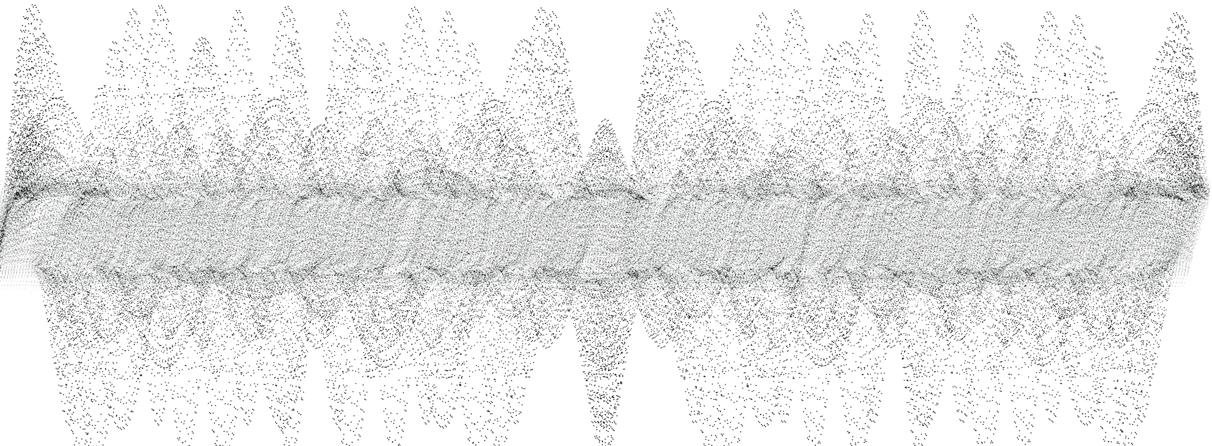

The implementation of the *in situ* referencing protocol in Papers II and III is based on the control of the polarisation state of the resonant and NR CRS signals as a function of the linear polarisation of the input laser fields. In the theoretical description of the CRS process given in Chapter 2 the tensor nature of Equations (2.23) and (2.24) is neglected as well as the effect of the polarisation of the pump, Stokes and probe fields, by assuming all the fields to have the same linear polarisation. The resulting CRS field is thus described by Equation (2.28), where the third-order optical susceptibility is reduced to the scalar quantity $\chi^{(3)}(\Omega)$ computed according to Equation (2.29). In order to introduce the polarisation dependence of the CRS signal on the input laser fields, the tensorial nature of $\boldsymbol{\chi}^{(3)}$ is

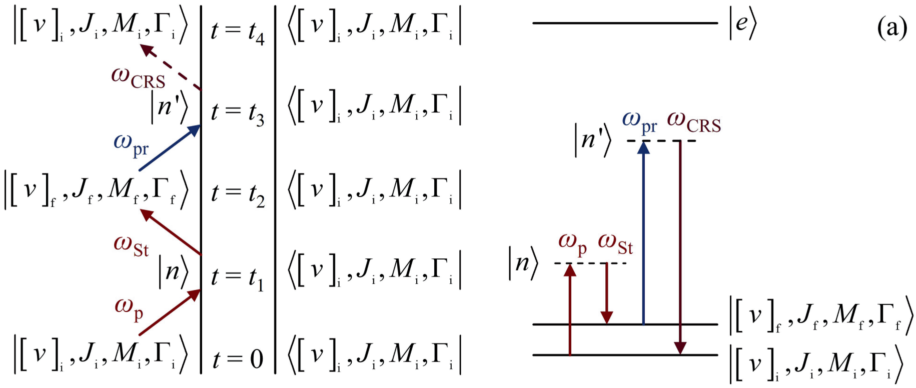

Resonant CRS

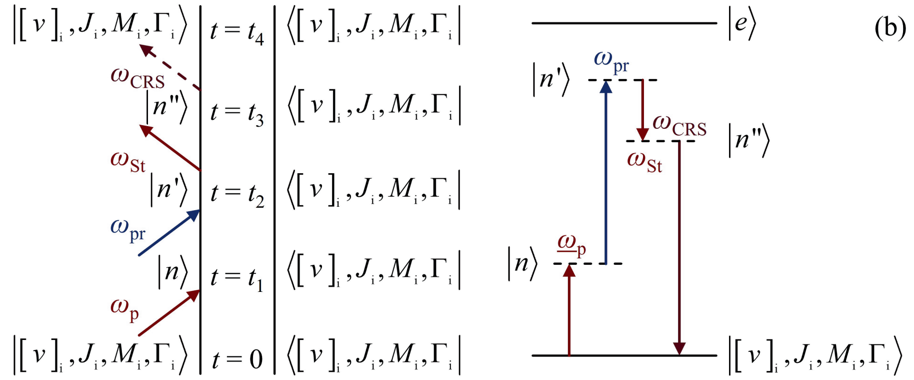

Non-resonant CRS

Figure D.1: The resonant and non-resonant CRS processes. (a) Double-sided Feynman and energy diagrams for one resonant CRS pathway. As a result of the interaction with the pump (ω_{p}) and Stokes (ω_{St}) fields, the medium –represented by the density operator $\hat{\rho} = |[v],J,M,\Gamma\rangle\langle[v],J,M,\Gamma|$– evolves into a coherent rotational-vibrational state. (b) Double-sided Feynman and energy diagrams for one NR CRS pathway. All the intermediate states following the interaction of the medium with the input laser fields are virtual electronic states: no nuclear resonance is involved in this process.

considered in the following:

$$\boldsymbol{\chi}^{(3)} = \boldsymbol{\chi}^{(3)}_{\mathrm{res}} + \boldsymbol{\chi}^{(3)}_{\mathrm{NR}} = \left[\chi^{(3)}\right]_{i,j,k,l} \tag{D.1}$$

Where the indexes i, j, k and l identify, respectively, the polarisation directions of the CRS, pump, Stokes, and probe fields. $\chi^{(3)}_{i,j,k,l}$ is thus the $ijkl^{\mathrm{th}}$ element of the fourth-rank non-linear susceptibility tensor.

$\boldsymbol{\chi}^{(3)}_{\mathrm{res}}$ in Equation (D.1) introduces the contributions to the third-order susceptibility due to all the possible interactions of the input laser fields with the optical medium resulting in rotational-vibrational Raman coherence. $\boldsymbol{\chi}^{(3)}_{\mathrm{NR}}$ on the contrary represents contributions that are entirely electronic in nature, without a coupling to the nuclear motion of the molecules. According to the semi-classical description of third-order non-linear optical phenomena (see e.g. Ref. [31]), unless there is a strict temporal ordering of the input laser pulses, a total of 48 possible combinations of the input laser fields (also called "*pathways*") contribute to the non-linear polarisation field $\boldsymbol{P}^{(3)}$. These contributions can be represented by double-sided Feynman diagrams, which depict the interaction of the input laser fields with the density of operator of the optical medium (see Appendix A), as shown in Figure D.1.

The resonant pathway in Figure D.1(a) can then be interpreted as follows:

1. At time t=0 a molecule in the gas-phase medium is assumed to be in the initial state $|[v]_i, J_i, M_i, \Gamma_i\rangle$, such that it is described by the density operator $\hat{\rho}(0)$=$|[v]_i, J_i, M_i, \Gamma_i\rangle \langle [v]_i, J_i, M_i, \Gamma_i|$;
2. At time t=t_1 the molecule interact with the pump field oscillating at angular frequency ω_1: under the Born-Oppenheimer approximation, the field only interacts with the electrons and the molecule is assumed to instantaneously change its state to $\hat{\rho}(t_1)$=$\hat{H}_{\mathrm{pump}}|[v]_i, J_i, M_i, \Gamma_i\rangle\langle [v]_i, J_i, M_i, \Gamma_i|$=$|e\rangle\langle [v]_i, J_i, M_i, \Gamma_i|$;
3. At time t=t_2 the interaction with the Stokes field (ω_2) brings the molecule into the coherent nuclear state $\hat{\rho}(t_2)$=$|[v]_f, J_f, M_f, \Gamma_f\rangle\langle [v]_i, J_i, M_i, \Gamma_i|$;
4. At time t=t_3 the (off-resonant) probe field (ω_3) interacts with the molecule as $\hat{\rho}(t_3) = \hat{H}_{\mathrm{probe}}|[v]_f, J_f, M_f, \Gamma_f\rangle\langle [v]_i, J_i, M_i, \Gamma_i|$=$|e'\rangle\langle [v]_i, J_i, M_i, \Gamma_i|$;
5. With the emission of the CRS field (ω_4) at time t=t_4 the molecule returns to the initial state $|[v]_i, J_i, M_i, \Gamma_i\rangle$, and the total energy of the system is conserved in this *parametric* process.

Figure D.1(b) represents a parametric non-resonant pathway, as no nuclear coherence is established in this process; it also illustrates why the pump, Stokes and probe fields must temporally overlap to generate a NR CRS signal.

The polarisation theory of the CRS process employed in Papers II and III is based on the model of the non-linear optical response of isotropic media developed by Owyoung [285]. The third-order optical susceptibility of the gas-phase medium is written as a linear combination of the electronic (σ) and nuclear response functions, the latter being divided in a isotropic (a) and an anisotropic (b) contribution (see appendix C) as:

$$\begin{aligned}
\chi^{(3)}_{i,j,k,l}(-\omega_4;\omega_1,-\omega_2,\omega_3) = \frac{1}{24}\Big\{ &\left[\sigma + 2a(-\omega_2+\omega_3) + b(\omega_1+\omega_3) + b(\omega_1-\omega_2)\right]\delta_{ij}\delta kl \\
&+ \left[\sigma + 2a(\omega_1-\omega_2) + b(\omega_1+\omega_3) + b(-\omega_2+\omega_3)\right]\delta_{il}\delta jk \\
&+ \left[\sigma + 2a(\omega_1+\omega_3) + b(-\omega_2+\omega_3) + b(\omega_1-\omega_2)\right]\delta_{ik}\delta jl \Big\}
\end{aligned} \tag{D.2}$$

With δ being the Kronecker delta, and the input laser fields being modelled as monochromatic waves. Note that Equation (D.2) assumes that the non-resonant response of the medium is independent of the laser frequencies when these are off-resonant with the optical medium, a condition known as *Kleinman symmetry* [286]. The depolarisation ratio defined in Equation (2.22) can be recast in terms of the isotropic and anisotropic response functions as:

$$\rho = \frac{b}{2(a+b)} \tag{D.3}$$

Using the depolarisation ratio is possible to write the anisotropic response function as proportional to the isotropic one:

$$b = \frac{2\rho}{1-2\rho} a = \xi a \tag{D.4}$$

The $ijkl^{\text{th}}$ element of the susceptibility tensor is thus written as

$$\begin{aligned}
\chi^{(3)}_{i,j,k,l}(-\omega_4;\omega_1,-\omega_2,\omega_3) = {} & \frac{1}{24}\Big\{\sigma + a\big[2(-\omega_2+\omega_3)+\xi(\omega_1+\omega_3)+\xi(\omega_1-\omega_2)\big]\Big\}\delta_{ij}\delta kl \\
& + \frac{1}{24}\Big\{\sigma + a\big[2(\omega_1+\omega_3)+\xi(-\omega_2+\omega_3)+\xi(\omega_1-\omega_2)\big]\Big\}\delta_{il}\delta jk \\
& + \frac{1}{24}\Big\{\sigma + a\big[2(\omega_1+\omega_3)+\xi(-\omega_2+\omega_3)+\xi(\omega_1-\omega_2)\big]\delta_{ik}\delta jl\Big\}
\end{aligned} \tag{D.5}$$

Equation (D.5) can be simplified by invoking the RWA, whereby terms of the form $|\omega_i{+}\omega_j|$ that oscillate at optical frequencies are neglected. The only non-vanishing components of the third-order optical susceptibility tensor are:

$$\begin{aligned}
\chi^{(3)}_{1111} &= \frac{1}{24}\Big\{3\sigma + 2(1+\xi)\big[(-\omega_2+\omega_3)+(\omega_1-\omega_2)\big]\Big\} \\
\chi^{(3)}_{1122} &= \frac{1}{24}\Big\{\sigma + a\big[2(-\omega_2+\omega_3)+\xi(\omega_1-\omega_2)\big]\Big\} \\
\chi^{(3)}_{1221} &= \frac{1}{24}\Big\{\sigma + a\big[\xi(-\omega_2+\omega_3)+2(\omega_1-\omega_2)\big]\Big\} \\
\chi^{(3)}_{1212} &= \frac{1}{24}\Big\{\sigma + a\xi\big[(-\omega_2+\omega_3)+(\omega_1-\omega_2)\big]\Big\}
\end{aligned} \tag{D.6}$$

The non-linear polarisation field at the CRS frequency can be written as:

$$P^{(3)}_i(\omega_4) = \varepsilon_0 \sum_{ijkl} \chi^{(3)}_{ijkl} \cdot E_l(\omega_3) \cdot E^*_k(\omega_2) \cdot E_j(\omega_1) \tag{D.7}$$

The input fields are all assumed as linearly polarised and the polarisation angles of the CRS, Stokes and probe fields, relative to the polarisation of the pump field, are named α, θ and ϕ respectively, as shown in Figure D.2(a). Introducing the relations in Equation (D.6) into Equation (D.7) and projecting the resulting field onto the polarisation direction of the pump field:

$$
\begin{aligned}
P_{\alpha}^{(3)}(\omega_4) = \Bigg\{ a\bigg[&\bigg(\big(\xi(-\omega_2+\omega_3) + 2(\omega_1-\omega_2) \big) \cos\theta \sin\phi \\
&\quad + \big(2(-\omega_2+\omega_3) + \xi(\omega_1-\omega_2) \big) \sin\theta \cos\phi \bigg) \sin\alpha \\
&+ \bigg(2(1+\xi)\big((-\omega_2+\omega_3) + (\omega_1-\omega_2) \big) \cos\theta \cos\phi \\
&\quad + \big(\xi(-\omega_2+\omega_3) + (\omega_1-\omega_2) \big) \sin\theta \sin\phi \bigg) \cos\alpha \bigg] \\
&+ \sigma \Big[(\cos\theta \sin\phi + \sin\theta \cos\phi) \sin\alpha \\
&\quad + (3\cos\theta\cos\phi + \sin\theta\sin\phi)\cos\alpha \Big] \Bigg\} E(\omega_1)E^{*}(\omega_2)E(\omega_3)
\end{aligned}
\tag{D.8}
$$

As discussed in Section 4.1.1 the probe pulse is generated at double the frequency of the pump/Stokes one ($\omega_3 \approx 2\omega_1 \approx \omega_2$), so that the term proportional to $(-\omega_2+\omega_3)$ oscillates at optical frequency and can be neglected under the RWA:

$$
\begin{aligned}
P_{\alpha}^{(3)}(\omega_4) = \Big\{ a\big[&\big(2\cos\theta\sin\phi + \xi\sin\theta\cos\phi \big) \sin\alpha \\
&+ \big(2(1+\xi)\cos\theta\cos\phi + \xi\sin\theta\sin\phi \big)\cos\alpha \big] \\
+\sigma\big[&\big(\cos\theta\sin\phi + \sin\theta\cos\phi \big)\sin\alpha \\
&+ \big(3\cos\theta\cos\phi + \sin\theta\sin\phi \big)\cos\alpha \big] \Big\} E(\omega_1)E^{*}(\omega_2)E(\omega_3)
\end{aligned}
\tag{D.9}
$$

The resonant and non-resonant components of the CRS field can thus be separated as the ones originating from the nuclear and electronic response functions, respectively:

$$
\begin{aligned}
P_{\mathrm{res}}^{(3)}(\omega_4) &= a\big[\big(2\cos\theta\sin\phi + \xi\sin\theta\cos\phi \big)\sin\alpha \\
&\quad + \big(2(1+\xi)\cos\theta\cos\phi + \xi\sin\theta\sin\phi \big)\cos\alpha \big] E(\omega_1)E^{*}(\omega_2)E(\omega_3) \\
P_{\mathrm{NR}}^{(3)}(\omega_4) &= \sigma\big[\big(\cos\theta\sin\phi + \sin\theta\cos\phi \big)\sin\alpha \\
&\quad + \big(3\cos\theta\cos\phi + \sin\theta\sin\phi \big)\cos\alpha \big] E(\omega_1)E^{*}(\omega_2)E(\omega_3)
\end{aligned}
\tag{D.10}
$$

The polarisation angles of the resonant and NR CRS signals are thus computed as:

$$
\begin{aligned}
\tan\beta &= \frac{(1-2\rho)\cos\theta\sin\phi + \rho\sin\theta\cos\phi}{\cos\theta\cos\phi + \rho\sin\theta\sin\phi} \\
\tan\delta &= \frac{\cos\theta\sin\phi + \sin\theta\cos\phi}{3\cos\theta\cos\phi + \sin\theta\sin\phi}
\end{aligned}
\tag{D.11}
$$

The formulas in Equation (D.11) describe the polarisation of the CRS signals for a general three-beam CRS instrument. In the case of the two-beam fs/ps CRS instrument employed in Papers II and III the pump and Stokes fields are combined in a single broadband fs laser pulse (i.e. θ=0), hence:

$$
\begin{aligned}
\tan\beta &= (1-2\rho)\tan\phi \\
\tan\delta &= \frac{1}{3}\tan\phi
\end{aligned}
\tag{D.12}
$$

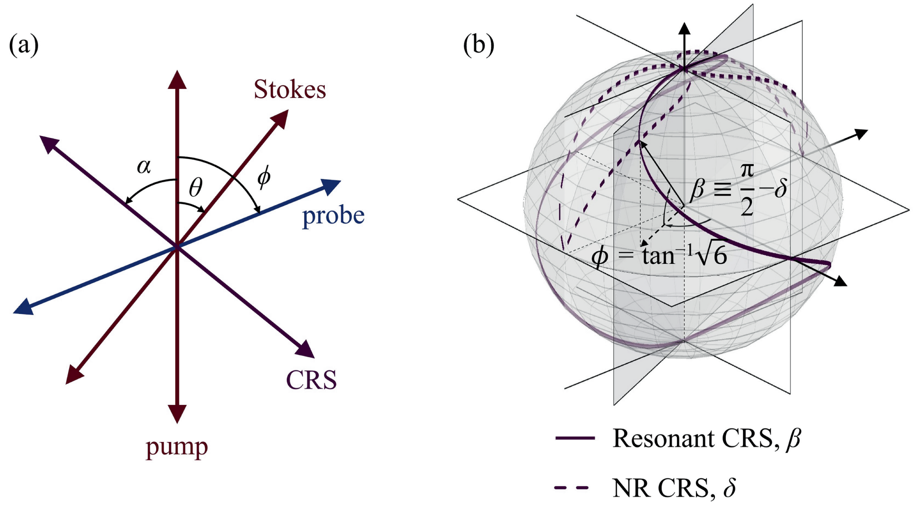

Figure D.2: Polarisation of the resonant and NR CRS signals. (a) Angle convention for the linearly polarised laser fields: all the angles are measured with respect to the polarisation direction of the pump/Stokes beam. ϕ, probe polarisation angle; β, resonant CRS polarisation angle; δ, NR CRS polarisation angle. (b) Polarisation curves for the resonant and NR CRS signals as functions of the probe polarisation angle, represented on the unit sphere (reproduced from Ref. [27]). For clarity the polarisation curve of the resonant signal is turned by $\pi/2$: the polarisation separation of the resonant and NR components of the CRS signals is thus possible at the intersection of the two curves. For a completely depolarised Raman transition this condition is satisfied for $\phi=\tan^{-1}\sqrt{6}$.

In order to implement the polarisation-based *in situ* referencing protocol, the resonant and NR CRS signals must be cross-polarised:

$$|\beta - \delta| = \frac{\pi}{2} \tag{D.13}$$

Substituting this polarisation separation condition into Equation (D.12) and solving for the polarisation angle of the probe field ϕ:

$$\phi = \tan^{-1}\left(\pm \frac{\sqrt{3}}{\sqrt{2\rho - 1}} \right) \tag{D.14}$$

Equation (D.14) has real solutions only if the depolarisation ratio is $\rho \geq 1/2$.

As discussed in Section 2.2.1, completely depolarised Raman transitions have the maximum possible value of the depolarisation ratio (i.e. $\rho = 3/4$), so that the *in situ* referencing protocol is always possible for the corresponding CRS spectra. This is the case for pure-rotational CRS and e.g. for the ro-vibrational ν_2 mode spectrum of CH_4 discussed in Section 6.4. For partially polarised Raman transitions, on the other hand, the *in situ* referencing can only be implemented as long as the depolarisation ratio is greater or equal to the limit value of 0.5, for which the probe angle that generates cross-polarised resonant and NR CRS signals is $\phi=\pm\pi/2$. In Figure D.2(b) the solutions to Equation (D.12) in the case ρ=3/4 are represented as curves on the unit sphere. The probe polarisation angle (relative to the pump/Stokes) is the azimuth and the polarisation angle angle of the NR signal is represented as the elevation of the dashed curve. The elevation angle of the solid curve represents the polarisation angle of the resonant signal, offset by $\pi/2$ for clarity: the polarisation separation condition in Equation (D.13) is thus represented by the crossing of the two curves for ϕ=$\tan^{-1}\sqrt{6}$.

Bibliography

[1] A. C. Eckbreth. *Laser diagnostics for combustion temperature and species.* CRC Press, London, 1996.

[2] P. D. Maker and R. W. Terhune. Study of Optical Effects Due to an Induced Polarization Third Order in the Electric Field Strength. *Physical Review*, 137(3A):801–818, 1965.

[3] K. Kohse-Höinghaus, R. S. Barlow, M. Aldén, and J. Wolfrum. Combustion at the focus: Laser diagnostics and control. *Proceedings of the Combustion Institute*, 30:89–123, 2005.

[4] F. Moya, S. A. J. Druet, and J.-P. E. Taran. Gas spectroscopy and temperature measurement by coherent Raman anti-stokes scattering. *Optics Communications*, 13(2):169–174, 1975.

[5] R. L. Farrow, P. L. Mattern, and L. A. Rahn. Comparison between CARS and corrected thermocouple temperature measurements in a diffusion flame. *Applied Optics*, 21(17):3119–3125, 1982.

[6] R. D. Hancock, K. E. Bertagnolli, and R. P. Lucht. Nitrogen and hydrogen CARS temperature measurements in a hydrogen/air flame using a near-adiabatic flat-flame burner. *Combustion and Flame*, 109:323–331, 1997.

[7] S. Roy, T. R. Meyer, R. P. Lucht, M. Afzelius, P.-E. Bengtsson, and J. R. Gord. Dual-pump dual-broadband coherent anti-Stokes Raman scattering in reacting flows. *Optics Letters*, 29(16):1843–1845, 2004.

[8] M. Aldén, P.-E. Bengtsson, H. Edner, S. Kröll, and D. Nilsson. Rotational CARS: a comparison of different techniques with emphasis on accuracy in temperature determination. *Applied Optics*, 28(15):3206–3219, 1989.

[9] P. R. Régnier and J.-P. E. Taran. On the possibility of measuring gas concentrations by stimulated anti-Stokes scattering. *Applied Physics Letters*, 23(5):240–242, 1973.

[10] P. R. Régnier, F. Moya, and J.-P. E. Taran. Gas concentration measurement by coherent raman anti-stokes scattering. *AIAA Journal*, 12(6):826–831, 1974.

[11] R. L. Farrow, R. P. Lucht, G. L. Clark, and R. E. Palmer. Species concentration measurements using CARS with nonresonant susceptibility normalization. *Applied Optics*, 24(14):2241–2251, 1985.

[12] L. Martinsson, P.-E. Bengtsson, and M. Aldén. Oxygen concentration and temperature measurements in N_2-O_2 mixtures using rotational coherent anti-Stokes Raman spectroscopy. *Applied Physics B*, 62:29–37, 1996.

[13] K. Müller-Dethlefs, M. Pealat, and J.-P. E. Taran. Temperature and Hydrogen Concentration Measurements by CARS in an Ethylene-Air Bunsen Flame. *Berichte der Bunsengesellschaft für physikalische Chemie*, 85(8):803–807, 1981.

[14] F. Grisch, P. Bouchardy, and W. Clauss. CARS thermometry in high pressure rocket combustors. *Aerospace Science and Technology*, 7:317–330, 2003.

[15] S. Roy, T. R. Meyer, R. P. Lucht, V. M. Belovich, E. Corporan, and J. R. Gord. Temperature and CO_2 concentration measurements in the exhaust stream of a liquid-fueled combustor using dual-pump coherent anti-Stokes Raman scattering (CARS) spectroscopy. *Combustion and Flame*, 138:273–284, 2004.

[16] T. R. Meyer, S. Roy, R. P. Lucht, and J. R. Gord. Dual-pump dual-broadband CARS for exhaust-gas temperature and CO_2-O_2-N_2 mole-fraction measurements in model gas-turbine combustors. *Combustion and Flame*, 142:52–61, 2005.

[17] J. Warnatz, U. Maas, and R. W. Dibble. *Combustion: Physical and Chemical Fundamentals, Modeling and Simulation, Experiments, Pollutant Formation.* Springer-Verlag, 4th edition, 2006.

[18] S. M. Correa. A review of NO_x formation under gas-turbine combustion conditions. *Combustion Science and Technology*, 87:329–362, 1993.

[19] J. E. Retter, D. R. Richardson, and S. P. Kearney. Rotational hydrogen thermometry by hybrid fs/ps coherent anti-Stokes Raman scattering in the plume of a burning metalized propellant. *Applied Physics B*, 126(83):1–14, 2020.

[20] A. Farooq, A. B. S. Alquaity, M. Raza, E. F. Nasir, S. Yao, and W. Ren. Laser sensors for energy systems and process industries: Perspectives and directions. *Progress in Energy and Combustion Science*, 91:100997, 2022.

[21] W. D. Kulatilaka, H. U. Stauffer, J. R. Gord, and S. Roy. One-dimensional single-shot thermometry in flames using femtosecond-CARS line imaging. *Optics Letters*, 36(21):4182–4184, 2011.

[22] A. Bohlin and C. J. Kliewer. Communication: Two-dimensional gas-phase coherent anti-Stokes Raman spectroscopy (2D-CARS): Simultaneous planar imaging and multiplex spectroscopy in a single laser shot. *Journal of Chemical Physics*, 138:221101, 2013.

[23] A. Bohlin, B. D. Patterson, and C. J. Kliewer. Communication: Simplified two-beam rotational CARS signal generation demonstrated in 1D. *Journal of Chemical Physics*, 138:081102, 2013.

[24] A. Bohlin and C. J. Kliewer. Two-beam ultrabroadband coherent anti-Stokes Raman spectroscopy for high resolution gas-phase multiplex imaging. *Applied Physics Letters*, 104:031107, 2014.

[25] A. Bohlin and C. J. Kliewer. Direct Coherent Raman Temperature Imaging and Wideband Chemical Detection in a Hydrocarbon Flat Flame. *Journal of Physical Chemistry Letters*, 6:643–649, 2015.

[26] F. Mazza, N. Griffioen, L. Castellanos, D. Kliukin, and A. Bohlin. High-temperature rotational-vibrational O_2-CO_2 coherent Raman spectroscopy with ultrabroadband femtosecond laser excitation generated *in-situ*. *Combustion and Flame*, 237:111738, 2022.

[27] F. Mazza, A. Stutvoet, L. Castellanos, D. Kliukin, and A. Bohlin. Coherent Raman spectroscopy on hydrogen with *in-situ* generation, *in-situ* use, and *in-situ* referencing of the ultrabroadband excitation. *Optics Express*, 30(20):35232–35245, 2022.

[28] F. Mazza, L. Castellanos, D. Kliukin, and A. Bohlin. Coherent Raman imaging thermometry with *in-situ* referencing of the impulsive excitation efficiency. *Proceedings of the Combustion Institute*, 38:1895–1904, 2021.

[29] C. M. Penney, R. L. St. Peters, and M. Lapp. Absolute rotational Raman cross sections for N_2, O_2, and CO_2. *Journal of the Optical Society of America*, 64(5):712–716, 1974.

[30] G. O. Ariunbold. *Ultrafast cooperative phenomena in coherently prepared media - From superfluorescence to coherent Raman scattering and applications.* PhD thesis, Texas A&M University, 2011.

[31] R. W. Boyd. *Nonlinear Optics.* Academic Press, 3rd edition, 2008.

[32] C. C. Gerry and P. L. Knight. *Introductory Quantum Optics.* Cambridge University Press, 1st edition, 2005.

[33] S. Roy, J. R. Gord, and A. K. Patnaik. Recent advances in coherent anti-Stokes Raman scattering spectroscopy: Fundamental developments and applications in reacting flows. *Progress in Energy and Combustion Science*, 36:280–306, 2010.

[34] J. Kiefer and P. Ewart. Laser diagnostics and minor species detection in combustion using resonant four-wave mixing. *Progress in Energy and Combustion Science*, 37:525–564, 2011.

[35] B. Lavorel, H. Tran, E. Hertz, O. Faucher, P. Joubert, M. Motzkus, T. Buckup, T. Lang, H. Skenderovi, G. Knopp, P. Beaud, and H. M. Frey. Femtosecond Raman time-resolved molecular spectroscopy. *Comptes Rendus Physique*, 5:215–229, 2004.

[36] M. Dantus, R. M. Bowman, and A. H. Zewail. Femtosecond laser observations of molecular vibration and rotation. *Nature*, 343:737–739, 1990.

[37] F. Mazza, H. Buurmeijer, L. Castellanos, and A. Bohlin. Coherent N_2^+ emission mediated by coherent Raman scattering for gas-phase thermometry. *Optics Letters*, 47(23):6105–6108, 2022.

[38] M. J. Hollas. *High resolution spectroscopy.* Butterworths, 1st edition, 1982.

[39] D. A. Long. *The Raman effect: A unified treatment of the theory of Raman scattering by molecules.* John Wiley & Sons, Ltd., 1st edition, 2002.

[40] E. O. Potma and S. Mukamel. Theory of coherent Raman scattering. In J.-X. Cheng and X. S. Xie, editors, *Coherent Raman Scattering Microscopy*, pages 3–42. CRC Press, 1st edition, 2013.

[41] T. Okino, Y. Furukawa, Y. Nabekawa, S. Miyabe, A. A. Eilanlou, E. J. Takahashi, K. Yamanouchi, and K. Midorikawa. Direct observation of an attosecond electron wave packet in a nitrogen molecule. *Science Advances*, 1(8):1–8, 2015.

[42] O. Roslyak and S. Mukamel. *Spontaneous, stimulated, coherent and incoherent nonlinear wave mixing and Hyper-Rayleigh scattering; a unified quantum-field description.* Lecture notes, Wydział Chemiczny Politechniki Łódzkiej, 2010.

[43] P. F. Bernath. *Spectra of Atoms and Molecules.* Oxford University Press, Inc., 2nd edition, 2005.

[44] L. D. Landau and E. M. Lifshitz. *Course of theoretical physics Vol.3 Quantum mechanics - Non relativistic theory.* Pergamon Press, Ltd., 2nd edition, 1982.

[45] A. C. Eckbreth. BOXCARS: Crossed-beam phase-matched CARS generation in gases. *Applied Physics Letters*, 32:421, 1978.

[46] C. J. Kliewer. High-spatial-resolution one-dimensional rotational coherent anti-Stokes Raman spectroscopy imaging using counterpropagating beams. *Optics Letters*, 37(2):229–231, 2012.

[47] D. Strickland and G. Mourou. Compression of amplified chirped optical pulses. *Optics Communications*, 56(3):219–221, 1985.

[48] M. O. Scully, G. W. Kattawar, R. P. Lucht, T. Opatrný, H. Pilloff, A. Rebane, A. V. Sokolov, and M. S. Zubairy. FAST CARS: Engineering a laser spectroscopic technique for rapid identification of bacterial spores. *Proceedings of the National Academy of Sciences of the United States of America*, 99(17):10994–11001, 2002.

[49] R. P. Lucht. Femtosecond lasers for molecular measurements. *Science*, 316:207–208, 2007.

[50] M. Marrocco. Closed-form solutions to time model for hybrid fs/ps coherent anti-Stokes Raman scattering. *Journal of Raman Spectroscopy*, 48:1033–1039, 2017.

[51] R. P. Lucht, P. J. Kinnius, S. Roy, and J. R. Gord. Theory of femtosecond coherent anti-Stokes Raman scattering spectroscopy of gas-phase transitions. *Journal of Chemical Physics*, 127:044316, 2007.

[52] F. M. Kamga and M. G. Sceats. Pulse-sequenced coherent anti-Stokes Raman scattering spectroscopy: a method for suppression of the nonresonant background. *Optics Letters*, 5(3):126–128, 1980.

[53] D. K. Lauriola, P. S. Hsu, N. Jiang, M. N. Slipchenko, T. R. Meyer, and S. Roy. Burst-mode 100 kHz N_2 ps-CARS flame thermometry with concurrent nonresonant background referencing. *Optics Letters*, 46(21):5489–5492, 2021.

[54] T. Lang, K. Kompa, and M. Motzkus. Femtosecond CARS on H_2. *Chemical Physics Letters*, 310:65–72, 1999.

[55] T. Lang, M. Motzkus, H. M. Frey, and P. Beaud. High resolution femtosecond coherent anti-Stokes Raman scattering: Determination of rotational constants, molecular anharmonicity, collisional line shifts, and temperature. *Journal of Chemical Physics*, 115:5418, 2001.

[56] N. Dudovich, D. Oron, and Y. Silberberg. Single-pulse coherently controlled nonlinear Raman spectroscopy and microscopy. *Nature*, 418:512–514, 2002.

[57] D. Oron, N. Dudovich, D. Yelin, and Y. Silberberg. Narrow-Band Coherent Anti-Stokes Raman Signals from Broad-Band Pulses. *Physical Review Letters*, 88(6):063004, 2002.

[58] D. Oron, N. Dudovich, and Y. Silberberg. Femtosecond Phase-and-Polarization Control for Background-Free Coherent Anti-Stokes Raman Spectroscopy. *Physical Review Letters*, 90(21):1–4, 2003.

[59] H. Li, D. A. Harris, B. Xu, P. J. Wrzesinski, V. V. Lozovoy, and M. Dantus. Coherent mode-selective Raman excitation towards standoff detection. *Optics Express*, 16(8):5499–5504, 2008.

[60] S. Roy, P. Wrzesinski, D. Pestov, T. Gunaratne, M. Dantus, and J. R. Gord. Single-beam coherent anti-Stokes Raman scattering spectroscopy of using a shaped 7 fs laser pulse. *Applied Physics Letters*, 95:074102, 2009.

[61] S. Roy, P. J. Wrzesinski, D. Pestov, M. Dantus, and J. R. Gord. Single-beam coherent anti-Stokes Raman scattering (CARS) spectroscopy of gas-phase CO_2 via phase and polarization shaping of a broadband continuum. *Journal of Raman Spectroscopy*, 41:1194–1199, 2010.

[62] T. Lang and M. Motzkus. Single-shot femtosecond coherent anti-Stokes. *Journal of the Optical Society of America B*, 19(2):340–344, 2002.

[63] S. Roy, W. D. Kulatilaka, D. R. Richardson, R. P. Lucht, and J. R. Gord. Gas-phase single-shot thermometry at 1 kHz using fs-CARS spectroscopy. *Optics Letters*, 34(24):3857–3859, 2009.

[64] D. R. Richardson, R. P. Lucht, W. D. Kulatilaka, S. Roy, and J. R. Gord. Chirped-probe-pulse femtosecond coherent anti-Stokes Raman scattering concentration measurements. *Journal of the Optical Society of America B*, 30(1):188–196, 2013.

[65] C. N. Dennis, C. D. Slabaugh, I. G. Boxx, W. Meier, and R. P. Lucht. Chirped probe pulse femtosecond coherent anti-Stokes Raman scattering thermometry at 5 kHz in a Gas Turbine Model Combustor. *Proceedings of the Combustion Institute*, 35:3731–3738, 2015.

[66] A. Lowe, L. M. Thomas, A. Satija, R. P. Lucht, and A. R. Masri. Chirped-probe-pulse femtosecond CARS thermometry in turbulent spray flames. *Proceedings of the Combustion Institute*, 37:1383–1391, 2019.

[67] M. Gu, A. Satija, and R. P. Lucht. CO_2 chirped-probe-pulse femtosecond CARS thermometry. *Proceedings of the Combustion Institute*, 38:1599–1606, 2021.

[68] S. Legros, C. Brunet, P. Domingo-Alvarez, P. Malbois, E. Salaun, G. Godard, M. Caceres, B. Barviau, G. Cabot, B. Renou, G. Lartigue, V. Moureau, S. Puggelli, S. Richard, M. Abdelkrim, and F. Grisch. Combustion for aircraft propulsion: Progress in advanced laser-based diagnostics on high-pressure kerosene/air flames produced with low-NO_x fuel injection systems. *Combustion and Flame*, 224:273–294, 2021.

[69] B. D. Prince, A. Chakraborty, B. M. Prince, and H. U. Stauffer. Development of simultaneous frequency- and time-resolved coherent anti-Stokes Raman scattering for ultrafast detection of molecular Raman spectra. *Journal of Chemical Physics*, 125:044502, 2006.

[70] D. Pestov, R. K. Murawski, G. O. Ariunbold, X. Wang, M. Zhi, A. V. Sokolov, V. A. Sautenkov, Y. V. Rostovtsev, A. Dogariu, Y. Huang, and M. O. Scully. Optimizing the laser-pulse configuration for coherent Raman spectroscopy. *Science*, 316:265–268, 2007.

[71] D. Pestov, X. Wang, G. O. Ariunbold, R. K. Murawski, V. A. Sautenkov, A. Dogariu, A. V. Sokolov, and M. O. Scully. Single-shot detection of bacterial endospores via coherent Raman spectroscopy. *Proceedings of the National Academy of Sciences of the United States of America*, 105(2):422–427, 2008.

[72] L. Castellanos, F. Mazza, and A. Bohlin. Water vapor in hydrogen flames measured by time-resolved collisional dephasing of the pure-rotational N_2 CARS signal. *Proceedings of the Combustion Institute*, 39:In press (corrected proof), 2022.

[73] J. D. Miller, C. E. Dedic, S. Roy, J. R. Gord, and T. R. Meyer. Interference-free gas-phase thermometry at elevated pressure using hybrid femtosecond/picosecond rotational coherent anti-Stokes Raman scattering. *Optics Express*, 20(5):5003–5010, 2012.

[74] M. Afzelius, P.-E. Bengtsson, J. Bood, J. Bonamy, F. Chaussard, H. Berger, and T. Dreier. Dual-broadband rotational CARS modelling of nitrogen at pressures up to 9 MPa. II. Rotational Raman line widths. *Applied Physics B*, 75:771–778, 2002.

[75] J. D. Miller, S. Roy, J. R. Gord, and T. R. Meyer. Communication: Time-domain measurement of high-pressure N_2 and O_2 self-broadened linewidths using hybrid femtosecond/picosecond coherent anti-Stokes Raman scattering anti-Stokes Raman scattering. *Journal of Chemical Physics*, 135:201104, 2011.

[76] H. U. Stauffer, J. D. Miller, S. Roy, J. R. Gord, and T. R. Meyer. Communication: Hybrid femtosecond/picosecond rotational coherent anti-Stokes Raman scattering thermometry using a narrowband time-asymmetric probe pulse. *Journal of Chemical Physics*, 136:111101, 2012.

[77] C. E. Dedic, T. R. Meyer, and J. B. Michael. Single-shot ultrafast coherent anti-Stokes Raman scattering of vibrational/rotational nonequilibrium. *Optica*, 4(5):563–570, 2017.

[78] C. E. Dedic and J. B. Michael. Thermalization dynamics in a pulsed microwave plasma-enhanced laminar flame. *Combustion and Flame*, 227:322–334, 2021.

[79] S. A. Steinmetz, T. Y. Chen, B. M. Goldberg, and C. M. Limbach. Resolved rotation–vibration non-equilibrium with rotational VIPA-CARS. *Optics Letters*, 47(20):5429–5432, 2022.

[80] J. D. Miller, M. N. Slipchenko, T. R. Meyer, H. U. Stauffer, and J. R. Gord. Hybrid femtosecond/picosecond coherent anti-Stokes Raman scattering for high-speed gas-phase thermometry. *Optics Letters*, 35(14):2430–2432, 2010.

[81] J. D. Miller, S. Roy, M. N. Slipchenko, J. R. Gord, and T. Meyer. Single-shot gas-phase thermometry using pure-rotational hybrid femtosecond/picosecond coherent anti-Stokes Raman scattering. *Optics express*, 19(16):15627–15640, 2011.

[82] S. P. Kearney, D. J. Scoglietti, and C. J. Kliewer. Hybrid femtosecond/picosecond rotational coherent anti-Stokes Raman scattering temperature and concentration measurements using two different picosecond-duration probes. *Optics Express*, 21(10):12327–12339, 2013.

[83] S. P. Kearney. Hybrid fs/ps rotational CARS temperature and oxygen measurements in the product gases of canonical flat flames. *Combustion and Flame*, 162:1748–1758, 2015.

[84] D. V. Murphy, M. B. Long, R. K. Chang, and A. C. Eckbreth. Spatially resolved coherent anti-Stokes Raman spectroscopy from a line across a CH_4 jet. *Optics Letters*, 4(6):167–169, 1979.

[85] J. B. Snow, J.-B. Zheng, and R. K. Chang. Spatially and spectrally resolved multipoint coherent anti-Stokes Raman scattering from N_2 and O_2 flows. *Optics Letters*, 8(12):599–601, 1983.

[86] J. Jonuscheit, A. Thumann, M. Schenk, T. Seeger, and A. Leipertz. One-dimensional vibrational coherent anti-Stokes Raman-scattering thermometry. *Optics Letters*, 21(19):1532–1534, 1996.

[87] J. Bood, C. Brackmann, P.-E. Bengtsson, and M. Aldén. Multipoint temperature and oxygen-concentration measurements using rotational coherent anti-Stokes Raman spectroscopy. *Optics Letters*, 25(20):1535–1537, 2000.

[88] A. Bohlin, M. Mann, B. D. Patterson, A. Dreizler, and C. J. Kliewer. Development of two-beam femtosecond/picosecond one-dimensional rotational coherent anti-Stokes Raman spectroscopy: Time-resolved probing of flame wall interactions. *Proceedings of the Combustion Institute*, 35:3723–3730, 2015.

[89] S. A. Steinmetz and C. J. Kliewer. Phase matching in two-dimensional coherent Raman imaging. *Optics Express*, 28(23):34586–34596, 2020.

[90] A. Bohlin, C. Jainski, B. D. Patterson, A. Dreizler, and C. J. Kliewer. Multiparameter spatio-thermochemical probing of flame-wall interactions advanced with coherent Raman imaging. *Proceedings of the Combustion Institute*, 36:4557–4564, 2017.

[91] D. Escofet-Martin, A. O. Ojo, N. T. Mecker, M. A. Linne, and B. Peterson. Simultaneous 1D hybrid fs/ps rotational CARS, phosphor thermometry, and CH* imaging to study transient near-wall heat transfer processes. *Proceedings of the Combustion Institute*, 38:1579–1587, 2021.

[92] A. Bohlin and C. J. Kliewer. Diagnostic Imaging in Flames with Instantaneous Planar Coherent Raman Spectroscopy. *Journal of Physical Chemistry Letters*, 5:1243–1248, 2014.

[93] J. D. Miller, M. N. Slipchenko, J. G. Mance, S. Roy, and J. R. Gord. 1-kHz two-dimensional coherent anti-Stokes Raman scattering (2D-CARS) for gas-phase thermometry. *Optics Express*, 24(22):24971–24979, 2016.

[94] C. H. Camp, Y. J. Lee, J. M. Heddleston, C. M. Hartshorn, A. R. H. Walker, J. N. Rich, J. D. Lathia, and M. T. Cicerone. High-speed coherent Raman fingerprint imaging of biological tissues. *Nature Photonics*, 8:627–634, 2014.

[95] F. Träger. *Springer Handbook of Laser and Optics*. Springer, 2nd edition, 2007.

[96] L. Praxmeyer and K. Wodkiewicz. Time and Frequency description of Optical Pulses. *Laser Physics*, 15(10):1477, 2005.

[97] T. Seeger, F. Beyrau, A. Braeuer, and A. Leipertz. High-pressure pure rotational CARS: comparison of temperature measurements with O_2, N_2 and synthetic air. *Journal of Raman Spectroscopy*, 34:932–939, 2003.

[98] C. Brackmann, J. Bood, M. Afzelius, and P.-E. Bengtsson. Thermometry in internal combustion engines via dual-broadband rotational coherent anti-Stokes Raman spectroscopy. *Measurement Science and Technology*, 15:13–15, 2004.

[99] A. Bohlin, F. Vestin, P. Joubert, and P.-E. Bengtsson. Improvement of rotational CARS thermometry in fuel-rich hydrocarbon flames by inclusion of N_2-H_2 Raman line widths. *Journal of Raman Spectroscopy*, 40:788–794, 2009.

[100] C. Brackmann, J. Bood, P.-E. Bengtsson, T. Seeger, M. Schenk, and A. Leipertz. Simultaneous vibrational and pure rotational coherent anti-Stokes Raman spectroscopy for temperature and multispecies concentration measurements demonstrated in sooting flames. *Applied Optics*, 41(3):564–572, 2002.

[101] E. Nordström, A. Bohlin, and P.-E. Bengtsson. Pure rotational Coherent anti-Stokes Raman spectroscopy of water vapor and its relevance for combustion diagnostics. *Journal of Raman Spectroscopy*, 44:1322–1325, 2013.

[102] R. J. Hall, J. A. Shirley, and A. C. Eckbreth. Coherent anti-Stokes Raman spectroscopy: spectra of water vapor in flames. *Optics Letters*, 4(3):87–89, 1979.

[103] R. J. Hall and J. A. Shirley. Coherent Anti-Stokes Raman Spectroscopy of Water Vapor for Combustion Diagnostics. *Applied Optics*, 37(2):196–202, 1983.

[104] D. A. Greenhalgh, R. J. Hall, F. M. Porter, and W. A. England. Application of the Rotational Diffusion Model to the CARS Spectra of High-Temperature, High-pressure Water Vapour. *Journal of Raman Spectroscopy*, 15:71–79, 1984.

[105] F. M. Porter and D. R. Williams. Quantitative CARS Spectroscopy of the ν_1 of Water Vapour. *Applied Physics B*, 54:103–108, 1992.

[106] K. Fox. Theory of pure rotational transitions in the vibronic ground state of methane. *Physical Review Letters*, 27(5):233, 1971.

[107] T. Chen, B. Goldberg, B. Patterson, E. Kolemen, J. Yiguang, and C. J. Kliewer. 1-D imaging of rotation-vibration non-equilibrium from pure rotational ultrafast coherent anti-Stokes Raman scattering. *Optics Letters*, 45(15):4252–4255, 2020.

[108] S. A. Tedder, J. L. Wheeler, A. D. Cutler, and P. M. Danehy. Width-increased dual-pump enhanced coherent anti-Stokes Raman spectroscopy. *Applied Optics*, 49(8):1305–1313, 2010.

[109] A. Bohlin and C. J. Kliewer. Single-shot hyperspectral coherent Raman planar imaging in the range 0-4200 cm^{-1}. *Applied Physics Letters*, 105:161111, 2014.

[110] T. L. Courtney, A. Bohlin, B. D. Patterson, and C. J. Kliewer. Pure-rotational H_2 thermometry by ultrabroadband coherent anti-stokes Raman spectroscopy. *Journal of Chemical Physics*, 146:224202, 2017.

[111] M. Kerstan, I. Makos, S. Nolte, A. Tünnermann, and R. Ackermann. Two-beam femtosecond coherent anti-Stokes Raman scattering for thermometry. *Applied Physics Letters*, 110:021116, 2017.

[112] Y. Ran, M. Junghanns, A. Boden, S. Nolte, A. Tünnermann, and R. Ackermann. Temperature and gas concentration measurements with vibrational ultra-broadband two-beam femtosecond/picosecond coherent anti-Stokes Raman scattering and spontaneous Raman scattering. *Journal of Raman Spectroscopy*, 50:1268–1275, 2019.

[113] Y. Ran, A. Boden, F. Küster, F. An, A. Richter, S. Guhl, S. Nolte, and R. Ackermann. In situ investigation of carbon gasification using ultrabroadband coherent anti-Stokes Raman scattering. *Applied Physics Letters*, 119:243905, 2021.

[114] F. Calegari, C. Vozzi, S. De Silvestri, and S. Stagira. Molecular rotovibrational dynamics excited in optical filamentation. *Optics Letters*, 33(24):2922–2924, 2008.

[115] A. Couairon and A. Mysyrowicz. Femtosecond filamentation in transparent media. *Physics Reports*, 441:47–189, 2007.

[116] S. L. Chin. *Femtosecond Laser Filamentation.* Springer, 1st edition, 2010.

[117] F. Théberge, N. Aközbek, W. Liu, A. Becker, and S. L. Chin. Tunable ultrashort laser pulses generated through filamentation in gases. *Physical Review Letters*, 97:023904, 2006.

[118] A. Couairon, J. Biegert, C. P. Hauri, W. Kornelis, F. W. Helbing, U. Keller, and A. Mysyrowicz. Self-compression of ultra-short laser pulses down to one optical cycle by filamentation. *Journal of Modern Optics*, 53(1-2):75–85, 2006.

[119] A. Mysyrowicz, A. Couairon, and U. Keller. Self-compression of optical laser pulses by filamentation. *New Journal of Physics*, 10:025023, 2008.

[120] S. I. Hwang, S. Be. Park, J. Mun, W. Cho, C. H. Nam, and K. T. Kim. Generation of a single-cycle pulse using a two-stage compressor and its temporal characterization using a tunnelling ionization method. *Scientific Reports*, 9:1613, 2019.

[121] E. T. M. Dlugosz. *Development and applications of filament-assisted impulsive vibrational and rotational Raman spectroscopies.* PhD thesis, Temple University, 2016.

[122] J. H. Odhner, D. A. Romanov, and R. J. Levis. Rovibrational Wave-Packet Dispersion during Femtosecond Laser Filamentation in Air. *Physical Review Letters*, 103:075005, 2009.

[123] D. R. Richardson, S. P. Kearney, and D. R. Guildenbecher. Post-detonation fireball thermometry via femtosecond-picosecond coherent anti-Stokes Raman Scattering (CARS). *Proceedings of the Combustion Institute*, 38:1657–1664, 2021.

[124] J. Barros, M. Scherman, E. Lin, N. Fdida, R. Santagata, B. Attal-Tretout, and A. Bresson. 5 kHz single shot hybrid fs/ps-CARS thermometry in an atmospheric flame. *Optics Express*, 28(23):34656–34664, 2020.

[125] L. Castellanos, F. Mazza, D. Kliukin, and A. Bohlin. Pure-rotational 1D-CARS spatiotemporal thermometry with a single regenerative amplifier system. *Optics Letters*, 45(17):4662–4665, 2020.

[126] T. Y. Chen, C. J. Kliewer, B. M. Goldberg, E. Kolemen, and Y. Ju. Time-domain modelling and thermometry of the CH_4 ν_1 Q-branch using hybrid femtosecond/picosecond coherent anti-Stokes Raman scattering. *Combustion and Flame*, 224:183–195, 2021.

[127] T. L. Courtney, N. T. Mecker, B. D. Patterson, M. Linne, and C. J. Kliewer. Generation of narrowband pulses from chirped broadband pulse frequency mixing. *Optics Letters*, 44(4):835–838, 2019.

[128] H. Zhao, Z. Tian, T. Wu, Y. Li, and H. Wei. Dynamic and sensitive hybrid fs/ps vibrational CARS thermometry using a quasi-common-path second-harmonic bandwidth-compressed probe. *Applied Physics Letters*, 118(071107), 2021.

[129] M. A. Yuratich. Effects of laser linewidth on coherent antiStokes Raman spectroscopy. *Molecular Physics*, 38(2):625–655, 1979.

[130] S. A. Tedder, M. C. Weikl, T. Seeger, and A. Leipertz. Determination of probe volume dimensions in coherent measurement techniques. *Applied Optics*, 47(35):6601–6605, 2008.

[131] Y. Liu, Y. Brelet, G. Point, A. Houard, and A. Mysyrowicz. Self-seeded lasing in ionized air pumped by 800 nm femtosecond laser pulses. *Optics Express*, 21(19):22791–22798, 2013.

[132] W. Chu, G. Li, H. Xie, J. Ni, J. Yao, B. Zeng, H. Zhang, C. Jing, H. Xu, Y. Cheng, and Z. Xu. A self-induced white light seeding laser in a femtosecond laser filament. *Laser Physics Letters*, 11:015301, 2014.

[133] J. W. Hahn and E. S. Lee. Measurement of nonresonant third-order susceptibilities of various gases by the nonlinear interferometric technique. *Journal of the Optical Society of America B*, 12(6):1021–1027, 1995.

[134] R. L. Farrow, R. P. Lucht, and L. A. Rahn. Measurements of the nonresonant third-order susceptibilities of gases using coherent anti-Stokes Raman spectroscopy. *Journal of the Optical Society of America B*, 4(8):1241–1246, 1987.

[135] J. Jiang, Y. Zhong, Y. Zheng, Z. Zeng, X. Ge, and R. Li. Broadening of white-light continuum by filamentation in BK7 glass at its zero-dispersion point. *Physics Letters A*, 379:1929–1933, 2015.

[136] X. Zhao, A. Boden, S. Nolte, and R. Ackermann. Spectral properties of IR-filamentation in air induced by 1 ps pulses for coherent anti-Stokes Raman scattering. *Optics Continuum*, 2(4):720–726, 2023.

[137] A. Houard, V. Jukna, G. Point, Y-B. André, S. Klingebiel, M. Schultze, K. Michel, T. Metzger, and A. Mysyrowicz. Study of filamentation with a high power high repetition rate ps laser at 1.03 μm. *Optics Express*, 24(7):7437–7448, 2016.

[138] B. Broers, H. B. van Linden van den Heuvell, and L. D. Noordam. Large interference effects of small chirp observed in two-photon absorption. *Optics Communications*, 91(1-2):57–61, 1992.

[139] J.-F. Ripoche, G. Grillon, B. Prade, M. Franco, E. Nibbering, R. Lange, and A. Mysyrowicz. Determination of the time dependence of n_2 in air. *Optics Communications*, 135:310–314, 1997.

[140] W. Liu and S. L. Chin. Direct measurement of the critical power of femtosecond Ti:sapphire laser pulse in air. *Optics Express*, 13(15):5750–5755, 2005.

[141] X.-L. Liu, X. Lu, X. Liu, L.-B. Feng, J.-L. Ma, Y.-T. Li, L.-M. Chen, Q.-L. Dong, W.-M. Wang, Z.-H. Wang, Z.-Y. Wei, Z.-M. Sheng, and J. Zhang. Broadband supercontinuum generation in air using tightly focused femtosecond laser pulses. *Optics Letters*, 36(19):3900–3902, 2011.

[142] V. Vaičaitis, M. Kretschmar, R. Butkus, R. Grigonis, U. Morgner, and I. Babushkin. Spectral broadening and conical emission of near-infrared femtosecond laser pulses in air. *Journal of Physics B*, 51:045402, 2018.

[143] M. Gu, A. Satija, and R. P. Lucht. Impact of moderate pump/Stokes chirp on femtosecond coherent anti-Stokes Raman scattering spectra. *Journal of Raman Spectroscopy*, 51:115–124, 2020.

[144] M. Pealat, P. Bouchardy, M. Lefebvre, and J.-P. E. Taran. Precision of multiplex CARS temperature measurements. *Applied Optics*, 24(7):1012–1022, 1985.

[145] E. H. van Veen and D. J. E. M. Roekaerts. Thermometry for turbulent flames by coherent anti-Stokes Raman spectroscopy with simultaneous referencing to the modeless excitation profile. *Applied Optics*, 44(32):6995–7004, 2005.

[146] D. R. Richardson, H. U. Stauffer, S. Roy, and J. R. Gord. Comparison of chirped-probe-pulse and hybrid femtosecond/picosecond coherent anti-Stokes Raman scattering for combustion thermometry. *Applied Optics*, 56(11):37–49, 2017.

[147] J.-L. Oudar, W. R. Smith, and Y. R. Shen. Polarization-sensitive coherent anti-Stokes Raman spectroscopy Polarization-sensitive coherent anti-Stokes Raman spectroscopy. *Applied Physics Letters*, 34:758, 1979.

[148] D. Kliukin, F. Mazza, L. Castellanos, and A. Bohlin. Cascaded coherent anti-Stokes Raman scattering for high-sensitivity number density determination in the gas phase. *Journal of Raman Spectroscopy*, 52:1589–1597, 2021.

[149] J. A. van Oijen and L. P. H. de Goey. Modelling of premixed laminar flames using flamelet-generated manifolds. *Combustion Science and Technology*, 161(1):113–137, 2000.

[150] E. R. Peck and D. J. Fisher. Dispersion of Argon. *Journal of the Optical Society of America*, 54(11):1362–1364, 1964.

[151] P. E. Ciddor. Refractive index of air: new equations for the visible and near infrared. *Applied Optics*, 35(9):1566–1573, 1996.

[152] S. Rostami, J.-C. Diels, and L. Arissian. Polarization evolution of ultrashort pulses in air. *Optics Express*, 23(3):3299–3307, 2015.

[153] D. V. Petrov. Depolarization Ratios of Methane Raman Bands as a Function of Pressure. *Molecules*, 25(8):1951, 2020.

[154] G. Magnotti, U. KC, P. L. Varghese, and R. S. Barlow. Raman spectra of methane, ethylene, ethane, dimethyl ether, formaldehyde and propane for combustion applications. *Journal of Quantitative Spectroscopy and Radiative Transfer*, 163:80–101, 2015.

[155] N. F. Zobov, O. L. Polyansky, C. Ruth Le Sueur, and J. Tennyson. Vibration-rotation levels of water beyond the Born-Oppenheimer approximation. *Chemical Physics Letters*, 260:381–387, 1996.

[156] N. L. Wagner, A. Wüest, I. P. Christov, T. Popmintchev, X. Zhou, M. M. Murnane, and H. C. Kapteyn. Monitoring molecular dynamics using coherent electrons from high harmonic generation. *Proceedings of the National Academy of Sciences of the United States of America*, 103(36):13279–13285, 2006.

[157] Joseph Daniel Miller. *Hybrid femtosecond/picosecond coherent anti-Stokes Raman scattering for gas-phase temperature measurements.* PhD thesis, Iowa State University, 2012.

[158] H. U. Stauffer, J. D. Miller, M. N. Slipchenko, T. R. Meyer, B. D. Prince, S. Roy, and J. R. Gord. Time- and frequency-dependent model of time-resolved coherent anti-Stokes Raman scattering (CARS) with a picosecond-duration probe pulse. *Journal of Chemical Physics*, 140:024316, 2014.

[159] J. Komasa, K. Piszczatowski, Grzegorz Łach, M. Przybytek, B. Jeziorski, and K. Pachucki. Quantum Electrodynamics Effects in Rovibrational Spectra of Molecular Hydrogen. *Journal of Chemical Theory and Computation*, 7:3105–3115, 2011.

[160] C. Asawaroengchai and G. M. Rosenblatt. Rotational Raman intensities and the measured change with internuclear distance of the polarizability anisotropy of H_2, D_2, N_2, O_2, and CO. *Journal of Chemical Physics*, 72:2664, 1980.

[161] M. Marrocco. Comparative analysis of Herman-Wallis factors for uses in coherent anti-Stokes Raman spectra of light molecules. *Journal of Raman Spectroscopy*, 41:741–747, 2009.

[162] R. H. Tipping and J. F. Ogilvie. Herman-wallis factors for Raman transitions of $^1\Sigma$-state diatomic molecules. *Journal of Raman Spectroscopy*, 15:38–40, 1984.

[163] G. Herzberg. *Molecular Spectra and Molecular Structure. I. Spectra of Diatomic Molecules.* Van Nostrand Reinhold Company, Inc., 2nd edition, 1950.

[164] G. Rouillé, G. Millot, R. Saint-Loup, and H. Berger. High-resolution stimulated Raman spectroscopy of O_2. *Journal of Molecular Spectroscopy*, 154:372–382, 1992.

[165] R. J. Hall. CARS spectra of combustion gases. *Combustion and Flame*, 35:47–60, 1979.

[166] T. Dreier and G. Schiff. High Temperature O_2-CARS Thermometry. *Applied Physics B*, 55:388–390, 1992.

[167] T. A. Reichardt, P. E. Schrader, and R. L. Farrow. Comparison of gas temperatures measured by coherent anti-Stokes Raman spectroscopy (CARS) of O_2 and N_2. *Applied Optics*, 40(6):741–747, 2001.

[168] T. Dreier, B. Lange, J. Wolfrum, and M. Zahn. Determination of Temperature and Concentration of Molecular Nitrogen , Oxygen and Methane with Coherent Anti-Stokes Raman Scattering. *Applied Physics B*, 45:183–190, 1988.

[169] D. Kilian, S. Engel, B. Borsdorf, Y. Gao, A. F. Kögler, S. Kobler, T. Seeger, S. Will, A. Leipertz, and W. Peukert. Spatially resolved flame zone classification of a flame spray nanoparticle synthesis process by combining different optical techniques. *Journal of Aerosol Science*, 69:82–97, 2014.

[170] J. W. Tröger, C. Meißner, and T. Seeger. High temperature O_2 vibrational CARS thermometry applied to a turbulent oxy-fuel combustion process. *Journal of Raman Spectroscopy*, 47:1149–1156, 2016.

[171] J. I. Hölzer, C. Meißner, and T. Seeger. Oxygen rotational Raman linewidth determination considering nonmonoexponential decoherence behavior. *Journal of Raman Spectroscopy*, 50:1260–1267, 2019.

[172] T. L. Courtney and C. J. Kliewer. Rotational coherence beating in molecular oxygen: Coupling between electronic spin and nuclear angular momenta. *Journal of Chemical Physics*, 149:234201, 2018.

[173] M. A. Buldakov, V. N. Cherepanov, B. V. Korolev, and I. I. Matrosov. Role of intramolecular interactions in Raman spectra of N_2 and O_2 molecules. *Journal of Molecular Spectroscopy*, 217(1):1–8, 2003.

[174] L. A. Rahn and R. E. Palmer. Studies of nitrogen self-broadening at high temperature with inverse Raman spectroscopy. *Journal of the Optical Society of America B*, 3(9):1164–1169, 1986.

[175] G. Millot, R. Saint-Loup, J. Santos, R. Chaux, H. Berger, and J. Bonamy. Collisional effects in the stimulated Raman Q-branch of O_2 and O_2–N_2. *Journal of Chemical Physics*, 96:961, 1992.

[176] V. Masson-Delmotte, P. Zhai, A. Pirani, S. L. Connors, C. Péan, S. Berger, N. Caud, Y. Chen, L. Goldfarb, M. I. Gomis, M. Huang, K. Leitzell, E. Lonnoy, J. B. R. Matthews, T. K. Maycock, T. Waterfield, O. Yelekçi, R. Yu, and B. Zhou. IPCC, 2021: Climate Change 2021: The Physical Science Basis. Contribution of Working Group I to the Sixth Assessment Report of the Intergovernmental Panel on Climate Change. Technical report, Intergovernmental Panel on Climate Change, Cambridge, United Kingdom and New York, NY, USA, 2021.

[177] R. J. Hall and J. H. Stufflebeam. Quantitative CARS spectroscopy of CO_2 and N_2O. *Applied Optics*, 23(23):4319–4327, 1984.

[178] R. P. Lucht, V.-N. Viswanathan, C. D. Carter, K. D. Grinstead Jr., J. R. Gord, P. M. Danehy, G. J. Fiechtner, and R. L. Farrow. Dual-Pump Coherent Anti-Stokes Raman Scattering Temperature and CO_2 Concentration Measurements. *AIAA Journal*, 41(4):679–686, 2003.

[179] G. Herzberg. *Molecular Spectra and Molecular Structure. II. Infrared and Raman Spectra of Polyatomic Molecules.* Van Nostrand Reinhold Company, Inc., 1st edition, 1945.

[180] R. Lemus, M. Sánchez-Castellanos, F. Pérez-Bernal, J. M. Fernández, and M. Carvajal. Simulation of the Raman spectra of CO_2: Bridging the gap between algebraic models and experimental spectra. *Journal of Chemical Physics*, 141:054306, 2014.

[181] R. S. Mulliken and A. Christy. Λ-type doubling and electron configurations in diatomic molecules. *Physical Review*, 38:87–119, 1931.

[182] M. Basire, F. Mouhat, G. Fraux, A. Bordage, J.-L. Hazemann, M. Louvel, S. Bonella, and R. Vuilleumier. Fermi resonance in CO_2: Mode assignment and quantum nuclear effects from first principles molecular dynamics. *Journal of Chemical Physics*, 146:134102, 2017.

[183] V. G. Arakcheev, V. V. Kireev, V. B. Morozov, A. N. Olenin, V. G.Tunkin, A.A. Valeev, and D. V. Yakovlev. Collisionally induced dephasing and rotational energy transfer in the CO_2 Fermi dyad 'red' Q-branch 1285 cm^{-1}. *Journal of Raman Spectroscopy*, 38:1038–1045, 2007.

[184] V. G. Arakcheev, V. V. Kireev, V. B. Morozov, A. N. Olenin, V. G.Tunkin, A.A.Valeev, and D. V. Yakovlev. Collisionally induced dephasing and rotational energy transfer in the CO_2 Fermi dyad 'blue' Q-branch 1388 cm^{-1}. *Journal of Raman Spectroscopy*, 38:1046–1051, 2007.

[185] Y.-J. Jin, Y.-Q. Yu, Y.-X. Wang, K. Lin, X.-G. Zhou, and S.-L. Liu. Accurate Measurement of Raman Depolarization Ratio in Gaseous CO_2. *Chin. J. Chem. Phys.*, 28:17, 2015.

[186] B. Lavorel, G. Millot, R. Saint-Loup, H. Berger, L. Bonamy, J. Bonamy, and D. Robert. Study of collisional effects on band shapes of the $\nu_1/2\nu_2$ Fermi dyad in CO_2 gas with stimulated Raman spectroscopy. I . Rotational and vibrational relaxation in the $2\nu_2$ band. *Journal of Chemical Physics*, 93:2176, 1990.

[187] F. Mazza, O. Thornquist, L. Castellanos, T. Butterworth, C. Richard, V. Boudon, and A. Bohlin. The ro-vibrational ν_2 mode spectrum of methane investigated by ultrabroadband coherent Raman spectroscopy. *Journal of Chemical Physics*, 158:094201, 2023.

[188] V. Boudon, J.-P. Champion, T. Gabard, M. Lo, M. Rotger, and C. Wenger. Spherical Top Theory and Molecular Spectra. In Martin Quack and Frédéric Merkt, editors, *Handbook of High-resolution Spectroscopy.* John Wiley & Sons, Ltd., 2011.

[189] Y. Awa Ba, C. Wenger, R. Surleau, V. Boudon, M. Rotger, L. Daumont, D. A. Bonhommeau, V. G. Tyuterev, and M. L. Dubernet. MeCaSDa and ECaSDa: Methane and ethene calculated spectroscopic databases for the virtual atomic and molecular data centre. *Journal of Quantitative Spectroscopy and Radiative Transfer*, 130:62–68, 2013.

[190] G. Millot, B. Lavorel, R. Chaux, R. Saint-Loup, G. Pierre, H. Berger, J. I. Steinfeld, and B. Foy. High-Resolution Stimulated Raman Spectroscopy of Methane $^{13}CD_4$ in the Pentad Region. *Journal of Molecular Spectroscopy*, 127:156–177, 1988.

[191] D. Bermejo, J. Santos, and P. Cancio. High-Resolution q-cw SRS Spectrum of $^{12}CH_4$ in the Region of the Level Crossing between ν_1 and $\nu_2 + \nu_4$. *Journal of Molecular Spectroscopy*, 156:15–21, 1992.

[192] J. J. Barrett and R. F. Begley. Low-power cw generation of coherent anti-Stokes Raman radiation in CH_4 gas. *Applied Physics Letters*, 27(3):129–131, 1975.

[193] D. N. Kozlov and V. V. Smirnov. Coherent spectroscopy of high-resolution Raman scattering of methane. *Pis'ma v Zhurnal Èksperimental'noi i Teoreticheskoi Fiziki*, 26(1):31–34, 1977.

[194] D. N. Kozlov, A. M. Prokhorov, and V. V. Smirnov. The methane $\nu_1(a_1)$ vibrational state rotational structure obtained from high-resolution CARS-spectra of the Q-branch. *Journal of Molecular Spectroscopy*, 77(1):21–28, 1979.

[195] H. Frunder, D. Illig, H. Finsterhölzl, H. W. Schrotter, B. Lavorel, G. Roussel, J. C. Hilico, J.-P. Champion, G. Pierre, G. Poussigue, and E. Pascaud. Revised analysis of the structure of the ν_1 band of methane. *Chemical Physics Letters*, 100(1):110–114, 1983.

[196] G. Millot, B. Lavorel, and J. I. Steinfeld. Collisional broadening, line shifting, and line mixing in the stimulated Raman $2\nu_2$ Q-branch of CH_4. *Journal of Chemical Physics*, 95:7938, 1991.

[197] M. Ridder, A. A. Suvernev, and T. Dreier. Collision effects in nitrogen and methane coherent anti-Stokes Raman isotropic Q-branch spectra at high densities. *Journal of Chemical Physics*, 105:3376, 1996.

[198] M. L. Strekalov. Rotational energy relaxation in CH_4 and CH_4-He, Ar collisions calculated from coherent and stimulated Raman spectroscopy data. *Molecular Physics*, 100(7):1049–1056, 2002.

[199] E. Jourdanneau, T. Gabard, F. Chaussard, R. Saint-Loup, H. Berger, E. Bertseva, and F. Grisch. CARS methane spectra: Experiments and simulations for temperature diagnostic purposes. *Journal of Molecular Spectroscopy*, 246:167–179, 2007.

[200] F. Grisch, E. Bertseva, M. Habiballah, E. Jourdanneau, F. Chaussard, R. Saint-Loup, T. Gabard, and H. Berger. CARS spectroscopy of CH_4 for implication of temperature measurements in supercritical LOX/CH_4 combustion. *Aerospace Science and Technology*, 11:48–54, 2007.

[201] S. R. Engel, J. D. Miller, C. E. Dedic, T. Seeger, A. Leipertz, and T. R. Meyer. Hybrid femtosecond/picosecond coherent anti- Stokes Raman scattering for high-speed CH_4/N_2 measurements in binary gas mixtures. *Journal of Raman Spectroscopy*, 44:1336–1343, 2013.

[202] E. Jourdanneau, F. Chaussard, R. Saint-Loup, T. Gabard, and H. Berger. The methane Raman spectrum from 1200 to 5500 cm^{-1}: A first step toward temperature diagnostic using methane as a probe molecule in combustion systems. *Journal of Molecular Spectroscopy*, 233:219–230, 2005.

[203] C. Richard, V. Boudon, and M. Rotger. Calculated spectroscopic databases for the VAMDC portal: New molecules and improvements. *Journal of Quantitative Spectroscopy and Radiative Transfer*, 251:107096, 2020.

[204] T. D. Butterworth, B. Amyay, D. van den Bekerom, A. van de Steeg, T. Minea, N. Gatti, Q. Ong, C. Richard, C. van Kruijsdijk, J. T. Smits, A. P. van Bavel, V. Boudon, and G. J. van Rooij. Quantifying methane vibrational and rotational temperature with Raman scattering. *Journal of Quantitative Spectroscopy and Radiative Transfer*, 236:106562, 2019.

[205] J.-P. Champion, M. Loéte, and G. Pierre. *Spherical Top Spectra.* Academic Press, 1992.

[206] A. E. DePristo, S. D. Augustin, R. Ramaswamy, and H. Rabitz. Quantum number and energy scaling for nonreactive collisions. *Journal of Chemical Physics*, 71:850, 1979.

[207] A. E. DePristo and H. Rabitz. The effect of elastic and reorientation collisions on vibration-rotation lineshapes: A semi-empirical approach. *Journal of Quantitative Spectroscopy and Radiative Transfer*, 22:65–79, 1979.

[208] A. H. Nielsen and H. H. Nielsen. The Infrared Absorption Bands of Methane. *Physical Review*, 48:864–867, 1935.

[209] H. A. Jahn. A new Coriolis perturbation in the methane spectrum I. Vibrational-rotational Hamiltonian and wave functions. *Proceedings of the Royal Society of London A*, 168(935):469–495, 1938.

[210] H. A. Jahn. A new Coriolis perturbation in the methane spectrum II. Energy levels. *Proceedings of the Royal Society of London A*, 168(935):495–518, 1938.

[211] W. H. J. Childs and H. A. Jahn. A new Coriolis perturbation in the methane spectrum III. Intensities and optical spectrum. *Proceedings of the Royal Society of London A*, 169(939):451–463, 1939.

[212] H. A. Jahn. Coriolis perturbations in the methane spectrum. IV. Four general types of Coriolis perturbation. *Proceedings of the Royal Society of London A*, 171(947):450–468, 1939.

[213] L. D. Landau and E. M. Lifshitz. *Course of theoretical physics Vol.1 Mechanics.* Pergamon Press, Ltd., 2nd edition, 1982.

[214] A. Chakraborty, D. G. Truhlar, J. M. Bowman, and S. Carter. Calculation of converged rovibrational energies and partition function for methane using vibrational-rotational configuration interaction. *Journal of Chemical Physics*, 121:2071, 2004.

[215] D. L. Gray and A. G. Robiette. Simultaneous analysis of the ν_2 and ν_4 bands of methane. *Molecular Physics*, 32(6):1609–1625, 1976.

[216] M. A. Thomas and H. L. Welsh. The Raman spectrum of methane. *Canadian Journal of Physics*, 38:1291–1303, 1960.

[217] J.-P. Champion and H. Berger. Spectre Raman à haute résolution de la bande ν_2 de $^{12}CH_4$. *Journal de Physique*, 36(2):135–139, 1975.

[218] J.-P. Champion. Analyse de la bande fondamentale ν_2 de $^{12}CH_4$. *Journal de Physique*, 36(2):141–151, 1975.

[219] L. I-K. Lin. A Concordance Correlation Coefficient to Evaluate Reproducibility. *Biometrics*, 45:255–268, 1989.

[220] J. Jiang, X. Jiang, and M. Zhu. A computational study of preferential diffusion and scalar transport in nonpremixed hydrogen-air flames. *International Journal of Hydrogen Energy*, 40:15709–15722, 2015.

[221] B. Ranganath and T. Echekki. Effects of preferential and differential diffusion on the mutual annihilation of two premixed hydrogen-air flames. *Combustion Theory and Modelling*, 9(4):659–672, 2005.

[222] R. S. Barlow, M. J. Dunn, M. S. Sweeney, and S. Hochgreb. Effects of preferential transport in turbulent bluff-body-stabilized lean premixed CH_4/air flames. *Combustion and Flame*, 159:2563–2575, 2012.

[223] W. Meier, S. Prucker, M.-H. Cao, and W. Stricker. Characterization of Turbulent hytVAir Jet Diffusion Flames by Single-Pulse Spontaneous Raman Scattering. *Combustion Science and Technology*, 118:293–312, 1996.

[224] A. Cavaliere and M. De Joannon. Mild combustion. *Progress in Energy and Combustion Science*, 30:329–366, 2004.

[225] M. D. Smooke, P. Lin, J. K. Lam, and M. B. Long. Computational and experimental study of a laminar axisymmetric methane-air diffusion flame. *Proceedings of the Combustion Institute*, 23:575–582, 1991.

[226] C. Zhang, G. Hu, S. Liao, Q. Cheng, C. Xiang, and C. Yuan. Comparative study on the effects of nitrogen and carbon dioxide on methane/air flames. *Energy*, 106:431–442, 2016.

[227] N. Sánchez-Bastardo, R. Schlögl, and H. Ruland. Methane Pyrolysis for CO_2-Free H_2 Production: A Green Process to Overcome Renewable Energies Unsteadiness. *Chemie-Ingenieur-Technik*, 92(10):1596–1609, 2020.

[228] T. D. Butterworth, A. van de Steeg, D. van den Bekerom, T. Minea, T. Righart, Q. Ong, and G. J. van Rooij. Plasma induced vibrational excitation of CH_4 – A window to its mode selective processing. *Plasma Sources Science and Technology*, 29:095007, 2020.

[229] T. L. Courtney, N. T. Mecker, B. D. Patterson, M. Linne, and C. J. Kliewer. Hybrid femtosecond/picosecond pure rotational anti-Stokes Raman spectroscopy of nitrogen at high pressures (1-70 atm) and temperatures (300-1000 K). *Applied Physics Letters*, 114:101107, 2019.

[230] J. E. Retter, M. Koll, D. R. Richardson, and S. P. Kearney. Time-domain self-broadened and air-broadened nitrogen S-branch Raman linewidths at 80-200 K recorded in an underexpanded jet. *Journal of Chemical Physics*, 156:194201, 2022.

[231] M. Scherman, R. Santagata, E. Lin, P. Nicolas, J.-P. Faleni, A. Vincent-Randonnier, P. Cherubini, F. Guichard, A. Mohamed, D. Gaffie, B. Attal-tretout, and A. Bresson. 1-kHz hybrid femtosecond/picosecond coherent anti-Stokes Raman scattering thermometry of turbulent combustion in a representative aeronautical test rig. *Journal of Raman Spectroscopy*, 52:1643–1650, 2021.

[232] J. E. Retter, G. S. Elliott, and S. P. Kearney. Dielectric-barrier-discharge plasma-assisted hydrogen diffusion flame. Part 1: Temperature, oxygen, and fuel measurements by one-dimensional fs/ps rotational CARS imaging. *Combustion and Flame*, 191:527–540, 2018.

[233] A. Dogariu, J. B. Michael, M. O. Scully, and R. B. Miles. High-gain backward lasing in air. *Science*, 331:442–445, 2011.

[234] P. R. Hemmer, R. B. Miles, P. Polynkin, T. Siebert, A. V. Sokolov, P. Sprangle, and M. O. Scully. Standoff spectroscopy via remote generation of a backward-propagating laser beam. *Proceedings of the National Academy of Sciences of the United States of America*, 108(8):3130–3134, 2011.

[235] P. Ding, M. Ruchkina, Y. Liu, M. Aldén, and J. Bood. Femtosecond two-photon-excited backward lasing of atomic hydrogen in a flame. *Optics Letters*, 43(5):1183–1186, 2018.

[236] P. Ding, S. Mitryukovskiy, A. Houard, E. Oliva, A. Couairon, A. Mysyrowicz, and Y. Liu. Backward Lasing of Air plasma pumped by Circularly polarized femtosecond pulses for the saKe of remote sensing (BLACK). *Optics Express*, 22(24):29964–29977, 2014.

[237] P. N. Malevich, R. Maurer, D. Kartashov, S. Ališauskas, A. A. Lanin, A. M. Zheltikov, M. Marangoni, G. Cerullo, A. Baltuška, and A. Pugžlys. Stimulated Raman gas sensing by backward UV lasing from a femtosecond filament. *Optics Express*, 40(11):2469–2472, 2015.

[238] X. Zhang, R. Danylo, Z. Fan, P. Ding, C. Kou, and Q. Liang. Backward lasing of singly ionized nitrogen ions pumped by femtosecond laser pulses. *Applied Physics B*, 126(53):1–7, 2020.

[239] F. Zhang, H. Xie, L. Yuan, Z. Zhang, B. Fu, S. Yu, G. Li, N. Zhang, X. Lu, J. Yao, Y. Cheng, and Z. Xu. Background-free single-beam coherent Raman spectroscopy assisted by air lasing. *Optics Letters*, 47(3):481–484, 2022.

[240] Z. Zhang, F. Zhang, B. Xu, H. Xie, B. Fu, X. Lu, N. Zhang, S. Yu, J. Yao, Y. Cheng, and Z. Xu. High-Sensitivity Gas Detection with Air-Lasing-Assisted Coherent Raman Spectroscopy. *Ultrafast Science*, 2022:1–8, 2022.

[241] R. R. Smith, D. R. Killelea, D. F. DelSesto, and A. L. Utz. Preference for Vibrational over Translational Energy in a Gas-Surface Reaction. *Science*, 304:992–995, 2004.

[242] C. M. Penney, L. M. Goldman, and M. Lapp. Raman Scattering Cross Sections. *Nature Physical Science*, 235:110–112, 1972.

[243] A. Guardone, P. Colonna, M. Pini, and A. Spinelli. Nonideal compressible fluid dynamics of dense vapors and supercritical fluids. *Annual Review of Fluid Mechanics*, to be publ, 2024.

[244] S. A. Akhmanov, S. M. Gladkov, M. G. Karimov, N. I. Koroteev, V. N. Zadkov, and G. Marowsky. CARS Thermometry of Polyatomic Gases: SF6. *IEEE Journal of Quantum Electronics*, 20(4):424–428, 1984.

[245] H. Ke, V. Boudon, C. Richard, V. Madhur, M. Faye, and L. Manceron. Analysis and modeling of combination bands of sulfur hexafluoride $^{32}SF_6$ based on global fits. Update of the SHeCaSDa database. *Journal of Molecular Spectroscopy*, 368:1–14, 2020.

[246] J. C. Denton. On the internal partition functions for the diatomic molecules, N_2, O_2, NO, and their ions – I. Symmetry and spin considerations. *Energy Conversion*, 17(4):147–152, 1977.

[247] P. A. M. Dirac. *The Principles of Quantum Mechanics.* Oxford University Press Inc., 3rd edition, 1982.

[248] C. Maïnos and M. C. Castex. The single path rotational structure of n-photon transitions in diatomic molecules. *Molecular Physics*, 68(3):615–628, 1989.

[249] A. Bohlin. *Development and Application of Pure Rotational CARS for Reactive Flows.* PhD thesis, Lund University, 2012.

[250] P. Zeeman. On the Influence of Magnetism on the Nature of the Light Emitted by a Substance. *Reports of the Ordinary Sessions of the Mathematical and Physical Section (Royal Academy of Sciences in Amsterdam)*, 5:181–184, 1896.

[251] J. Stark. Beobachtungen über den Effekt des elektrischen Feldes auf Spektrallinien. I. Quereffekt. *Annalen der Physik*, 348(7):965–982, 1914.

[252] S. H. Autlert and C. H. Townes. Stark Effect in Rapidly Varying Fields. *Physical Review*, 100(2):703–722, 1955.

[253] S. L. Altmann and P. Herzig. *Point-Group Theory Tables.* Clarendon Press, 2nd edition, 2011.

[254] A. Hosseinnia. *On the Use of Rotational CARS on Polyatomics and in Time Domain.* PhD thesis, Lund University, 2020.

[255] A. Hosseinnia, E. Nordström, J. Bood, and P.-E. Bengtsson. Ethane thermometry using rotational coherent anti-Stokes Raman scattering (CARS). *Proceedings of the Combustion Institute*, 36:4461–4468, 2017.

[256] A. Hosseinnia, C. Brackmann, and P.-E. Bengtsson. Pure rotational coherent anti-Stokes Raman spectroscopy of ethylene, experiments and modelling. *Journal of Quantitative Spectroscopy and Radiative Transfer*, 234:24–31, 2019.

[257] A. M. Walser. *Time-Resolved Four-Wave Mixing Spectroscopy of Gaseous Formaldehyde.* PhD thesis, ETH Zürich, 2008.

[258] A. M. Walser, P. Beaud, P. P. Radi, M. Tulej, T. Gerber, and G. Knopp. Time-resolved investigation of the ν_1 ro-vibrational Raman band of H_2CO with fs-CARS. *Journal of Raman Spectroscopy*, 38:147–153, 2007.

[259] E. Bright Wilson. The statistical weights of the rotational levels of polyatomic molecules, including methane, ammonia, benzene, cyclopropane and ethylene. *Journal of Chemical Physics*, 3:276, 1935.

[260] S. Mukamel. *Principles of nonlinear optical spectroscopy.* Oxford University Press Inc., 1st edition, 1995.

[261] N. Mankoč-Borštnik, L. Fonda, and B. Bortnik. Coherent rotational states and their creation and time evolution in molecular and nuclear systems. *Physical Review A*, 35(10):4132, 1987.

[262] A. K. Patnaik, S. Roy, and J. R. Gord. Saturation of vibrational coherent anti-Stokes Raman scattering mediated by saturation of the rotational Raman transition. *Physical Review A*, 87:043801, 2013.

[263] S. J. Weber, M. Oppermann, and J. P. Marangos. Role of rotational wave packets in strong field experiments. *Physical Review Letters*, 111:263601, 2013.

[264] M. Oppermann, S. J. Weber, and J. P. Marangos. Characterising and optimising impulsive molecular alignment in mixed gas samples. *Physical Chemistry Chemical Physics*, 14(27):9785–9791, 2012.

[265] R. G. Bray and R. M. Hochstrasser. Two-photon absorption by rotating diatomic molecules. *Molecular Physics*, 31(4):1199–1211, 1976.

[266] M. Bermúdez-Montaña, M. Carvajal, F. Pérez-Bernal, and R. Lemus. An algebraic alternative for the accurate simulation of CO_2 Raman spectra. *Journal of Raman Spectroscopy*, 51:569–583, 2020.

[267] V. Boudon, J.-P. Champion, T. Gabard, M. Loëte, F. Michelot, G. Pierre, M. Rotger, Ch Wenger, and M. Rey. Symmetry-adapted tensorial formalism to model rovibrational and rovibronic spectra of molecules pertaining to various point groups. *Journal of Molecular Spectroscopy*, 228:620–634, 2004.

[268] G. Placzek and E. Teller. Die Rotationsstruktur der Raman banden mehratomiger Molekuele. *Zeitschrift für Physik*, 81:209–258, 1933.

[269] K. Altmann and G. Strey. Application of spherical tensors and Wigner 3-j-symbols to the calculation of relative intensities of rotational lines in Raman bands of molecular gases. *Journal of Molecular Spectroscopy*, 44:571–577, 1972.

[270] R. Herman and R. F. Wallis. Line intensities in vibration-rotation bands of diatomic molecules. *Journal of Chemical Physics*, 23:637, 1955.

[271] A. Bohlin, P.-E. Bengtsson, and M. Marrocco. On the sensitivity of rotational CARS N_2 thermometry to the Herman-Wallis factor. *Journal of Raman Spectroscopy*, 43:599–603, 2012.

[272] M. Marrocco. Herman-Wallis factor to improve thermometric accuracy of vibrational coherent anti-Stokes Raman spectra of H_2. *Proceedings of the Combustion Institute*, 32:863–870, 2009.

[273] T. C. James and W. Klemperer. Line Intensities in the Raman Effect of $^1\Sigma$ Diatomic Molecules. *Journal of Chemical Physics*, 31:130, 1959.

[274] L. Martinsson, P.-E. Bengtsson, M. Aldén, S. Kröll, and J. Bonamy. A test of different rotational Raman linewidth models: Accuracy of rotational coherent anti-Stokes Raman scattering thermometry in nitrogen from 295 to 1850 K. *Journal of Chemical Physics*, 99:2466, 1993.

[275] N. Owschimikow, F. Königsmann, J. Maurer, P. Giese, A. Ott, B. Schmidt, and N. Schwentner. Cross sections for rotational decoherence of perturbed nitrogen measured via decay of laser-induced alignment. *Journal of Chemical Physics*, 133:044311, 2010.

[276] J. Bonamy, D. Robert, J. M. Hartmann, M. L. Gonze, R. Saint-Loup, and H. Berger. Line broadening, line shifting, and line coupling effects on N_2-H_2O stimulated Raman spectra. *Journal of Chemical Physics*, 91:5916, 1989.

[277] M. L. Gonze, R. Saint-Loup, J. Santos, B. Lavorel, R. Chaux, G. Millot, H. Berger, L. Bonamy, J. Bonamy, and D. Robert. Collisional line broadening and line shifting in N_2-CO_2 mixture studied by inverse Raman spectroscopy. *Chemical Physics*, 148:417–428, 1990.

[278] S. A. Magnitskiĭ and V. G. Tunkin. Determination of the Dicke Narrowing in Gaseous Hydrogen By Direct Measurement of the Dephasing Time. *Soviet journal of quantum electronics*, 11(9):1218–1220, 1981.

[279] W. D. Kulatilaka, P. S. Hsu, H. U. Stauffer, J. R. Gord, and S. Roy. Direct measurement of rotationally resolved H_2 Q-branch Raman coherence lifetimes using time-resolved picosecond coherent anti-Stokes Raman scattering. *Applied Physics Letters*, 97:081112, 2010.

[280] C. J. Kliewer, A. Bohlin, E. Nordström, B. D. Patterson, P. E. Bengtsson, and T. B. Settersten. Time-domain measurements of S-branch N_2-N_2 Raman linewidths using picosecond pure rotational coherent anti-Stokes Raman spectroscopy. *Applied Physics B*, 108:419–426, 2012.

[281] A. Bohlin, E. Nordström, B. D. Patterson, P.-E. Bengtsson, and C. J. Kliewer. Direct measurement of S-branch N_2-H_2 Raman linewidths using time-resolved pure rotational coherent anti-Stokes Raman spectroscopy. *Journal of Chemical Physics*, 137:074302, 2012.

[282] S. Roy, P. S. Hsu, N. Jiang, J. R. Gord, W. D. Kulatilaka, H. U. Stauffer, and J. R. Gord. Direct measurements of collisionally broadened Raman linewidths of CO_2 S-branch transitions. *Journal of Chemical Physics*, 138:024201, 2013.

[283] C. Meißner, J. I. Hölzer, and T. Seeger. Determination of N_2-N_2 and N_2-O_2 S-branch Raman linewidths using time-resolved picosecond pure rotational coherent anti-Stokes Raman scattering. *Applied Optics*, 58(10):47–54, 2019.

[284] N. T. Mecker. *Hybrid rotational femtosecond/picosecond coherent anti-Stokes Raman Spectroscopy of Nitrogen at high Pressures and Temperatures.* PhD thesis, University of Edinburgh, 2020.

[285] A. Owyoung. *The origin of the nonlinear refractive index of liquids and glasses.* PhD thesis, California Institute of Technology, 1972.

[286] D. A. Kleinman. Nonlinear dielectric polarization in optical media. *Physical Review*, 126(6):1977–1979, 1962.

Curriculum Vitae

Name: Francesco Mazza
Born: 23/06/1991 in Macerata, Italy
Mobile: +31 (0) 6 19680231
Email: f.mazza@tudelft.nl
Web: https://research.tudelft.nl/en/persons/f-mazza

RESEARCH AND WORK EXPERIENCE

06/2019-06/2023	**TU Delft, Delft, the Netherlands – Ph.D. candidate** Development of ultrabroadband fs/ps CRS with fs laser induced-filamentation for combustion diagnostics, Development of time domain spectral models for major (diatomic and polyatomic) combustion species.
09/2018-06/2019	**Leonardo S.p.a., Torino, Italy – Fatigue specialist** Monitoring and airworthiness maintenance of fighter aircrafts.
02/2017-02/2018	**Universität Stuttgart, Stuttgart, Germany – Guest researcher** Investigation of inertial electrostatic confinement of plasmas for space application.

EDUCATION

06/2019-06/2023	**Ph.D. in non-linear optical spectroscopy** TU Delft, Aerospace Engineering, The Netherlands *Thesis:* Ultrabroadband coherent Raman spectroscopy for reacting flows *Promotor:* Prof. dr. ir. P. Colonna di Paliano *Supervisor:* Dr. ir. A. Bohlin
10/2014-02/2018	**M.Sc. degree in Aerospace engineering** Politecnico di Torino, Italy *GPA:* 107/110
10/2010-02/2014	**B.Sc. degree in Aerospace engineering** Università di Bologna, Italy *GPA:* 110/110 *cum laude*

PUBLICATIONS

1. L. Castellanos, F. Mazza, D. Kliukin, and A. Bohlin, *Optics Letters*, 45(17):4662-4665, 2020 [Editor's Pick].
2. F. Mazza, L. Castellanos, D. Kliukin, and A. Bohlin, *Proceedings of the Combustion Institute*, 38:1895, 2021.
3. D. Kliukin, F. Mazza, L. Castellanos, and A. Bohlin, *Journal of Raman Spectroscopy*, 52:1589-1597, 2021 [Special Issue].
4. F. Mazza, N. Griffioen, L. Castellanos, D. Kliukin, and A. Bohlin, *Combustion and Flame*, 237:111738, 2022.
5. F. Mazza, A. Stutvoet, L. Castellanos, D. Kliukin, and A. Bohlin, *Optics Express*, 30(20):35232-35245, 2022.
6. L. Castellanos, F. Mazza, and A. Bohlin, *Proceedings of the Combustion Institute*, 39, *In press, corrected proof*, 2022 [Distinguished paper].
7. F. Mazza, H. Buurmeijer, L. Castellanos, and A. Bohlin, *Optics Letters*, 47(23):6105-6108, 2022.
8. F. Mazza, O. Thornquist, L. Castellanos, T. Butterworth, V. Boudon, C. Richard, and A. Bohlin, *Journal of Chemical Physics*, 158:094201, 2023.

CONFERENCE CONTRIBUTIONS

- F. Mazza, L. Castellanos, D. Kliukin, A. Bohlin, "Coherent Raman imaging thermometry with *in-situ* referencing of the impulsive excitation efficiency", 38th International Symposium on Combustion, Adelaide, Australia, 24-29 January 2021. Talk given by F. Mazza.
- F. Mazza, A. Stutvoet, L. Castellanos, D. Kliukin, A. Bohlin, "Ultrabroadband fs/ps coherent Raman spectroscopy behind optical windows via *in-situ* fs laser-induced filamentation", 19th European Conference on Non-linear Optical Spectroscopy (ECONOS)/39th European CARS workshop, Karlsruhe, Germany, 26-29 September 2021. Talk given by F. Mazza.
- D. L. Castellanos, F. Mazza, D. Kliukin, A. Bohlin, "Water vapor concentration in hydrogen flames measured by the collisional dephasing of the pure-rotational N_2 CARS signal", Combura 2021 Symposium, Soesterberg, The Netherlands, 10-11 November 2021.
- F. Mazza, A. Stutvoet, L. Castellanos, D. Kliukin, A. Bohlin, "Ultrabroadband fs/ps coherent Raman thermometry behind the combustor windows via fs laser-induced filamentation", Combura 2021 Symposium, Soesterberg, The Netherlands, 10-11 November 2021. Talk given by F. Mazza.
- L. Castellanos, F. Mazza, A. Bohlin, "Water vapor in hydrogen flames measured by time-resolved collisional dephasing of the pure-rotational N_2 CARS signal", 39th International Symposium on Combustion, Vancouver, Canada, 24-29 July 2022. Talk given by F. Mazza.

- L. Castellanos, F. Mazza, A. Bohlin, “Ultrabroadband fs/ps coherent Raman spectroscopy behind optical windows via *in-situ* fs laser-induced filamentation”, Talk at the 20th European Conference on Non-linear Optical Spectroscopy (ECONOS)/40th European CARS workshop, Kiruna, Sweden, 25-28 September 2022.
- F. Mazza, O. Thornquist, L. Castellanos, A. Bohlin, “The ro-vibrational ν_2 mode spectrum of methane investigated by ultrabroadband coherent Raman spectroscopy”, Talk at the 20th European Conference on Non-linear Optical Spectroscopy (ECONOS)/40th European CARS workshop, Kiruna, Sweden, 25-28 September 2022. Talk given by F. Mazza.
- L. Castellanos, F. Mazza, A. Bohlin, “Direct measurements of preferential diffusion in turbulent H_2 flames using multi-field CARS imaging”, Combura 2022 Symposium, Soesterberg, The Netherlands, 23-24 November 2022.
- F. Mazza, O. Thornquist, L. Castellanos, A. Bohlin, “Ultrabroadband coherent Raman spectroscopy for methane thermometry and relative concentration measurements”, Combura 2022 Symposium, Soesterberg, The Netherlands, 23-24 November 2022. Talk given by F. Mazza.
- F. Mazza, L. Castellanos, A. Bohlin, “Air lasing seeded by coherent Raman scattering and its application to gas-phase thermometry”, N_2^+ Air Lasing Workshop, Palaiseau, France, 2-5 May 2023. Invited talk given by F. Mazza.

SUPERVISED STUDENTS

Student: Nathan Griffioen
Degree: M.Sc. degree in Aerospace engineering
Title: Development of CO_2-O_2 CARS thermometry and concentration measurements for applied flame diagnostics
Graduation date: 09/04/2021

Student: Aert Stutvoet
Degree: M.Sc. degree in Aerospace engineering
Title: Supercontinuum generation via *in situ* femtosecond laser-induced filamentation for ultrabroadband femtosecond/picosecond coherent Raman spectroscopy
Graduation date: 19/11/2021

Student: Anand Vijayaraghavan
Degree: M.Sc. degree in Aerospace engineering
Title: Enhanced single-shot flame thermometry with femtosecond/picosecond CARS using a phase-characterized picosecond probe
Graduation date: 26-11-2021

Student: Hugo Buurmeijer
Degree: Honours Programme Bachelor in Aerospace engineering
Title: Analysis of the emission spectrum of nitrogen molecular ions generated in femtosecond plasma filamentation
Graduation date: 31-08-2022

Student: Ona Thornquist
Degree: M.Sc. degree in Aerospace engineering
Title: Time-domain investigation of the ro-vibrational CH_4 ν_2 Raman spectrum via fs/ps CRS for combustion diagnostics
Graduation date: 19-12-2022

List of publications

The present thesis is based on the following publications, referred to in Roman numerals in the text. The order in which these papers are presented is meant to convey the path followed in the doctoral research here discussed, even if it does not reflect the publication history. The relevant publications are appended to this document in the listed order. Additional publications authored, which bear a limited relevance to the present research, are also listed in the following.

Relevant publications

🗎 I. **F. Mazza**, N. Griffioen, L. Castellanos, D. Kliukin, and A. Bohlin, High-temperature rotational-vibrational O_2-CO_2 coherent Raman spectroscopy with ultrabroadband femtosecond laser excitation generated *in-situ*, *Combustion and Flame*, 237:111738, 2022.

🗎 II. **F. Mazza**, L. Castellanos, D. Kliukin, and A. Bohlin, Coherent Raman imaging thermometry with *in-situ* referencing of the impulsive excitation efficiency, *Proceedings of the Combustion Institute*, 38:1895, 2021.

🗎 III. **F. Mazza**, A. Stutvoet, L. Castellanos, D. Kliukin, and A. Bohlin, Coherent Raman spectroscopy on hydrogen with *in-situ* generation, *in-situ* use, and *in-situ* referencing of the ultrabroadband excitation, *Optics Express*, 30(20):35232-35245, 2022.

🗎 IV. **F. Mazza**, O. Thornquist, L. Castellanos, T. Butterworth, V. Boudon, C. Richard, and A. Bohlin, The ro-vibrational ν_2 mode spectrum of methane investigated by ultrabroadband coherent Raman spectroscopy, *Journal of Chemical Physics*, 158:094201, 2023.

Additional publications

V. L. Castellanos, **F. Mazza**, D. Kliukin, and A. Bohlin, Pure-rotational 1D-CARS spatiotemporal thermometry with a single regenerative amplifier system, *Optics Letters*, 45(17):4662-4665, 2020 [Editor's pick].

🗎 VI. **F. Mazza**, H. Buurmeijer, L. Castellanos, and A. Bohlin, Coherent N_2^+ emission mediated by coherent Raman scattering for gas-phase thermometry, *Optics Letters*, 47(23):6105-6108, 2022.

VII. D. Kliukin, **F. Mazza**, L. Castellanos, and A. Bohlin, Cascaded coherent anti-Stokes Raman scattering for high-sensitivity number density determination in the gas phase, *Journal of Raman Spectroscopy*, 52:1589-1597, 2021 [Special Issue: ECONOS/ECW 2020 Special Issue in memoriam of Marcus Motzkus].

🗎 Publication included in the present thesis.

VIII. L. Castellanos, **F. Mazza**, and A. Bohlin, Water vapor in hydrogen flames measured by time-resolved collisional dephasing of the pure-rotational N_2 CARS signal, *Proceedings of the Combustion Institute*, 39, *In press, corrected proof*, 2022 [Distinguished paper in the Diagnostics colloquium for the 39th International Symposium on Combustion].

Combustion and Flame 237 (2022) 111738

Contents lists available at ScienceDirect

Combustion and Flame

journal homepage: www.elsevier.com/locate/combustflame

High-temperature rotational-vibrational O_2-CO_2 coherent Raman spectroscopy with ultrabroadband femtosecond laser excitation generated *in-situ*

Francesco Mazza[a,*], Nathan Griffioen[a], Leonardo Castellanos[a], Dmitrii Kliukin[a], Alexis Bohlin[a,b]

[a] *Advanced Laser Diagnostics and Flames Laboratory, Aerodynamics, Wind Energy, Flight Performance & Propulsion (AWEP) Department, Delft University of Technology, Kluyverweg 1, 2629 HS Delft, the Netherlands*
[b] *Space Propulsion Laboratory, Department of Computer Science, Electrical and Space Engineering, Luleå University of Technology, Bengt Hultqvists väg 1, 981 92 Kiruna, Sweden*

ARTICLE INFO

Article history:
Received 6 March 2021
Revised 30 August 2021
Accepted 5 September 2021
Available online 24 September 2021

Keywords:
Laser diagnostics
Gas-phase thermometry
Lean premixed flames
Femtosecond/picosecond CARS

ABSTRACT

We present ultrabroadband two-beam femtosecond/picosecond coherent Raman spectroscopy on the ro-vibrational spectra of CO_2 and O_2, applied for multispecies thermometry and relative concentration measurements in a standard laminar premixed hydrocarbon flame. The experimental system employs fs-laser-induced filamentation to generate the compressed supercontinuum *in-situ*, resulting in a ∼24 fs full-width-at-half-maximum pump/Stokes pulse with sufficient bandwidth to excite all the ro-vibrational Raman transitions up to 1600 cm^{-1}. We report the simultaneous recording of the ro-vibrational CO_2 Q-branch and the ro-vibrational O_2 O-, Q- and S-branch coherent Stokes Raman spectra (CSRS) on the basis of a single-laser-shot. The use of filamentation as the supercontinuum generation mechanism has the advantage of greatly simplifying the experimental setup, as it avoids the use of hollow-core fibres and chirped mirrors to deliver a near-transform-limited ultrabroadband pulse at the measurement location. Time-domain models for the ro-vibrational Q-branch spectrum of CO_2 and the ro-vibrational O-, Q- and S-branch spectra of O_2 were developed. The modelling of the CO_2 Q-branch spectrum accounts for up to 180 vibrational bands and for their interaction in Fermi polyads, and is based on recently available, comprehensive calculations of the vibrational transition dipole moments of the CO_2 molecule: the availability of spectroscopic data for these many vibrational bands is crucial to model the high-temperature spectra acquired in the flue gases of hydrocarbon flames, where the temperature can exceed 2000 K. The numerical code was employed to evaluate the CSRS spectra acquired in the products of a laminar premixed methane/air flame provided on a Bunsen burner, for varying equivalence ratio in the range 0.6–1.05. The performance of the CO_2 spectral model is assessed by extracting temperatures from 40-laser-shots averaged spectra, resulting in thermometry accuracy and precision of ∼5% and ∼1%, respectively, at temperatures as high as 2220 K.

1. Introduction

Coherent Raman scattering spectroscopy – both in its Stokes (CSRS) and anti-Stokes (CARS) implementation [1,2] – has found vast application in the experimental study of chemically-reacting flows, especially in the context of combustion [3] and non-equilibrium thermodynamics [4]. CARS in particular has been extensively employed in combustion diagnostics for temperature [5–7] and concentration measurements [8–10], and is regarded as the gold-standard for high-fidelity thermometry in flames [11–13]. In principle, CARS is a form of four-wave mixing (FWM) [14], i.e. a third-order non-linear optical process, in which the frequency difference of two photons –called the "pump" photon (with angular frequency ω_p) and the "Stokes" photon (ω_{St})– coherently excite a Raman-active molecule to a higher rotational-vibrational (ro-vibrational) energy state; a third photon, the "probe" (ω_{pr}), is then scattered by the molecule, resulting in the emission of a coherent CARS photon at frequency $\omega_{CARS} = \omega_p - \omega_{St} + \omega_{pr}$. In the CARS process, the pump/Stokes photon-pairs couple to the internal energy states of the Raman-active molecules: the CARS

---

[*] Corresponding author.
E-mail address: f.mazza@tudelft.nl (F. Mazza).

https://doi.org/10.1016/j.combustflame.2021.111738

signal thus carries information on the molecular distribution over the ro-vibrational energy manifold, usually described in terms of the vibrational and total-angular-momentum quantum numbers (v and J, respectively). In the context of ro-vibrational spectroscopy ($\Delta v = \pm 1$) it is customary to use the labels "Q-", "O-", and "S-branch" to indicate ro-vibrational transitions with $\Delta J = 0$, -2, and $+2$, respectively [15].

The commercial availability, in recent years, of ultrafast regenerative amplifiers, has prompted the development of a number of time-resolved CARS techniques, allowing for nearly collision-independent measurements at high repetition rate [10]. In addition, the typical CARS setup can be greatly simplified when a broadband laser source is employed, as the constructive photon-pairs, typically provided by two distinct laser pulses, can be found across the bandwidth of a single pump/Stokes pulse. This technique is called "two-beam CARS" [11]. A single ultrafast regenerative amplifier, providing <50 fs duration pulses, can impulsively excite all the rotational energy states that are significantly populated by N_2 molecules at flame temperatures [16]. Nevertheless, the bandwidth of the laser pulses provided by commercially-available ultrafast regenerative amplifiers is not sufficient to efficiently excite Raman transitions further than ~400 cm^{-1}. In order to achieve impulsive excitation and perform ro-vibrational two-beam CARS spectroscopy in the "molecular fingerprint" region (i.e. in the range 800–1800 cm^{-1}) it is necessary to compress the pump/Stokes pulse to a duration comparable to the vibrational period of the target molecules [17], this being e.g. ~25 fs for CO_2 and ~21 fs for O_2. Thus, when compressing the pump/Stokes pulse below 25 fs duration, the resulting ultrabroadband pulse has enough spectral bandwidth to provide a significant number of constructive photon-pairs at Raman shifts up to ~1600 cm^{-1}. The use of ultrabroadband laser pulses to excite the whole ro-vibrational energy manifold of the Raman-active molecules in the probe volume dramatically enlarges the interrogation window for quantitative multiplex spectroscopy. Roy et al. [18] demonstrated the use of supercontinuum generation, through an argon-filled hollow-core fibre, in a single-beam CARS setup to measure the number density of CO_2 in a binary mixture with argon at room temperature and at different pressures. Bohlin and Kliewer [19] employed a hollow-core fibre to compress the 45 fs duration output of a Ti:Sapphire regenerative amplifier below 7 fs, enough to impulsively excite Raman transitions in the spectral range 0–4200 cm^{-1}. They demonstrated single-shot one-dimensional imaging of the ro-vibrational spectra of N_2, O_2, H_2, CO_2, and CH_4 in a two-beam femtosecond/picosecond (fs/ps) CARS setup. The application of this experimental technique to combustion diagnostics was furthermore demonstrated, firstly in a flat hydrocarbon flame [20] and subsequently in the investigation of flame-wall interaction [21]. Odhner et al. [22] demonstrated time-resolved ultrabroadband Raman spectroscopy employing fs-laser-induced air filamentation to generate the supercontinuum excitation pulse. They employed a 2 mJ, 45 fs duration laser pulse to generate a plasma filament in atmospheric air: the self-phase modulation experienced by the pulse resulted in its temporal compression to ~14 fs; furthermore, they showed the use of this "heterodyned, impulsive filament-based, stimulated Raman technique" in a CH_4/O_2 flame.

The diagnostic technique presented in this work relies on such filament-based supercontinuum generation to achieve quantitative time-resolved coherent Raman spectroscopy in the molecular fingerprint region. The possibility of performing measurements in the molecular fingerprint region is particularly appealing for combustion diagnostics, as almost all major combustion species possess ro-vibrational Raman spectral lines in this spectral range. The ro-vibrational Raman spectrum of O_2 is located at ~1556 cm^{-1} [23], while CO_2 appears a Fermi dyad at ~1285 cm^{-1} and ~1388 cm^{-1} [24], and the pure-rotational Raman spectrum of H_2 spans from ~354 cm^{-1} to ~1815 cm^{-1}, at high temperatures [25]. In addition, almost all hydrocarbons (e.g. methane, ethylene and ethane) have Raman-active vibrational transitions in the range ~882–1791 cm^{-1} [26], corresponding to the bending mode of the H–C–H bond. The scope of the present work is limited to the development of ultrabroadband two-beam fs/ps coherent Raman spectroscopy for the measurement of the ro-vibrational CO_2 and O_2 spectra in the region 1200–1600 cm^{-1}. The simultaneous detection of these two main combustion species makes the technique appealing for the study of Moderate or Intense Low oxygen Dilution (MILD) combustion [27–29] applications, where hot flue gases are recirculated as a thermal control mechanism to abate the emission of nitric oxide, leading to O_2 dilution and relatively low temperatures. Moreover, the availability of both O_2 and CO_2 as thermometric species in this spectral region makes the technique suited to applications such as oxy-fuel combustion, where molecular nitrogen is not available as a thermometer [30]. Multiplex CARS spectroscopy on the CO_2 Q-branch spectrum has been an active research area since the first applications of CARS to gas-phase media. In 1984, Hall and Stufflebeam [31] reported on CO_2 CARS thermometry performed at temperatures up to ~1600 K in a gas cell. A dual-pump nanosecond CARS system was employed by Lucht et al. [32] to simultaneously detect the Q-branch spectra of CO_2 and N_2 (at ~2330 cm^{-1}): they measured temperatures up to ~2000 K and achieved single-shot detection of the CO_2 signal at values of the mole fraction down to ~1–2%. Dual-pump N_2-CO_2 CARS was furthermore used for thermometry and CO_2 concentration measurements in the exhaust of a swirl-stabilized JP-8-fuelled combustor [33]. Recently, Kerstan et al. [34] demonstrated the first use of ultrabroadband two-beam fs/ps CARS for CO_2 thermometry. They used a neon-filled hollow-core fibre to compress the ~35 fs duration laser pulse, resulting in a ~7 fs duration, ~25 µJ pump/Stokes pulse. Due to the relatively low average power of the laser pulses employed, their measurements were limited to a pressurized gas-cell and the maximum temperature measured from the CO_2 spectrum was 937 K. The same research group demonstrated the use of ultrabroadband CARS –attained in this case through an optical parametric chirped-pulse amplifier, providing a ~7 fs duration, 7.5 µJ pump/Stokes pulse– to measure relative CO/CO_2 concentrations, as well as temperature, in a gas oven heated up to ~800 K [35].

In the present work, we employ fs-laser-induced filamentation for the *in-situ* generation of the compressed supercontinuum. Two-beam ultrabroadband fs/ps coherent Raman spectroscopy on the ro-vibrational spectra of O_2 and CO_2 is demonstrated in the hot flue gases of a standard laminar premixed CH_4/air flame, at temperatures higher than 2000 K, allowing for simultaneous thermometry and relative O_2/CO_2 concentration measurements.

2. Experimental setup

2.1. Two-beam femtosecond/picosecond CARS setup

The experimental setup for two-beam fs/ps coherent Raman thermometry is detailed in [16] and depicted in Fig. 1; in the following a brief summary of the main features of the system is given. The two laser pulses employed are provided by a single regenerative amplifier system (Astrella, Coherent), operating at 1 kHz and providing an overall pulse energy of 7.5 mJ at 800 nm. The temporally uncompressed output of the amplifier is split 65%–35%: the larger portion is compressed before being fed to a second-harmonic bandwidth compressor (SHBC, Light Conversion), providing a 5 ps duration pulse at 402.7 nm, to serve as the probe pulse. A spatial 4f-filter in transmission, placed in the probe beam path, allows for tuning the duration of the pulse: in

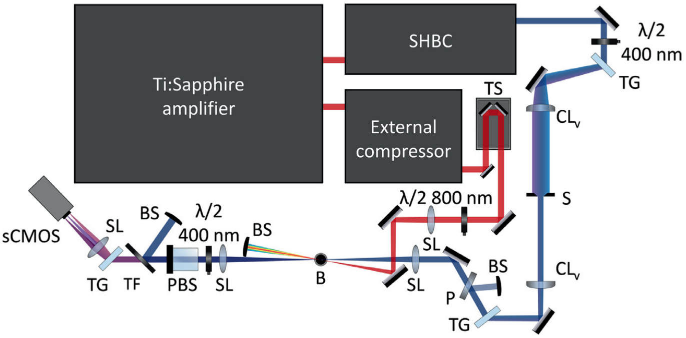

Fig. 1. Schematic of the ultrabroadband two-beam CSRS system. The output of a 1 kHz Ti:Sapphire regenerative amplifier system is split 65%–35% to feed a second-harmonic bandwidth compressor (SHBC) and an external compressor, respectively. The transform-limited 35 fs duration output of the external compressor is focused by a 500 mm focal-length spherical lens (SL) resulting in fs-laser-induced filamentation. The ultrabroadband pump/Stokes beam is crossed by the probe beam at a distance of ~4 mm after exiting the filament: the resulting probe volume is located over the Bunsen burner (B). The ultrabroadband CSRS signal is collected in a coherent imaging spectrometer and imaged to a sCMOS detector. TG, transmission gratings; S, slit; CL_v, cylindrical lenses with vertical alignment symmetry axis; TS, automated translation stage; λ/2, half-wave plates; P, polarizer; PBS, polarization beam splitter; TF, angle-tuneable band-pass filter; BS, beam stop.

the present work, a ~6.6 ps duration probe pulse is employed, with ~300 µJ/pulse. The second output beam is compressed by an external compressor unit providing a transform-limited 35 fs duration pump/Stokes pulse, with 2.3 mJ/pulse. The external compressor furthermore provides an active control on the pulse dispersion, allowing for pulse pre-chirping, to compensate for the effect of group velocity dispersion of the different optical media along the beam path. The use of a single regenerative amplifier to provide all the laser pulses has the advantage of the pulses being automatically synchronised with no temporal jitter. The path-length difference between the pump/Stokes and the probe pulses is compensated for by an optical delay line, and the probe delay is set by the position of an automated translation stage (Thorlabs), with a resolution <10 fs. Half-wave plates for 800 nm and 400 nm (Eksma Optics) are employed to control the orientation of the linearly-polarized pump/Stokes and probe pulses, respectively. In order to ensure the same polarization of the different spectral branches in the CSRS signal, the probe polarization is set parallel to the pump/Stokes: under this condition, both the CO_2 and O_2 Q-branch and the ro-vibrational O_2 O- and S-branch have the same polarization as the pump/Stokes and probe pulses [36,37]. The pump/Stokes and probe beams are both focused at the measurement location by spherical lenses and crossed according to the phase-matching scheme demonstrated in [38]. The probe pulse is focused by a 300 mm focal-length lens, resulting in a measured beam waist of ~30 µm ($1/e^2$), and its energy at the measurement location is measured to be 194 µJ; the pump/Stokes pulse energy, focused by a 500 mm focal-length lens, is measured to be 1.6 mJ. The extremely high peak irradiance (estimated to be ~4.46×10^{14} W/cm^2) of the fs pulse results in the non-linear self-focusing of the pulse (Kerr effect) and the multiphoton ionization of the gas medium, producing a visible plasma channel (i.e. the filament), which can be observed near the focal plane of the focusing lens. This process is also accompanied by the non-linear self-phase modulation of the pulse, resulting in supercontinuum generation and providing, at the measurement location, an ultrabroadband pump/Stokes pulse. The interaction length is estimated by measuring the beam crossing angle (~5°) and the divergence of the beam out of the filament, yielding a pump/Stokes beam waist of ~130 µm ($1/e^2$) at the probe volume location. The probe volume is thus measured to be ~60 µm (width, $1/e^2$) × 3.3 mm (length, $1/e^2$) × ~60 µm (height, $1/e^2$), and is located ~4 mm after the filament. The details of the fs-laser-induced filamentation and of the resulting compressed ultrabroadband pulse are discussed in Section 2.2.

The co-propagating probe beam and CSRS signals are collected by a collimating lens (f:=400 mm). The angle-tuning of a spectral band-pass filter (Semrock) is used to suppress the probe beam and select the spectral window of interest (~1200–1600 cm^{-1}) and a 400 nm half-wave plate (Eksma Optics) turns the polarization of the CARS signal to maximize the diffraction efficiency of a high-resolution transmission grating (3040 lines/mm, Ibsen Photonics). The dispersed signal is then collected by an imaging lens (f:=200 mm) onto a cropped region (100 × 2048 pixels) of the sCMOS detector (Zyla 4.2, Andor) frame, providing 1 kHz frame-rate signal acquisition.

2.2. *Compressed supercontinuum generation*

In order to achieve the ultrabroadband excitation of the ro-vibrational Raman coherences, we employ a pulse compression technique based on *in-situ* filamentation, as demonstrated in [22]. The propagation of ultrashort pulses in any dielectric medium is accompanied by several nonlinear effects such as Kerr effect, self-phase modulation, and multiphoton ionization [39]. The Kerr effect causes a transient increase of the refractive index of the optical medium at high-pulse intensity, resulting in the self-focusing of the laser beam and the self-phase modulation of the pulse, leading to the generation of new spectral components. Above an input pulse energy threshold of ~40 µJ (corresponding to an estimated irradiance of ~1.14×10^{13} W/cm^2), a fraction of the molecules is ionized through multiphoton absorption (11 photons for N_2 [40] and 8 photons for O_2 [41], at 800 nm laser wavelength) reducing the refractive index and causing self-defocusing of the laser beam. The competition between self-focusing and self-defocusing occurs until the pulse energy, consumed in multiphoton ionization, is sufficient to maintain the nonlinear optical processes. Moreover, the complex dispersion of the ionized gas medium causes self-pulse compression, which may result in pulse durations as low as <5 fs with sufficiently long filaments [42]. In this work we employ relatively fast focusing of the pump/Stokes femtosecond pulse with f:=500 mm, with the Gaussian beam diameter being ~10.5 mm ($1/e^2$) and the pulse energy being ~1.6 mJ, producing a visible filament with a measured length of ~13.2 mm ($1/e^2$). The longitudinal spatial jitter of the filament is assessed by detecting the initiation and the ending point of the visible filament in a sample of 300 single-shot images, and it is measured to be ~350 µm and ~300 µm, respectively. We characterise the supercontinuum generation by measuring the pulse energy of the ultrabroadband pulse, output by the filament, as a function of the input energy of the 35

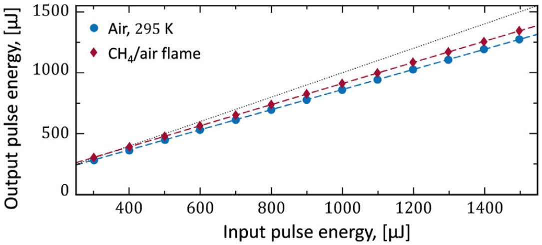

Fig. 2. Power scaling of the ultrabroadband pump/Stokes pulse output by the filament generated in room-temperature air and in the products of a laminar premixed methane/air flame. The pulse energy is measured after the filament collapse: for varying input pulse energy in the range 0.3–1.5 mJ, before the filament initiation, the energy of the compressed ultrabroadband pulse out of the filament scales linearly. The dotted line represents the ideal limit when no pulse energy is lost to the filamentation process.

fs duration pulse, measured before the initiation of the filament. Figure 2 illustrates the dependence of the ultrabroadband pulse energy on the energy of the fs laser pulse, for the filament generated in room-temperature air and in the product gases of a laminar premixed CH_4/air flame. The energy output of the filament scales linearly with the energy of the input laser pulse over the whole measured range of 0.3–1.5 mJ, with the energy-conversion efficiency of the supercontinuum generation being ~82% in air and ~86% in the flame (see Fig. 2). The higher energy conversion of the filamentation process in the flame is explained by the ionization rate of the gas medium being larger in the denser room-temperature air than in the hot flame products. The increment of the input energy, from 0.3 mJ to 1.5 mJ, leads to higher irradiance and an earlier onset of the Kerr effect, resulting in the elongation of the filament towards the laser focusing lens, while the location of the ending point of the filament is unaltered: therefore, the probe volume is always maintained at a fixed distance from the filament. Although the filament is partly generated inside the flame, the coherent Raman signal is generated on a ps timescale, so that the molecular ensemble probed in the measurement is not affected by the perturbation of the flame introduced by the ionization process. Furthermore, the electron-ion recombination timescale is in the order of nanoseconds [39], which is much faster than the repetition rate of the regenerative amplifier system, operating at 1 kHz. Hence, even if multiple laser-shots are averaged in the signal acquisition, each measurement is unaffected by the filament generated by the previous laser-shot. In this respect, coherent Raman spectroscopy with ultrabroadband femtosecond laser excitation generated *in-situ* can be claimed to be a non-intrusive diagnostic technique for gas-phase measurements.

In the present work, we demonstrate the *in-situ* generation and *in-situ* use of the filament to compress the pump/Stokes pulse and excite the ro-vibrational Raman transitions of O_2 and CO_2 in the range 1200–1600 cm^{-1}, on the Stokes side. The choice of acquiring the CSRS signal rather than the CARS is motivated by the intensity of the former being significantly larger: at room temperature, the O_2 Q-branch spectrum was detected with two orders of magnitude higher intensity on the Stokes side than on the anti-Stokes side. This is in contrast with the predicted theoretical ratio of the CARS and CSRS signals, which is computed to be ~1.29, owing to the higher carrier frequency of the CARS signal [43]. The observed enhancement in the CSRS signal intensity can be partly attributed to the quantum efficiency (QE) of the sCMOS detector. According to the QE curve reported by the manufacturer, at 1556 cm^{-1}, i.e. at the fundamental band of the O_2 Q-branch spectrum, the QE is approximately 1.75 times higher on the Stokes side than on the anti-Stokes side. In addition, the diffraction efficiency of the transmission grating employed in the coherent imaging spectrometer (see Section 2.1) is reduced on the anti-Stokes side by a factor of ~1.20, according to the diffraction efficiency curve reported by the manufacturer. Finally, we report an asymmetric excitation profile delivered by the ultrabroadband pump/Stokes pulse, as mapped by the non-resonant (NR) signal recorded on the Stokes and anti-Stokes sides: the NR CSRS spectrum at 1556 cm^{-1} is ~20 times higher than the NR CARS spectrum measured at the same Raman shift (see Supplementary Figure S1). Additional experiments are required to explain the asymmetric excitation profile observed in coherent Raman spectroscopy with ultrabroadband femtosecond laser excitation generated *in-situ*.

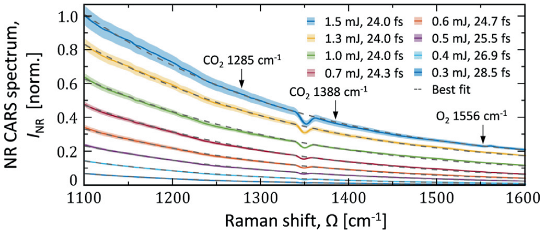

Fig. 3. Averaged NR CSRS spectrum acquired in room temperature argon generated with 0.3–1.5 mJ pump/Stokes pulse energy and the theoretical curve corresponding to 24–28.5 fs pulse duration. The coloured area represents the standard deviation of the NR spectrum over 300 single-shot acquisitions. The visible dip in the NR CSRS spectrum at ~1350 cm^{-1} is due to interference with the N_2^+ fluorescence emission from the filament (see e.g., [45]).

We estimate the duration of the self-compressed pump/Stokes pulse using the NR CSRS signal. This signal is routinely employed in CARS spectroscopy to map the frequency-dependant excitation efficiency of the Raman coherence: the standard experimental protocols thus entail the generation of the NR CSRS signal from the electronic susceptibility in argon, by setting zero-delay time between the pump/Stokes and probe pulses. The third-order polarization induced by the electronic susceptibility of the optical medium can be estimated as [44]:

$$P_{NR}^{(3)}(t) \propto \left(-\frac{i}{\hbar}\right)^3 E_{12}^*(t)E_{12}(t)E_3(t) \tag{1}$$

where E_{12} and E_{12}^* are the envelopes of the pump/Stokes pulse and its complex conjugate, E_3 is the probe pulse envelope. The spectrum of the NR CSRS signal can then be computed as the Fourier transform of $P_{NR}^{(3)}(t)$. The compressed time-domain pump/Stokes pulse envelope (E_{12}) is assumed to be transform-limited (TL) and to have a Gaussian profile, with the pulse duration being a fitting parameter to determine the pulse compression in the filament. The time-domain envelope of the probe pulse (E_3) is measured experimentally, by performing a probe delay-scan in room-temperature argon, employing a pump/Stokes pulse energy below the filamentation threshold. Figure 3 shows the NR CSRS spectra (averaged over 300 single-shots) acquired for a pump/Stokes pulse energy varying between 0.3 and 1.5 mJ and the fit to the theoretical spectra computed according to Eq. (1). The increase of the pulse energy leads to a stronger self-phase modulation, resulting in a larger bandwidth of the laser pulse at the output of the filament, as shown by the increased excitation efficiency at larger Raman shifts. The fit to the theoretical NR spectrum simulated for a Gaussian TL pulse shows the corresponding temporal compression of the pump/Stokes pulse from 28.5 fs to 24 fs. A plateau in the pulse compression is reached at ~1 mJ/pulse: increasing the pulse energy above this threshold does not result in a further compression of the pulse, but only increases the electronic Raman coherence, enhancing the NR signal intensity. The experimental NR spectra presented in Fig. 3 show a consistent dip at ~1350 cm^{-1} due to the destructive interference at the detector of the NR CSRS signal and the fluorescence signal produced by the N_2^+ ions generated in the filament [45,46]. The shot-to-shot fluctuations in the overall energy of the pump/Stokes pulse output by the filament stay within ~0.5% and the relative standard deviation of its bandwidth, evaluated in the region 1200–1600 cm^{-1}, is below 10%.

2.3. Bunsen burner

We performed ultrabroadband two-beam fs/ps coherent Raman spectroscopy in a quasi-adiabatic laminar premixed CH_4/air flame, provided on a Bunsen burner. The burner consists of a seamless stainless steel pipe with ~12 mm inner diameter and a length-to-diameter ratio (~100:1) chosen to dampen coherent flow structures at the exit plane. The fuel and the oxidizer are provided by separated pressurised vessels and the flows are independently controlled by rotameters (Omega), and mixed afterwards to deliver the combustible mixture to the burner. The volumetric flow rate is maintained below 5 standard litre per minute (SLPM): the Reynolds number is thus computed to be <1000, resulting in a laminar flow. The probe volume is placed ~ 7 mm above the tip of the conical flame. The equivalence ratio of the combustible mixture is varied in the fuel-lean regime from $\varphi=0.6$ to slightly fuel rich conditions ($\varphi=1.05$), to simultaneously acquire the CSRS spectra by O_2 and CO_2. In correspondence of the two leanest cases tested, the flame is stabilized as a V-shaped flame to avoid lean blow-off, employing a 4 mm diameter steel rod placed at a height of ~12 mm above the burner rim; in these flame conditions the probe volume is placed ~5 mm above the rod.

3. Time-resolved CSRS model

3.1. Ro-vibrational fs/ps CSRS processes

The principles underlying the time-domain modelling of the fs/ps coherent Raman scattering process have been thoroughly elaborated upon in the literature (e.g., [47–50]), for both pure-rotational and ro-vibrational CARS: in the following, we provide only a brief summary of the main assumptions and equations employed. In the present work, we report on the experimental acquisition of CSRS spectra; however, from a theoretical perspective, the time-resolved model of the ro-vibrational O_2_CO_2 CARS spectra can be readily extended to simulate the CSRS spectra, under electronically non-resonant conditions [51,52].

The third-order polarisation resulting from the FWM process can be described, in the time domain, as the convolution of the envelopes of the input electromagnetic fields with the ordinary response function of the gas-phase medium, represented by its macroscopic electric susceptibility $\chi^{(3)}$ [14,49]:

$$P^{(3)}(t,\ t_{12},\tau_{23},t_3)=\left(-\frac{i}{\hbar}\right)^3\int_{-\infty}^{t}dt_3\int_{-\infty}^{t_3}dt_{12}\chi^{(3)}$$
$$\times\,(t,t_3,t_{12})E_3(t-t_3)e^{i(\omega_1-\omega_2+\omega_3)t_3} \tag{2}$$
$$\times\ E_{12}^*(t+\tau_{23}-t_3-t_{12})e^{i(\omega_1-\omega_2)t_{12}}E_{12}(t+\tau_{23}-t_3-t_{12})e^{i\omega_1 t_{12}}$$

where ω_i is the frequency of the i th photon (with index $i=1$, 2 and 3 corresponding to the pump, Stokes and probe photons, respectively), E_{12} and E_{12}^* are the envelopes of the pump/Stokes pulse and its complex conjugate, E_3 is the envelope of the probe pulse, t_{12} is the coherence timescale between the pump/Stokes and probe pulse, t_3 is the coherence timescale in the scattering of the probe pulse, and τ_{23} is the delay of the probe pulse relative to the pump/Stokes pulse. Under the assumptions of instantaneous dephasing of the electronic coherence in non-resonant single-photon interactions, and of infinite bandwidth of the pump/Stokes excitation pulse [44], Eq. (2) is greatly simplified as:

$$P^{(3)}(t)=\left(-\frac{i}{\hbar}\right)^3E_3(t-t_3)\chi^{(3)}(t) \tag{3}$$

Under these assumptions, the conceptual core in the fs/ps CSRS model is represented by the third-order non-linear susceptibility of the optical medium. This term is typically treated phenomenologically [47], as the weighted sum of dampened oscillations at the frequencies corresponding to the transitions in the ro-vibrational energy manifold of the Raman-active species in the medium:

$$\chi_{\mathrm{CSRS}}^{(3)}(t)=\sum_k\sum_v\sum_J \mathrm{X}_k I_{(v_\mathrm{f},J_\mathrm{f})\leftarrow(v_\mathrm{i},J_\mathrm{i})}^{(k)}\exp\left[\left(i\omega_{(v_\mathrm{f},J_\mathrm{f})\leftarrow(v_\mathrm{i},J_\mathrm{i})}^{(k)}-\Gamma_{(v_\mathrm{f},J_\mathrm{f})\leftarrow(v_\mathrm{i},J_\mathrm{i})}^{(k)}\right)t\right] \tag{4}$$

where X_k is the mole fraction of the k-th species considered, $I_{(v_\mathrm{f},J_\mathrm{f})\leftarrow(v_\mathrm{i},J_\mathrm{i})}$ is the strength of the spectral line corresponding to the Raman transition between the initial $(v_\mathrm{i},J_\mathrm{i})$ and the final energy state $(v_\mathrm{f},J_\mathrm{f})$, which carries the temperature sensitivity of the Raman spectrum as a dependence on the Boltzmann distribution over these ro-vibrational energy states. $\omega_{(v_\mathrm{f},J_\mathrm{f})\leftarrow(v_\mathrm{i},J_\mathrm{i})}^{(k)}$ and $\Gamma_{(v_\mathrm{f},J_\mathrm{f})\leftarrow(v_\mathrm{i},J_\mathrm{i})}^{(k)}$ are, respectively, the frequency and the dephasing coefficient of the Raman transition, representing the position and the linewidth (full-width-at-half-maximum, FWHM) of the corresponding spectral line in the frequency domain. The strength of the ro-vibrational Raman lines is computed according to [4,15]:

$$I_{(v,J)\leftarrow(v+1,J)}=\left[F_\alpha^{(k)}\left(\alpha_{(v,J)\leftarrow(v+1,J)}^{(k)}\right)^2+\frac{4}{45}F_\gamma^{(k)}b_{J,J}^{(k)}\left(\gamma_{(v,J)\leftarrow(v+1,J)}^{(k)}\right)^2\right]N^{(k)}\Delta\rho_{(v,J)\leftarrow(v+1,J)}$$
$$I_{(v,J)\leftarrow(v+1,J\pm2)}=\frac{4}{45}F_\gamma^{(k)}b_{J,J\pm2}^{(k)}\left(\gamma_{(v,J)\leftarrow(v+1,J\pm2)}^{(k)}\right)^2N^{(k)}\Delta\rho_{(v,J)\leftarrow(v+1,J\pm2)} \tag{5}$$

where $\alpha_{(v_\mathrm{f},J_\mathrm{f})\leftarrow(v_\mathrm{i},J_\mathrm{i})}^{(k)}$ and $\gamma_{(v_\mathrm{f},J_\mathrm{f})\leftarrow(v_\mathrm{i},J_\mathrm{i})}^{(k)}$ are the isotropic and anisotropic invariants of the (transition) polarizability tensor, $b_{J_\mathrm{f}J_\mathrm{i}}^{(k)}$ is the Placzek-Teller coefficient for the rotational transition $(J_\mathrm{f}\leftarrow J_\mathrm{i})$, $F_{\alpha/\gamma}^{(k)}$ are the Herman-Wallis factors for isotropic/anisotropic transitions, $N^{(k)}$ is the number density of the k-th species, and $\Delta\rho_{(v_\mathrm{i},\ J_\mathrm{i})\to(v_\mathrm{f}J_\mathrm{f})}$ is the differential Boltzmann distribution between the initial and the final energy states. The summations in Eq. (4) are intended over all the Raman-active species (k), and for all the ro-vibrational energy levels (v, J) that are significantly populated in the thermal ensemble. The labels ”v” and “J” are employed here to represent the quantised vibrational and rotational levels in the energy manifold of a certain species. In reality, more than two quantum numbers might be required to completely characterise the quantum state of a specific molecule: this is the case e.g. for CO_2.

The phenomenological model represented by Eq. (4) can thus be employed to compute the non-linear optical response of the gas-phase medium, for different input values of its temperature and composition. By combining this response with the experimentally-measured envelope of the probe pulse, one can

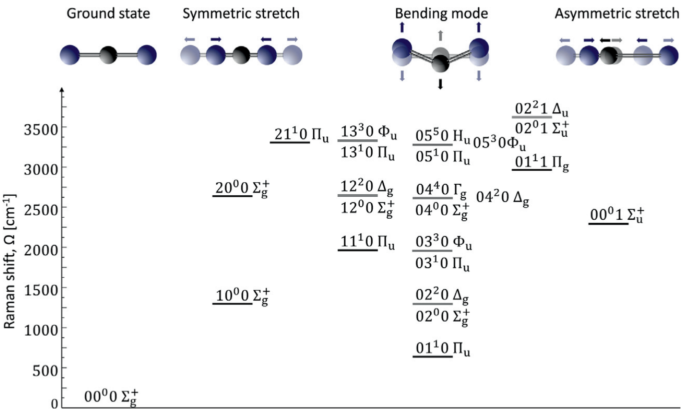

Fig. 4. Energy diagram detailing the structure of the vibrational energy manifold for the CO_2 molecule up to 3500 cm^{-1}. The vibrational energy state of the molecule is described by four quantum numbers, $v_1v_2lv_3$, according to the notation in [53]: v_1 is the symmetric stretch quantum number, v_2 is the bending mode quantum number, l is the vibrational angular momentum quantum number, and v_3 is the asymmetric stretch quantum number.

simulate the ro-vibrational CO_2 and O_2 Raman spectra for temperatures and compositions relevant to combustion studies.

3.2. Ro-vibrational CO_2 spectrum

In order to synthesise the ro-vibrational Q-branch spectrum of CO_2, an accurate description of the structure of its ro-vibrational energy manifold is required. CO_2 is a triatomic molecule made of two oxygen atoms and a carbon atom forming two double covalent bonds: the resulting molecule is linear and centrosymmetric. This structure results in three distinct normal vibrational modes: the symmetric stretch, the scissoring bend and the asymmetric stretch mode (see inlet in Fig. 4). Because of the point-symmetry of the molecule, the symmetric stretch is the only Raman-active mode, while the bending and asymmetric mode are IR-active only. The vibrational energy states of the CO_2 molecule can thus be labelled, according to the notation in Herzberg [53], as $v_1v_2lv_3$, where v_1 is the symmetric stretch quantum number, v_2 is the bending quantum number, l is the vibrational angular momentum quantum number, and v_3 is the asymmetric stretch quantum number. The vibrational angular momentum is due to the asymmetric motion of the nuclei with respect to the inter-nuclear axis in the bending mode, resulting in a rotational motion about the (equilibrium) inter-nuclear axis [15,53,54]. This additional angular momentum is quantized, with quantum number l=-v_2,-v_2+2,…,v_2–2,v_2. The energy levels associated to the bending mode are therefore (v_2+1)-fold degenerate and the corresponding ro-vibrational energy is computed according to [54]:

$$E(v,J) = G_v + B_v\left[J(J+1) - l^2\right] - D_v\left[J(J+1) - l^2\right]^2 + H_v\left[J(J+1) - l^2\right]^3 \qquad (6)$$

where G_v, B_v, D_v and H_v are the spectroscopic constants of CO_2 (with $v = v_1v_2lv_3$), and J is the total angular momentum quantum number, which includes the contribution of the vibrational angular momentum, so that $J \geq |l|$ [15,54]. In addition, as the vibrational angular momentum is parallel to the inter-nuclear axis, when it is in a degenerate bending state, CO_2 behaves as a prolate symmetric top molecule [15], and the Placzek-Teller coefficients for the corresponding Raman band are computed as:

$$b(J,l) = \frac{\left[J(J+1) - 3l^2\right]^2}{J(J+1)(2J-1)(2J+3)} \qquad (7)$$

The ro-vibrational Q-branch CARS spectrum of CO_2 is thus made of the spectral lines corresponding to the excitation of the symmetric stretch mode, according to the selection rules: Δv_1=1, Δv_2=Δv_3=Δl=0. Vibrational states characterised by an active bending mode (i.e. for $v_2 \neq 0$) are (v_2+1)-fold degenerate, as the vibrational angular momentum has quantized values l=-v_2,-v_2+2,…,v_2–2,v_2. Each degenerate bending mode accompanied by vibrational angular momentum (i.e. for $l \neq 0$) is double-degenerate and, in analogy with the Λ-type doubling due to spin-orbit interaction, capital Greek letters are used to label these states, as shown in Fig. 4. Moreover, when two different vibrational states characterised by the same vibrational wave function symmetry have similar energy, their respective wave function can “mix”, a phenomenon known as Fermi resonance [32,55]. As the unperturbed (i.e. as described by a harmonic potential Hamiltonian) v_1 and $2v_2$ states have almost identical energy, due to Fermi resonance the IR-active $2v_2$ lines appear in the Raman spectrum and the anharmonic terms in the exact Hamiltonian result in the “repulsion” of the spectral lines in the v_1+$2v_2$ dyad [54].

The ro-vibrational CO_2 fs/ps CARS model developed in the present work employs the ro-vibrational constants given in [56], to compute the molecular energy according to Eq. (6). In the thermal ensemble, these energy levels are populated as described by Boltzmann distribution:

$$\rho(v,J) = g_S\, g_v\, g_J \frac{\exp(-E(v,J)/(k_B T))}{Z} \qquad (8)$$

where k_B is the Boltzmann constant, T is the temperature, Z is the partition function, $g_J = 2J+1$ is the rotational degeneracy, g_v is the vibrational degeneracy, and g_S is the nuclear spin degeneracy. The latter is respectively 1 and 0 for even and odd rotational states in those vibrational bands characterised by an even symmetry of the nuclear wave function (e.g. in the vibrational ground state), while the opposite holds for odd-symmetric states. As the temperature increases, higher energy states became substantially populated in the vibrational Boltzmann population of CO_2. The values of the transition polarizability isotropic (α) and anisotropic (γ) invariants are required to compute the Raman line-strengths in Eq. (5). Lemus et al. [57] used an algebraic approach to compute the vibrational transition dipole moments of CO_2: their calculations are in good agreement with experimental values in [58]. The resulting polarizability transition moments for ro-vibrational transition in the range 1100–1600 cm^{-1} are employed extensively in the present work. On the other hand, no reliable measurement of the dependence of the

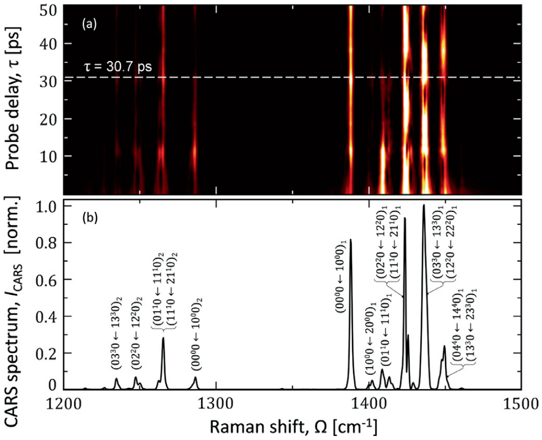

Fig. 5. (a) Spectrochronogram of the ro-vibrational CO_2 Q-branch spectrum, simulated by the time-domain CSRS code for an input temperature of 2200 K and an experimental probe duration measured to be 6.6 ps. The simulated fs/ps CO_2 CSRS spectrum is affected by a severe beating of all the spectral lines, due to the unresolved transitions between the many ro-vibrational energy states populated at flame temperature. (b) CO_2 Q-branch spectrum simulated for a probe delay of 30.7 ps. The main ro-vibrational bands contributing to the unresolved spectral lines are reported, the labelling follows the notation in [34].

transition dipole moments on the rotational energy state could be found in the literature, and the same values of $\alpha_{v+1\rightarrow v}$ are employed for all the rotational lines within the same vibrational band [59]. To the best of our knowledge, the anisotropic polarizability $\gamma_{v+1\rightarrow v}$, is also not known with sufficient accuracy: in absence of accurate experimental data or computations, the CO_2 model only includes the isotropic contribution to the Q-branch CO_2 spectrum. This assumption is justified by the well-established value of the depolarization ratio of the fundamental vibrational band in the CO_2 Raman spectrum at 1388 cm^{-1}, amounting to 0.027 [60]. The spectral model includes temperature-dependant linewidths for self-broadened CO_2 and for CO_2 perturbed by N_2, as this is the most abundant species in air-fed combustion. The linewidths are fitted, according to the modified exponential energy-gap (MEG) scaling law [61], from the experimental data reported in [24] for the self-broadened CO_2 spectral lines; the collisional broadening due to nitrogen, on the other hand, is modelled according to [62].

Figure 5 shows the ro-vibrational Q-branch spectrum of CO_2, in the spectral range 1200–1500 cm^{-1}, simulated by the time-domain CARS code, for an input temperature of 2200 K and assuming a probe duration of 6.6 ps. The spectrochronogram in Fig. 5(a) reveals the strong beating of the vibrational hot bands due to unresolved ro-vibrational lines pertaining to different vibrational transitions: these unresolved vibrational bands are identified in Fig. 5(b), and labelled according to the notation in Herzberg. The structure of the Fermi resonances between the v_1 and $2v_2$ vibrational bands is clearly visible and identified in the labels by the subscripts. The fundamental band corresponding to the first symmetric stretch is the Fermi dyad, comprising a lower-frequency spectral line located at 1285 cm^{-1} (referred to the “red” branch of the dyad [63]), and a higher-frequency line at 1388 cm^{-1} (the “blue” branch of the dyad [64]). The beating of the spectrum with the probe pulse delay is particularly evident on the second, third and fourth hot bands on the blue Q-branch spectrum (spanning the spectral region >1350 cm^{-1}), which are characterised by similar beating patterns, with a period of about 36 ps. This behaviour is explained by the close separation (~0.2 cm^{-1}) of two distinct vibrational bands, in each spectral peak, being smaller than the probe bandwidth (~2.23 cm^{-1}). In this respect, the use of a single regenerative amplifier system, providing automatically synchronised pump/Stokes and probe beam pulses at the measurement location, can improve the single-shot precision of vibrational CO_2 coherent Raman thermometry.

3.3. Ro-vibrational O_2 spectrum

Compared to CO_2, the oxygen molecule presents a much simpler energy manifold: molecular vibration is only possible along the direction of the inter-nuclear axis: only one quantum number (v) is thus required to describe the vibrational energy state of O_2. On the other hand, the ground electronic state of O_2 ($X\ ^3\Sigma_g^-$) is characterised by unpaired electrons [65,66], resulting in an electronic spin angular momentum quantum number $S = 1$: the coupling of this angular momentum component to the nuclear angular momentum (with quantum number N) is accounted for by adopting the Hund’s case (b) [53]. Under such conditions, the total angular momentum J is the direct sum of the electronic spin and nuclear components, $J = N + S$, resulting in each energy state with nuclear angular momentum N, being a triplet with $J = N$, $N \pm 1$. Courtney and Kliewer [67] experimentally demonstrated the effect of this coupling on the S-branch Raman spectrum: a significant temporal beating was measured the time-resolved hybrid fs/ps CARS signal, for probe delays larger than 100 ps. In the present work, the ro-vibrational time-domain model of the O_2 CSRS spectra is simplified by considering the triplets as degenerate states: this assumption is justified by the lower transition frequency separation for the ro-vibrational Q-branch lines, with respect to the O- and S-branch lines [23], and the relatively short probe delay of ~31 ps employed in the flame experiment. The energy of a molecule in the ro-vibrational state (v, J) is thus described by a simplified form of Eq. (6), as:

$$E(v,J) = G_v + B_v[J(J+1)] - D_v[J(J+1)]^2 + H_v[J(J+1)]^3 \tag{9}$$

The ro-vibrational constants of diatomic oxygen in the ground electronic state can be found in [23]. Eq. (8) and (9) are used to compute the differential Boltzmann population for the ro-vibrational Q-, O- and S-branch Raman transitions. Placzek-Teller coefficients are computed for the line strengths of the Q-, O- and S-branch spectra respectively, as [15]:

$$\begin{aligned} b_{J\leftarrow J-2}(J) &= \frac{3J(J-1)}{2(2J+1)(2J-1)} \\ b_{J\leftarrow J}(J) &= \frac{J(J+1)}{(2J-1)(2J+3)} \\ b_{J\leftarrow J+2}(J) &= \frac{3(J+1)(J+2)}{2(2J+1)(2J+3)} \end{aligned} \tag{10}$$

According to Eq. (5), the intensity of the spectral lines furthermore depends on the Herman-Wallis factor, and on the isotropic (α) and anisotropic (γ) invariants of the transition polarizability tensor, here computed according to the formulae provided in [68]. The spectral linewidths employed in the model account for the collisional broadening due to self-perturbed O_2 and for the O_2–N_2 collisional system. The temperature-dependant Q-branch linewidths are determined by applying the MEG law to the experimental data reported by Millot et al. [69] for both O_2-O_2 and O_2-N_2 collisional broadening. The linewidths of the ro-vibrational O_2 O- and S-branch spectra are computed from the Q-branch linewidths, by applying the random phase approximation [70].

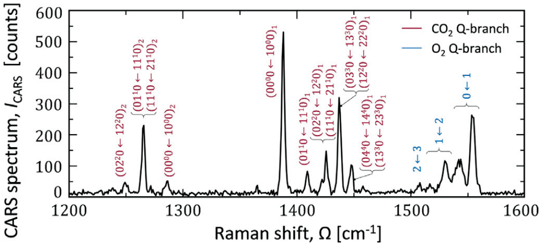

Fig. 6. Single-shot O_2-CO_2 CSRS spectrum acquired in the products of a laminar premixed CH_4/air flame (φ=0.77). The red labels denote the Q-branch CO_2 transitions according to the notation in [53]; blue labels are employed to indicate the fundamental and hot band transitions in the O_2 Q-branch spectrum.

4. Results and discussion

4.1. O_2-CO_2 coherent Raman spectroscopy in a laminar premixed CH_4/air flame

We demonstrate the use of ultrabroadband coherent Raman spectroscopy, over the spectral range 1200–1600 cm^{-1}, to perform thermometry and relative O_2/CO_2 concentration measurements in a typical hydrocarbon flame. As discussed in Section 2.3, the measurements were performed in the products of a laminar premixed CH_4/air flame, provided on a Bunsen burner: six different values of the equivalence ratio, from 0.6 to 1.05, were tested in the flame experiments.

An example of a single-shot ro-vibrational O_2-CO_2 CSRS spectrum, acquired in the products of the laminar premixed CH_4/air flame (φ=0.77), is depicted in Fig. 6. The three peaks visible in the range ~1200–1300 cm^{-1} represent the "red" CO_2 Q-branch spectrum, consisting of the fundamental and the first three hot bands; the "blue" CO_2 Q-branch lies in the spectral region from the fundamental transition at 1388 cm^{-1} to ~1450 cm^{-1}, with many vibrational bands convolved with each other and giving rise to the beating patterns simulated in Fig. 5(a). The ro-vibrational O_2 Q-branch is positioned at larger Raman shifts and consists, at the present temperature, of the fundamental band –labelled as "0←1", according to the change in its only vibrational number–, and the first two hot bands. The signal-to-noise ratio (SNR) of the single-shot spectra acquired at this flame condition is measured to be ~48, employing full-vertical binning and a factor of 2 horizontal binning (effective pixel width of 11 µm) as the acquisition mode. A sample of one thousand single-shot spectra, acquired in these flame conditions, is fitted to the theoretical models discussed in the previous section to extract the temperature and the relative O_2/CO_2 concentration. The temperature assessed from the CO_2 spectrum is 1921 K with a standard deviation of 27 K, which, compared to the adiabatic flame temperature (1951 K), result in an accuracy of −1.5% and a single-shot precision of 1.4%. The O_2 thermometry yields an average temperature of 1749 K, with a standard deviation of 81 K, corresponding to an accuracy of −11.6% and a single-shot precision of 4.7%. The relative O_2/CO_2 concentration is measured to be 0.66, with a standard deviation of 0.03: the corresponding accuracy and precision are thus assessed to 33.0% and 4.1%, respectively. A significant bias in the measured relative O_2/CO_2 concentration is reported at all flame conditions: this issue is addressed more in the details in Section 4.3.

While single-shot detection of the CSRS signal is possible in all the flame conditions tested in the present work, the SNR is severely affected by the increased temperature, resulting in SNR~3 at φ=1.05. In order to assess the performance of the time-domain CSRS model at temperatures higher than 2000 K, 40 flame spec-

Table 1
Comparison of the CARS thermometry performed on the ro-vibrational Q-branch spectra of the CO_2 and O_2 molecules in the products of the laminar premixed CH_4/air flame, for the different values of the equivalence ratio. For φ>0.84 the O_2 CSRS signal is too weak to provide a reliable estimation of the gas temperature. The results of ro-vibrational thermometry performed on the 40-shot averaged ro-vibrational CSRS spectra of O_2 and CO_2, are compared to the adiabatic flame temperature and the results of pure-rotational thermometry performed on the single-shot pure-rotational CARS spectra of O_2 and N_2.

Equivalence ratio φ	Adiabatic flame temperature $T_{ad.}$	Pure-rotational N_2-O_2 thermometry			Ro-vibrational CO_2 thermometry			Ro-vibrational O_2 thermometry		
		$T_{avg.}$	$(T_{avg.}-T_{ad.})/ T_{avg.}$	σ_T / $T_{avg.}$	$T_{avg.}$	$(T_{avg.}-T_{ad.})/ T_{avg.}$	σ_T / $T_{avg.}$	$T_{avg.}$	$(T_{avg.}-T_{ad.})/ T_{avg.}$	σ_T / $T_{avg.}$
[-]	[K]	[K]	[%]	[%]	[K]	[%]	[%]	[K]	[%]	[%]
0.60	1669	1622	−2.9	0.4	1619	−3.1	1.5	1636	−2.0	2.0
0.66	1775	1783	+0.5	0.4	1711	−3.7	1.2	1711	−3.7	1.0
0.77	1951	1909	−2.2	0.3	1836	−6.3	1.1	1787	−9.1	1.5
0.84	2059	2019	−2.0	0.4	1939	−6.2	1.1	2045	−0.7	5.4
0.93	2167	2086	−3.9	0.4	2081	−4.1	0.8	–	–	–
1.05	2226	2132	−4.4	0.5	2113	−5.3	0.7	–	–	–

Table 2
Comparison of the CARS relative concentration measurements performed on the ro-vibrational Q-branch spectra of the CO_2 and O_2 molecules in the product of the laminar premixed CH_4/air flame, for the different values of the equivalence ratio. The relative O_2/CO_2 concentrations assessed from the 40-shot averaged ro-vibrational CSRS spectra of O_2 and CO_2 are compared to the values predicted by a one-dimensional laminar flame code [72].

Equivalence ratio φ	Relative O_2/CO_2 concentration $X_{O_2-CO_2}$	Relative O_2/CO_2 CARS measurements		
		$X_{O_2-CO_2}$	ΔX / $X_{O_2-CO_2}$	σ_X / $X_{O_2-CO_2}$
[-]	[-]	[-]	[%]	[%]
0.60	0.97	1.56	+61.2	5.9
0.66	0.75	1.16	+54.4	5.4
0.77	0.44	0.79	+79.9	3.5
0.84	0.28	0.38	+32.9	2.1
0.93	0.13	–	–	–
1.05	0.02	–	–	–

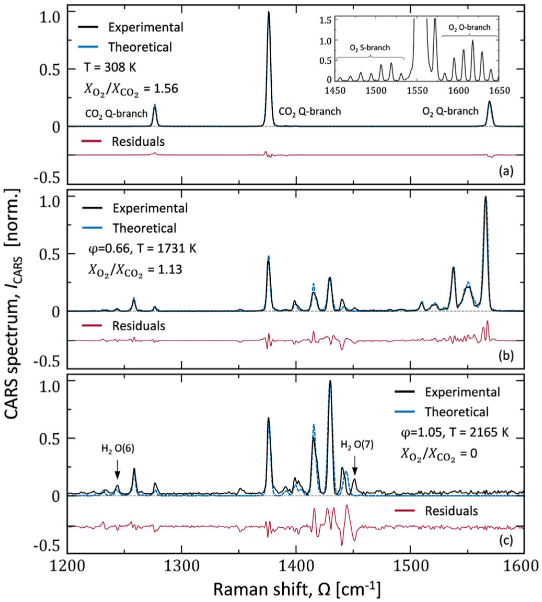

Fig. 7. (a) Single-shot ro-vibrational CO_2 and O_2 CSRS spectra acquired, in the spectral range 1200–1600 cm^{-1}, in a room-temperature CO_2/air mixture (9%–91%). The O_2 CSRS signal is dominated by the Q-branch spectrum, centred at ~1556 cm^{-1}; the CO_2 Q-branch spectrum is represented, at this temperature, by the sole Fermi dyad at 1285 cm^{-1} and 1388 cm^{-1}. The inset shows the ro-vibrational O- and S-branch spectra of O_2, these are two orders of magnitude weaker than the ro-vibrational Q-branch spectrum. (b) 40-shot averaged ro-vibrational CO_2 and O_2 CSRS spectra acquired in the hot product gases of a laminar premixed CH_4/air flame at φ=0.66. (c) 40-shot averaged ro-vibrational CO_2 and O_2 CSRS spectra acquired in the hot product gases of a laminar premixed CH_4/air flame at φ=1.05.

tra are averaged so as to guarantee a sufficient signal level over the whole set of experimental conditions. Therefore, 40-shot averaged spectra are presented in Fig. 7 and employed to assess the ro-vibrational thermometry and relative concentration measurements in Tables 1 and 2, respectively.

Figure 7(a) shows a single-shot ro-vibrational CSRS spectrum acquired in a room-temperature (295 K) air/CO_2 mixture (9%–91%); Fig. 7(b) and (c) show 40-shot averaged CSRS spectra acquired in the product gases of the flame for φ = 0.66 and 1.05, respectively: for better clarity the absolute value of the Raman shift is given on the abscissa. Comparing the Raman spectra in the progression from Fig. 7(a) to Fig. 7(c), one should notice the combined effect of the temperature increment and of the variation in the relative O_2/CO_2 concentrations. At room temperature, only the ground vibrational states of the CO_2 and O_2 molecules are significantly populated so that only one vibrational band can be identified in the resulting Q-branch CSRS spectra. The inset in Fig. 7(a) shows the ro-vibrational O- and S-branch spectra of O_2 detected on the sides of the ro-vibrational Q-branch spectrum. As the corresponding transitions are only due to the anisotropic polarizability of the molecule, as shown in Eq. (5), the ro-vibrational O- and S-branch spectra are two orders of magnitude weaker than the Q-branch spectrum. The O_2 Q-branch spectra in Fig. 7(a) and (b) show a clear temperature dependence as higher vibrational energy states become populated in the Boltzmann distribution, and the corresponding spectral bands appear at lower Raman shifts with respect to the fundamental band centred at ~1556 cm^{-1}. An even stronger temperature dependence is shown by the CO_2 Q-branch spectrum, where the energy states corresponding to all the normal vibrational modes become populated at high temperature: this behaviour is reflected in a number of vibrational spectral bands appearing in both the red and blue Q-branch spectra. At slightly fuel-rich conditions (φ=1.05), O_2 is completely consumed in the chemical reaction and is absent from the CSRS spectra acquired in the flame products; on the other hand, the spectral signature of molecular hydrogen (H_2) appears as a strong spectral line, corresponding to O(7) at ~1447 cm^{-1}, and a much weaker line at 1246 cm^{-1}, corresponding to O(6) [71]. As shown in Fig. 7(c), these lines are overlapped to the CO_2 Q-branch spectrum and skew the experimental spectrum with respect to the synthetic one. This is particularly evident for the O(7) line being approximately stronger than O(6), as the nuclear spin degeneracy of H_2 is respectively 1 and 3 for even and odd values of *J*; this line was therefore excluded by the spectral fitting routine. The comparison of the experimental and synthetic spectra presented in Fig. 7 moreover shows a mismatch in correspondence of the second and fourth hot bands of the CO_2 blue Q-branch spectrum: this is attributed to the uncertainty in the experimental and computed line positions and transition dipole moments for higher vibrational bands found in the literature, resulting in a different beating pattern between the underlying ro-vibrational transitions.

4.2. Ro-vibrational coherent Raman thermometry

In the present work, CO_2 is employed as the main thermometric species as, being one of the main combustion products, it is present in the hot flue gases in significant concentrations for any equivalence ratio employed in the experiment. The time-domain CO_2 CSRS code was validated by performing coherent Raman thermometry on a sample of one thousand Raman spectra acquired in a room-temperature CO_2/air mixture: the average temperature was estimated to 308 K with a standard deviation of 12 K, resulting in a measurement accuracy of 2.7% and precision of 4.0%.

The relatively low accuracy of the low-temperature ro-vibrational CO_2 thermometry is not surprising as only two lines, corresponding to the Fermi dyad of the fundamental vibrational band, are available for the spectral fitting. In the flame experiment, on the other hand, the CSRS spectra are dominated by a number of spectral lines, corresponding to the ro-vibrational transitions between the many vibrational energy states populated at higher temperatures. Table 1 presents the results of ro-vibrational CO_2 thermometry performed at the six values of the equivalence ratio employed in the experiment: a sample of one thousand CSRS spectra was acquired at each flame condition. The experimental results are validated by the comparison to both the adiabatic flame temperatures and to the temperatures measured by pure-rotational CARS thermometry. The adiabatic flame temperature is predicted for the different values of equivalence ratio by a one-dimensional laminar flame code (CHEM1D [72]), while the single-shot CARS measurements were performed on the pure-rotational spectra of N_2 and O_2 in the spectral region 0–400 cm^{-1} according to [16]. Ro-vibrational CO_2 thermometry shows a reasonable agreement with pure-rotational N_2-O_2 thermometry and with the expected flame temperature: depending on the equivalence ratio considered, the agreement between the pure-rotational N_2-O_2 and ro-vibrational CO_2 thermometry varies between 0.2% (for φ=0.60 and 0.93) and 4% (for φ=0.84). When compared to the adiabatic flame temperature, the accuracy of CO_2 thermometry, quantified in terms of the systematic bias of the experimental temperature, varies between 3.1% (for φ=0.60) and 6.3% (for φ=0.77 and 0.84). These values are in line with those computed for the corresponding RCARS measurements at the same flame conditions, yielding a systematic bias between 0.5% (for φ=0.66) and 4.4% (for φ=1.05). As far as the precision of ro-vibrational CO_2 thermometry is concerned, it is interesting to point out how the relative standard deviation (σ_T/T_{avg}) of the temperature measurements decreases for increasing equivalence ratios and flame temperatures. The corresponding thermometric precision is improved from 1.5% (for φ=0.60) to 0.7% (for φ=1.05). This result is in contrast with the most commonly reported CARS measurements, where in general the precision is negatively impacted by the increasing temperature, which determines a reduction in the number density of the scattering species and, consequently, a degrading SNR [73,74]: indeed, this the case for ro-vibrational CO_2 thermometry as well. At higher equivalence ratio, on the other hand, CO_2 thermometry benefits both from the increased CO_2 concentration and from the much richer ro-vibrational spectrum with pronounced hot bands, resulting in a more robust temperature assessment.

Furthermore, for values of the equivalence ratio below 0.84, the concentration of excess oxygen in the hot products is large enough to experimentally detect the O_2 CSRS signal with a signal-to-noise ratio greater than ~3. As shown in Fig. 7(b), at high temperature the O_2 Q-branch spectrum presents a number of vibrational bands: alongside the fundamental band at ~1556 cm^{-1}, the second and third vibrational hot bands can be identified at ~1532 and ~1509 cm^{-1} [23], respectively. Due to the limited spectral resolution, each vibrational band appears as two distinct peaks in the experimental spectrum (see Supplementary Figure S2). The comparison between the temperature measurements performed on the CO_2 and O_2 CSRS spectra is provided in Table 1, for values of the equivalence ratio up to 0.84. Ro-vibrational thermometry was performed by two independent contour-fitting routines on the ro-vibrational O_2 and CO_2 spectra acquired simultaneously in the 1200–1600 cm^{-1} spectral region. The good agreement of the temperatures measured by independently fitting the spectra of the two chemicals thus provides an additional mean of validation for the time-domain CARS code developed in the present work. As a matter of fact, ro-vibrational CO_2 and O_2 thermometry agree to within 2.7% of the measured temperature for all the considered equivalence ratios, with the only exception of φ=0.84, where the two temperature measurements diverge by 5.5%. At this latter flame condition, the O_2 signal is significantly affected by the reduction in O_2 concentration (SNR~3), as attested by the reduced precision of the corresponding thermometry (5.4%).

4.3. Relative O_2/CO_2 concentration measurements

The relative O_2/CO_2 concentrations in the flue gases of the hydrocarbon flame can be measured by comparing the spectral signatures of the O_2 and CO_2 molecules in the experimental CSRS spectra. A contour-fitting routine is employed to compare the experimental ro-vibrational O_2-CO_2 spectra to a library of synthetic spectra, computed for relative O_2/CO_2 concentrations ranging from 0 to 4, in steps of 0.1. As mentioned in the previous paragraph, in the flame experiment the O_2 spectrum is only detected with a reasonable SNR up to φ=0.84, so that the relative O_2/CO_2 concentrations can be measured for four lean flame conditions. Table 2 summarises the experimental relative O_2/CO_2 concentrations measured from the ro-vibrational Raman spectra, at the different flame conditions. As expected, the relative oxygen content in the product of the premixed laminar flame is reduced for increasing values of the equivalence ratio up to 0.84: for the richer flame conditions tested (φ=0.93, 1.05) the ro-vibrational O_2 spectrum was, respectively, too weak to perform quantitative measurements on it and not detected altogether. When compared to the expected relative concentrations, the experimental measurements result in a significant overestimation of the oxygen content relative to carbon dioxide.

One of the possible reasons for this measurement bias is identified in the spectral referencing of the ro-vibrational O_2-CO_2 spectra, performed by subdividing the experimental resonant spectra by the spectrum of the NR CSRS signal, generated in a gas with no ro-vibrational degree of freedom (i.e. argon), which maps the excitation efficiency at different Raman shifts. As it propagates through different optical media, the ultrabroadband pump/Stokes pulse can be affected by changes in the group velocity dispersion [75], resulting in temporal chirp, which limits the bandwidth effective excitation efficiency at the measurement location [76–80]. In addition, the self-phase modulation experienced by the pulse during the pulse propagation in the filament –being a third-order nonlinear optical process– depends on the composition and temperature of the gas-phase medium. It is, therefore, possible that the NR CSRS signal acquired *ex-situ*, in argon, does not perfectly map the ultrabroadband excitation efficiency, when this is generated *in-situ*. This would have a negligible effect on ro-vibrational thermometry, as the ro-vibrational O_2 and the “blue” CO_2 Q-branch spectra span less than 60 cm^{-1} at high temperatures. An imperfect spectral referencing, on the other hand, could significantly affect the relative intensity of the ro-vibrational spectra of the two species and, thus, the relative O_2/CO_2 concentration measurements.

5. Conclusions and outlook

We have demonstrated ultrabroadband two-beam fs/ps coherent Raman spectroscopy for simultaneous O_2-CO_2 thermometry and relative concentration measurements, employing fs-laser-induced filamentation for the supercontinuum generation. The 35 fs duration output of a regenerative Ti:Sapphire amplifier system, with 1.6 mJ/pulse, is focused to the measurement location so as to induce Kerr effect in the gas-phase medium resulting in the beam self-focusing and the generation of a plasma filament. While travelling inside this filament the pulse experiences self-phase modulation and temporal compression resulting in the generation of a compressed supercontinuum. The pulse energy conversion efficiency in the filamentation process is constant over the whole range of input pulse energy measured, and it only slightly depends on the temperature and composition of the gas-phase medium: in the hot products of a CH_4/air flame the conversion efficiency was measured to be ~86%, as compared to the ~82% efficiency measured in air. The resulting ~24 fs duration output of the filament is thus employed as the pump/Stokes pulse in a two-beam fs/ps CARS setup: the bandwidth of the pulse is sufficient to impulsively excite the ro-vibrational coherences of the Raman-active molecules up to 1600 cm^{-1}. The use of the fs-laser-induced filament as the supercontinuum source thus allows for the practical implementation of ultrabroadband coherent Raman spectroscopy with a single regenerative laser amplifier. Furthermore, the *in-situ* generation and *in-situ* use of the filament can pave the way to the application of ultrabroadband CARS spectroscopy in combustion scenarios where the pulse needs to be transmitted through thick optical windows, which severely limit the effective excitation bandwidth delivered by broadband pulses generated *ex-situ* [81]. The demonstration of coherent Raman spectroscopy with ultrabroadband femtosecond laser excitation generated *in-situ* behind thick optical ports, and the characterization of its performance for thermometry and relative species concentration measurements represents the next step in our research on this topic.

A time-domain model for the ro-vibrational O_2 and CO_2 CSRS signal has been developed, in order to fit the experimental spectra and extract temperatures and relative O_2/CO_2 concentrations. The time-domain modelling of the CO_2 spectrum, in particular, employs recently available comprehensive calculations of the polarizability transition moments for Raman transitions in the range 1150–1500 cm^{-1} [57]. The availability of these data allows for up to 180 vibrational bands to be included in the time-domain simulation of the CSRS signal. In order to validate this spectral model, and demonstrate simultaneous ro-vibrational thermometry and relative concentration measurements on the ro-vibrational O_2 and CO_2 spectra, filament-based ultrabroadband coherent Raman spectroscopy was successfully employed in the product gases of a laminar premixed methane/air flame. The flame measurements are performed on a Bunsen burner, at six different values of the equivalence ratio, from 0.6 to 1.05. The experimental spectra are acquired on the Stokes side (CSRS), rather than on the anti-Stokes one (CARS), owing to the larger excitation efficiency provided on the Stokes side by the ultrabroadband pump/Stokes pulse generated *in-situ*. Single-shot detection of the ro-vibrational O_2 and CO_2 spectra is demonstrated in all of the flame conditions tested; nevertheless, the signal rapidly degrades with the temperature increment, significantly reducing the single-to-noise-ratio. This fact limits the applicability of the proposed diagnostic technique to high temperatures: such a limitation could be overcome by increasing the energy content of the probe pulse or by employing a separate high-power ps laser source. In addition, the signal detection could be improved by employing a more sensitive CCD detector, instead of the sCMOS one currently in use in our set-up. In order to guarantee a sufficient SNR to validate the spectral model at temperatures higher than 2000 K, in the present work, the CSRS spectra acquired in the flame are therefore averaged over 40 laser-shots.

The ro-vibrational temperature is independently measured by fitting the ro-vibrational spectra of the two species –ranging 1480–1560 cm^{-1} for O_2 and 1375–1450 cm^{-1} for the CO_2 “blue” dyad–to distinct spectral libraries: the experimental results show a good agreement between O_2 and CO_2 thermometry. The measured temperatures are moreover validated by comparison to the adiabatic flame temperature and by performing pure-rotational N_2-O_2 CARS thermometry at the same flame conditions: ro-vibrational CO_2 thermometry presents an accuracy of −5.3% and a precision of 0.7% at 2200 K. The relatively complex vibrational energy structure of the CO_2 molecule results in the high temperature sensitivity of its ro-vibrational Raman spectrum. In this respect, possible refinements of the position and strength of its ro-vibrational spectral lines could further improve CO_2 vibrational thermometry at temperatures higher than 2000 K. Simultaneously to thermometry, relative O_2/CO_2 concentration measurements are performed by comparing the relative intensity of the ro-vibrational spectra of the two species. When employed to measure the relative concentrations in the flame products, this technique results in a significant overestimation of the oxygen content, relative to carbon dioxide. We speculate that this mismatch can be attributed, at least in part, to the *ex-situ* spectral referencing of the ultrabroadband femtosecond laser excitation generated *in-situ*.

In conclusion, the present work represents a further step towards quantitative ultrabroadband fs/ps coherent Raman spectroscopy in the molecular fingerprint region, for simultaneous thermometry and relative concentration measurements in chemically-reacting flows. We are currently pursuing the development and validation of time-domain models of the ro-vibrational Raman spectra of major species for combustion diagnostics, such as CH_4 [82] and H_2.

Declaration of Competing Interest

The authors declare that they have no known competing financial interests or personal relationships that could have appeared to influence the work reported in this paper.

Acknowledgments

We gratefully acknowledge the financial support provided by the Netherlands Organization for Scientific Research (NWO), obtained through a Vidi grant in the Applied and Engineering Sciences domain (AES) (15690). In addition, A. Bohlin is thankful for support through the RIT project/European Regional Development Fond. We thank Dr. Michele Marrocco for his valuable comments on the application of the time-domain CARS model to CSRS spectra, and M.Sc. thesis student Aert Stutvoet for technical assistance in the experiments.

Supplementary materials

Supplementary material associated with this article can be found, in the online version, at doi:10.1016/j.combustflame.2021.111738.

References

[1] J.B. Zheng, A. Leipertz, J.B. Snow, R.K. Chang, Simultaneous observation of rotational coherent Stokes Raman scattering and coherent anti-Stokes Raman scattering in air and nitrogen, Opt. Lett. 8 (7) (1983) 350–352.

[2] A.C. Eckbreth, T.J. Anderson, Simultaneous rotational coherent anti-Stokes Raman spectroscopy and coherent Stokes Raman spectroscopy with arbitrary pump-Stokes spectral separation, Opt. Lett. 11 (8) (1986) 496–498.

[3] A.C. Eckbreth, Laser Diagnostics For Combustion Temperature and Species, Second Edi, Gordon and Breach Publishers, 1996.

[4] W.R. Lempert, I.V. Adamovich, Coherent anti-Stokes Raman scattering and spontaneous Raman scattering diagnostics of nonequilibrium plasmas and flows, J. Phys. D. Appl. Phys. 47 (2014) 433001.

[5] F. Moya, S.A.J. Druet, J.P.E. Taran, Gas spectroscopy and temperature measurement by coherent Raman anti-stokes scattering, Opt. Commun. 13 (2) (1975) 169–174.

[6] A.C. Eckbreth, CARS thermometry in practical combustors, Combust. Flame 39 (2) (1980) 133–147.

[7] T. Seeger, A. Leipertz, Experimental comparison of single-shot broadband vibrational and dual-broadband pure rotational coherent anti-Stokes Raman scattering in hot air, Appl. Opt. 35 (15) (1996) 2665–2671.

[8] P.R. Régnier, J.P.E. Taran, On the possibility of measuring gas concentrations by stimulated anti-Stokes scattering, Appl. Phys. Lett. 23 (5) (1973) 240–242.

[9] P.R. Régnier, F. Moya, J.P.E. Taran, Gas concentration measurement by coherent raman anti-stokes scattering, AIAA J. 12 (6) (1974) 826–831.

[10] S. Roy, J.R. Gord, A.K. Patnaik, Recent advances in coherent anti-Stokes Raman scattering spectroscopy: fundamental developments and applications in reacting flows, Prog. Energy Combust. Sci. 36 (2) (2010) 280–306.

[11] A. Bohlin, B.D. Patterson, C.J. Kliewer, Communication: simplified two-beam rotational CARS signal generation demonstrated in 1D, J. Chem. Phys. 138 (2013) 081102.

[12] M. Scherman, et al., 1-kHz hybrid femtosecond/picosecond coherent anti-Stokes Raman scattering thermometry of turbulent combustion in a representative aeronautical test rig, J. Raman Spectrosc (2021) In press.

[13] S. Legros, et al., Combustion for aircraft propulsion: progress in advanced laser-based diagnostics on high-pressure kerosene/air flames produced with low-NOx fuel injection systems, Combust. Flame 224 (2021) 273–294.

[14] R.W. Boyd, Nonlinear Optics, 3rd Ed., Academic Press Inc., 2013.

[15] D.A. Long, The Raman effect: A unified Treatment of the Theory of Raman scattering By Molecules, 1st Ed., John Wiley & Sons Ltd., 2002.

[16] L. Castellanos, F. Mazza, D. Kliukin, A. Bohlin, Pure-rotational 1D-CARS spatiotemporal thermometry with a single regenerative amplifier system, Opt. Lett. 45 (17) (2020) 4662–4665.

[17] P. Polynkin, Y. Chen, Air Lasing, 1st ed., Springer International Publishing, 2018.

[18] S. Roy, P. Wrzesinski, D. Pestov, T. Gunaratne, M. Dantus, J.R. Gord, Single-beam coherent anti-Stokes Raman scattering spectroscopy of using a shaped 7 fs laser pulse, Appl. Phys. Lett. 95 (2009) 074102.

[19] A. Bohlin, C.J. Kliewer, Two-beam ultrabroadband coherent anti-Stokes Raman spectroscopy for high resolution gas-phase multiplex imaging, Appl. Phys. Lett. 104 (2014) 031107.

[20] A. Bohlin, C.J. Kliewer, Direct Coherent Raman Temperature Imaging and Wideband Chemical Detection in a Hydrocarbon Flat Flame, J. Phys. Chem. Lett. 6 (2015) 643–649.

[21] A. Bohlin, C. Jainski, B.D. Patterson, A. Dreizler, C.J. Kliewer, Multiparameter spatio-thermochemical probing of flame-wall interactions advanced with coherent Raman imaging, Proc. Combust. Inst. 36 (3) (2017) 4557–4564.

[22] J.H. Odhner, D.A. Romanov, R.J. Levis, Rovibrational wave-packet dispersion during femtosecond laser filamentation in air, Phys. Rev. Lett. 103 (2009) 075005.

[23] G. Rouillé, G. Millot, R. Saint-Loup, H. Berger, High-resolution stimulated Raman spectroscopy of O_2, J. Mol. Spectrosc. 154 (1992) 372–382.

[24] B. Lavorel, et al., Study of collisional effects on band shapes of the $\nu_1/2\nu_2$ Fermi dyad in CO_2 gas with stimulated Raman spectroscopy. I. Rotational and vibrational relaxation in the $2\nu_2$ band, J. Chem. Phys. 174 (1994) 2176–2184 1998.

[25] T.L. Courtney, A. Bohlin, B.D. Patterson, C.J. Kliewer, Pure-rotational H_2 thermometry by ultrabroadband coherent anti-stokes Raman spectroscopy, J. Chem. Phys. 146 (2017) 224202.

[26] G. Magnotti, U. KC, P.L. Varghese, R.S. Barlow, Raman spectra of methane, ethylene, ethane, dimethyl ether, formaldehyde and propane for combustion applications, J. Quant. Spectrosc. Radiat. Transf. 163 (2015) 80–101.

[27] A. Cavaliere, M. De Joannon, Mild combustion, Prog. Energy Combust. Sci. 30 (2004) 329–366.

[28] D. Tabacco, C. Innarella, C. Bruno, Theoretical and numerical investigation in flameless combustion, Combust. Sci. Technol. 174 (7) (2002) 1–35.

[29] A.A.V. Perpignan, A.Gangoli Rao, D.J.E.M. Roekaerts, Flameless combustion and its potential towards gas turbines, Prog. Energy Combust. Sci. 69 (2018) 28–62.

[30] J.W. Tröger, C. Meißner, T. Seeger, High temperature O_2 vibrational CARS thermometry applied to a turbulent oxy-fuel combustion process, J. Raman Spectrosc. 47 (2016) 1149–1156.

[31] R.J. Hall, J.H. Stufflebeam, Quantitative CARS spectroscopy of CO_2 and N_2O, Appl. Opt. 23 (23) (1984) 4319–4327.

[32] R.P. Lucht, et al., Dual-pump coherent anti-stokes Raman scattering temperature and CO_2 concentration measurements, AIAA J. 41 (4) (2003) 679–686.

[33] S. Roy, T.R. Meyer, R.P. Lucht, V.M. Belovich, E. Corporan, J.R. Gord, Temperature and CO_2 concentration measurements in the exhaust stream of a liquid-fueled combustor using dual-pump coherent anti-Stokes Raman scattering (CARS) spectroscopy, Combust. Flame 138 (3) (2004) 273–284.

[34] M. Kerstan, I. Makos, S. Nolte, A. Tünnermann, R. Ackermann, Two-beam femtosecond coherent anti-Stokes Raman scattering for thermometry, Appl. Phys. Lett. 110 (2017) 021116.

[35] Y. Ran, M. Junghanns, A. Boden, S. Nolte, A. Tünnermann, R. Ackermann, Temperature and gas concentration measurements with vibrational ultra-broadband two-beam femtosecond/picosecond coherent anti-Stokes Raman scattering and spontaneous Raman scattering, J. Raman Spectrosc. 50 (2019) 1268–1275.

[36] R.P. Lucht, R.E. Palmer, M.A. Maris, Simultaneous acquisition of pure rotational and vibrational nitrogen spectra using three-laser coherent anti-Stokes Raman spectroscopy, Opt. Lett. 12 (6) (1987) 386–388.

[37] F. Vestin, M. Afzelius, P.E. Bengtsson, Development of rotational CARS for combustion diagnostics using a polarization approach, Proc. Combust. Inst. 31 (1) (2007) 833–840.

[38] A. Bohlin, M. Mann, B.D. Patterson, A. Dreizler, C.J. Kliewer, Development of two-beam femtosecond/picosecond one-dimensional rotational coherent anti-Stokes Raman spectroscopy: time-resolved probing of flame wall interactions, Proc. Combust. Inst 35 (3) (2015) 3723–3730.

[39] S.L. Chin, *Femtosecond Laser Filamentation*, First Edit, Springer, New York, NY, 2010.

[40] A. Mysyrowicz, A. Couairon, U. Keller, Self-compression of optical laser pulses by filamentation, New J. Phys. 10 (2008) 025023.

[41] A. Couairon, M. Franco, G. Méchain, T. Olivier, B. Prade, A. Mysyrowicz, Femtosecond filamentation in air at low pressures: part I: theory and numerical simulations, Opt. Commun. 259 (2006) 265–273.

[42] A. Couairon, et al., Self-compression of ultra-short laser pulses down to one optical cycle by filamentation, J. Mod. Opt. 53 (1–2) (2006) 75–85.

[43] M.A. Yuratich, Effects of laser linewidth on coherent antiStokes Raman spectroscopy, Mol. Phys. 38 (2) (1979) 625–655.

[44] H.U. Stauffer, et al., Time- and frequency-dependent model of time-resolved coherent anti-Stokes Raman scattering (CARS) with a picosecond-duration probe pulse, J. Chem. Phys. 140 (2014) 024316.

[45] Y. Liu, P. Ding, G. Lambert, A. Houard, V. Tikhonchuk, A. Mysyrowicz, Recollision-Induced Superradiance of Ionized Nitrogen Molecules, Phys. Rev. Lett. 115 (2015) 133203.

[46] Z. Liu, et al., Extremely nonlinear Raman interaction of an ultrashort nitrogen ion laser with an impulsively excited molecular wave packet, Phys. Rev. A 101 (2020) 043404.

[47] B.D. Prince, et al., Development of simultaneous frequency- and time-resolved coherent anti-Stokes Raman scattering for ultrafast detection of molecular Raman spectra, J. Chem. Phys 125 (2006) 044502.

[48] J.D. Miller, S. Roy, M.N. Slipchenko, J.R. Gord, T. Meyer, Single-shot gas-phase thermometry using pure-rotational hybrid femtosecond/picosecond coherent anti-Stokes Raman scattering, Opt. Express 19 (16) (2011) 15627–15640.

[49] S.P. Kearney, D.J. Scoglietti, C.J. Kliewer, Hybrid femtosecond/picosecond rotational coherent anti-Stokes Raman scattering temperature and concentration measurements using two different picosecond-duration probes, Opt. Express 21 (10) (2013) 12327–12339.

[50] T.Y. Chen, C.J. Kliewer, B.M. Goldberg, E. Kolemen, Y. Ju, Time-domain modelling and thermometry of the CH_4 ν_1 Q-branch using hybrid femtosecond/picosecond coherent anti-Stokes Raman scattering, Combust. Flame 224 (2021) 183–195.

[51] K. Bito, M. Okuno, H. Kano, P. Leproux, V. Couderc, H. Hamaguchi, Three--pulse multiplex coherent anti-Stokes/Stokes Raman scattering (CARS/CSRS) microspectroscopy using a white-light laser source, Chem. Phys. 419 (2013) 156–162.

[52] P.V. Kolesnichenko, J.O. Tollerud, J.A. Davis, Background-free time-resolved coherent Raman spectroscopy (CSRS and CARS): heterodyne detection of low-energy vibrations and identification of excited-state contributions, APL Photonics 4 (2019) 056102.

[53] G. Herzberg, Molecular Spectra and Molecular Structure, II. Infrared and Raman Spectra of Polyatomic Molecules, First Edit. D. Van Nostrand Company Inc, 1945.

[54] P.F. Bernath, *Spectra of Atoms and Molecules*, Second Edi, Oxford University Press Inc., 2005.

[55] M. Basire, et al., Fermi resonance in CO_2: mode assignment and quantum nuclear effects from first principles molecular dynamics, J. Chem. Phys. 146 (2017) 134102.

[56] L.S. Rothman, R.L. Hawkins, R.B. Wattson, R.R. Gamache, Energy levels, intensities, and linewidths of atmospheric carbon dioxide bands, J. Quant. Spectrosc. Radiat. Transf 48 (5–6) (1992) 537–566.

[57] R. Lemus, M. Sánchez-Castellanos, F. Pérez-Bernal, J.M. Fernández, M. Carvajal, Simulation of the Raman spectra of CO_2: bridging the gap between algebraic models and experimental spectra, J. Chem. Phys 141 (2014) 054306.

[58] G. Tejeda, B. Maté, S. Montero, Overtone Raman spectrum and molecular polarizability surface of CO_2, J. Chem. Phys. 103 (2) (1995) 568–576.

[59] M. Gu, A. Satija, R.P. Lucht, CO_2 chirped-probe-pulse femtosecond CARS thermometry, Proc. Combust. Inst. 38 (1) (2021) 1599–1606.

[60] C.M. Penney, L.M. Goldman, M. Lapp, Raman Scattering Cross Sections, Nat. Phys. Sci. 235 (1972) 110–112.

[61] L.A. Rahn, R.E. Palmer, Studies of nitrogen self-broadening at high temperature with inverse Raman spectroscopy, J. Opt. Soc. Am. B 3 (9) (1986) 1164–1169.

[62] L. Rosenmann, J.M. Hartmann, M.Y. Perrin, J. Taine, Accurate calculated tabulations of IR and Raman CO_2 line broadening by CO_2, H_2O, N_2, O_2 in the 300-2400-K temperature range, Appl. Opt 27 (18) (1988) 3902–3907.

[63] V.G. Arakcheev, et al., Collisionally induced dephasing and rotational energy transfer in the CO_2 Fermi dyad 'red' Q-branch 1285 cm^{-1}, J. Raman Spectrosc. 38 (2007) 1038–1045.

[64] V.G. Arakcheev, et al., Collisionally induced dephasing and rotational energy transfer in the CO_2 Fermi dyad 'blue' Q-branch 1388 cm^{-1}, J. Raman Spectrosc. 38 (2007) 1046–1051.

[65] L. Martinsson, P.-E. Bengtsson, M. Aldén, Oxygen concentration and temperature measurements in N_2-O_2 mixtures using rotational coherent anti-Stokes Raman spectroscopy, Appl. Phys. B Lasers Opt. 62 (1996) 29–37.

[66] J.I. Hölzer, C. Meißner, T. Seeger, Oxygen rotational Raman linewidth determination considering nonmonoexponential decoherence behavior, J. Raman Spectrosc. 50 (2019) 1260–1267.

[67] T.L. Courtney, C.J. Kliewer, Rotational coherence beating in molecular oxygen: coupling between electronic spin and nuclear angular momenta, J. Chem. Phys. 149 (2018) 234201.

[68] M.A. Buldakov, V.N. Cherepanov, B.V. Korolev, I.I. Matrosov, Role of intramolecular interactions in Raman spectra of N_2 and O_2 molecules, J. Mol. Spectrosc. 217 (1) (2003) 1–8.

[69] G. Millot, R. Saint-Loup, J. Santos, R. Chaux, H. Berger, J. Bonamy, Collisional effects in the stimulated Raman Q-branch of O_2 and O_2-N_2," *J*, Chem. Phys 96 (2) (2011) 961–971.

[70] A.E. DePristo, S.D. Augustin, R. Ramaswamy, H. Rabitz, Quantum number and energy scaling for nonreactive collisions, J. Chem. Phys. 71 (2) (1979) 850–865.

[71] D.K. Veirs, G.M. Rosenblatt, Raman line positions in molecular hydrogen: H_2, HD, HT, D_2, DT, and T_2,, J. Mol. Spectrosc. 121 (2) (1987) 401–419.

[72] J.A. van Oijen, L.P.H. de Goey, Modelling of premixed laminar flames using flamelet-generated manifolds, Combust. Sci. Technol. 161 (1) (2000) 113–137.
[73] S.P. Kearney, Hybrid fs/ps rotational CARS temperature and oxygen measurements in the product gases of canonical flat flames, Combust. Flame 162 (5) (2014) 1748–1758.
[74] D.R. Richardson, H.U. Stauffer, S. Roy, J.R. Gord, Comparison of chirped-probe-pulse and hybrid femtosecond/picosecond coherent anti-Stokes Raman scattering for combustion thermometry, Appl. Opt. 56 (11) (2017) 37–49.
[75] P.J. Wrzesinski, D. Pestov, V.V. Lozovoy, J.R. Gord, S. Roy, Group-velocity-dispersion measurements of atmospheric and combustion-related gases using an ultrabroadband-laser source, Opt. Express 19 (6) (2011) 8394–8401.
[76] M. Gu, A. Satija, R.P. Lucht, Impact of moderate pump/Stokes chirp on femtosecond coherent anti-Stokes Raman scattering spectra, J. Raman Spectrosc. 51 (2020) 115–124.
[77] F. Mazza, L. Castellanos, D. Kliukin, A. Bohlin, Coherent Raman imaging thermometry with *in-situ* referencing of the impulsive excitation efficiency, Proc. Combust. Inst 38 (1) (2021) 1895–1904.
[78] J.-.L. Oudar, Y.R. Shen, Nonlinear spectroscopy by multiresonant four-wave mixing, Phys. Rev. A 22 (3) (1980) 1141–1158.
[79] R.L. Farrow, P.L. Mattern, L.A. Rahn, Comparison between CARS and corrected thermocouple temperature measurements in a diffusion flame, Appl. Opt. 21 (17) (1982) 3119–3125.
[80] R.L. Farrow, R.P. Lucht, G.L. Clark, R.E. Palmer, Species concentration measurements using CARS with nonresonant susceptibility normalization, Appl. Opt 24 (14) (1985) 2241–2251.
[81] S.P. Kearney, Bandwidth optimization of femtosecond pure-rotational coherent anti-Stokes Raman scattering by pump/Stokes spectral focusing, Appl. Opt 53 (28) (2014) 6579–6585.
[82] T.D. Butterworth, B. Amyay, T. Minea, N. Gatti, Q. Ong, Quantifying methane vibrational and rotational temperature with Raman scattering, J. Quant. Spectrosc. Radiat. Transf 236 (2019) 106562.

High-temperature rotational-vibrational O_2-CO_2 coherent Raman spectroscopy with ultrabroadband femtosecond laser excitation generated *in-situ*

Francesco Mazza*, Nathan Griffioen, Leonardo Castellanos, Dmitrii Kliukin, and Alexis Bohlin

Faculty of Aerospace Engineering, Delft University of Technology, Kluyverweg 1, 2629 HS Delft, The Netherlands
*Corresponding Author: f.mazza@tudelft.nl

Supplementary Figures

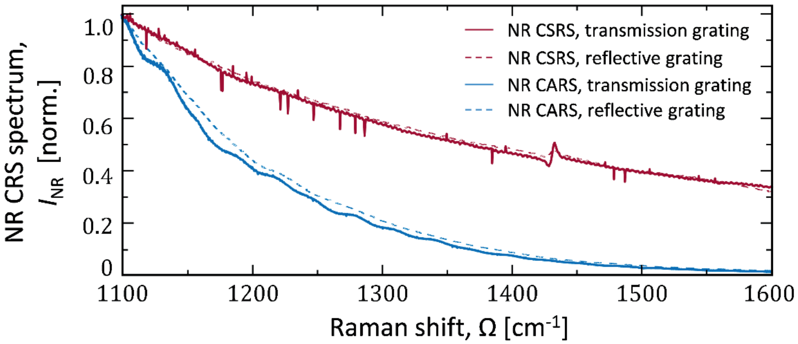

Fig. S1 Spectra of the non-resonant CARS and CSRS signals recorded in argon in the spectral region 1100-1600 cm^{-1}. Two different diffraction gratings were tested: a high-resolution transmission grating (3040 lines/mm), and a ruled reflective grating (1200 lines/mm).

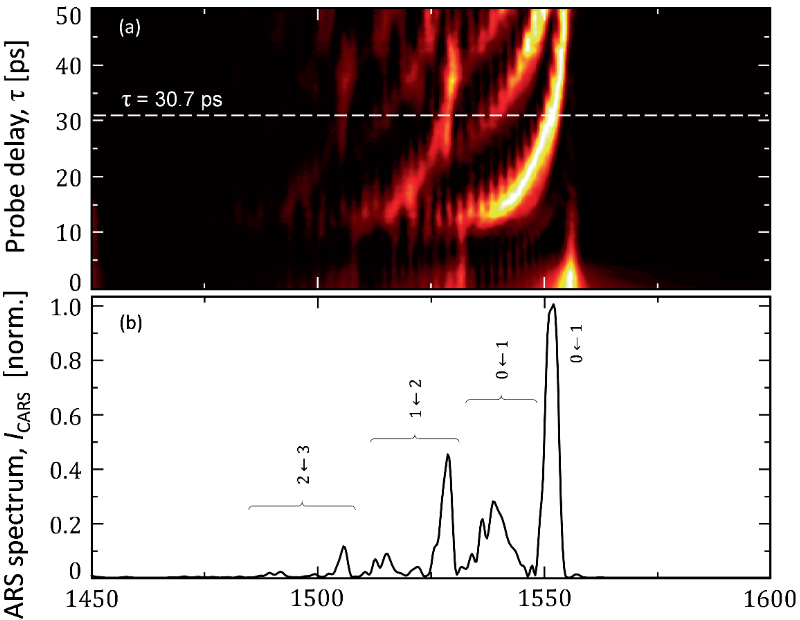

Fig. S2 (a) Spectrochronogram of the O$_2$ ro-vibrational Q-branch spectrum, simulated by the time-domain CSRS code for an input temperature of 1800 K and an experimental probe duration measured to be 6.6 ps. The simulated fs/ps O$_2$ CSRS spectrum is affected by a severe beating, due to the unresolved transitions between the many ro-vibrational energy states populated at flame temperature. (b) O$_2$ Q-branch spectrum simulated for a probe delay of 30.7 ps. Labels are employed to identify the fundamental vibrational band 0←1 at ~1556 cm^{-1}, and the first two hot bands 1←2 and 2←3, at ~1532 cm^{-1} and 1509 cm^{-1}, respectively.

Available online at www.sciencedirect.com

ScienceDirect

Proceedings of the Combustion Institute 38 (2021) 1895–1904

Proceedings of the Combustion Institute

www.elsevier.com/locate/proci

Coherent Raman imaging thermometry with *in-situ* referencing of the impulsive excitation efficiency

Francesco Mazza, Leonardo Castellanos, Dmitrii Kliukin, Alexis Bohlin*

Faculty of Aerospace Engineering, Delft University of Technology, Kluyverweg 1, 2629 HS Delft, the Netherlands

Received 7 November 2019; accepted 28 June 2020
Available online 14 October 2020

Abstract

Simultaneous detection of resonant and non-resonant femtosecond/picosecond coherent anti-Stokes Raman spectroscopy (CARS) signals has been developed as a viable technique to provide *in-situ* referencing of the impulsive excitation efficiency for temperature assessments in flames. In the framework of CARS thermometry, the occurrence of both a resonant and a non-resonant contribution to the third-order susceptibility is well known. While the resonant part conceives the useful spectral information for deriving temperature and species concentrations in the probed volume, the non-resonant part is often disregarded. It nonetheless serves the CARS technique as an essential reference to map the finite bandwidth of the laser excitation fields and the transmission characteristics of the signal along the detection path. Hence, the standard protocols for CARS flame measurements include the time-averaged recording of the non-resonant signal, to be performed sequentially to the experiment. In the present work we present the successful single-shot recordings of both the resonant and non-resonant CARS signals, split on the same detector frame, realizing the *in-situ* referencing of the impulsive excitation efficiency. We demonstrate the use of this technique on one-dimensional CARS imaging spectra, acquired across the flame front of a laminar premixed methane/air flame. The effect of pulse dispersion on the laser excitation fields, while propagating in the participating medium, is proved to result, if not accounted for, in an ~1.3% systematic bias of the CARS-evaluated temperature in the oxidation region of the flame.

Keywords: Gas-phase thermometry; CARS; Femtosecond laser excitation; Non-linear optical spectroscopy; Combustion diagnostics

---

1. Introduction

Laser diagnostics is an important tool in the effort to develop clean combustion technologies, which is on the agenda for the propulsion and power industry, in-line with the current energy transition. These optical techniques have the ability to realize non-intrusive measurements *in-situ,* and to provide scalar information (e.g. temperature and species) with excellent spatial and temporal resolution. Laser diagnostics has been successfully employed over the years in multiple energy and combustion science applications where high-fidelity data are needed [1,2], e.g. by providing direct obser-

---

* Corresponding author.
E-mail address: g.a.bohlin@tudelft.nl (A. Bohlin).

https://doi.org/10.1016/j.proci.2020.06.360
1540-7489

vations and validating results from predictive engineering combustion models.

Coherent anti-Stokes Raman spectroscopy (CARS) is a versatile technique for assessing temperature and species concentrations in flames. It is unparalleled in the level of accuracy and precision it can provide, and the strong “laser-like” signal, which can be remotely detected, makes it well-suited for the application in extremely harsh and luminous environments such as combustion flows [3–5]. The conventional setup for CARS is based on nanosecond pulses; however, many variants exist, in which the inaccuracy and precision are technique-specific and need to be quantified respective to the measurement environment (e.g. nanosecond CARS thermometry has an approximate inaccuracy of ~2–3%, and a single-shot imprecision of ~4–5% [6,7]). In air-fed flames, the temperature sensitivity arises from the relative strength of the N_2 spectral lines. The spectrum uncovers the Boltzmann distribution (in principle) over the entire manifold of molecular rotational-vibrational states in the thermal ensemble. The retrieval of the quantitative temperature information from a CARS experiment is enabled by the combination of unobstructed detection of the spectrum and adequate spectroscopic modelling: the recorded data is evaluated using a goodness-of-fit routine [8].

The uncertainty in the CARS-evaluated temperature is related to critical parameters leading to either systematic (inaccuracy) or stochastic (imprecision) deviation from the true temperature. Much effort has been spent in quantifying the overall accuracy of the technique and limiting the impact of uncertainties originating e.g. from pressure broadening (Raman linewidths) [9], from the vibrational-rotational matrix-elements (Herman–Wallis factor) [10], and from the mode-amplitude and phase-mode fluctuations on the broadband laser emission profiles [11,12]. The influence of the uncertainty originating from the non-resonant susceptibility has also been investigated [13], although most of the effort in dealing with this parameter in CARS thermometry has been spent on the spectral fitting routine. This is partly because the total non-resonant susceptibility depends not only on the active molecule (e.g. N_2), but also on contributions from the background species [14,15]. A perfectly validated theoretical value of the non-resonant susceptibility, to be included in the spectral fitting routine, would then require the complete experimental retrieval of the chemical composition of the sample. The relative strength of the resonant and non-resonant CARS susceptibility is not only relevant for thermometry, but has been commonly employed for extracting species concentrations as well. This technique is particularly interesting for detecting water vapour [16,17], which is a recognized challenge for CARS diagnostics because of the relatively low Raman cross-section of the H_2O molecule [18].

The implementation of time-resolved CARS allows for reducing the impact of many of the aforementioned sources of uncertainty [19–21]. With “time-resolved CARS probing” we refer not only to the freezing of the energy-containing scale in the combustion flow, but also to the fact that the probing time is well within the characteristic molecular response time (dephasing). This temporal window for probing combustion-relevant species is usually on a picosecond timescale, the relatively long dephasing time of hydrogen being an exception [22]. On this short timescale the impact on the CARS spectrum of the Raman linewidths is small. Also the mode-amplitude and phase-mode fluctuations, affecting the emission profile of the broadband laser, are significantly reduced by using a near transform-limited femtosecond laser pulse, as compared to the broadband output from a nanosecond pumped dye-laser. In addition, with a time-resolved CARS technique, it is possible to suppress the non-resonant four-wave mixing signal by simply delaying the probe pulse relative the pump and Stokes pulses [23,24]. Recent investigations aimed at the benchmarking of time-resolved CARS thermometry [25–27] have shown a considerably reduced relative standard deviation with respect to nanosecond CARS thermometry, reaching the unprecedented single-shot precision of ~1% in room air and ~1-3% in flames. When operating in flames, it is nonetheless difficult to make perfect statements about the statistical uncertainty inherent to the CARS technique. Indeed, the measured temperature might be affected by fluctuations in the experimental boundary conditions e.g. originating from factors related to the flow controllers and vibrations of the platform. In order to determine the overall accuracy of CARS-evaluated temperature, a similarity test with other experimental techniques and comparison to numerical simulations is thus important [28].

In the present work, we develop a technique aimed at minimizing the influence of the CARS thermometric uncertainty resulting from the effective bandwidth of the laser excitation fields. In turbulent flames and flows, the temperature and species gradients (and, accordingly, the number density of the gas mixture) change constantly with respect to the alignment of the laser excitation fields [29]. Therefore, shot-to-shot fluctuations may occur *in-situ*, affecting the delivery of a uniform bandwidth and the phase-matching condition necessary to coherently drive the temperature-sensitive Raman transitions. However, even in more still, stationary measurement conditions (e.g. in a laminar flame), which allow statistics to be obtained from signal averaging, the CARS spectrum depends on the effective bandwidth of the laser excitation fields as imposed by the measurement condition. In this framework, the simultaneous referencing of the excitation efficiency has been developed to improve the CARS thermometric measurements obtained on the principle of a single-laser-shot [16,30]. Here, we use the non-resonant CARS susceptibility, measured *in-situ*, to extract information on the effective impulsive efficiency, as mapped directly by the spectrum of the non-resonant four-wave mixing signal. Concurrent resonant and non-resonant CARS signals are generated in the flame, and simultaneous, spatially divided detection of both signals is achieved through a novel polarization-sensitive wide-field coherent imaging spectrometer. We demonstrate the use of this spectrometer on spatially-correlated data, generated through single-shot hybrid femtosecond/picosecond 1D-CARS. We analyze the potential of the simultaneous, *in-situ* referencing in reducing the thermometric uncertainty, as compared to a standard protocol, where the spectral referencing is provided by a recording sequential to the experiment.

2. Theoretical considerations

In dual-broadband pure-rotational CARS [31,32], two-photon constructive pairs, available across the bandwidth of the laser excitation fields, coherently drive specific Raman shifts in the spectral range ~0–500 cm^{-1}. This corresponds to N_2 pure-rotational S-branch transitions from quantum numbers J‘s = 0–60, zwith line separation $\Delta\varepsilon_{J,\ J\ +2} = 4B\ (J{+}3/2)$, and $4B$ ~8 cm^{-1} for N_2. In hybrid femtosecond/picosecond CARS [26,33–39], the excitation efficiency across a specific Raman-active window is dictated by the finite bandwidth of the transform-limited fs-duration driving pulse. When considering pure-rotational CARS transitions (Δv=0, ΔJ=+/−2, ΔM_J=0), the laser excitation of the molecules results in a non-adiabatic interaction (here termed “impulsive”) if the laser pulse duration is about one tenth of the molecular rotational period [40]. The impulsive excitation of N_2, for which the rotational periods are in the order of ~500 fs, would thus require a ~50 fs duration laser pulse. The high excitation efficiency provided by the impulsive drive of the rotational Raman transitions, is a prerequisite for generating non-resonant four-wave mixing at appreciable signal levels, for the instantaneous detection in high-temperature gaseous environments. In general, the strength of the CARS signal scales to the number density squared, and the number density is inversely proportional to the temperature in the sample.

The polarization dependence on the resonant and non-resonant CARS signals [41] is described with angles $\tan\beta = -\ \sin\phi\ /\ 2\cos\phi$ for the resonant CARS signal, and $\tan\delta = \sin\phi\,/\,3\cos\phi$ for the non-resonant CARS signal, determined as a function of the relative polarization angle, ϕ, between the probe beam and the pump/Stokes beams, respectively. A probe angle of 67.5°, relative to the vertically polarized pump/Stokes beam, results in orthogonally polarized resonant and non-resonant CARS signals.

3. Experimental

The experimental setup was developed according to the two-beam femtosecond/picosecond phase-matching scheme for 1D-CARS imaging [42], here implemented with a single regenerative amplifier laser system [43]. The laser pulses originate as the ~35 fs output of a high-power femtosecond regenerative amplifier, with a pulse energy of ~7.5 mJ provided at a 1 kHz repetition-rate (Astrella, Coherent). A narrowband ~7 ps-duration full-width-at-half-maximum (FWHM) probe pulse centered at ~402 nm, is efficiently produced by means of the second-harmonic bandwidth compression [44,45] (Light Conversion) of a ~65% portion of the fs laser output. This results in the ps probe pulse being both repetition-wise synchronized with the fs pump/Stokes pulse and automatically phase-locked at the CARS measurement, with an arbitrary arrival time. The near transform-limited fs pump/Stokes pulse is produced by an external compressor operating on a ~35% portion of the uncompressed output from the amplifier. This design allows for flexible compensation (pre-chirping) of dispersion terms possibly arising along the optical path, thus providing impulsive excitation in the CARS measurement. The alignment of the laser beams and the polarization-sensitive detection of the single-shot hybrid femtosecond/picosecond 1D-CARS signals is depicted in Fig. 1.

The ~2.3 mJ impulsive excitation beam (femtosecond laser pulse) and the ~0.4 mJ probe beam (picosecond laser pulse) are intersected in a crossed-plane geometry, forming a one-dimensional spatial coordinate. The two beams are synchronized by an optical delay-line made of a high-finesse translation stage, ensuring sub-picosecond temporal resolution. The leveling and relative polarization of the laser beams are controlled with turning periscopes and a half-wave plate (Eksma optics) mounted in the pump/Stokes beam path; the shaping of the laser beams is performed with low-dispersion, sheet-forming optics. The irradiance of the probe beam (~1 $\mathrm{J/cm^2}$) is significantly enhanced at the measurement location by means of astigmatic convergence [46], here realized by two cylindrical lenses with focal lengths f:=300 mm (v,h) -the indexes v (vertically) and h (horizontally) express the alignment symmetry axis. In efforts to match the phase-matching condition homogeneously across the line-image, a combination of focal lengths f:=500 mm (v) and f:=1000 mm (h) is employed in the pump/Stokes

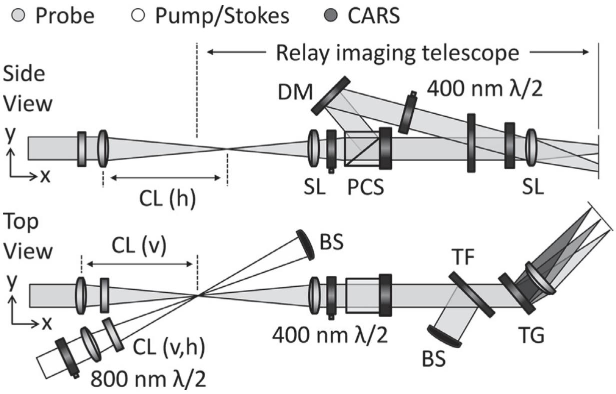

Fig. 1. The polarization-sensitive wide-field coherent imaging spectrometer used for spatially divided detection of resonant - and non-resonant hybrid femtosecond/picosecond one-dimensional (1D) coherent anti-Stokes Raman spectroscopy (CARS) signals. The indexes v (vertically) and h (horizontally) express the alignment symmetry axis of the cylindrical lenses cylindrical lenses (CL). Two separate detection channels for P- and S-polarized light, with orientation determined with respect to the transmission grating (TG), are relay-imaged with ∼1:1 magnification from the signal generation plane to the position of the detector. DM-dichroic mirror, PCS-polarization cube splitter, BS-beam stop, TF-tunable filter, and SL-spherical lens.

beam path. However, the phase-matching condition is relaxed for driving pure-rotational N_2 CARS transitions with the current beam configuration. The excitation beam is dumped before the first collection lens in the wide-field, one-to-one plane, coherent imaging spectrometer, while the probe beam is separated from the pure-rotational CARS signal through the angle-tuning of a spectral bandpass filter (Semrock). The resonant and non-resonant CARS signals are separated in two polarization-dependent detection channels, composed by two 400 nm half-wave plates and a polarization cube splitter (Eksma optics). Both channels are directed through a transmission grating (3040 lines/mm, Ibsen Photonics) and relay-imaged onto the same detector plane (Zyla 4.2, Andor). The first half-wave plate rotates the cross-polarized resonant and non-resonant CARS signals to fit the orthogonal S- and P-polarization transmission axes of the analyser. The second half-wave plate is mounted after the analyser to turn the polarization of the non-resonant CARS signal from P- to S-polarization and achieve the maximum grating transmission efficiency of >90% at 400 nm.

The measurement was performed across the flame front of a laminar premixed methane/air flame (Φ=0.95), provided on a Bunsen burner. The fuel (methane) and oxidizer (air) are delivered from separate containers, and variable-area flow meters (rotameters) provide independent control over each of the flows. Upon exiting the rotameters the flow lines are connected to a junction, after which the gases are mixed and the mixture is provided with a total bulk flow velocity of ∼1 m/s. The combustible mixture is then channeled through a seamless stainless burner pipe, designed with a length-to-diameter ratio (∼1:100) sufficient to dampen coherent flow structures and provide a laminar flow at the exit (Reynolds number < 2000). The 10 mm inner diameter nozzle is tapered to minimize heat losses at the burner rim. The probe volume was positioned in proximity of the chemical reaction layer, and oriented so as to provide measurements along a line orthogonal to the flame front.

The crossing angle (θ) of the pump/Stokes and probe beams was measured to 3°, providing a probe volume of ∼0.03 mm (width) x ∼0.6 mm (length) x ∼1.3 mm (height), estimated from the assumption of a near diffraction-limited beam waist (e_0) of 30 μm FWHM (width), yielding an interaction length of $e_0/\sin(\theta) = 0.6$ mm. The total field-of-view (FOV) was measured to ∼1.3 mm (height) and the image quality was retrieved with a ∼40 μm line-spread function (LSF). These parameters were measured as the translation and steepness of an edge response in the signal, by inserting a razor blade at the plane of the two-beam crossing. A ∼3 ps relative temporal delay between the excitation beam and the probe beam was employed in the experiment, to generate the resonant and non-resonant CARS signals simultaneously. The “time equal zero” and the probe pulse duration were calibrated by performing a probe-delay measurement scan in argon, a monoatomic gas with no rotational degree of freedom. Consequently, the only signal component is the instantaneous four-wave mixing signal, which maps the temporal profile of the ps probe beam, synchronized with the fs pump/Stokes beam. The time-averaged argon spectrum also quantifies the constructive two-photon pairs available for the ex-

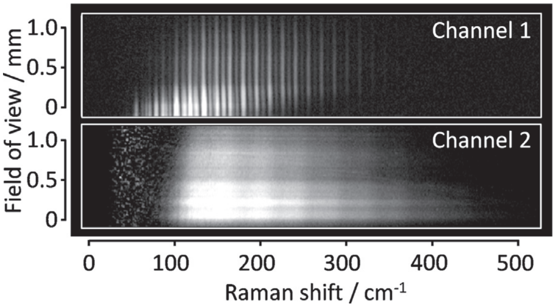

Fig. 2. Single-shot detection of concurrent resonant and non-resonant pure-rotational femtosecond/picosecond 1D-CARS signals acquired *in-situ* across the flame-front of a laminar premixed methane/air flame (Φ=0.95). The label "Channel 1" indicates the portion of the detector frame employed for the acquisition of the resonant CARS signal, which is dominated by the characteristic spectral signature of N_2. "Channel 2" indicates the detection channel for the broadband non-resonant CARS signal (due to four-wave-mixing), which is scattered from all the species present in the probed volume.

citation of a specific Raman shift and is thus employed for the spectral referencing in standard protocols.

A sample of 900 single-shot, resonant and non-resonant CARS spectra was recorded simultaneously in the flame and analyzed to assess the thermometric accuracy and precision. The procedure was compared to a standard protocol, where the single-shot resonant CARS spectra are instead referenced by a time-averaged spectrum recorded in argon sequentially to the experiment.

4. Results and discussion

Figure 2 shows the simultaneous, single-shot detection of resonant and non-resonant 1D-CARS signals, generated across the flame front of a laminar premixed methane/air flame, and acquired on two distinct portions of the same detector frame. The labels "Channel 1" and "Channel 2" identify the portions of the detector where the resonant and non-resonant CARS signals are relayed, respectively.

As it can be seen in Fig. 2, the resonant CARS signal is dominated by the spectral lines of the nitrogen molecules, spanning Raman shifts from ~60 cm^{-1} to ~300 cm^{-1}, which result from the high-rotational energy levels being populated by the elevated temperature in the flame. The non-resonant CARS signal is instead continuous in nature, resulting from the four-wave-mixing from all the molecular species present in the sample. The highest signal intensity is detected in both channels around 180 cm^{-1}, while at frequencies lower than ~150 cm^{-1} the signals are attenuated by the angle-tuning of a spectral band-pass filter, to avoid spurious stray-light and residual probe beam reaching the detector.

Figure 3 shows a single-shot resonant spectrum acquired in the first detection channel, which is referenced by the non-resonant spectrum measured *in-situ* and detected simultaneously in the second channel.

The spectral resolution of the resonant CARS signal is dictated by the linewidth of the probe beam, measured to 2.1 cm^{-1} (FWHM), as well as by the instrumental broadening resulting from the wide-field coherent imaging spectrometer. In addition, the stray light covering the leftmost portion of the detector currently limits the spectral range available. This is nevertheless considered to have an insignificant impact on the N_2 thermometry, since, in correspondence of the elevated temperature in the product gases of the flame, the energy levels above 160 cm^{-1} are the most populated. The resonant CARS signal strength at room-temperature is several orders of magnitude stronger than the flame-temperature signal: the signal to background ratio (SNB) rapidly degrades as a function of temperature. The estimation of the temperature from the experimental CARS spectra was performed through a non-linear least-square contour fitting routine, comparing the acquired resonant spectra to a library of theoretical spectra pre-calculated for different input temperatures. These synthetic Raman spectra were computed by means of a time-domain CARS model, similar to previously-reported ones [34,26]. The broadening of the spectral linewidths due to the imaging system was accounted for by convolving the synthetic spectra with a Voigt instrument-response-function with a 1.6 cm^{-1} -wide Gaussian component (FWHM) and a 0.5 cm^{-1} -wide Lorentzian component (FWHM). The acquired resonant spectra were background-subtracted, introducing an area-averaged factor, thus accounting for possible shot-to-shot fluctuation in the magnitude of the background. Subsequently, the spectral referencing of the impulsive excitation efficiency was performed by dividing the resonant spectrum with the non-resonant spectrum (NR) obtained through two independent meth-

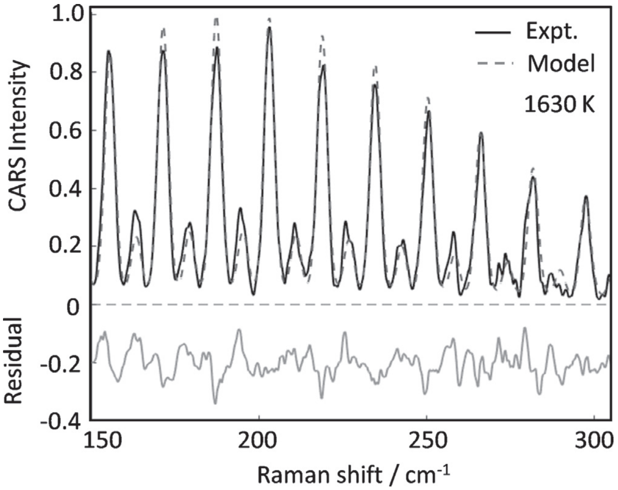

Fig. 3. Single-shot hybrid femtosecond/picosecond CARS spectrum, generated at short pump-probe pulse delay (~3 ps) in the flame. The resulting temperature in the measurement location was estimated to 1630 K. The performance of the spectral fitting can be evaluated by the residuals of the theoretical and experimental spectra, which are presented in the figure, with an offset of −0.2 for clarity purposes.

ods: 1. non-resonant spectrum acquired in room-temperature argon (*ex-situ*); 2. non-resonant spectrum acquired in the flame (*in-situ*).

In Fig. 4, the comparison of the non-resonant CARS signal, as provided by the two techniques, is presented. The measurements were performed with spatially and temporally overlapped probe and pump/Stokes fields, at a ~3 ps relative delay, for concurrent generation of the non-resonant CARS signal.

The signal quality from each of the single-shot recordings is sufficient to perform the spectral referencing: the signal counts of the single-shot spectra for the most critical condition (i.e. non-resonant signal from the flame) was ~700 counts above the detector baseline. The non-resonant spectra show a clear decay for increasing values of the Raman shift: in this respect, the non-resonant signal provides an effective mapping of the laser bandwidth available for the excitation of the Raman-active molecules in the ensemble. If this pronounced slope were not taken into account in the spectral fitting routine (by spectral referencing), its effect would resemble a strong *J*-dependence similar to any other critical uncertainty factor, and result in a systematic bias (inaccuracy) in the CARS evaluated temperature. The comparison of the non-resonant spectra acquired *ex-situ* and *in-situ* clearly shows that the effective bandwidth available for the excitation of the temperature-sensitive Raman transitions in the combustion products is broader than the one mapped by the non-resonant spectrum acquired in room-temperature argon. This is explained by the strong dependence of the refractive index of the participating medium (i.e. the gaseous mixture in the probe volume) on its temperature. Indeed, the group-velocity dispersion (GVD) of the fs pump/Stokes pulse induces a temporal broadening of the pulse itself as it propagates through the medium, resulting in a reduction of the effective bandwidth [47]. As the GVD for most gases at atmospheric pressure scales linearly with the density, the high temperature of the product gases in the flame determines a significant reduction of the GVD of the pump/Stokes pulse and the increase in the effective bandwidth shown in Fig. 4.

Furthermore, if a time-average NR spectrum, acquired *ex-situ*, is employed for the spectral referencing, possible variations in the excitation bandwidth available shot-to-shot would be neglected. This behavior is expected e.g. in turbulent flames, where the temperature field, as well as the chemical composition of the gas mixture in the probe volume, is highly dynamic in nature. Seemingly, this shot-to-shot variability in the slope of the NR spectra measured in the flame (*in-situ*) is neglected in the *ex-situ* measurement of the NR spectrum: this would lead to a stochastic uncertainty in the measurement. The bottom panel in Fig. 4 shows the relative standard deviation (RSTD) of the NR spectra acquired *in-situ* and *ex-situ*, as a function of the Raman shift: the trend of these curves thus represents the *J*-dependence of the shot-to-shot fluctuations in the NR spectrum, i.e. in the impulsive excitation efficiency. The RSTD of the *in-situ* NR spectrum is one order of magnitude higher across the whole spectral range compared to the *ex-situ* one: this is due to the reduced SNB available in the *in-situ* measurement, as compared to the *ex-situ*, because of the decreased number density of

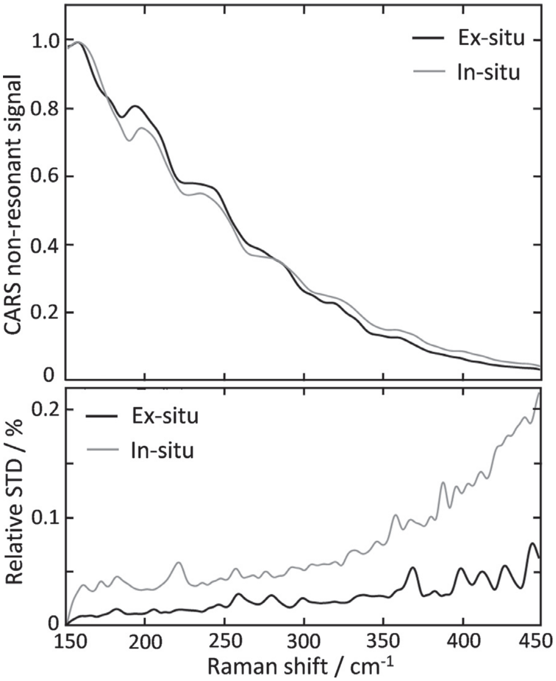

Fig. 4. (Top) Comparison of the average non-resonant spectra acquired in room-temperature argon (*ex-situ*) and at ~390 µm from the flame-front in the oxidation region of the flame. (Bottom) The relative standard deviation as obtained from the 900 single-shot recordings.

the participating medium at high temperature. The difference in the RSTD values is more significant at the high-rotational energy levels populated at elevated temperatures: the variance of the available effective bandwidth in the fs pulse is shown to be higher in the *in-situ* measurements.

The use of the *in-situ* referencing of the impulsive excitation was demonstrated in CARS imaging thermometry, performed across the flame front of a laminar premixed methane/air flame (Φ=0.95). In the scope of the present work, the location of the flame front is defined as the measurement point yielding the closest temperature to 1192 K; this value corresponding to the inflection point of the temperature profile across the reaction layer of the measured flame, as computed by the CHEM1D code [48]. The comparison of the temperature evaluations, obtained by applying the two referencing methods on 900 single-shot CARS spectra acquired in the flame, is discussed in the following.

In Fig. 5, the probability density functions (PDFs) of the temperature measurements are provided as a mean of comparison for the *ex-situ* and *in-situ* referencing techniques. The same resonant spectra, acquired in a 900 frames sample, were thus referenced by: 1. the time-averaged non-resonant spectrum acquired in room-temperature argon (*ex-situ*), and 2. the single-shot non-resonant spectra acquired in the second detection channel, simultaneously to the resonant one (*in-situ*).

In the temperature measurements at ~390 µm from the flame front, the *ex-situ* and *in-situ* referencing of the resonant spectra yielded, respectively: 1. an average temperature of 1696 K, with standard deviation 11 K (~0.7%); 2. an average temperature of 1674 K with standard deviation 18 K (~1.1%). The *ex-situ* referencing of the resonant CARS spectra results in a consistent bias towards higher temperatures, as compared to the results of the *in-situ* referencing: the systematic bias being quantified in 22 K (~1.3%) at this flame location. This behavior is in good agreement with the aforementioned discrepancy in the available excitation bandwidth as mapped by NR spectra acquired *in-situ* and *ex-situ*: the lower density of the hot product gases is expected to have a lesser GVD on the laser excitation fields, thus resulting in a broader effective bandwidth. The effect of the temperature of the gaseous medium on the GVD of the fs pump/Stokes pulse, is even more evident when comparing the CARS measurements provided by *ex-situ* and *in-situ* referencing at lower temperatures. Indeed, at the flame front the two referencing techniques yielded the following results: 1. an average temperature of 1210 K (*ex-situ*) and

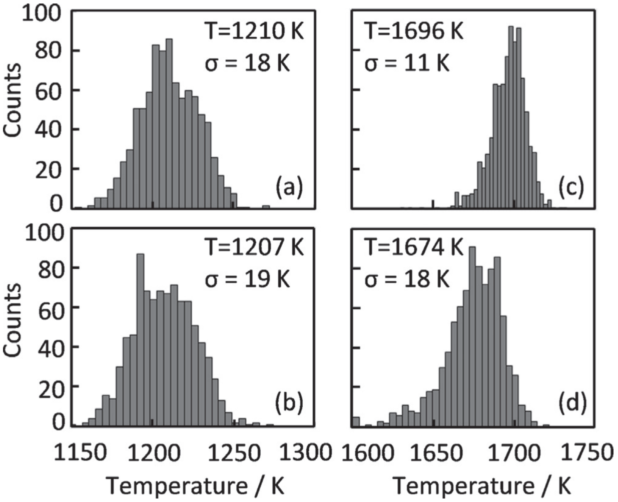

Fig. 5. Probability density functions of the 900 single-shot CARS-evaluated temperatures in the oxidation region of a laminar premixed methane/air flame. (a,b) Comparison for the measurements performed at the flame front. The *ex-situ* CARS measurement resulted in an average temperature of 1210 K, with standard deviation of 18 K (~1.5%); the *in-situ* referencing provided an average temperature of 1207 K, with standard deviation of 19 K (~1.6%). (c,d) Comparison of the temperature assessment provided by *ex-situ* and *in-situ* referencing of the resonant CARS spectra acquired at ~390 µm from the flame front. The *ex-situ* referencing resulted in an average temperature of 1696 K, with standard deviation 11 K (~0.7%); the *in-situ* provided an average temperature of 1674 K with standard deviation 18 K (~1.1%).

2. an average temperature of 1207 K (*in-situ*). The evident decrease in the systematic bias of the *ex-situ*-referenced CARS thermometry is well understood as a lesser impact the GVD on the fs pump/Stokes pulse.

It is nonetheless important to note that the CARS-evaluated temperatures seem to be significantly lower than as predicted by the numerical model in this spatial region of the flame: the expected temperature is indeed ~1870 K. This higher temperature value was moreover confirmed by performing CARS measurements at longer probe pulse delay (~27 ps), i.e. where the probe pulse is not temporally overlapped to the pump/Stokes pulse, and the self-referencing technique can thus not be employed. As a matter of fact, these measurement provide an average temperature of ~1840 K (inacurracy: ~1.6%). The reported discrepancy between the temperature measurements performed at long and short (i.e. within the temporal overlap of the pump/Stokes and probe pulses) pump-probe delays was consistently observed in different measurement locations within the flame front and for different values of the delay itself. This behavior seems to indicate the presence of a source of uncertainty in the evaluation of the temperature through the resonant CARS spectra generated at short pump-probe delays, which our theoretical model fails to take into account. Nevertheless, this uncertainty is not inherent to the *in-situ* referencing of the impulsive excitation, as it was also clearly observed in the temperature measurements provided by the standard protocol, with *ex-situ* referencing by room-temperature argon.

As far as the relative standard deviation of the temperature measurements is concerned, the self-referencing shows a slightly worse precision as compared to the *ex-situ* referencing. This is attributed to the reduced SNB ratio available in the single-shot detection of the non-resonant signal in the self-referencing approach. Seemingly, this effect was more pronounced than any shot-to-shot variation in the effective excitation bandwidth, that the *in-situ* referencing could have accounted for. Nonetheless, the use of the self-referencing technique here described is foreseen to provide a substantial improvement in the precision of the CARS thermometric measurements in a number of applications of practical interest. We anticipate, for example, that the inherent compensation of the shot-to-shot fluctuations of the laser excitation fields can improve the thermometry in turbulent flows and flames. Future work in our laboratory will moreover quantify the impact of this technique on the performance of CARS systems employing laser sources which are more unstable in nature, such as supercontinuum generation.

5. Conclusions

In the present work, we have presented the application of a novel, *in-situ* referencing technique for CARS imaging thermometry. The simultaneous, *in-situ* referencing of the resonant Raman spectra was achieved by the concurrent, spatially divided detection of the resonant and non-resonant CARS signals in two distinct portions of the same detector frame. The non-resonant CARS signal detected in Channel 2 was thus employed as a spectral reference to the resonant CARS signal detected in Channel 1. Furthermore, we successfully demonstrated the application of this technique to the spatially correlated data provided by a single-shot one-dimensional CARS imaging system. Moreover, we have investigated the impact of the spectral referencing on CARS flame thermometry. A consistent bias of the *ex-situ* referencing towards higher temperatures was reported. This is understood in terms of the effect of the GVD change in the less dense product gases, as compared to the room-temperature argon employed to measure the *ex-situ* non-resonant spectrum. Nonetheless, the mean temperatures provided by both referencing methods were lower than predicted by the numerical evaluation of the measured flame front. This temperature bias was furthermore confirmed by additional CARS measurements performed at longer pump-probe delays, where no *in-situ* referencing is possible. In terms of relative standard deviation, the CARS-evaluated temperature obtained by applying the *in-situ* referencing was slightly worse than the *ex-situ* case. Nevertheless, the self-referencing technique here proposed is foreseen to improve the thermometric precision in more challenging measurement conditions.

Declaration of Competing Interest

The authors declare that they have no known competing financial interests or personal relationships that could have appeared to influence the work reported in this paper.

Acknowledgments

We gratefully acknowledge the financial support provided by the Netherlands Organization for Scientific Research (NWO), obtained through a Vidi grant in the Applied and Engineering Sciences domain (AES) (15690).

References

[1] K. Kohse-Höinghaus, R.S. Barlow, M. Aldén, E. Wolfrum, *Proc. Combust. Inst.* 30 (2005) 89–123.

[2] A.C. Eckbreth, *Laser Diagnostics for Combustion Temperature and Species*, 2nd ed., Gordon and Breach, Amsterdam, 1996.

[3] S. Druet, J.P. Taran, *Prog. Quant. Electr.* 7 (1981) 1–72.

[4] D.I. Greenhalgh, *Adv. Spectrosc.* 15 (1988) 193–251.

[5] S. Roy, J.R. Gord, A.K. Patnaik, *Prog. Energy Combust.* 36 (2010) 280.

[6] T. Seeger, A. Leipertz, *Appl. Opt.* 35 (1996) 2665–2671.

[7] A. Bohlin, E. Nordström, H. Carlsson, X.-S. Bai, P.-E. Bengtsson, *Proc. Combust. Inst.* 34 (2013) 3629.

[8] R.E. Palmer, *Sandia CARSFT Code*, Sandia National Laboratories, Livermore, CA, USA, 1989 Report No. SAND89-8206.

[9] L. Martinsson, P.-E. Bengtsson, M. Aldén, S. Kröll, J. Bonamy, *J. Chem. Phys.* 99 (4) (1993) 2466.

[10] M. Marrocco, *Proc. Combust. Inst.* 32 (2009) 863–870.

[11] S. Kröll, M. Aldén, T. Berglind, R.J. Hall, *Appl. Opt.* 26 (1987) 1068–1073.

[12] J.P. Kuehner, M.A. Woodmansee, R.P. Lucht, J.C. Dutton, *Appl. Opt.* 42 (2003) 6757–6767.

[13] M. Woyde, W. Stricker, *Appl. Phys. B* 50 (1990) 519–525.

[14] T. Lundeen, S.Y. Hou, J.W. Nibler, *J. Chem. Phys.* 79 (1983) 6301–6305.

[15] R.L. Farrow, R.P. Lucht, L.A. Rahn, *J. Opt. Soc. Am. B* 4 (1987) 1241–1246.

[16] F. Grisch, P. Bouchardy, W. Clauss, *Aerosp. Sci. Technol.* 7 (2003) 317–330.

[17] S.A. Tedder, J.L. Wheeler, A.D. Cutler, P.M. Danehy, *Appl. Opt.* 49 (2010) 1305–1313.

[18] W.F. Murphy, *J. Chem. Phys.* 67 (1977) 5877–5882.

[19] C.C. Hayden, D.W. Chandler, *J. Chem. Phys.* 103 (1995) 10465–10472.

[20] T. Lang, M. Motzkus, *J. Opt. Soc. Am. B* 19 (2002) 340.

[21] R.P. Lucht, S. Roy, T.R. Meyer, J.R. Gord, *Appl. Phys. Lett.* 89 (2006) 251112.

[22] W.D. Kulatilaka, P.S. Hsu, H.U. Stauffer, J.R. Gord, S. Roy, *Appl. Phys. Lett.* 97 (2010) 081112.

[23] D. Pestov, R.K. Murawski, G.O. Ariunbold, et al., *Science* 316 (2007) 265–268.

[24] T. Seeger, J. Kiefer, A. Leipertz, B.D. Patterson, C.J. Kliewer, T.B. Settersten, *Opt. Lett.* 34 (2009) 3755–3757.

[25] D.R. Richardson, H.U. Stauffer, S. Roy, J.R. Gord, *Appl. Opt.* 56 (2017) 37–49.

[26] S.P. Kearney, *Combust. Flame* 162 (2015) 1748–1758.

[27] A. Bohlin, C.J. Kliewer, *J. Phys. Chem. Lett.* 6 (2015) 643–649.

[28] R.S. Barlow, *Proc. Combust. Inst.* 31 (2007) 49–75.

[29] G. Magnotti, A.D. Cutler, P.M. Danehy, *Appl. Opt.* 51 (2012) 4730–4741.

[30] E.H. van Veen, D. Roekaerts, *Appl. Opt.* 44 (2005) 6995–7004.

[31] A.C. Eckbreth, T.J. Anderson, *Opt. Lett.* 11 (1986) 496–498.

[32] M. Aldén, P.-E. Bengtsson, H. Edner, *Appl. Opt.* 25 (1986) 4493–4500.

[33] B.D. Prince, A. Chakraborty, B.M. Prince, H.U. Stauffer, *J. Chem. Phys.* 125 (2006) 044502.

[34] J.D. Miller, S. Roy, M.N. Slipchenko, J.R. Gord, T.R. Meyer, *Opt. Express* 19 (2011) 15627–15640.

[35] A. Bohlin, M. Mann, B.D. Patterson, A. Dreizler, C.J. Kliewer, *Proc. Combust. Inst.* 35 (2015) 3723–3730.

[36] M. Scherman, M. Nafa, T. Schmid, et al., *Opt. Lett.* 41 (2016) 488–491.

[37] C.B. Yang, D. Escofet-Martin, D. Dunn-Rankin, Y.C. Chien, X. Yu, S. Mukamel, *J. Raman Spectrosc.* 48 (2017) 1881.

[38] Y. Ran, M. Junghanns, A. Boden, S. Nolte, A. Tünnermann, R. Ackermann, *J. Raman Spectrosc.* 50 (9) (2019) 1268.
[39] J.E. Retter, G.S. Elliott, *Appl. Opt.* 58 (2019) 2557–2566.
[40] N. Owschimikow, B. Schmidt, N. Schwentner, *Phys. Chem. Chem. Phys.* 13 (2011) 8671–8680.
[41] F. Vestin, M. Afzelius, P.-E. Bengtsson, *Proc. Combust. Inst.* 31 (2007) 833–840.
[42] A. Bohlin, B.D. Patterson, C.J. Kliewer, *J. Chem. Phys.* 138 (2013) 081102.
[43] L. Castellanos, F. Mazza, D. Kliukin, A. Bohlin, *Opt. Lett.* 45 (2020) 4662–4665.
[44] S.P. Kearney, D.J. Scoglietti, *Opt. Lett.* 38 (2013) 833–835.
[45] F. Raoult, A.C.L. Boscheron, D. Husson, C. Sauteret, A. Modena, V. Malka, F. Dorchies, A. Migus, *Opt. Lett.* 23 (1998) 1117–1119.
[46] A. Bohlin, C.J. Kliewer, *Appl. Phys. Lett.* 105 (2014) 161111.
[47] P.J. Wrzesinski, D. Pestov, V.V. Lozovoy, J.R. Gord, R.J. Sukesh, *Opt. Express* 19 (2011) 5163–5171.
[48] J.A. van Oijen, L.P.H. de Goey, *Combust. Sci. Technol.* 161 (2000) 113–137.

Research Article
Vol. 30, No. 20 / 26 Sep 2022 / *Optics Express* 35232
Optics EXPRESS

Coherent Raman spectroscopy on hydrogen with *in-situ* generation, *in-situ* use, and *in-situ* referencing of the ultrabroadband excitation

Francesco Mazza,[1] **Aert Stutvoet,**[1] **Leonardo Castellanos,**[1] **Dmitrii Kliukin,**[1,2] **and Alexis Bohlin**[1,3,*]

[1] *Faculty of Aerospace Engineering, Delft University of Technology, Kluyverweg 1, 2629 HS Delft, The Netherlands*
[2] *LaserLaB, Department of Physics and Astronomy, Vrije Universiteit Amsterdam, De Boelelaan 1081, 1081 HV Amsterdam, The Netherlands*
[3] *Space Propulsion Laboratory, Department of Computer Science, Electrical and Space Engineering, Luleå University of Technology, 98128 Kiruna, Sweden*
[*] *alexis.bohlin@ltu.se*

Abstract: Time-resolved spectroscopy can provide valuable insights in hydrogen chemistry, with applications ranging from fundamental physics to the use of hydrogen as a commercial fuel. This work represents the first-ever demonstration of *in-situ* femtosecond laser-induced filamentation to generate a compressed supercontinuum behind a thick optical window, and its *in-situ* use to perform femtosecond/picosecond coherent Raman spectroscopy (CRS) on molecular hydrogen (H_2). The ultrabroadband coherent excitation of Raman active molecules in measurement scenarios within an enclosed space has been hindered thus far by the window material imparting temporal stretch to the pulse. We overcome this challenge and present the simultaneous single-shot detection of the rotational H_2 and the non-resonant CRS spectra in a laminar H_2/air diffusion flame. Implementing an *in-situ* referencing protocol, the non-resonant spectrum measures the spectral phase of the supercontinuum pulse and maps the efficiency of the ultrabroadband coherent excitation achieved behind the window. This approach provides a straightforward path for the implementation of ultrabroadband H_2 CRS in enclosed environment such as next-generation hydrogen combustors and reforming reactors.

1. Introduction

Molecular hydrogen (H_2) is the object of an ever-increasing scientific interest, in view of its prospect use as the main energy carrier in the current energy transition [1], and a significant research effort is being spent on the development of technologies enabling H_2-based carbon-neutral combustion. The experimental investigation of H_2 chemistry [2,3], which plays a significant role in its storage and utilization, requires the availability of time-resolved spectroscopic techniques, providing information on the molecular dynamics on picosecond (ps) and femtosecond (fs) timescales [4]. The current state-of-the-art technique for gas-phase molecular spectroscopy is coherent Raman scattering (CRS) spectroscopy [5], which has found vast application to high fidelity *in-situ* measurements of the temperature field and chemical flow composition in combustion environments [6,7], and in non-equilibrium thermodynamic systems [8,9]. Since the first observation of rotational coherent Raman scattering in gas-phase media [10], CRS has been successfully demonstrated in gaseous H_2, both as a test-bench for fundamental physics (e.g. dynamic Stark effect [11]) and for enabling the development of novel photonic technologies [12]. Despite the research effort spent over the years, the application of CRS techniques to perform direct broadband multiplex spectroscopy on H_2 still presents a significant challenge due to sparse ro-vibrational energy manifold of the H_2 molecule [13]. Vibrational H_2 CRS

#465817
Journal © 2022
https://doi.org/10.1364/OE.465817
Received 1 Jun 2022; revised 25 Aug 2022; accepted 25 Aug 2022; published 13 Sep 2022

spectroscopy has been applied in combustion environments [14], as well as in plasmas [15], by employing broadband nanosecond dye lasers. Further development of H_2 CRS has been more recently promoted by the availability of ultrafast regenerative laser amplifiers, producing pulses a few tens of fs long, which have sprung the development of time-resolved spectroscopic techniques to investigate chemical reactions in real time [16]. Lang *et al.* were the first to employ fs pulses to perform coherent anti-Stokes Raman spectroscopy (CARS) on H_2, resolving the temporal dynamics of its ro-vibrational wave packet with sub-ps resolution [17]. Tran *et al.* used fs-CRS to study the H_2-N_2 collisional system and the speed-memory effects due to the high motility of the H_2 molecules [18]. Magnitskiĭ and Tunkin investigated the Dicke narrowing of the H_2 Q-branch, using ps-CRS to measure its coherence lifetime with high temporal and spectral resolution [19]; similar ps-CRS measurements of the H_2 Q-branch coherence lifetime were performed by Kulatilaka *et al.* [20]. The idea of combining broadband fs pulses to generate maximal quantum coherence of the Raman-active molecules [21] and relatively-narrowband ps pulses to perform simultaneously temporally- and spectrally-resolved measurements [22] has led to the development of hybrid fs/ps CRS [23]. The introduction of ultrabroadband fs laser sources greatly enhanced the spectral interrogation window of fs/ps CRS [24], allowing for the detection of virtually all the rotationally Raman-active species in the probed volume and for the investigation of their chemistry. Bohlin and Kliewer [25] demonstrated the use of a ~7 fs compressed supercontinuum, generated in an argon-filled hollow-core fiber, to simultaneously excite both the pure-rotational H_2 S-branch and the vibrational H_2 Q-branch transitions, in the range 0-4200 cm^{-1}. Despite the huge versatility of ultrabroadband fs/ps CRS, its application to perform measurements behind thick optical windows is limited by the significant chirp that these impart to broadband [26] and ultrabroadband fs pulses.

In the present work, we employ fs laser-induced filamentation [27] to generate a compressed supercontinuum pulse *in-situ*, where it is employed as a single pump/Stokes excitation pulse [28] to drive the pure-rotational Raman coherence up to ~1500 cm^{-1}. This approach is combined

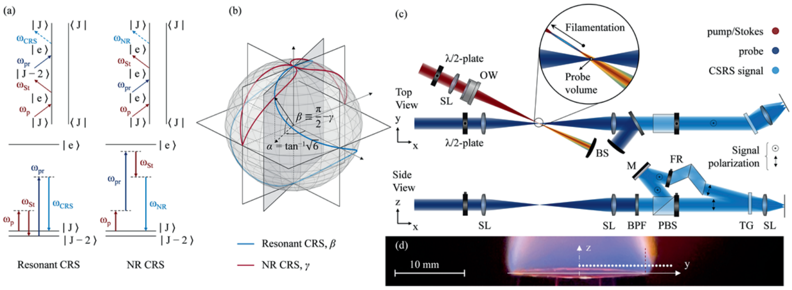

Fig. 1. (a) Energy and Feynman diagrams of a resonant (left) and a non-resonant (right) CRS pathways. (b) Polarization angles of the resonant (blue line) and non-resonant (red line) CRS signals, β and γ, represented as the elevation angle on the unit sphere as a function of the relative polarization angle (azimuthal angle) of the pump/Stokes and probe fields, α. (c) Schematic of the polarization-sensitive coherent imaging spectrometer. OW, optical window; SL, spherical lenses; M, mirror; BPF, band-pass filter; PBS, polarization beam splitter; FR, Fresnel rhomb; BS, beam stop. Inset: probe volume. The probe crosses the ultrabroadband pump/Stokes beam ~2mm after the end of the filament. The increment of input energy results in the elongation of the filament towards the focusing optics (arrow direction) (d) Measurements points across the H_2/air flame front, the dashed red line identifies the location of the burner rim at y = 9.5 mm.

with the simultaneous shot-to-shot measurement of the non-resonant (NR) CRS signal, due to the instantaneous electronic optical response of the medium (Fig. 1(a)), to map the spectral efficiency of the coherent excitation, which can significantly impact the accuracy and precision of the H_2 spectroscopy [29]. We use a polarization approach to simultaneously generate and detect the resonant and NR CRS signals with orthogonal polarization [30], as shown in Fig. 1(b). This *in-situ* spectral referencing allows us to monitor the spectrochronographic properties of the compressed supercontinuum and the bandwidth of the coherent Raman excitation. We demonstrate the application of fs/ps H_2 CRS with *in-situ* generation, use and referencing of the ultrabroadband coherent excitation to perform thermometric measurements in a laminar H_2/air diffusion flame as shown in Fig. 1(d), and to experimentally demonstrate preferential diffusion of H_2 [31].

2. Theory and methods

2.1. Analytical framework

The excitation efficiency of the H_2 Raman active modes depends on the spectrochronographic characteristics of the broadband pump/Stokes pulse, and is effectively controlled by its spectral phase [32,33], as shown in the application of coherent control theory to CRS [34,35]. We measure the excitation bandwidth provided by the combined pump/Stokes pulse using the intensity spectrum of the NR CRS signal. The NR CRS signal is here modelled in the time domain under the assumptions of instantaneous dephasing of the electronic coherence induced by the non-resonant two-photon excitation pathways in Fig. 1(a) and temporal overlap of the probe field E_3 with the pump/Stokes field E_{12} [24]:

$$P^{(3)}_{\mathrm{NR}}(t) = \left(\frac{i}{\hbar}\right)^3 \chi^{(3)}_{\mathrm{NR}} \cdot E_3(t) \cdot E^*_{12}(t) \cdot E_{12}(t) \tag{1}$$

The pump/Stokes pulse is assumed to have a Gaussian envelope in the time domain with duration Δt_{12} (FWHM):

$$E_{12}(t) \propto \exp[-2\ln 2(t-t_{12})^2/\Delta t_{12}^2] \cdot \exp(i\omega_{12}t) + c.c. \tag{2}$$

with t_{12} being the arrival time of the combined pump/Stokes pulse, and ω_{12} the carrier (angular) frequency of the pulse ($\omega_{12} = 2.34$ rad/fs for 806.7 nm). The spectrum of the NR CRS field, resulting from the pump/Stokes photon-pairs found across the instantaneous bandwidth of the pulse, is then computed via the Fourier transform of Eq. (1), and is thus proportional to the spectral autocorrelation of the pump/Stokes laser field [36]:

$$P^{(3)}_{\mathrm{NR}}(\omega) \propto \chi^{(3)}_{\mathrm{NR}} E_3(\omega) * [E_{12}(\omega) \star E_{12}(\omega)] \tag{3}$$

$$I_{\mathrm{NR}}(\omega) \propto |\chi^{(3)}_{\mathrm{NR}} E_3(\omega) * [E_{12}(\omega) \star E_{12}(\omega)]|^2 \tag{4}$$

where $\star$ and $*$ represent the cross-correlation and convolution operators, respectively. Hence, the intensity spectrum in Eq. (4) is used to measure the spectral autocorrelation of the fs pump/Stokes pulse and deduce information on its spectral phase. Equation (2) and Eq. (4) are employed to generate a library of synthetic NR CRS spectra for varying pulse duration, and fit the experimental NR CRS spectra acquired in a non-resonant gas (e.g. methane or argon) flow. The spectral phase of the pump/Stokes pulse is introduced in the model through the Taylor expansion:

$$\varphi(\omega) = \sum_n L \cdot k_{(n)}(\omega_{12}) \cdot \frac{(\omega-\omega_{12})^n}{n!} \tag{5}$$

with L being the thickness of the optical window, and $k_{(n)}$ the n$^{\mathrm{th}}$-order derivative of the wave vector $k(\omega)$ in the dispersive medium ($k_{(2)}$ thus representing the group velocity dispersion of the fs pulse). The chirped pump/Stokes pulse is thus represented in the frequency domain as:

$$E_{12}(\omega) \propto \exp\left[-2\ln 2(\omega-\omega_{12})^2/\Delta\omega_{12}^2\right]\cdot\exp\left[-i\sum_n \varphi_{(n)}\cdot\frac{(\omega-\omega_{12})^n}{n!}\right] \tag{6}$$

Substituting Eq. (6) into Eq. (3), the spectral autocorrelation of the pump/Stokes pulse is computed according to the integral:

$$(E_{12}\star E_{12})(\Omega) = \int_{-\infty}^{\infty} d\omega E_{12}^{*}(\omega)E_{12}(\omega+\Omega) \propto \\ \exp\left[-\left(\frac{\ln 2}{\Delta\omega_{12}^2}+i\frac{\varphi_2}{2}\right)\Omega^2\right]\cdot\int_{-\infty}^{\infty} d\omega \exp\left\{\frac{4\ln 2}{\Delta\omega_{12}^2}\left[\Omega+\frac{(\omega-\omega_{12})}{2}\right]^2 - i\varphi_2\Omega\frac{(\omega-\omega_{12})}{2}\right\} \tag{7}$$

where only the quadratic phase term (φ_2) has been included. Note that including the third-order dispersion (TOD, φ_3) would only contribute to the real part of the argument of the exponential integrand, as the imaginary part factors out in the product with the complex-conjugated field: this is true for all the odd terms in the spectral phase expansion of Eq. (5). A closed-form solution to the integral in Eq. (7) is given in the form:

$$(E_{12}\star E_{12})(\Omega) \propto \sqrt{\pi(4\log 2 + i\varphi_2\Delta\omega_{12}^2)}\exp\left[\left(-\frac{4\ln 2}{\Delta\omega_{12}^2}+i\varphi_2\right)\Omega^2\right] \tag{8}$$

which represents a Gaussian envelope modulated by non-linear harmonic oscillations, having the form of the derivative of Fresnel sine integral function, with local frequency proportional to the quadratic phase term. Equation (4) and Eq. (8) are employed to generate a library of synthetic NR CRS spectra for varying pulse duration, and fit the experimental NR CRS spectra, as shown in Fig. 2.

2.2. *Experimental setup*

The laser system employed for ultrabroadband fs/ps CRS spectroscopy is detailed in Ref. [37]. A single ultrafast regenerative amplifier system (Astrella, Coherent) combined with a second-harmonic bandwidth compressor unit (Light Conversion), provides the combined pump/Stokes (35 fs, 1650 µJ/pulse at 806.7 nm) and the probe (12.6 ps, 117 µJ/pulse at 403.4 nm) fields which are auto-synchronized at 1 kHz repetition rate and focused to the measurement location using spherical lenses (f: 500 and 300 mm, respectively). We demonstrate its applicability to measurements behind thick optical windows by transmitting the fs beam through a ~22 mm thick BK7 glass window. This glass has larger group velocity dispersion at 800 nm (~45 fs^2/mm) than other optical window materials (e.g. fused silica ~36 fs^2/mm), which demonstrates the application of this methodology to the more extreme conditions. The window is placed ~200 mm after the focusing lens to prevent white light generation inside the glass. The energy of the fs beam after the transmission thought the optical window is ~1500 µJ/pulse. We control the temporal chirp of the fs pulse prior the *in-situ* filamentation using an external pulse-compressor. Thin-film polarizers ensure the linear polarization of the pump/Stokes and the probe beams, and half-wave plates control their polarization angles. Ensuring the linearity of the polarization of the fs beam before it undergoes filamentation is critical to control the polarization state of the compressed supercontinuum, since electronic Kerr nonlinearity, electron plasma, and molecular alignment in the filament result in the rotation of the polarization ellipse [38]. Linearly polarized pulses maintain their polarization state in fs laser-induced filamentation and in the post-filamentation propagation [39]. Adopting a two-beam nearly phase-matched configuration

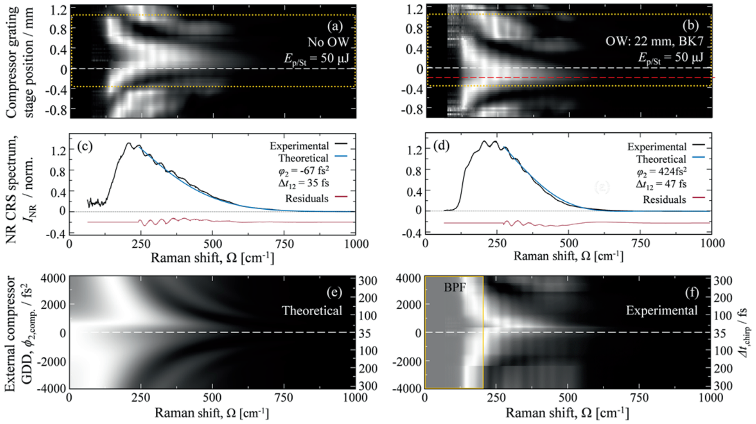

Fig. 2. (a) 1000-shot-averaged NR CRS spectra recorded, by varying the position of the compressor grating, in a flow of CH_4 without the optical window (No OW). The white dashed line identifies the condition of a near transform-limited (TL) pulse. (b) Corresponding NR CRS spectra after the introduction of a BK7 optical window (OW) in the pump/Stokes beam path. The red dashed line identifies the condition of a TL pulse obtained after transmission through the window. The dotted boxes represent the region of interest (ROI) analyzed in the present work. (c) NR CRS spectrum for a near TL pump/Stokes pulse as compared to the time-domain NR CRS model (No OW). (d) NR CRS spectrum for TL pump/Stokes pulse transmitted through the optical window (OW). (e) NR CRS signal for varying linear chirp in the input fs pump/Stokes pulse, as predicted by the time-domain model. For values of the pulse GDD larger than ~1000 fs^2 the spectral autocorrelation of the pulse results in the formation of sidebands in the CRS spectrum and in the narrowing of the excitation window. (f) Experimental autocorrelation of the fs pulse as measured by the NR CRS signal of room temperature CH_4 in the ROI. The opaque box represents the spectral region affected by the edge of the band pass filter (BPF).

[28], the pump/Stokes beam is crossed by the probe beam ~2 mm after the end of the filament to avoid ionization inside the probe volume. The ending point of the filamentation generated both across the flame and in non-resonant gases (i.e. argon and methane) is always fixed regardless of the input pulse energy and the local thermodynamic properties of the gas [37]. The resulting dimensions of the probe volume are thus estimated geometrically to be 20 μm (width, FWHM) x 2.5 mm (length, FWHM) x 20 μm (height, FWHM). The coherent imaging spectrometer developed for the simultaneous acquisition of the resonant and NR CRS signals in Ref. [30] is here adapted for the *in-situ* referencing of the ultrabroadband excitation generated in the flame. A Fresnel Rhomb rotates the polarization of the NR signal to maximize the efficiency of a high-resolution transmission diffraction grating (>90% diffraction efficiency for S-polarization, Ibsen Photonics). The signals are imaged onto the sCMOS detector (Zyla, Andor) through a fast-focusing lens (f: 100 mm), resulting in a detection bandwidth of 1900 cm^{-1}, with a dispersion of 0.93 cm^{-1}/pixel. The resolution of the H_2 CRS spectra is limited by the linewidth of the ps probe pulse which is measured to be ~2.7 cm^{-1}, and by the instrumental broadening of the spectrometer, which is fitted to a Voigt profile with a ~0.1 cm^{-1} FWHM Lorentzian and a ~1.7 cm^{-1} FWHM Gaussian contribution. For high-resolution spectroscopy in the pure-rotational region (~50-600 cm^{-1}) the spectrometer is adapted by changing the imaging lens to a slower

focus (f: 400 mm), resulting in a dispersion of ~0.27 cm^{-1}. H_2 CRS measurements were performed across the flame front of a laminar H_2/air diffusion flame, provided on a Bunsen burner: the probe volume was moved from the center of the burner towards its rim, in steps of 0.5 mm as shown in Fig. 1(d). A steel mesh was placed ~15 mm above the burner to stabilize the flame and the measurements were performed ~0.5 mm (H_2 CRS thermometry) and ~1 mm (preferential diffusion) above its nozzle. The H_2 flow was diluted in a 50% mixture with nitrogen (N_2) to perform conventional N_2 CRS thermometry for validation purposes. The *ex-situ* spectral referencing protocol is performed by measuring the NR CRS signal from the compressed supercontinuum generated in a flow of room temperature argon (which has no rotational degree of freedom).

3. Results

3.1. Autocorrelation measurements of the fs pump/Stokes pulse

The effect of temporal chirp in the pump/Stokes pulse on the spectral excitation efficiency is illustrated in Fig. 2. 1000-shot-averaged NR CRS spectra were recorded as a function of the pulse dispersion, controlled by the external compressor unit in Fig. 2 (a) and introduced by the optical window in Fig. 2 (b), in a non-resonant gas flow (methane, CH_4). The input pump/Stokes pulse energy was 50 μJ, i.e. lower than the filamentation onset. The amount of chirp in the input pulse is controlled by varying the angle of the diffraction grating in the external compressor unit (details in Supplement 1). A strong periodic modulation of the NR CRS spectra in Fig. 2(a) results from the introduction of quadratic phase to the pump/Stokes pulse, in accordance with the theoretical result of Eq. (8). The pulse transmission through the thick optical material only introduces linear chirp, as proven by the translation of the spectrochronogram from Fig. 2(a) to Fig. 2(b). The dependence of the NR CRS spectrum on the spectral phase of the pump/Stokes pulse can be exploited to measure its spectrochronographic properties: we do this by fitting the experimental spectra to our time-domain NR CRS model. We quantify the quadratic phase introduced by the external compressor, resulting in a stretching of the 35 fs near transform-limited (TL) pump/Stokes pulse in Fig. 2(c) to ~150 fs by either negative or positive dispersion. The same input chirp is combined with transmission through the window in Fig. 2(d), allowing for a direct evaluation of the positive group delay dispersion (GDD) arising due to the optical material: this is measured to be 424 fs^2, resulting in a stretching of the pulse duration to 47 fs. When the combined GDD is larger (in magnitude) than ~1000 fs^2, the autocorrelation of the pump/Stokes pulse results in the shift of the local maximum of the spectral excitation in the range ~300-1000 cm^{-1}, evident in the raw data of Fig. 2(a-b). For large pulse GDD, the NR CRS spectrum departs from the usual monotonic trend with the Raman shift, presenting multiple local maxima at locations which depend on the GDD itself. This behavior is similar to what has been shown by applying spectral focusing [40] and pulse shaping [41] techniques, but is here realized without any intra-pulse delay as our CRS system employs a single combined pump/Stokes pulse. Figure 2(e-f) shows the comparison of the experimental and the theoretical spectral autocorrelation of the fs pump/Stokes pulse as measured by the NR CRS signal. The time-domain CRS model illustrated by Fig. 2(e) predicts the parallel formation of spectral sidebands: this prediction is experimentally verified in Fig. 2(f). This behavior is analogous to the spectral focusing technique first demonstrated by T. Hellerer *et al.* [42] for CARS microscopy: introducing the same amount of GDD in their broadband fs pump and Stokes pulses, they demonstrated the coherent excitation of a narrow spectral region with spectral selectivity enabled by the tuning of the intrapulse delay. The experimental NR CRS spectra in Fig. 2(f) thus map the effect of the linear chirp in the input fs pulse, which results in the narrowing of the spectral excitation, and in its shift to values of the Raman shift $|\Omega| > 0$, even with a null intrapulse delay for our combined pump/Stokes pulse.

3.2. Generation of ultrabroadband coherent excitation behind the optical window

The use of ultrabroadband CRS techniques at measurement scenarios with an enclosed space (e.g. high-pressure combustors, optical cells, etc.) requires the experimentalist to maintain control of the spectral phase while the compressed supercontinuum pulse is transported through the optical windows, which is impractical, perhaps even impossible. In the present work we demonstrate that fs laser-induced filamentation [43,44] can be used to generate a compressed supercontinuum pulse *in-situ* behind an optical window, thus maximizing the rotational Raman coherence in gaseous H_2. The time-domain NR CSR model is extended to the ultrabroadband NR signal generated by the compressed supercontinuum acting as the pump/Stokes pulse. We let the duration of the fs pulse vary and used it as an additional fitting parameter, thus accounting for the increment of the pulse bandwidth due to its self-phase modulation in the filamentation process. The temporal compression of the resulting spectrally-broadened pulse, due to its non-linear propagation in the plasma medium, is again modelled by the GDD of the medium. The most stringent assumption introduced here is that of a symmetric broadening of the pulse spectrum, preserving its original Gaussian shape. The validity of this assumption could be limited when the pulse is compressed in air under tight focusing conditions: if the contribution of the non-linear refractive index of the dense plasma medium to self-phase modulation is greater than the one due to Kerr effect, an asymmetric broadening of the pulse spectrum would result to higher frequencies. Within the scope of the present work we nonetheless find the assumption reasonable, given the limited energy of the input fs pulse and the much-reduced density of the plasma generated in the hot environment of the flame. The pulse compression achieved via fs laser-induced filamentation can also be experimentally investigated as a function of the linear chirp in the input fs pulse, as shown in Fig. 3. The generation of the compressed supercontinuum in the filament depends on the complex interplay between multiple non-linear optical processes, whose relative magnitude is determined by the non-linear susceptibility of the gaseous medium where the filament is generated. While for non-resonant molecules (e.g. argon) the third-order non-linear susceptibility is entirely electronic in nature, the generation of rotational nuclear wave packets in Raman-active molecules (e.g. N_2 and O_2) can play a role in the pulse compression through self-phase modulation and non-linear light propagation. This explain the different output of the filamentation process, in terms of pulse compression and corresponding ultra-broad excitation bandwidth, in CH_4 and in air.

Figure 3(b) shows the ultrabroadband NR CRS spectra acquired in a room-temperature flow of CH_4, as a function of the linear chirp in the input pulse. The pulse compression –here quantified by the contour line at half maximum of the NR CRS spectrum in the region 200-1600 cm^{-1} (i.e. HWHM)– shows only a slight dependence on the input chirp pulse in the range between -500 fs^2 and 500 fs^2, and it decreases dramatically for larger (absolute) values of the pulse GDD. When realized in air, on the other hand, fs laser-induced filamentation has a more complex dependence on the input chirp, and the HWHM bandwidth contour shown in Fig. 3(a) remarkably presents a local minimum close to the condition of a TL pulse. Introducing a small amount of GDD in the input pulse enhances the pulse compression resulting in two local maxima of the excitation bandwidth for $\varphi_2 = 397$ fs^2 and $\varphi_2 = -492$ fs^2; the latter was found to optimize the pulse compression for ultrabroadband H_2 CRS spectroscopy in the flame. Furthermore, comparing the bandwidth of the compressed supercontinuum generated in CH_4 and in air, the higher electronic third-order susceptibility of CH_4, being almost thrice as large as that of N_2 and O_2 (see Table S1 in Supplement 1), results in a larger pulse compression via fs laser-induced filamentation. We operated the external compressor so as to optimize the pulse compression via filamentation in the flame environment, introducing a GDD of -492 fs^2 to the input pulse, which is thus stretched to $\sim$52 fs, as measured by the NR CRS signal in Fig. 3(c), recorded in flow of a non-resonant gas (argon) at low pulse energy (i.e. without filamentation).

Figure 3(d) shows the application of the NR CRS model to estimate the duration and the residual chirp of the compressed supercontinuum generated via fs laser-induced filamentation

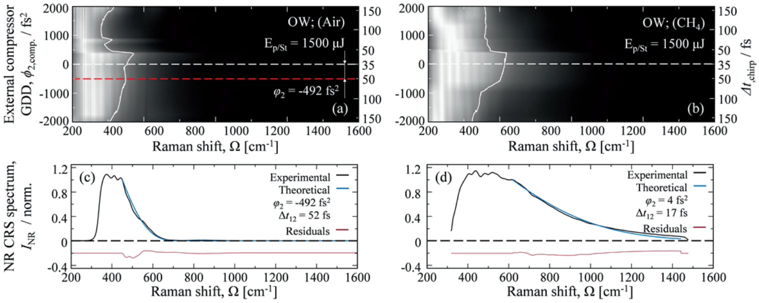

Fig. 3. Pulse compression by fs laser-induced filamentation behind the optical window. The ultrabroadband NR CRS signal is generated in room-temperature (a) air and (b) CH_4, for varying linear chirp in the input fs pump/Stokes pulse. 1000-shot-averaged spectra are shown. The white contour line identifies the HWHM excitation bandwidth. For moderate input chirp (i.e. $|\varphi_2| < 500$ fs^2) the bandwidth of the compressed supercontinuum generated in CH_4 is almost unaffected by the input chirp. In air, a local minimum in the bandwidth of the supercontinuum pulse is obtained for a TL input pulse, while two local maxima are achieved for slightly chirped pulses. The setting $\varphi_2 = -492$ fs^2 (dashed red line) of the external compressor was employed to optimize the pulse compression in the flame experiments. (c) 1000-shot-averaged NR CRS spectrum of the chirped input fs pulse optimized for pulse compression via filamentation in the flame environment (d) 1000-shot-averaged ultrabroadband NR CRS spectrum recorded in a flow of argon. The spectrum clearly displays the success of generating a compressed supercontinuum behind the optical window, which can be used for ultrabroadband CRS in enclosed spaces.

in argon (*ex-situ*): this is measured to be a near-TL pulse with a duration of 17 fs. Finally, we can estimate the impact that the optical window would have on the transmission of this supercontinuum pulse generated *ex-situ*, when employed as the pump/Stokes pulse for H_2 CRS behind the window itself. The ~424 fs^2 GDD introduced by 22 mm of BK7 glass would result in a significant stretch of the compressed supercontinuum generated *ex-situ*, to ~68 fs requiring additional phase control techniques to guarantee a sufficient excitation bandwidth and perform ultrabroadband CRS on H_2.

3.3. In-situ referencing of the compressed supercontinuum generated in the flame

The experimental protocol for the *in-situ* referencing [30] of the fs laser excitation of the Raman-active modes relies on the simultaneous generation of the resonant and NR CRS signals with orthogonal polarization. The theory of polarization control over the generation of the resonant and NR CRS signals is detailed in Supplement 1. We assume the polarization of our combined pump/Stokes pulse as a reference, and define the relative polarization angles of the probe, and the resonant and the NR components of the CRS signal respectively as α, β, and γ. The polarization angles of the resonant and NR CRS signals, as a function of the relative probe polarization angle, are:

$$\begin{gathered}\tan\beta = (1-2\rho)\tan\alpha \\ \tan\gamma = \tfrac{1}{3}\tan\alpha\end{gathered} \qquad (9)$$

where ρ is the depolarization ratio of the Raman-active molecules. The functional relations in Eq. (9) are represented on the unit sphere in Fig. 1(b). Coupling Eq. (9) with the condition for simultaneous generation of cross-polarized resonant and NR CRS signals, i.e. $|\beta - \gamma| = \pi/2$, we determine the required relative probe polarization angle:

$$\alpha = \tan^{-1}\left(\pm\frac{\sqrt{3}}{\sqrt{2\rho - 1}}\right) \tag{10}$$

Equation (10) has real solutions only for $\rho>1/2$: the applicability of the *in-situ* referencing protocol is thus limited to weakly-polarized or depolarized Raman transitions. In the present work we are interested in applying the *in-situ* referencing protocol to the pure-rotational CRS spectrum of H_2, whose Raman-activity is entirely due to their anisotropic polarizability: the pure-rotational H_2 Raman spectrum is thus entirely depolarized and $\rho = 3/4$. Equation (10) then gives the relative probe polarization angle that results in cross-polarized resonant H_2 and NR CRS signals: $\alpha = \tan^{-1}\sqrt{6}$.

Figure 4(a) shows the average NR CRS spectra acquired *in-situ* at each measurement location across the flame front (see Fig. 1(d)) and is compared to the average NR CRS spectrum generated *ex-situ* in room-temperature argon (same as Fig. 3 (d)). The ultrabroadband CRS signal spans over 1600 cm^{-1}, and the band-pass filter is tuned to transmit the spectral region ~300-1500 cm^{-1}. The comparison between the fs laser excitation efficiency, as mapped by the NR signal generated *in-situ versus ex-situ*, illustrates the significant impact of the boundary conditions to the supercontinuum generation via *in-situ* filamentation in the flame. The instantaneous bandwidth of the compressed supercontinuum is here defined as half-width-at-half-maximum (HWHM) of the signal over the measured spectral range ~300-1500 cm^{-1}, and it is measured to be 394 cm^{-1} for the compressed supercontinuum generated *ex-situ* in argon. For comparison the excitation bandwidth provided by a 35 fs TL pump/Stokes pulse over the spectral range ~300-1500 cm^{-1} is 126 cm^{-1}. In the flame, the bandwidth of the supercontinuum varies from 206 cm^{-1} at y = 0 mm to 136 cm^{-1} at y = 8 mm, corresponding to a pulse duration of respectively 26 fs (GDD = 100 fs^2) and 30 fs (GDD = 100 fs^2). This reduction in the pulse compression is due to the lower effective refractive index of the optical medium along the filament propagation across the flame front. This has a comparable effect on the two non-linear optical effects underlying fs laser-induced filamentation, i.e. optical Kerr effect and multi-photon ionization. The lesser effective refractive index of the optical medium at higher temperatures determines a reduction of the self-phase modulation of the fs pulse and of the plasma density in the filament, resulting in a lesser pulse compression. This effect is of course highly dependent on the spatio-temporal boundary conditions to the filamentation process, requiring the *in-situ* referencing protocol to faithfully map the excitation efficiency of the different Raman transitions. The locality of the supercontinuum generation is moreover evident looking at the progressive reduction in the excitation bandwidth from the center of the burner to its rim, due to the three-dimensional curvature of the conical flame.

3.4. Pure-rotational H_2 CSR spectroscopy

Figure 4(b) presents the single-shot resonant H_2 CRS spectra acquired across the flame front. Six rotational lines of H_2 –from O(2) at 354 cm^{-1} to O(7) at 1447 cm^{-1}– were detected simultaneously, at high temperature, in the detection bandwidth of the spectrometer and within the dynamic range of the sCMOS detector. The rotational lines in the resonant spectra show the characteristic alternating intensity of even and odd lines, in accordance with the degeneracy of the single and triplet spin states [29]. The progression along the transverse axis clearly shows the shift in the rotational Boltzmann population of the H_2 molecules with the increasing temperature across the flame front. At y = 0 the relatively low temperature of the molecular ensemble results in the lower rotational states, in particular $J = 1 \leftarrow 3$, being the most populated. Moving towards the rim of the burner, the increment in temperature results in the shift of the rotational population toward higher energy states: for y > 4.5 mm the transition $J = 3 \leftarrow 5$ dominates the rotational spectrum.

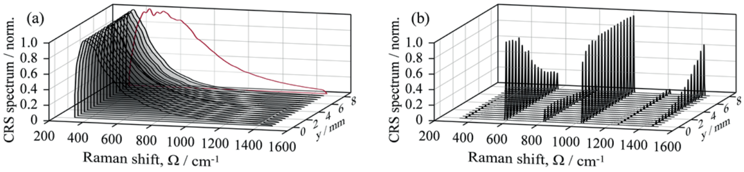

Fig. 4. (a) Ultrabroadband NR CRS spectra acquired *ex-situ* in room temperature argon (red curve) and *in-situ* at the different measurement locations across the flame front (black curves). Each curve represents the average of 1200 single-shot spectra. (b) Single-shot pure-rotational H_2 CRS spectra acquired across the flame front of a laminar H_2/air diffusion flame. Up to six rotational lines are detected simultaneously within the dynamic range of the sCMOS detector.

The single-shot H_2 spectra are fitted to a time-domain model similar to that presented in Ref. [29] (details in Supplement 1) to extract the local temperature across the flame front. An example of the spectral fit is shown in Fig. 5(a) and Fig. 5(b), where the comparison between the conventional *ex-situ* and the *in-situ* referencing protocol is presented. The larger bandwidth of the NR CRS signal generated *ex-situ* in room-temperature argon (Fig. 5(a)) overestimates the effective excitation efficiency of the higher Raman transitions, resulting in spectral cooling. This behavior severely skews the envelope of the Raman spectrum so that, even for the best-fitting temperature, the *ex-situ*-referenced spectrum does not follow Boltzmann distribution, as illustrated by the large misfit of most rotational lines. The use of the correct spectral reference, provided by the NR signal generated *in-situ* (Fig. 5(b)), is thus critical to perform quantitative spectroscopy on the pure-rotational H_2 spectrum. The temperature profile across the flame front, as measured by H_2 CRS thermometry, is shown in Fig. 5(c), along with the validation measurements performed by conventional N_2 CRS thermometry. As N_2-dilution of the H_2 flow is employed, conventional N_2 CRS measurements are possible on both sides of the flame front, allowing for a complete reconstruction of the temperature profile. H_2 on the other hand is rapidly consumed in the chemical reaction, so that the H_2 CRS signal rapidly decreases moving towards the burner rim, for the combined effect of the increasing temperature and the reduced H_2 concentration: ultrabroadband H_2 CRS measurements were performed up to $y = 8$ mm. The temperatures measured by N_2 CRS and H_2 CRS are well in agreement when the *in-situ* NR signal is employed for the spectral referencing of the ultrabroadband H_2 CRS spectra: the accuracy of the H_2 thermometry is below 1% for most measurement locations across the flame front. H_2 CRS thermometry employing *ex-situ* referencing, on the other hand, results in a significant bias (up to 80%) towards lower temperatures at all the measurement locations, as shown in Fig. 5(d).

The precision of ultrabroadband H_2 CRS thermometry was estimated as the standard deviation of the measured temperature over a sample of 1200 single-shot spectra. This is comparable to that of conventional N_2 CRS, varying in the range ~1-3%, for $y \leq 6.5$ mm, while it is negatively impacted by the H_2 consumption in the reaction zone of the flame, with a significant reduction of the signal intensity. At the last three measurement locations, this abatement of the signal impaired the detection of the O(2) line (see Fig. 4(b)), and the signal-to-background ratio (SBR) of the O(6) line was reduced to ~2. At the last measurement point, the O(5) line was barely detectable (SBR~1.3) and the spectral fit only relied on four lines, reducing the precision to ~9%. These temperature measurements are in good agreement with the values reported by Toro *et al* for a similar laminar H_2/air diffusion flame [45].

Ultrabroadband CRS further provides new insights in the molecular transport processes taking place in the measurement environment presented here. Figure 6(a) shows the experimental temperature and relative H_2/N_2 concentration profiles, measured by ultrabroadband CRS across

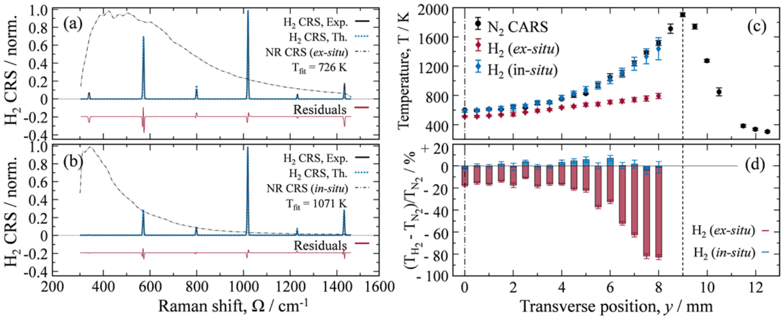

Fig. 5. (a) Single-shot experimental H_2 CRS spectrum (solid line) acquired in the flame at y = 6 mm, referenced by the NR CRS (dot-dashed line) spectrum acquired *ex-situ* in argon, and comparison to the time-domain H_2 CRS model (dotted line) to fit the Boltzmann distribution. (b) The same experimental spectrum is referenced by the NR CRS spectrum simultaneously acquired *in-situ*, and fitted to the time-domain H_2 CRS model. (c) Temperature profile measured by conventional pure-rotational N_2 CRS and ultrabroadband H_2 CRS spectroscopy. (d) Comparison of the measurement accuracy of H_2 CRS thermometry for the *ex-situ* and *in-situ* referencing protocols: the standard (*ex-situ*) protocol results in a consistent underestimation of the H_2 temperature.

the flame front: moving from the center of the burner to the chemical reaction zone, the H_2 concentration significantly reduces, from 50% to 40%, while the temperature presents only a minor increment up to y = 3.5 mm as shown in Fig. 6(b). This small change in temperature (~57 K) is attributed to heat transfer from the high-temperature reaction zone, rather than to the onset of the chemical reaction itself: H_2 is not consumed in this region, but it is rapidly transported towards the reaction zone, owing to its large mass diffusivity [31]. To the best of our knowledge, this represents the first direct observation of molecular preferential diffusion in a H_2/air flame.

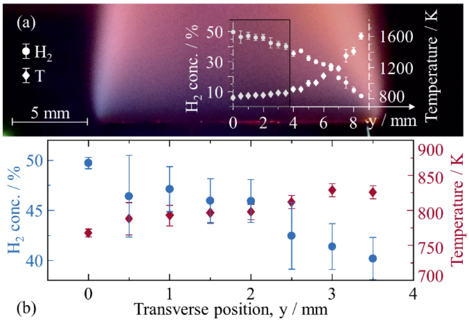

Fig. 6. (a) Simultaneous CRS measurement of the temperature and relative H_2/N_2 concentration across the flame front (1 mm above the nozzle). The black box represents the area of interest for H_2 preferential diffusion. (a) A significant reduction of the H_2 concentration, from 50% at y = 0 mm to 40% at y = 3.5 mm, is measured in the face of an almost constant temperature profile and is thus attributed to preferential diffusion.

4. Conclusions

A novel approach to ultrabroadband CRS is proposed as a straightforward pathway to rotational H_2 spectroscopy in closed environments, such as high-pressure combustors or chemical reactors. The investigation of H_2 chemistry by time-resolved coherent Raman techniques requires a compressed supercontinuum to generate coherence between the widely spaced states in the rotational energy manifold [29], but is hindered by the introduction of non-linear contributions to its spectral phase. To date ultrabroadband fs/ps H_2 CRS has not been applied in closed measurement scenarios.

The technique here proposed is based on the *in-situ* generation, use and referencing of the coherent excitation provided by supercontinuum compression in fs laser-induced filamentation. The 35 fs output of a regenerative fs laser amplifier was negatively chirped before its transmission through a 22 mm BK7 glass window, resulting in a residual negative chirp of ~490 fs^2: this value is experimentally demonstrated to optimize the multiphoton ionization and the optical Kerr effects that underpin the pulse compression in the filamentation process. We have shown that the NR CRS signal, which has often been considered detrimental to CRS, with much effort dedicated to its suppression [24,46], not only maps the efficiency of the coherent excitation delivered by the pump/Stokes pulse, but can be effectively used to perform spectral autocorrelation measurements of the pump/Stokes pulse and to characterize its transmission through optical media. This result is particularly powerful when combined to the last piece of the present diagnostic puzzle: the *in-situ* referencing protocol to monitor the ultrabroadband spectral excitation delivered by the compressed supercontinuum. This novel experimental protocol utilizes polarization control over the input laser fields to generate the resonant and NR signals with relative orthogonal polarization, and realizes their simultaneous separated detection in a polarization-sensitive coherent imaging spectrometer. Altogether *in-situ* generation, *in-situ* use, and *in-situ* referencing of the ultrabroadband coherent Raman excitation define a new diagnostics to investigate the rotational energy distribution in gaseous H_2.

Ultrabroadband H_2 CRS measurements were demonstrated over a wide range of temperature and H_2 concentration across a canonical H_2/air diffusion flame (Fig. 5), and validated against conventional N_2 CRS thermometry. The potential of our technique is further exemplified by what, to the best of our knowledge, is the first direct observation of H_2 preferential diffusion in H_2/air flames. The effect of the mass transport mechanism for the lightweight H_2 molecules is uncovered by the spatial mismatch of the temperature and relative H_2/N_2 concentration, as measured by pure-rotational CRS (Fig. 6). Although this configuration is designed for rather large-scale combustor test rigs (approximately 0.5 m in width), it can be extended to smaller-scale housings as in Ref. [26], provided that the numerical aperture and therefore the filament properties are maintained. For instance, the input beam diameter can be modified accordingly to reduce the field irradiance inside the window when short focal-length optics are required. We prospect the far ranging application of this diagnostics in all the research fields where H_2 chemistry plays a key role, from novel sustainable combustion technologies to methane reforming for H_2 production. To name one, liquid oxygen/gaseous H_2 rocket combustion is a thriving research field with application to low-Earth commercialization and sustainable space exploration [47]. Our technique has clear advantages in such high-pressure environments, where both the fs pulse compression and the coherent Raman excitations are enhanced, while time-resolved measurements can be realized probing the Raman coherences below the collisional time-scale.

Funding. Nederlandse Organisatie voor Wetenschappelijk Onderzoek (15690).

Acknowledgements. We gratefully acknowledge the financial support provided by the Netherlands Organization for Scientific Research (NWO), obtained through a Vidi grant in the Applied and Engineering Sciences domain (AES) (15690). A. Bohlin is thankful for support through the RIT (Space for Innovation and Growth) project/European Regional Development Fond in Kiruna, Sweden.

Disclosures. The authors declare no conflicts of interest.

Data availability. Data underlying the results presented in this paper are not publicly available at this time, but may be obtained from the authors upon reasonable request**.**

Supplemental document. See Supplement 1 for supporting content.

References

1. “Hydrogen on the rise,” Nat. Energy 1, 16127 (2016).
2. Y. Shagam, A. Klein, W. Skomorowski, R. Yun, V. Averbukh, C. P. Koch, and E. Narevicius, “Molecular hydrogen interacts more strongly when rotationally excited at low temperatures leading to faster reactions,” Nat. Chem. **7**(11), 921–926 (2015).
3. S. A. Lahankar, J. Zhang, K. G. McKendrick, and T. K. Minton, “Product-state-resolved dynamics of the elementary reaction of atomic oxygen with molecular hydrogen, $O(^3P) + D2 \longrightarrow OD(X\,^2\Pi) + D$,” Nat. Chem. **5**(4), 315–319 (2013).
4. N. G. Kling, S. Díaz-Tendero, R. Obaid, M. R. Disla, H. Xiong, M. Sundberg, S. D. Khosravi, M. Davino, P. Drach, A. M. Carroll, T. Osipov, F. Martín, and N. Berrah, “Time-resolved molecular dynamics of single and double hydrogen migration in ethanol,” Nat. Commun. **10**(1), 2813 (2019).
5. R. P. Lucht, “Femtosecond lasers for molecular measurements,” Science **316**(5822), 207–208 (2007).
6. D. A. Greenhalgh, “Raman: An eye for combustion studies,” Nature **291**(5816), 535–536 (1981).
7. S. Roy, J. R. Gord, and A. K. Patnaik, “Recent advances in coherent anti-Stokes Raman scattering spectroscopy: Fundamental developments and applications in reacting flows,” Prog. Energy Combust. Sci. **36**(2), 280–306 (2010).
8. C. E. Dedic, T. R. Meyer, and J. B. Michael, “Single-shot ultrafast coherent anti-Stokes Raman scattering of vibrational/rotational nonequilibrium,” Optica **4**(5), 563–570 (2017).
9. T. Chen, B. Goldberg, B. Patterson, E. Kolemen, C. Kliewer, K. Olemen, J. Yiguang, and C. H. J. K. Liewer, “1-D imaging of rotation-vibration non-equilibrium from pure rotational ultrafast coherent anti-Stokes Raman scattering,” Opt. Lett. **45**(15), 4252–4255 (2020).
10. I. R. Beattie, T. R. Gilson, and D. A. Greenhalgh, “Low frequency coherent anti-Stokes Raman spectroscopy of air,” Nature **276**(5686), 378–379 (1978).
11. R. L. Farrow and L. A. Rahn, “Optical Stark Splitting of Rotational Raman Transitions,” Phys. Rev. Lett. **48**(6), 395–398 (1982).
12. F. Benabid, F. Couny, J. C. Knight, T. A. Birks, and P. S. J. Russell, “Compact, stable and efficient all-fibre gas cells using hollow-core photonic crystal fibres,” Nature **434**(7032), 488–491 (2005).
13. R. L. Farrow and L. a Rahn, “Measurement of the self-broadening of the H_2 Q(0-5) Raman transitions from 295 to 1000 K,” Phys. Rev. A **43**(11), 6075–6088 (1991).
14. V. Bergmann and W. Stricker, “H_2 CARS thermometry in a fuel-rich, premixed, laminar CH_4/air flame in the pressure range between 5 and 40 bar,” Appl. Phys. B **61**(1), 49–57 (1995).
15. V. A. Shakhatov, O. De Pascale, M. Capitelli, K. Hassouni, G. Lombardi, and A. Gicquel, “Measurement of vibrational, gas, and rotational temperatures of H_2 $(X\,^1\Sigma_g{}^+)$ in radio frequency inductive discharge plasma by multiplex coherent anti-Stokes Raman scattering spectroscopy technique,” Phys. Plasmas **12**(2), 023504 (2005).
16. A. H. Zewail, “Laser Femtochemistry,” Science **242**(4886), 1645–1653 (1988).
17. T. Lang, K. Kompa, and M. Motzkus, “Femtosecond CARS on H_2,” Chem. Phys. Lett. **310**(1-2), 65–72 (1999).
18. H. Tran, P. Joubert, L. Bonamy, B. Lavorel, V. Renard, F. Chaussard, O. Faucher, and B. Sinardet, “Femtosecond time resolved coherent anti-Stokes Raman spectroscopy: Experiment and modelization of speed memory effects on H_2-N_2 mixtures in the collision regime,” J. Chem. Phys. **122**(19), 194317 (2005).
19. S. A. Magnitskiĭ and V. G. Tunkin, “Determination of the Dicke Narrowing in Gaseous Hydrogen By Direct Measurement of the Dephasing Time,” Sov. J. quantum Electron. **11**(9), 1218–1220 (1981).
20. W. D. Kulatilaka, P. S. Hsu, H. U. Stauffer, J. R. Gord, and S. Roy, “Direct measurement of rotationally resolved H_2 Q-branch Raman coherence lifetimes using time-resolved picosecond coherent anti-Stokes Raman scattering,” Appl. Phys. Lett. **97**(8), 081112 (2010).
21. M. O. Scully, G. W. Kattawar, R. P. Lucht, T. Opatrný, H. Pilloff, A. Rebane, A. V. Sokolov, and M. S. Zubairy, “FAST CARS: Engineering a laser spectroscopic technique for rapid identification of bacterial spores,” Proc. Natl. Acad. Sci. U. S. A. **99**(17), 10994–11001 (2002).
22. D. Pestov, R. K. Murawski, G. O. Ariunbold, X. Wang, M. Zhi, A. V. Sokolov, V. A. Sautenkov, Y. V. Rostovtsev, A. Dogariu, Y. Huang, and M. O. Scully, “Optimizing the laser-pulse configuration for coherent Raman spectroscopy,” Science **316**(5822), 265–268 (2007).
23. B. D. Prince, A. Chakraborty, B. M. Prince, and H. U. Stauffer, “Development of simultaneous frequency- and time-resolved coherent anti-Stokes Raman scattering for ultrafast detection of molecular Raman spectra,” J. Chem. Phys. **125**(4), 044502 (2006).
24. N. Dudovich, D. Oron, and Y. Silberberg, “Single-pulse coherently controlled nonlinear Raman spectroscopy and microscopy,” Nature **418**(6897), 512–514 (2002).
25. A. Bohlin and C. J. Kliewer, “Single-shot hyperspectral coherent Raman planar imaging in the range 0-4200 cm^{-1},” Appl. Phys. Lett. **105**(16), 161111 (2014).
26. D. R. Richardson, S. P. Kearney, and D. R. Guildenbecher, “Post-detonation fireball thermometry via femtosecond-picosecond coherent anti-Stokes Raman Scattering (CARS),” Proc. Combust. Inst. **38**(1), 1657–1664 (2021).

27. J. H. Odhner, D. A. Romanov, and R. J. Levis, "Rovibrational Wave-Packet Dispersion during Femtosecond Laser Filamentation in Air," Phys. Rev. Lett. **103**(7), 075005 (2009).
28. A. Bohlin, B. D. Patterson, and C. J. Kliewer, "Communication: Simplified two-beam rotational CARS signal generation demonstrated in 1D," J. Chem. Phys. **138**(8), 081102 (2013).
29. T. L. Courtney, A. Bohlin, B. D. Patterson, and C. J. Kliewer, "Pure-rotational H_2 thermometry by ultrabroadband coherent anti-stokes Raman spectroscopy," J. Chem. Phys. **146**(22), 224202 (2017).
30. F. Mazza, L. Castellanos, D. Kliukin, and A. Bohlin, "Coherent Raman imaging thermometry with in-situ referencing of the impulsive excitation efficiency," Proc. Combust. Inst. **38**(1), 1895–1904 (2021).
31. R. S. Barlow, M. J. Dunn, M. S. Sweeney, and S. Hochgreb, "Effects of preferential transport in turbulent bluff-body-stabilized lean premixed CH_4/air flames," Combust. Flame **159**(8), 2563–2575 (2012).
32. D. Meshulach and Y. Silberberg, "Coherent quantum control of two-photon transitions by a femtosecond laser pulse," Nature **396**(6708), 239–242 (1998).
33. A. A. Lanin, I. V. Fedotov, A. B. Fedotov, D. A. Sidorov-Biryukov, and A. M. Zheltikov, "The phase-controlled Raman effect," Sci. Rep. **3**(1), 1842 (2013).
34. U. Gaubatz, P. Rudecki, S. Schiemann, and K. Bergmann, "Population transfer between molecular vibrational levels by stimulated Raman scattering with partially overlapping laserfields. A new concept and experimental results," J. Chem. Phys. **92**(9), 5363–5376 (1990).
35. S. Zhdanovich, E. A. Shapiro, M. Shapiro, J. W. Hepburn, and V. Milner, "Population transfer between two quantum states by piecewise chirping of femtosecond pulses: Theory and experiment," Phys. Rev. Lett. **100**(10), 103004 (2008).
36. C. H. Camp, Y. J. Lee, J. M. Heddleston, C. M. Hartshorn, A. R. H. Walker, J. N. Rich, J. D. Lathia, and M. T. Cicerone, "High-speed coherent Raman fingerprint imaging of biological tissues," Nat. Photonics **8**(8), 627–634 (2014).
37. F. Mazza, N. Griffioen, L. Castellanos, D. Kliukin, and A. Bohlin, "High-temperature rotational-vibrational O_2-CO_2 coherent Raman spectroscopy with ultrabroadband femtosecond laser excitation generated in-situ," Combust. Flame **237**, 111738 (2022).
38. S. Rostami, J.-C. Diels, and L. Arissian, "Polarization evolution of ultrashort pulses in air," Opt. Express **23**(3), 3299–3307 (2015).
39. A. H. Sheinfux, E. Schleifer, J. Papeer, G. Fibich, B. Ilan, and A. Zigler, "Measuring the stability of polarization orientation in high intensity laser filaments in air," Appl. Phys. Lett. **101**(20), 201105 (2012).
40. E. T. J. Nibbering, D. A. Wiersma, and K. Duppen, "Ultrafast Nonlinear Spectroscopy with Chirped Optical Pulses," Phys. Rev. Lett. **68**(4), 514–517 (1992).
41. Y. J. Yan and S. Mukamel, "Pulse shaping and coherent Raman spectroscopy in condensed phases," J. Chem. Phys. **94**(2), 997–1005 (1991).
42. T. Hellerer, A. M. K. Enejder, and A. Zumbusch, "Spectral focusing: High spectral resolution spectroscopy with broad-bandwidth laser pulses," Appl. Phys. Lett. **85**(1), 25–27 (2004).
43. F. Théberge, N. Aközbek, W. Liu, A. Becker, and S. L. Chin, "Tunable ultrashort laser pulses generated through filamentation in gases," Phys. Rev. Lett. **97**(2), 023904 (2006).
44. A. Mysyrowicz, A. Couairon, and U. Keller, "Self-compression of optical laser pulses by filamentation," New J. Phys. **10**(2), 025023 (2008).
45. V. V Toro, A. V Mokhov, H. B. Levinsky, and M. D. Smooke, "Combined experimental and computational study of laminar, axisymmetric hydrogen–air diffusion flames," Proc. Combust. Inst. **30**(1), 485–492 (2005).
46. L. Gong, W. Zheng, Y. Ma, and Z. Huang, "Higher-order coherent anti-Stokes Raman scattering microscopy realizes label-free super-resolution vibrational imaging," Nat. Photonics **14**(2), 115–122 (2020).
47. F. Grisch, P. Bouchardy, and W. Clauss, "CARS thermometry in high pressure rocket combustors," Aerosp. Sci. Technol. **7**(4), 317–330 (2003).

Equation Chapter 1 Section 1
Coherent Raman spectroscopy on hydrogen with *in-situ* generation, *in-situ* use, and *in-situ* referencing of the ultrabroadband excitation: supplementary material

FRANCESCO MAZZA,[1] AERT STUTVOET,[1] LEONARDO CASTELLANOS,[1] DMITRII KLIUKIN,[1,2] AND ALEXIS BOHLIN[1,3,*]

[1]*Faculty of Aerospace Engineering, Delft University of Technology, Kluyverweg 1, 2629 HS Delft, The Netherlands*
[2]*LaserLaB, Department of Physics and Astronomy, Vrije Universiteit Amsterdam, De Boelelaan 1081, 1081 HV Amsterdam, The Netherlands*
[3]*Space Propulsion Laboratory, Department of Computer Science, Electrical and Space Engineering, Luleå University of Technology, 98128, Kiruna, Sweden*
**alexis.bohlin@ltu.se*

This document provides supplementary information to "Coherent Raman spectroscopy on hydrogen with *in-situ* generation, *in-situ* use, and *in-situ* referencing of the ultrabroadband excitation". The theory of the polarization of the non-linear CRS field is presented along with the derivation of the relative polarization angle between the probe and pump/Stokes beams to generate the resonant and non-resonant (NR) CRS signals with orthogonal polarization. The details of the time-domain model employed to simulate the H_2 CSRS signal, are provided. The experimental details of the NR CRS signal measurements are discussed along with the use of the time-domain NR CRS model to measure the spectrochronographic properties of the fs pump/Stokes pulse transmitted through a thick optical window.

1. Polarization theory of coherent Raman scattering

The theory of polarization control over the generation of the resonant and NR CRS signals relies on the model of the non-linear optical response of isotropic media developed by A. Owyoung [1]. The third-order susceptibility tensor $\chi^{(3)}$ of gaseous H_2 is written as a linear combination of the electronic response function σ, and the nuclear response function with isotropic and anisotropic components, respectively a and b:

$$\begin{aligned}\chi^{(3)}_{ijkl}=\frac{1}{24}\Big\{&\left[\sigma+2a\left(-\omega_2+\omega_3\right)+b\left(\omega_1+\omega_3\right)+b\left(\omega_1-\omega_2\right)\right]\delta_{ij}\delta_{kl}\\&+\left[\sigma+2a\left(\omega_1-\omega_2\right)+b\left(\omega_1+\omega_3\right)+b\left(-\omega_2+\omega_3\right)\right]\delta_{ij}\delta_{kl}+\\&\left[\sigma+2a\left(\omega_1+\omega_3\right)+b\left(-\omega_2+\omega_3\right)+b\left(\omega_1-\omega_2\right)\right]\delta_{ij}\delta_{kl}\Big\}\end{aligned}\qquad\text{(S1)}$$

where the indexes l, k, j and i represent the polarization direction of the pump, Stokes, probe and CRS field, modelled in the frequency domain as monochromatic waves at frequencies ω_1, ω_2, ω_3 and ω_4. The CRS polarization field is thus computed as the combination of the input pump, Stokes and probe fields with the susceptibility tensor:

$$P^{(3)}_i\left(\omega_4\right)=\varepsilon_0\sum_{ijkl}\chi^{(3)}_{ijkl}\left(-\omega_4,\omega_1,-\omega_2,\omega_3\right)\cdot E_l\left(\omega_3\right)\cdot E^*_k\left(\omega_2\right)\cdot E_j\left(\omega_1\right)\qquad\text{(S2)}$$

where ε_0 is the dielectric constant of vacuum and E_j, E_k, and E_l represent the complex spectral envelopes of the pump, Stokes and probe fields, respectively. We can here invoke the rotating wave approximation (RWA) to simplify Eq. (S1), neglecting the terms of the form $|\omega_i+\omega_j|$, which oscillate at optical frequencies, and introduce the parameter $\zeta = 2\rho/(1-\rho)$, with $\rho = b/2(a+b)$ being the depolarization ratio of the Raman-active molecules. The only non-vanishing terms in Eq. (S1) are then:

$$\begin{cases}\chi^{(3)}_{1111}=\frac{1}{24}\left\{3\sigma+2\left(1+\zeta\right)\left[\left(-\omega_2+\omega_3\right)+\left(\omega_1-\omega_2\right)\right]\right\}\\\chi^{(3)}_{1122}=\frac{1}{24}\left\{\sigma+a\left[2\left(-\omega_2+\omega_3\right)+\zeta\left(\omega_1-\omega_2\right)\right]\right\}\\\chi^{(3)}_{1221}=\frac{1}{24}\left\{\sigma+a\left[\zeta\left(-\omega_2+\omega_3\right)+2\left(\omega_1-\omega_2\right)\right]\right\}\\\chi^{(3)}_{1212}=\frac{1}{24}\left\{\sigma+a\zeta\left[\left(-\omega_2+\omega_3\right)+\left(\omega_1-\omega_2\right)\right]\right\}\end{cases}\qquad\text{(S3)}$$

Substituting Eq. (S3) into Eq. (S2), and defining α the relative polarization angles of the probe with respect to the polarization direction of the combined pump/Stokes field (with frequency ω_{12}), we can project the CRS polarization along an arbitrary direction, identified by the angle ξ, as:

$$\begin{aligned}P_{\xi}^{(3)}(\omega_4)=\{a[&(\zeta(-\omega_2+\omega_3)+2(\omega_1-\omega_2))\sin\alpha\sin\xi+\\&2(1+\zeta)((-\omega_2+\omega_3)+(\omega_1-\omega_2))\cos\alpha\cos\xi]+\\&\sigma[\sin\alpha\sin\xi+3\cos\alpha\cos\xi]\}E(\omega_3)E^{*}(\omega_{12})E(\omega_{12})\end{aligned}\tag{S4}$$

Eq. (S4) can be further simplified assuming the probe field to be far detuned from any electronic resonance of the Raman active molecules so that $|\omega_3-\omega_2|>>|\omega_1-\omega_2|$, and by again invoking the RWA:

$$\begin{aligned}P_{\xi}^{(3)}(\omega_4)\propto\{a[&2(\omega_1-\omega_2)\sin\alpha\sin\xi+\\&2(1+\zeta)(\omega_1-\omega_2)\cos\alpha\cos\xi]+\\&\sigma[\sin\alpha\sin\xi+3\cos\alpha\cos\xi]\}E(\omega_3)E^{*}(\omega_{12})E(\omega_{12})\end{aligned}\tag{S5}$$

We now define the relative polarization angles of the resonant and the non-resonant components of the CRS field respectively as β and γ:

$$\begin{aligned}P_{\text{resonant}}^{(3)}(\omega_4)&\propto a(\omega_1-\omega_2)[2\sin\alpha\sin\beta+\\&\qquad 2(1+\zeta)\cos\alpha\cos\beta]E(\omega_3)E^{*}(\omega_2)E(\omega_1)\\P_{\text{non-resonant}}^{(3)}(\omega_4)&\propto\sigma(\sin\alpha\sin\gamma+\\&\qquad 3\cos\alpha\cos\gamma)E(\omega_3)E^{*}(\omega_{12})E(\omega_{12})\end{aligned}\tag{S6}$$

Eq. (S6) is used to compute the polarization angles of the resonant and NR CRS fields as functions of the relative probe polarization angle:

$$\begin{aligned}\tan\beta&=(1-2\rho)\tan\alpha\\\tan\gamma&=\frac{1}{3}\tan\alpha\end{aligned}\tag{S7}$$

The functional relationships in Eq. (S7) are represented on the unit sphere in Fig. S1, representing the probe polarization angle as the azimuthal angle and the polarization angles of the resonant and non-resonant CRS signals as the elevation angle.

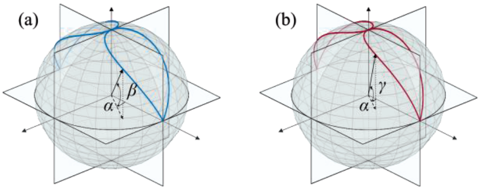

Fig. S1. (a) Polarization angle of the resonant pure-rotational H_2 CRS signal (β), represented as the elevation angle of a point on the unit sphere, as a function of the polarization of the probe field with respect to the pump/Stokes field (α), represented as the azimuthal angle of said point, according to Eq. (S7). (a) Polarization angle of the non-resonant CRS signal (γ) as a function of the polarization of the probe field with respect to the pump/Stokes field (α), according to Eq. (S7).

2. Time-domain H_2 CSRS model

The time-domain model of the H_2 CSRS signal follows the mathematical treatment presented in Ref. [2]. The third-order non-linear polarization field can be modelled in the time domain as:

$$\begin{aligned}P^{(3)}(t,\tau_{12},\tau_{23})=\left(\frac{i}{h}\right)^{3}\int_0^\infty dt_3\int_0^\infty dt_2\int_0^\infty dt_1\Big[&\left(\chi_{\text{CSRS}}^{(3)}+\chi_{\text{NR}}^{(3)}\right)\cdot\\&E_3(t+t_1-\tau_{12}+t_2-\tau_{23}+t_3)e^{i(\omega_1-\omega_2+\omega_3)t_3}\cdot\\&E_2^{*}(t+t_1-\tau_{12}+t_2)e^{i(\omega_1-\omega_2)t_2}\cdot E_1(t+t_1)e^{i\omega_1 t_1}\Big]\end{aligned}\tag{S8}$$

with E_1, E_2, and E_3 being the complex time-domain envelopes of the pump, Stokes and probe fields, oscillating at frequencies ω_1, ω_2, and ω_3, respectively. The integration times t_1, t_2, and t_3 represent the coherence timescales after the interaction with the corresponding fields, while τ_{12} and τ_{23} are the intra-pulse delay between the pump and Stokes and the Stokes and probe pulses, respectively.

The two contributions to the third-order optical susceptibility $\chi^{(3)}$ represent the effect of the resonant and non-resonant non-linearities in the optical response of the Raman-active molecules, where the first one is due to the stimulated Raman excitation of ro-vibrational wave packets for the nuclear wave function, by the pump and Stokes fields. The second contribution is due to the electronic coherence induced in the medium by the far-detuned pump, Stokes and probe fields, and is discussed in details in the next section. The resonant contribution to the third-order non-linear polarization field in Eq. (S8) is computed assuming that the molecular Raman frequencies of the gas-phase medium are matched by frequency pairs found across the bandwidth of a single broadband combined pump/Stokes pulse, $E_{12}(t)e^{i(\omega_2-\omega_1)t}+c.c.$ with "*c.c.*" denoting the complex conjugate. Eq. (S8) is thus recast as:

$$P^{(3)}_{\text{CSRS}}(t,\tau)=\left(\frac{i}{\hbar}\right)^3\int_0^\infty dt_3\int_0^\infty dt_{12}\Big[\chi^{(3)}_{\text{CSRS}}\cdot E_3\left(t+t_{12}-\tau+t_3\right)\cdot e^{i(\omega_1-\omega_2+\omega_3)t_3}\left(E_{12}*E^*_{12}\right)\left(t+t_{12}\right)e^{i(\omega_1-\omega_2)t_{12}}\Big] \tag{S9}$$

Under the assumptions of impulsive excitation of the rotational Raman coherence by the combined pump/Stokes field, and of instantaneous dephasing of the electronic coherence induced by the detuned probe field, the resonant non-linear susceptibility induced in the medium as a function of time can be written as:

$$\chi^{(3)}_{\text{CSRS}}(t)=\chi^{(3)}_{\text{CSRS}}(t,t_3)\delta(t_3) \tag{S10}$$

The temporal evolution of the resonant CSRS field is thus obtained by substituting Eq. (S10) into Eq. (S9):

$$P^{(3)}_{\text{CSRS}}(t,\tau)=\left(\frac{i}{\hbar}\right)^3 E_3(t-\tau)\cdot\chi^{(3)}_{\text{CSRS}}(t) \tag{S11}$$

The resonant CSRS signal can thus be computed in the time domain as the product of the experimentally-measured temporal envelope of the probe field and the third-order non-linear optical susceptibility of the gas-phase medium. The latter is computed according to a phenomenological model as the linear combination of dampened harmonic oscillators at the frequencies of the rotational Raman resonances of the H_2 molecules [3], with the combination coefficients representing the probability for the different rotational transitions:

$$\chi^{(3)}(t)=\sum_v\sum_J W_{v,J-2\leftarrow v,J}\cdot\exp\left[\left(i\omega_{v,J-2\leftarrow v,J}-\Gamma_{v,J-2\leftarrow v,J}\right)t\right] \tag{S12}$$

Here, $\omega_{v,J-2\leftarrow v,J}$ is the angular frequencies of the pure-rotational Stokes Raman transition $|v,J-2\rangle\leftarrow|v,J\rangle$ taken from Ref. [4], $\Gamma_{v,J-2\leftarrow v,J}$ is the coefficient associated to its temporal dephasing due to molecular collisions, and $W_{v,J-2\leftarrow v,J}$ is the overall transition probability. In the present work we neglect the effect of collisional dephasing of the H_2 Raman coherences in the light of its large timescale at ambient pressure [5] and of the short probe delay employed to simultaneously generate the resonant and NR CRS signals. The transition probabilities are computed as:

$$W_{v,J-2\leftarrow v,J}=\gamma^2_{v,J}\cdot b_{J-2\leftarrow J}\cdot F_J\cdot\left|N_{v,J}-N_{v,J-2}\right| \tag{S13}$$

with $\gamma^2_{v,J}$ being the polarizability anisotropy of the H_2 molecule, $b_{J-2\leftarrow J}$ the Placzek-Teller coefficients accounting for the coupling of the angular momenta, F_J the Herman-Wallis factors accounting for the vibrational-rotational coupling, $N_{v,J}$ and $N_{v,J-2}$ the Boltzmann populations in the initial and final ro-vibrational states, respectively. The Placzek-Teller coefficients for the pure-rotational O-branch spectrum is given by the algebraic formula

$$b_{J-2\leftarrow J}=\frac{3J(J-1)}{2(2J+3)(2J+1)} \tag{S14}$$

The Herman-Wallis factors play a significant role in the Raman spectra of light-weight molecules, such as H_2, which show a significant coupling between the vibrational and rotational degrees of freedom [6]. In the present work the Herman-Wallis factors are computed as [7]:

$$F_J=\left[1+\frac{\eta^2}{\chi}\left(J^2+3J+3\right)\right]^2 \tag{S15}$$

where $\eta = 2B_e/\omega_e$ is the ratio between the equilibrium values of the rotational (B_e = 60.8 cm^{-1} [8]) and vibrational constants (ω_e = 4401 cm^{-1} [8]), and χ here represents the ratio of the first two terms in the Taylor expansion of polarizability anisotropy as a function of the inter-nuclear distance, with value χ = 0.38 for H_2 [9].

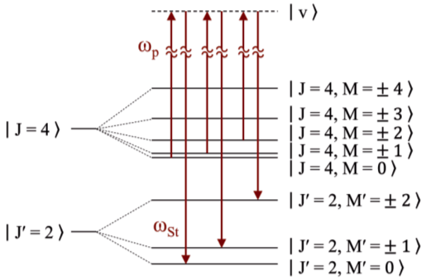

Fig. S2. Coherent transition between rotational states of the H_2 molecule. According to the selection rules of the pure-rotational CSRS process ($\Delta J = -2$ and $\Delta M = 0$), transitions are only possible between states of equal magnetic quantum number: the multiplicity of these degenerate Zeeman substates is thus taken to be $g_z = 2J'+1$, with J' being the lower (final) rotational state in the transition. An example is here presented, where the stimulated Raman transition from the Zeeman substates $|J = 4, M = \pm 3\rangle$ and $|J = 4, M = \pm 4\rangle$ are forbidden, and the Zeeman multiplicity is $g_z = 5$.

The differential Boltzmann population between the initial and final ro-vibrational states is computed as the product of the number density of scatters N, the difference between the Boltzmann populations in the initial and final states, their nuclear spin degeneracy, and the Zeeman degeneracy of the lower J-state:

$$\left|N_{v,J} - N_{v,J-2}\right| = N \cdot g_N \cdot g_Z \cdot \left|\rho_{v,J} - \rho_{v,J-2}\right| \qquad \text{(S16)}$$

with nuclear spin degeneracy g_N being respectively 1 or 3 for even or odd values of the total angular momentum quantum number J (called the “para-” and “ortho-” spin-isomeric forms of the H_2 molecule), and the Zeeman degeneracy ($g_z = 2J - 3$), quantifying the multiplicity of magnetic sub-states. According to the selection rules for the pure-rotational Raman transitions, $\Delta J = -2$ and $\Delta M = 0$ (with M magnetic quantum number), the multiplicity of magnetic sub-states is taken to be the one of the final rotational state (i.e. the lower energy state, $|J', M'\rangle$) for the O-branch spectrum, as shown in Fig. S2.

The time-domain model was further simplified, with regard to the spectral linewidths, by assuming the dephasing of the H_2 CRS signal to be entirely due to the frequency spread of the rotational wave packet, and neglecting the effect of molecular collisions. This assumption is justified, under the experimental conditions of the present work, as the H_2 CRS signal shows a low rotational energy transfer at ambient pressure (as compared to other diatomic molecules such as N_2), and the H_2 CRS signal was generated with a probe pulse delay varying in the range 0-10 ps, so that the effect of molecular collisions is negligible.

3. Autocorrelation measurements – Experimental details

A folded grating compressor [10] is employed in the setup to compress the output of the regenerative chirped-pulse amplifier, and the diffraction grating is mounted on a motorized tilt stage to control its angle relative to the beam path. This can be changed to introduce linear pre-chirp to the pulse, and compensate for the group delay dispersion (GDD) introduced along the fs beam path, e.g. by the thick optical window.

Table S1 Electronic third-order susceptibilities of various gases.

Gas	$\chi^{(3)}_{\mathrm{NR}}$
Ar	9.46
CH_4	22.7
N_2	7.90
O_2	7.98
H_2	5.90

Experimental values taken from Ref. [11].

Methane was selected for this experiment owing to its large third-order electronic susceptibility –more than twice the one of argon and almost four times the one of H_2, as shown in Table S1–, which allowed us to maintain a signal-to-background ratio greater than 10 for all the acquired datasets. Modelling the output of the regenerative Ti:Sapphire amplifier as a Gaussian laser pulse with a measured bandwidth of 27.2 nm at 806.7 nm, the spectrochronographic properties of the pump/Stokes pulse are represented in Fig. S3(a-c) by the Wigner function for a negatively-chirped, TL and positively-chirped pulse, respectively, corresponding to a two-dimensional Gaussian function. A sketch of the behavior of the spectral autocorrelation for a linearly chirped degenerate pump/Stokes pulse, and thus for of the NR CRS spectrum, is provided in Fig. S3(d-l).

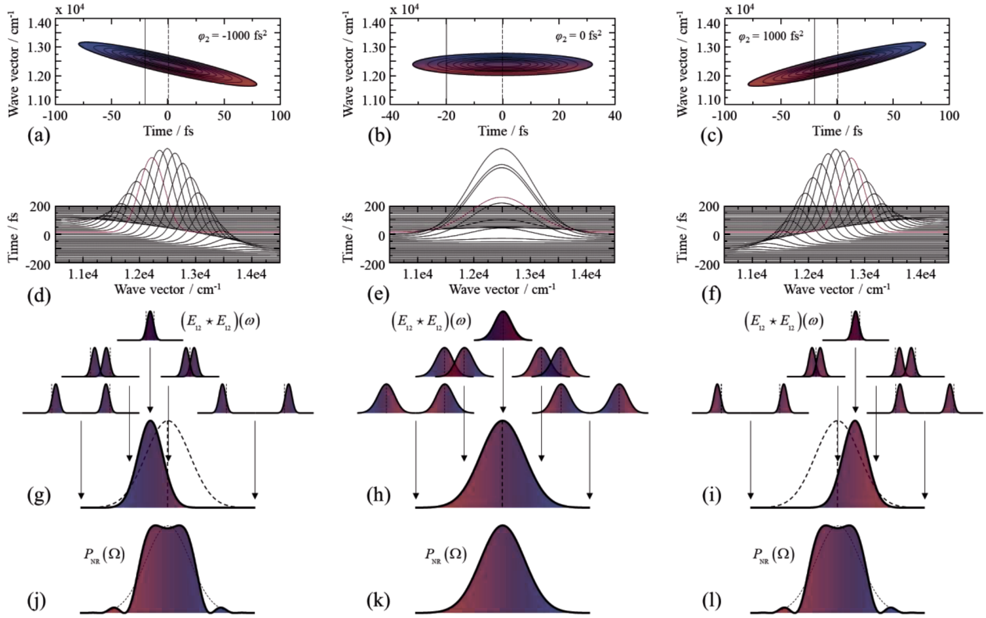

Fig. S3 (a) Wigner function of a negatively-chirped pump/Stokes pulse ($\varphi_2 = -1000$ fs^2). (b) Wigner function of a transform-limited pump/Stokes pulse. (c) Wigner function of a positively-chirped pump/Stokes pulse ($\varphi_2 = 1000$ fs^2). (d) Amplitude spectrum of the negatively-chirped pulse field at different times: the red curve represents the spectrum of the instantaneous sub-pulse at time $t = -20$ fs. The linear chirp results in an asymmetric profile of the sub-pulse spectrum for $t \neq 0$ fs. (e) Amplitude spectrum of the TL pulse field at different times: the red curve represents the spectrum of the instantaneous sub-pulse at time $t = -20$ fs. As the spectral phase is linear for the TL pulse, all the instantaneous sup-pulses have Gaussian spectra. (f) Amplitude spectrum of the positively-chirped pulse field at different times: the red curve represents the spectrum of the instantaneous sub-pulse at time $t = -20$ fs. (g) Spectral autocorrelation of the negatively-chirped sub-pulse at time $t = -20$ fs: the maximum excitation efficiency available at this time instant is shifted to $\Omega < 0$. (h) Spectral autocorrelation of the TL sub-pulse at time $t = -20$ fs: the resulting excitation efficiency profile is a Gaussian with maximum at $\Omega = 0$. (i) Spectral autocorrelation of the positively-chirped sub-pulse at time $t = -20$ fs: the maximum excitation efficiency available at this time instant is shifted to $\Omega > 0$. (j) Amplitude spectrum of the NR CRS signal generated by the negatively-chirped pump/Stokes pulse: this results from the temporal integration of the excitation efficiency provided by each instantaneous sub-pulse. The introduction of negative chirp in the pump/Stokes pulse thus results in the shift of the maximum at $|\Omega| \neq 0$, and in the formation of spectral sidebands. (k) Amplitude spectrum of the NR CRS signal generated by the TL pump/Stokes pulse: in absence of the quadratic phase term, the spectrum is a Gaussian centered at $\Omega = 0$. (l) Amplitude spectrum of the NR CRS signal generated by the negatively-chirped pump/Stokes pulse: analogous to the case of negative chirp, the quadratic phase results in the generation of spectral sidebands, but the magnitude of the focusing effect is not symmetric with respect to $\pm\varphi_2$.

The temporal instantaneous intensity of the pulse can be obtained by integration of the Wigner function over the frequency domain, while integration over the time domain yields the power spectrum of the pulse [12]. Introducing a quadratic phase –represented in Fig. S3(a-c) by the change in color– to the pump/Stokes pulse, the covariance matrix of the time and frequency variables is non-diagonal and thus quantifies the linear change in the carrier frequency over the temporal duration of the pulse. The NR CRS is generated by the FWM interaction of the degenerate pump/Stokes and probe fields, through the virtual electronic states represented in Fig. 1(a) of the main text, so that the process is assumed to be instantaneous. Hence, at each instant of time, the coherent excitation delivered by the pump/Stokes pulse, as mapped by the NR CRS signal, is the spectral autocorrelation of the sub-pulse given as the local section of the Wigner surface, an example being given by the red curves in Fig. S3(d-f), representing the sub pulse at time $t = -20$ fs. The results of the autocorrelation of these sub pulses, shown in Fig. S3(g-i), depends on the shape of the spectrum of each sub pulse: in case of a TL pump/Stokes pulse, this is obviously a Gaussian. When a linear chirp is introduced in the pump/Stokes pulse, on the other hand, the resulting spectral asymmetry determines a shift of the maximum excitation efficiency at values of the Raman shift $|\Omega| \neq 0$, with the sign depending on the chirp being negative or positive, as well as on the instant of time considered. The NR CRS signal of course results from the integration of this process over the duration of the pump/Stokes pulse: the experimental NR CRS spectrum being recorded by the sCMOS detector over a timeframe (1 ms) much larger than the tens of fs spanned by the pump/Stokes pulse. Fig. S3(j-l) show the resulting amplitude spectra of the NR CRS signal: in case of a TL pulse this is trivially a Gaussian, but when temporal chirp is present in the pulse, the quadratic phase term results in the periodic modulation predicted by the NR CRS model.

References

1. A. Owyoung, "The origin of the nonlinear refractive index of liquids and glasses," California Institute of Technology (1972).
2. B. D. Prince, A. Chakraborty, B. M. Prince, and H. U. Stauffer, "Development of simultaneous frequency- and time-resolved coherent anti-Stokes Raman scattering for ultrafast detection of molecular Raman spectra," J. Chem. Phys. **125**, 044502 (2006).
3. T. L. Courtney, A. Bohlin, B. D. Patterson, and C. J. Kliewer, "Pure-rotational H_2 thermometry by ultrabroadband coherent anti-stokes Raman spectroscopy," J. Chem. Phys. **146**, 224202 (2017).
4. J. Komasa, K. Piszczatowski, M. Przybytek, B. Jeziorski, and K. Pachucki, "Quantum Electrodynamics Effects in Rovibrational Spectra of Molecular Hydrogen," J. Chem. Theory Comput. **7**, 3105–3115 (2011).
5. W. D. Kulatilaka, P. S. Hsu, H. U. Stauffer, J. R. Gord, and S. Roy, "Direct measurement of rotationally resolved H_2 Q-branch Raman coherence lifetimes using time-resolved picosecond coherent anti-Stokes Raman scattering," Appl. Phys. Lett. **97**, 2–5 (2010).
6. M. Marrocco, "Herman-Wallis factor to improve thermometric accuracy of vibrational coherent anti-Stokes Raman spectra of H_2," Proc. Combust. Inst. **32**, 863–870 (2009).
7. R. H. Tipping and J. F. Ogilvie, "Herman-wallis factors for Raman transitions of $^1\Sigma$-state diatomic molecules," J. Raman Spectrosc. **15**, 38–40 (1984).
8. G. Herzberg, *Molecular Spectra and Molecular Structure. I. Spectra of Diatomic Molecules*, 2nd ed. (Van Nostrand Reinhold Company, 1950).
9. C. Asawaroengchai and G. M. Rosenblatt, "Rotational Raman intensities and the measured change with internuclear distance of the polarizability anisotropy of H_2, D_2, N_2, O_2, and CO," J. Chem. Phys. **72**, 2664–2669 (1980).
10. F. Träger, *Springer Handbook of Laser and Optics* (2007).
11. J. W. Hahn and E. S. Lee, "Measurement of nonresonant third-order susceptibilities of various gases by the nonlinear interferometric technique," J. Opt. Soc. Am. B **12**, 1021–1027 (1995).
12. L. Praxmeyer and K. Wodkiewicz, "Time and Frequency description of Optical Pulses," Laser Phys. **15**, 1477 (2005).

The ro-vibrational ν_2 mode spectrum of methane investigated by ultrabroadband coherent Raman spectroscopy

Francesco Mazza,[1,a)] Ona Thornquist,[1] Leonardo Castellanos,[1] Thomas Butterworth,[2] Cyril Richard,[3] Vincent Boudon,[3] and Alexis Bohlin[1,4]

[1]Faculty of Aerospace Engineering, Delft University of Technology, Kluyverweg 1, 2629 HS Delft, The Netherlands

[2]Faculty of Science and Engineering, Maastricht University, Paul Henri Spaaklaan 1, 6229 GS Maastricht, The Netherlands

[3]Laboratoire Interdisciplinaire Carnot de Bourgogne, UMR 6303 CNRS - Université Bourgogne Franche-Comté 9 Avenue Alain Savary, BP 47 870, F-21078 Dijon Cedex, France

[4]Space Propulsion Laboratory, Department of Computer Science, Electrical and Space Engineering, Luleå University of Technology, Bengt Hultqvists väg 1, 981 92 Kiruna, Sweden

[a)] Author to whom correspondence should be addressed: f.mazza@tudelft.nl

---

ABSTRACT

We present the first experimental application of coherent Raman spectroscopy (CRS) on the ro-vibrational ν_2 mode spectrum of methane (CH_4). Ultrabroadband femtosecond/picosecond (fs/ps) CRS is performed in the molecular fingerprint region from 1100 to 2000 cm^{-1}, employing fs laser-induced filamentation as the supercontinuum generation mechanism to provide the ultrabroadband excitation pulses. We introduce a time-domain model of the CH_4 ν_2 CRS spectrum, including all the five ro-vibrational branches allowed by the selection rules $\Delta v=1$, $\Delta J=0, \pm1, \pm2$; the model includes collisional linewidths, computed according to a modified exponential gap scaling law and validated experimentally. The use of ultrabroadband CRS for *in-situ* monitoring of the CH_4 chemistry is demonstrated in a laboratory CH_4/air diffusion flame: CRS measurements in the fingerprint region, performed across the laminar flame front, allow the simultaneous detection of molecular oxygen (O_2), carbon dioxide (CO_2), and molecular hydrogen (H_2), along with CH_4. Fundamental physicochemical processes, such as H_2 production via CH_4 pyrolysis, are observed through the Raman spectra of these chemical species. In addition, we demonstrate ro-vibrational CH_4 ν_2 CRS thermometry, and we validate it against CO_2 CRS measurements. The present technique offers an interesting diagnostics approach to *in-situ* measurement of CH_4-rich environments e.g. in plasma reactors for CH_4 pyrolysis and H_2 production.

I. INTRODUCTION

Methane (CH_4) is the simplest hydrocarbon molecule and one of the most abundant chemical species in the universe, with its ubiquitous chemistry having important implications in planetary[1,2] and life[3] science. In recent years, the challenges posed by anthropogenic climate change have highlighted the critical role played by CH_4 in the oil and gas industry and in combustion technologies. CH_4 is one of the most powerful greenhouse gases and, despite being short-lived in the Earth's atmosphere, it has the second largest effective climate forcing potential after carbon dioxide (CO_2)[4]: CH_4 is the major component of natural gas and it's associated with all hydrocarbon fuels. On the other hand, (compressed or liquefied) natural gas is the main alternative fuel for internal combustion engines[5], reducing the emission of transport vehicles with respect to typical diesel and gasoil engines, and CH_4 can be produced in a sustainable fashion as a bio-[6] and e-fuel[7]. In this respect, CH_4 can also be used as a chemical energy storage to enable the development of the hydrogen economy[7]: CH_4 can be transported within the existing infrastructure for natural gas and valorised via chemical reforming to molecular hydrogen[8] (H_2) or other commodity hydrocarbons[9,10].

In view of this, CH_4 has been extensively investigated by laser diagnostics with linear optical techniques, based on absorption or scattering, providing *in-situ* detection and ro-vibrational spectroscopy in energy systems. Optical probes based on laser absorption have been developed using e.g.

near-[11] and mid-IR[12] diode lasers, quantum-cascade lasers[13], and frequency combs[14], and have been vastly employed for CH_4 detection in atmospheric environments[15] and for combustion diagnostics[16]. Absorption techniques have the advantage of simplicity and robustness, as well as the availability of large spectroscopic databases for the interpretation of experimental spectra[17], they can realise ultrafast spectroscopy employing femtosecond (fs) laser sources[18], and the capability for imaging measurements has also been demonstrated[19,20]. On the other hand they suffer from the lack of spatial resolution in the longitudinal direction as they are line-of-site techniques[16], which can severely limit the accuracy of quantitative spectroscopy in inhomogeneous gas-phase media, such as turbulent combustion environments.

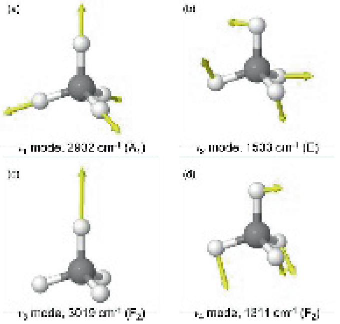

FIG. 1. The normal vibrational modes of methane[21]. (a) Symmetric C-H stretch mode. (b) Doubly degenerate H-C-H bend mode. (c) Triply degenerate asymmetric C-H stretch mode. (d) Triply degenerate H-C-H bend mode. (*Jmol: an open-source Java viewer for chemical structures in 3D.* http://www.jmol.org/)

The use of spontaneous Raman scattering in these contexts allows for spatially-resolved measurements, with the possibility for imaging and high repetition rates[22]. Spontaneous Raman spectroscopy has been thoroughly applied to the study of CH_4[23,24], both in combustion[25–29] and plasma[21,30] environments, demonstrating its suitability as a probe molecule for the direct measurement of the rotational and vibrational temperature even in non-equilibrium systems, with important implications for CH_4 chemistry[31]. The main drawback of spontaneous Raman is the typically low cross section for this incoherent scattering process, which complicates its application in luminous environments, requiring large laser pulse energies to achieve single-shot measurements, with the risk of inducing the optical breakdown of the gas-phase medium or molecular photofragmentation[27]. Additionally, further incoherent emission processes (e.g. chemiluminescence, fluorescence, *etc.*) can shadow the Raman signal, and the use of nanosecond (ns) laser pulses limits the temporal resolution so that spontaneous Raman spectroscopy cannot resolve ultrafast dynamics such as energy redistribution and relaxation processes[32].

The limitations due to the incoherent nature of the Raman scattering process can be overcome by resorting to non-linear optics, in particular in the form of stimulated (SRS) and coherent Raman scattering (CRS). Despite the different nature of their emission[33], SRS and CRS share the use of driving pump and Stokes laser fields with frequency difference matching the ro-vibrational transitions of the Raman-active molecules, resulting in the emission of a coherent signal, which can be remotely detected even in harsh environments. Since the very beginning of their development, continuous-wave SRS[34,35] and CRS[36–39] have been employed to perform high-resolution measurements of the ro-vibrational Raman spectrum of CH_4 in the so-called pentad region, allowing for the assignment of individual rotational lines in the isotropic Q-branch of the symmetric C-H stretch (ν_1 mode, see **FIG. 1(a)**). They were further employed to investigate the rotational energy transfer in molecular collisions[40–42] between the vibrationally coherent CH_4 molecules and other collisional partners, e.g. N_2 and argon (Ar). In the context of combustion diagnostics, the CH_4 CRS signal was recorded at temperatures as high as 1273 K in a furnace[43], and CH_4 ns CRS was used to measure the temperature in a laminar CH_4/air diffusion flame[44] and in supercritical LOX/CH_4 combustion[45].

In recent years, the introduction of ultrafast laser sources, providing pulses of the duration of pico- (ps) and femtosecond (fs), has led to the development of various kind of time-resolved CRS techniques, able to directly measure the rotational and vibrational wave packets of Raman-active molecules[46]. In particular, hybrid fs/ps CRS[47], employing a combination of broadband fs pump and Stokes and narrowband ps probe pulses, achieved simultaneous time- and frequency resolution, measuring the CRS spectrum below the relaxation timescale of the ro-vibrational energy. Different kinds of time-resolved CRS have been applied to CH_4. Relative CH_4 concentrations measurements in binary mixtures with N_2 were demonstrated via hybrid CRS by Engel *et al.*[48] and via chirped-probe-pulse (CPP) CRS by Dennis *et al.*[49]. Bohlin and Kliewer at Sandia National Laboratories (SNL), Livermore, CA, employed a hollow-core fibre to compress a 45 fs pulse to <7 fs supercontinuum to excite the ro-vibrational Raman modes up to the pentad region of the CH_4 Raman spectrum, realising ultrabroadband

PLEASE CITE THIS ARTICLE AS DOI: 10.1063/5.0138803

fs/ps CRS imaging[50]. In a later work[51], the same group employed ultrabroadband CRS imaging to investigate CH_4/air flame-wall interaction, realising the simultaneous detection of N_2, H_2, molecular oxygen (O_2), carbon monoxide (CO), CO_2, and CH_4. Recently, researchers at SNL Livermore and at the Plasma Physics Laboratory, Princeton, NJ, have presented a thorough investigation of the ν_1 mode spectrum of by hybrid fs/ps CRS[52]: they demonstrated the viability of CH_4 CRS thermometry up to 1000 K, realised time-resolved measurements of the collisional dephasing of the Raman coherence of CH_4 perturbed by itself, by N_2 and by Ar, and developed a time-domain model of the CH_4 ν_1 CRS spectrum.

All the applications of CRS to CH_4 have been focused on the pentad region of its spectrum (~2600-3300 cm^{-1}), which is dominated by the fundamental bands of the ν_1 mode and of the asymmetric C-H stretch (ν_3) mode (see **FIG. 1(c)**). The so-called dyad region (~1200-1900 cm^{-1}), due to the doubly and triply degenerate bending of the H-C-H bonds[23] (ν_2 and ν_4 modes, in **FIG. 1(b)** and **FIG. 1(d)** respectively), has been thus far neglected as the Raman cross section of the bending modes is more than one order of magnitude smaller than that of the stretch modes. On the other hand, this represents an important region for combustion and plasma diagnostics, as it overlaps with the ro-vibrational spectra of CO_2[53] and O_2[54], as well as with the pure-rotational spectrum of H_2, thus offering an interesting window for the study of CH_4 chemistry with high spatio-temporal resolution. In view of this we here present the first CRS investigation of the ν_2 mode of CH_4, dominating the dyad region of its Raman spectrum. We employ a two-beam hybrid fs/ps CRS system[55] to perform ultrabroadband CRS spectroscopy in the region 1100-1200 cm^{-1} of the Raman spectrum, using *in-situ* fs-laser-induced filamentation as the compressed supercontinuum generation mechanism[54,56,57]. The use of hybrid fs/ps allows us to simultaneously access the frequency and time-domain to investigate the coupling of the rotational and vibrational energy degrees of freedom of the CH_4 molecule, as well as the rotational energy transfer in molecular collisions. In order to demonstrate the potential of CH_4 ν_2 CRS as a diagnostic tool for combustion and plasma technologies, we performed spatially-resolved multiplexed measurements across a laminar CH_4/air diffusion flame.

II. METHODS

A. Optical setup

The experimental setup for two-beam ultrabroadband fs/ps CRS is similar to the one detailed in a previous work[54], only a brief summary is here provided. A regenerative chirped-pulse amplifier (CPA) system (Astrella, Coherent) is employed as the single light source, providing fs laser pulses at 800 nm, with a pulse energy of ~7.5 mJ, at a repetition rate of 1 kHz. A 65% split of the total pulse energy is temporally compressed to 35 fs and fed to a second-harmonic bandwidth compressor (SHBC, Light Conversion), to generate a frequency-doubled ~5 ps pulse, which serves as the narrow-band probe pulse. Its duration and spectral linewidth are tuned by a 4f-pulse shaper to 7.3 ps and 4.1 cm^{-1} (time-bandwidth product: 0.89 for a top-hat pulse[58]), with a resulting probe pulse energy of 200 μJ. The remainder of the CPA output is employed as a single degenerate fs pump/Stokes pulse in a two-beam phase CRS matching configuration[55,59]: an external compressor unit provides independent control the spectral phase of the fs pulse, so as to compensate for the dispersion due to the optical elements on the pump/Stokes beam path. As demonstrated in previous works[54,60], fs laser-induced filamentation can be used to generate a compressed supercontinuum, which acts as a single ultrabroadband pump/Stokes pulse, coherently exciting all the Raman-active modes whose characteristic period is longer than the supercontinuum pulse. Here this *in-situ* generation/*in-situ* use scheme is employed to perform ultrabroadband CRS in the vibrational fingerprint region: a spherical lens (f:=500 mm) focuses the ~1.2 mJ pump/Stokes pulse, with a theoretical irradiance of ~357 TW/cm^2 at the focal point, thus resulting in the formation of a laser-induced plasma filament, which propagates for ~13 mm before collapsing. The laser focusing lens is mounted on a linear stage, whose position is adjusted to maintain the filament ~4 mm before the probe volume. As the fs pulse experiences self-phase modulation and non-linear propagation in the plasma medium inside the filament, these result in a compressed supercontinuum output, which serves as the ultrabroadband pump/Stokes pulse.

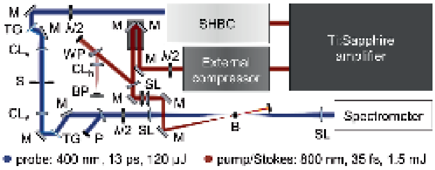

FIG. 2. Schematic of the ultrabroadband two-beam fs/ps CRS instrument. A single Ti:sapphire regenerative amplifier is employed to generate the 35 fs pump/Stokes and the 7 ps probe pulses. *In-situ* fs filamentation is employed as the supercontinuum generation mechanism: the ultrabroadband pump/Stokes beam is crossed by the probe beam at a distance of ~4 mm after exiting the filament. TG, transmission grating; S, slit; TS, translation stage; CL, cylindrical lens with horizontal (h) and vertical (v) symmetry axes; λ/2, half-wave plate; WP, wedge plate; BP, beam profiler; B, burner; P, polariser; SL, spherical lens; M, mirror.

A crossed beam quasi-phase-matched configuration is adopted with the probe beam focused by a spherical lens (f:=300 mm) to the measurement location and crossing the pump/Stokes at a ~3° angle, resulting in an estimated 20 µm (width, FWHM) x 2.5 mm (length, FWHM) x 20 µm (height, FWHM) probe volume. The relative delay of the probe pulse is tuned by controlling an automated delay line on the pump/Stokes beam path with a <10 fs resolution (Thorlabs). A combination of 800 nm half-wave plate and thin-film polariser is employed to split a ~50 µJ portion of the beam: a single reflection from a wedge plate is focused by a cylindrical lens (f:=300 mm) onto a sCMOS beam profiler (WinCamD, Dataray), so as to monitor the (most sensitive) vertical alignment of the pump/Stokes beam over the whole range of motion of the automated stage. The ultrabroadband CRS signal is collimated through a spherical lens (f:=400 mm) and a band-pass filter (20 nm bandwidth FWHM, Semrock) is employed to suppress the probe, almost co-propagating with the signal in this geometry. The signal is finally dispersed through a high-resolution transmission grating (3039 lines/mm, Ibsen Photonics) and imaged by a relatively fast-focusing lens (f:=200 mm) onto the sCMOS detector (Zyla, Andor), resulting in a detection bandwidth of 900 cm^{-1}, with a dispersion of 0.43 cm^{-1}/pixel. The 4.1 cm^{-1} spectral linewidth of the ps probe pulse is the limiting factor for the resolution of the ultrabroadband CRS signal; the instrumental broadening due to the spectrometer is evaluated by fitting a Voigt profile with ~0.1 cm^{-1} FWHM Lorentzian and ~1.7 cm^{-1} FWHM Gaussian contributions. Half-wave plates are employed to maximise the efficiency of the transmission grating (measured to >90% for S-polarisation at 400 nm) in the 4f-filter and to control the relative polarisation angle between the pump/Stokes and the probe field: in the present work the beams were set to have same polarisation, so as to maximise the signal generation efficiency, and a 400 nm half-wave plate is employed to turn the polarisation of the (completely depolarised) CH_4 ν_2 CRS signal and optimise its diffraction efficiency in the spectrometer.

B. Time-resolved CRS measurements

The ν_2 mode Raman spectrum of CH_4 is here investigated under a number of different experimental conditions, by varying the collisional environment to measure its dephasing coefficients, and by performing ultrabroadband spectroscopy in a CH_4/air flame, demonstrating single-shot detection of the CH_4 ν_2 CRS spectrum at temperatures as high as ~800 K.

The collisional dephasing of the CH_4 ν_2 CARs signal was measured by performing time-resolved measurements of its spectrum and delaying the probe pulse relative to the pump/Stokes up to 220 ps, in steps of 5.1 ps. Samples of 1000 single-shot CH_4 ν_2 CRS spectra were recorded up to ~80-100 ps, where the collisional dephasing results in a reduction of the signal-to-background ratio (SBR) to ~3.3, and 10-shot-averaged spectra were recorded from that point onward: at the transition point both single-shot and shot-averaged datasets were acquired and compared, computing a scaling factor over the different dynamic ranges of the dephasing experiments. Collisional dephasing measurements were performed, at atmospheric pressure, in different mixtures of combustion-relevant gases. The measurements were performed in an open flow, regulated by digital flow controllers (Bronkhorst), provided inside a stainless steel T-junction: two set of measurements for binary mixtures of 75% and 50% CH_4 in combination with N_2, H_2 and argon were performed. The demonstration of the single-shot detection of the CH_4 ν_2 CRS spectrum at high temperatures in a chemically-reacting flow was realised in a laminar CH_4/air flame, provided on a Bunsen burner. The burner is a seamless steel pipe with an inner diameter of 19 mm, through which the CH_4 flow was delivered with an exit plane velocity of 2.65 cm/s, ensuring a laminar flow (Reynolds number ~35); a steel mesh was placed ~15 mm above the burner to stabilise the flame, while the measurements were performed ~1 mm above its nozzle. Point-wise ultrabroadband CRS measurements were performed at 25 locations across the flame front, moving from the centre of the burner (location y=0 mm) with a 0.5 mm step size. In order to extend the detection limit at lower concentrations and higher temperatures, a set of 1000 10-shot-averaged CRS spectra was acquired at each measurement location.

C. Time-domain CRS model

The modelling of the CH_4 ν_2 coherent Raman spectrum follows the modelling approach of the CH_4 ν_1 spectrum presented by T. Chen *et al.*[52], based on assumption of impulsive excitation of the Raman coherence, and on a phenomenological description of the resulting third-order nonlinear optical susceptibility following Prince *et al.*[47] This approach has been successfully demonstrated for both pure-rotational[61–63] and ro-vibrational[54,64] CRS of multiple combustion-relevant species. The main assumptions of the time-domain model can be outlined as follows: the nonlinear interaction of the electronically off-resonant pump, Stokes probe laser fields (at angular frequencies ω_i with i=1, 2, and 3, for the pump, Stokes and probe) with the gas-phase medium induces the macroscopic third-order polarisation:

$$\begin{aligned} P^{(3)}\left(t,\tau_{12},\tau_{23}\right) = \left(-\frac{i}{\hbar}\right)^3 \int_{-\infty}^{t} \mathrm{d}t_3 \int_{-\infty}^{t_3} \mathrm{d}t_2 \int_{-\infty}^{t_2} \mathrm{d}t_1 \Big[E_3\left(t-t_3\right) \mathrm{e}^{i(\omega_3-\omega_2+\omega_1)} \cdot \\ \delta\left(t_3\right) \chi^{(3)}\left(t_2\right) E_2^*\left(t-t_3+\tau_{23}-t_2\right) \mathrm{e}^{i(-\omega_2+\omega_1)} \cdot \\ E_1\left(t-t_3+\tau_{23}-t_2+\tau_{12}-t_1\right) \mathrm{e}^{i\omega_1} \delta\left(t_1\right) \end{aligned} \qquad (1)$$

where E_{i} and E_{i}^* are the envelope of the ith field and its complex conjugate, t_{i} is the coherence timescale for the molecules after the interaction with the i$^{\mathrm{th}}$ field, τ_{ij} is the delay of the interaction with the i$^{\mathrm{th}}$ and j$^{\mathrm{th}}$ fields, δ is the Dirac function, representing the instantaneous dephasing of the (virtual) electronic coherence, and $\chi^{(3)}$ is the third-order susceptibility of the gas-phase medium. Under the assumption of impulsive excitation of the ro-vibrational Raman coherence we can disregard the temporal envelope of the combined pump/Stokes field (in case of two-beam CRS[55]) and write:

$$P^{(3)}\left(t,\tau_{23}\right) = \left(-\frac{i}{\hbar}\right)^3 E_3\left(t+\tau_{23}-t_2\right) \chi^{(3)}\left(t_2\right) \qquad (2)$$

Hence the CRS intensity spectrum is obtained, upon Fourier transforming the polarisation field, as:

$$I_{\mathrm{CRS}}\left(\omega,\tau_{23}\right) = \left|\mathscr{F}\left\{P^{(3)}\left(t,\tau_{23}\right)\right\}\right|^2 \qquad (3)$$

$\chi^{(3)}$ represents the core of the model outlined so far, and is typically treated phenomenologically as:

$$\chi^{(3)}\left(t_2\right) = \sum_{(v,J)} W_{(v_{\mathrm{i}},J_{\mathrm{i}})\to(v_{\mathrm{f}},J_{\mathrm{f}})} \exp\left[\left(i\omega_{(v_{\mathrm{i}},J_{\mathrm{i}})\to(v_{\mathrm{f}},J_{\mathrm{f}})} - \Gamma_{(v_{\mathrm{i}},J_{\mathrm{i}})\to(v_{\mathrm{f}},J_{\mathrm{f}})}\right)t\right] \qquad (4)$$

with summation running over all the possible initial and final ro-vibrational states (represented by the total angular momentum and vibrational quantum numbers, *v* and *J*) allowed by the Raman selection rules for the molecular species considered. The temporal evolution of $\chi^{(3)}$ is thus computed as the interferogram of damped harmonic oscillations –at the Raman frequencies $\omega_{(v_{\mathrm{i}},J_{\mathrm{i}})\to(v_{\mathrm{f}},J_{\mathrm{f}})}$ and with damping coefficients $\Gamma_{(v_{\mathrm{i}},J_{\mathrm{i}})\to(v_{\mathrm{f}},J_{\mathrm{f}})}$ dominated by the collisional rotational energy transfer (RET) at atmospheric pressure[65]–, weighted by the semi-classical transition probabilities[66]. Eq. (4) thus introduces in the time-domain CRS model the spectroscopic properties of the Raman-active species, which in turn depend on the chemical structure of the molecule considered.

The case of CH_4 is considerably more complicated than simple diatomic molecules, as early studies of its absorption spectrum revealed[67]. CH_4 is a polyatomic spherical top molecule, possessing three 3-fold and 2-fold axes of symmetry, and six planes of symmetry: in terms of these symmetry elements, CH_4 belongs to the tetrahedral point group (T_d)[68]. Since the molecule has five nuclei, there are nine possible vibrational modes which, according to group theory, can be clustered in the four normal modes illustrated **FIG. 1**, called by the Greek letter "*ν*" and identified by the vibrational quantum numbers (v_1, v_2, v_3, v_4) and by the symmetry labels A, E, and F, for non-degenerate, doubly degenerate and triply degenerate modes, respectively. The first normal mode (ν_1 at 2932.4 cm^{-1}), as already mentioned, is the non-degenerate symmetric stretch of the C-H bonds, which preserves the symmetry of the molecule in the vibrational ground state (0000), so that the instantaneous polarisability tensor has zero anisotropic invariant, and the associated Raman spectrum consists only of the isotropic Q-branch (with selection rules: $\Delta v=1$, $\Delta J=0$). The ν_2 mode (at 1533.3 cm^{-1}) is a doubly degenerate bend of the H-C-H bonds: this mode, as all the other vibrational modes of CH_4 is Raman active, with selection rules $\Delta J=0, \pm1, \pm2$, so that the Raman spectrum is composed of O-, P-, Q-, R- and S-branch lines. The asymmetric C-H stretch mode (ν_3 at 3018.5 cm^{-1}) and the ν_4 bend mode (at 1310.8 cm^{-1}), being the least symmetric modes, are triply degenerate and the reduced symmetry results in the selection rules: $\Delta J=0, \pm1, \pm2$. Experimental measurements on the depolarisation ratio of the fundamental ν_2 and ν_3 Raman spectra have shown that these modes are completely depolarised (i.e. $\rho=0.75$), with the Raman activity entirely due to the anisotropic part of the polarisability tensor. The normal frequencies of the stretch modes are roughly double than the bending modes (i.e. $\nu_1 \approx \nu_3 \approx 2\nu_2 \approx 2\nu_4$), so that vibrational bands can be grouped into polyads, denoted P_n, with polyad number $n = (2v_1 + 2v_3 + v_2 + v_4)$. P_0 is the vibrational ground state; P_1 has two vibrational levels, and Raman transitions $P_0 \leftarrow P_1$ involving the fundamental bands of ν_2 and ν_4 constitute the dyad region of the Raman spectrum; similarly, P_2 has five vibrational levels, and transitions $P_1 \leftarrow P_2$ involve the fundamental ν_1 and ν_3 modes, as well as the overtones ($2\nu_2$ and $2\nu_4$) and combination ($\nu_2+\nu_4$) of the bending modes, defining the pentad region.

The concept of symmetry plays an essential role in molecular spectroscopy, as it constraints the form of the molecular wave function according to Pauli's exclusion principle. Under the assumption of the Born-Oppenheimer approximation, the total wave function of the CH_4 molecule is written as the product of separable functions:

$$\psi = \psi_{\mathrm{T}} \psi_{\mathrm{E}} \psi_{\mathrm{V}} \psi_{\mathrm{R}} \psi_{\mathrm{S}} \qquad (5)$$

with ψ_{T} translational wave function, ψ_{E} electronic wave function (including the electron spin), ψ_{V} vibrational wave function, ψ_{R} rotational wave function, and ψ_{S} nuclear spin wave function. As the translational motion doesn't involve any internal degree of freedom, ψ_{T} is completely symmetrical (A symmetry), and so is ψ_{E} in the electronic ground state. The symmetry of the vibrational wave function depends on the symmetry of the irreducible representations of the T_d point group corresponding to the normal vibrational modes in **FIG. 1**. The rotational state of a CH_4 molecule can be specified by the quantum numbers J, M, where M represents the projection of the total angular momentum with respect to an inertial frame of reference: the associated wave function is a solution of the spherical top wave equation. E.W. Wilson Jr. showed that this solution is a linear combination of irreducible representations of symmetry A, E and F[69]: his results are summarised in **TABLE 1**. The rotational wave function has $(2J+1)$ degenerate projections with respect to an arbitrary inertial axis (i.e. $M = 0, \pm1, \dots, \pm J$), hence the common factor in the table: this degeneracy cannot be lifted by intramolecular interaction, but only by application of an external field (e.g. in Stark effect)[68].

TABLE 1 Symmetry of the rotational wave function of CH_4 (with p = 0, 1, 2, 3, 4, or 5).

$J = 6p$	$(2J+1)\,[\,(p+1)A + 2p\,E + 3p\,F\,]$
$J = 6p+1$	$(2J+1)\,[\,p\,A + 2p\,E + 3(3p+1)\,F\,]$
$J = 6p+2$	$(2J+1)\,[\,p\,A + 2(p+1)\,E + 3(3p+1)\,F\,]$
$J = 6p+3$	$(2J+1)\,[\,(p+1)A + 2p\,E + 3(3p+2)\,F\,]$
$J = 6p+4$	$(2J+1)\,[\,(p+1)A + 2(3p+1)\,E + 3(3p+2)\,F\,]$
$J = 6p+5$	$(2J+1)\,[\,p\,A + 2(p+1)\,E + 3(3p+3)\,F\,]$

Finally, CH_4 has 16 possible nuclear spin wave functions: 2 are singlet states (with nuclear spin quantum number $I = 0$, and associated projection $M_I = 0$), 3 are triplet states ($I = 1$, $M_I = 0, \pm1$) and one is a quintet states ($I = 2$, $M_I = 0, \pm1, \pm2$). In terms of symmetry, ψ_{S} is the combination[69]: $5A + E + 3F$. The CH_4 molecule has 4 identical ^{1}H nuclei, which obey the Fermi-Dirac statistics: according to Pauli's principle, the total wave function must be symmetric with respect to any proper rotation of the T_d point group, so that its overall symmetry must be A.

TABLE 2 Multiplication table for the irreducible representations.

	A	E	F
A	$A = A$	$E \not\supset A$	$F \not\supset A$
E	$E \not\supset A$	$(2A + E) \supseteq A$	$F \not\supset A$
F	$F \not\supset A$	$F \not\supset A$	$(A + E + 2F) \supseteq A$

Under the multiplication in Eq. (5) the symmetry label obeys the rules in **TABLE 2**, and only wave functions with resulting symmetry A are allowed. This has important implications for the statistical weights of the ro-vibrational energy levels included in the calculation of Boltzmann distribution:

$$\rho = g_{\mathrm{V}} g_{\mathrm{R}} g_{\mathrm{S}} \frac{\exp\left(-\hbar c E_{\mathrm{v},J} / \mathrm{k_B} T\right)}{Z} \tag{6}$$

where $E_{\mathrm{v},J}$ is the ro-vibrational energy (expressed in cm^{-1}) of the molecule (v is a short-hand notation for the complete set of vibrational quantum numbers), g_{V} is the vibrational degeneracy, g_{R} is the degeneracy of the rotational wave function according to the entries of **TABLE 1**, and g_{S} is the nuclear spin degeneracy, being 5, 2 and 3 for A, E and F symmetry labels, respectively. According to the symmetry multiplication rules in **TABLE 2** only the product of identical symmetry labels produces a representation with A symmetry: hence the often statement, in the literature, that ro-vibrational states (i.e. $\psi_{\mathrm{V}}\psi_{\mathrm{R}}$) of symmetry A, E, and F are 5-, 2- and 3-fold degenerate.

In order to model the temporal evolution of the nonlinear susceptibility according to Eq. (4), one must know the frequencies of the allowed Raman transitions, and the corresponding polarisabilities of the CH_4 molecule, which enter the weighting factors as[44]:

$$W_{(\mathrm{v_i}, J_\mathrm{i}) \to (\mathrm{v_f}, J_\mathrm{f})} = \left| \left\langle \mathrm{v_i}, J_\mathrm{i} \right| \hat{\alpha} \left| \mathrm{v_f}, J_\mathrm{f} \right\rangle \right|^2 \left(\rho_{(\mathrm{v_f}, J_\mathrm{f})} - \rho_{(\mathrm{v_i}, J_\mathrm{i})} \right) \tag{7}$$

These quantities can be computed adopting a tetrahedral formalism developed for the analysis of spherical top molecules[70], which removes inter-polyad contributions to the higher order thanks to implicit contact transformations[71], while explicitly retaining inter-polyad contributions, due to the strong coupling between vibrational states within individual polyads. This approach was developed at the University of Burgundy and allowed the derivation of effective ro-vibrational Hamiltonians for polyads up to the tetradecad (i.e. P_4, at ~6200 cm^{-1}), from which the position and intensities of the spontaneous Raman spectrum of CH_4 are computed[72–74]. The resulting spectral database has been employed by multiple research groups to simulate the spontaneous CH_4 Raman spectrum in both the dyad[75] and pentad region[21,30,76], and recently its application has been extended to the v_1 CH_4 CRS spectrum[52]. According to the notation of Jourdanneau *et al.* the spontaneous Raman line intensities in the spectral database are computed as[76]:

$$I_{(\mathrm{v_i}, J_\mathrm{i}) \to (\mathrm{v_f}, J_\mathrm{f})} \propto \rho_{(\mathrm{v_i}, J_\mathrm{i})} \left[S_0 \mathscr{I}^2_{(\mathrm{v_i}, J_\mathrm{i}) \to (\mathrm{v_f}, J_\mathrm{f})} + S_2 \mathscr{A}^2_{(\mathrm{v_i}, J_\mathrm{i}) \to (\mathrm{v_f}, J_\mathrm{f})} \right] \tag{8}$$

where $S_{0,2}$ are the Stone coefficients, depending on the observation geometry in a spontaneous Raman experiment, while $\mathscr{I}$ and $\mathscr{A}$ are the transition values of the isotropic and anisotropic components of the polarisability tensor. As already mentioned, the v_2 mode Raman spectrum is completely depolarised, so that its transition polarisability has only an anisotropic component, and the corresponding Stone coefficient become an irrelevant scaling factor. In contrast to the incoherent spontaneous Raman scattering, the probability amplitude for the coherent Raman scattering process depends on the differential of the Boltzmann population in the initial and final ro-vibrational states, as shown in Eq. (7). The weight factors in Eq. (4) are thus computed from the line intensities in the spectral database as:

$$W_{(v_i,J_i)\to(v_f,J_f)} = I_{(v_i,J_i)\to(v_f,J_f)}\left(\frac{\rho_{(v_f,J_f)}-\rho_{(v_i,J_i)}}{\rho_{(v_i,J_i)}\big|_{T_0}}\right) \qquad (9)$$

with T_0 (~1500 K) being the reference temperature for the calculation of the line intensities in the spectral database[21]. The spectral database contains ~16 million lines in the dyad region –involving vibrational states up to the tetradecad and rotational states up to $J = 23$: of these ~11 million correspond to v_2 mode Raman transitions (i.e. $\Delta v_2 = 1$, $\Delta v_4 = 0$) and ~5 million are v_4 mode transitions. The v_4 mode band is the weakest of the ro-vibrational Raman spectrum of CH_4 and could not be observed in our CRS experiments: the time-domain CH_4 CRS model was thus limited to the v_2 mode spectrum. Each of the v_2 mode transitions gives rise to a damped harmonic contribution which is computationally evaluated on a temporal grid up to 1 ns, with 8 fs step size, corresponding to a resolution of 0.03 cm^{-1} for the Fourier-transformed CRS signal. As pointed out by Chen *et al.*[52], the main challenge in the development of an accurate time-domain model for the CH_4 CRS spectrum is the staggering number of Raman transitions included in the MeCaSDa calculated spectral database computed at the University of Burgundy[72,73] (and accessible at the following url: http://vamdc.icb.cnrs.fr/PHP/methane.php) and the resulting computational cost. Implementing the calculation of $\chi^{(3)}$ as a running sum for every transition input avoids exceeding memory limits of the available computational resources; each spectral calculation still needs to be iterated for different input values of temperature and, if the effects of molecular collisions are not negligible, of species concentrations in the probe volume. Hence, the calculation of spectral libraries for quantitative spectroscopy can be a cumbersome task, especially when the possibility of CH_4 CRS thermometry in non-equilibrium environments is considered[21]. The computational cost can be reduced by implementing a filter to exclude transitions whose intensity is lesser than the a cut-off value of strongest transition in the spectrum[52], depending on both the strength of the associated instantaneous dipole and on the Boltzmann population.

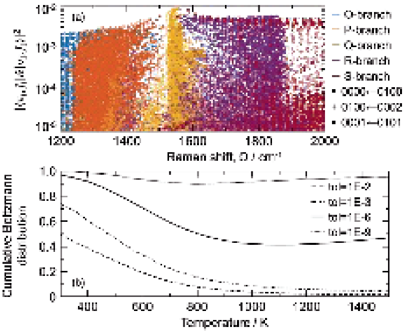

FIG. 3. The spontaneous Raman cross-section for CH_4 v_2 mode transitions. (a) Transition moment of the polarisability anisotropy for the fundamental band (0000←0100) and the first two hot bands (0100←0200 and 0001←0101) of the v_2 mode, according to the different Raman selection rules. (b) The cumulative distribution function, representing the fraction of the Boltzmann population included in the calculation of $\chi^{(3)}$ as a function of the input temperature and cut-off value selected for the filtering of the spectral database.

FIG. 3(a) shows the transition polarisability for a small fraction of the Raman transitions considered in the database, corresponding to the fundamental band of the v_2 mode spectrum (0000←0100) and its first two hot bands (0001←0101 and 0100←0002): the overall database spans more than 18 orders of magnitude in the Raman polarisability. These are combined with the differential Boltzmann population between the initial and final transition states at different temperatures, between 300 and 1500 K in **FIG. 3(b)**, to compute the overall line intensities of the CRS spectrum. Implementing different cut-off values the number of Raman transitions taken into account in the calculation of $\chi^{(3)}$ can be significantly reduced, at cost of considering only a fraction of the Boltzmann population. In particular, adopting a tolerance of 1% or 0.1% of the strongest line in each branch most of the cumulative distribution function (CDF) is neglected. Increasing the tolerance to a millionth (billionth) of the strongest line, more than 40% (90%) of the CDF is taken into account at all temperatures considered in the theoretical CRS library. The non-monotonic behaviour shown by the corresponding curve in **FIG. 3(b)** depends on the combination of the different Raman polarisabilities and of the spreading Boltzmann distribution at higher temperatures. A cut-off value of 1E-4 was found to be sufficient to model the time-domain behaviour of the CH_4 v_2 CRS spectrum at room temperature, where the effect of vibrational hot bands is measured to be negligible. In the flame experiment, on the other hand, the cut-off value needs to be increased to guarantee the independence of CH_4 v_2 CRS thermometry from the spectral filtering. An unfiltered spectral library was used to fit the flame spectra up to ~800 K, and a cut-off value of 1E-6 was then found to perfectly reproduce these results while including only half of the cumulative Boltzmann distribution as shown in **FIG. 3(b)**.

The time-domain CH_4 v_2 CRS model is complemented by the inclusion of Raman linewidths, representing the collisional dephasing of the signal. The collisional dephasing coefficients of the Q-branch spectrum $\Gamma_{(v_i,J)\to(v_f,J)}$ are modelled according to the modified exponential gap (MEG) law[77,78], as:

$$\Gamma_{(v_i,J)\to(v_f,J)} = \sum_{k\neq j}\gamma_{kj} \tag{10}$$

with upward and downward collisional transition rates, between the i^{th} and j^{th} rotational energy states, given by:

$$\gamma_{ji} = \alpha p\left(\frac{T_0}{T}\right)^n\left(\frac{1+a\,E_i/k_BT\delta}{1+a\,E_i/k_BT}\right)^2\exp\left[\frac{-\beta\left(E_j-E_i\right)}{k_BT}\right] \tag{11}$$

$$\gamma_{ij} = \frac{2J_i+1}{2J_j+1}\gamma_{ij}\exp\left(\frac{E_j-E_i}{k_BT}\right) \tag{12}$$

where p is the pressure, T_0=296 K is the reference temperature, E_i and E_j represent the ro-vibrational energy in the upper and lower vibrational states (so that the energy gap is always positive), and α, β, δ, a and n are fitting parameter for the scaling law. In the present linewidth model the effect of the symmetry of ro-vibrational wave function is neglected[42], so that the linewidth computed for a specific value of the rotational quantum number J is applied to all its symmetry components in **TABLE 1**; similarly, the same RET rate is assumed for all the vibrational hot bands. Following the work of Chen *et al.*[52] the species-specific constant a is set to 2, and the number of fitting parameter to be simultaneously determined is reduced by independently fitting α and β at room temperature, assuming δ=1 and n=0. While the MEG model has been successfully applied to isotropic v_1 Q-branch CRS spectrum of CH_4 in multiple studies[44,45,52], the sum rule in Eq. (10) is not rigorously satisfied in the case of the anisotropic CH_4 v_2 lines, where molecular reorientation and degenerate levels are present[79]. To a first approximation this fact can be neglected, and the corresponding Raman lines can be assumed to satisfy Eq. (10): this approximation, though coarse, was employed with satisfactory results to model the collisional line broadening of the P- and R-branch lines in the absorption spectra of CO_2[80]. We justify the present use of the MEG scaling law as a first-approximation model of the collisional dephasing of the anisotropic CH_4 v_2 Q-branch spectrum in view of the fact that only atmospheric pressure experiments are here reported, so that the molecular reorientation in inelastic collisions and the intra-branch coupling can be reasonably neglected. On the other hand, the sum rule in Eq. (10) is not directly used to compute the dephasing coefficients of the O-, P-, R- and S-branch lines, as the inter-branch coupling is assumed to dominate over the intra-branch contribution[79]. The collisional dephasing rates of these lines are computed assuming the "random phase approximation" (RPA), whereby the width of an anisotropic line involving a change in the rotational quantum number ($J_i \rightarrow J_f$) depends only on the relaxation of the rotational energy levels labelled by the quantum numbers J_i and J_f, as[81]:

$$\Gamma_{(v_i,J_i)\to(v_f,J_f)} = \frac{1}{2}\left(\Gamma_{(v_i,J_i)\to(v_f,J_i)} + \Gamma_{(v_i,J_f)\to(v_f,J_f)}\right) \tag{13}$$

III. RESULTS AND DISCUSSION

A. Time-resolved CH_4 v_2 spectrum

An example of a single-shot CH_4 v_2 coherent Raman Stokes spectrum (CSRS), acquired in a room-temperature methane flow, in the spectral range 1100-2000 cm^{-1} is given in **FIG. 4**. The CH_4 v_2 spectrum presents all five branches corresponding to the selection rules ΔJ=0, ±1, and ±2. The spectral resolution of our CRS instrument (limited by the 4.1 cm^{-1} width of the probe spectrum) is insufficient to resolve the rotational structure of the Q-branch, which is then a single convolved feature at ~1535 cm^{-1}. The ordering of the branch labels with the Raman shift on the Stokes of the probe line is opposite to the one on the anti-Stokes side (CARS), as shown in **FIG. 4**: the O- and P-branch appearing at larger Raman shifts than the R- and S-branch.

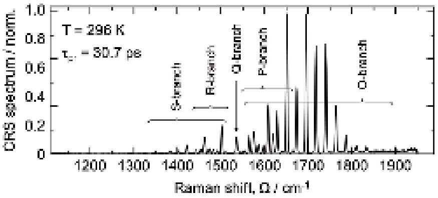

FIG. 4. Single-shot CH_4 v_2 CSRS spectrum at room-temperature. The v_2 mode Raman-activity is completely anisotropic and the selection rules allow for O-, P-, Q-, R-, and S-branch transitions. Note that, as the CRS signal is acquired in the Stokes side, the usual branch ordering is reverted, with negative changes in the total angular momentum quantum number (ΔJ=-1,-2 for the P- and O-branch, respectively) determining a larger frequency transition.

The spectroscopic data for the CH_4 Raman spectrum discussed in Section II can be directly applied to the CSRS spectrum, with the only caveat that the branch labels for negative and positive changes in *J* need to be interchanged. A comparison of the experimental measurements and model prediction of the dynamic behaviour of the CH_4 ν_2 CRS spectrum is provided in **FIG. 5**.

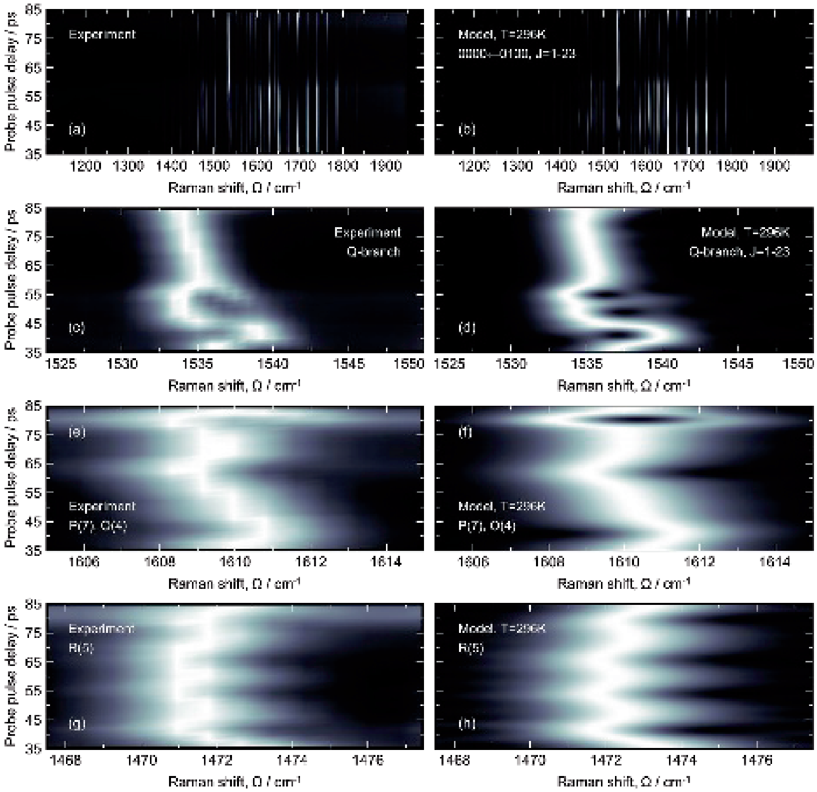

FIG. 5. Time-resolved CH_4 ν_2 CRS spectra: comparison between experiments and time-domain model. (a) Experimental spectrochronogram of the ro-vibrational CH_4 ν_2 mode, acquired in a room-temperature CH_4 flow over for values of the probe pulse delay spanning over 50 ps. A 1000-shot-averaged CRS spectrum is shown at each probe delay. (b) Modelled spectrochronogram including only the fundamental band of the ν_2 mode (i.e. 0000←0100), and rotational states up to J=23. (c) Experimental spectrochronogram of the ν_2 Q-branch spectrum. (d) Modelled spectrochronogram of the ν_2 Q-branch spectrum. (e) Experimental spectrochronogram of the convolved P(7) and O(4) ro-vibrational lines. (f) Modelled spectrochronogram of the convolved P(7) and O(4) ro-vibrational lines. (g) Experimental spectrochronogram of the R(5) line of the P-branch spectrum. (h) Modelled spectrochronogram of the P(6) line of the P-branch spectrum.

The coherence beating in time-resolved CRS spectra is a well-known phenomenon, due to the presence of unresolved spectral lines at the resolution of the CRS instrument. Examples of this are found in hybrid fs/ps CRS spectra of air, where some N_2 and O_2 lines cannot be resolved for probe pulse durations lesser then ~60 ps, and in high-temperature N_2 spectra due to the presence of unresolved hot bands[82]. The presence of significant vibrational hot bands in room-temperature CRS spectra is uncommon for diatomic molecules, with relatively high vibrational constant (e.g. ~2330 cm^{-1} for N_2), but more complex polyatomic molecules can have vibrational modes at lower frequencies (e.g. ~667 cm^{-1} for the bending mode of CO_2), so that excited vibrational states can have a significant Boltzmann population[54]. In order to assess the impact of vibrational hot bands on the temporal beating of the room-temperature CH_4 ν_2 CRS spectrum, the time-domain model was here limited to the inclusion of fundamental transitions between the ground and first vibrationally excited states: as the model correctly reproduces the beating pattern in the experimental spectrogram, vibrational hot bands must have a negligible impact on this behaviour.

It is useful to distinguish the dynamics of the different branches in the CH_4 ν_2 CRS spectrum to understand the origin of its beating. As shown in **FIG. 5(c)**, the Q-branch lines appear as a single unresolved spectral feature centred approximately at 1535 cm^{-1} and shifting by ~5 cm^{-1} on either side, depending on the probe pulse delay. Its beating is captured by the model in **FIG. 5(d)**, including rotational lines up to state J=23: it is reasonable to interpret this as the interferogram of these unresolved lines. It is then interesting to analyse the other spectral branches, which are fully resolved in **FIG. 5**. As an example, the dynamic behaviour O(4) at ~1610 cm^{-1} is represented in **FIG. 5(e)** and modelled in **FIG. 5(f)**: a severe beating is still observed, which even leads to the line splitting at a probe delay of ~80 ps. While the beating can be partly attributed to the fact that the O- (and S-) branch lines are as a matter of fact not isolated, but overlap to the P- (R-) branch lines, the interference of only two harmonic contribution is expected to give rise to a simple sinusoidal pattern. A non-trivial beating pattern is also observed for line R(5) in **FIG. 5(g),(h)**, which does not overlap to any line of the S-branch and is perfectly isolated. Besides unresolved lines due to different chemical species, and to vibrational hot bands, coherence beating in time-resolved CRS spectra can arise from intra-molecular interaction, whereby the coupling of two energy degrees of freedom breaks some implicit symmetry of the molecular wave function, thus splitting otherwise degenerate energy states. This is the case e.g. in the pure-rotational CRS spectrum of O_2, where the spin-orbit coupling give rise to the beating of unresolved triplet transitions[83], and for the ν_2 mode Raman spectrum of CH_4. In this case, the gyroscopic coupling between the ro-vibrational levels of the ν_2 and ν_4 modes in the CH_4 dyad, lifts the degeneracy of the ro-vibrational energy associated to the total angular momentum quantum number J. This effect can be thought of in classical terms as the introduction of a non-inertial Coriolis force[84,85] in the molecule-fixed frame of reference, which introduces an orientation-dependent contribution to the rotational energy of the molecule. The ν_2-ν_4 Coriolis coupling is explicitly taken into account in the tetrahedral formalism employed to compute the spectral database[86], so that the rotational sub-states associated to the same J are treated as non-degenerate, and the time-domain CRS model correctly reproduce their coherence beating.

B. Linewidth measurements

The collisional dephasing of the CH_4 ν_2 CRS spectrum is presented in **FIG. 6**.

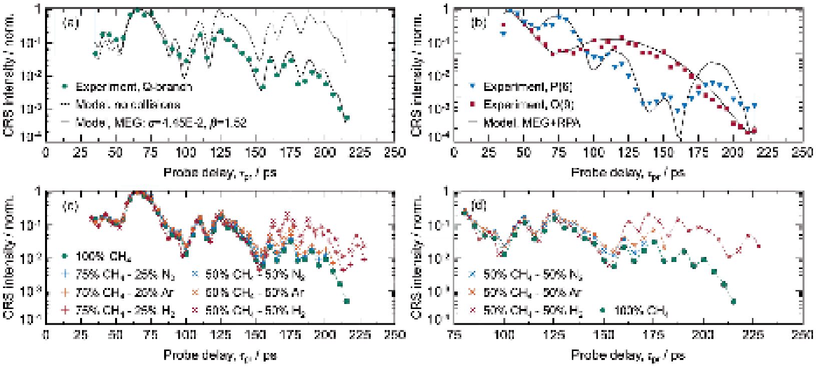

FIG. 6. Collisional dephasing of the CH_4 ν_2 CRS signal. (a) Comparison of the experimental dephasing of the spectrally-integrated Q-branch signal and the MEG model in a room-temperature atmospheric CH_4 flow. (b) Experimental dephasing of isolated lines of the CH_4 ν_2 spectrum in a room-temperature atmospheric CH_4 flow: O(9), and P(6) are selected as an example. The experimental behaviour is compared to the linewidths computed adopting the RPA. (c) Experimental dephasing of the of the spectrally-integrated isotropic Q-branch signal in binary mixtures with N_2, H_2 and argon, compared to the dephasing in a pure CH_4 flow. (d) Detail of the experimental dephasing of the CH_4 signal self-perturbed and in 50%-50% binary mixtures with N_2, H_2 and argon, for probe delays 100-225 ps.

First, the dephasing of the spectrally-integrated Q-branch signal in a room-temperature, atmospheric flow of CH_4 is shown in **FIG. 6(a)**: the beating of the unresolved *J*-lines in the Q-branch spectrum has a significant impact on the CRS signal intensity. The temporal behaviour of the CRS signal is thus determined by both the coherence beating and the collisional dephasing of the rotational lines. The collisional dephasing is modelled according to the MEG scaling law in Eq. (10)-(12), by fitting simultaneously the α and β parameters. In order to highlight the effect of the molecular collisions, the theoretical behaviour in their absence is also given (dashed line) in **FIG. 6(a)**. The experimental dephasing of the CH_4 ν_2 Q-branch spectrum and the prediction of the collisional model show a satisfactory agreement over the measured probe delay range 20-180 ps, and prove that, at least to a first approximation and at ambient conditions, the collisional dephasing of the anisotropic Q-branch lines can be well approximated by the sum rule with a MEG scaling law for the state-to-state relaxation rates. The effect of inter-branch coupling on the other hand is taken into account in the collisional dephasing model for the O-, P-, R- and S-branch lines, by introducing the RPA. The corresponding dephasing rates are thus computed according to Eq. (13) from the dephasing of the Q-branch lines, previously calculated by the MEG scaling law. **FIG. 6(b)** shows the experimental dephasing of two isolated lines in the O- and P- branches (namely O(9) and P(6)) and presents a comparison to the prediction of the RPA applied to the MEG-modelled Q-branch dephasing coefficients. The model predicts the collisional dephasing of these lines to a reasonable agreement with the experimental data, in particular for line O(6), although the predicted dephasing introduces an undue damping of the coherence beating of P(9) for probe delays larger than ~150 ps.

The effect of different collisional partners in binary mixtures with CH_4 was also investigated, as shown in **FIG. 6(c)**. The experimental decay of the CH_4 ν_2 Q-branch signal, as measured in pure CH_4 or in the binary mixtures with N_2, H_2, and argon, shows a negligible dependence on the actual mixture composition for a probe delay lesser than ~80 ps. This observation confirms for the ν_2 mode spectrum the same behaviour reported for the CH_4 ν_1 Q-branch in binary mixtures with N_2 by Engel et *al.*[48]. Chen *et al.* defined a critical probe delay for the collisional partner independence of the CH_4 ν_1 CRS signal and estimated this to be ~100 ps[52]: they experimentally confirmed it by measuring the collisional dephasing of the CH_4 CRS signal in binary mixtures with argon, as well as N_2. They employed a simple model based on gas kinetics to estimate the mean time between molecular collisions and thus define a collision sensitivity time. Below such a timescale, coherence beating dominates the temporal evolution of the CH_4 ν_2 CRS signal in **FIG. 6(c)**. For probe delays larger than ~80 ps the dephasing of the signal shows sensitivity to the collisional environment, as shown more in details in **FIG. 6(d)**. N_2 and argon present similar behaviours as collisional partners to the CH_4 molecules: this and confirm the findings by Chen *et al.*, who estimated the collisional linewidths of the CH_4 ν_1 Q-branch at room temperature and 500 Torr to be 0.167 cm^{-1} and 0.158 cm^{-1} for binary mixtures with 90% N_2 and argon, respectively. On the other hand, H_2 is a much weaker perturber to the CH_4 ν_2 CRS signal as demonstrated by the comparison with the self-perturbed behaviour in **FIG. 6(d)**: at 210 ps, the CH_4 CRS signal in a binary mixture with 50% H_2 is almost two orders of magnitude larger than the corresponding signal in a flow of pure CH_4. This observation is explained by the largely different rotational energy manifolds of the CH_4 and H_2 molecules, such that any rotational state of the CH_4 scatterers has a low density of neighbouring states of the H_2 perturbers. The collisional RET is thus significantly lessened in case of binary mixtures of CH_4 and H_2. In the case of N_2, on the other hand, radiator and perturber have plenty neighbouring rotational energy states, promoting the RET in inelastic collisions.

C. CH_4/air diffusion flame spectroscopy

The potential of CH_4 ν_2 CRS spectroscopy for *in-situ* diagnostics in chemically reactive flows is demonstrated by performing spatially-resolved measurements across a laminar CH_4/air diffusion flame.

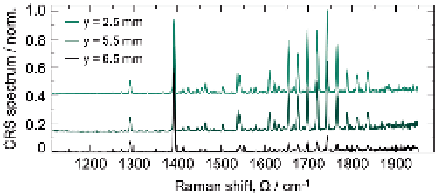

FIG. 7. Single-shot CRS spectra acquired at locations y=2.5, 5.5 and 6.5 mm across the CH_4/air diffusion flame front. The probe delay 30.7 ps is for all spectra. The peaks at 1265 and 1285 cm^{-1} belong to the "red" dyad of the CO_2 spectrum, while the peaks at 1388 and 1409 cm^{-1} belong to the "blue" dyad. O_2 can also be detected by its ro-vibrational Q-branch spectrum at 1553 cm^{-1}, which presents a clear increment moving towards the oxidiser stream. The rest of the spectral lines are attributed to the ν_2 mode spectrum of CH_4.

CRS measurements over the spectral range ~1100-2000 cm^{-1} were performed with a probe delay of 30.7 ps at each of the 25 locations, spaced by 0.5 mm across the flame front, moving from the fuel stream at the centre of the burner (y = 0 mm) to the oxidiser stream (y = 12 mm). The probe delay was chosen to time-gate the NR background and to maximise the signal-to-noise ratio (SNR), balancing the detection of the different branches of the CH_4 spectrum as visible in **FIG. 6(a)** and **FIG. 6(b)**. The single-shot detection of the CH_4 v_2 CRS signal was achieved up to location 6.5 mm, at temperatures as high as ~800 K: **FIG. 7** presents different examples of single-shot CH_4 v_2 CRS spectra acquired at three different locations (y=2.5, 5.5 and 6.5 mm) in the flame. Moving from the centre of the burner towards the chemical reaction zone of the flame, the CH_4 v_2 CRS signal is negatively impacted by the combination of increasing temperature and reducing CH_4 concentration so that at y=6.5 mm the SNR is reduced to less than 10. In order to extend the detection limit of the CH_4 v_2 CRS signal and validate the time-domain model at higher temperatures, 10-shot-averaged spectra were acquired at each flame location: the CH_4 could be detected up to 1020 K at y=8 mm. **FIG. 8** shows the ultrabroadband CRS spectra acquired across the CH_4/air flame front. Four different chemical species are detected in the vibrational fingerprint region of the Raman spectrum from 1100 to 2000 cm^{-1}: namely, the ro-vibrational v_2 spectrum of CH_4 (from 1300 to 1950 cm^{-1}), the CO_2 Fermi dyad (with fundamental Q-branch at 1285 and 1388 cm^{-1}), the pure-rotational spectrum of H_2 (four O-branch lines at 1246, 1447, 1637, and 1815 cm^{-1}), and the ro-vibrational spectrum of O_2 (with fundamental Q-branch at 1556 cm^{-1}). Spatially-resolved ultrabroadband CRS thus provide a window to monitor the physical-chemical processes *in-situ*, by measuring the local temperature and detecting some of the major reactants and products. The spectrum in **FIG. 8(a)** is representative of the fuel stream from the centre of the burner to y≈5 mm (as shown also in the comparison of the single-shot spectra at y=2.5 and 5.5 mm in **FIG. 7**): the spectrum is dominated by the ro-vibrational v_2 mode lines of CH_4 and by the characteristics Fermi dyad of the CO_2 spectrum, in particular the “blue” fundamental band of CO_2 at 1388 cm^{-1} is the single highest spectral feature. Such an abundance of CO_2 at the centre of the fuel stream can be explained by buoyancy of the lightweight CH_4 molecule (relative molecular mass: m=16) against the heavier CO_2 (m=44) produced in the whole reaction zone volume of the flame. This results in the internal recirculation of the high-temperature CO_2 and its local mixing with the room-temperature CH_4 flow at the burner inlet: upon thermalisation the local temperature is higher than 296 K as attested by the clear detection of the first hot band in the CO_2 spectrum[54] at ~1265 and ~1409 cm^{-1}, and even a second hot band in the red dyad at 1244 cm^{-1} as shown in the inset of **FIG. 8(a)**. It is worth noting here that this local CO_2 recirculation is expected to impact on the combustion chemistry due to its large heat capacity: this point will be further discussed when presenting the results of CRS thermometry. A small amount of fuel mixing with air is also visible in the spectrum: the small peak at 1556 cm^{-1} is indeed the ro-vibrational Q-branch of O_2. This becomes much more pronounced in the high-temperature spectrum of **FIG. 8(b)**, acquired in the reaction zone at y=8.5 mm.

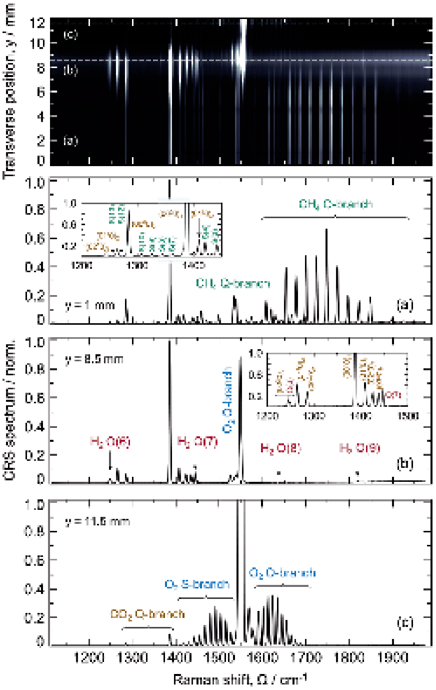

FIG. 8. Ultrabroadband CRS spectra in the molecular fingerprint region, measured across the laminar CH_4/air diffusion flame. The probe delay 30.7 ps is for all spectra. Note that gamma compression is employed in the image post-processing. (a) Fuel steam (y=1 mm): low-temperature ro-vibrational spectra of CO_2 and CH_4 (b) Reaction layer (y=8.5 mm): moving toward the reaction zone, CH_4 undergoes pyrolysis producing H_2, which is then rapidly consumed in the chemical reaction. Four lines of the pure-rotational Raman spectrum of H_2 are detected in the window ~1100-2000 cm^{-1}. The increased temperature is evident in the multiple hot bands of the ro-vibrational CO_2 and O_2 spectra (c) Oxidiser stream (y=11.5 mm): the oxidiser is ambient air, so that the Raman spectrum in the fingerprint region is dominated by the ro-vibrational spectrum of O_2. A small amount of the CO_2 produced in the combustion reaction diffuses into the oxidiser stream.

In this region of the flame the combustion reaction sustains itself by releasing heat that in turns provides the activation energy for the dissociation of the CH_4 molecules into radicals leading to the generation of H_2, which is then rapidly oxidised. Indeed the CH_4 ν_2 CRS spectrum is barely detectable at this location, while four lines of the pure-rotational H_2 O-branch spectrum are identified: namely, O(6) at 1246 cm^{-1} (overlapping with the second hot band of the CO_2 spectrum, as highlighted in the inset), O(7) at 1447 cm^{-1}, O(8) at 1637 cm^{-1} and O(9) at 1815 cm^{-1}. The heat released in the oxidation of the fuel increases the local temperature as marked by the pronounced hot bands in the Q-branch spectra of CO_2, these are marked in the figure by the lowest vibrational state, denoted according to the notation in Herzberg[87] as $\nu_1\nu_2^l\nu_3$. As the oxidiser is ambient air, the temperature rapidly drops moving away from the reaction zone and the spectrum at y=11.5 mm is dominated by the low-temperature O_2 CRS signal, with the ro-vibrational O- and S-branch spectra also visible in **FIG. 8(c)**.

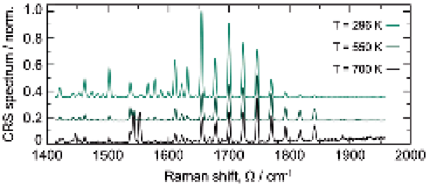

FIG. 9. Temperature dependence of the CH_4 ν_2 CRS spectrum. Single-shot spectrum acquired in an open room-temperature CH_4 flow (light green), and 10-shot-averaged spectra acquired at 550 K (dark green) and 700 K (black) at location y=3.5 and 6 mm, respectively.

FIG. 9 illustrates how the CH_4 ν_2 CRS spectrum is affected by temperature, by comparing a single-shot spectrum acquired in at room temperature, and two 10-shot-averaged spectra acquired at two different locations across the flame and fitted to the time-domain model measuring the local temperature to 550 K and 700 K, respectively. As the temperature increases higher rotational state become populated, as reflected by the spread of the spectral envelope; in addition, the coherence beating of the O- and P-branch lines, and possibly of the vibrational hot bands, determines a shift of the strongest line from O(6) at room temperature to O(10) in the flame, while the probe delay is kept at 30.7 ps for all the spectra. An analogous behaviour is shown by the S-branch spectrum, with the dominating line at room temperature being S(0), and shifting to S(2) at 550 K. The small peak at 1447 cm^{-1} at 700 K is attributed to line O(7) in the pure-rotational H_2 CRS spectrum. A significant change is also observed in the unresolved Q-branch spectrum as the temperature increases, although the effect is somewhat obscured at T=700 K because of the overlap with the ro-vibrational O_2 Q-branch spectrum, whose intensity increases moving towards the oxidiser stream.

Ultrabroadband CRS in the fingerprint region has so far provided us with qualitative insights into the mixing and chemical processes taking place across the diffusion flame. In order to perform quantitative measurements, it is necessary to validate the time-domain model for the CH_4 ν_2 CRS spectrum at high temperature. This is done by performing direct CH_4 thermometry –matching the experimental 10-shot-averaged spectra up to y=6.5 mm against the synthetic library– and comparing the results to CO_2 CRS thermometry, developed and validated in our previous study[54]. An example of the fitting of an experimental CH_4 ν_2 CRS spectrum (at y=0 mm) to the time-domain CRS model is shown in **FIG. 10(a)**. All the five ro-vibrational branches of the CH_4 ν_2 spectrum in the region ~1400-1950 cm^{-1} are fitted simultaneously to the synthetic spectra in the library employing a damped least-squares algorithm. As the temperature increases toward the reaction zone, the hot bands of the CO_2 spectrum cover the S- and R-branch lines of the CH_4 spectrum; similarly, the increasing oxygen concentration moving to the oxidiser stream, results in the mixing of the Q-branch lines of the CH_4 and O_2 spectra. Hence, from location y=4 mm up to 7 mm the fit was limited to the P- and O-branch lines of the CH_4 ν_2 spectrum. All the five ro-vibrational branches of the CH_4 ν_2 spectrum in the region ~1400-1950 cm^{-1} are fitted simultaneously to the synthetic spectra in the library employing a damped least-squares algorithm. As the temperature increases toward the reaction zone, the hot bands of the CO_2 spectrum cover the S- and R-branch lines of the CH_4 spectrum; similarly, the increasing oxygen concentration moving to the oxidiser stream, results in the mixing of the Q-branch lines of the CH_4 and O_2 spectra. Hence, from location y=4 mm up to 7 mm the fit was limited to the P- and O-branch lines of the CH_4 ν_2 spectrum.

FIG. 10(b) presents the validation of CH_4 ν_2 CRS thermometry (green markers) by means of comparison with ro-vibrational CO_2 CRS (black markers): the abundance of CO_2 in the diffusion flame tested and its detection at all the measurement locations allow us to use CO_2 to measure the temperature profile across the whole flame front. As briefly mentioned in the previous paragraph, the large concentration of CO_2 in the centre of the burner, as detected in the ultrabroadband CRS spectra of **FIG. 8**, has a significant impact on the combustion chemistry, given the large heat capacity of the CO_2 molecules, which thus act as heat sinks in the reaction zone on the flame. The result is a smoother temperature profile than expected for a laminar CH_4/air diffusion flame[88]: the temperature at the centre of the fuel stream (y=0 mm) is larger than the room-temperature of the inlet CH_4 flow, while the maximum temperature in the reaction zone (~1430 K) is significantly lower than expected for a laminar axisymmetric methane/air diffusion flame[88]. The thermal effect of the back-diffusing CO_2 on the measured flame temperature in our experiment is comparable to the reduction in the adiabatic flame temperature measured in laminar premixed CH_4/air flames for a 20% CO_2 dilution[89]. Comparing the temperature measurements obtained by CH_4 ν_2 CRS and CO_2 CRS we can validate our time-domain CH_4 CRS model at temperatures as high as ~800 K, and quantify the accuracy of CH_4 ν_2 CRS thermometry. The two thermometric techniques show a very satisfactory agreement not only in terms of the average temperature measured at each flame location, but also within each temporal sequence of 1000 frames, as shown in **FIG. 10(c)** for y=0 mm.

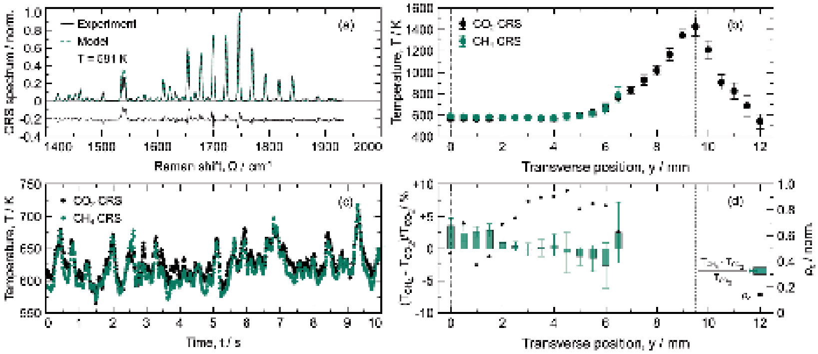

FIG. 10. Ro-vibrational CH_4 ν_2 CRS thermometry. (a) Experimental 10-shot-averaged CH_4 ν_2 CRS spectrum acquired at location y=0 mm and comparison to the time-domain CRS model for thermometry. (b) Average temperature profile across the laminar CH_4/air diffusion flame as measured by ultrabroadband fs/ps CRS thermometry: ro-vibrational CO_2 thermometry (black) provides validation to ro-vibrational CH_4 thermometry (green). (c) Comparison of CO_2 and CH_4 CRS thermometry over sample of 1000 ultrabroadband spectra, acquired at y=5.5 mm: the same dynamics is reproduced by the two independent methods, which proves the physical nature of the temperature oscillations. (d) Accuracy and precision of CH_4 ν_2 CRS thermometry as compared to CO_2 CRS thermometry: the thermometric accuracy (green bars) is better than 3% at all measurement locations, while the precision is fundamentally limited by the physical fluctuations in the flame. Concordance correlation (black dots) quantifies the agreement of the temperature dynamics measured by CO_2 and CH_4 CRS at each location.

The agreement between CH_4 ν_2 and CO_2 CRS thermometry is quantified in **FIG. 10(d)** evaluating the systematic bias between the two methodologies (bar plot), and by means of Lin's concordance correlation coefficient, defined as[90]:

$$\rho_c = \frac{2\sigma_{CO_2,CH_4}}{\sigma^2_{CO_2} + \sigma^2_{CH_4} + \left(\mu_{CO_2} - \mu_{CH_4}\right)^2} \qquad (14)$$

where μ_{CO_2} and μ_{CH_4} are the mean temperature measured by CO_2 and CH_4 CRS respectively, with corresponding standard deviations σ_{CO_2}, σ_{CO_4}, and covariance σ_{CO_2,CH_4}.

The formula in Eq. (14) quantifies the correlation between the two temperature measurements independently of the possible systematic bias between them and of the temperature fluctuations in the sample. The temperature dynamics measured by CO_2 CRS thermometry can thus be adequately reproduced by CH_4 ν_2 CRS, with an accuracy better than 3% at all measurements location. The satisfactory frame-by-frame comparison between CO_2 and CH_4 ν_2 CRS thermometry, as quantifies by the concordance correlation factor, also allow us two establish the origin of the fluctuations in the measured temperature, due to oscillations in the flame.

FIG. 11(a) shows the spectra of the temperature dynamics as measured by CO_2 and CH_4 ν_2 CRS thermometry at y=3 mm and represented by circles in **FIG. 11(b)**. These spectra present common frequencies in the range ~0.1-12.5 Hz (the upper limit being the value where the spectra of T_{CH_4} and T_{CO_2} diverge), corresponding to the frequencies associated to the flame oscillations. Applying a spectral filter in this window[91], it is possible to isolate the inherent noise in the measurements, represented by the solid lines in **FIG. 11(b)**, even though a lower-frequency oscillation (<0.1 Hz), unresolved over the 10 s acquisition window, can still be made out in the smoothened profiles. The thermometric precision was thus improved from 1.9% for CH_4 ν_2 CRS and 2.4 % for CO_2 CRS to 0.57% and 0.91%, respectively. The identification of the frequency at which the two spectra diverge depends on the metric used to define this divergence, but this has only a minor effect on the quantification of the measurement precision: filtering oscillations only up to 10 Hz resulted in a precision of 0.61% for CH_4 ν_2 CRS and 1.0% for CO_2 CRS, while extending the filter to 15 Hz changed it to 0.54% and 0.90% respectively. The 12.5 Hz value was found to be the lowest applicable to all the datasets acquired in the flame: the resulting thermometric precision was better than 2% at all measurements locations for both CO_2 and CH_4 ν_2 CRS thermometry.

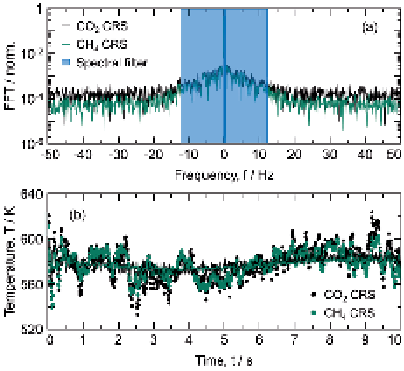

FIG. 11. Temperature dynamics measured by ro-vibrational CRS thermometry performed on CO_2 (black) and CH_4 (green). (a) Spectrum of the temperature dynamics: common frequencies, due to physical oscillations in the flame environment, are identified in the range ~0.1-12.5 Hz. (b) Original (circle) and filtered (solid line) temperature dynamics: removing the temperature fluctuations with common frequencies we estimate the inherent precision of CH_4 ν_2 CRS thermometry to be better than 1% for this sample.

IV. CONCLUSIONS

We have reported the first investigation of the ν_2 mode Raman spectrum of CH_4 by means of coherent Raman spectroscopy: ultrabroadband two-beam fs/ps CRS was employed to perform time-resolved measurements of the ro-vibrational CH_4 ν_2 spectrum and to demonstrate its application as a combustion diagnostic tool. Our CRS instrument employs a single regenerative fs amplifier to generate both broadband fs and narrowband ps pulses; fs laser-induced filamentation is employed *in-situ* to compress the fs pulse to <20 fs, so as to excite the ro-vibrational Raman modes in the vibrational fingerprint region. This spectral region is of particular interest in the investigation of chemical reactions in gas-phase environments, as a number of Raman-active species have a spectral signature in the range ~1100-2000 cm^{-1}.

We developed a time-domain CRS model for the CH_4 ν_2 spectrum employing the MeCaSDa calculated spectroscopic database with the position and cross section of ~10 million Raman lines, as computed at the University of Burgundy[72,73]. We employed this line list by rescaling the spontaneous Raman cross section by the differential Boltzmann population between the two ro-vibrational states involved in the CRS process, and we applied a spectral filter, considering only CRS lines stronger than a cut-off value of the strongest lines, to reduce the computational time of the temperature-dependent synthetic CRS libraries. We then validated the CRS model by performing CH_4 ν_2 thermometry in a laminar CH_4/air diffusion flame: the temperature estimations by CH_4 ν_2 CRS were found to converge for cut-off values smaller than 1E-6, for all the measured temperatures up to ~800 K.

The CRS model include collisional Raman linewidths computed by a modified energy-gap scaling law for the Q-branch lines and adopting the random phase approximation for the derivation of the O-, P-, R- and S-branch collisional dephasing rates. The collisional dephasing of the self-perturbed CRS signal in a room-temperature CH_4 flow is used to fit the α and β parameters of the MEG model. The use of the sum rule for the calculation of the total collisional dephasing rate of the anisotropic Q-branch for the completely depolarized CH_4 ν_2 Raman spectrum is a rather coarse approximation, but it is here justified by the fact that only atmospheric measurements are reported. The extension of the present model to high pressure measurements should include the impact of inelastic collisions, determining molecular reorientation[92,93], and the effect of intra-branch coupling of the vibrationally-degenerate lines[94] of the CH_4 ν_2 spectrum. The effect of different collisional partners was furthermore investigated by performing dephasing measurements in binary mixtures of CH_4 with N_2, H_2, and Ar, in varying concentrations. We employed the model to study the time-domain behaviour of the CH_4 ν_2 CRS spectrum at room temperature: a strong coherence beating is observed, not only for the unresolved rotational lines in the Q-branch, but also for the well-resolved lines in the other branches. The beating of perfectly isolated in the P- and R-branch spectra, in particular, was demonstrated to be due to the Coriolis splitting[23,84,85] of the fine structure of the rotational states due to the different symmetry of the wave function components, and was well captured by our the time-domain CRS model.

We then performed spatially resolved ultrabroadband fs/ps CRS measurements across the laminar CH_4/air diffusion flame front, identifying the Raman signature of four major combustion species. We demonstrated the single-shot detection of the CH_4 ν_2 CRS signal at temperatures as high as ~800 K, and we employed the ro-vibrational CO_2 CRS spectrum, detected at all measurement locations, to perform (10-shot-averaged) CRS thermometry across the flame front and to validate CH_4 ν_2 thermometry. The accuracy of CH_4 ν_2 thermometry was better than 2% at all measurement locations, while the precision was intrinsically limited by fluctuations in the flame, as proven by the same temperature dynamics being measured independently by CO_2 and CH_4 ν_2 CRS.

The detection of CH_4, CO_2, O_2 and H_2 across the flame front is particularly appealing for the prospect use of ultrabroadband fs/ps CRS the *in-situ* investigation of CH_4 pyrolysis and chemical reforming in non-equilibrium environments, such as plasma reactors, for e.g. production of turquoise hydrogen[95]. The extension of the present work to concentration measurements is currently limited by the lack of reported data on the absolute Raman cross section for the CH_4 ν_2 mode, which are required to meaningfully compare the CRS spectra of different chemical species, and should be addressed in future works. An additional difficulty is represented by the unknown spectral excitation efficiency provided by the compressed supercontinuum generated by filamentation in the flame environment: in a recent work we have demonstrated a novel experimental protocol for the *in-situ* referencing of the ultrabroadband spectral excitation[57]. The implementation of this protocol is based on the polarisation control of the CRS signal generation and required the Raman spectrum to have a depolarisation ratio larger than 0.5. The completely depolarised CH_4 ν_2 CRS signal could thus be generated with the same polarisation as the pure-rotational H_2 CRS signal for accurate H_2/CH_4 concentration measurements via ultrabroadband fs/ps CRS.

Furthermore, the modelling of the CH_4 ν_2 Raman spectrum can serve as blueprint for heavier hydrocarbon molecules, such as ethane and dimethyl ether, which also have a Raman-active vibrational mode due to the bending of the H-C-H bond[27,96]. The availability of spectral data for such molecules could pave the way to the extension of ultrabroadband fs/ps CRS to the *in-situ* investigation of oxy-fuel combustion in a number of practical applications[97].

ACKNOWLEDGEMENTS

We acknowledge the financial support provided by the Netherlands Organization for Scientific Research (NWO), obtained through a Vidi grant in the Applied and Engineering Sciences domain (AES) (15690). A. Bohlin is thankful for support through the RIT (Space for Innovation and Growth) project/European Regional Development Fond in Kiruna, Sweden.

REFERENCES

[1] J.I. Lunine and S.K. Atreya, Nat. Geosci. **1**, 159 (2008).

[2] C.R. Webster, P.R. Mahaffy, S.K. Atreya, J.E. Moores, G.J. Flesch, C. Malespin, C.P. Mckay, G. Martinez, C.L. Smith, J. Martin-Torres, J. Gomez-Elvira, M.-P. Zorzano, M.H. Wong, M.G. Trainer, A. Steele, D. Archer Jr., B. Sutter, P.J. Coll, C. Freissinet, P.-Y. Meslin, R. V. Gough, C.H. House, A. Pavlov, J.L. Eigenbrode, D.P. Glavin, J.C. Pearson, D. Keymeulen, L.E. Christensen, S.P. Schwenzer, R. Navarro-Gonzalez, J. Pla-García, S.C.R. Rafkin, Á. Vicente-Retortillo, H. Kahanpää, D. Viudez-Moreiras, M.D. Smith, A.-M. Harri, M. Genzer, D.M. Hassler, M. Lemmon, J. Crisp, S.P. Sander, R.W. Zurek, and A.R. Vasavada, Science **360**, 1093 (2018).

[3] L. Ernst, B. Steinfeld, U. Barayeu, T. Klintzsch, M. Kurth, D. Grimm, T.P. Dick, J.G. Rebelein, I.B. Bischofs, and F. Keppler, Nature **603**, 482 (2022).

[4] V. Masson-Delmotte, P. Zhai, A. Pirani, S.L. Connors, C. Péan, S. Berger, N. Caud, Y. Chen, L. Goldfarb, M.I. Gomis, M. Huang, K. Leitzell, E. Lonnoy, J.B.R. Matthews, T.K. Maycock, T. Waterfield, O. Yelekçi, R. Yu, and B. Zhou, editors , *IPCC, 2021: Climate Change 2021: The Physical Science Basis. Contribution of Working Group I to the Sixth Assessment Report of the Intergovernmental Panel on Climate Change* (Cambridge University Press, Cambridge, United Kingdom and New York, NY, USA, 2021).

[5] T.W. Hesterberg, C.A. Lapin, and W.B. Bunn, Environ. Sci. Technol. **42**, 6437 (2008).

[6] D.E. Holmes and J.A. Smith, Adv. Appl. Microbiol. **97**, 1 (2016).

[7] M. Qi, J. Lee, S. Hong, J. Kim, Y. Liu, J. Park, and I. Moon, Energy **256**, 124583 (2022).

[8] L. Bromberg, D.R. Cohn, A. Rabinovich, C. O'Brien, and S. Hochgreb, Energy and Fuels **12**, 11 (1998).

[9] J.R. Fincke, R.P. Anderson, T. Hyde, B.A. Detering, R. Wright, R.L. Bewley, D.C. Haggard, and W.D. Swank, Plasma Chem. Plasma Process. **22**, 105 (2002).

[10] A.I. Olivos-Suarez, À. Szécsényi, E.J.M. Hensen, J. Ruiz-Martinez, E.A. Pidko, and J. Gascon, ACS Catal. **6**, 2965 (2016).

[11] S.-I. Chou, D.S. Baer, and R.K. Hanson, Appl. Opt. **36**, 3288 (1997).

[12] P. Werle and A. Popov, Appl. Opt. **38**, 1494 (1999).

[13] A.A. Kosterev, R.F. Curl, F.K. Tittel, C. Gmachl, F. Capasso, D.L. Sivco, J.N. Baillargeon, A.L. Hutchinson, and A.Y. Cho, Opt. Lett. **24**, 1762 (1999).

[14] E. Baumann, F.R. Giorgetta, W.C. Swann, A.M. Zolot, I. Coddington, and N.R. Newbury, Phys. Rev. A **84**, (2011).

[15] P. Werle, Spectrochim. Acta Part A **54**, 197 (1998).

[16] C.S. Goldenstein, R.M. Spearrin, J.B. Jeffries, and R.K.

Hanson, Prog. Energy Combust. Sci. **60**, 132 (2017).

[17] I.E. Gordon, L.S. Rothman, C. Hill, R. V Kochanov, Y. Tan, P.F. Bernath, M. Birk, V. Boudon, A. Campargue, K. V Chance, B.J. Drouin, J. Flaud, R.R. Gamache, J.T. Hodges, D. Jacquemart, V.I. Perevalov, A. Perrin, K.P. Shine, M.H. Smith, J. Tennyson, G.C. Toon, H. Tran, V.G. Tyuterev, A. Barbe, A.G. Császár, V.M. Devi, T. Furtenbacher, J.J. Harrison, J. Hartmann, A. Jolly, T.J. Johnson, T. Karman, I. Kleiner, A.A. Kyuberis, J. Loos, O.M. Lyulin, S.T. Massie, S.N. Mikhailenko, N. Moazzen-ahmadi, H.S.P. Müller, O. V Naumenko, A. V Nikitin, O.L. Polyansky, J. Vander Auwera, G. Wagner, J. Wilzewski, P. Wcis, S. Yu, and E.J. Zak, J. Quant. Spectrosc. Radiat. Transf. **203**, 3 (2017).

[18] R.J. Tancin and C.S. Goldenstein, Opt. Express **29**, 30140 (2021).

[19] W. Cai and C.F. Kaminski, Prog. Energy Combust. Sci. **59**, 1 (2017).

[20] C. Wei, K.K. Schwarm, D.I. Pineda, and R.M. Spearrin, Opt. Lett. **45**, 2447 (2020).

[21] T.D. Butterworth, B. Amyay, D. v. d. Bekerom, A. v. d. Steeg, T. Minea, N. Gatti, Q. Ong, C. Richard, C. van Kruijsdijk, J.T. Smits, A.P. van Bavel, V. Boudon, and G.J. van Rooij, J. Quant. Spectrosc. Radiat. Transf. **236**, 106562 (2019).

[22] T.F. Guiberti, Y. Krishna, W.R. Boyette, C. Yang, W.L. Roberts, and G. Magnotti, Proc. Combust. Inst. **38**, 1647 (2021).

[23] T. Feldman, J. Romanko, and H.L. Welsh, Can. J. Phys. **33**, 138 (1955).

[24] M.A. Thomas and H.L. Welsh, Can. J. Phys. **38**, 1291 (1960).

[25] W. Meier, R.S. Barlow, Y.L. Chen, and J.Y. Chen, Combust. Flame **123**, 326 (2000).

[26] R.S. Barlow, S. Meares, G. Magnotti, H. Cutcher, and A.R. Masri, Combust. Flame **162**, 3516 (2015).

[27] G. Magnotti, U. KC, P.L. Varghese, and R.S. Barlow, J. Quant. Spectrosc. Radiat. Transf. **163**, 80 (2015).

[28] D. Butz, S. Hartl, S. Popp, S. Walther, R.S. Barlow, C. Hasse, A. Dreizler, and D. Geyer, Combust. Flame **210**, 426 (2019).

[29] D. V. Petrov, I.I. Matrosov, A.R. Zaripov, and A.S. Maznoy, Appl. Spectrosc. **74**, 948 (2020).

[30] T. Butterworth, A. van de Steeg, D. van den Bekerom, T. Minea, T. Righart, Q. Ong, and G. van Rooij, Plasma Sources Sci. Technol. **29**, 095007 (2020).

[31] R.R. Smith, D.R. Killelea, D.F. DelSesto, and A.L. Utz, Science **304**, 992 (2004).

[32] J.W.L. Lee, D.S. Tikhonov, P. Chopra, S. Maclot, A.L. Steber, S. Gruet, F. Allum, R. Boll, X. Cheng, S. Düsterer, B. Erk, D. Garg, L. He, D. Heathcote, M. Johny, M.M. Kazemi, H. Köckert, J. Lahl, A.K. Lemmens, D. Loru, R. Mason, E. Müller, T. Mullins, P. Olshin, C. Passow, J. Peschel, D. Ramm, D. Rompotis, N. Schirmel, S. Trippel, J. Wiese, F. Ziaee, S. Bari, M. Burt, J. Küpper, A.M. Rijs, D. Rolles, S. Techert, P. Eng-Johnsson, M. Brouard, C. Vallance, B. Manschwetus, and M. Schnell, Nat. Commun. **12**, 6107 (2021).

[33] C.A. Marx, U. Harbola, and S. Mukamel, Phys. Rev. A **77**, 1 (2008).

[34] G. Millot, B. Lavorel, R. Chaux, G. Pierre, H. Berger, J.I. Steinfeld, and B. Foy, J. Mol. Spectrosc. **127**, 156 (1988).

[35] D. Bermejo, J. Santos, and P. Cancio, J. Mol. Spectrosc. **156**, 15 (1992).

[36] J.J. Barrett and R.F. Begley, Appl. Phys. Lett. **27**, 129 (1975).

[37] D.N. Kozlov and V. V. Smirnov, Pis'ma Zh. Eksp. Teor. Fiz. **26**, 31 (1977).

[38] D.N. Kozlov, A.M. Prokhorov, and V. V. Smirnov, J. Mol. Spectrosc. **77**, 21 (1979).

[39] H. Frunder, D. Illig, H. Finsterhölzl, H.W. Schrotter, B. Lavorel, G. Roussel, J.C. Hilico, J.P. Champion, G. Pierre, G. Poussigue, and E. Pascaud, Chem. Phys. Lett. **100**, 110 (1983).

[40] G. Millot, B. Lavorel, and J.I. Steinfeld, J. Chem. Phys. **95**, 7938 (1991).

[41] M. Ridder, A.A. Suvernev, and T. Dreier, J. Chem. Phys. **105**, 3376 (1996).

[42] M.L. Strekalov, Mol. Phys. **100**, 1049 (2002).

[43] T. Dreier, B. Lange, J. Wolfrum, and M. Zahn, Appl. Phys. B **45**, 183 (1988).

[44] E. Jourdanneau, T. Gabard, F. Chaussard, R. Saint-Loup, H. Berger, E. Bertseva, and F. Grisch, J. Mol. Spectrosc. **246**, 167 (2007).

[45] F. Grisch, E. Bertseva, M. Habiballah, E. Jourdanneau, F. Chaussard, R. Saint-Loup, T. Gabard, and H. Berger, Aerosp. Sci. Technol. **11**, 48 (2007).

[46] R. Leonhardt, W. Holzapfel, W. Zinth, and W. Kaiser, Chem. Phys. Lett. **133**, 373 (1987).

[47] B.D. Prince, A. Chakraborty, B.M. Prince, and H.U. Stauffer, J. Chem. Phys. **125**, 044502 (2006).

[48] S.R. Engel, J.D. Miller, C.E. Dedic, T. Seeger, A. Leipertz, and T.R. Meyer, J. Raman Spectrosc. **34**, 1336 (2013).

[49] C.N. Dennis, D.L. Cruise, H. Mongia, G.B. King, and R.P. Lucht, in *53rd AIAA Aerosp. Sci. Meet.* (2015), pp. 1–13.

[50] A. Bohlin and C.J. Kliewer, Appl. Phys. Lett. **104**, 031107 (2014).

[51] A. Bohlin, C. Jainski, B.D. Patterson, A. Dreizler, and C.J. Kliewer, Proc. Combust. Inst. **36**, 4557 (2017).

[52] T.Y. Chen, C.J. Kliewer, B.M. Goldberg, E. Kolemen, and Y. Ju, Combust. Flame **224**, 183 (2021).

[53] Y. Ran, A. Boden, F. Küster, F. An, A. Richter, S. Guhl, S. Nolte, and R. Ackermann, Appl. Phys. Lett. **119**, 243905 (2021).

[54] F. Mazza, N. Griffioen, L. Castellanos, D. Kliukin, and A. Bohlin, Combust. Flame **237**, 111738 (2022).

[55] L. Castellanos, F. Mazza, D. Kliukin, and A. Bohlin, Opt. Lett. **45**, 4662 (2020).

[56] Z. Tian, H. Zhao, Y. Gao, H. Wei, Y. Tan, and Y. Li, Appl. Phys. Lett. **121**, 081102 (2022).

[57] F. Mazza, A. Stutvoet, L. Castellanos, D. Kliukin, and A. Bohlin, Opt. Express **30**, 35232 (2022).

[58] F. Träger, *Springer Handbook of Laser and Optics* (Springer, New York, 2007).

[59] A. Bohlin, B.D. Patterson, and C.J. Kliewer, J. Chem. Phys. **138**, 081102 (2013).

[60] J.H. Odhner, D.A. Romanov, and R.J. Levis, Phys. Rev. Lett. **103**, 075005 (2009).

[61] J.D. Miller, S. Roy, M.N. Slipchenko, J.R. Gord, and T. Meyer, Opt. Express **19**, 15627 (2011).

[62] S.P. Kearney, D.J. Scoglietti, and C.J. Kliewer, Opt. Express **21**, 12327 (2013).

[63] T.L. Courtney, A. Bohlin, B.D. Patterson, and C.J. Kliewer, J. Chem. Phys. **146**, 224202 (2017).

[64] J.D. Miller, M.N. Slipchenko, T.R. Meyer, H.U. Stauffer, and J.R. Gord, Opt. Lett. **35**, 2430 (2010).

[65] N. Owschimikow, F. Königsmann, J. Maurer, P. Giese, A. Ott, B. Schmidt, and N. Schwentner, J. Chem. Phys. **133**, 044311 (2010).

[66] F. Metz, W.E. Howard, L. Wunsch, H.J. Neusser, and E.W. Schlag, Proc. R. Soc. Lond. A **363**, 381 (1978).

[67] A.H. Nielsen and H.H. Nielsen, Phys. Rev. **48**, 864 (1935).

[68] M.J. Hollas, *High Resolution Spectroscopy*, 1st ed. (Butterworths, London, 1982).

[69] E. Bright Wilson, J. Chem. Phys. **3**, 276 (1935).

[70] V. Boudon, J. Champion, T. Gabard, M. Lo, M. Rotger, and C. Wenger, in *Handb. High-Resolution Spectrosc.*, edited by M. Quack and F. Merkt (John Wiley & Sons, Ltd., 2011).

[71] J.-P. Champion, M. Loéte, and G. Pierre, *Spherical Top Spectra* (1992).

[72] Y.A. Ba, C. Wenger, R. Surleau, V. Boudon, M. Rotger, L. Daumont, D.A. Bonhommeau, V.G. Tyuterev, and M.L. Dubernet, J. Quant. Spectrosc. Radiat. Transf. **130**, 62 (2013).

[73] C. Richard, V. Boudon, and M. Rotger, J. Quant. Spectrosc. Radiat. Transf. **251**, 107096 (2020).

[74] B. Amyay and V. Boudon, J. Quant. Spectrosc. Radiat. Transf. **219**, 85 (2018).

[75] A.S. Tanichev and D. Petrov, J. Raman Spectrosc. **53**, 654 (2021).

[76] E. Jourdanneau, F. Chaussard, R. Saint-loup, T. Gabard, and H. Berger, J. Mol. Spectrosc. **233**, 219 (2005).

[77] L.A. Rahn and R.E. Palmer, J. Opt. Soc. Am. B **3**, 1164 (1986).

[78] T. Seeger, F. Beyrau, A. Braeuer, and A. Leipertz, J. Raman Spectrosc. **34**, 932 (2003).

[79] G. Fanjoux, B. Lavorel, and G. Millot, J. Raman Spectrosc. **29**, 391 (1998).

[80] J. Boissoles, C. Boulet, L. Bonamy, and D. Robert, J. Quant. Spectrosc. Radiat. Transf. **42**, 509 (1989).

[81] A.E. DePristo, S.D. Augustin, R. Ramaswamy, and H. Rabitz, J. Chem. Phys. **71**, 850 (1979).

[82] T.Y. Chen, N. Liu, C.J. Kliewer, A. Dogariu, E. Kolemen, and Y. Ju, Opt. Lett. **47**, 1351 (2022).

[83] T.L. Courtney and C.J. Kliewer, J. Chem. Phys. **149**, 234201 (2018).

[84] H.A. Jahn, Proc. R. Soc. London. Ser. A. Math. Phys. Sci. **168**, 469 (1938).

[85] H.A. Jahn, Phys. Rev. **56**, 680 (1939).

[86] J.P. Champion and G. Pierre, J. Mol. Spectrosc. **79**, 255 (1980).

[87] G. Herzberg, *Molecular Spectra and Molecular Structure. II. Infrared and Raman Spectra of Polyatomic Molecules*, 10th ed. (Van Nostrand Reinhold Company, New York, 1945).

[88] M.D. Smooke, P. Lin, J.K. Lam, and M.B. Long, Proc. Combust. Inst. **23**, 575 (1991).

[89] C. Zhang, G. Hu, S. Liao, Q. Cheng, C. Xiang, and C. Yuan, Energy **106**, 431 (2016).

[90] L.I. Lin, Biometrics **45**, 255 (1989).

[91] J. Barros, M. Scherman, E. Lin, N. Fdida, R. Santagata, B. Attal-Tretout, and A. Bresson, Opt. Express **28**, 34656 (2020).

[92] S.I. Temkin, L. Bonamy, J. Bonamy, and D. Robert, Phys. Rev. A **47**, 1543 (1993).

[93] L. Bonamy, J. Bonamy, D. Robert, S.I. Temkin, G. Millot, and B. Lavorel, J. Chem. Phys. **101**, 7350 (1994).

[94] A.S. Pine, J. Quant. Spectrosc. Radiat. Transf. **57**, 145 (1997).

[95] N.N. Morgan and M. ElSabbagh, Plasma Chem. Plasma Process. **37**, 1375 (2017).

[96] Ö. Andersson, H. Neij, J. Bood, B. Axelsson, and M. Aldén, Combust. Sci. Technol. **137**, 299 (1998).

[97] J.W. Tröger, C. Meißner, and T. Seeger, J. Raman Spectrosc. **47**, 1149 (2016).

Coherent N_2^+ emission mediated by coherent Raman scattering for gas-phase thermometry

FRANCESCO MAZZA,[1,*] HUGO BUURMEIJER,[1] LEONARDO CASTELLANOS,[1] AND ALEXIS BOHLIN[1,2]

[1]*Faculty of Aerospace Engineering, Delft University of Technology, Kluyverweg 1, 2629 HS Delft, The Netherlands*
[2]*Space Propulsion Laboratory, Department of Computer Science, Electrical and Space Engineering, Luleå University of Technology, 98128, Kiruna, Sweden*
**Corresponding author: f.mazza@tudelft.nl*

Received 26 September 2022; revised 20 October 2022; accepted 30 October 2022; posted 1 November 2022; published 17 November 2022

We report on the generation of coherent emission from fs laser-induced filaments mediated by ultrabroadband coherent Raman scattering (CRS), and we investigate its application for high-resolution gas-phase thermometry. Broadband 35 fs, 800 nm pump pulses generate the filament through photoionization of the N_2 molecules, while narrowband ps pulses at 400 nm seed the fluorescent plasma medium via generation of a ultrabroadband CRS signal, resulting in a narrowband and highly spatiotemporally coherent emission at 428 nm. This emission satisfies the phase-matching for the crossed pump-probe beams geometry, and its polarization follows the CRS signal polarization. We perform spectroscopy on the coherent N_2^+ signal to investigate the rotational energy distribution of the N_2^+ ions in the excited $B\,^2\Sigma_u^+$ electronic state, and demonstrate that the ionization mechanism of the N_2 molecules preserves the original Boltzmann distribution to within the experimental conditions tested.

A remarkable feature associated with femtosecond (fs) laser filamentation [1] is the generation of coherent emission, from the electronically excited atomic [2] and molecular [3,4] ions in the plasma filament, both in the forward and backward directions. A number of experimental and theoretical studies have been dedicated to the coherent emission from nitrogen cations (N_2^+) [5], with particular focus on the first negative band $B\,^2\Sigma_u^+ \rightarrow X\,^2\Sigma_g^+$. Narrowband coherent emission at 391 nm and 428 nm is consistently reported, corresponding to the ro-vibronic transitions $v=0 \rightarrow v'=0$ and $v=0 \rightarrow v'=1$ respectively, with v and v' being the vibrational quantum numbers in excited and ground electronic states (Fig. 1). There is no clear consensus on the mechanism behind this "air lasing" action [5], with stimulated amplification or superradiant emission [6] from an inverted population [7,8], and lasing-without-inversion [9,10] being proposed as alternatives. Four-wave mixing and stimulated Raman scattering were rejected as amplification mechanisms on the basis of the experimental observations by Ni *et al.* [11]. The possibility to generate an air laser remotely has potential for the development of new remote-sensing techniques of e.g. pollutants in the atmosphere [12]. Combustion researchers have recently employed filament-induced nonlinear spectroscopy to detect intermediate combustion species [13] and fs laser excitation tagging (FLEET) to measure the velocity field [14]. Filamentation has also been combined with coherent Raman spectroscopy (CRS) for the *in-situ* generation of a compressed supercontinuum to achieve ultrabroadband excitation of major combustion species [15–18], or to generate a narrowband probe pulse [19] via N_2^+ lasing. This lasing is particularly interesting for combustion diagnostics given the abundance of N_2 in air and its low

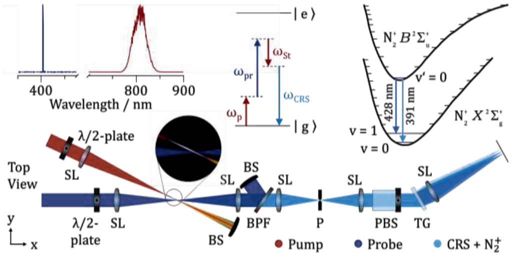

Fig. 1. Generation of air lasing mediated by NR CRS. The 1.5 mJ, ~50 fs pump pulse generates a filament and it is compressed to ~17 fs TL [17], providing the pump (ω_p) and Stokes (ω_{St}) frequencies to the ultrabroadband CRS process; the narrowband frequency-doubled (ω_{pr}) ~4 ps probe pulse undergoes NR CRS generating a broadband signal, which seeds the fluorescent emission from the excited N_2^+. SL, spherical lens; λ/2, half-wave plate; BS, beam stop, BPF, band-pass filter, P, pinhole; PBS, polarization beam splitter; TG, transmission grating.

chemical reactivity, and the demonstration of backward lasing from singly ionized N_2 pumped by near-infrared (IR) fs pulses [4].

In the present work we report on air lasing mediated by CRS, whereby a filament is generated by a fs near-IR pump pulse, and the coherent N_2^+ emission at 428 nm is seeded by a narrowband picosecond (ps) probe pulse, via non-resonant (NR) CRS of the latter. The seeding mechanism observed here is clearly different from that of similar experiments, where the coherent emission results from self-seeding [20,21] or by the use of two-color collinear pump-probe schemes employing fs seed pulses, spectrally broad enough to cover the fluorescence wavelength [11,22,23]. We employ a single regenerative amplifier system (7.5 mJ, 1 kHz, Astrella Coherent) to generate the fs pump and the ps probe pulses. A 1.5 mJ portion of the broadband output of the amplifier (19.2 nm, centered at 806.7 nm) is focused through a 500 mm spherical lens to generate a ~13 mm long filament: the pulse dispersion prior filamentation is controlled by an external compressor unit and a residual linear chirp of ±500 fs^2 is found to optimize the filamentation process in air [17]. The estimated pulse fluence is ~446 TW/cm^2 so that quantum tunneling is the main ionization mechanism [1]. The probe pulse is generated via second-harmonic bandwidth compression of the second 35 fs transform-limited amplifier output, producing a narrowband ~4 ps pulse (0.08 nm, centered at 403.4 nm), with 0.9 mJ/pulse [24]. The probe beam is focused through a 300 mm lens resulting in a beam diameter at the focus of ~21.5 μm ($M^2=1.2$), and it crosses the filament at a distance of ~5 mm from its leading edge, at an angle of ~3.5°. A delay line controls the relative delay of the two pulses, and we use polarization optics (half-wave plates and thin-film polarizers) to control the energy and polarization angle for the linear polarized pump and probe beams before the focusing lenses. The filament emission at 428 and 391 nm has high spatial coherence and satisfies the near-phase-matching condition of the CRS process for our two-beam CRS setup [24]. This emission is collected through a polarization-sensitive coherent imaging spectrometer, dispersed by a high-density diffraction grating and imaged through a pinhole to a sCMOS camera by a 1000 mm spherical lens. A tunable band-pass filter (20 nm bandwidth, Semrock) suppresses the probe beam, nearly co-propagating with the signal. A Glan-laser polarizer acts as polarization gate to the spectrometer, allowing us to measure the polarization of the coherent N_2^+ emission.

The main features of the coherent emission generated by the fs filamentation at 428 nm are presented in Fig. 2. The role of the probe pulse in the generation of air lasing is shown in Fig. 2(a): the emission is only observed in correspondence of the temporal overlap of the pump and probe pulses. The relative arrival time of the two pulses is changed in steps of 100 fs and the resulting integrated signal maps the temporal envelope of the ps probe pulse, with a duration estimated to ~7 ps full-with-at-half-maximum (FWHM). The emission also shows high spatial coherence as it is imaged through a pinhole in the spectrometer, and satisfies the phase-matching requirements of the CRS process, co-propagating with the probe beam. On the other hand, the probe pulse is off-resonant with respect to the $B^2\Sigma_u^+ \rightarrow X^2\Sigma_g^+$ ro-vibronic transition, and its bandwidth is clearly too narrow to have any significant overlap with the fluorescence spectrum of N_2^+, so that it cannot directly stimulate emission from the electronically-excited ions. This behavior is in contrast to the one observed by Ni *et al.* [11], who reported coherent emission at 391 nm with no phase-matching requirements, but only for a resonant probe pulse. We identify the reason for the peculiar behavior observed in our experiment in a different seeding mechanism. The narrowband ps probe does not act directly as a seed pulse for the N_2^+ emission, but undergoes four-wave mixing (NR CRS) with the ultrabroadband ~17 fs compressed supercontinuum pulse generated by filamentation. CRS thus mediates the N_2^+ emission, providing a seeding mechanism for the coherent emission at 428 nm, although this does not represent a gain mechanism alternative to those mentioned in the introduction. This process is additionally confirmed by the polarization properties of the coherent emission, as shown in Fig. 2(b). We performed a parametric study by rotating the polarization of the pump pulse relative to the polarization gate of our spectrometer from 0° to 90° in steps of 15° and, for each of these settings, we rotated the polarization of the probe pulse from 0° to 360° in steps of 10°. The experimental points (black) in the polar plot in Fig. 2(b) represents the intensity of the coherent N_2^+ emission transmitted through the polarization gate as a function of the relative probe polarization, for a pump polarization angle of 60°. The blue curve represents the theoretical behavior of the NR CRS signal as predicted by the CRS polarization theory in Ref. [17], and a similar agreement is found for all the pump polarization angles tested in our experiment. The coherent N_2^+ emission thus has the polarization of the NR CRS signal rather than that of the probe field, which confirms CRS to be the seeding mechanism, according to the experimental observations of Li *et al.*, who showed that the lasing emission is linearly polarized as the seed pulse [25].

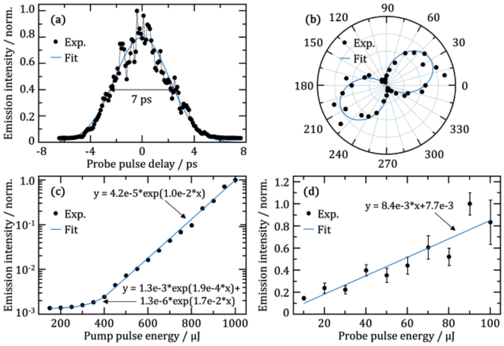

Fig. 2. Characterization of the coherent N_2^+ emission from the plasma filament. (a) Intensity of the N_2^+ emission as a function of the delay of the probe pulse relative to the pump. (b) Polarization of the N_2^+ emission (black) as a function of the probe polarization angle, and comparison with the theoretical polarization of the NR CRS signal. The pump polarization is oriented at 60° from the polarization gate in the spectrometer. (c) Power scaling of the N_2^+ emission a function of the pump pulse energy. (d) Power scaling of the N_2^+ emission a function of the probe pulse energy.

The N_2^+ emission strongly depends on the pump pulse energy, and two distinct regimes are identified in Fig. 2(c), with a transition at ~400 μJ/pulse: for low pump energy (100-400 μJ/pulse), the emission intensity grows more than exponentially, while at larger pump energies the growth is exponential. The experimental data in the low power regime are fitted by a linear combination of two exponential functions: this hints at a two different phenomena contributing to the emission. On the one hand, the N_2^+ fluorescence has been observed to grow exponentially with the power of the pump laser [26]; on the other, the compression of the pump pulse itself grows non-linearly in the range 100-400 μJ/pulse, leading to an exponential growth of the seed power at 428 nm [16]. In contrast, the emission intensity grows linearly with the energy of the probe pulse, as shown in Fig. 2(d), in agreement with the linear scaling of the CRS signal with the probe.

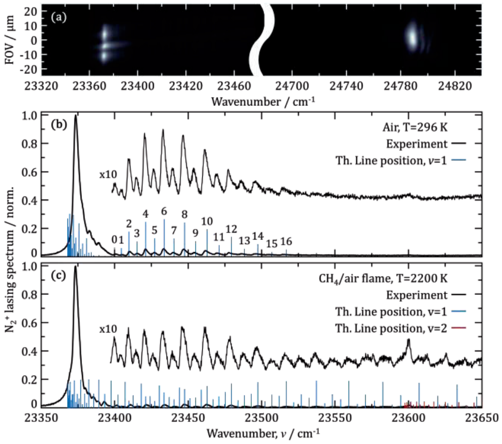

Fig. 3. Hyperspectral imaging of the coherent N_2^+ emission from the filament. (a) The multi-filament structure (on the left) as imaged by the N_2^+ emission at the probe focus (on the right). (b) Single-shot spectrum of the N_2^+ emission at 428 nm generated in air (black) and theoretical position of the rotational lines in the fundamental vibrational band (blue). (b) Single-shot spectrum of the N_2^+ emission at 428 nm generated in a CH_4/air flame (black) and position of the rotational lines in the fundamental (blue) and first hot (red) vibrational bands.

The coherent emission from the filament is imaged through the spectrometer, with ~1:3 magnification, onto the sCMOS detector with 6.5 μm pixel-size: the multi-filament structure [1] of the plasma medium is visible in the imaged N_2^+ emission in Fig. 3(a). For reference the probe beam waist is also imaged on the camera: the size of the probe at its focus was independently measured with a beam profiler (WinCam D, Dataray) to be ~21.5 μm. The diameter of the single filaments is thus estimated to be ~10 μm: this is well in agreement with the experimental results obtained by Centurion *et al.* for a 2 mJ, 150 fs near-IR pulse focused in carbon disulfide [27]. High-resolution single-shot N_2^+ spectra, acquired in room-temperature air and in the hot products of a laminar premixed methane/air flame (equivalence ratio φ=1), are shown in Fig. 3(b) and Fig. 3(c), respectively. The rotational structure of the N_2^+ emission spectrum is evident in the R-branch (23400-23500 cm^{-1}), where each line correspond to the transition $N \rightarrow N-1$, with N being the nuclear angular momentum quantum number. The alternation in the intensity of adjacent lines reflects the multiplicity of triplet and heptet spin states for odd and even values of N, respectively. The P-branch ($N \rightarrow N+1$) spectrum is much more congested and gives rise to the large spectral feature at ~23360-23380 cm^{-1}. The spectrum acquired in the hot product gases of the flame has a much broader envelope and presents a clear feature at ~23600 cm^{-1}: this is the vibrational hot band, corresponding to the transition v=2 → v'=1. The change in the spectral envelope between the N_2^+ spectrum in room-temperature air and in the flame must reflect the different rotational and vibrational energy distribution of the N_2 population, according to Boltzmann statistics. This proves that, at least to a certain extent, the original ro-vibrational energy distribution is preserved in the tunneling ionization process: the N_2^+ emission spectrum could then be used for gas-phase thermometry.

We show this in Fig. 4 by comparing the experimental spectra – acquired in a flow of N_2 at room-temperature and heated to 775 K (as measured by pure-rotational N_2 CRS)– and a simplified theoretical model for the emission spectrum of N_2^+. A similar model has been successfully employed by Azarm *et al.* to fit air lasing spectra at 428 nm and estimate the impact on the optical gain of different rotational energy distributions in the upper and lower electronic states [28]. The emission from the microscopic N_2^+ dipoles is treated as a coherent process by summing their contributions to the emitted field and computing the resulting intensity spectrum as the squared amplitude spectrum, in analogy to superradiant emission [29]. Additional simplifying assumptions are: a homogeneous spectral density of the seeding NR CRS signal on the region 23350-23650 cm^{-1}, and negligible dependence on the N quantum number of the angular momenta [30] and rotational-vibrational [31] coupling in the emission process. The theoretical position of the rotational lines in the P- and R-branch spectra (ν) is converted from the energy difference between the initial ($B\,^2\Sigma_u^+$, v, N) and final ($X\,^2\Sigma_g^+$, v', N') ro-vibronic states of the cation:

$$\begin{aligned} \nu &= \mathrm{B_v} N(N+1) - \mathrm{D_v}\left[N(N+1)\right]^2 \\ \nu' &= 23392.1\,\mathrm{cm^{-1}} + \mathrm{B'_v} N'(N'+1) - \mathrm{D'_v}\left[N'(N'+1)\right]^2 \end{aligned} \tag{1}$$

with B_v, D_v, B'_v and D'_v being the rotational and centrifugal constants of N_2^+ as a function of the vibrational quantum number [32]. The emission cross-section is taken to be proportional to the Boltzmann distribution of the original N_2 population, thus introducing the temperature sensitivity of the N_2^+ spectrum:

$$\rho(\mathrm{v}', N') = \exp\left[-\nu(\mathrm{v}', N')\hbar c / \mathrm{k_B T}\right] \tag{2}$$

The line shape is due to interference between the N_2^+ emission and the NR CRS background, and is computed using a Fano profile [33], with resonance width γ=2.5 cm^{-1} and a Fano parameter of q=2:

$$\Gamma = \frac{(q\gamma/2 + \omega - \nu)^2}{(\gamma/2)^2 + (\omega - \nu)^2} \tag{3}$$

The comparison between the experimental spectra and the theoretical model is somewhat complicated by the presence of the NR CRS, which on the one hand acts as a seed for the N_2^+ emission, but on the other is a background to its spectrum. The interference between the N_2^+ spectrum and the NR background results in a distortion of the spectral envelopes in Fig. 4. This is particularly significant at larger wavenumbers, where the intensity of the rotational lines of the N_2^+ spectrum is reduced according to their Boltzmann population, while the NR background grows for reducing Raman shifts with respect to the probe line at 24790 cm^{-1}, as shown in Fig. 4. The room-temperature spectrum in Fig. 4(a) is almost unaffected by the presence of the background and shows a good agreement with the theoretical model. In Fig. 4(b) higher rotational lines are populated at 775 K, giving rise to interference with the NR background: this completely suppresses line R(16) at ~23517 cm^{-1}, and the following lines are identified with the negative peaks in the continuous background.

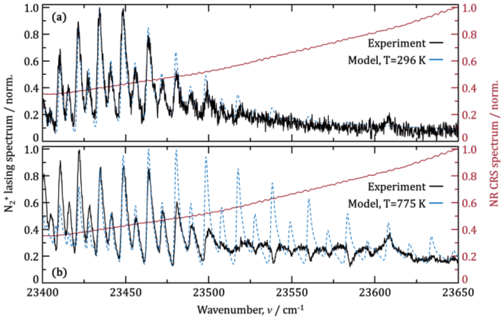

Fig. 4. Comparison of experimental N_2^+ spectra and spectral model. (a) Single-shot N_2^+ spectrum acquired in a room-temperature N_2 flow. (b) Single-shot N_2^+ spectrum acquired in a heated N_2 flow at 775 K. In red the spectrum of the NR CRS signal acquired in argon.

In conclusion we reported the observation of air lasing from a filament generated by near-IR fs pulses, mediated by NR CRS as the seeding mechanism. The dynamics of the seeding process are demonstrated by the phase-matching of the coherent emission from the filament, according to the crossing angle of the narrowband ps probe beam, and by its polarization dependence on the linearly polarized pump and probe pulses. We investigated the temperature dependence of the coherent emission from excited N_2^+, recording single-shot spectra in air, a heated N_2 flow, and in a laminar CH_4/air flame. The N_2^+ spectrum shows a clear temperature dependence, which points to an isothermal population transfer from N_2 to N_2^+ in the tunneling ionization regime. The experimental spectra are compared to a simple spectral model: a good agreement is shown at room temperature, while the interference between the N_2^+ emission and the NR CRS seed suppresses higher rotational lines in the spectrum of the former, severely skewing the spectral envelope at larger temperatures. Modelling of the NR CRS spectrum or background suppression schemes could improve the quantitative comparison and lead to the development of air lasing thermometry (ALT) as a robust diagnostics technique, with potential for remote sensing and single-ended optical probing, as well as for spatial resolution below the diffraction limit. Future work should address questions about the impact of the ionization efficiency [34] on the ro-vibrational energy distribution of N_2^+, the possible rotational non-equilibrium in inverted population systems [28], as well as the effect of rotational wave packet created by stimulated Raman scattering [35], and incorporate these in the spectral model for the coherent N_2^+ emission.

Funding. Dutch Research Council (NWO) (AES-15690).

Acknowledgments. We gratefully acknowledge the financial support provided by the Netherlands Organization for Scientific Research (NWO). A. Bohlin is thankful for support through the RIT (Space for Innovation and Growth) project/European Regional Development Fond in Kiruna, Sweden.

Disclosures. The authors declare no conflicts of interest.

Data Availability. Data underlying the results presented in this paper are not publicly available at this time, but may be obtained from the authors upon reasonable request.

References

1. A. Couairon and A. Mysyrowicz, Phys. Rep. **441**, 47 (2007).
2. A. Dogariu, J. B. Michael, M. O. Scully, and R. B. Miles, Science **331**, 442 (2011).
3. S. Mitryukovskiy, Y. Liu, P. Ding, A. Houard, and A. Mysyrowicz, Opt. Express **22**, 12750 (2014).
4. X. Zhang, R. Danylo, Z. Fan, P. Ding, C. Kou, and Q. Liang, Appl. Phys. B **126**, 53 (2020).
5. P. Polynkin and Y. Chen, 1st ed. (Springer International Publishing, 2018).
6. Y. Liu, P. Ding, G. Lambert, A. Houard, V. Tikhonchuk, and A. Mysyrowicz, Phys. Rev. Lett. **115**, 133203 (2015).
7. H. Xu, E. Lötstedt, A. Iwasaki, and K. Yamanouchi, Nat. Commun. **6**, 8347 (2015).
8. J. Yao, S. Jiang, W. Chu, B. Zeng, C. Wu, R. Lu, Z. Li, H. Xie, G. Li, C. Yu, Z. Wang, H. Jiang, Q. Gong, and Y. Cheng, Phys. Rev. Lett. **116**, 143007 (2016).
9. A. Mysyrowicz, R. Danylo, A. Houard, V. Tikhonchuk, X. Zhang, Z. Fan, Q. Liang, S. Zhuang, L. Yuan, and Y. Liu, APL Photonics **4**, 110807 (2019).
10. M. Richter, M. Lytova, F. Morales, S. Haessler, O. Smirnova, M. Spanner, and M. Ivanov, Optica **7**, 586 (2020).
11. J. Ni, W. Chu, C. Jing, H. Zhang, B. Zeng, J. Yao, G. Li, H. Xie, C. Zhang, H. Xu, S.-L. Chin, Y. Cheng, and Z. Xu, Opt. Express **21**, 8746 (2013).
12. P. R. Hemmer, R. B. Miles, P. Polynkin, T. Siebert, A. V. Sokolov, P. Sprangle, and M. O. Scully, PNAS **108**, 3130 (2011).
13. H.-L. Li, H.-L. Xu, B.-S. Yang, Q.-D. Chen, T. Zhang, and H.-B. Sun, Opt. Lett. **38**, 1250 (2013).
14. J. B. Michael, M. R. Edwards, A. Dogariu, and R. B. Miles, Appl. Opt. **50**, 5158 (2011).
15. J. H. Odhner, D. A. Romanov, and R. J. Levis, Phys. Rev. Lett. **103**, 075005 (2009).
16. F. Mazza, N. Griffioen, L. Castellanos, D. Kliukin, and A. Bohlin, Combust. Flame **237**, 111738 (2022).
17. F. Mazza, A. Stutvoet, L. Castellanos, D. Kliukin, and A. Bohlin, Opt. Express **30**, 35232 (2022).
18. Z. Tian, H. Zhao, Y. Gao, H. Wei, Y. Tan, and Y. Li, Appl. Phys. Lett. **121**, 081102 (2022).
19. X. Zhao, S. Nolte, and R. Ackermann, Opt. Lett. **45**, 3661 (2020).
20. T. J. Wang, J. Ju, J. F. Daigle, S. Yuan, R. Li, and S. L. Chin, Laser Phys. Lett. **10**, 125401 (2013).
21. Y. Liu, Y. Brelet, G. Point, A. Houard, and A. Mysyrowicz, Opt. Express **21**, 22791 (2013).
22. J. Yao, G. Li, C. Jing, B. Zeng, W. Chu, J. Ni, H. Zhang, H. Xie, C. Zhang, H. Li, H. Xu, S. L. Chin, Y. Cheng, and Z. Xu, New J. Phys. **15**, (2013).
23. Y. Fu, E. Lötstedt, H. Li, S. Wang, D. Yao, T. Ando, A. Iwasaki, F. H. M. Faisal, K. Yamanouchi, and H. Xu, Phys. Rev. Res. **2**, 012007 (2020).
24. L. Castellanos, F. Mazza, D. Kliukin, and A. Bohlin, Opt. Lett. **45**, 4662 (2020).
25. H. Li, Q. Song, J. Yao, Z. Liu, J. Chen, B. Xu, K. Lin, J. Qiang, B. He, H. Xu, Y. Cheng, H. Zeng, and J. Wu, Phys. Rev. A **99**, 053413 (2019).
26. Q. Luo, W. Liu, and S. L. Chin, Appl. Phys. B **76**, 337 (2003).
27. M. Centurion, Y. Pu, M. Tsang, and D. Psaltis, Phys. Rev. A **71**, 063811 (2005).
28. A. Azarm, P. Corkum, and P. Polynkin, Phys. Rev. A **96**, 051401 (2017).
29. M. Gross and S. Haroche, Phys. Rep. **93**, 301 (1982).
30. H. Hönl and F. London, Zeitschrift für Phys. **35**, 286 (1926).
31. R. Herman and R. F. Wallis, J. Mol. Spectrosc. **2**, 369 (1958).
32. R. R. Laher and F. R. Gilmore, J. Phys. Chem. Ref. Data **20**, 685 (1991).
33. U. Fano, Phys. Rev. **124**, 1866 (1961).
34. I. V. Litvinyuk, K. F. Lee, P. W. Dooley, D. M. Rayner, D. M. Villeneuve, and P. B. Corkum, Phys. Rev. Lett. **90**, 233003 (2003).
35. H. Xie, B. Zeng, G. Li, W. Chu, H. Zhang, C. Jing, J. Yao, J. Ni, Z. Wang, Z. Li, and Y. Cheng, Phys. Rev. A **90**, 042504 (2014).